Advances in Polymer Technology

Intelligent Technologies for Polymer Injection Molding

Lead Guest Editor: Yun Zhang
Guest Editors: Lih-sheng Turng, Huamin Zhou, Peng Zhao, and Srikanth Pilla

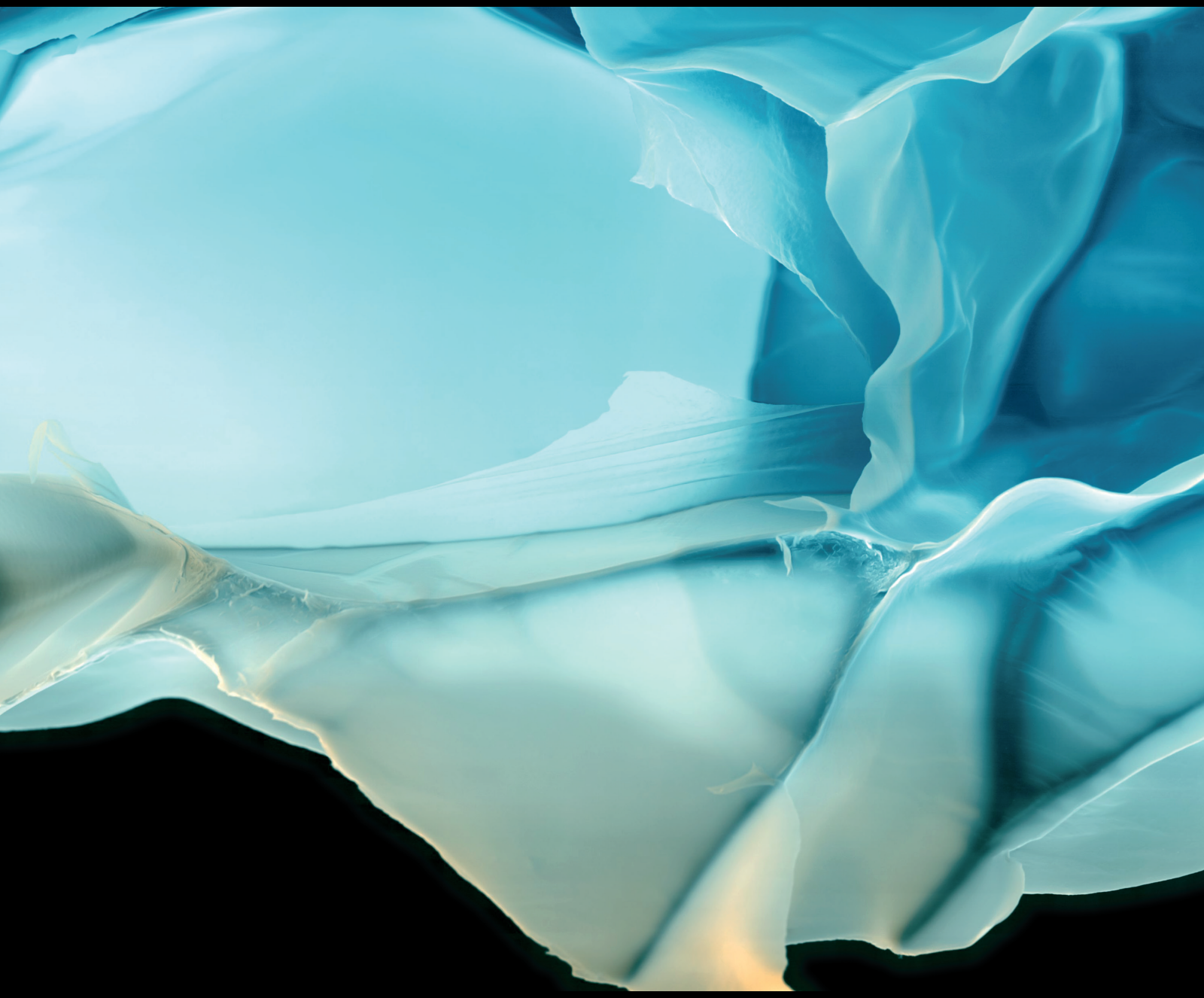

Intelligent Technologies for Polymer Injection Molding

Advances in Polymer Technology

Intelligent Technologies for Polymer Injection Molding

Lead Guest Editor: Yun Zhang
Guest Editors: Lih-sheng Turng, Huamin Zhou, Peng Zhao, and Srikanth Pilla

Copyright © 2020 Hindawi Limited. All rights reserved.

This is a special issue published in "Advances in Polymer Technology." All articles are open access articles distributed under the Creative Commons Attribution License, which permits unrestricted use, distribution, and reproduction in any medium, provided the original work is properly cited.

Chief Editor

Ning Zhu, China

Associate Editors

Maria L. Focarete, Italy
Leandro Gurgel, Brazil
Lu Shao, China

Academic Editors

Nasir M. Ahmad, Pakistan
Sheraz Ahmad, Pakistan
B Sridhar Babu, India
Xianglan Bai, USA
Lucia Baldino, Italy
Matthias Bartneck, Germany
Anil K. Bhowmick, India
Marcelo Calderón, Spain
Teresa Casimiro, Portugal
Sébastien Déon, France
Alain Durand, France
María Fernández-Ronco, Switzerland
Wenxin Fu, USA
Behnam Ghalei, Japan
Kheng Lim Goh, Singapore
Chiara Gualandi, Italy
Kai Guo, China
Minna Hakkarainen, Sweden
Christian Hopmann, Germany
Xin Hu, China
Puyou Jia, China
Prabakaran K, India
Adam Kiersnowski, Poland
Ick Soo Kim, Japan
Siu N. Leung, Canada
Chenggao Li, China
Wen Li, China
Haiqing Lin, USA
Jun Ling, China
Wei Lu, China
Milan Marić, Canada
Dhanesh G. Mohan, United Kingdom
Rafael Muñoz-Espí, Spain
Kenichi Nagase, Japan
Mohamad A. Nahil, United Kingdom
Ngoc A. Nguyen, USA
Daewon Park, USA
Kinga Pielichowska, Poland
Nabilah Afiqah Mohd Radzuan, Malaysia
Sikander Rafiq, Pakistan
Vijay Raghunathan, Thailand
Filippo Rossi, Italy
Sagar Roy, USA
Júlio Santos, Brazil
Mona Semsarilar, France
Hussein Sharaf, Iraq
Melissa F. Siqueira, Brazil
Tarek Soliman, Egypt
Mark A. Spalding, USA
Gyorgy Szekely, Saudi Arabia
Song Wei Tan, China
Faisal Amri Tanjung, Indonesia
Vijay K. Thakur, USA
Leonard D. Tijing, Australia
Lih-sheng Turng, USA
Kavimani V, India
Micaela Vannini, Italy
Surendar R. Venna, USA
Pierre Verge, Luxembourg
Ren Wei, Germany
Chunfei Wu, United Kingdom
Jindan Wu, China
Zhenhao Xi, China
Bingang Xu, Hong Kong
Yun Yu, Australia
Liqun Zhang, China
Xinyu Zhang, USA

Contents

Five-Axis Tool Path Generation of Injection Mold Represented by T-Spline Surface
Ce Shang, Hongyao Shen, Jianzhong Fu, Yangfan Sun, Shuhua Yue, and Jianfeng Zhang
Research Article (11 pages), Article ID 2075434, Volume 2020 (2020)

Reducing the Sink Marks of a Crystalline Polymer Using External Gas-Assisted Injection Molding
Shaofei Jiang, Taidong Li, Xinxin Xia, Xiang Peng, and Jiquan Li
Research Article (8 pages), Article ID 3793505, Volume 2020 (2020)

Design and Research of Skin Injection Molded TPE Materials Based on Genetic Algorithm
Kui Yan, Yizhe Chen, Hui Wang, Cheng Gao, and Qiuyang Bai
Research Article (9 pages), Article ID 6910535, Volume 2020 (2020)

Optimization of Residual Wall Thickness Uniformity in Short-Fiber-Reinforced Composites Water-Assisted Injection Molding Using Response Surface Methodology and Artificial Neural Network-Genetic Algorithm
Haiying Zhou, Hesheng Liu, Tangqing Kuang, Qingsong Jiang, Zhixin Chen, and Weipei Li
Research Article (10 pages), Article ID 6154694, Volume 2020 (2020)

Simulation and Optimization of Short Fiber Circumferential Orientation in Short-Fiber-Reinforced Composites Overflow Water-Assisted Injection Molded Tube
Haiying Zhou, Hesheng Liu, Tangqing Kuang, Qingsong Jiang, Zhixin Chen, and Weiping Li
Research Article (10 pages), Article ID 6135270, Volume 2019 (2019)

Quality Indexes Design for Online Monitoring Polymer Injection Molding
Jian-Yu Chen, Chien-Chou Tseng, and Ming-Shyan Huang
Research Article (20 pages), Article ID 3720127, Volume 2019 (2019)

Multiobjective Optimization Method for Polymer Injection Molding Based on a Genetic Algorithm
Zhijun Yuan, Hui Wang, Xuebing Wei, Kui Yan, and Cheng Gao
Research Article (17 pages), Article ID 9012085, Volume 2019 (2019)

Improving the Consistency of Injection Molding Products by Intelligent Temperature Compensation Control
Yufei Ruan, Huang Gao, and Dequn Li
Research Article (13 pages), Article ID 1591204, Volume 2019 (2019)

Effect of Process Parameters on Repeatability Precision of Weight for Microinjection Molding Products
Quan Wang, Jinrong Wang, Chongying Yang, Kaihui Du, Wenli Zhu, and Xiaoli Zhang
Research Article (8 pages), Article ID 2604878, Volume 2019 (2019)

Hindawi
Advances in Polymer Technology
Volume 2020, Article ID 3718670, 13 pages
https://doi.org/10.1155/2020/3718670

Research Article

Numerical Simulation during Short-Shot Water-Assisted Injection Molding Based on the Overflow Cavity for Short-Glass Fiber-Reinforced Polypropylene

Zhong Yu,[1,2] He-Sheng Liu,[1,3] Tang-Qing Kuang,[4] Xing-Yuan Huang,[1] Wei Zhang,[1] Zhong-Shi Chen,[1] and Kai Zhang[2]

[1]*Polymer Processing Laboratory, Nanchang University, Nanchang 330031, China*
[2]*Jiangxi Province Key Laboratory of Polymer Preparation and Processing, Shangrao Normal University, Shangrao 334001, China*
[3]*School of Chemical Biology and Materials, East China University of Technology, Nanchang 330013, China*
[4]*School of Mechanical & Electrical Engineering, East China Jiaotong University, Nanchang 330013, China*

Correspondence should be addressed to He-Sheng Liu; hsliu@vip.163.com

Received 18 July 2019; Revised 31 December 2019; Accepted 4 February 2020; Published 5 May 2020

Academic Editor: Huamin Zhou

Copyright © 2020 Zhong Yu et al. This is an open access article distributed under the Creative Commons Attribution License, which permits unrestricted use, distribution, and reproduction in any medium, provided the original work is properly cited.

Compared with water penetration condition of short-shot water-assisted injection molding with or without overflow cavity, it can be known from theory and common knowledge that short-shot water-assisted injection molding with overflow cavity has many advantages, such as it can save materials and energy. Then, the effects of melt short shot size, water injection delay time, melt temperature and water injection pressure on the penetration of water after penetration, and the orientation distribution of short fibers during water-assisted injection molding of the overflow cavity short-shot method were studied. It is found that the melt short shot size had the greatest influence on it, followed by water injection pressure, water injection delay time, and finally, melt temperature. With the increase of the melt short shot size, the thickness of the residual wall of the whole main cavity becomes thinner, the orientation of short fiber along the melt flow direction becomes higher, and the degree of fiber orientation changes becomes lower. In the front half of the main cavity, with the decrease of water injection pressure, the delay time of water injection, and the melt temperature, in the front part of the main cavity, the residual wall thickness becomes thinner, the fiber orientation along the melt flow direction becomes lower, and the fiber orientation changes degree becomes higher; in the latter half of the main cavity, the influence of the water penetration and the orientation distribution of short fibers along the melt flow direction are not significant.

1. Introduction

Fluid-assisted injection molding is a new injection molding technique that uses high-pressure fluid to push molten polymer forward to form a hollow or partially hollow product. It consists of gas-assisted injection molding and water-assisted injection molding. Because the gas-assisted system was more mature than the water-assisted system, gas-assisted injection molding first entered the researcher's field of vision. With the development of science and technology, the technology of the water-assisted system has gradually improved, and water-assisted injection molding has gradually entered the field of researchers. Compared with gas, water has the advantages of high thermal conductivity, specific heat capacity, and recyclability, so water-assisted injection molding can shorten the molding cycle, reduce the production cost, and improve the inner surface smoothness, and so on [1, 2]. Therefore, in recent years, water-assisted injection molding has been widely concerned.

In water-assisted injection molding, according to whether the molten polymer is fully filled with the main cavity before high-pressure water injection, it can be divided into short-shot water-assisted injection molding and overflow water-assisted injection molding. Whether it is short-shot

or overflow molding, researchers focus on the influence of process parameters on macrostructure such as the water penetration length and residual wall thickness [3]. For example, Huang and Deng [4] studied the influence of process parameters on the water penetration length and residual wall thickness of PP curved pipe products by using a single-factor method. Zhang et al. [5] and Zhang et al. [6] studied the influence of relevant process parameters on the residual wall thickness of water-assisted injection molded products. Polynkin et al. [7] simulated the influence of water injection pressure on the residual wall thickness of water-assisted injection molded circular pipe products. Pudpong et al. [8] used Moldflow to simulate the influence of process parameters on the residual wall thickness of overflow water-assisted injection molding PP products by an overflow method. Park et al. [9] found that the residual wall thickness of the workpiece decreases with the increase of polymer melt temperature and water injection pressure through experiments and theories. Tangqing et al. and Tang-Qing et al. [10, 11] studied the influence of the water pressure and water delay time on the residual wall thickness of water-assisted coinjection molding by experiment. Recently, the researchers also conducted correlation studies on the microstructure and performance control of water-assisted injection molding products by changing process parameters and physical parameters [12]. For example, Wang et al. [13] prepared polypropylene/acrylonitrile-styrene copolymer products with four mass ratios through different water injection pressure and melt temperature and studied the formation mechanism of transverse crystal. Xianhu et al. [14, 15] studied the effect of HDPE with different molecular weights on the crystal morphology of water-assisted injection molded products. Haiying et al. [16] studied the effect of process parameters on the short fiber circumferential orientation by experiments and theories. In the literature investigation, there are many researches on short-shot water-assisted injection molding without the overflow cavity. However, there are few researches on the short-shot water-assisted injection molding based on the overflow cavity.

In this paper, the numerical calculation is carried out based the short-shot water-assisted injection molding with and without overflow cavity. The residual wall thickness and water penetration length were compared when the short-shot molding with and without the overflow cavity is used under the same process parameters. It is proved by common sense and theory that short injection with overflow cavity can save more materials than short injection without overflow cavity. Then, the influence of process parameters on the residual wall thickness and fiber orientation distribution degree of short fiber-reinforced PP products by short-shot water-assisted injection molding with the overflow cavity is analyzed. At the same time, it also broadens the basic theoretical and experimental research content of short-shot water-assisted injection molding.

2. Numerical Research Method

The short-shot water-assisted injection molding process based on the overflow cavity, which first fills short glass fiber-reinforced polymer composite melt into the main cavity, and then injects high-pressure water into the main cavity to push the melt forward to the overflow cavity, which finally keeps pressure and cooling. Due to the intervention of high-pressure water, the whole process involves many process parameters. The melt short shot size, water injection delay time, melt temperature, and water injection pressure are the main research objects in the calculation.

3. Mathematical Model and Assumption

Short-shot water-assisted injection molding based on the overflow cavity involves both short fiber-reinforced polymer composites with viscoelastic melt and high-pressure water for Newtonian fluids. In order to make the calculation convergence and the calculation process conform to the actual molding conditions, the mathematical model is simplified as follows: (1) the density, heat capacity, and thermal conductivity in the fluid remain unchanged; (2) no slip between the melt and the mold wall; (3) ignoring surface tension, gravity, inertial force, and body force; and (4) not considering the phase transition enthalpy during melt crystallization. Therefore, the three-dimensional nonisothermal flow behavior governing equation is obtained as follows:

Continuity equation:

$$\frac{\partial \rho}{\partial t} + \nabla \cdot \rho \boldsymbol{u} = 0 \tag{1}$$

Momentum equation:

$$\frac{\partial}{\partial t}(\rho \boldsymbol{u}) + \nabla \cdot (\rho \boldsymbol{u}\boldsymbol{u} + \boldsymbol{\tau}) = -\nabla p + \rho \boldsymbol{g} \tag{2}$$

Energy equation:

$$\rho C_p \left(\frac{\partial T}{\partial t} + \boldsymbol{u} \cdot \nabla T \right) = \nabla \cdot (k \nabla T) + \eta \dot{\gamma}^2 \tag{3}$$

where $\boldsymbol{u}$ is the velocity vector, T is temperature, t is time, p is pressure, $\boldsymbol{\tau}$ is stress tensor, $\boldsymbol{g}$ is acceleration vector of gravity, ρ is density, η is viscosity, k is thermal conductivity, C_p is specific heat, and $\dot{\gamma}$ is shear rate.

In order to describe the rheological properties of polymer melt in the mold flow channel, one of the classical constitutive equations reflecting the short fiber-reinforced polymer composites, the White-Metzner constitutive equation, is selected:

$$\begin{aligned}
&\boldsymbol{\tau} + \lambda \left(\frac{\partial \boldsymbol{\tau}}{\partial t} + \boldsymbol{u} \cdot \nabla \boldsymbol{\tau} - \nabla \boldsymbol{u}^{\mathrm{T}} \cdot \boldsymbol{\tau} - \boldsymbol{\tau} \cdot \nabla \boldsymbol{u} \right) = \eta \left(\nabla \boldsymbol{u} + \nabla \boldsymbol{u}^{\mathrm{T}} \right), \\
&\lambda(T, \dot{\gamma}) = \frac{\eta(T, \dot{\gamma})}{G}, \\
&\eta = \frac{\eta_0}{1 + (\eta_0 \dot{\gamma} / \tau^*)^{1-n}}, \\
&\eta_0 = \mathrm{D}_1 \exp\left(\frac{-\mathrm{A}_1 (T - T_c)}{\mathrm{A}_2 + (T - T_c)} \right), \\
&T_c = \mathrm{D}_2 + \mathrm{D}_3 p, \\
&\mathrm{A}_2 = \tilde{\mathrm{A}}_2 + \mathrm{D}_3 p,
\end{aligned} \tag{4}$$

Table 1: Characteristics of polypropylene composites (10% by weight of short fibers).

Thermal conductivity	$k = 0.1776\text{W/(m.K)}$
Specific heat capacity	$C_P = 2700\text{J/(kg.K)}$
White-Metzner constitutive equation parameters	$n = 0.20426$, $\tau^* = 33086.7\text{Pa}$, $D_1 = 4.58\text{E} + 20\text{Pa} \cdot \text{s}$, $D_2 = 263.15\text{K}$, $D_3 = 0\text{K/Pa}$, $A_1 = 40.388$, $\tilde{A}_2 = 51.6\text{K}$, and $G = 2.1\text{E} + 05\text{Pa}$
Fiber orientation model iARD-PRP parameters	$C_I = 0.005$, $C_M = 0$, ansd $\alpha = 0.7$

where T is the melt temperature, G is shear modulus, η_0 is zero shear viscosity, τ^* is the parameter of the transition region between the zero shear rate and the power law region of the viscosity curve, n is the power law index, and D_1, D_2,D_3, A_1, and $\tilde{A}_2$ are all the material constants.

In fiber orientation simulation, orientation probability distribution function and orientation tensor are often used to describe fiber orientation. The orientation distribution function can describe the fiber orientation state directly, but the complexity limits its use. The orientation tensor describes the fiber orientation state in the form of the matrix of the orientation distribution function. In previous studies, the standard Folgar-Tucker orientation equation combined with the fluid dynamics model of the IRD model was a useful method to theoretically determine the orientation of isotropic fibers in the concentrated suspension, but when quantitatively compared with the relevant experimental observations, the equation showed the inaccuracy of excessive prediction. Recently, the Phelps-Tucker anisotropic rotational diffusion (ARD) model has demonstrated the ability to deal with the orientation of primary anisotropic fibers; however, ARD tensors dependent on HD tensors are generally difficult to apply. In this paper, the recently improved iARD-RPR orientation model [17] is adopted, which not only considers the interaction between fibers but also considers the rotation resistance of fibers in three-dimensional space. Its expression is as follows:

$$\begin{aligned} \dot{\mathbf{A}} &= \dot{\mathbf{A}}^{\text{HD}} + \dot{\mathbf{A}}^{\text{iARD}}(C_I, C_M) + \dot{\mathbf{A}}^{\text{RPR}}(\alpha), \\ \dot{\mathbf{A}}^{\text{HD}} &= (\mathbf{W} \cdot \mathbf{A}\text{-}\mathbf{A} \cdot \mathbf{W}) + \xi(\mathbf{D} \cdot \mathbf{A} + \mathbf{A} \cdot \mathbf{D}\text{-}2\mathbf{A}_4 : \mathbf{D}), \end{aligned} \tag{5}$$

where $\dot{\mathbf{A}}^{\text{iARD}}$ has two available parameters: the fiber-fiber interaction parameter C_I and the fiber-matrix interaction parameter C_M; $\dot{\mathbf{A}}^{\text{RPR}}$ has one parameter α, which is meant to slow down the response rate of the fiber orientation.

In this paper, the material selected was a short fiber-reinforced polypropylene (SGFPP) with a mass content of 10% short fibers, which was produced by LyondellBasell Industries. According to the equations mentioned above, the physical parameters involved are shown in Table 1.

3.1. Melt front tracking. A volume percent function is introduced to describe the melt front position and the evolution of fluid penetration with respect to time. Here, $f = 0$ is defined as the fluid phase, $f = 1$ as the plastic melt phase, whereas the melt front is located in the $0 < f < 1$ unit. The increase in the volume percent fraction from the kinematics process is governed by the following advection equation:

$$\frac{\partial f}{\partial t} + \nabla \cdot (\boldsymbol{u} f) = 0, \tag{6}$$

where f is the volume percent fraction; $\boldsymbol{u}$ is the velocity vector.

In this paper, based on the White-Metzner constitutive equation describing the short fiber-reinforced polymer composite and the short fiber orientation model iRAD-PRP, a mathematical model was constructed based on three major equations of fluid dynamics. Using the finite volume method and the melt front tracking method, three fluid equations, constitutive equations, and fiber orientation models were calculated based on the given process parameters and physical parameters.

4. Model Structure and Process Parameters

Short-shot water-assisted injection molding with the overflow cavity is different from the general short-shot water-assisted injection molding by adding an overflow cavity. Its model consists mainly of the main cavity, overflow cavity, melt injection nozzle, and water injection nozzle. Its main structural parameters: the main cavity size is $\Phi 16 * 245$, the overflow cavity diameter is $\Phi 10$. Compared with short-shot water-assisted injection molding based on the overflow cavity, there is no overflow cavity for the short-shot water-assisted injection molding without the overflow cavity. The schematic diagrams and physical figure are shown in Figure 1 and Figure 2, respectively.

In this paper, firstly, the residual wall thickness and water penetration length were compared when the short-shot molding without the overflow cavity and the short-shot molding with the overflow cavity are used under the same process parameters. The following, the influence of process parameters on the residual wall thickness and fiber orientation distribution degree of short fiber-reinforced PP products by short-shot water-assisted injection molding with the overflow cavity, are further analyzed; the process parameters studied are shown in Table 2.

5. Materials and Experiments

5.1. Materials. In the experiments, short glass fiber-reinforced polyethylene (SGFPP, Grade Hostacom SB224-1, LyondellBasell Industries, Germany) was used. The materials were 10% reinforced by the mass content of short glass fiber.

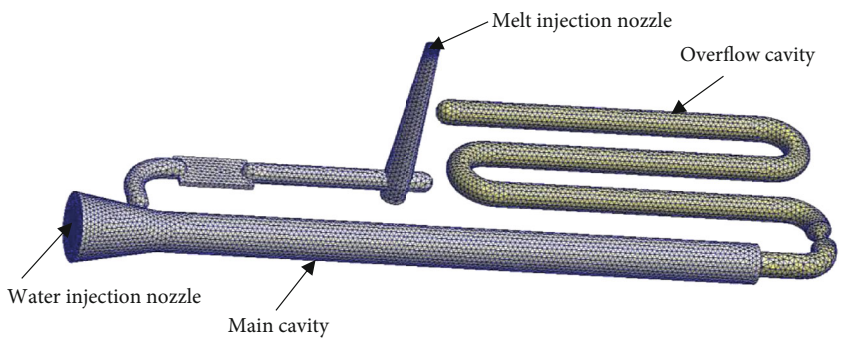

Figure 1: The schematic diagrams.

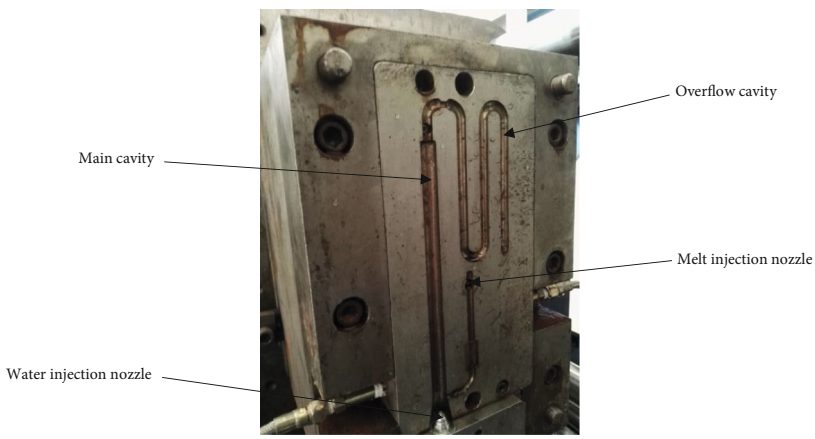

Figure 2: The physical figure.

Table 2: The process parameters.

Melt short shot size (%)	Water injection delay time(s)	Melt temperature (°C)	Water injection pressure(MPa)
70	0	210	4
75	**1**	**230**	6
80	3	250	**8**
85	5	270	10

Note: The numerical bolding in the table is the basic parameter to investigate the melt short shot size, water injection delay time, melt temperature, and water injection pressure.

Its flow index MFI $(230, 2.16) = 7\,\mathrm{g}/10$ min, and its density was 0.9 g/cc.

5.2. Experiments. The experimental platform is mainly composed of injection molding machine, water injection system, and mold, as shown in Figure 3. The experiment adopts a single-factor experiment, in which the injection molding machine mainly implements melt short shot size and melt temperature, and the water injection system mainly implements injection water injection delay time and water injection pressure.

Figure 3: The experimental platform.

5.3. Theoretical and Experimental Data Processing

5.3.1. Residual Wall Thickness and Its Percentage. The residual wall thickness of the product refers to the radial thickness of the melt after filling, and the percentage of residual wall thickness refers to the ratio of the residual wall thickness to the main cavity diameter. The larger the percentage of the residual wall thickness, the larger the cross-section of melt penetrated by water, and vice versa.

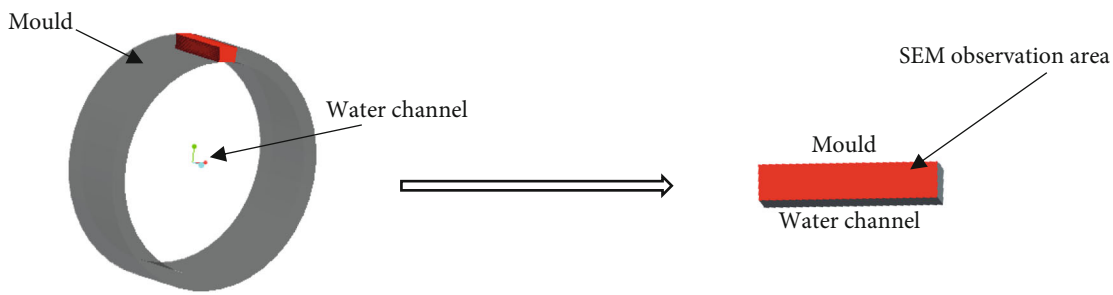

Figure 4: Schematic diagram of SEM sample sampling position and detection area.

5.3.2. Fiber Orientation. Fiber orientation refers to the orientation value of the fiber along the melt flow direction. The more the orientation value fluctuates or the more chaotic the orientation value is, the greater the orientation change degree is. In this paper, the main cavity is divided into three sections on average. At the end of each section, a 5 mm ring is cut out (Figure 4) and then placed in a liquid nitrogen container for half an hour cooling and brittle fracture treatment. Finally, the brittle section is sliced and placed in a carrier platform with conductive adhesive for gold spraying (Figure 5) and scanning electron microscope (Figure 6).

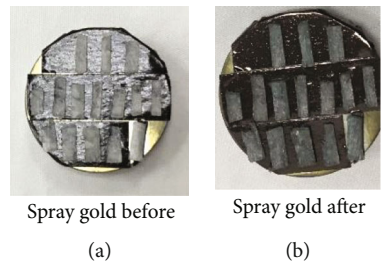

Figure 5: Experimental test sample.

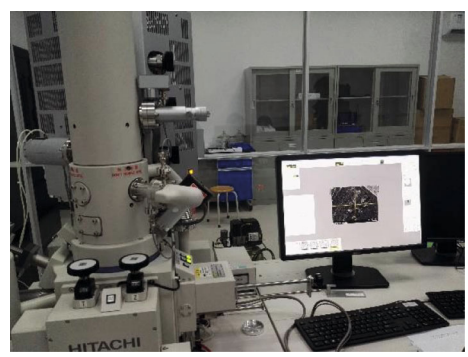

Figure 6: SEM observation.

6. Results and Analysis

Figure 7 shows the water penetration of the two water-assisted injection moldings along the melt flow direction at the melt short shot size of 75%, the water injection delay time of 1 s, the melt temperature of 230° C, and the water injection pressure of 8 MPa. It can be seen from the figure that the main cavity is completely penetrated by water during short-shot water-assisted injection molding with the overflow cavity, while the main cavity is penetrated by water more than half during short-shot water-assisted injection molding without the overflow cavity.

The reason is that in the short-shot water-assisted injection molding without the overflow cavity, the volume of the main cavity corresponds to the sum of the volume of the melt penetrated by water and the volume of the residual wall thickness, and the more the melt is penetrated by water, the smaller the residual wall thickness. On the contrary, the less the melt is penetrated by water, the larger the residual wall thickness. In short-shot water-assisted injection molding with the overflow cavity, although the volume of the main cavity is equal to the sum of the volume of the melt penetrated by water and the volume of the residual wall thickness, the overflow cavity is connected with the main cavity causes the excess melt to gradually flow into the overflow cavity during the process of the melt penetrated by water. Under the same process parameters, compared with the short-shot water-assisted injection molding without the overflow cavity, when the short-shot water-assisted injection molding with the overflow cavity is used, the melt is longer penetrated by water and the residual wall thickness is thinner; the short-shot water-assisted injection molding with the overflow cavity saves more material or energy, such as melt short shot size.

Therefore, both in theory and in common sense, the short-shot water-assisted injection molding with the overflow cavity is more advantageous than that without the overflow cavity. Subsequently, the influence of different process parameters on water penetration and fiber orientation distribution along the melt flow direction will be analyzed during the short-shot water-assisted injection molding with the overflow cavity.

6.1. Water Penetration. Figure 8 shows the residual wall thickness percentage along the melt flow direction when the melt short shot size of the short-shot water-assisted injection molding with the overflow cavity is 70%, 75%, 80%, and 85%, respectively; other process parameters are the basic parameters. As can be seen from the figure, as the melt short shot size increases, residual wall thickness percentage increases, and residual wall thickness is thickening. At a distance from the water injection port to the end of the main cavity, as the melt short shot size is smaller, the residual wall thickness percentage is flatter and smaller, and the residual wall thickness is more uniform. The reason is

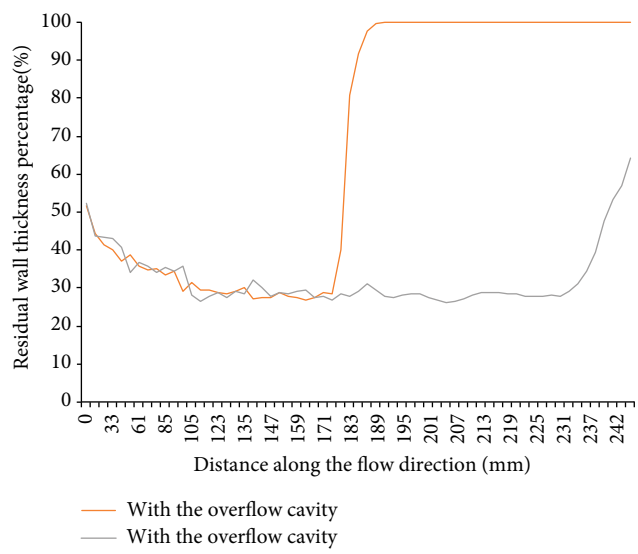

Figure 7: Water penetration of two short-shot water-assisted injection molding at the melt injection volume of 75%.

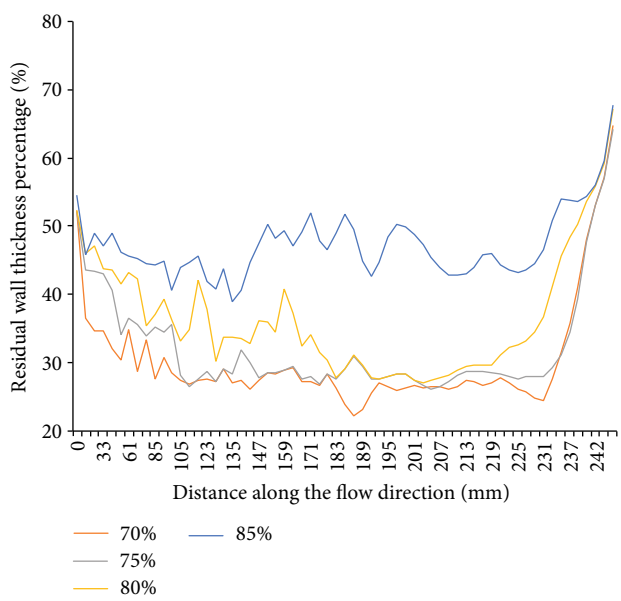

Figure 8: Effect of melt short shot size on water penetration.

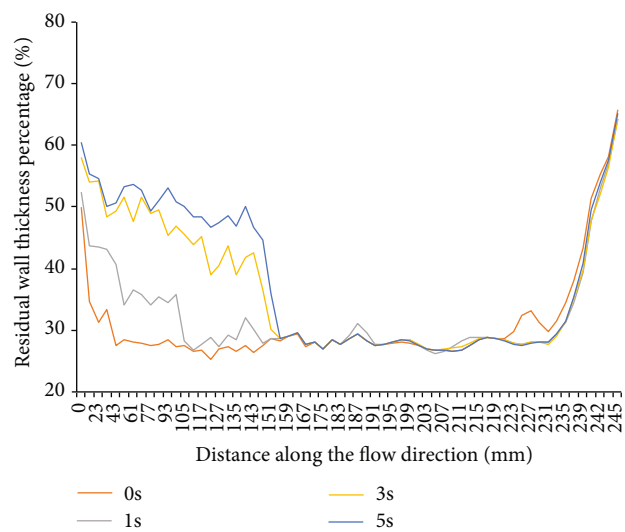

Figure 9: Effect of water injection delay time on water penetration.

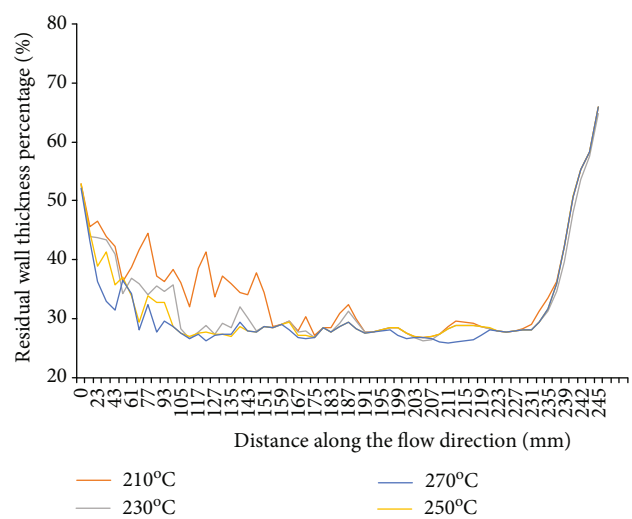

Figure 10: Effect of melt temperature on water penetration.

that as the melt short shot size increases, the resistance of water penetrates increases, and the longer the cooling time of the melt that is not penetrated by the water at the low temperature mold wall, the greater the effect.

Figure 9 shows that the residual wall thickness percentage along the melt flow direction when the injection delay time of the short-shot water-assisted injection molding with the overflow cavity is 0 s, 1 s, 3 s, and 5 s, respectively; other process parameters are the basic parameters. It can be seen from the figure that with the longer of water injection delay time, residual wall thickness percentage increases in the front half of the main cavity, and residual wall thickness percentage in the latter half is basically the same. The reason is that before the high-pressure water is injected, the high-temperature melt mainly stays in the front half of the main cavity, and as the cooling time of low-temperature mold wall becomes longer, the thickness of solidified layer becomes larger. After the high-pressure water is injected, the melt of the front half of the main cavity is pushed into the overflow cavity through the latter half of the main cavity. In this process, the residual wall thickness of the latter half of the main cavity is determined by the mold surface and the water cooling period. This period is very short, resulting in substantially the same percentage of residual wall thickness in the latter half. In addition, it can be seen that when the water injection time is 0 s, residual wall thickness percentage is the flattest along the melt flow direction.

Figure 10 shows that the residual wall thickness percentage along the melt flow direction when the melt temperature of the short-shot water-assisted injection molding with the

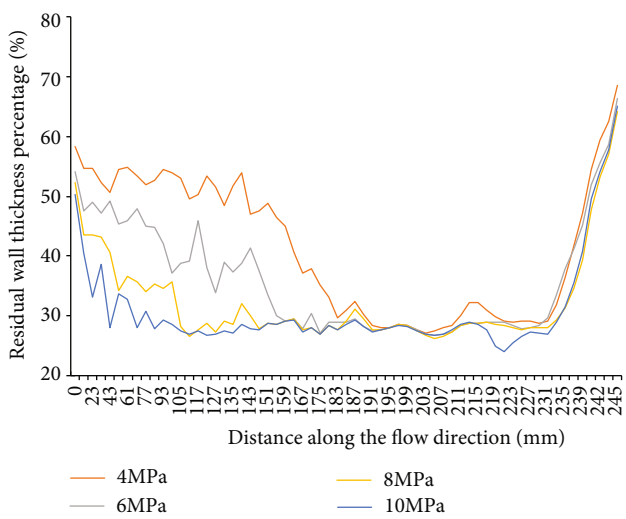

Figure 11: Effect of water injection pressure on water penetration.

overflow cavity is 210°C, 230°C, 250°C, and 270°C, respectively; other process parameters are the basic parameters. According to the figure, as the melt temperature increases, residual wall thickness percentage decreases relatively, but not significant. The reason is that as the melt temperature increases, the melt viscosity decreases, the resistance of high-pressure water pushing melt decreases, and residual wall thickness percentage also decreases.

Figure 11 shows that the residual wall thickness percentage along the melt flow direction when the water injection pressure of the short-shot water-assisted injection molding with the overflow cavity is 4 MPa, 6 MPa, 8 MPa, and 10 MPa, respectively; other process parameters are the basic parameters. It can be seen from the figure that as the water injection pressure increases, residual wall thickness percentage decreases, and the distribution of residual wall thickness is flatter along the melt flow direction, and the percentage of residual wall thickness in the latter half of the main cavity is almost the same. The reason is that as the water injection pressure increases, the water diameter becomes large when the high-pressure water enters from the water injection nozzle, thereby pushing the water penetration cross-section to be larger. In the latter half of the main cavity, the melt here is driven by the high-pressure water in the first half of the main cavity and continues to be pushed into the overflow cavity by the high-pressure water. During this process, the melt is pushed by the high-pressure water for a short time, resulting in a shorter time for the melt to be cooled by water and mold wall.

6.2. Degree of Fiber Orientation Distribution. Figure 12 shows that the fiber orientation distribution along the melt flow direction when the melt short shot size of the short-shot water-assisted injection molding with the overflow cavity is 70%, 75%, 80%, and 85%, respectively; other process parameters are the basic parameters. As can be seen from the figure, as the melt short shot size increases, the fiber orientation is lower and the degree of change in the fiber orientation distribution is higher along the melt flow direction. According to the characteristics of short fiber-reinforced polymer water-assisted injection molding products, the products are divided into a wall layer, core layer, and water channel layer along the direction of thickness. The fiber at the wall layer and water channel layer has a high orientation along the melt flow direction and a low degree of change, while the fiber at the core layer has a random orientation along the melt flow direction and a high degree of change. The reasons are as follows: as can be seen from Figure 8, as the melt short shot size increases, residual wall thickness percentage increases, and residual wall thickness is thickening. The thickening of residual wall thickness means that the smaller the percentage of wall thickness of the wall layer and water channel layer, the higher the percentage of core layer, resulting in the lower orientation and higher degree of change of fiber along the melt flow direction.

Figure 13 shows that the fiber orientation distribution along the melt flow direction when the water injection delay time of the short-shot water-assisted injection molding with the overflow cavity is 0 s, 1 s, 3 s, and 5 s, respectively; other process parameters are the basic parameters. As can be seen from the figure, in the front half of the main cavity, as the water injection delay time is prolonged, the fiber orientation is lower and the degree of the fiber orientation change is higher along the melt flow direction. In the latter half of the main cavity, the change in the water injection delay time has little effect on it. The reasons are as follows: as can be seen from Figure 9, with the longer of water injection delay time, residual wall thickness percentage increases in the front half of the main cavity, and residual wall thickness percentage in the latter half is basically the same. With the extension of water injection delay time, the percentage of residual wall thickness in the front half of the main cavity increases and the residual wall thickness thickens, resulting in the percentage of core layer in the wall thickness increases and the lower orientation and higher change degree of the fibers in the front half of the main cavity along the melt flow direction.

Figure 14 shows that the fiber orientation distribution along the melt flow direction when the melt temperature of the short-shot water-assisted injection molding with the overflow cavity is 210°C, 230°C, 250°C, and 270°C, respectively; other process parameters are the basic parameters. As can be seen from the figure, in the front half of the main cavity, as the melt temperature increases, the fiber orientation is higher and the degree of change in the fiber orientation distribution is lower along the melt flow direction. In the latter half of the main cavity, the change in the melt temperature has little effect on it. The reasons are as follows: as can be seen from Figure 10, as the melt temperature increases, the residual wall thickness percentage decreases in the front half of the main cavity, and the residual wall thickness percentage in the latter half is basically the same, but not significant in the main cavity. With the increase of melt temperature, the percentage of residual wall thickness in the front half of the main cavity increases and the residual wall thickness thickens, resulting in the percentage of core layer in the wall thickness increases

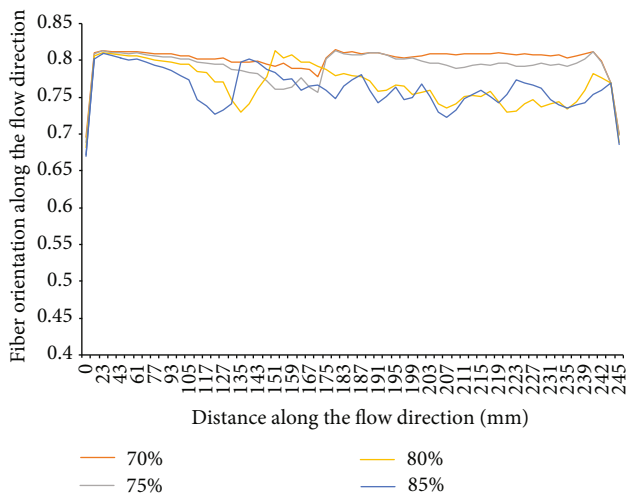

(a) Numerical analysis of water injection delay time on fiber orientation

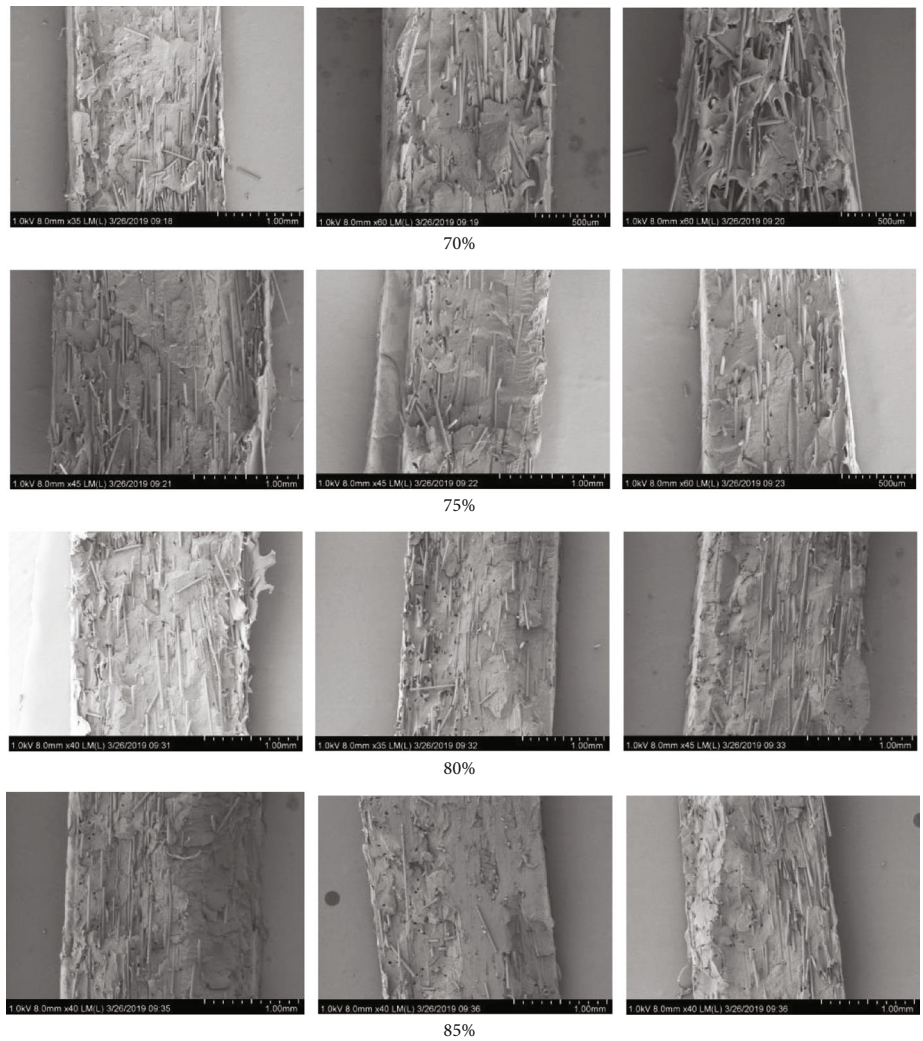

(b) SEM image of fiber orientation, the left side of each picture is the mold wall, the right side is the channel, and the three pictures of each process parameter are the near water end, the middle end, and the far water end, respectively, from left to right (the result of 0 s the same as the result of 1 s)

Figure 12: Effect of melt short shot size on fiber orientation distribution along the melt flow direction.

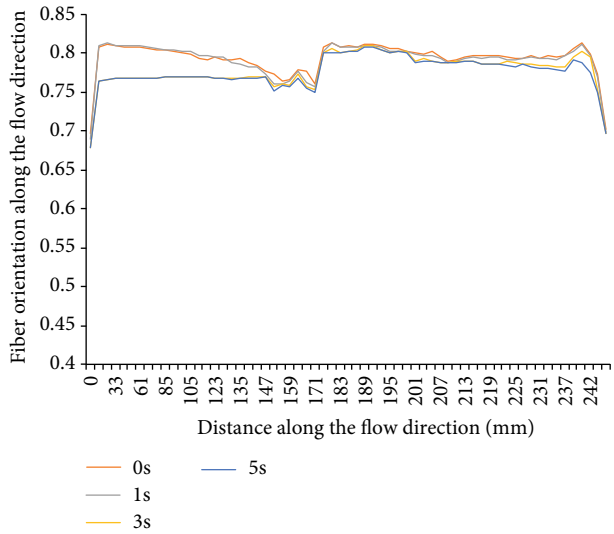

(a) numerical analysis of water injection delay time on fiber orientation

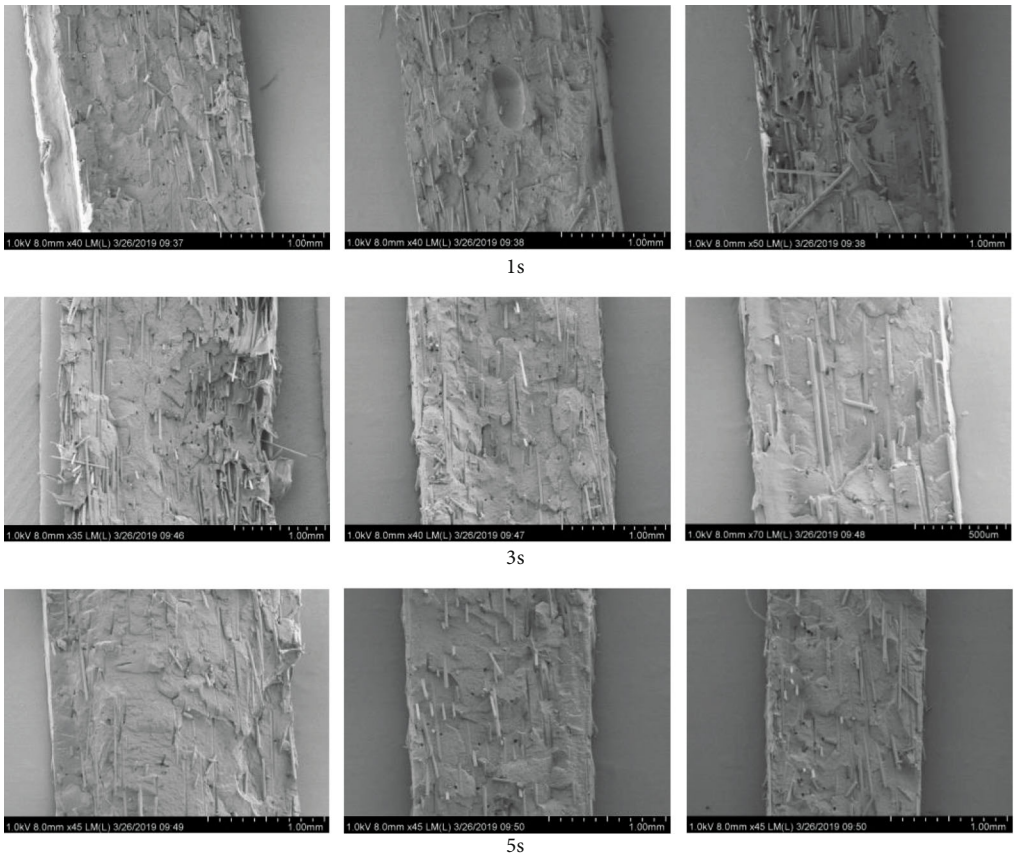

(b) SEM image of fiber orientation, the left side of each picture is the mold wall, the right side is the channel, and the three pictures of each process parameter are the near water end, the middle end and the far water end respectively from left to right (the result of 0 s the same as the result of 1 s)

Figure 13: Effect of water injection delay time on fiber orientation distribution along the melt flow direction.

and the lower orientation and higher change degree of the fibers in the front half of the main cavity along the melt flow direction.

Figure 15 shows that the fiber orientation distribution along the flow direction when the water injection pressure of the short-shot water-assisted injection molding with the overflow cavity is 4 MPa, 6 MPa, 8 MPa, and 10 MPa, respectively; other process parameters are the basic parameters. As can be seen from the figure, in the front half of the main cavity, as the water injection pressure increases, the fiber orientation is higher and the degree of change in the fiber orientation distribution is lower along the melt flow

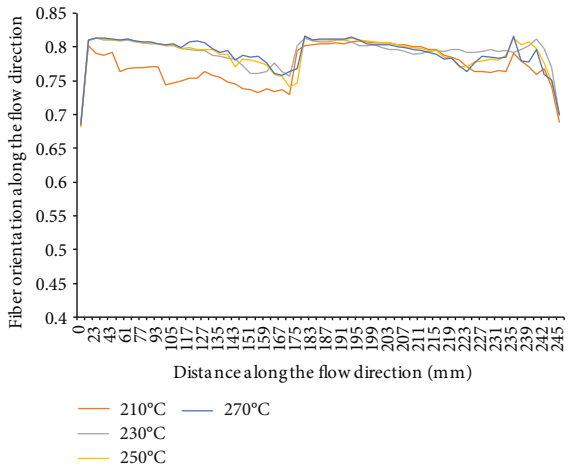

(a) Numerical analysis of melt temperature on fiber orientation

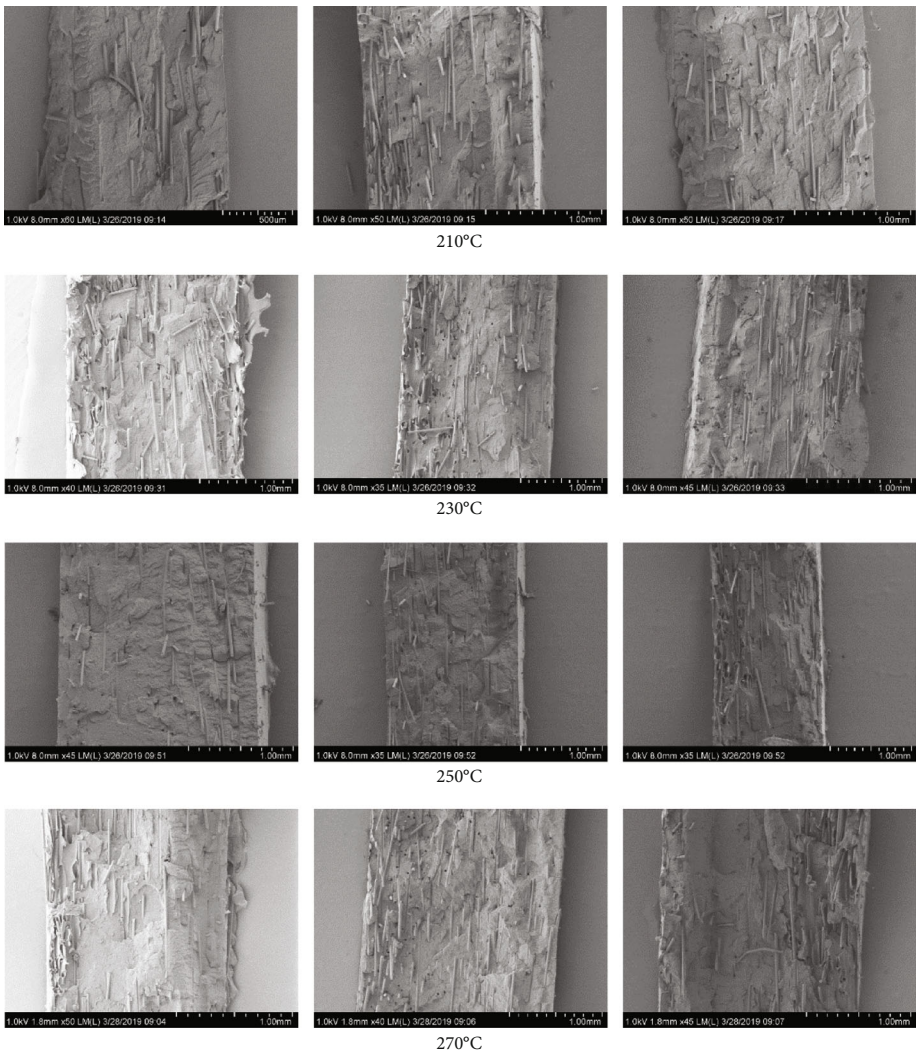

(b) SEM image of fiber orientation, the left side of each picture is the mold wall, the right side is the channel, and the three pictures of each process parameter are the near water end, the middle end and the far water end, respectively, from left to right

Figure 14: Effect of melt temperature on fiber orientation distribution along the melt flow direction.

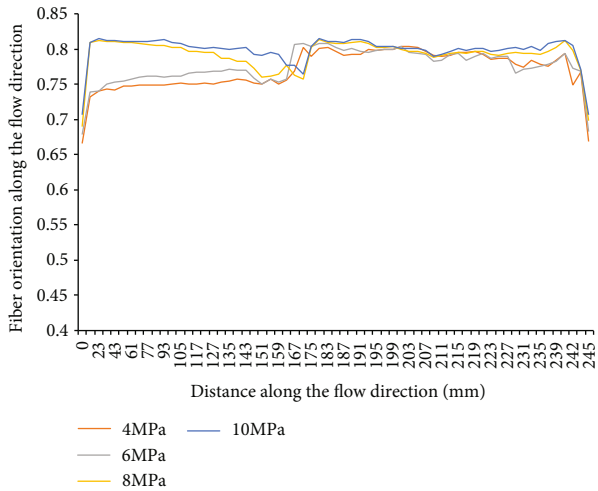

(a) Numerical analysis of water injection pressure on fiber orientation

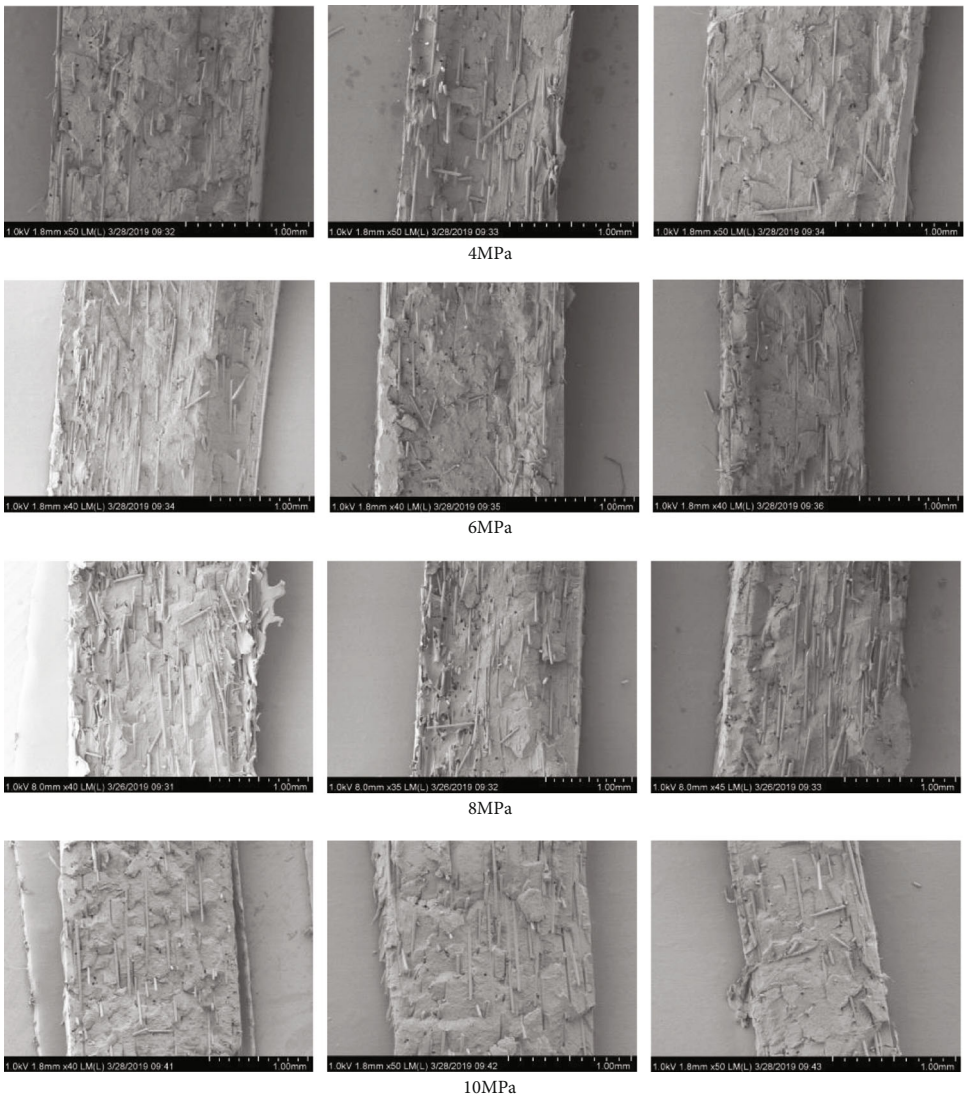

(b) SEM image of fiber orientation, the left side of each picture is the mold wall, the right side is the channel, and the three pictures of each process parameter are the near water end, the middle end and the far water end, respectively, from left to right

Figure 15: Effect of water injection pressure on fiber orientation distribution along the melt flow direction.

direction. In the latter half of the main cavity, the change in the melt temperature has little effect on it. The reasons are as follows: as can be seen from Figure 11, as the water injection pressure increases, residual wall thickness percentage decreases in the front half of the main cavity, and residual wall thickness percentage in the latter half is basically the same. With the increase of water injection pressure, the percentage of residual wall thickness in the front half of the main cavity decreases and the residual wall thickness thins, resulting in the percentage of core layer in the wall thickness decreases and the higher orientation and lower change degree of the fibers in the front half of the main cavity along the melt flow direction.

7. Conclusion

The numerical calculation is carried out by combining the viscoelastic constitutive equation White-Metzner and the fiber orientation model iARD-RPR and then verified by experiment. Firstly, the water penetration condition of the short-shot water-assisted injection molding with and without the overflow cavity is compared. From theory and common sense, the short-shot water-assisted injection molding with the overflow cavity is more advantageous than that without the overflow cavity. And then, during short-shot water-assisted injection molding with the overflow cavity, the effects of the melt short shot size, water injection delay time, melt temperature, and water injection pressure on the penetration of water after penetration and the orientation distribution of short fibers along the melt flow direction were analyzed.

It is known that the melt short shot size has the most significant influence on the penetration condition and the orientation distribution of short fibers along the melt flow direction after water penetration, followed by the water injection pressure, the water injection delay time, and finally, the melt temperature. To a certain extent, as the melt short shot size increases, the residual wall thickness becomes larger after water penetration, and the orientation of short fibers is lower and the degree of the fiber orientation change is higher along the melt flow direction; as the water injection pressure increases, the residual wall thickness becomes thinner after water penetration, and the orientation of short fibers is higher (especially in the front half of the main cavity) and the degree of the fiber orientation change is lower along the melt flow direction; as the water injection delay time is prolonged, the residual wall thickness becomes thicker after water penetration, and the orientation of short fibers is lower and the degree of the fiber orientation change is higher along the melt flow direction in the front half of the main cavity; however, the penetration of the water and the orientation distribution of short fibers along the melt flow direction in the latter half of the main cavity have little effect; as the melt temperature increases, the residual wall thickness becomes thinner after water penetration, and the orientation of short fibers is higher and the degree of the fiber orientation change is lower along the melt flow direction in the front half of the main cavity, and the influence of the water penetration and the orientation distribution of short fibers along the melt flow direction in the latter half of the main cavity is minimal.

Data Availability

All data included in this study are available upon request by contact with the corresponding author.

Conflicts of Interest

The authors declare that they have no conflicts of interest.

Acknowledgments

This work forms part of a project supported by the National Natural Science Foundation of China (NSFC, No. 21664002, No. 51563010, and No. 51403165) and the Science and Technology Association of Jiangxi Province (No. GJJ161049).

References

[1] M. Knights, "Water injection molding makes hollow parts faster," *Plastics Technology*, vol. 48, no. 4, pp. 42–47, 2002.

[2] T. Juntgen and W. Michaeli, "The water injection technique(-WIT) as an attractive alternative and supplement to gas-assisted injection molding (GAIM)," in *ANTEC 2002-Conference Proceedings*, pp. 386–391, San Fransisco, CA, USA, 2002.

[3] S.-J. Liu, "Water assisted injection molding: a review," *International Polymer Processing*, vol. 24, no. 4, pp. 315–325, 2009.

[4] H. X. Huang and Z. W. Deng, "Effects and optimization of processing parameters in water-assisted injection molding," *Journal of Applied Polymer Science*, vol. 108, no. 1, pp. 228–235, 2008.

[5] Z. Zeng-meng, Z. Hua, Y.'a. Gao, and H. Yang, "Simulation simulation and analysis on cavity filling process in water-assisted injection molding," *Journal of Mechanical Engineering*, vol. 46, no. 8, pp. 140–146, 2010.

[6] K. Zhang, T. Kuang, H. Liu, X. Zeng, Y. Deng, and H. Jasak, "Simulation analysis of water-assisted injection filling process based on viscoelastic constitutive," *Polymer Materials Science and Engineering*, vol. 30, no. 9, pp. 93–96, 2014.

[7] A. Polynkin, L. Bai, J. F. T. Pittman et al., "Water assisted injection moulding: development of insights and predictive capabilities through experiments on instrumented process in parallel with computer simulations," *Plastics, Rubber and Composites*, vol. 37, no. 2-4, pp. 131–141, 2008.

[8] T. Pudpong, P. Buahom, S. Areerat, W. Rungseesantivanon, I. Satoh, and T. Saito, "The effects of processing parameters on the residual wall thickness distribution at the sharp angle corner of water assisted injection molded parts," *International Polymer Processing*, vol. 28, no. 5, pp. 528–540, 2013.

[9] H. Park, B. S. Cha, and B. Rhee, "Experimental and Numerical Investigation of the Effect of Process Conditions on Residual Wall Thickness and Cooling and Surface Characteristics of Water- Assisted Injection Molded Hollow Products," *Advances in Materials Science and Engineering*, vol. 2015, Article ID 161938, 11 pages, 2015.

[10] T. Kuang, C. Yu, B. Xu, and L.-S. Turng, "Experimental study of penetration interfaces in the overflow fluid-assisted co-

injection molding process," *Journal of Polymer Engineering*, vol. 36, no. 2, pp. 139–148, 2016.

[11] T.-Q. Kuang, K. Zhou, L.-X. Wu, G.-F. Zhou, and L.-S. Turng, "Experimental study on the penetration interfaces of pipes with different cross-sections in the overflow water-assisted coinjection molding," *Journal of Applied Polymer Science*, vol. 132, 2016.

[12] X. Liu, Y. Pan, G. Zheng et al., "Overview of the experimental trends in water-assisted injection molding," *Macromolecular Materials and Engineering*, vol. 303, no. 8, article 1800035, 2018.

[13] B. Wang, H.-x. Huang, and Z.-y. Wang, "Formation mechanism of transcrystals in PP/SAN blends prepared via water-assisted injection molding," *Acta Polymerica Sinica*, vol. 8, pp. 825–830, 2012.

[14] X. Liu, C. Zhang, K. Dai, G. Zheng, C. Liu, and C. Shen, "Unexpected molecular weight dependence of shish kebab in water-assisted injection molded HDPE," *Polymers for Advanced Technologies*, vol. 24, no. 2, pp. 270–272, 2013.

[15] X. Liu, Y. Pan, C. Peng et al., "Twisted lamellae in water-assisted injection molded high density polyethylene," *Materials Letters*, vol. 172, no. 1, pp. 19–22, 2016.

[16] H. Zhou, H. Liu, T. Kuang, Q. Jiang, Z. Chen, and W. Li, "Simulation and optimization of short fiber circumferential orientation in short-fiber-reinforced composites overflow water-assisted injection molded tube," *Advances in Polymer Technology*, vol. 2019, Article ID 6135270, 10 pages, 2019.

[17] H.-C. Tseng, R.-Y. Chang, and C.-H. Hsu, "Phenomenological improvements to predictive models of fiber orientation in concentrated suspensions," *Journal of Rheology*, vol. 57, no. 6, pp. 1597–1631, 2013.

Hindawi
Advances in Polymer Technology
Volume 2020, Article ID 8946591, 10 pages
https://doi.org/10.1155/2020/8946591

Research Article

Tensile Behavior of Acrylonitrile Butadiene Styrene at Different Temperatures

Jiquan Li,[1] Yadong Jia,[1] Taidong Li,[1] Zhou Zhu,[1] Hangchao Zhou,[2] Xiang Peng,[1] and Shaofei Jiang[1]

[1]*Key Laboratory of E&M, Ministry of Education, Zhejiang University of Technology, Hangzhou 310014, China*
[2]*Mechanical Light Industry Inspection Department, Zhejiang Fangyuan Test Group Co., Ltd, Hangzhou 310018, China*

Correspondence should be addressed to Shaofei Jiang; jsf75@zjut.edu.cn

Received 30 July 2019; Accepted 15 November 2019; Published 4 April 2020

Guest Editor: Yun Zhang

Copyright © 2020 Jiquan Li et al. This is an open access article distributed under the Creative Commons Attribution License, which permits unrestricted use, distribution, and reproduction in any medium, provided the original work is properly cited.

Temperature greatly influences the mechanical response of acrylonitrile butadiene styrene (ABS). The tensile behavior of ABS was explored in this study. The tensile experiments were conducted at a wide range of temperatures (from 40°C to 130°C). A model was established to reveal the quantitative relationship between temperature and tensile behavior of ABS. The results of tensile experiments showed that tensile behavior of ABS exhibited glassy state and high-elastics state. The model was also divided into two parts that rely on the boundary of glass transition temperature, in which the parameters of the model were calculated by the fitting method. The model predictions showed a good agreement with the results of the experimental tensile test. This study provides the quantitative relationship between temperature and tensile behavior of ABS, which saves time and experimental costs.

1. Introduction

Mechanical behavior of amorphous polymers has been studied for many decades, and the basic features of the stress-strain curves are well known [1–3]. At very small strains, the behavior is elastic. At slightly larger strains, yielding occurs when intermolecular barriers to segmental rearrangements are overcome. Following yielding, strain softening may happen, which means a reduction in stress to a level corresponding to plastic flow [4, 5]. Due to their light weight and excellent mechanical properties, amorphous polymers are widely used in automotive industries [6], packaging applications [7], and electronic products [8].

The complex mechanical behavior of amorphous polymers is generally temperature dependent [3, 9, 10]. Over the years, many models have been proposed for the determination of relationship between temperature, stress, and strain [11–13]. Richeton et al. [14] carried out uniaxial compression stress-strain tests at a wide range of temperatures (−40°C to 180°C) to study the influence of temperature on the mechanical behavior of three amorphous polymers. Blumenthal et al. [15] examined the influence of both strain rate and temperature on the deformation response of PMMA and PC. Cady et al. [16] studied the mechanical response of several polymers under dynamic loading at high temperatures. The aforementioned studies resulted in guidelines of how to construct tailored materials, which could serve our needs of improved materials without the need of extensive trial and error work [17].

ABS is an important component of amorphous polymers, especially in the electronics industry, machinery industry, transportation, and building materials industry. [18, 19]. According to the latest report released by Global Market Insights [20], ABS market sales will increase to $38 billion in 2024, with a compound annual growth rate of 6.0%. The potential growth of household appliances, electronic appliances, automobiles, and construction industry will promote the rapid development of ABS market. Thus, the use of ABS has become commonplace.

However, the influence of temperature on the tensile behavior of ABS has received much less attention. The purpose of this work is to propose a mathematical model for

describing tensile behavior of ABS at different temperatures (from 40°C to 130°C), in which the parameters of the model were calculated by a fitting method. To verify the accuracy of the model, the prediction results from the model were compared with the experimental results. This study provides the quantitative relationship between temperature and tensile behavior of ABS, which saves time and experimental costs.

2. Modeling

The amorphous polymer sequentially presents glassy state, high-elastics state, and viscous flow state with an increase in temperature. The tensile test is impossible with the temperature higher than viscous flow temperature. So this paper focuses on the tensile properties of glassy state and high-elastics state of amorphous polymer.

In the glassy state of amorphous polymer, the typical stress vs. strain curves are divided into two parts bounded by the yield point. Before the yield point, the polymer shows elastic properties, and the yield point is the critical point of the elastic stage; after the yield point, the polymer enters the plastic stage. However, the relationship between stress and strain is not completely linear elasticity at the end of the elastic stage. Therefore, the model is divided into three parts as follows: elastic stage, the stage of elastic critical point to yield point, and strain softening stage, which describes the quantitative relationship of stress, strain, and temperature in the glassy state.

The stress-strain relationship is linear in the elastic stage, which is defined as follows [21]:

$$\sigma = E(T) \times \varepsilon; \quad \varepsilon \leq 0.25\%, \tag{1}$$

where σ and ε are the stress and strain, respectively. The critical point of elastic stage is 0.25%, referencing the test standard of elastic modulus [22]. $E(T)$ is the elastic modulus relevant to the absolute temperature T; in this paper, the relationship of elastic modulus and temperature can be written as

$$E(T) = a_1 \times T^2 + b_1 \times T + c_1, \tag{2}$$

where a_1, b_1, and c_1 are the material constants, respectively.

The trend in the range of elastic critical point to yield point is no longer completely linear, which is described by the power-hardening model [23]:

$$\sigma = A(T)\varepsilon^{B(T)}; \quad 0.25\% < \varepsilon \leq \varepsilon_s, \tag{3}$$

where $A(T)$ and $B(T)$ are material parameters considered as the function of the temperature, that is,

$$A(T) \times B(T) = a_2 \times T + b_2, \tag{4}$$

with

$$A(T) = a_3 \times T + b_3, \tag{5}$$

and ε_s is the yield strain, which is introduced as follows:

$$\varepsilon_s = a_4 \times T^2 + b_4 \times T + c_4, \tag{6}$$

where a_2, a_3, a_4, b_2, b_3, b_4, and c_4 are the material constants, respectively.

The relationship of stress and strain in the strain-softening stage is described by the following modified models from the power-hardening model:

$$\sigma = C(T)\varepsilon^{D(T)} + F(T); \quad \varepsilon > \varepsilon_s, \tag{7}$$

where $C(T)$, $D(T)$, and $F(T)$ are the material parameters relevant to the temperature; the quantitative relationships are shown in the following equations:

$$\begin{cases} C(T) = a_5 \times T^2 + b_5 \times T + c_3, \\ F(T) = a_6 \times T^2 + b_6 \times T + c_4, \\ D(T) = \dfrac{a_7 \times T^3 + b_7 \times T^2 + c_5 \times T + d_1}{C(T) \times F(T)}, \end{cases} \tag{8}$$

where a_5, a_6, a_7, b_5, b_6 b_7, c_3, c_4, c_5, and d_1 are the material constants, respectively.

The sample exhibits high elasticity as the temperature is higher than the glass transition temperature T_g. There is no yield point on the stress vs. strain curves, but a longer platform. This property can be expressed as [21]

$$\sigma = H(T)\varepsilon^{G(T)}, \tag{9}$$

where $H(T) = a_8 \times T^2 + b_8 \times T + c_6$, $G(T) = a_9 \times T^2 + b_9 \times T + c_7$, and a_8, a_9, b_8, b_9, c_6, and c_7 are the material constants.

The model is divided into two parts for describing the quantitative relationship according to material properties at different temperatures. Conclusively, the relationship of temperature and tensile properties of ABS is given as follows:

When $T < T_g$,

$$\sigma = \begin{cases} E(T)\varepsilon; & 0 < \varepsilon \leq 0.25\%, \\ A(T)\varepsilon^{B(T)}; & 0.25\% < \varepsilon \leq \varepsilon_s, \\ C(T)\varepsilon^{D(T)} + F(T); & \varepsilon > \varepsilon_s. \end{cases} \tag{10}$$

Also, when $T \geq T_g$,

$$\sigma = H(T)\varepsilon^{G(T)}. \tag{11}$$

3. Experiments

The tensile samples were made by the amorphous material ABS (XR-401, LG Chemical Information Electronic Materials Co Ltd, Korea), and the tensile specimens were produced by an injection molding machine (HTFX5-MA3800/2250). The processing parameters are shown in Table 1. The tensile tests were performed at different temperatures (40°C, 50°C, 60°C, 70°C, 80°C, 90°C, 100°C, 110°C, 120°C, and 130°C) using a testing machine (Instron-5966, Instron Engineering Corporation, USA), and the tensile rate was 50 mm/min. Further, to verify the correctness of the proposed model, the tensile data of samples at 75°C and 115°C (above and below the glass transition temperature) were carried out for comparison with the data from the proposed model.

Table 1: Processing parameters of ABS in injection molding.

Processing parameters	Values
Injection temperature (°C)	210
Filling time (s)	3
Injection pressure (Mpa)	30
Cooling time (s)	15
Cooling temperature (°C)	25

4. Results and Discussion

4.1. Parameter Identification. Tensile properties of ABS vary at different temperatures; in this paper, the temperature of ABS was divided into two parts including below and above the transition temperature. Previous studies had shown that the range of glass transition temperature is 100°C–110°C [24], so the glass transition temperature 105°C was chosen as the boundary between glassy state and high-elastics state of ABS.

4.1.1. Parameters of Model below the Transition Temperature. The experimental results of ABS below 105°C are shown in Figure 1. ABS undergoes elastic deformation and plastic deformation in turn as the strain increases. Obviously, the stress gradually increases with the increase of temperature under same strain, and the slope of the stress vs. strain curves decreases correspondingly. The difference of yield stress at 40°C and 90°C is 27.1 MPa, and the tensile properties of ABS are greatly affected by temperature.

The elastic modulus of ABS at different temperature is shown in Table 2, which develops an upward trend with the increase in temperature. This trend is consistent with that of literature [24]. The data were also fitted to obtain the parameters of the model, as shown in Figure 2.

The relationship between elastic modulus and temperature is well described by unary quadratic equation. The value of R-square is 0.99969, which means that the deviation between the fitting curve and experimental data is controlled in a mini confine. The parameters $a_1 = -0.5847$, $b_1 = 360.4405$, and $c_1 = 53035.8534$ of equation (2) were calculated from the fitting curve.

The tensile properties of ABS are obviously affected by temperature due to the viscoelasticity, so the relationship between stress and strain is not linear before yield point. Combining with the test standard, the range of elastic stage is 0–0.25% of strain, in which the relationship between stress and strain is linear. When the strain is in the range of 0.25% to yield strain, the relationship between stress and strain is described by equation (3). The fitting results are shown in Figure 3.

The values of R-square are all greater than 0.93, the largest of which is 0.99398, which means that equation (3) is suitable for describing the relationship between stress and strain in the range of 0.25% to yield strain at different temperatures. The parameters of equation (3) were obtained by the fitting equation, as shown in Table 3.

To explore the relationship between parameters and temperature, the A and $A{\times}B$ vs. temperature curves are

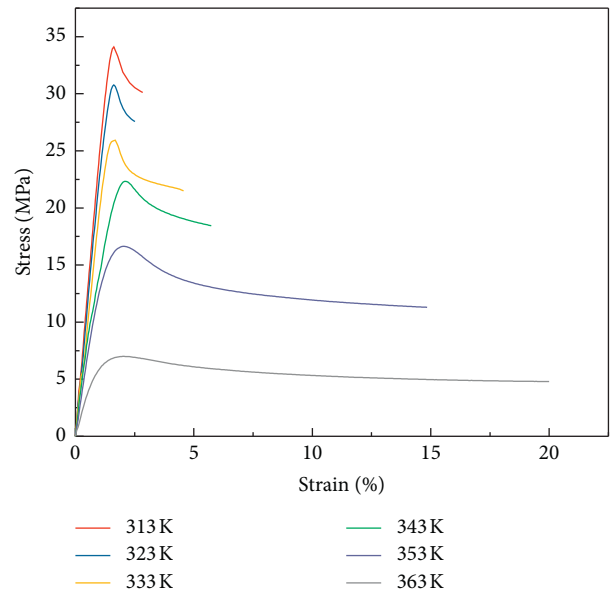

Figure 1: Tensile data of ABS at different temperature (below glass transition temperature).

shown in Figure 4. A and A×B decreases monotonously with the increase of temperature, and linear equations were applied to fitting data. A and $A{\times}B$ of R-square are all larger than 0.97. The acceptable fit results were used for calculating the parameters in equations fd4(4) and (5)fd5. a_2, b_2, a_3, and b_3 are −0.3875, 143.7337, −0.3582, and 136.8874, respectively.

The yield stress ε_s was also counted (Figure 5) at different temperatures. The yield stress decreased gradually with the increase of temperature, which decreases from 34.1036 MPa to 6.9964 MPa in the range of 313 K to 363 K. The quadratic functional equation is suitable for the relationship between yield stress and temperature, so the parameters of equation (6) were obtained; a_4, b_4, and c_4 are −0.0063, 3.7049, and −513.8276, respectively.

In the strain softening stage, the fitting results of experimental data are shown in Figure 6. The values of R-square indicated that equation (7) commendably represents the relationship between stress and strain in the strain softening stage. On the basis of the fitting results, the values of C, F, and D were calculated(Figure 7).

All the parameters of equation (7) were fitted by equation (8), and the parameters of equation (8) were obtained as follows: $a_5 = -0.0078$, $b_5 = 5.0474$, $c_3 = -800.3438$, $a_7 = -0.0474$, $b_7 = 48.2651$, $c_5 = -16316.8925$, $d_1 = 1.8322 \times 10^6$, $a_6 = -0.0065$, $b_6 = 3.8487$, and $c_4 = -540.2021$.

The parameters of the aforementioned model were obtained on the basis of acceptable fitting results. These models reflect the relationship between stress and strain below the glass transition temperature.

4.1.2. Parameters of the Model above the Transition Temperature. The tensile properties of ABS at the high-elastics state are different from those at the glassy state,

Table 2: Elastic modulus of ABS at different temperatures.

Temperature (K)	313	323	333	343	353	363
Elastic modulus, *E (T)* (MPa)	2499.8156	2381.4532	2146.4725	1823.3530	1322.6141	761.9812

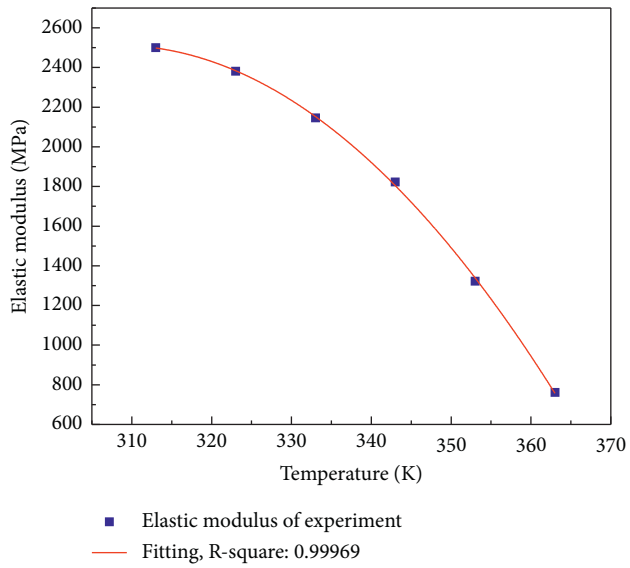

Figure 2: Fitting curve of the elastic modulus at different temperatures.

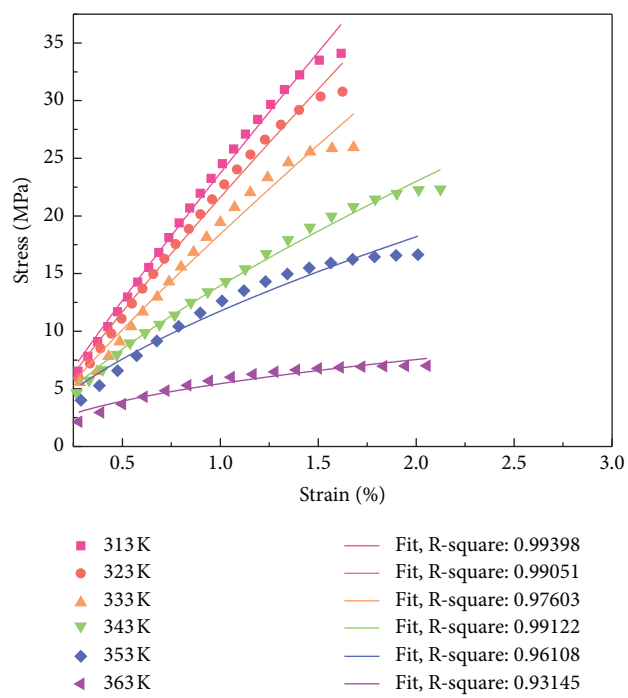

Figure 3: Fitting curve at different temperatures in the range of 0.25% to yield strain.

Table 3: Parameters of equation (3) calculated by the fitting equation.

Temperature (K)	313	323	333	343	353	363
A	23.7047	21.6101	18.4354	13.9403	11.7421	5.4501
B	0.9043	0.8891	0.8613	0.7216	0.6313	0.4689
A×*B*	21.4362	19.2135	15.8784	10.0593	7.4128	2.5556

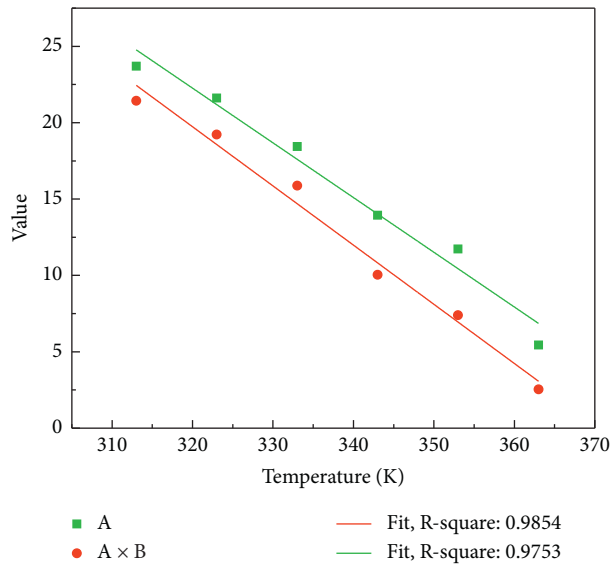

Figure 4: Fitting curves of A and $A{\times}B$ at different temperatures in equation (3).

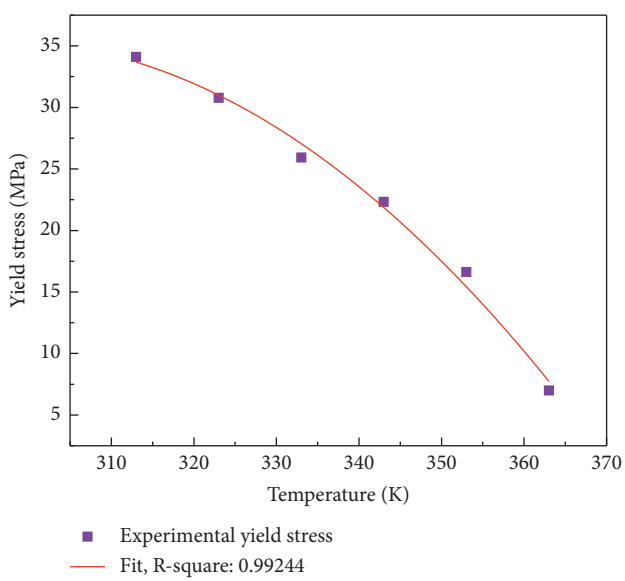

Figure 5: Fitting result of yield stress at different temperatures.

which does not show obvious strain softening and enters directly the plastic stage, as shown in Figure 8.

Equation (9) can be well matched with the experimental results of ABS above the glass transition temperature. The parameters H and G could be calculated on the basis of fitting results, as shown in Figure 9, where $a_8 = 9.0263 \times 10^{-4}$, $b_8 = -0.7160$, $c_6 = 141.9836$, $a_9 = -6.4360 \times 10^{-4}$, $b_9 = 0.5046$, and $c_7 = -98.4584$.

In summary, the parameters of the model were obtained by the fitting in this paper, and the model described the quantitative relationship between stress and strain in a certain temperature range. The quantitative relationship is as follows:When $T < T_g$,

$$\sigma = \begin{cases} (-0.5847 \times T^2 + 360.4405 \times T + 530335.8534) \times \varepsilon; & 0 < \varepsilon \leq 0.25\%, \\ (-0.3582 \times T + 136.8874) \times \varepsilon^{B(T)}; & 0.25\% < \varepsilon \leq \varepsilon_s, \\ (-0.0078 \times T^2 + 5.0474 \times T - 800.33438) \times \varepsilon^{D(T)} + (-0.0065 \times T^2 + 3.8487 \times T - 540.2021); & \varepsilon > \varepsilon_s. \end{cases} \quad (12)$$

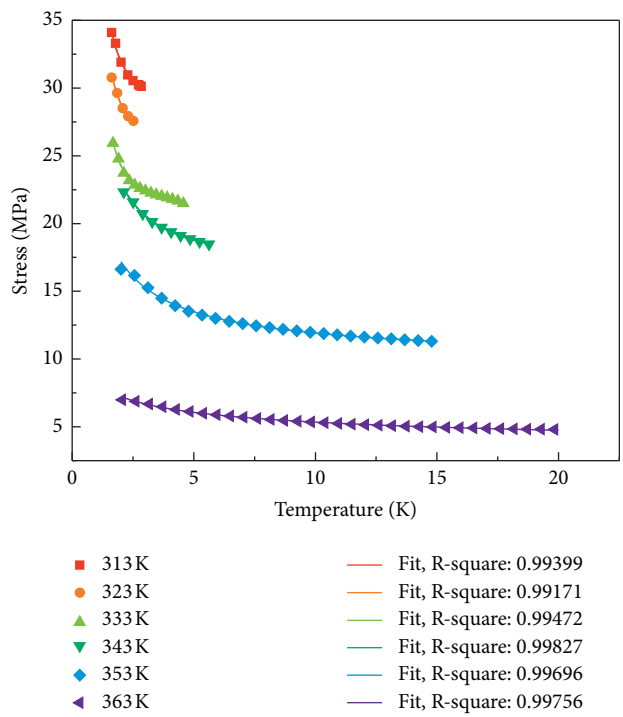

Figure 6: Fitting result of stress in the strain softening stage at different temperatures.

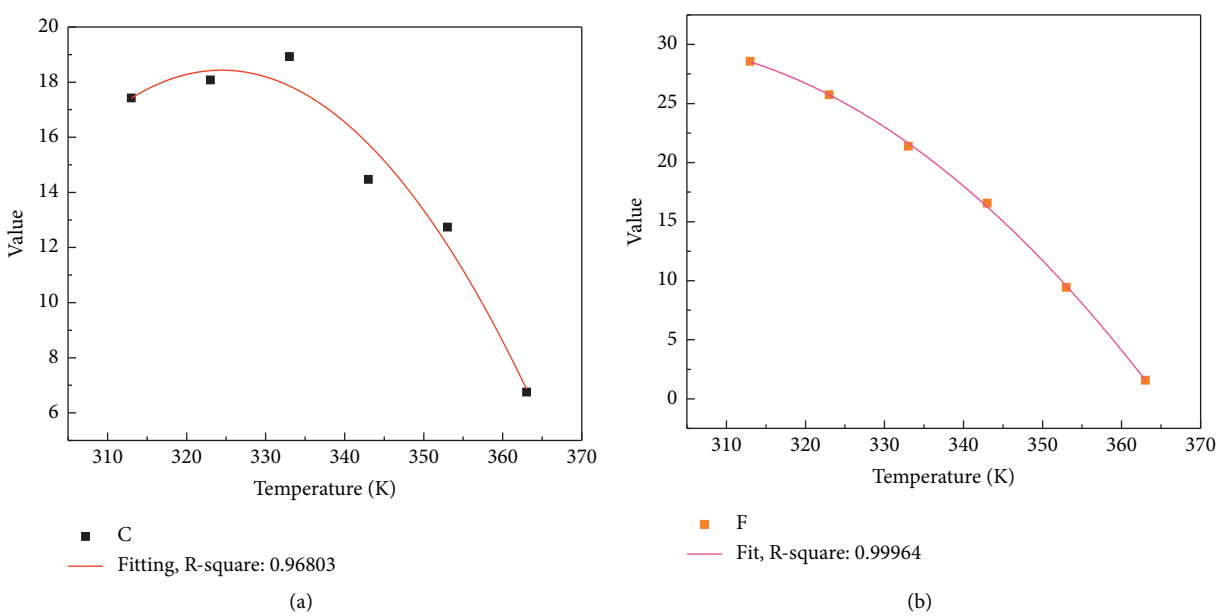

Figure 7: Continued.

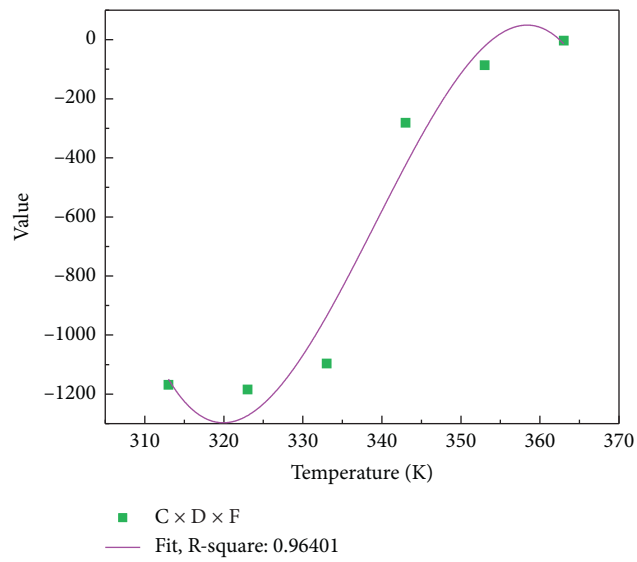

(c)

Figure 7: Fitting result of C, F, and $C \times D \times F$ at different temperatures. (a) C, (b) F, and (c) $C \times D \times F$.

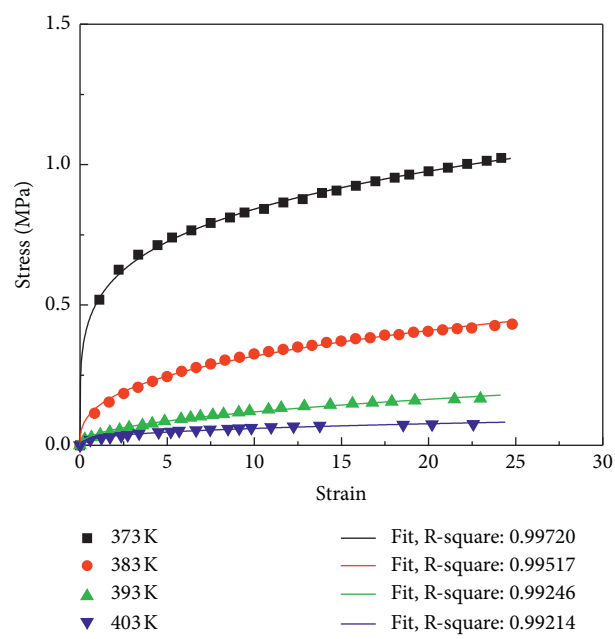

Figure 8: Tensile data of ABS at different temperature (above glass transition temperature).

Also when $T \geq T_g$,

$$\sigma = \left(9.0263 \times 10^{-4} \times T^2 - 0.7160 \times T + 141.9836\right) \times \varepsilon^{G(T)}, \tag{13}$$

where $B(T) = (-0.3875 \times T + 14.7337)/(-0.3572 \times T + 136.8874)$, $\varepsilon_s = -0.0063 \times T^2 + 3.7049 \times T - 513.8276$, $D(T) = (-0.04744 \times T^3 + 48.2651 \times T^2 - 16316.8925 \times T + 1.8322 \times 10^6)/((-0.0078 \times T^2 + 5.0474 \times T - 800.33438) \times (-0.0065 \times T^2 + 3.8487 \times T - 540.2021))$, and $G(T) = -6.4360 \times 10^{-4} + 0.5046 \times T - 98.4584$.

4.2. Verification. To verify the accuracy of the proposed model, the tensile data at 75°C and 115°C were carried out to compare with the data from this model. Combined with the parametric models, the parameters were calculated (Table 4).

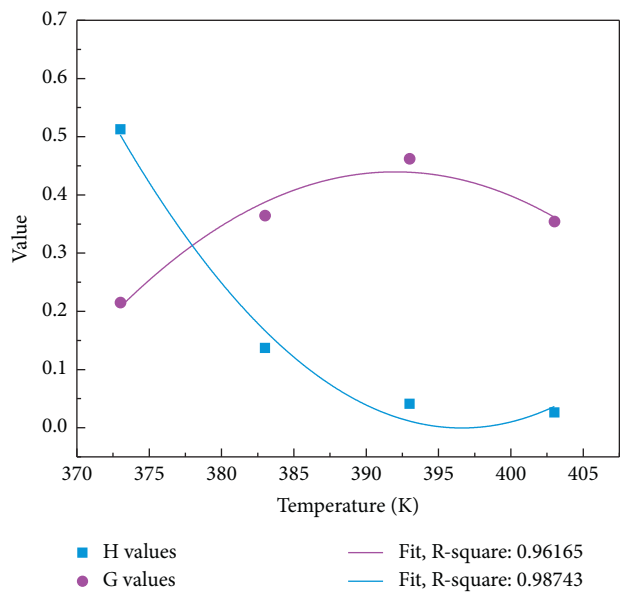

Figure 9: Fitting results of H and G at different temperatures.

Table 4: Parameters of the model at 348 K and 378 K.

Parameters								
348 K ($T < T_g$)				388 K ($T \geq T_g$)				
E	A	B	ε_s	C	D	F	H	G
1587.9318	12.2338	0.7262	1.7748	13.9484	−1.8776	1.1666	0.0681	0.4200

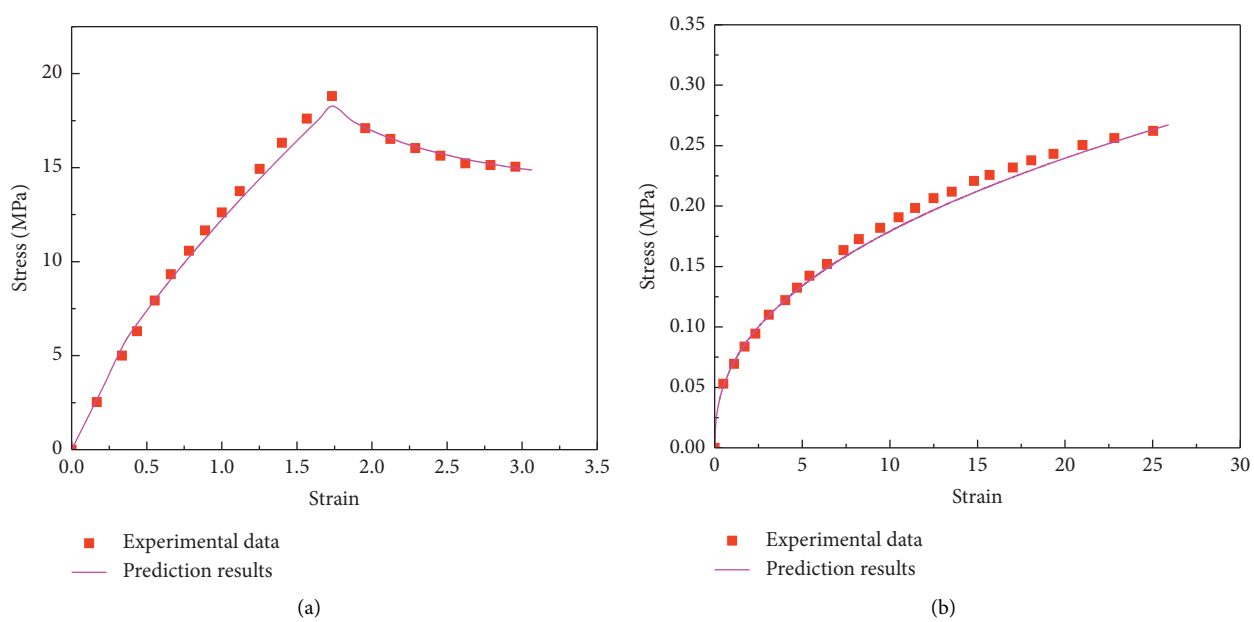

Figure 10: Comparison of experimental data and prediction results at different temperature. (a) 348 K and (b) 388 K.

The comparison of experimental and predicted results at 348 K and 388 K is shown in Figure 10. Clearly, Figure 10 shows that the experimental results agree well with the model predictions by estimated parameters. The small discrepancy can be attributed to material response, which is very complex. Moreover, it is important to emphasize that

the model proposed in this work quantitatively describes the stress-strain relationship of ABS atdifferent temperatures, which reduces the number of experiments.

5. Conclusion

In this study, a model is proposed to describe the tensile behavior of ABS at different temperatures. The temperature significantly influences the properties of ABS, and the model is divided into two parts based on the glass transition temperature. The proposed model equations combine mathematical simplicity that facilitates their application to engineering problems with a physically realistic description of the mechanical behavior of ABS. In addition to that, the model was also verified by comparing the experimental data to prediction data from the proposed model. In general, the proposed model accurately describes the tensile behavior of ABS performed at different temperatures, saving time and experimental costs.

Data Availability

The data used to support the findings of this study are included within the article.

Conflicts of Interest

The authors declare that they have no conflicts of interest.

Acknowledgments

This work was supported by the National Natural Science Foundation under Grant nos. 51575491, 51875525, and U1610112 and by the Natural Science Foundation of Zhejiang Province under Grant nos. LY19E050004, LY18E050020, LY20E050020, and LY19E050009.

References

[1] R. S. Hoy and M. O. Robbins, "Strain hardening of polymer glasses: effect of entanglement density, temperature, and rate," *Journal of Polymer Science Part B Polymer Physics*, vol. 44, no. 24, pp. 3487–3500, 2010.

[2] A. Kozanecka-Szmigiel, J. Antonowicz, D. Szmigiel et al., "On stress-strain responses and photoinduced properties of some azo polymers," *Polymer*, vol. 140, pp. 117–121, 2018.

[3] Y. J. Deng, L. F. Peng, X. M. Lai, M. W. Fu, and Z. Q. Lin, "Constitutive modeling of size effect on deformation behaviors of amorphous polymers in micro-scaled deformation," *International Journal of Plasticity*, vol. 89, pp. 197–222, 2017.

[4] J. Bicerano, N. K. Grant, J. T. Seitz, and K. Pant, "Microstructural model for prediction of stress-strain curves of amorphous and semicrystalline elastomers," *Journal of Polymer Science Part B Polymer Physics*, vol. 35, no. 16, pp. 2715–2739, 2015.

[5] J. Q. Li, T. D. Li, Y. D. Jia et al., "Modeling and characterization of crystallization during rapid heat cycle molding," *Polymer Testing*, vol. 71, 2018.

[6] M. Lei, K. Yu, H. Lu, and H. J. Qi, "Influence of structural relaxation on thermomechanical and shape memory performances of amorphous polymers," *Polymer*, vol. 109, pp. 216–228, 2017.

[7] R. Muthuraj, M. Misra, and A. K. Mohanty, "Biodegradable compatibilized polymer blends for packaging applications: a literature review," *Journal of Applied Polymer Science*, vol. 135, no. 24, 2017.

[8] K. L. Camera, B. Wenning, A. Lal, and C. K. Ober, "Transient materials from thermally-sensitive polycarbonates and polycarbonate nanocomposites," *Polymer*, vol. 101, pp. 59–66, 2016.

[9] X. Rui and T. D. Nguyen, "An effective temperature theory for the nonequilibrium behavior of amorphous polymers," *Journal of the Mechanics & Physics of Solids*, vol. 82, pp. 62–81, 2015.

[10] R. M. Shay and J. M. Caruthers, "A predictive model for the effects of thermal history on the mechanical behavior of amorphous polymers," *Polymer Engineering & Science*, vol. 30, no. 20, pp. 1266–1280, 2010.

[11] T. Yokoyama and K. Nakai, "Determination of high strain-rate compressive stress-strain loops of selected polymers," *Applied Mechanics and Materials*, vol. 24-25, pp. 349–355, 2010.

[12] C. Park, H. Huh, J. Kim, and C. Ahn, "Determination of true stress-true strain curves of polymers at various strain rates using force equilibrium grid method," *Journal of Composite Materials*, vol. 46, no. 17, pp. 2065–2077, 2012.

[13] S. Behzadi and F. R. Jones, "Yielding behavior of model epoxy matrices for fiber reinforced composites: effect of strain rate and temperature," *Journal of Macromolecular Science, Part B*, vol. 44, no. 6, pp. 993–1005, 2005.

[14] J. Richeton, S. Ahzi, K. S. Vecchio, F. C. Jiang, and R. R. Adharapurapu, "Influence of temperature and strain rate on the mechanical behavior of three amorphous polymers: characterization and modeling of the compressive yield stress," *International Journal of Solids and Structures*, vol. 43, no. 7-8, pp. 2318–2335, 2006.

[15] W. Blumenthal, C. Cady, and D. J. Idar, "Influence of temperature and strain rate on the compressive behavior of PMMA and polycarbonate polymers," *AIP Conference Proceedings*, vol. 620, pp. 665–668, 2002.

[16] C. M. Cady, W. R. Blumenthal, G. T. Gray, and D. J. Idar, "Determining the constitutive response of polymeric materials as a function of temperature and strain rate," *Journal de Physique IV*, vol. 110, no. 1, pp. 27–32, 2003.

[17] E. H. M. Han and L. E. Govaert, "Mechanical performance of polymer systems: the relation between structure and properties," *Progress in Polymer Science*, vol. 30, no. 8, pp. 915–938, 2005.

[18] M. M. K. Khan, C. J. Hilado, S. Agarwal, and R. K. Gupta, "Flammability properties of virgin and recycled polycarbonate (PC) and acrylonitrile-butadiene-styrene (ABS) recovered from end-of-life electronics," *Journal of Polymers and the Environment*, vol. 15, no. 3, pp. 188–194, 2007.

[19] C.-Y. Chang, J.-S. Chang, Y.-W. Lin, L. Erdei, and S. Vigneswaran, "Quantification of air stripping and biodegradation of organic removal in acrylonitrile-butadiene-styrene (ABS) industry wastewater during submerged membrane bioreactor operation," *Desalination*, vol. 191, no. 1–3, pp. 162–168, 2006.

[20] Global ABS Market Sales Will Grow by 6% Annually to $38 Billion, http://info.plas.hc360.com/2017/06/261155615858.shtml.

[21] Y. Yao, N. Liao, Z. Miao, and F. Li, "Evaluation of the elastic-plastic properties of SiCN coating system by finite element

simulations," *Journal of the European Ceramic Society*, vol. 37, no. 13, 2017.

[22] J. D. Wang, *General Engineering Plastics Standards Compilation*, Standards Press of China, Beijing, China, 2013.

[23] S. Dul, L. Fambri, and A. Pegoretti, "Fused deposition modeling with ABS-graphene nanocomposites," *Composites Part A: Applied Science and Manufacturing*, vol. 85, pp. 182–191, 2016.

[24] E. Bociaga, "The effect of mold temperature and injection velocity on selected properties of polyethylene moldings," *Polimery*, vol. 45, no. 11/12, pp. 830–836, 2000.

Hindawi
Advances in Polymer Technology
Volume 2020, Article ID 7023616, 22 pages
https://doi.org/10.1155/2020/7023616

Review Article

Intelligent Injection Molding on Sensing, Optimization, and Control

Peng Zhao,[1,2] **Jianfeng Zhang**,[1,2] **Zhengyang Dong**,[1,2] **Junye Huang**,[1,2] **Hongwei Zhou**,[3] **Jianzhong Fu**,[1,2] **and Lih-Sheng Turng**[4,5]

[1]*The State Key Laboratory of Fluid Power and Mechatronic Systems, College of Mechanical Engineering, Zhejiang University, Hangzhou 310027, China*
[2]*Key Laboratory of 3D Printing Process and Equipment of Zhejiang Province, College of Mechanical Engineering, Zhejiang University, Hangzhou 310027, China*
[3]*Tederic Machinery Co., Ltd., Hangzhou 311224, China*
[4]*Department of Mechanical Engineering, University of Wisconsin-Madison, Madison, WI 53706, USA*
[5]*Wisconsin Institute for Discovery, University of Wisconsin-Madison, Madison, WI 53715, USA*

Correspondence should be addressed to Peng Zhao; pengzhao@zju.edu.cn and Lih-Sheng Turng; turng@engr.wisc.edu

Received 1 August 2019; Accepted 25 November 2019; Published 31 March 2020

Academic Editor: Federico Carosio

Copyright © 2020 Peng Zhao et al. This is an open access article distributed under the Creative Commons Attribution License, which permits unrestricted use, distribution, and reproduction in any medium, provided the original work is properly cited.

Injection molding is one of the most significant material processing methods for mass production of plastic products. It is widely used in various industry sectors, and its products are ubiquitous in our daily life. The settings and optimization of the injection molding process dictate the geometric precision and mechanical properties of the final products. Therefore, sensing, optimization, and control of the injection molding process have a crucial influence on product quality and have become an active research field with abundant literature. This paper defines the concept of intelligent injection molding as the integral application of these three procedures—sensing, optimization, and control. This paper reviews recent studies on methods for the detection of relevant physical variables, optimization of process parameters, and control strategies of machine variables in the molding process. Finally, conclusions are drawn to discuss future research directions and technologies, as well as algorithms worthy of being explored and developed.

1. Introduction

The Society of the Plastics Industry (SPI) has reported that, in the United States, the plastics industry is the third largest manufacturing industry. In 2017, the US plastics industry accounted for $432.32 billion in annual shipments and directly employed nearly one million people [1]. Hence, the plastics industry has a large contribution to the nation's economy. Plastics are now among the most widely used materials and their use covers the entire spectrum of industries worldwide [2]. Injection molding is regarded as the most important and efficient process used to manufacture plastic products. It accounts for approximately 80% of the plastic merchandise in the modern plastics industry [2], and as such, it is one of the important pillars of the manufacturing industry. As a highly complicated process, plastic injection molding can be divided into three stages: filling, packing, and cooling. During the entire process, the polymer is subject to large and dynamic changes in pressure and temperature. The whole process is complicated because the process variables are strongly coupled and hard to analyze accurately. For now, manufacturing of qualified products by injection molding still mainly relies on manual operation and trial-and-error methods [3–5]. Obviously, this traditional approach has disadvantages of low production efficiency, poor reliability and repeatability, and dependence on prior experience. Therefore, it is imperative and crucial to develop an advanced injection molding method that is science based and technology oriented.

Recently, much attention has been focused on intelligent (smart) manufacturing, which represents an in-depth integration of next-generation artificial intelligence (AI) technology and advanced manufacturing technology. It runs through every link in the full life cycle of design, production, product, and service [6]. Intelligent injection molding refers to the production process that employs AI technology—such as extracting information from production, computer optimization methods, and control strategies—to develop an online production optimization system. Through the comprehensive use of sensing, optimization, and control methods, the intelligent injection molding production process can increase production efficiency and product quality.

During the production process, when material and mold are preselected, an intelligent injection molding method is required to obtain high quality and stable production. As shown in Figure 1, intelligent injection molding contains three phases—sensing, optimization, and control—all of which are interrelated. Process sensing is first needed to realize real-time detection of variables from the injection-molding process and further on to diagnose and guide the manufacturing process. Moreover, optimal process parameters should be determined by process optimization since it is the key to obtaining high-quality injection molded products with high precision. Finally, sufficient machine control accuracy and repeatability—which means robust control over machine parameters—are required. Furthermore, advanced control strategies will help to conserve energy in manufacturing [7]. Integrating these three phases into an effective online quality control model, which is the section in the dotted-line frame in Figure 1, is one of the major goals of intelligent injection molding. It has attracted extensive attentions from many researchers in the field of injection molding.

In a 2005 review article, injection molding control [8] after process setup was classified into three levels—machine control, process control, and quality control. Due to the lack of quality sensors and the process and quality relationship model, there is a potential opportunity for advancement in the optimization and control of the product quality in injection molding. Moreover, with further development of science and technology in injection molding, and the fact that there has been very little review of process sensing, this paper aims to review and summarize the research on intelligent injection molding in recent years. It will focus on sensing, optimization, and control so that readers will be able to obtain useful information and an overview of the intelligent injection molding process. This paper is outlined as follows. Section 1 provides a brief introduction of intelligent injection molding. Sections 2, 3, and 4 discuss sensing, optimization, and control methods for the injection molding process and present up-to-date developments in these fields. The last section provides a summary of and future directions for intelligent injection molding.

2. Process Sensing

The sensing of the injection molding process is focused on the temperature, pressure, position, speed, etc., which reflect the physical state of the process. Temperature and pressure are the two fundamental physical variables that are the most important in the injection molding process. Furthermore, among various sensing technologies, temperature and pressure sensors are the most well developed and the most widely utilized. By means of sensing the temperature and pressure, one can obtain abundant information about the mold and polymer melt. With continuing technology development, some new methods have emerged in the field of injection molding. Some of them are capable of characterizing more variables besides temperature, pressure, position, and speed. This section will briefly introduce the conventional and emerging methods used in injection molding processes and the up-to-date research progress. Finally, a conclusion and analysis will be put forward and discussed.

2.1. Conventional Methods. Temperature and pressure are the most important variables in the injection molding process. As such, they have received the most attention. Therefore, traditional pressure and temperature sensors are maturely developed and have been the most important tools in measuring the melt state and in characterizing product quality (cf. Figure 2(a)).

2.1.1. Pressure Measurement. Pressure sensors come in mainly two types—resistance and piezoelectricity—which generate resistance changes and voltage changes, respectively, in response to the different pressure levels to characterize the value of the pressure. Commercial pressure sensors have advanced rapidly. In recent years, commercial pressure sensors have been widely used to study the correlation between melt pressure and various parameters of the injection molding process [12–15]. Furthermore, pressure sensors have also been utilized to study the correlation between the cavity pressure curve during the injection/packing stage and the final deformation of the molded part [16]. The results indicated that the pressure difference of the melt at two locations along the radial flow path was related to the part deformation, which could then be used to characterize the warpage of the molded product. Mao et al. [17] proposed a novel automatic feature learning method using cavity pressure data. The results showed that the proposed method could achieve higher classification accuracies and offer more optimal solutions for process monitoring. Based on these studies, online cavity pressure curves can be used to characterize injection process parameters and product quality. Since the value of cavity pressure that the pressure sensor detects usually turns out to be a one-dimensional (1D) value (in the normal direction), Heinle and Drummer [18] therefore proposed a standard three-way force sensor, which was stiffly connected to the measurement element in the cavity to measure the 3D force in a cavity. However, installing direct pressure sensors sometimes introduces product defects in the form of surface sensor marks.

In recent studies, researchers have put forward some alternative methods for cavity pressure measurements in order to maintain the integrity of the part and mold. Gim et al. [10] installed indirect pressure sensors under the lens

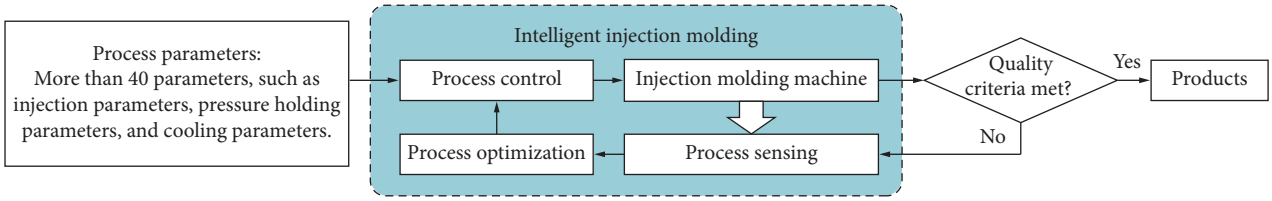

Figure 1: Schematic of an intelligent injection molding process.

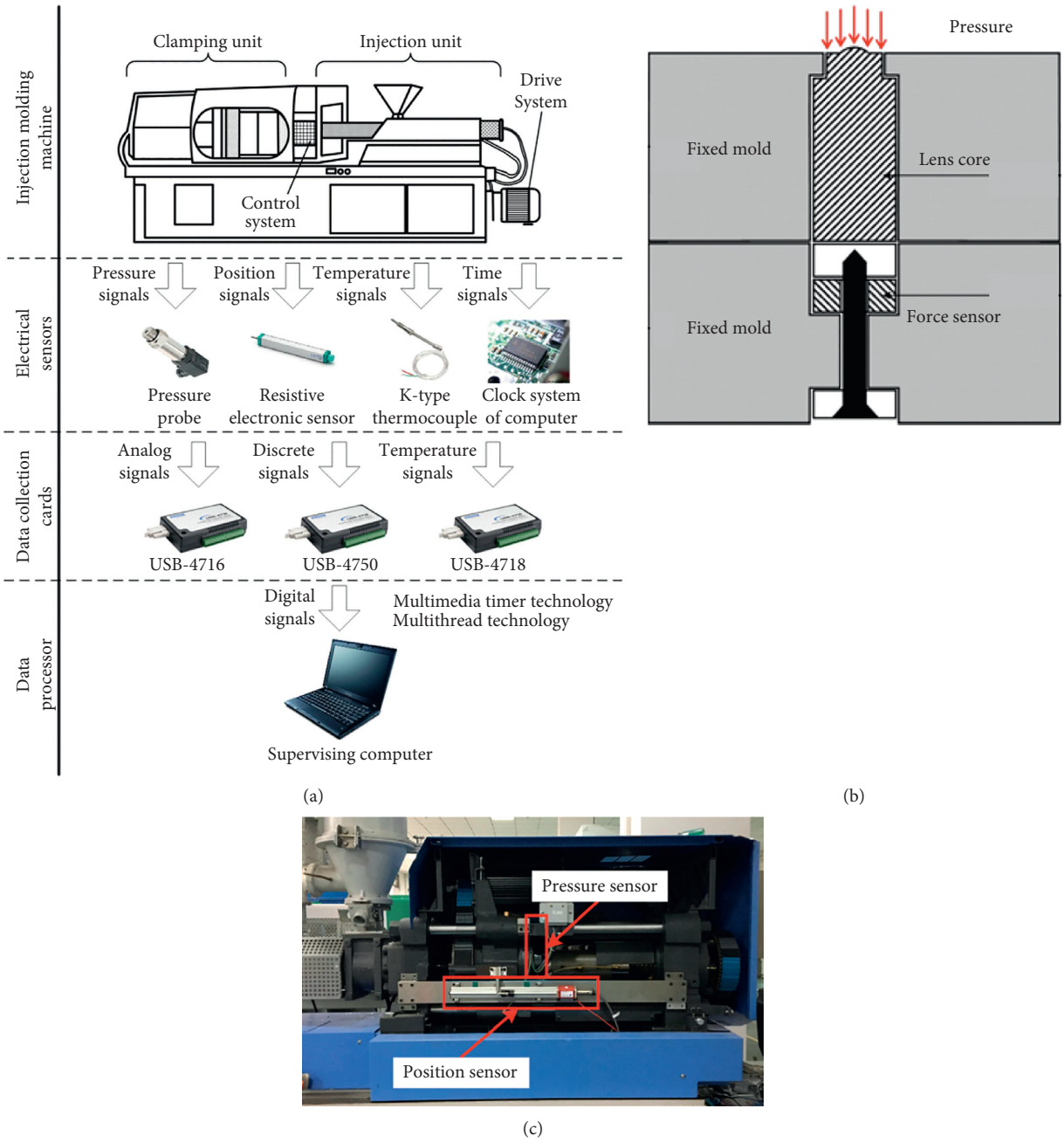

Figure 2: (a) Conventional sensors used in online sensing of injection molding process [9]. (b) Illustration of an indirect pressure sensor [10]. (c) The injection molding machine with respect to position and pressure sensors equipped [11].

core to monitor filling imbalance and short shots without causing product defects (cf. Figure 2(b)). Tsai and Lan [19] investigated the correlation between melt pressure and cavity pressure in different runner positions and identified the runner position where the local runner pressure represented the cavity pressure. In addition, product quality can be monitored by installing sensors at different runner positions. Guan and Huang [20] used a surface strain sensor and pressure sensors installed at the cavity and surface of the mold, respectively, and found that the cavity pressure was proportional to the mold surface strain through a data-based regression method. Using this correlation, the precise cavity pressure distribution could be obtained indirectly via mold surface strain data. Furthermore, some quality monitoring methods using other pressure sensors have also been proposed. Zhang et al. [21] proposed a statistical quality monitoring method for injection molding, which used only hydraulic pressure and screw position data obtained from built-in machine sensors. With the present method, the rate of successful fault detection was excellent. Zhou et al. [11] established a quality prediction model based on polymer melt properties to monitor product weigh variation online. The pressure integral, which was obtained by using the machine's built-in injection pressure sensor, was used as an effective process variable to predict product weight variation (cf. Figure 2(c)).

2.1.2. Temperature Measurement. Thermocouples and infrared temperature sensors are the two most common sensors for online temperature detection in the injection molding process. A thermocouple is a kind of sensor that transforms thermal potential difference into electrical potential difference. According to the selected conductive material, it can be classified into S, B, K, E, T, and J types. Considering the cost and the working environment, J-type and K-type thermocouples are usually used. Thermocouples are widely used in the development and operation of rapid heat cycle molding (RHCM) [22–27], which is a process that rapidly changes the surface temperature of the mold during the injection and cooling stages for the purpose of producing products with special features, such as high-gloss surfaces, without prolonging the cycle time. Temperature sensors can feasibly monitor the temperature of the mold, cavity surface, and heat transfer medium (e.g., the coolant).

However, when detecting the melt temperature, the thermocouple can only measure the contact temperature at the contact point between the material (mold or melt) and the sensor, and this measurement is unlikely to be characteristic of the bulk temperature of the melt. Johnston et al. [28] developed an analysis that used the data from an in-mold thermocouple to predict the bulk melt temperature of a plastic. The heat flux through the mold steel was taken into account to calculate the overall melt temperature and the result was verified by an infrared (IR) temperature sensor. In another study, by measuring the instantaneous melt temperature, Yang et al. [29] investigated the crystallization and solidification kinetics during injection molding, which represented another usage of a thermocouple in injection molding.

Injection molding is known as a process that is accompanied by drastic changes in both temperature and pressure. In order to reveal more online process information during injection molding, the comprehensive use of various sensors has become a commonly used research approach. Gao et al. [30, 31] obtained online melt viscosity and speed through the combined use of a variety of sensors (thermocouples, infrared temperature sensors, pressure sensors, and multitemperature and pressure sensors, cf. Figure 3). The viscosity and speed were calculated from the measured values from those sensors. Mendibil et al. [32] monitored pressure and temperature transducers located in a runner system and microfeatured cavity and further achieved online quality inspection and quality test results from a confocal microscope.

2.2. Emerging Methods. To obtain melt information other than temperature and pressure, some emerging methods have been employed for injection molding process sensing. Such emerging methods include ultrasound, visualization molds, X-ray computed tomography, capacitive sensors, and magnetic levitation detection. These methods will be introduced as follows.

2.2.1. Ultrasound. Ultrasound waves are mechanical waves whose frequencies are greater than 20 kHz [33]. Ultrasonic technology is a promising method for the characterization of polymer processes as it can be applied in real time and online, as well as being nondestructive and environmentally friendly [34–36]. Ultrasound waves reflect at the surface of the media, and the attenuation and speed of the waves change according to the properties of the media. By studying the relationship between the attenuation and speed of ultrasound pulse-echoes and the physical properties of the polymer, this method has been applied in many studies for offline detection of injection molded parts [37, 38]. Similarly, ultrasound can be applied online for quality detection during the production process [39].

Based on the principle of the ultrasonic method, online detection of the material in the barrel and nozzle during injection molding can be realized. For example, the solid bed to melt pool ratio has been quantified using a noninvasive ultrasound system based on reflection measurements [40]. Automated analyses of the reflected pulses were also realized, which means that the plasticization process can be monitored online at different axial positions along the barrel. Praher and Steinbichler [41] measured the clearance between screw and barrel in the plasticization unit of an injection molding machine, where the wear status of the tribomechanical screw-barrel system and unsuitable process conditions could be detected. Moreover, besides the melt content and melt condition in the plasticizing process being detected by ultrasound, a noninvasive ultrasound tomography system was also proposed by Praher et al. [42, 43]. An ultrasound transmitter and five ultrasound receivers were employed, and five individual sound paths through the polymer melt were achieved (cf. Figure 4(a)). Thus, the temperature distribution in the polymer melt could be

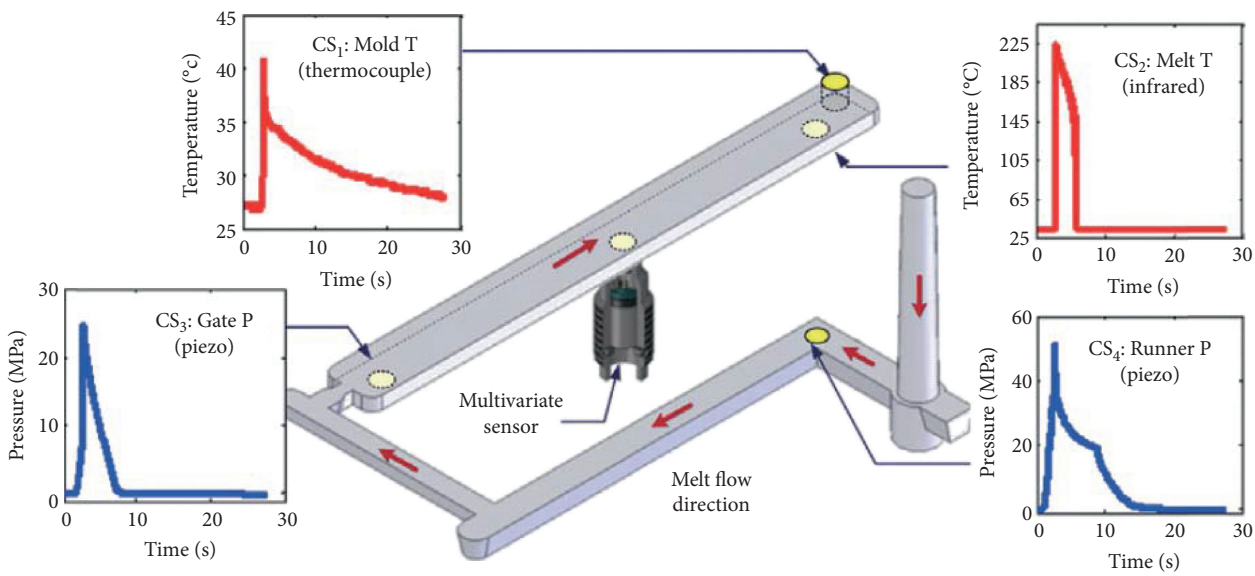

Figure 3: Process instrumentation using commercial sensors (CS) for pressure (P) and temperature (T), as well as a developed multivariate sensor (MVS) within an injection mold cavity [30].

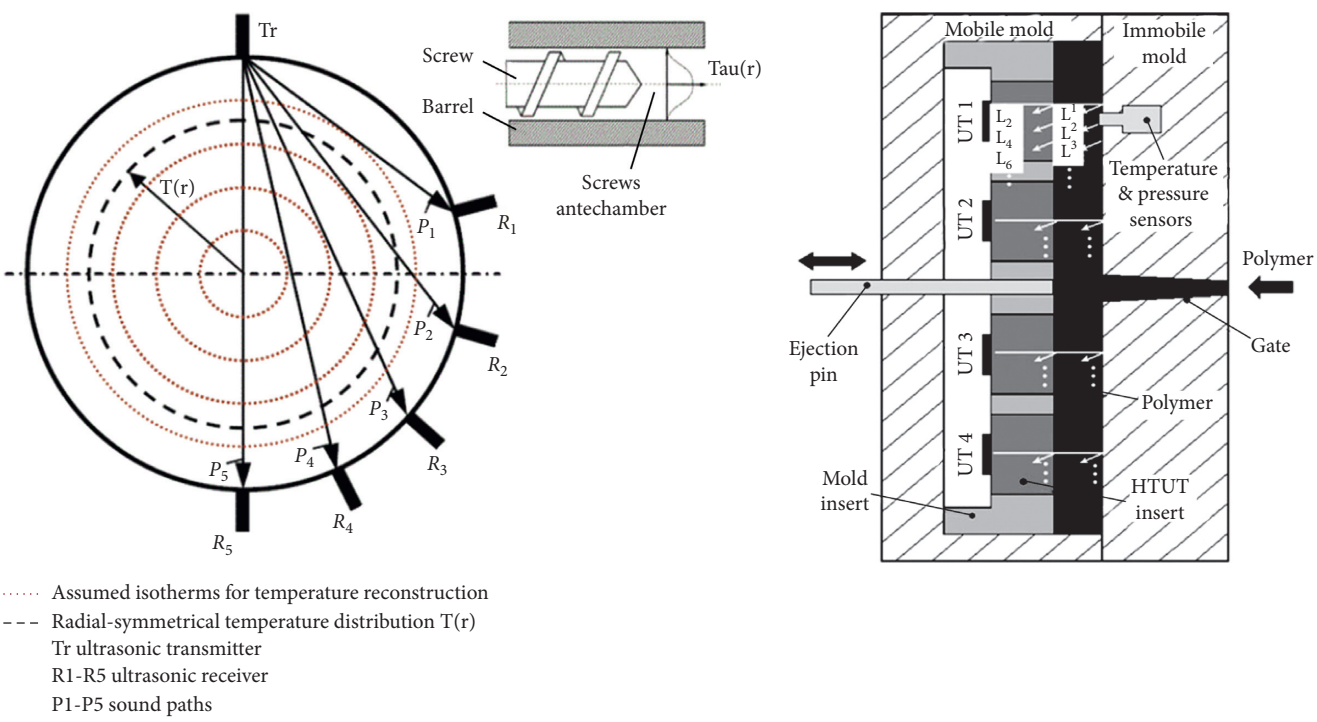

Figure 4: (a) Positions of the ultrasound transducers and resulting sound paths through the concentric ring segments used in ultrasound tomography [43]. (b) A cross-sectional view of an in-mold detection system [44].

calculated by analyzing the transmission times of the ultrasound pulses through different sound paths. Ultrasound probe design strategies were also discussed, given that conventional ultrasound transducers cannot endure high temperature environments, such as the injection barrel.

Ono et al. made a great contribution in this area. Specifically, a high temperature ultrasonic transducer was invented and applied in microinjection molding [45], coinjection molding [46], and gas-assisted injection molding processes [47] for online polymer characterization. By installing high temperature ultrasound transducers at the nozzle location, Wu et al. [48, 49] revealed the flow characteristics of the polymer melt and the flow conditions at the nozzle. The melt flow characteristics at the nozzle, including

the dynamic flow speed and density of the polymer melt, can be monitored online.

The detection of in-mold information by ultrasound reveals abundant information about the process and the properties of the melt during the injection molding process. The microcellular injection molding (MIM) process was also characterized by an in situ ultrasonic method [50] (cf. Figure 5). In this study, cell size, surface roughness, and skin layer thickness of the products were characterized by ultrasonic echo signal. Moreover, the detection of longitudinal waves characterized the injection process data and polymer morphological changes in real time, including the melt front arrival time, injection time, filling and packing stages, polymer solidification process, and morphological changes in the polymer crystallization [44, 51]. Shear waves in real time diagnosed Young's modulus and shear storage modulus, as well as the anisotropic properties of the polymer in the injection molding process [44] (cf. Figure 4(b)). Although the methods and theory used here are quite similar to those used to detect plasticization, this part of the measurement is an online, nonisothermal process that is quite difficult to implement. The data is difficult to analyze as well.

Our research group proposed an ultrasonic methodology to measure cavity pressure during the injection molding process via the Gaussian process [9, 52]. Recently, we employed an ultrasonic method to measure the stress on the tie bars of an injection molding machine, therefore monitoring the service situation of the machine [53, 54]. We also established a physical model to estimate the correlation between the cavity pressure and stress on the tie bars and as such achieved an indirect measurement of the cavity pressure via the stress on the tie bars [55].

2.2.2. Visualization Molds. Because the molten polymer behavior during the injection molding process is carried out in a closed cavity, the molding process cannot be observed by the naked eye. Therefore, researchers often develop a visualization mold combined with a high-speed camera to observe the molding process [56–60]. Guerrier et al. [56, 57] developed a visualization mold by replacing part of the mold steel with glass to observe and verify the accuracy of a 3D numerical simulation of the injection molding process carried out by computer molding and obtained ideal results (cf. Figure 6). Jong et al. [58] added aluminum glitter powder to the melt to observe and track the flow trajectory of the particles in the melt to observe the fountain flow effect at the melt front. Jiang et al. also developed a visualized experimental device to observe the flow of the polymer melt of coinjection molding and ultrasonic-assisted injection molding process [59, 60].

2.2.3. X-Ray Computed Tomography. For injection molding parts, the researchers paid most attention to the mechanical properties of the products. However, the surface replicability and internal structure of the parts could be more concerned in a considerable part of the situation. These properties of the products have yet been difficult to be characterized and there is rarely related research. The application of computed tomography (CT) in industry is rapidly increasing. CT scanning is capable of evaluating the voxel-based and surface-based characteristic [61]. As being voxel based, it can serve as a visualization method and give the images of the inner structure of the work pieces. It is widely applied in the defect detection and fiber orientation distribution observation [62–64] of the injection molded parts (cf. Figure 7(a)). As being surface based, such as digitization and dimensional metrology [65], it can measure the surface profile and deviation of injection molded parts (cf. Figure 7(b)). Certainly, it requires accuracy and traceability. In addition, CT scanning still has its limitations; the faster cycle time and better economy need to be achieved for wider manufacturing applications.

2.2.4. Capacitive Sensors. Capacitance is a useful physical phenomenon for sensor design. It has been successfully applied for measuring the distance, area, volume, force, humidity, etc., in industry [66]. If two metal plates can be separately installed on the two mold halves and isolated from each other, they can form the two electrodes of a capacitor. Such a capacitive sensor for the measurements of the melt front position and melt front velocity has been proposed for injection molding process monitoring [66–69]. Due to the filling of the polymer melt, the capacitance between the two electrodes changes, resulting in a change of voltage on the capacitor. The principle and installation scheme of a capacitive transducer are shown in Figure 8(a). The ratio of polymer to air causes variations in the dielectric properties of the capacitor, further resulting in a change of voltage on the electrodes.

Capacitive sensors can detect not only the polymer melt front position and melt flow rate [69], but also the start and end of mold filling, the time of gate freezing, and overpacking [66]. The sensor outputs can be further correlated to online part weight prediction and also the measurement of the part solidification rate [68]. Combined with data-based regression analysis, this type of sensor could be used for online monitoring, part weight prediction, and check-ring failure detection for injection molding [67].

Based on the same principles as dielectrics, a rheodielectric sensor, also called a planar capacitor sensor, has been developed with interdigitated electrodes deposited on the surface of the substrate adjacent to the dielectric material [70]. Interdigitated electrodes are electrode strips arranged like the interlocking fingers of two hands folded together (cf. Figures 8(b) and 8(c)). This kind of sensor can be mounted on the cavity surface, where the voltage variation on the electrodes reflects the dielectric constant of the material, which is related to the shear stress and orientation of the material [71–73]. Therefore, the planar capacitor sensor is able to measure the shear stress and orientation of the material in the injection molding process.

2.2.5. Magnetic Levitation. Quality detection of final parts is an important component of injection molding production. In the field of materials science, there are several characterization methods including wide angle X-ray diffraction

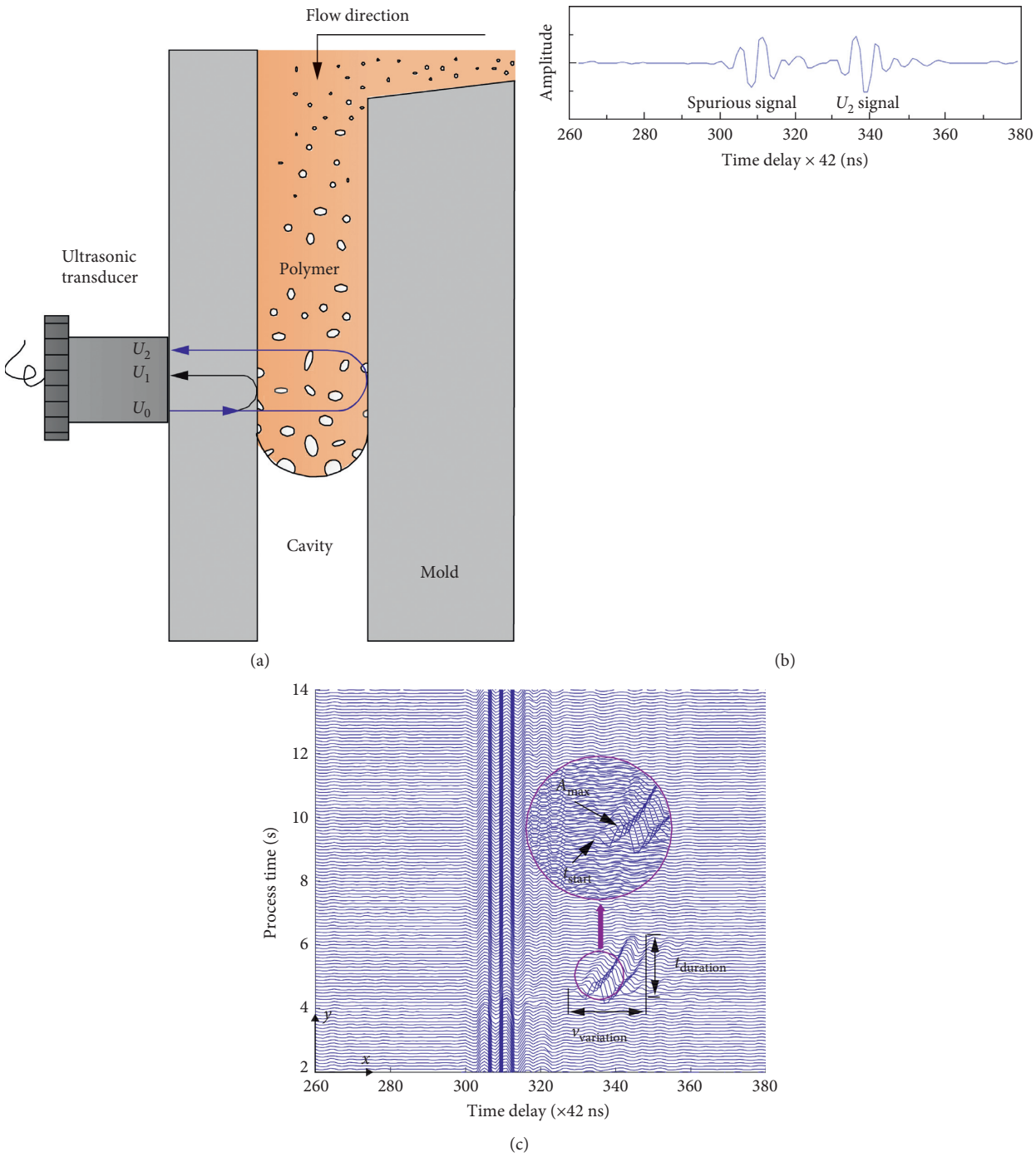

Figure 5: An ultrasonic pulse-echo measurement method for online characterization of (a) a cross-sectional schematic view of a mold with an ultrasonic transducer, (b) a typical single signal received with the transducer, and (c) typical U2 ultrasonic signals over a microcellular injection molding (MIM) process cycle [50].

(WAXD) [74–79], nanocalorimetry [80], and X-ray tomography [62, 63]. These methods are generally and widely utilized for measuring physical properties of final products. They have excellent characterization accuracy, but the cost of equipment is usually very high.

A magnetic levitation detection method has been proposed by Mirica and colleagues in 2009 for measuring density [81], which also is called the MagLev method. The device consists of two identical permanent magnets set 45 mm apart, with identical poles facing each other. The sample is immersed in paramagnetic media and is then levitated at an equilibrium position along the centerline of the device (cf. Figure 9(a)). According to the levitation height, the density of the sample can be calculated. The accuracy of the device is estimated as 0.0002 g/cm^3. Many researchers focus on developing MagLev technology and

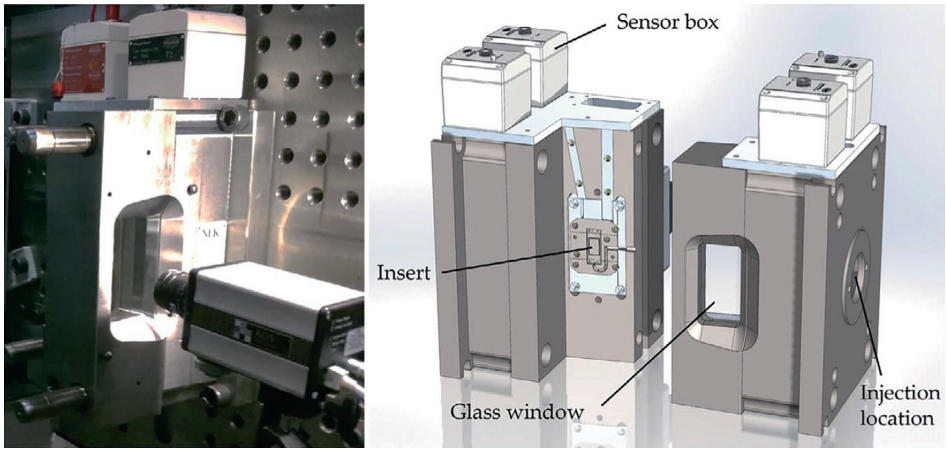

Figure 6: Schematic overview of the visualization mold [57].

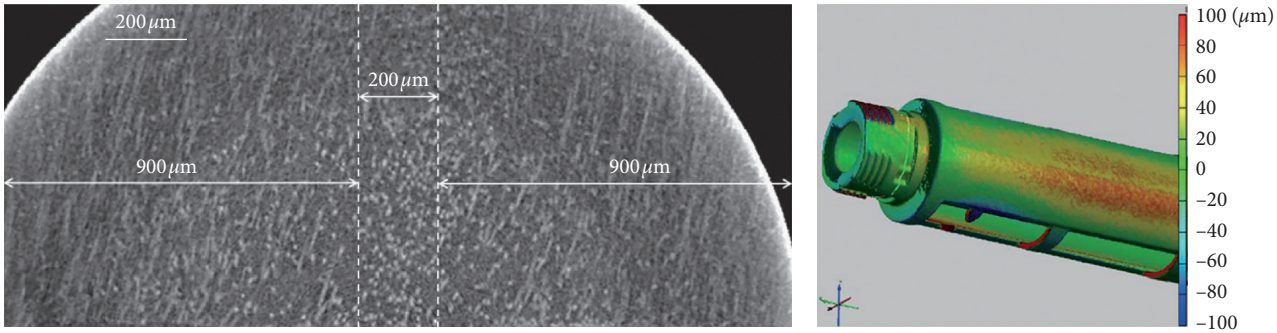

(a) (b)

Figure 7: (a) Fiber orientation of the GF/PA6 specimen shown by the longitudinal section X-ray CT image [64]. (b) Comparison with the CAD model of an injection molded cartridge holder [61].

have done many works and achievements on this particular field [81, 82, 85–87]. By flattening the device (cf. Figure 9(b)), the ability to measure samples with large densities was achieved [83, 88, 89]. Moreover, our research group employed ring magnets to MagLev [90, 91] ensuring better visibility, accessibility, and operability of the samples.

The research by Subramanian and colleagues found that the levitation posture of a sample was correlated with the sample's shape [92]. Hence, Hennek's work explored the possibility of using the MagLev method for quality control of plastic parts [93]. Recently, our research group further analyzed the correlation between the position of the defects and the levitation posture of the sample [94, 95]. This method is further applied in the evaluation of washers [82] and injection molded lens [96] and subtle differences could be detected (cf. Figure 9(c)). Besides, based on its high accuracy, the MagLev method was also studied in separating and recycling different polymers via small differences in density [84, 97, 98] (cf. Figure 9(d)).

In summary, ultrasound is an outstanding and integrated method for online process sensing of injection molding as it is a nondestructive method that provides rich information. CT scanning can provide abundant product quality features. MagLev is a good emerging method for product defect detection. It has excellent measurement accuracy at a low cost, making it worthy of pursuing.

3. Optimization of Process Parameters

The injection molding process involves dozens of process parameters such as injection speed and pressure, packing duration and pressure, mold temperature, and cooling time. The effects of these parameters are coupled to each other, which makes it very difficult to set the process parameters and often relies heavily on the long-term experience of skilled operators.

Many studies have been conducted for the optimization of injection molding processes in order to reduce the time to market and to obtain consistent quality molded parts, and some methods have been put forward. Generally, these optimization methods can be classified into three categories. The first category involves identifying optimal process settings by noniterative analysis based on experimental or simulated results. It also involves analysis based on past experience. The second category establishes relationships between process parameters and product quality through experiments based on the approximate mathematical function obtained by a surrogate model. The third category

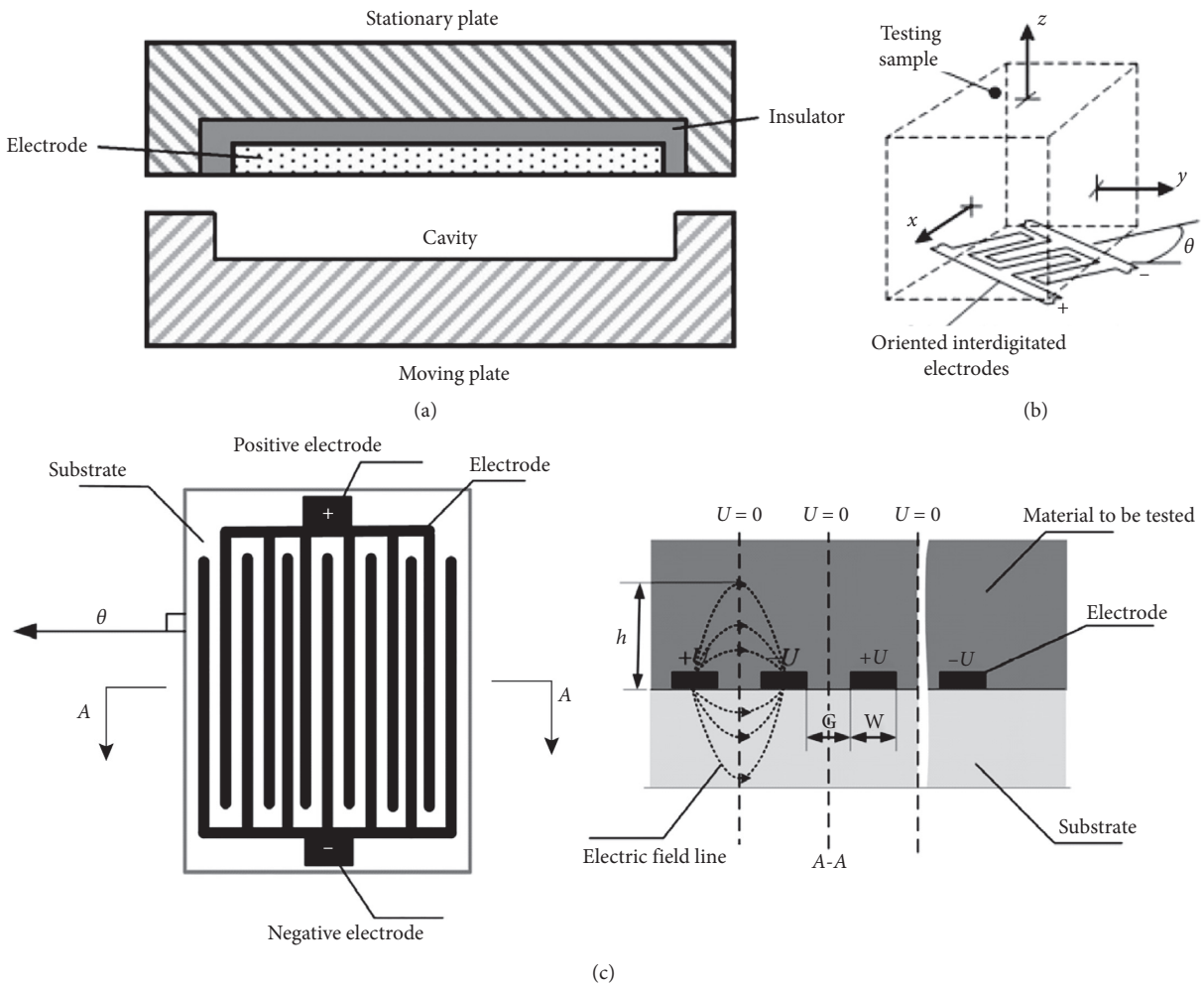

Figure 8: (a) Schematic view of the capacitive transducer installed in the injection mold [68]. (b) Interdigitated electrodes located in the *xy*-plane form an angle, θ, with respect to the *y*-axis [70]. (c) Schematic diagram of interdigitated electrodes.

uses a global search process in a given parameter area, as established by a surrogate model, using intelligent optimization algorithms that follow some rules in nature. These three categories are usually integrated when solving a practical problem and will be introduced in this section.

3.1. Noniterative Optimization Methods. Noniterative methods are generally based on experimental results and practical experiences. They can provide initial process settings or give a direction or route toward optimization. Noniterative optimization methods are easy to implement and require less computation. They have been widely used in research, including the following methods: case-based reasoning (CBR) [3], expert system, fuzzy system [99], and the Taguchi method [100–116].

When optimizing process parameters, implementing a set of real injection molding experiments [111] is a reliable way to gain product quality information under certain parameter settings. However, due to time, expense, and other reasons, a method using simulation analysis [101–104, 107–110, 117–120] is more likely to be used in research to characterize the impact of various levels of various parameters on the product quality. Some common software packages for simulation include Moldflow, Moldex3D, HsCAE, and ANSYS.

3.1.1. Taguchi Method. The Taguchi method is an effective approach for optimizing the throughput in various manufacturing-related processes. It has been extensively used in the engineering design and analysis of optimal manufacturing parameters [121, 122]. It provides an optimization framework according to experiments and data analysis. Its concrete steps can be divided into (1) determination of the experimental parameters and their levels, (2) design of experiments, (3) implementation of experiments, and (4) data analysis. By analyzing the quality of injection molded products with different parameters, the influence of the process parameters on product quality can be accessed by means of analysis of variance (ANOVA), range analysis, and analysis of signal-to-noise ratio (S/N). Finally, relatively optimal parameter settings can be determined.

Applying the Taguchi method, Kuo and Liao [100] and Lin and Hsieh [101] investigated the influence of parameters on the accuracy of lens geometry. Many other

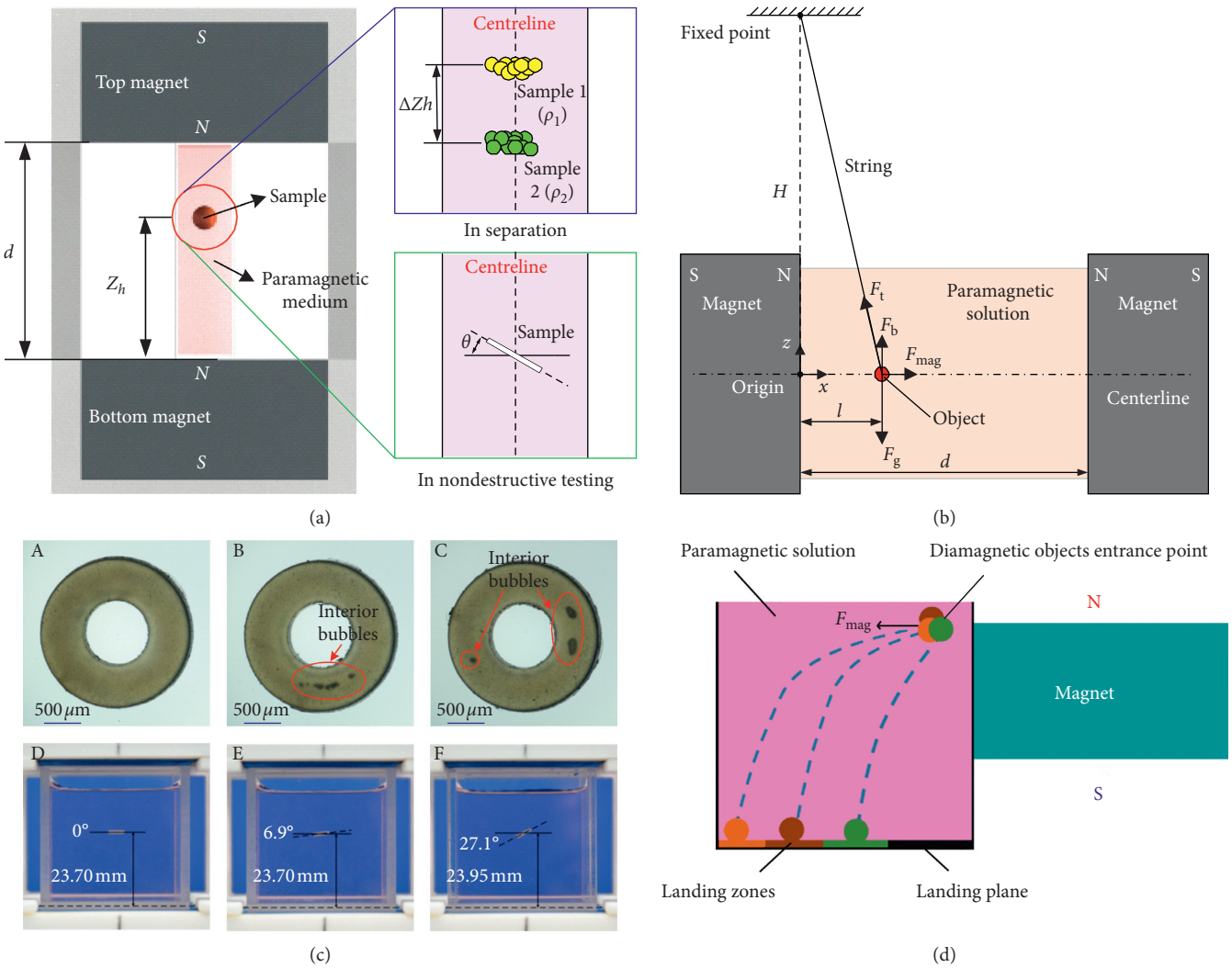

FIGURE 9: (a) Schematic view of the magnetic levitation detection device [82]. (b) Horizontal magnetic levitation for enlarging density measurement range [83]. (c) Samples and their levitation posture and position in MagLev device [82]. (d) A novel separation device using the magnetic levitation method [84].

researchers have also applied the Taguchi method to optimize residual stress, volume shrinkage, and warpage properties [102–104]. Xie et al. [106] took four parameters into account and investigated the effect of key injection molding process parameters on the density and strength of a specimen. Wang et al. [108] extended the range of variables investigated to the number of gates, gate size, mold temperature, polymer temperature, fill volume conversion, V/P switch over, and cooling time. Analysis of the signal-to-noise ratio (S/N) and analysis of variance (ANOVA) were conducted and the best process parameters were found. Using this method, the compression strength increased 12% compared to the average of the experiment. Sánchez-Sánchez et al. [114] employed the Taguchi method to achieve the optimum level of ultrasonic-assisted injection molding parameters and to maximize the tensile strength of the ultrahigh molecular weight polyethylene (UHMWPE)/graphite composites; the tensile strength was increased by 8.8%.

The foundation of designing an experiment with the Taguchi methodology is the orthogonal array. By using an orthogonal array, a better design on sets of samples can be achieved and results can be obtained by running the simulation code or performing corresponding experiments.

An orthogonal array is a typical design of experiments (DOE) method. Besides the Taguchi method, it is widely applied in other optimization solutions for designing sets of samples. The practical process usually contains multiple influencing factors. The full-factor design includes all possible combinations of all factors and levels and as such it requires a large number of trials that take a lot of time and is too costly to implement. DOE, however, can significantly reduce the number of experiments needed while still revealing the main effects. DOE are almost exclusively used in iterative and noniterative methods. The orthogonal experimental design (OED) used in the Taguchi method is the most extensively used DOE method. In addition, there are many other DOE methods such as CCD, BBD, and LHD.

Table 1 exhibits the most common DOE methods used in the literature.

3.1.2. Intelligent Methods. Case-based reasoning (CBR) is a procedure that uses an old solution to solve new problems and to evaluate new solutions for further application. CBR is a good method to determine the initial process parameters. The difficulty lies mainly in the description and definition of new problems and finding old solutions to match. The optimization results are strongly dependent on the case library.

Expert systems (ESs) are a subbranch of artificial intelligence that solve problems and give advice using the knowledge of human experts within a specific domain. ESs employ expert-level knowledge to achieve expert performance for the sake of solving specific problems. Their knowledge is both theoretical and practical; that is, the human experts who provide the system's knowledge have generally augmented their own theoretical understanding on the problem domain.

Fuzzy systems are an approximate inference methodology based on the concept of fuzzy set theory. The fuzzy rules and their membership functions compose the system's knowledge base [3, 4]. The fuzzification procedure converts the input variables into fuzzy values, while the defuzzification procedure transforms fuzzy results into crisp output variables. The fuzzy inference engine uses fuzzy rules during each evaluation cycle.

Expert systems and fuzzy reasoning are methods of modifying process parameters, combined with process parameters and product defects, based on some refined knowledge of the human experience. These methods can guide optimization [132] and optimize some product defects that cannot be quantitatively described, such as flash, flow lines, and pores.

Zhou et al. [4] adopted the idea of case-based reasoning (CBR) to determine the initial process parameters and discussed four case-adaptation strategies. The ideology of fuzzy inference based on expert knowledge and practical experience was utilized for defect correction and process parameter optimization. The fuzzy rules and membership function were discussed. Finally, an integrated intelligent optimization system based on CBR and fuzzy reasoning was constructed. A CBR adaptation strategy was employed to simplify the model into a combination of several basic geometries, and a simplified simulation model was applied to the CBR method to obtain initial parameter settings [5]. Furthermore, based on the previous work, Zhao et al. [3] introduced the empirical model (EM) into the optimization system, combined with the CBR method, to give the initial process parameters, and fuzzy logic algorithm was then combined to optimize the defects, and this system was effectively applied in practical production.

3.2. Surrogate Models. Surrogate models are not an independent method for optimization. They were originally used as a tool for fitting data and can be applied to the optimization process. The optimization results obtained by a noniterative method are often only a local optimal combination of parameters. In order to obtain a global optimal result, some surrogate models are needed to correlate process parameters and objectives because it is expensive and impractical if the techniques involve a time-consuming simulation for each function evaluation. Commonly used surrogate models include the response surface method (RSM), artificial neural network (ANN), support vector regression (SVR), Kriging model, and the Gaussian process. A survey of surrogate models for injection molding optimization in recent years is shown in Table 2. Some surrogate models, such as RSM and ANN, can be utilized in the noniterative method as an experimental data processing method, where a reasonable interval of parameters can be given as a process window. Generally, surrogate models serve as an approximation function for each iteration of the intelligent algorithm, which will be introduced in the next section.

Table 1: A brief summary of DOE methods for injection molding optimization.

Method of DOE	Optimization objective
Orthogonal experimental design (OED)	Warpage [103, 104, 109, 115, 116, 123] Shrinkage [103, 109, 111] Mechanical properties [105, 106, 108] Multiple properties [102, 107] Dimensional accuracy [100] Residual stress [101, 103]
Central composite design (CCD)	Tensile properties [124] Shrinkage and warpage [125, 126]
Box–Behnken design (BBD)	Conversion of RIM [127]
Latin hypercube design (LHD)	Warpage and cycle time [128, 129] Shrinkage and clamping force [130] Warpage [131]

The polynomial models generated by RSM are often referred to as response surface (RS) models in the literature. RS is a model building technique based on the statistical design of experiment (DOEe) and least-square-error fitting methods. When constructing an RSM model, regression analysis is performed. If the user has prior knowledge about the objective problem, the proper model can be chosen. Otherwise, several models need to be constructed from first to third or fourth order, with the best one being selected among the models according to the predicted errors. Heidari et al. [125] constructed an RSM to optimize the shrinkage and warpage of three polylactic acid (PLA)based bone screws. Using this method, they successfully obtained the minimum shrinkage and warpage of the product.

ANNs are widely accepted as a type of technology that offers an alternative way of simulating complex and ill-defined problems. They have been used in diverse applications and are particularly useful in system modeling similar to RSM. An ANN is made up of one or more hidden layers placed between the input and output layers. It has a computational structure that consists of a number of highly interconnected processing units called neurons. The neurons sum up weighted inputs and then apply a linear or nonlinear

Table 2: A survey of surrogate models for injection molding optimization.

Surrogate model	Application
RSM [112, 124, 125, 127, 133, 134]	Shrinkage and warpage Conversion of RIM Tensile properties Energy efficiency
Artificial neural network [113, 123, 128–131, 135–139]	Shrinkage and warpage Cycle time Clamping force Mechanical properties
Kriging model [140–142]	Warpage

function to the resulting sum in order to determine the output. The ANN learns to approximate the functions through a training process and adjusts their weights and biases until a performance index reaches a preset threshold value. Kitayama et al. [128, 129] developed an injection mold with a conformal cooling channel, combined with computer simulation, using a radial basis function network for multiobjective optimization of the injection process. The cycle time improved by 26%, and the warpage improved by 14% using an optimal combination of process parameters. Jou et al. [112] and Oliaei et al. [113] optimized the injection parameters using response surface methodology and neural network methods, respectively, and a lower product shrinkage was achieved. Also, the Taguchi method was applied and compared with those surrogate models, and the results were in good agreement.

There are many other surrogate models that are utilized for constructing approximation functions based on experiments or simulation such as support vector machines (SVM) [143] and the Kriging model. They have similar roles in optimization and will not be specifically introduced here. These surrogate models serve an objective function for the characterization of the iteration results when conducting iterate optimization strategies, thus making the evaluation of iteration results less time-consuming [123, 130, 131, 133, 135, 136, 141, 144, 145].

3.3. Iterative Optimization Methods. As mentioned above, a simple optimization algorithm based on experiments and data analysis is unlikely to give a global optimal solution. In order to obtain better optimization results, iterative optimization algorithms are often utilized to obtain a convergent global optimal combination of parameters. Iterative optimization approaches can be classified into deterministic and stochastic approaches according to the methods of improving the optimal point within each iteration [132]. Stochastic approaches have been mostly employed for injection molding process parameter optimization and are generally referred to as intelligent optimization algorithms. These algorithms include the genetic algorithm (GA) [123, 133, 134, 146–155], particle swarm optimization (PSO) [99, 131, 136, 147, 151–153, 156, 157], simulated annealing, and hill climbing. These algorithms start with random variables and iterate for the next variables according to their own iterative principles until the optimal points are found. Iterative directions are determined similar to the evolution of natural phenomena. Surrogate models are applied to characterize the quality of the products under the parameters settings after every iteration. Global optimal parameter settings are expected to be found after several runs or iterations, and thus, they become a feasible approach for the optimization of injection molding parameters. However, the probability of finding the global optimal solution decreases as the problem size increases.

Genetic algorithms are search algorithms designed to mimic the principles of biological evolution in a natural genetic system. GAs can be used to solve difficult problems in terms of objective functions that possess "bad" properties, such as those that are multimodal, discontinuous, and nondifferentiable. These algorithms maintain and manipulate a population of solutions and implement their search for better solutions based on a "survival of the fittest" strategy. This provides an implicit as well as explicit parallelism that allows for the exploitation of several promising areas for a given solution space at the same time. Applying the genetic algorithm combined with an RSM model, Park and Nguyen [133] solved the multiobjective optimization problem of energy consumption and product quality. Li et al. [123] minimized warpage for fiber-reinforced composite injection molding by combining a GA with a BP neural network. Zhao et al. [146] employed the improved effective global optimization (IEGO) algorithm to approximate the nonlinear correlation between process parameters and quality indicators of a final product, and then the nondominated sorting genetic algorithm II (NSGA-II) was developed to find the combination of process parameters for the smallest warpage and volume shrinkage of plastic products.

The particle swarm optimization methods were first inspired by the biological and social behavior of bird flocks and fish schools [158]. This behavior was collectively referred to as *swarming*. When a swarm looks for food, its individuals will spread out in the environment and move around independently. Each individual has a degree of freedom or randomness in its movements, which enables it to find food. Sooner or later, one of them will find something digestible and, as being social, will announce this to its neighbors [159]. In PSO, the potential solutions, called *particles*, are analogous to birds or fish. These particles fly according to their own flying experiences and their companions' flying experiences.

Applying PSO, Kramar and Cica [99] maximized the tensile strength of molded products. Zhang et al. [131] carried out a multiobjective optimization of injection molding process parameters of diesel engine oil cooler covers based on the ellipsoid basis function neural network. Xu et al. [136] developed a back-propagation neural network model to reflect the complex nonlinear correlation between process parameters and product mechanical properties. They found that the particle swarm optimization algorithm significantly improved the mechanical properties—and hence the performance—of the product.

There are many other evolutionary algorithms, such as simulated annealing algorithms and ant colony algorithms, which share many similarities with other GA and PSO models. They both initialize a population in a similar manner and search for an optimal solution by updating generations. They have been successfully applied in many research and industry applications.

Ideal injection molding process optimization results always come from a combination of using a variety of methods. This is summarized in Figure 10. Generally, it starts with a noniterative method like CBR to give an initial process setting and then the design of experiments (DOEe) technique is used to provide sets of samples. After performing the experiments and analyzing the influence of different parameters, a local optimal combination of parameters can be given like a process window. Furthermore, surrogate models can be employed to correlate process parameters and objectives. Hence, one can optimize the process parameters and obtain an optimized product quality with the application of intelligent iterative algorithms such as genetic algorithms and particle swarm optimization models.

For example, the GA approach was combined with BPNN [149], RSM [134, 150], and the Kriging model [148] as surrogate models. The optimal combination of process parameters was obtained and became stable. Also, the PSO algorithm was applied with BPNN to optimize the flash and volume shrinkage of injection molded parts [157]. Moreover, a GA/PSO hybrid approach was developed to serve as an iterative method [147, 152, 153] and with the assistance of BPNN or RSM the warpage was reduced by 38.6%.

The model-free optimization (MFO) algorithm is also an effective method. Johnston et al. [160] and Yang et al. [161] developed an online, model-free process optimization method and obtained ideal convergent results. A systematic approach that combined digital image processing (DIP) and model-free optimization (MFO) was proposed to solve optimization problems [161]. MFO uses measurements like DIP as feedback to determine the optimal settings, which is a typical online intelligent optimization approach.

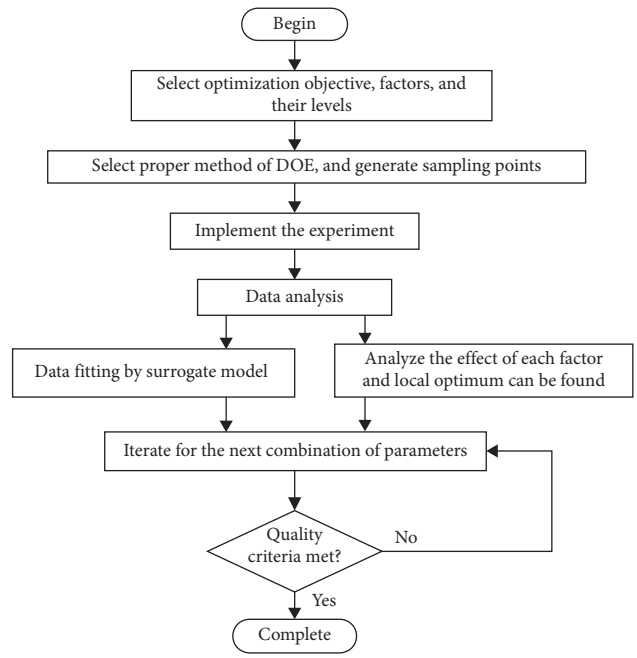

Figure 10: A flowchart of the overall optimization of injection molding parameters.

4. Process Control

The control target of the machine includes the injection speed, shot size, screw rotation speed, cylinder pressure, injection pressure, packing pressure, packing pressure, barrel temperature, and coolant temperature. These quantifiable and easily measured variables are the most common control variables in modern industrial injection molding. The precise closed-loop control of these variables ensures high repeatability of the injection molded process and the resultant product.

The injection molding process is a typical cyclic batch process. Obviously, the control algorithm for the batch process is different from the continuous process. Due to the nonlinear and time-varying complex dynamic characteristics of the batch process, it is much more difficult than a continuous process. Therefore, the development of injection molding process control has gradually transferred from the traditional continuous-control strategy to control strategies that focus on batch-direction characteristics. The research group of Gao F has made great advances in this field [144, 162–175]. This section will introduce the application of two typical strategies in injection molding—traditional feedback control and iterative learning control—and summarize and analyze them. Finally, the latest relevant studies will be introduced.

4.1. Feedback Control

4.1.1. Proportional-Integral-Derivative (PID) Controller. The PID controller is the most standard feedback control algorithm and measures the controlled variable, calculates the error between the output and set point, and generates the controller output based on the proportional, the integral, and the derivative of the errors. In brief, a PID controller makes use of the error to adjust the output to obtain the set variables. Researchers have achieved control of mold temperature [176], servohydraulic systems [177], and the stability of product quality [143] using PID controllers.

However, traditional PID control does not work well for the injection molding process due to its batch operation nature and the nonlinear and time-varying characteristics of the process. Adaptive control is a good alternative for this kind of control. Its parameters are adapted in a certain way to conform to the nonlinear or time-varying process dynamics and provide good control performance. Yang and Gao proposed a self-tuning adaptive controller [162] for injection velocity control, and robustness and tracking performance were improved.

4.1.2. Model Predictive Control. Model predictive control (MPC) can obtain the control signal by optimizing future

behavior through minimizing a cost function and making explicit use of a prediction model. It predicts the process output of future time over a certain period, called the prediction horizon. MPC calculates a set of future input for certain steps by minimizing a cost function, called the control horizon, so that the predicted output reaches the set point in an optimal manner. It is suitable for batch processes since the reference trajectories of the process settings are known before the cycle starts. This controller has been successfully applied in the injection molding process to control the screw speed and hydraulic back pressure [178, 179], coolant flow, coolant temperature [180], and cavity pressure [181, 182]. The group of Zhang et al. [166, 167, 170, 173, 183] designed fault-tolerant control through a predictive functional control framework for a batch process with unknown disturbances and partial actuator failures to achieve the desired closed-loop response.

Based on the fuzzy logic and neural network systems, establishing a precise model in process control can be avoided. If constructed from human knowledge in the form of fuzzy IF-THEN rules, it can easily perform multi-input, single-output, nonlinear mapping from a multidimensional vector to a scalar. This method has been used to control the injection speed and repeatability [184, 185]. Kanagalakshmi et al. [186] developed a multimodel control strategy that comprehensively included a variety of approaches, such as PID, fuzzy, and adaptive neurofuzzy inference system (ANFIS) control. The weighted average of these three strategies was utilized to control the barrel plasticizing temperature.

4.2. Learning Control. Injection molding is a batch process with a repetitive property. It is different from continuous process control where past control information can be used to improve current and future cycles. This kind of cycle-to-cycle improvement is similar to the human learning process; therefore, it is called learning control.

4.2.1. Conventional Iterative Learning Control. The batch process is usually described by two dimensions—the time dimension and the cycle dimension (batch dimension). The repetitive nature of the batch dimension can be used to guide the control output of the system. Generally, there are two ways to improve the learning control performance along the cycle direction: controller parameter learning and iterative learning control. Controller parameter learning adjusts and updates the controller parameters from cycle to cycle. Control signal learning control, also called iterative learning control (ILC), adjusts the controller output directly. The ILC method has been widely used in injection molding to achieve stable tracking of the time and batch sequence of the set point trajectory so as to improve process accuracy and repeatability [164, 169, 187, 188].

4.2.2. Two-Dimensional (2D) Control. Conventional ILC is only cycle-wise feedback control, with cycle-wise integral action that ensures performance improvement along the cycle direction. Two-dimensional feedback control is the strategy to ensure performance improvement along both time and cycle directions. The integral action along these two directions forms a 2D integrator cascade for eliminating the control error within and along the time and cycle directions.

The research on this control approach was also mainly studied by Gao's group. They proposed a robust 2D feedback control combined with an iterative learning control (FILC) method for batch processes [165, 171, 172]. They further proposed iterative learning fault-tolerant control (ILFTC) for uncertain disturbances and fault conditions [168]. Then, a novel 2D predictive functional iterative learning control (ILC) scheme [175, 189] was developed, thus introducing a new model formulation and error compensation approach. They also proposed some hybrid methods that combined conventional MPC with ILC to yield two-dimensional time model predictive control [174], combined with ILC and predictive function control (PFC) [163].

Due to the nonlinear and time-varying characteristics of the injection molding process, conventional feedback control strategies are not very effective for batch process control. This is because the information in the batch direction is an important guidance for control strategies. The iterative learning control method is the earliest effective strategy. After that, by introducing the feedback control of the time dimension, one can achieve faster convergence and better tracking performance. Using control strategies involves a lot of expertise in control discipline. Readers who are interested can consult more detailed references [2, 190] in this field.

4.2.3. Reinforcement Learning Control. Reinforcement learning (RL) is the learning from the environment to behavior mapping, which aims at allowing the agent to learn how to behave in an environment through the interaction with the environment. Intelligent system through interaction with the environment achieves the maximum reward signal. Recently, with the combination of artificial neural networks (ANNs), RL has attracted more attention in solving practical control problems [191]. Reinforcement learning control (RLC) can effectively handle nonlinear and highly uncertain systems. It is a powerful algorithm for solving optimal control problems.

Ruan et al. [192] first proposed applying RLC to the field of injection molding control. They proposed a hybrid method that combined RLC with ILC to solve the motion control problem in injection molding. RLC is ideal for optimal control, but it is not suitable for precise tracking control. Therefore, by combining with other tracking control algorithms, such as iterative learning control, it can effectively solve the motion control problems in injection molding.

5. Conclusions and Prospects

This review introduces methods and strategies on the sensing, optimization, and control of intelligent injection molding and summarizes recent studies in these three areas. As for process sensing, conventional methods like pressure

and temperature sensors are still indispensable, while emerging methods like ultrasound can obtain other important physical variables to enrich the information extracted from the process. In terms of parameter optimization, intelligent algorithms combined with surrogate models have gradually become the widely used optimization method and have delivered increasingly excellent results. In machine control, feedback control and learning control are currently the most effective control algorithms for typical batch processes. At present, these three areas have achieved considerable development. Furthermore, it can be concluded that the main research trend in the future lies in the integration of these three areas and in achieving reliable and real-time control of product quality in a more efficient and intelligent manner. However, there are still some problems that need to be further studied in order to achieve intelligent injection molding, including the following aspects.

5.1. Perception and Reconstruction of Multiple Physical Fields. There are many methods for detecting or diagnosing the physical parameters of the molding process. However, it can be found in the literature that the methods can only detect physical variables at some finite points. Some papers have suggested a data-fitting method to obtain the distribution of certain physical fields in the cavity. There is also an ultrasound "tomography scan" to construct the temperature field. But such methods are indirectly calculated and there are considerable errors. How to develop advanced sensing technology in the future and realize the perception of the physical field will continue to attract much interest, such as using a pressure detection film to detect the pressure distribution of the entire domain. In addition, it is still quite difficult to detect some microscopic physical variables online. A number of investigations applying ultrasound and dielectric methods to detect microphysical variables have emerged, but they are still in the early stages. Moreover, it is worth looking forward to the advancement in physics and modeling; it could directly enhance the observability of many physical variables in what are otherwise confounded states (e.g., barrel temperature and melt pressure). In this field, there are many scientific and engineering problems worth exploring.

5.2. Autonomous Learning Driven by Big Data. With the development of information technology, more and more data can be collected in the current industrial production process, including the process parameters and product quality of each batch. If autonomous learning based on big data analysis can be realized, higher efficiency in the optimization of process parameters can be achieved. It is without a doubt though that this process contains many difficulties, such as data standards and protocols, the accurate acquisition of data samples, and the integration of various complicated methods. It is believed that future technological breakthroughs in this area will bring fruition to industrial integration and production.

5.3. Definition of Product Quality Characteristics. It is well known that many types of defects in injection molded parts cannot be accurately described under certain circumstances. Some process optimization methods already have the capability of giving a better combination of process parameters, but these methods are often offline. To realize the combination of online detection and process optimization, a definition of quality characteristics of injection molded parts is very important. The approach may be to estimate their physical valuables per area. At present, the online detection mode for product weight, density, warpage, etc., is insufficient, and a direct quality feedback control system has yet to be developed. Hopmann and Heinisch [185] have made a great attempt in this direction even though they characterized the viscosity of the melt rather than the part quality. In addition, there are some product defects such as flow marks and bubbles that cannot be characterized quantitatively, thus rendering quantitative optimization methods inadequate. Therefore, how to properly characterize defects and further promote them will be a new trend in future optimization studies.

5.4. Model Identification Based on the Learning Method. For a batch process like injection molding, the development of feedback control and learning control reduces the dependence of the algorithm on the model. However, for model-based control algorithms, an accurate model has a crucial influence on the control result. And a good model can still accelerate the convergence of the algorithm and improve the tracking performance. During the injection molding process, the batch-direction data can be considered as a basis for system modeling and the characteristics of the batch can be further exploited. In addition, owing to changes in molds and materials, previous algorithms cannot necessarily be continued, which also puts forward new requirements for the modeling of the process.

Conflicts of Interest

The authors declared no potential conflicts of interest with respect to the research, authorship, and/or publication of this article.

Acknowledgments

The authors would like to acknowledge the financial support of the National Natural Science Foundation Council of China (nos. 51875519, 51635006, and 51821093), the Zhejiang Provincial Natural Science Foundation of China (no. LZ18E050002), and the Key Research and Development Plan of Zhejiang Province (no. 2020C01113).

References

[1] State & Congressional Data, 2019, http://www.plasticsindustry.org/advocacy/state-congressional-data.

[2] H. Zhou, *Computer Modeling for Injection Molding: Simulation, Optimization, and Control*, John Wiley & Sons, Hoboken, NJ, USA, 2013.

[3] N. Zhao, Z. Zhao, S. Liao, and S.-B. Cui, "Probabilistic model combination for support vector machine using positive-

definite kernel-based regularization path," *Advances in Intelligent and Soft Computing*, vol. 12, no. 3, pp. 201–206, 2011.

[4] H. Zhou, P. Zhao, and W. Feng, "An integrated intelligent system for injection molding process determination," *Advances in Polymer Technology*, vol. 26, no. 3, pp. 191–205, 2007.

[5] D. Li, H. Zhou, P. Zhao, and Y. Li, "A real-time process optimization system for injection molding," *Polymer Engineering & Science*, vol. 49, no. 10, pp. 2031–2040, 2009.

[6] J. Zhou, P. Li, Y. Zhou, B. Wang, J. Zang, and L. Meng, "Toward new-generation intelligent manufacturing," *Engineering*, vol. 4, no. 1, pp. 11–20, 2018.

[7] H. Zhang, L. Ren, Y. Gao, and B. Jin, "A comprehensive study of energy conservation in electric-hydraulic injection-molding equipment," *Energies*, vol. 10, no. 11, p. 1768, 2017.

[8] Z. Chen and L.-S. Turng, "A review of current developments in process and quality control for injection molding," *Advances in Polymer Technology*, vol. 24, no. 3, pp. 165–182, 2005.

[9] P. Zhao, H. Zhou, Y. He, K. Cai, and J. Fu, "A nondestructive online method for monitoring the injection molding process by collecting and analyzing machine running data," *The International Journal of Advanced Manufacturing Technology*, vol. 72, no. 5–8, pp. 765–777, 2014.

[10] J.-S. Gim, J.-S. Tae, J.-H. Jeon, J.-H. Choi, and B.-O. Rhee, "Detection method of filling imbalance in a multi-cavity mold for small lens," *International Journal of Precision Engineering and Manufacturing*, vol. 16, no. 3, pp. 531–535, 2015.

[11] X. Zhou, Y. Zhang, T. Mao, and H. Zhou, "Monitoring and dynamic control of quality stability for injection molding process," *Journal of Materials Processing Technology*, vol. 249, pp. 358–366, 2017.

[12] Q. Wang, M. Zhen, Z. Wu, Y. Cai, T. Kuo-Ming, and L. Jun-Kai, "Effect of process parameters on cavity pressure in injection molding," *AIP Conference Proceedings*, vol. 1820, no. 1, Article ID 050005, 2017.

[13] H. Hassan, "An experimental work on the effect of injection molding parameters on the cavity pressure and product weight," *The International Journal of Advanced Manufacturing Technology*, vol. 67, no. 1–4, pp. 675–686, 2013.

[14] X. Zhou, Y. Zhang, T. Mao, Y. Ruan, H. Gao, and H. Zhou, "Feature extraction and physical interpretation of melt pressure during injection molding process," *Journal of Materials Processing Technology*, vol. 261, pp. 50–60, 2018.

[15] H. S. Park, D. X. Phuong, and S. Kumar, "AI based injection molding process for consistent product quality," *Procedia Manufacturing*, vol. 28, pp. 102–106, 2019.

[16] H. Zamani, S. Azmoudeh, and K. Shelesh-Nezhad, "Warpage characterization of thin and centrally-gated injection molded part by applying cavity pressure measurement," in *Advanced Research in Material Science and Mechanical Engineering, Pts 1 and 2*, H. Rui, Ed., pp. 1099–1103, Trans Tech Pubilcations, Beijing, China, 2014.

[17] T. Mao, Y. Zhang, Y. Ruan, H. Gao, H. Zhou, and D. Li, "Feature learning and process monitoring of injection molding using convolution-deconvolution auto encoders," *Computers & Chemical Engineering*, vol. 118, pp. 77–90, 2018.

[18] M. Heinle and D. Drummer, "Measuring mechanical stresses on inserts during injection molding," *Advances in Mechanical Engineering*, vol. 7, no. 5, p. 6, 2015.

[19] K. M. Tsai and J. K. Lan, "Correlation between runner pressure and cavity pressure within injection mold," *The International Journal of Advanced Manufacturing Technology*, vol. 79, no. 1–4, pp. 273–284, 2015.

[20] W. S. Guan and H. X. Huang, "A proposed technique to acquire cavity pressure using a surface strain sensor during injection-compression molding," *Journal of Manufacturing Science and Engineering*, vol. 135, no. 2, p. 6, 2013.

[21] Y. Zhang, T. Mao, Z. Huang, H. Gao, and D. Li, "A statistical quality monitoring method for plastic injection molding using machine built-in sensors," *The International Journal of Advanced Manufacturing Technology*, vol. 85, no. 9–12, pp. 2483–2494, 2016.

[22] G. Wang, G. Zhao, and X. Wang, "Development and evaluation of a new rapid mold heating and cooling method for rapid heat cycle molding," *International Journal of Heat and Mass Transfer*, vol. 78, pp. 99–111, 2014.

[23] F. De Santis and R. Pantani, "Development of a rapid surface temperature variation system and application to micro-injection molding," *Journal of Materials Processing Technology*, vol. 237, pp. 1–11, 2016.

[24] G.-L. Wang, G.-Q. Zhao, and X.-X. Wang, "Heating/cooling channels design for an automotive interior part and its evaluation in rapid heat cycle molding," *Materials & Design*, vol. 59, pp. 310–322, 2014.

[25] G. Wang, Y. Hui, L. Zhang, and G. Zhao, "Research on temperature and pressure responses in the rapid mold heating and cooling method based on annular cooling channels and electric heating," *International Journal of Heat and Mass Transfer*, vol. 116, pp. 1192–1203, 2018.

[26] L. Crema, M. Sorgato, and G. Lucchetta, "Thermal optimization of deterministic porous mold inserts for rapid heat cycle molding," *International Journal of Heat and Mass Transfer*, vol. 109, pp. 462–469, 2017.

[27] S. Liparoti, A. Sorrentino, and G. Titomanlio, "Temperature and pressure evolution in fast heat cycle injection molding," *Materials and Manufacturing Processes*, vol. 34, no. 4, pp. 422–430, 2019.

[28] S. P. Johnston, G. A. Mendible, R. X. Gao, and D. O. Kazmer, "Estimation of bulk melt-temperature from in-mold thermal sensors for injection molding, Part A: method," *International Polymer Processing*, vol. 30, no. 4, pp. 460–466, 2015.

[29] B. Yang, L. Hu, G.-J. Li et al., "An evaluation of the melt crystallisation behaviour of injection-moulded high-density polyethylene (HDPE) based on a solidification kinetics analysis," *Plastics, Rubber and Composites*, vol. 46, no. 5, pp. 200–211, 2017.

[30] R. X. Gao, X. Tang, G. Gordon, and D. O. Kazmer, "Online product quality monitoring through in-process measurement," *CIRP Annals*, vol. 63, no. 1, pp. 493–496, 2014.

[31] G. Gordon, D. O. Kazmer, X. Y. Tang, Z. Y. Fan, and R. X. Gao, "Quality control using a multivariate injection molding sensor," *The International Journal of Advanced Manufacturing Technology*, vol. 78, no. 9–12, pp. 1381–1391, 2015.

[32] X. Mendibil, I. Llanos, H. Urreta, and I. Quintana, "In process quality control on micro-injection moulding: the role of sensor location," *The International Journal of Advanced Manufacturing Technology*, vol. 89, no. 9–12, pp. 3429–3438, 2017.

[33] H. Wang, B. Cao, C. K. Jen, K. T. Nguyen, and M. Viens, "On-line ultrasonic monitoring of the injection molding process," *Polymer Engineering & Science*, vol. 37, no. 2, pp. 363–376, 1997.

[34] B. He, Y. Yang, H. Zou, Q. Zhang, and Q. Fu, "Fast determination of phase inversion in polymer blends using

ultrasonic technique," *Polymer*, vol. 46, no. 18, pp. 7624–7631, 2005.

[35] B. He, X. Yuan, H. Yang et al., "Ultrasonic measurement of orientation in HDPE/iPP blends obtained by dynamic packing injection molding," *Polymer*, vol. 47, no. 7, pp. 2448–2454, 2006.

[36] F. Lionetto and A. Maffezzoli, "Polymer characterization by ultrasonic wave propagation," *Advances in Polymer Technology*, vol. 27, no. 2, pp. 63–73, 2008.

[37] Y. Zhao, X. M. L. Lin, and M. K. Lei, "Simultaneous determination of the coating thickness and its longitudinal velocity by ultrasonic nondestructive method," *NDT & E International*, vol. 43, no. 7, pp. 579–585, 2010.

[38] R. Raisutis, R. Kazys, and L. Mazeika, "Application of the ultrasonic pulse-echo technique for quality control of the multi-layered plastic materials," *NDT E International*, vol. 41, pp. 300–311, 2008.

[39] W. Michaeli and C. Starke, "Ultrasonic investigations of the thermoplastics injection moulding process," *Polymer Testing*, vol. 24, no. 2, pp. 205–209, 2005.

[40] M. Aigner, B. Praher, C. Kneidinger, J. Miethlinger, and G. Steinbichler, "Verifying the melting behavior in single-screw plasticization units using a novel simulation model and experimental method," *International Polymer Processing*, vol. 29, no. 5, pp. 624–634, 2014.

[41] B. Praher and G. Steinbichler, "Ultrasound-based measurement of liquid-layer thickness: a novel time-domain approach," *Mechanical Systems and Signal Processing*, vol. 82, pp. 166–177, 2017.

[42] B. Praher, K. Straka, and G. Steinbichler, "An ultrasound-based system for temperature distribution measurements in injection moulding: system design, simulations and off-line test measurements in water," *Measurement Science And Technology*, vol. 24, no. 8, Article ID 084004, 2013.

[43] B. Praher, K. Straka, J. Usanovic, and G. Steinbichler, "Ultrasound based monitoring of the injection moulding process—methods, applications and limitations," *AIP Conference Proceedings*, vol. 1593, no. 1, pp. 159–162, 2014.

[44] L. Zhao, Y. Lai, C. Pei, C.-K. Jen, and K.-D. Wu, "Real-time diagnosing polymer processing in injection molding using ultrasound," *Journal of Applied Polymer Science*, vol. 126, no. 6, pp. 2059–2066, 2012.

[45] Y. Ono, B. R. Whiteside, E. C. Brown et al., "Real-time process monitoring of micromoulding using integrated ultrasonic sensors," *Transactions of the Institute of Measurement and Control*, vol. 29, no. 5, pp. 383–401, 2007.

[46] C.-C. Cheng, Y. Ono, and C.-K. Jen, "Real-time diagnosis of co-injection molding using ultrasound," *Polymer Engineering & Science*, vol. 47, no. 9, pp. 1491–1500, 2007.

[47] L. Mulvaney-Johnson, C. C. Cheng, Y. Ono, E. C. Brown, C. K. Jen, and P. D. Coates, "Real time diagnostics of gas/water assisted injection moulding using integrated ultrasonic sensors," *Plastics, Rubber and Composites*, vol. 36, no. 3, pp. 111–121, 2007.

[48] Y. L. Wu, C. H. Yang, C. C. Cheng, and M. Kobayashi, "Novel real-time diagnostic of injection molding process at nozzle by high-temperature ultrasonic transducer," in *Proceedings of the 2015 Ieee International Ultrasonics Symposium*, October 2015.

[49] Y.-L. Wu, C.-C. Cheng, M. Kobayashi, and C.-H. Yang, "Novel design of extension nozzle and its application on real-time injection molding process diagnosed by ultrasound," *Sensors and Actuators A: Physical*, vol. 263, pp. 430–438, 2017.

[50] P. Zhao, Y. Zhao, H. Kharbas et al., "In-situ ultrasonic characterization of microcellular injection molding," *Journal of Materials Processing Technology*, vol. 270, pp. 254–264, 2019.

[51] P. Zhao, Y. Peng, W. Yang, J. Fu, and L.-S. Turng, "Crystallization measurements via ultrasonic velocity: study of poly(lactic acid) parts," *Journal of Polymer Science Part B: Polymer Physics*, vol. 53, no. 10, pp. 700–708, 2015.

[52] P. Zhao, S. Wang, J. Ying, and J. Fu, "Non-destructive measurement of cavity pressure during injection molding process based on ultrasonic technology and Gaussian process," *Polymer Testing*, vol. 32, no. 8, pp. 1436–1444, 2013.

[53] Y. Zhao, P. Zhao, J. Zhang, J. Huang, N. Xia, and J. Fu, "Online measurement of clamping force for injection molding machine using ultrasonic technology," *Ultrasonics*, vol. 91, pp. 170–179, 2019.

[54] P. Zhao, Y. Zhao, J. Zhang, J. Huang, N. Xia, and J. Fu, "Ultrasonic measurement of clamping force for injection molding machine," *Journal of Polymer Engineering*, vol. 39, no. 4, pp. 388–396, 2019.

[55] J. Zhang, P. Zhao, Y. Zhao, J. Huang, N. Xia, and J. Fu, "Online measurement of cavity pressure during injection molding via ultrasonic investigation of tie bar," *Sensors and Actuators A: Physical*, vol. 285, pp. 118–126, 2019.

[56] P. Guerrier, G. Tosello, K. K. Nielsen, and J. H. Hattel, "Three-dimensional numerical modeling of an induction heated injection molding tool with flow visualization," *The International Journal of Advanced Manufacturing Technology*, vol. 85, no. 1–4, pp. 643–660, 2016.

[57] P. Guerrier, G. Tosello, and J. H. Hattel, "Flow visualization and simulation of the filling process during injection molding," *Cirp Journal Of Manufacturing Science and Technology*, vol. 16, pp. 12–20, 2017.

[58] W.-R. Jong, S.-S. Hwang, C.-C. Wu, C.-H. Kao, Y.-M. Huang, and M.-C. Tsai, "Using a visualization mold to discuss the influence of gas counter pressure and mold temperature on the fountain flow effect," *International Polymer Processing*, vol. 33, no. 2, pp. 255–267, 2018.

[59] K.-Y. Jiang, Z. Ji, H. Li, M.-J. Wang, and T.-M. Yu, "Polymer flow behavior analysis based on physical visualization technology for ultrasonic vibration-assisted injection molding," *International Polymer Processing*, vol. 32, no. 3, pp. 290–297, 2017.

[60] K.-Y. Jiang, Y. Zhang, L. Yang, and Y. Lu, "Study on influence of Co-injection molding process on self-reinforcing characteristics of self-reinforced polypropylene composite via visualization," *International Polymer Processing*, vol. 34, no. 4, pp. 408–415, 2019.

[61] L. De Chiffre, S. Carmignato, J.-P. Kruth, R. Schmitt, and A. Weckenmann, "Industrial applications of computed tomography," *CIRP Annals*, vol. 63, no. 2, pp. 655–677, 2014.

[62] A. Awal, M. Rana, and M. Sain, "Thermorheological and mechanical properties of cellulose reinforced PLA biocomposites," *Mechanics Of Materials*, vol. 80, pp. 87–95, 2015.

[63] D. Masato, J. Rathore, M. Sorgato, S. Carmignato, and G. Lucchetta, "Analysis of the shrinkage of injection-molded fiber-reinforced thin-wall parts," *Materials & Design*, vol. 132, pp. 496–504, 2017.

[64] T. B. Nguyen Thi, M. Morioka, A. Yokoyama, S. Hamanaka, K. Yamashita, and C. Nonomura, "Measurement of fiber orientation distribution in injection-molded short-glass-fiber composites using X-ray computed tomography," *Journal of Materials Processing Technology*, vol. 219, pp. 1–9, 2015.

[65] J. P. Kruth, M. Bartscher, S. Carmignato, R. Schmitt, L. De Chiffre, and A. Weckenmann, "Computed tomography for dimensional metrology," *CIRP Annals*, vol. 60, no. 2, pp. 821–842, 2011.

[66] X. Chen, G. Chen, and F. Gao, "Capacitive transducer for in-mold monitoring of injection molding," *Polymer Engineering And Science*, vol. 44, no. 8, pp. 1571–1578, 2004.

[67] K. T. Fung, F. Gao, and X. Chen, "Application of a capacitive transducer for online part weight prediction and fault detection in injection molding," *Polymer Engineering & Science*, vol. 47, no. 4, pp. 347–353, 2007.

[68] H. Y. Wong, K. T. Fung, and F. Gao, "Development of a transducer for in-line and through cycle monitoring of key process and quality variables in injection molding," *Sensors and Actuators A: Physical*, vol. 141, no. 2, pp. 712–722, 2008.

[69] X. Chen, L. Zhang, X. Kong, J. Lu, and F. Gao, "Automatic velocity profile determination for uniform filling in injection molding," *Polymer Engineering & Science*, vol. 50, no. 7, pp. 1358–1371, 2010.

[70] Y. Peng, H. Li, and L.-S. Turng, "Development of a rheo-dielectric sensor for online shear stress measurement during the injection molding process," *Polymer Engineering & Science*, vol. 50, no. 1, pp. 61–68, 2010.

[71] A. V. Mamishev, K. Sundara-Rajan, F. Fumin Yang, Y. Yanqing Du, and M. Zahn, "Interdigital sensors and transducers," *Proceedings of the IEEE*, vol. 92, no. 5, pp. 808–845, 2004.

[72] T. Yamwong, A. M. Voice, G. R. Davies et al., "Electrostrictive response of an ideal polar rubber," *Journal of Applied Physics*, vol. 91, no. 3, pp. 1472–1476, 2002.

[73] Y. Zhang, Z. Huang, H. Zhou, and X. Gao, "Capacitance to digital converter method for dielectrostriction of polymeric materials," in *Proceedings of the Annual Technical Conference-ANTEC Indianapolis*, pp. 1497–1501, Indianapolis, IN, USA, May 2016.

[74] V. Nagarajan, K. Zhang, M. Misra, and A. K. Mohanty, "Overcoming the fundamental challenges in improving the impact strength and crystallinity of PLA biocomposites: influence of nucleating agent and mold temperature," *ACS Applied Materials & Interfaces*, vol. 7, no. 21, pp. 11203–11214, 2015.

[75] J. Anakabe, A. M. Zaldua Huici, A. Eceiza, A. Arbelaiz, and L. Avérous, "Combined effect of nucleating agent and plasticizer on the crystallization behaviour of polylactide," *Polymer Bulletin*, vol. 74, no. 12, pp. 4857–4886, 2017.

[76] M. R. Kamal, R. El Otmani, A. Derdouri, and J.-S. Chu, "Flow and thermal history effects on morphology and tensile behavior of poly(oxymethylene) micro injection molded parts," *International Polymer Processing*, vol. 32, no. 5, pp. 590–605, 2017.

[77] M. Rinaldi, D. Puglia, F. Dominici, V. Cherubini, L. Torre, and F. Nanni, "Melt processing and mechanical property characterization of high-performance poly(ether ether ketone)-carbon nanotube composite," *Polymer International*, vol. 66, no. 12, pp. 1731–1736, 2017.

[78] S. J. A. Rizvi, "Effect of injection molding parameters on crystallinity and mechanical properties of isotactic polypropylene," *International Journal Of Plastics Technology*, vol. 21, no. 2, pp. 404–426, 2017.

[79] M. Zhou, D. Mi, F. Hou, and J. Zhang, "Insight into understanding the evolution of the epitaxy crystallization in isotactic polypropylene and polyethylene blends," *Polymers for Advanced Technologies*, vol. 28, no. 12, pp. 1750–1758, 2017.

[80] X. Tardif, B. Pignon, N. Boyard et al., "Experimental study of crystallization of PolyEtherEtherKetone (PEEK) over a large temperature range using a nano-calorimeter," *Polymer Testing*, vol. 36, pp. 10–19, 2014.

[81] K. A. Mirica, S. S. Shevkoplyas, S. T. Phillips, M. Gupta, and G. M. Whitesides, "Measuring densities of solids and liquids using magnetic levitation: fundamentals," *Journal of the American Chemical Society*, vol. 131, no. 29, pp. 10049–10058, 2009.

[82] J. Xie, P. Zhao, Z. Jing, C. Zhang, N. Xia, and J. Fu, "Research on the sensitivity of magnetic levitation (MagLev) devices," *Journal of Magnetism and Magnetic Materials*, vol. 468, pp. 100–104, 2018.

[83] C. Zhang, P. Zhao, J. Xie, N. Xia, and J. Fu, "Enlarging density measurement range for polymers by horizontal magneto-Archimedes levitation," *Polymer Testing*, vol. 67, pp. 177–182, 2018.

[84] X. Zhang, F. Gu, J. Xie, C. Zhang, J. Fu, and P. Zhao, "Magnetic projection: a novel separation method and its first application on separating mixed plastics," *Waste Management*, vol. 87, pp. 805–813, 2019.

[85] A. Winkleman, R. Perez-Castillejos, K. L. Gudiksen, S. T. Phillips, M. Prentiss, and G. M. Whitesides, "Density-based diamagnetic separation: devices for detecting binding events and for collecting unlabeled diamagnetic particles in paramagnetic solutions," *Analytical Chemistry*, vol. 79, no. 17, pp. 6542–6550, 2007.

[86] Q.-H. Gao, W.-M. Zhang, H.-X. Zou et al., "Tunable rotating-mode density measurement using magnetic levitation," *Applied Physics Letters*, vol. 112, no. 14, Article ID 142408, 2018.

[87] K. A. Mirica, S. T. Phillips, S. S. Shevkoplyas, and G. M. Whitesides, "Using magnetic levitation to distinguish atomic-level differences in chemical composition of polymers, and to monitor chemical reactions on solid supports," *Journal of the American Chemical Society*, vol. 130, no. 52, pp. 17678–17680, 2008.

[88] A. Nemiroski, S. Soh, S. W. Kwok, H.-D. Yu, and G. M. Whitesides, "Tilted magnetic levitation enables measurement of the complete range of densities of materials with low magnetic permeability," *Journal of the American Chemical Society*, vol. 138, no. 4, pp. 1252–1257, 2016.

[89] J. Xie, P. Zhao, C. Zhang, Y. Hao, N. Xia, and J. Fu, "A feasible, portable and convenient density measurement method for minerals via magnetic levitation," *Measurement*, vol. 136, pp. 564–572, 2019.

[90] C. Zhang, P. Zhao, F. Gu et al., "Single-ring magnetic levitation configuration for object manipulation and density-based measurement," *Analytical Chemistry*, vol. 90, no. 15, pp. 9226–9233, 2018.

[91] C. Zhang, P. Zhao, D. Tang et al., "Axial magnetic levitation: a high-sensitive and maneuverable density-based analysis device," *Sensors and Actuators B: Chemical*, vol. 304, no. 1, Article ID 127362, 2020.

[92] A. B. Subramaniam, D. Yang, H.-D. Yu et al., "Noncontact orientation of objects in three-dimensional space using magnetic levitation," *Proceedings of the National Academy of Sciences*, vol. 111, no. 36, pp. 12980–12985, 2014.

[93] J. W. Hennek, A. Nemiroski, A. B. Subramaniam et al., "Using magnetic levitation for non-destructive quality control of plastic parts," *Advanced Materials*, vol. 27, no. 9, pp. 1587–1592, 2015.

[94] N. Xia, P. Zhao, J. Xie, C. Zhang, and J. Fu, "Non-destructive measurement of three-dimensional polymeric parts by

magneto-Archimedes levitation," *Polymer Testing*, vol. 66, pp. 32–40, 2018.

[95] N. Xia, P. Zhao, J. Xie, C. Zhang, J. Fu, and L.-S. Turng, "Defect diagnosis for polymeric samples via magnetic levitation," *NDT & E International*, vol. 100, pp. 175–182, 2018.

[96] P. Zhao, J. Xie, J. Zhang, C. Zhang, N. Xia, and J. Fu, "Evaluation of polymer injection molded parts via density-based magnetic levitation," *Journal of Applied Polymer Science*, vol. 137, no. 7, Article ID 48431, 2020.

[97] M. B. J. Atkinson, D. K. Bwambok, J. Chen et al., "Using magnetic levitation to separate mixtures of crystal polymorphs," *Angewandte Chemie International Edition*, vol. 52, no. 39, pp. 10208–10211, 2013.

[98] P. Zhao, J. Xie, F. Gu, N. Sharmin, P. Hall, and J. Fu, "Separation of mixed waste plastics via magnetic levitation," *Waste Management*, vol. 76, pp. 46–54, 2018.

[99] D. Kramar and D. Cica, "Predictive model and optimization OF processing parameters for plastic injection moulding," *Materiali in Tehnologije*, vol. 51, no. 4, pp. 597–602, 2017.

[100] C. C. Kuo and H. Y. Liao, "Dimensional accuracy optimization of the micro-plastic injection molding process using the Taguchi design method," *Materials Science*, vol. 21, no. 2, pp. 244–248, 2015.

[101] C.-M. Lin and H.-K. Hsieh, "Processing optimization of Fresnel lenses manufacturing in the injection molding considering birefringence effect," *Microsystem Technologies*, vol. 23, no. 12, pp. 5689–5695, 2017.

[102] C. Kim and J. Park, "Optimization of an injection molding process for polycarbonate car switch buttons using the Taguchi method," *Composites Research*, vol. 29, no. 1, pp. 7–15, 2016.

[103] M. D. Azaman, S. M. Sapuan, S. Sulaiman, E. S. Zainudin, and A. Khalina, "Optimization and numerical simulation analysis for molded thin-walled parts fabricated using wood-filled polypropylene composites via plastic injection molding," *Polymer Engineering and Science*, vol. 55, no. 5, pp. 1082–1095, 2015.

[104] T. Wen, X. Chen, C. Yang, L.-T. Liu, and L. Hao, "Optimization of processing parameters for minimizing warpage of large thin-walled parts in whole stages of injection molding," *Chinese Journal of Polymer Science*, vol. 32, no. 11, pp. 1535–1543, 2014.

[105] H. Pervez, M. S. Mozumder, and A. H. I. Mourad, "Optimization of injection molding parameters for HDPE/TiO2 nanocomposites fabrication with multiple performance characteristics using the Taguchi method and grey relational analysis," *Materials*, vol. 9, no. 8, p. 12, 2016.

[106] X. C. Xie, C. G. Lin, C. G. H. Jia, and R. J. Cao, "Optimization of injection molding process parameters for ultrafine-grained WC-6Co cemented carbide," *Rare Metal Materials and Engineering*, vol. 44, no. 12, pp. 3202–3207, 2015.

[107] S. Yu, Y. Zhang, D. Yang, H. Zhou, and J. Li, "Offline prediction of process windows for robust injection molding," *Journal of Applied Polymer Science*, vol. 131, no. 18, 2014.

[108] Y.-Q. Wang, J.-G. Kim, and J.-I. Song, "Optimization of plastic injection molding process parameters for manufacturing a brake booster valve body," *Materials and Design (1980–2015)*, vol. 56, pp. 313–317, 2014.

[109] M. A. Barghash and F. A. Alkaabneh, "Shrinkage and warpage detailed analysis and optimization for the injection molding process using multistage experimental design," *Quality Engineering*, vol. 26, no. 3, pp. 319–334, 2014.

[110] Y. Wang, Z. Yan, and X. Shan, "Optimization of process parameters for vertical-faced polypropylene bottle injection molding," *Advances in Materials Science and Engineering*, vol. 2018, p. 9, 2018.

[111] B. Kc, O. Faruk, J. A. M. Agnelli, A. L. Leao, J. Tjong, and M. Sain, "Sisal-glass fiber hybrid biocomposite: optimization of injection molding parameters using Taguchi method for reducing shrinkage," *Composites Part A: Applied Science and Manufacturing*, vol. 83, pp. 152–159, 2016.

[112] Y.-T. Jou, W.-T. Lin, W.-C. Lee, and T.-M. Yeh, "Integrating the Taguchi method and response surface methodology for process parameter optimization of the injection molding," *Applied Mathematics and Information Sciences*, vol. 8, no. 3, pp. 1277–1285, 2014.

[113] E. Oliaei, B. S. Heidari, S. M. Davachi et al., "Warpage and shrinkage optimization of injection-molded plastic spoon parts for biodegradable polymers using Taguchi, ANOVA and artificial neural network methods," *Journal of Materials Science and Technology*, vol. 32, no. 8, pp. 710–720, 2016.

[114] X. Sánchez-Sánchez, A. Elias-Zuñiga, and M. Hernández-Avila, "Processing of ultra-high molecular weight polyethylene/graphite composites by ultrasonic injection moulding: Taguchi optimization," *Ultrasonics Sonochemistry*, vol. 44, pp. 350–358, 2018.

[115] G. Singh, M. K. Pradhan, and A. Verma, "Multi Response optimization of injection moulding Process parameters to reduce cycle time and warpage," *Materials Today: Proceedings*, vol. 5, no. 2, pp. 8398–8405, 2018.

[116] J. Zhang, X. Yin, F. Liu, and P. Yang, "The simulation of the warpage rule of the thin-walled part of polypropylene composite based on the coupling effect of mold deformation and injection molding process," *Science and Engineering of Composite Materials*, vol. 25, no. 3, pp. 593–601, 2018.

[117] F. Zhao, N. Lu, and J. Lu, "Quality control of batch processes using natural gradient based model-free optimization," *IFAC Proceedings Volumes*, vol. 47, no. 3, pp. 8335–8340, 2014.

[118] W. Guo, L. Hua, and H. Mao, "Minimization of sink mark depth in injection-molded thermoplastic through design of experiments and genetic algorithm," *International Journal of Advanced Manufacturing Technology*, vol. 72, no. 1–4, pp. 365–375, 2014.

[119] H. Shi, Y. Gao, and X. Wang, "Optimization of injection molding process parameters using integrated artificial neural network model and expected improvement function method," *International Journal of Advanced Manufacturing Technology*, vol. 48, no. 9–12, pp. 955–962, 2010.

[120] W. Xia, B. Luo, and X. P. Liao, "An enhanced optimization approach based on Gaussian process surrogate model for process control in injection molding," *International Journal of Advanced Manufacturing Technology*, vol. 56, no. 9–12, pp. 929–942, 2011.

[121] F. Gu, P. Hall, N. J. Miles, Q. Ding, and T. Wu, "Improvement of mechanical properties of recycled plastic blends via optimizing processing parameters using the Taguchi method and principal component analysis," *Materials and Design (1980–2015)*, vol. 62, pp. 189–198, 2014.

[122] A. Asfaram, M. Ghaedi, and S. Hajati, "Screening and optimization of highly effective ultrasound-assisted simultaneous adsorption of cationic dyes onto Mn-doped Fe_3O_4-nanoparticle-loaded activated carbon," *Ultrasonics Sonochemistry*, vol. 34, pp. 1–12, 2016.

[123] K. Li, S. L. Yan, W. F. Pan, and G. Zhao, "Warpage optimization of fiber-reinforced composite injection molding by combining back propagation neural network and genetic algorithm," *The International Journal of Advanced*

Manufacturing Technology, vol. 90, no. 1–4, pp. 963–970, 2017.

[124] S. J. A. Rizvi, A. K. Singh, and G. R. Bhadu, "Optimization of tensile properties of injection molded α-nucleated polypropylene using response surface methodology," *Polymer Testing*, vol. 60, pp. 198–210, 2017.

[125] B. S. Heidari, E. Oliaei, H. Shayesteh et al., "Simulation of mechanical behavior and optimization of simulated injection molding process for PLA based antibacterial composite and nanocomposite bone screws using central composite design," *Journal of the Mechanical Behavior of Biomedical Materials*, vol. 65, pp. 160–176, 2017.

[126] S. M. S. Mukras, H. M. Omar, and F. A. al-Mufadi, "Experimental-based multi-objective optimization of injection molding process parameters," *Arabian Journal for Science and Engineering*, vol. 44, no. 9, pp. 7653–7665, 2019.

[127] H.-G. Kim, H. J. Son, D.-K. Lee, D.-W. Kim, H. J. Park, and D.-H. Cho, "Optimization and analysis of reaction injection molding of polydicyclopentadiene using response surface methodology," *Korean Journal of Chemical Engineering*, vol. 34, no. 7, pp. 2099–2109, 2017.

[128] S. Kitayama, H. Miyakawa, M. Takano, and S. Aiba, "Multi-objective optimization of injection molding process parameters for short cycle time and warpage reduction using conformal cooling channel," *The International Journal of Advanced Manufacturing Technology*, vol. 88, no. 5–8, pp. 1735–1744, 2017.

[129] S. Kitayama, M. Yokoyama, M. Takano, and S. Aiba, "Multi-objective optimization of variable packing pressure profile and process parameters in plastic injection molding for minimizing warpage and cycle time," *The International Journal of Advanced Manufacturing Technology*, vol. 92, no. 9–12, pp. 3991–3999, 2017.

[130] S. Kitayama and S. Natsume, "Multi-objective optimization of volume shrinkage and clamping force for plastic injection molding via sequential approximate optimization," *Simulation Modelling Practice and Theory*, vol. 48, pp. 35–44, 2014.

[131] J. H. Zhang, J. Wang, J. W. Lin, Q. Guo, K. W. Chen, and L. Ma, "Multiobjective optimization of injection molding process parameters based on Opt LHD, EBFNN, and MOPSO," *The International Journal of Advanced Manufacturing Technology*, vol. 85, no. 9–12, pp. 2857–2872, 2016.

[132] H. Gao, Y. Zhang, X. Zhou, and D. Li, "Intelligent methods for the process parameter determination of plastic injection molding," *Frontiers of Mechanical Engineering*, vol. 13, no. 1, pp. 85–95, 2018.

[133] H. S. Park and T. T. Nguyen, "Optimization of injection molding process for car fender in consideration of energy efficiency and product quality," *Journal of Computational Design and Engineering*, vol. 1, no. 4, pp. 256–265, 2014.

[134] K. Li, S. Yan, Y. Zhong, W. Pan, and G. Zhao, "Multi-objective optimization of the fiber-reinforced composite injection molding process using Taguchi method, RSM, and NSGA-II," *Simulation Modelling Practice and Theory*, vol. 91, pp. 69–82, 2019.

[135] S. Kitayama, R. Onuki, and K. Yamazaki, "Warpage reduction with variable pressure profile in plastic injection molding via sequential approximate optimization," *The International Journal of Advanced Manufacturing Technology*, vol. 72, no. 5–8, pp. 827–838, 2014.

[136] Y. J. Xu, Q. W. Zhang, W. H. Zhang, and P. Zhang, "Optimization of injection molding process parameters to improve the mechanical performance of polymer product against impact," *The International Journal of Advanced Manufacturing Technology*, vol. 76, no. 9–12, pp. 2199–2208, 2015.

[137] S. Kitayama, K. Tamada, M. Takano, and S. Aiba, "Numerical and experimental investigation on process parameters optimization in plastic injection molding for weldlines reduction and clamping force minimization," *The International Journal of Advanced Manufacturing Technology*, vol. 97, no. 5–8, pp. 2087–2098, 2018.

[138] S. Kitayama, K. Tamada, M. Takano, and S. Aiba, "Numerical optimization of process parameters in plastic injection molding for minimizing weldlines and clamping force using conformal cooling channel," *Journal of Manufacturing Processes*, vol. 32, pp. 782–790, 2018.

[139] S. Kitayama, Y. Yamazaki, M. Takano, and S. Aiba, "Numerical and experimental investigation of process parameters optimization in plastic injection molding using multi-criteria decision making," *Simulation Modelling Practice and Theory*, vol. 85, pp. 95–105, 2018.

[140] X. Y. Wang, H. X. Li, J. F. Gu et al., "Pressure analysis of dynamic injection molding and process parameter optimization for reducing warpage of injection molded products," *Polymers*, vol. 9, no. 3, p. 23, 2017.

[141] X. Y. Wang, J. F. Gu, C. Y. Shen, and X. C. Wang, "Warpage optimization with dynamic injection molding technology and sequential optimization method," *The International Journal of Advanced Manufacturing Technology*, vol. 78, no. 1–4, pp. 177–187, 2015.

[142] H. Li, K. Liu, D. Zhao, M. Wang, Q. Li, and J. Hou, "Multi-objective optimizations for microinjection molding process parameters of biodegradable polymer stent," *Materials*, vol. 11, no. 11, p. 2322, 2018.

[143] P. Zhao, Z. Dong, J. Zhang et al., "Optimization of injection molding process parameters for weight control: converting optimization problem to classification problem," *Advances in Polymer Technology*, In press, 2019.

[144] J. Zhao, Y. Yang, X. Chen, and F. Gao, "An iterative modeling and trust-region optimization method for batch processes," *Industrial and Engineering Chemistry Research*, vol. 54, no. 12, pp. 3186–3199, 2015.

[145] S. Zhu, Y. Yang, B. Yang, Z. Shao, and X. Chen, "Model-free quality optimization strategy for a batch process with short cycle time and low operational cost," *Industrial and Engineering Chemistry Research*, vol. 53, no. 42, pp. 16384–16396, 2014.

[146] J. Zhao, G. D. Cheng, S. L. Ruan, and Z. Li, "Multi-objective optimization design of injection molding process parameters based on the improved efficient global optimization algorithm and non-dominated sorting-based genetic algorithm," *The International Journal of Advanced Manufacturing Technology*, vol. 78, no. 9–12, pp. 1813–1826, 2015.

[147] W. C. Chen, P. H. Liou, and S. C. Chou, "An integrated parameter optimization system for MIMO plastic injection molding using soft computing," *The International Journal of Advanced Manufacturing Technology*, vol. 73, no. 9–12, pp. 1465–1474, 2014.

[148] G.-J. Kang, C.-H. Park, and D.-H. Choi, "Metamodel-based design optimization of injection molding process variables and gates of an automotive glove box for enhancing its quality," *Journal of Mechanical Science and Technology*, vol. 30, no. 4, pp. 1723–1732, 2016.

[149] J. H. Liu, X. D. Chen, Z. Q. Lin, and S. P. Diao, "Multi-objective optimization of injection molding process

parameters for the precision manufacturing of plastic optical lens," *Mathematical Problems in Engineering*, vol. 2017, p. 13, 2017.

[150] M. Tian, X. Gong, L. Yin et al., "Multi-objective optimization of injection molding process parameters in two stages for multiple quality characteristics and energy efficiency using Taguchi method and NSGA-II," *The International Journal of Advanced Manufacturing Technology*, vol. 89, no. 1–4, pp. 241–254, 2017.

[151] K. Li, S. L. Yan, W. F. Pan, and G. Zhao, "Optimization of fiber-orientation distribution in fiber-reinforced composite injection molding by Taguchi, back propagation neural network, and genetic algorithm-particle swarm optimization," *Advances in Mechanical Engineering*, vol. 9, no. 9, p. 11, 2017.

[152] W. C. Chen, M. H. Nguyen, W. H. Chiu, T. N. Chen, and P. H. Tai, "Optimization of the plastic injection molding process using the Taguchi method, RSM, and hybrid GA-PSO," *The International Journal of Advanced Manufacturing Technology*, vol. 83, no. 9–12, pp. 1873–1886, 2016.

[153] W.-C. Chen and D. Kurniawan, "Process parameters optimization for multiple quality characteristics in plastic injection molding using Taguchi method, BPNN, GA, and hybrid PSO-GA," *International Journal of Precision Engineering and Manufacturing*, vol. 15, no. 8, pp. 1583–1593, 2014.

[154] C.-M. Lin and Y.-W. Chen, "Grey optimization of injection molding processing of plastic optical lens based on joint consideration of aberration and birefringence effects," *Microsystem Technologies*, vol. 25, no. 2, pp. 621–631, 2019.

[155] R. J. Bensingh, R. Machavaram, S. R. Boopathy, and C. Jebaraj, "Injection molding process optimization of a bi-aspheric lens using hybrid artificial neural networks (ANNs) and particle swarm optimization (PSO)," *Measurement*, vol. 134, pp. 359–374, 2019.

[156] J. L. Kuo and M. T. Chang, "Multiobjective design of turbo injection mode for axial flux motor in plastic injection molding machine by particle swarm optimization," *Mathematical Problems in Engineering*, vol. 2015, p. 11, 2015.

[157] G. Xu and Z. T. Yang, "Multiobjective optimization of process parameters for plastic injection molding via soft computing and grey correlation analysis," *The International Journal of Advanced Manufacturing Technology*, vol. 78, no. 1–4, pp. 525–536, 2015.

[158] R. Eberhart and J. Kennedy, "Particle swarm optimization," in *Proceeding of IEEE International Conference on Neural Network*, pp. 1942–1948, Perth, Australia, November 1995.

[159] T. Weise, *Global Optimization Algorithms-Theory and Application*, 2009.

[160] S. Johnston, C. McCready, D. Hazen, D. VanDerwalker, and D. Kazmer, "On-line multivariate optimization of injection molding," *Polymer Engineering and Science*, vol. 55, no. 12, pp. 2743–2750, 2015.

[161] Y. Yang, B. Yang, S. Zhu, and X. Chen, "Online quality optimization of the injection molding process via digital image processing and model-free optimization," *Journal of Materials Processing Technology*, vol. 226, pp. 85–98, 2015.

[162] Y. Yang and F. Gao, "Adaptive control of the filling velocity of thermoplastics injection molding," *Control Engineering Practice*, vol. 8, no. 11, pp. 1285–1296, 2000.

[163] B. Yang, Z. Xu, Y. Yang, and F. Gao, "Application of two-dimensional predictive functional control in injection molding," *Industrial and Engineering Chemistry Research*, vol. 54, no. 41, pp. 10088–10102, 2015.

[164] L. Wang, S. Mo, D. Zhou, F. Gao, and X. Chen, "Delay-range-dependent method for iterative learning fault-tolerant guaranteed cost control for batch processes," *Industrial and Engineering Chemistry Research*, vol. 52, no. 7, pp. 2661–2671, 2013.

[165] L. Wang, S. Mo, D. Zhou, F. Gao, and X. Chen, "Delay-range-dependent robust 2D iterative learning control for batch processes with state delay and uncertainties," *Journal of Process Control*, vol. 23, no. 5, pp. 715–730, 2013.

[166] R. Zhang, H. Zou, A. Xue, and F. Gao, "GA based predictive functional control for batch processes under actuator faults," *Chemometrics and Intelligent Laboratory Systems*, vol. 137, pp. 67–73, 2014.

[167] X. Hu, L. Wang, and F. Gao, "Genetic-algorithm-optimization-based infinite horizon linear quadratic control for injection molding batch processes with uncertainty," *Industrial and Engineering Chemistry Research*, vol. 57, no. 51, pp. 17462–17469, 2018.

[168] L. Wang, F. Liu, J. Yu, P. Li, R. Zhang, and F. Gao, "Iterative learning fault-tolerant control for injection molding processes against actuator faults," *Journal of Process Control*, vol. 59, pp. 59–72, 2017.

[169] L. Wang, X. Chen, and F. Gao, "An LMI method to robust iterative learning fault-tolerant guaranteed cost control for batch processes," *Chinese Journal of Chemical Engineering*, vol. 21, no. 4, pp. 401–411, 2013.

[170] R. Zhang, R. Lu, A. Xue, and F. Gao, "Predictive functional control for linear systems under partial actuator faults and application on an injection molding batch process," *Industrial and Engineering Chemistry Research*, vol. 53, no. 2, pp. 723–731, 2014.

[171] L. Wang, S. Mo, D. Zhou, F. Gao, and X. Chen, "Robust delay dependent iterative learning fault-tolerant control for batch processes with state delay and actuator failures," *Journal of Process Control*, vol. 22, no. 7, pp. 1273–1286, 2012.

[172] L. Wang, S. Mo, D. Zhou, and F. Gao, "Robust design of feedback integrated with iterative learning control for batch processes with uncertainties and interval time-varying delays," *Journal of Process Control*, vol. 21, no. 7, pp. 987–996, 2011.

[173] R. Zhang, J. Lu, H. Qu, and F. Gao, "State space model predictive fault-tolerant control for batch processes with partial actuator failure," *Journal of Process Control*, vol. 24, no. 5, pp. 613–620, 2014.

[174] Z. Cao, Y. Yang, J. Lu, and F. Gao, "Two-time-dimensional model predictive control of weld line positioning in Bi-injection molding," *Industrial and Engineering Chemistry Research*, vol. 54, no. 17, pp. 4795–4804, 2015.

[175] R. Zhang and F. Gao, "Two-dimensional iterative learning model predictive control for batch processes: a new state space model compensation approach," *IEEE Transactions on Systems, Man, and Cybernetics: Systems*, pp. 1–9, 2018.

[176] B.-H. Jeong, N.-H. Kim, and K.-Y. Lee, "Optimized digital proportional integral derivative controller for heating and cooling injection molding system," *Journal of Electrical Engineering and Technology*, vol. 10, no. 3, pp. 1383–1388, 2015.

[177] C.-J. Chen, K.-T. Wu, and S.-J. Hwang, "Development of a servo-hydraulic system with a self-tuning fuzzy PID controller to simulate injection molding process," *Microsystem Technologies*, pp. 1–22, 2018.

[178] R. Dubay, B. Hu, J. M. Hernandez, and M. Charest, "Controlling process parameters during plastication in plastic injection molding using model predictive control," *Advances in Polymer Technology*, vol. 33, p. 8, 2014.

[179] Y.-g. Peng, J. Wang, and W. Wei, "Model predictive control of servo motor driven constant pump hydraulic system in injection molding process based on neurodynamic optimization," *Journal of Zhejiang University Science C*, vol. 15, no. 2, pp. 139–146, 2014.

[180] S. Zhang, R. Dubay, and M. Charest, "A principal component analysis model-based predictive controller for controlling part warpage in plastic injection molding," *Expert Systems with Applications*, vol. 42, no. 6, pp. 2919–2927, 2015.

[181] C. Hopmann, A. Ressmann, M. Reiter, S. Stemmler, and D. Abel, "A self-optimising injection moulding process with model-based control system parameterisation," *International Journal of Computer Integrated Manufacturing*, vol. 29, no. 11, pp. 1190–1199, 2016.

[182] M. Reiter, S. Stemmler, C. Hopmann, A. Ressmann, and D. Abel, "Model predictive control of cavity pressure in an injection moulding process," *IFAC Proceedings Volumes*, vol. 47, no. 3, pp. 4358–4363, 2014.

[183] X. Hu, H. Zou, and L. Wang, "Design of the linear quadratic structure based predictive functional control for industrial processes against partial actuator failures using GA optimization," *International Journal of Control, Automation and Systems*, vol. 17, no. 3, pp. 597–605, 2019.

[184] F. Qi, S. Li, Y. Zhou, and Z. Zhou, *Design of Servo Control System of Precision Injection for Electro-Hydraulic Hybrid Injection Machine*, Springer, Berlin, Germany, 2014.

[185] C. Hopmann and J. Heinisch, "Process control strategies for injection molding processes with changing raw material viscosity," *Journal of Polymer Engineering*, vol. 38, no. 5, pp. 483–492, 2017.

[186] S. Kanagalakshmi, D. Manamalli, and M. Mohamedrafiq, "Implementation of multimodel-based PID and intelligent controller for simulated and real-time temperature control of injection molding machine," *Chemical Engineering Communications*, vol. 203, no. 4, pp. 452–462, 2016.

[187] C. Hopmann, D. Abel, J. Heinisch, and S. Stemmler, "Self-optimizing injection molding based on iterative learning cavity pressure control," *Production Engineering*, vol. 11, no. 2, pp. 97–106, 2017.

[188] D. Dorner, T. Radermacher, B. Wagner, and J. Weber, "Iterative learning control of a plastic injection moulding machine," *at–Automatisierungstechnik*, vol. 62, no. 3, pp. 226–236, 2014.

[189] R. Zhang, S. Wu, and J. Tao, "A new design of predictive functional control strategy for batch processes in the two-dimensional framework," *IEEE Transactions on Industrial Informatics*, vol. 15, no. 5, pp. 2905–2914, 2019.

[190] Y. Yang, X. Chen, N. Lu, and F. Gao, *Injection Molding Process Control, Monitoring, and Optimization*, Carl Hanser Verlag GmbH Co KG, Munich, Germany, 2016.

[191] V. Mnih, K. Kavukcuoglu, D. Silver et al., "Human-level control through deep reinforcement learning," *Nature*, vol. 518, no. 7540, pp. 529–533, 2015.

[192] Y. Ruan, Y. Zhang, T. Mao, X. Zhou, D. Li, and H. Zhou, "Trajectory optimization and positioning control for batch process using learning control," *Control Engineering Practice*, vol. 85, pp. 1–10, 2019.

Hindawi
Advances in Polymer Technology
Volume 2020, Article ID 5818606, 7 pages
https://doi.org/10.1155/2020/5818606

Research Article

FEM of Gas-Assisted Injection Molding Based on 3D Model

Xinchao Wang,[1,2] Tie Geng,[1] Liqun Yan,[1] Yonggang Guo,[1] and Lih-Sheng Turng[2,3]

[1]*School of Mechatronic Engineering, and National Engineering Laboratory for Wheat & Corn Further Processing, HeNan University of Technology, Zhengzhou 450001, China*
[2]*Wisconsin Institute for Discovery, University of WI–Madison, Madison, WI, USA*
[3]*Department of Mechanical Engineering, University of WI–Madison, Madison, WI, USA*

Correspondence should be addressed to Tie Geng; tiegeng2000@163.com

Received 29 July 2019; Revised 18 November 2019; Accepted 3 December 2019; Published 30 March 2020

Academic Editor: Gyorgy Szekely

Copyright © 2020 Xinchao Wang et al. This is an open access article distributed under the Creative Commons Attribution License, which permits unrestricted use, distribution, and reproduction in any medium, provided the original work is properly cited.

The gas-assisted injection molding (GAIM) process is so complicated that increasing reliance has been placed on CAE (Computer Aided Engineering) as a tool for both mold designers and process engineers. In this paper, a 3D theoretical model and numerical scheme is presented to simulate the GAIM process, in which an equal-order velocity-pressure formulation method is employed to eliminate the pressure oscillation. In addition, the whole flow field including the gas and melt regions is calculated using a uniform momentum equation with the viscosity of gas raised to a certain order of magnitude, and a 3D control volume scheme is employed to track the flow front of the melt and gas. Finally, the validity of the model has been tested through case studies and experimental verification.

1. Introduction

Gas-assisted injection molding (GAIM) is one of the important and innovative molding processes and considered to be a revolution in terms of injection molding technology [1, 2]. This new process came into practice as ripe technology in the 1990s, and has been spread widely due to its outstanding advantages. Compared with conventional injection molding (CIM), GAIM offers a considerable number of advantages, such as reduced part weight, injection pressure, clamp force, shrinkage, warpage, and residual stress. GAIM has four types: standard molding, vice cavity molding, melt backflow, and core activities [1]. This paper mainly focuses on standard molding, which is also called partial filling and inflation.

In gas-assisted injection molding, the mold cavity is partially, about 70–90% of the mold cavity, filled with the polymer melt, and then the gas with high pressure will be injected into the melt immediately or after some delay time. Three distinct regions can be indentified during the gas-assisted injection molding filling stage (as shown in Figure 1): the solidified melt layer close to the mold wall, the deforming viscous melt, and the penetration gas. The three regions are confined by the melt and gas fronts. In this process, the melt filling process in GAIM is the same as that in CIM, and the penetration of gas into melt will force the melt to fill the whole mold cavity.

But, with the gas injection, the GAIM process becomes so complicated that at present, the understanding of the characteristics of the process is still lagging behind.

In GAIM, two dramatically dissimilar materials flowing within complex cavities interact dynamically, and many additional parameters are introduced, such as the numbers and location of gas injection points, the short-shot size, gas delay time, the injected gas pressure, and the holding time for gas injection. So, the molding design and process control become more critical and difficult than conventional injection molding. Furthermore, previous experience about conventional injection molding is no longer sufficient to deal with this process.

So, the computer simulation for gas-assisted injection molding is needed urgently to improve the mold design and process control. Now, increasing reliance has been placed on computer-aided engineering (CAE), and commercially available computer simulation packages for the injection molding process have become routine tool for both mold

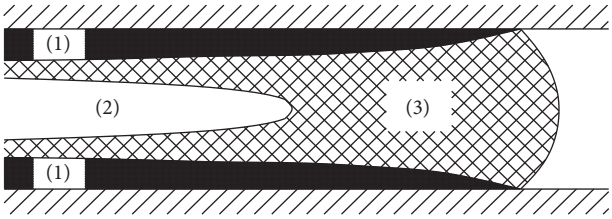

Figure 1: Schematic of gas-assisted injection molding.

designers and process engineers. With CAE simulation tools, engineers can optimize the mold and products, which used to be conducted by the trial-and-error method that is expensive and inefficient.

During the past decades, most of the papers on the simulation of GAIM are based on either a midplane model [3] or a surface model [4] which is both a so-called 2.5D approach. In the 2.5D method, the melt filling in the thin cavity is assumed as Hele-Shaw flow [5], and the velocity and the variation of pressure in the gapwise direction are neglected except that the temperature is solved by FDM, so the filling of a mold cavity becomes a 2D problem in flow direction and a 1D problem in gapwise direction. The residual wall thickness of a part is used to represent the gas penetration, which is determined by capillary number or empirical formula [6]. The influence of gas penetration on melt flow is taken only as a boundary condition of the melt filling region.

The models based on Hele-Shaw are simple and have less time cost, but they are used mainly for the analysis of shell structure parts without 3D features. As for these molded parts with the more complex three-dimensional geometries and uniform thickness walls often encountered in gas-assisted injection molding, the velocity and the changes of parameters in the gapwise direction are considerable and cannot be neglected. As for GAIM, the information obtained by 2.5-dimensional models is often limited and incomplete. Several phenomena occurring during mold filling, such as the fountain effect and fiber orientation, cannot be accurately predicted using the Hele-Shaw approximation. In many cases, the calculation results generated by the 2.5D model cannot coincide with experimental results [7].

At present, there are not many research papers on the simulation of three-dimensional GAIM. Literature [8] focuses on the 3D numerical simulation of the moving interfaces in GAIM using the CLSVOF method. Although several GAIM simulation commercial softwares, such as MOLDFLOW, MOLDEX3D, etc. [9, 10], have been developed, which have both three-dimensional analysis module of GAIM, their research results are regarded as the company's core technology and are strictly confidential, and the published articles on it are limited to the introduction of major functions, and the technical details are not disclosed to the public.

In this paper, a 3D finite element model is presented to deal with the melt filling, in which an equal-order velocity-pressure formulation method [11] for 3D flow field is employed to eliminate the pressure oscillation. The whole flow field including the gas and melt regions is calculated using a uniform momentum equation with the viscosity of gas raised to a certain order of magnitude. A 3D control volume scheme is employed to track the flow front of the melt and gas. The software based on this 3D model has been developed and can calculate the pressure field, velocity field, temperature field, and gas penetration in the injection process without pressure oscillation. The validity of the model has been tested through case studies and experimental verification.

2. Mathematical Model

Due to the absence of the Hele-Shaw approximation and the dynamic interaction of the gas and melt, the GAIM process becomes more complicated. Hence, several assumptions are needed and are listed below.

(1) The pressure of the melt is not very high during filling of the cavity; hence, the melt is considered incompressible and purely viscous.

(2) The polymer melt has high viscosity, so inertia, gravitation, and surface tension of melt are neglected as compared with the viscous force.

(3) The gas is treated as the incompressible fluid.

(4) Temperature in the gas regions is considered same everywhere and permanent. Furthermore, there is no thermal exchange between the melt and gas.

Given the abovementioned approximations, the governing equations, expressed in Cartesian coordinates, are as follows.

Momentum equations:

$$\frac{\partial}{\partial x}\left(2\eta\frac{\partial u}{\partial x}\right)+\frac{\partial}{\partial y}\left[\eta\left(\frac{\partial v}{\partial x}+\frac{\partial u}{\partial y}\right)\right]+\frac{\partial}{\partial z}\left[\eta\left(\frac{\partial w}{\partial x}+\frac{\partial u}{\partial z}\right)\right]-\frac{\partial(P)}{\partial x}=0, \tag{1a}$$

$$\frac{\partial}{\partial x}\left[\eta\left(\frac{\partial v}{\partial x}+\frac{\partial u}{\partial y}\right)\right]+\frac{\partial}{\partial y}\left(2\eta\frac{\partial v}{\partial y}\right)+\frac{\partial}{\partial z}\left[\eta\left(\frac{\partial w}{\partial y}+\frac{\partial v}{\partial z}\right)\right]-\frac{\partial(P)}{\partial y}=0, \tag{1b}$$

$$\frac{\partial}{\partial x}\left[\eta\left(\frac{\partial w}{\partial x}+\frac{\partial u}{\partial z}\right)\right]+\frac{\partial}{\partial y}\left[\eta\left(\frac{\partial v}{\partial z}+\frac{\partial w}{\partial y}\right)\right]+\frac{\partial}{\partial z}\left(2\eta\frac{\partial w}{\partial z}\right)-\frac{\partial(P)}{\partial z}=0. \tag{1c}$$

Continuity equation:

$$\frac{\partial u}{\partial x}+\frac{\partial v}{\partial y}+\frac{\partial w}{\partial z}=0. \tag{1d}$$

Energy equation:

$$\rho C_P \frac{\partial T}{\partial t} = \rho C_P \left(u \frac{\partial T}{\partial x} + v \frac{\partial T}{\partial y} + w \frac{\partial T}{\partial z} \right) + \frac{\partial}{\partial x}\left(K \frac{\partial T}{\partial x} \right) + \frac{\partial}{\partial y}\left(K \frac{\partial T}{\partial y} \right) + \frac{\partial}{\partial z}\left(K \frac{\partial T}{\partial z} \right) + \eta \dot{\gamma}^2, \tag{1e}$$

where x, y, z are the three-dimensional coordinates and u, v, w are the velocity components in the x, y, z directions, respectively. P, T, ρ, and η denote the pressure, temperature, density, and viscosity, respectively.

The cross viscosity model has been used for the simulations:

$$\eta = \frac{\eta_0 (T, P)}{1 + \left(\eta_0 \dot{\gamma} / \tau^* \right)^{1-n}}. \tag{2}$$

Because there is no notable change in the scope of the temperature of the polymer melt during filling, the Arrhenius model [12] for η_0 is employed as follows.

$$\eta_0 (T, P) = B \exp\left(\frac{T_b}{T} \right) \exp (\beta P). \tag{3}$$

3. Numerical Implementation

3.1. Melt Injection. For the 3D simulation of injection molding, the main difficulty is pressure oscillations, i.e., it is hard to obtain a stable solution during calculating the pressure and velocity. To solve this problem, an equal-order velocity-pressure formulation method is given here which uses 4-node tetrahedron elements based on FEM [13]. The main idea of this method is (1) the relationship between velocity and pressure is obtained from the discretized momentum equations, and then the pressure equation is obtained by substituting the velocity expressions into discretized continuity equation. (2) After pressure calculation, the velocity needs to be updated. (3) The overall calculation process is iterative.

The momentum equations are discretized using Galerkin's method with equal-order velocity-pressure formulation. The element equations are assembled in the conventional manner to form the discretized global momentum equations, and the nodal velocity may be expressed as following:

$$\begin{aligned} u_i &= \widehat{u}_i - K_i^u \frac{\partial P}{\partial x}, \\ v_i &= \widehat{v}_i - K_i^v \frac{\partial P}{\partial y}, \\ w_i &= \widehat{w}_i - K_i^w \frac{\partial P}{\partial z}, \end{aligned} \tag{4}$$

where $i$means the global node number and $\widehat{u}_i, \widehat{v}_i, \widehat{w}_i$, called virtual velocity of node i, are dependent on the velocity and velocity coefficients of the nodes around node i. K_i^u, K_i^v, K_i^w denote the nodal pressure coefficients in the direction of x, y, z coordinate, respectively.

Substitution of the velocity expressions (4) into the continuity equation, which is discretized using the Galerkin method, yields the following element equation for pressure:

$$\begin{aligned} &\int_V \left[\frac{\partial N_i}{\partial x} \left(N_j K_j^u \frac{\partial N_k}{\partial x} P_k \right) + \frac{\partial N_i}{\partial y} \left(N_j K_j^v \frac{\partial N_k}{\partial y} P_k \right) + \frac{\partial N_i}{\partial z} \left(N_j K_j^w \frac{\partial N_k}{\partial z} P_k \right) \right] \mathrm{d}V \\ &= \int_V \left(\frac{\partial N_i}{\partial x} N_j \widehat{u}_j + \frac{\partial N_i}{\partial y} N_j \widehat{v}_j + \frac{\partial N_i}{\partial z} N_j \widehat{w}_j \right) \mathrm{d}V, \end{aligned} \tag{5}$$

where N represents the element-based interpolation function. The element pressure equations are assembled in the conventional manner to form the global pressure equations.

Because the velocity field obtained by solving momentum equations does not satisfy continuity equation, the velocity values need be updated after the pressure field has been obtained from equation (5), using the following relations:

$$\begin{aligned} u_i &= \widehat{u}_i - \frac{1}{A_{ii}^x} \int_V N \frac{\partial P}{\partial x} \mathrm{d}V, \\ v_i &= \widehat{v}_i - \frac{1}{B_{ii}^y} \int_V N \frac{\partial P}{\partial y} \mathrm{d}V, \\ w_i &= \widehat{w}_i - \frac{1}{C_{ii}^z} \int_V N \frac{\partial P}{\partial z} \mathrm{d}V, \end{aligned} \tag{6}$$

where $A_{ii}^x, B_{ii}^y, C_{ii}^z$ denote the nodal velocity coefficients in the direction of x, y, z coordinate, respectively.

3.2. Calculation of the Temperature Field. The temperature field plays an important role during the injection molding process. Because the viscosity of the polymer varies with its temperature, the variation of the temperature of polymer will have important influence to the injection molding process. Only after the temperature field during filling has been calculated exactly, the simulations for packing and cooling are meaningful. This paper gives a 3D model for calculating the temperature field which considers the influence of convection items on three dimensions and suitable for the wider range of parts and has more exact results compared with the 2.5D models. According to the energy equation (1e), by the use of Galerkin's method, the equation for the temperature field can be expressed as follows:

$$\int_V N \rho C_p \frac{\partial T}{\partial t} \mathrm{d}V = \int_V N \left[-\rho C_p \left(u \frac{\partial T}{\partial x} + v \frac{\partial T}{\partial y} + w \frac{\partial T}{\partial z} \right) + \frac{\partial}{\partial x}\left(K \frac{\partial T}{\partial x} \right) + \frac{\partial}{\partial y}\left(K \frac{\partial T}{\partial y} \right) + \frac{\partial}{\partial z}\left(K \frac{\partial T}{\partial z} \right) + \eta \dot{\gamma}^2 \right] \mathrm{d}Vc. \tag{7}$$

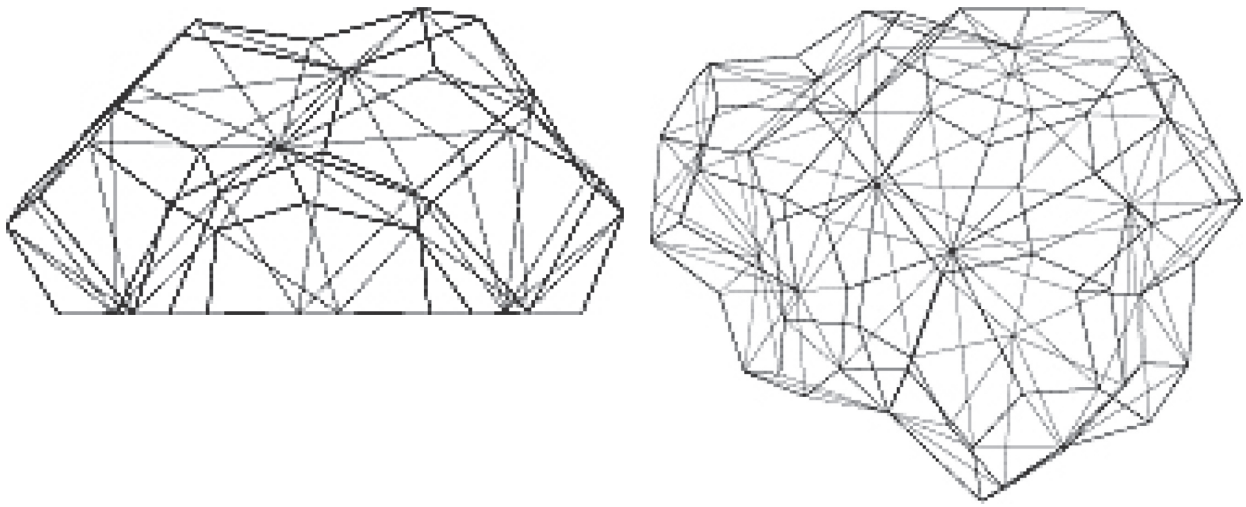

(a) (b)

Figure 2: 3D control volumes. (a) Control volume of an internal node. (b) Control volume of a boundary node.

Thermal convection item and viscous heat item are anisotropic and has to do with the direction of flow. To keep the numerical stability, the upwind method is employed to handle the convection item and viscous heat item, e.g., only the contributions of the upriver elements from the nodes are considered when the convection item and viscous heat item are calculated. In the abovementioned equations, the time T is discretized using a forward-difference method:

$$\frac{\partial T_j}{\partial t} = \frac{T_j^{n+1} - T_j^n}{\Delta t}, \tag{8}$$

where Δt denotes time step.

The element temperature equations are assembled in the conventional manner to form the global temperature equations. The overall procedure for temperature calculations is iterative. Because the pressure, velocity, and temperature influence each other during the calculation, the temperature and pressure are coupled during the procedure.

3.3. Gas Penetration. The pressure value of the gas gate node is equal to high-pressure gas pressure, and the values of temperature, viscosity, and pressure of other nodes have been gained at the end of the plastic melt filling stage, and the velocity of each node should be zero. These are the initial conditions when calculating the gas penetration and melt flow at the gas injection stage.

Here, the viscosity of gas is raised to a certain order of magnitude so that the gas and melt regions can be calculated with a uniform momentum equation although the viscosity of gas is much lower than that of polymer in fact. The adjacent nodes of the gas gate node are called the gas frontier nodes. The calculation of gas penetration is similar to calculating melt filling.

The filling time step is selected to ensure that only one node control volume is filled or replaced by gas at each time step to determine the new flow front of melt or gas. For this reason, according to the current pressure field, for melt flow, the flow rates per unit time to the melt front nodes are calculated, then the time taken for filling the first front node is determined; for gas penetration, the gas volume per unit time to the gas frontier nodes are calculated, and the time used by the gas frontier node that was first blown off is calculated. Finally, the shortest filling or blowing time is taken as the time step. The point is that the volume of the melt flowing out is equal to that of the gas penetration at each time step.

3.4. Trace of the Flow Fronts. The flow of plastic melt in the cavity and the penetration of gas in the melt are unsteady, and the positions of the flow fronts vary with time. Like in the 2.5D model, in this paper, the control volume method is employed to trace the position of the flow fronts of the melt and gas after the FAN (flow analysis network) [14]. But, 3D control volume is a special volume and more complex than the 2D control volume. It is required that 3D control volumes of all nodes fill the cavity without gap and hollow space. Two kinds of 3D control volumes are shown in Figure 2. The detailed description of the 3D control volume can be found in reference [13].

4. Verification

4.1. Experimental Product and Mould. An experimental cavity was employed for the purpose of verification. The experimental product was 200 mm long, with the cross-sectional shape, and the dimensions of the product are presented in Figure 3.

The mould used in this experiment was made by JiaRen Mould Company of Zhejiang province, China, shown as in Figure 4. PP Yuplene R370Y from SK Corporation, which is a common and representative material of GAIM [15], was selected as the simulative and experimental material. The short-shot size was 85%, injection melt temperature was 230°C, mould temperature was 40°C, gas pressure was 10 MPa, and gas injection time was 10 s.

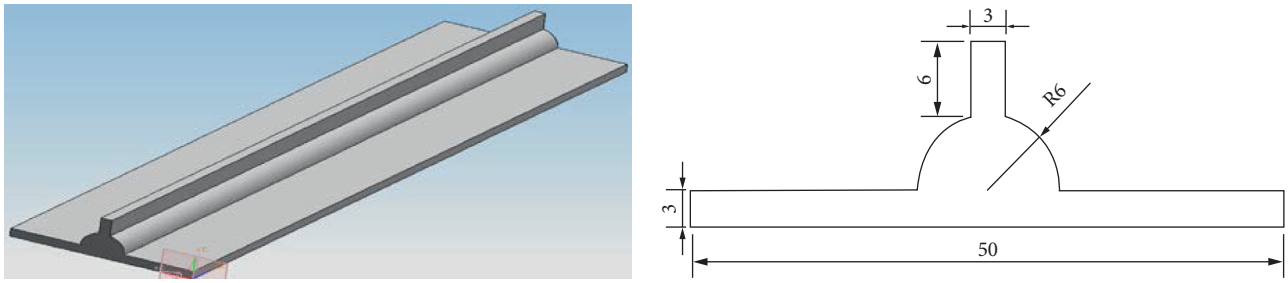

(a) (b)

Figure 3: Shape and dimensions of the product.

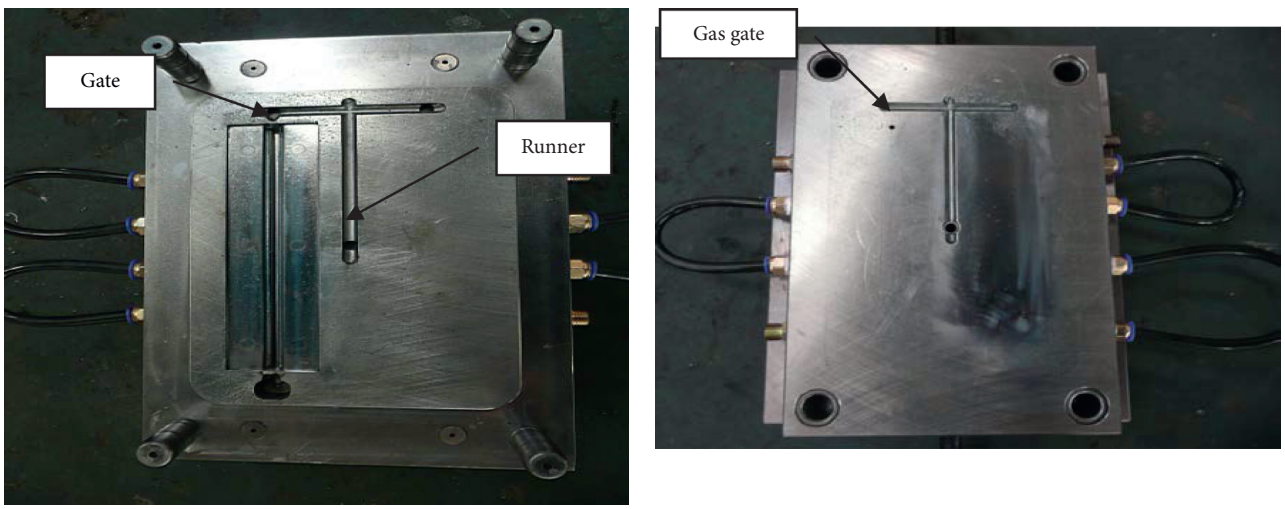

(a) (b)

Figure 4: Experimental moulds.

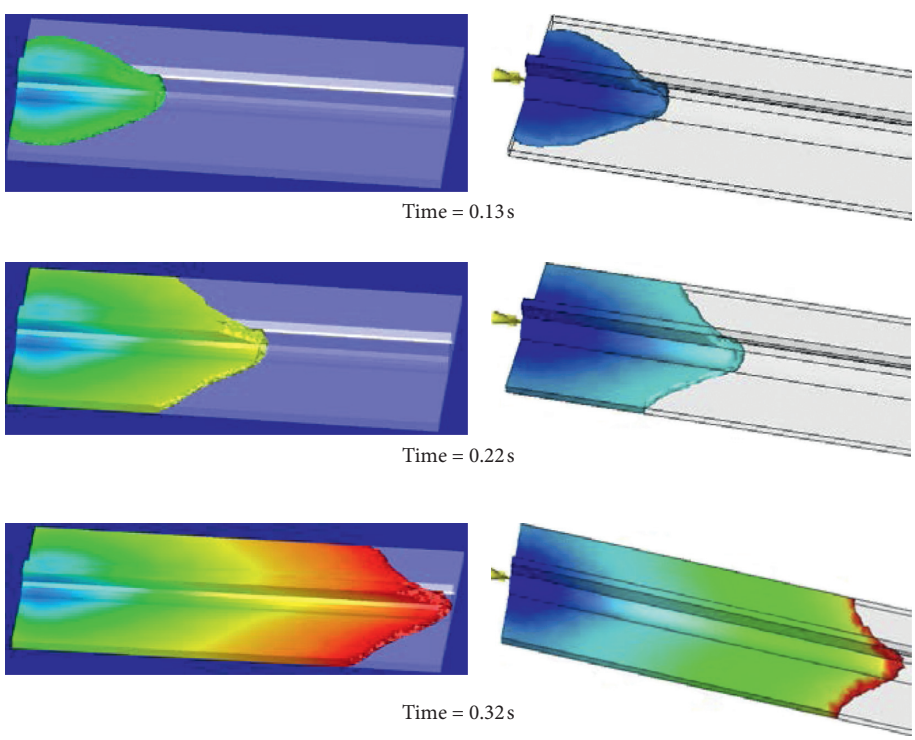

(a) (b)

Figure 5: Comparisons of the flow fronts predicted by (a) this model and (b) the commercial simulation software.

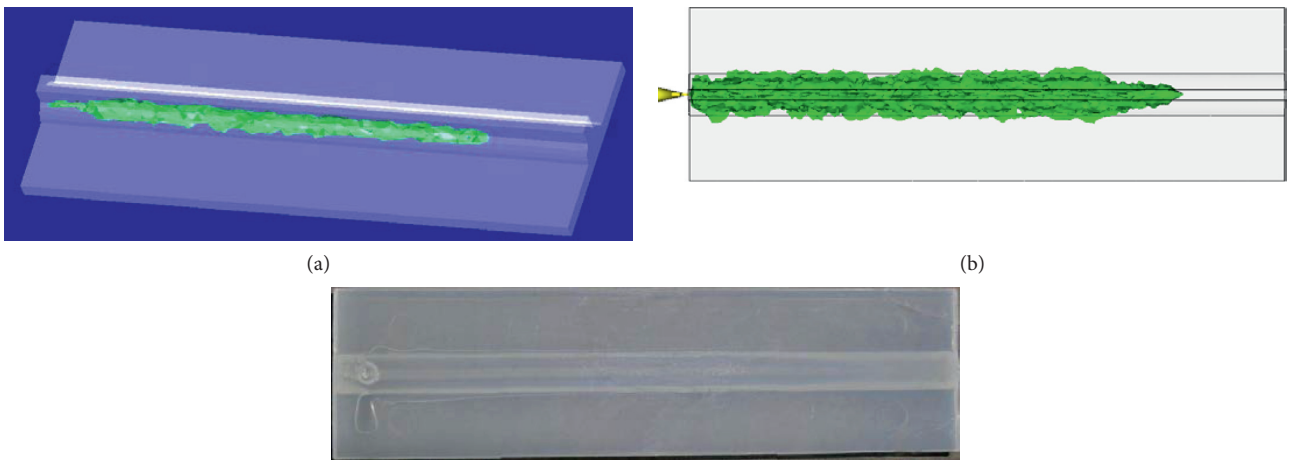

(a) (b)

(c)

Figure 6: Comparisons among predicted gas penetration length by this model, the commercial simulation software, and experimental observation. (a) Result by this model. (b) Result by the commercial software. (c) Experimental result.

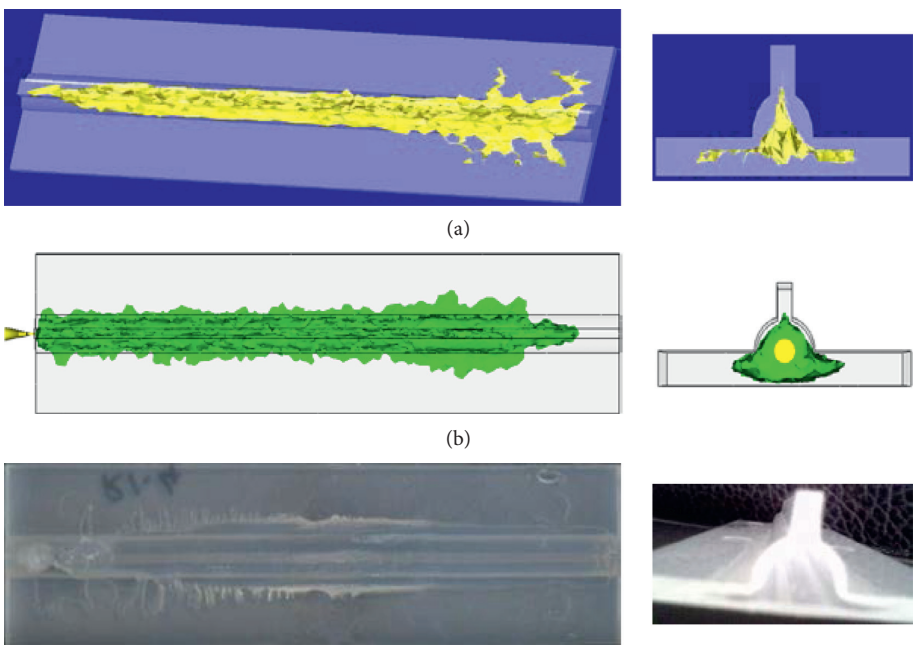

(a)

(b)

(c)

Figure 7: Comparisons among predicted fingering width range by this model, the commercial simulation software, and experimental observation. (a) Predicted result by this model. (b) Predicted result by commercial simulation software. (c) Experimental result.

4.2. Experimental Results and Discussion. In addition, the predicted result by this model was compared with that of certain a commercial simulation software to verify this model. The commercial software used was the Moldflow 2018 version in this study. The flow fronts of the melt at 3 different time steps simulated by this model and the commercial simulation software are shown in Figure 5. It can be seen that the injection sequence and the flow fronts of the melt at the same time step during the injection process predicted by the present model is in good agreement with that predicted by the commercial simulation software.

The comparison among predicted gas penetration length at certain gas injection time by this model, the commercial simulation software, and experimental observations is illustrated in Figure 6. It can be seen that the predicted direction and length of gas penetration based on this model agree well with that based on the commercial simulation software and also agree well with the experimental observation.

Another comparison among predicted fingering width range by this model, the commercial simulation software, and experimental observation is illustrated in Figure 7. It can

be seen that the maximum fingering width range predicted by both this model and the commercial simulation software are basically consistent with the experimental result. However, the cross-sectional shape of the gas channel predicted by the commercial simulation software agrees better with the experimental observation than that predicted by the present model.

5. Conclusions

A mathematic model and numerical algorithms to simulate the gas-assisted injection molding based on a 3D finite element method is presented in this paper. The model uses the equal-order velocity-pressure formulation method to prevent the potential numerical instabilities. The whole flow field including the gas and melt regions is calculated using a uniform momentum equation with the viscosity of gas raised to a certain order of magnitude. Also, a 3D control volume scheme is adopted to track the flow front of the melt and gas. The experimental verification and comparison show that the present model is valid and reliable.

Data Availability

The datasets used to support the findings of this study are available from the corresponding author upon request.

Conflicts of Interest

The authors declare that they have no conflicts of interest.

Acknowledgments

The authors would like to acknowledge financial support from the National Natural Science Foundation of China (Grant no. 51375143), the Henan Provincial Education Department Science and Technology Project (Grant no. 19A460016, and 18A430010), the Henan Provincial Science and Technology Project (Grant no. 182102210087), the Open Research Subject of National Engineering Laboratory for Wheat & Corn Further Processing (Grant no. NL201613), and Talent Support Fund of Henan University of Technology (Grant no. 2017QNJH25 and 216BS026).

References

[1] J. Avery, *Gas-Assist Injection Molding Principles and Applications*, Chemical Industry Press, Shanghai, China, 2003.

[2] S. Liang, N. Sun, and W. Yang, "The MPI 3D-simulation and experiment of the gas penetration behavior during gas-assisted injection molding," *Polymer Materials Science and Engineering*, vol. 25, no. 8, pp. 877–892, 2009.

[3] H. Zhou and D. Li, "Filling simulation and gas penetration modeling for gas-assisted injection molding," *Applied Mathematical Modelling*, vol. 27, no. 11, pp. 849–860, 2003.

[4] J. Li, L. Chen, H. Zhou, and D. Q. Li, "Surface model based modeling and simulation of filling process in gas-assisted injection molding," *Journal of Manufacturing Science and Engineering*, vol. 131, pp. 262–274, 2009.

[5] C. A. Hiebert and S. F. Shen, "A finite-element/finite-difference simulation of injection molding filling process," *Journal of Non-Newtonian Fluid Mechanics*, vol. 7, no. 1, pp. 152–164, 1980.

[6] R. A. Sousa, R. L. Reis, A. M. Cunha, and M. J. Bevis, "Structural development of HDPE in injection molding," *Journal of Applied Polymer Science*, vol. 89, no. 8, pp. 2079–2087, 2003.

[7] Y. Zhou, B. Dong, and J. B. Chen, "Numerical simulation of the filling stage in gas-assisted injection molding and contrast to experiment," *Polymer Materials Science and Engineering*, vol. 22, no. 5, pp. 28–31, 2006.

[8] Q. Li, J. Ouyang, B. Yang, and X. Li, "Numerical simulation of gas-assisted injection molding using CLSVOF method," *Applied Mathematical Modelling*, vol. 36, no. 5, pp. 2262–2274, 2012.

[9] C. Huang and J. F. Huang, *Moldflow Simulation of Injection Molding from Entry to Mastery*, Machinery Industry Press, South Norwalk, CT, USA, 2017.

[10] P. Thakre, A. S. Chauhan, E. Raj Kumar, E. R. Kumar, and R. Pradyumna, "Estimation of shrinkage & distortion in WaxInjection using Moldex3D simulation," *Materials Today: Proceedings*, vol. 5, no. 9, pp. 19410–19417, 2018.

[11] J. G. Rice and R. J. Schnipke, "An equal-order velocity-pressure formulation that does not exhibit spurious pressure modes," *Computer Methods in Applied Mechanics and Engineering*, vol. 58, no. 2, pp. 135–149, 1986.

[12] H. Zhou, T. Geng, and D. Li, "Numerical filling simulation of injection molding based on 3D finite element model," *Journal of Reinforced Plastics and Composites*, vol. 24, no. 8, pp. 823–830, 2005.

[13] G. Tie, L. Dequn, and Z. Huamin, "Three-dimensional finite element method for the filling simulation of injection molding," *Engineering with Computer*, vol. 21, no. 4, pp. 289–295, 2006.

[14] Z. Tadmor, E. Broyer, and C. Gutfinger, "Flow analysis network (FAN)-A method for solving flow problems in polymer processing," *Polymer Engineering and Science*, vol. 14, no. 9, pp. 660–665, 1974.

[15] H. L. Sheng and F. Liu, *Injection Molding Simulation Examples of Moldflow*, Publishing House of Electronics Industry, Beijing, China, 2014.

Hindawi
Advances in Polymer Technology
Volume 2020, Article ID 6861216, 15 pages
https://doi.org/10.1155/2020/6861216

Research Article

Numerical Simulation on the Penetration Behavior of the Projectile during the Water Injection Stage of Water-Projectile-Assisted Injection Molding Process

Tangqing Kuang,[1] Qiang Feng,[1] Tian Liu,[1] Luohao Zhong,[1] Yanqing Wang,[1] and Hesheng Liu[2]

[1]*East China Jiaotong University, Nanchang 330013, Jiangxi, China*
[2]*East China University of Technology, Nanchang 330013, Jiangxi, China*

Correspondence should be addressed to Tangqing Kuang; 545960963@qq.com

Received 22 May 2019; Revised 25 July 2019; Accepted 4 September 2019; Published 28 March 2020

Guest Editor: Yun Zhang

Copyright © 2020 Tangqing Kuang et al. This is an open access article distributed under the Creative Commons Attribution License, which permits unrestricted use, distribution, and reproduction in any medium, provided the original work is properly cited.

Water-projectile-assisted injection molding (W-PAIM) is a novel molding process for plastic pipes with complicated shape. It utilizes high-pressure water as a power to push a solid projectile to penetrate through the melt to form a hollow space. In order to investigate the penetration behavior of the projectile during the water injection stage of W-PAIM process, numerical simulation of the water injection stage of a W-PAIM pipe with straight and curved segments was carried out. A turbulent flow for the driving water was considered in the motion equation, and the dynamic mesh technology was used to deal with the moving solid projectile. The simulation results, including RWT and the flow fields, were compared with those of water-assisted injection molding (WAIM) pipe with the same outer dimensions. It was found that the residual wall thickness (RWT) of the W-PAIM pipe is much thinner than that of the WAIM pipe. The projectile has a crucial influence on the RWT. The pressure fields of W-PAIM and WAIM are very similar in both straight and curved segments. The velocity field and strain rate field near the penetration front in W-PAIM are quite different from those in WAIM due to the drag flow caused by the projectile penetration.

1. Introduction

The processing of plastic products occupies a large proportion in the current manufacture industry. [1] Water-assisted injection molding (WAIM) is one of the innovations of plastic injection molding processes [1]. In the Institute of Plastics Processing in Germany [2, 3], WAIM is developed to produce hollow or partially hollow parts in 1998. In the process, pressurized water following the melt injection step is injected into the core of the melt to form a hollow product. The development of this molding technique was made as a variant of the well-known gas-assisted injection molding process (GAIM), in which gas is used to core out the product. Both GAIM and WAIM techniques might produce complex pipe products with thin and thick sections, which are present in various branches of industry. Simultaneously, compared to the conventional injection molding process, they have the main strength of improving product characteristics and lowering production costs on the hollow products partiality. The use of water instead of gas leads to a further enhancement of some product characteristics and reduction of process costs, which is principally associated with the physical properties of water. More details on the specific advantages and disadvantages of both techniques are already extensively documented in earlier studies [4, 5].

Fluid-projectile-assisted injection molding (FPAIM, PIT in German) process, which is one process variant of fluid-assisted injection molding (FAIM, including WAIM and GAIM), can overcome the limitations of FAIM such as thicker residual wall thickness (RWT), fluctuation of RWT, and material selection. It was first documented in a Japanese patent [6]. In the process, a hollow channel in a part is

formed by a projectile which is pushed to core out polymer melt by a pressurized fluid. Compared with GAIM or WAIM, thinner and more uniform wall thicknesses with smoother surfaces can be achieved [7]. Moreover, the FPAIM process possesses a wider range of material applicability because molten core is displaced by a rigid projectile and the fluid comes only after the RWT is formed. FPAIM has two methods: short shot method and full shot method. The main difference between them is whether the cavity is partially or fully filled with a resin melt before the water injection. Analogous to the FAIM process, the FPAIM process can be classified as water-projectile-assisted injection molding (W-PAIM) and gas-projectile-assisted injection molding (G-PAIM). Liquid water has a higher cooling efficiency and can shorten cycle times in the W-PAIM process. Many researchers have investigated the penetration behaviors of water, the distribution of the RWT [8–12], and the optimization of processing parameters in WAIM via experimentation [13–15]. However, to the best knowledge of the authors, only some researchers from the Institute of Plastic Processing (IKV) at RWTH Aachen University have studied the FPAIM process via experimentation. They showed the potential and limitations of the new process [16–18]. As far as the authors know, the penetration behavior of the projectile during the water injection stage of W-PAIM process has not been theoretically studied.

This present research is devoted to studying the characteristics of flow filed and the penetration behavior of the projectile during the water injection stage of W-PAIM process. A W-PAIM pipe with straight and curved segments was used as a test case, and numerical simulation of the water injection stage of it was conducted. This study includes the following: (1) the influence of projectile on the size of penetrating section and the distribution of RWT; (2) the characteristics of velocity field, pressure field, and strain rate field when the projectile is penetrating through the straight segment; and (3) the flow field when the projectile is penetrating through the curved segment. The research results are helpful to understand the penetration mechanism of the projectile in melt and provide a theoretical basis for the process control of W-PAIM and quality improvement of W-PAIM part.

2. Modeling and Method

2.1. Mathematical Model. Generalized Hele-Shaw model was widely used in the numerical simulations of the conventional injection molding. But it is limited to the thin-walled cavity and laminal flow. The water injection stage of W-PAIM is a multiphase stratified unsteady flow involving fluid-structure interaction, which includes the non-Newtonian laminar of the melt with low Reynolds number, the turbulence of the water injection with high Reynolds number, and the interaction among the melt, water, and the projectile. Therefore, it is necessary to improve the mathematical model. To simplify the model and facilitate the simulation, the simplification assumptions are as follows based on CFD method: the water and melt are incompressible; the melt flow meets no-slip boundary; the body forces and surface tension are ignored; the melt fills mold cavity uniformly at the initial state, and the melt injection process does not affect the projectile penetration; and the plastic projectile with a high melting point was regarded as a moving solid boundary without thermal properties.

Governing equations include the continuity equation, motion equation, energy equation, constitutive equation, viscosity model, and volume fraction equation.

Based on the simplifications that water and melt are incompressible, the continuity equation is given by

$$\frac{\mathrm{d}u_i}{\mathrm{d}x_i} = 0, \tag{1}$$

where u_i is the fluid velocity.

During the penetration of projectile, the driving water is high Reynolds number turbulence. Therefore, the random nature of turbulent flow must be considered in motion equations. The Reynolds time-averaged motion equation is given by

$$\frac{\partial}{\partial t}(\rho u_i) + \frac{\partial}{\partial x_j}(\rho u_i u_j) = \frac{\partial}{\partial x_j}\left[\mu\left(\frac{\partial u_i}{\partial x_j} + \frac{\partial u_j}{\partial x_i} - \frac{2}{3}\delta_{ij}\frac{\partial u_l}{\partial x_l}\right)\right] - \frac{\partial p}{\partial x_i} + \frac{\partial}{\partial x_j}\left(-\rho\overline{u_i' u_j'}\right). \tag{2}$$

The equations are not closed and cannot be solved for the introduction of Reynolds stress in the last item of equation (2). To deal with Reynolds stress and make the equations close, the relationship between Reynolds stress and average velocity gradient is established based on the Bossiness eddy viscosity assumption:

$$-\rho\overline{u_i' u_j'} = \mu_t\left(\frac{\partial u_i}{\partial x_j} + \frac{\partial u_j}{\partial x_i}\right) - \frac{2}{3}\left(\rho k + \mu_t\frac{\partial u_i}{\partial x_i}\right)\delta_{ij}, \tag{3}$$

where μ_t is the turbulent viscosity and k is the turbulent kinetic energy.

In order to calculate the turbulent viscosity μ_t, a standard $k-\omega$ turbulent model was adopted, in which k is the turbulence kinetic energy and ω is the specific dissipation rate. The turbulent viscosity, μ_t, is computed by combining k and ω as follows:

$$\mu_t = \alpha^*\frac{\rho k}{\omega}, \tag{4}$$

where α^* is the modified coefficient of low Reynolds number.

k and ω are two basic unknown variables that are obtained from the following transport equations:

$$\frac{\partial}{\partial t}(\rho k) + \frac{\partial}{\partial x_i}(\rho k u_i) = \frac{\partial}{\partial x_j}\left[\left(\mu + \frac{\mu_t}{\sigma_k}\right)\frac{\partial k}{\partial x_j}\right] + G_k - Y_k,$$
$$\frac{\partial}{\partial t}(\rho \omega) + \frac{\partial}{\partial x_i}(\rho \omega u_i) = \frac{\partial}{\partial x_j}\left[\left(\mu + \frac{\mu_t}{\sigma_k}\right)\frac{\partial \omega}{\partial x_j}\right] + G_\omega - Y_\omega. \tag{5}$$

The cooling of the polymer melt by the water and mold wall is considered during the penetration of projectile, and the energy equation is given by

$$\frac{\partial}{\partial t}(\rho E)+\frac{\partial}{\partial x_i}(u_i(\rho E+p))=\frac{\partial}{\partial x_i}\left(\lambda_{\text{eff}}\frac{\partial T}{\partial x_i}+u_i\left(\tau_{ij}\right)_{\text{eff}}\right), \tag{6}$$

where E denotes the total energy of the fluid, λ_{eff} denotes the effective heat transfer coefficient, and $(\tau_{ij})_{\text{eff}}$ denotes the deviatoric stress tensor.

The melt in W-PAIM is regarded as a generalized Newtonian fluid because it is mainly affected by shear stress. Therefore, the elastic behavior of melt is ignored, and the melt constitutive equations is given by

$$\left(\tau_{ij}\right)_{\text{eff}}=\eta(p,T,\dot{\gamma})\dot{\gamma}, \tag{7}$$

where T is temperature and $\dot{\gamma}$ is deformed velocity tensor.

Due to the direct cooling of melt by water, Cross-WLF viscosity model with seven parameters was adopted to characterize the viscosity of the melt in a wide temperature range. The expression of Cross-WLF viscosity model with seven parameters is as follows:

$$\begin{aligned}\eta(\dot{\gamma},T,p)&=\frac{\eta_0(T,p)}{1+\left(\eta_0\dot{\gamma}/\tau^*\right)^{1-n}},\\ \eta_0(T,p)&=D_1\exp\left(-\frac{A_1(T-T^*)}{A_2+(T-T^*)}\right),\\ T^*(p)&=D_2+D_3p,\\ A_2&=\overline{A}_2+D_3p,\end{aligned} \tag{8}$$

where η_0 is the zero shear viscosity; τ^* is the material constant related to shear stress level transited from Newton viscosity to power-law viscosity; n is the non-Newtonian index in the high shear rate regime; and T^* is the glass transition temperature. A_1, $\overline{A}_2$, D_1, D_2, and D_3 are material constants.

In order to make a comparison between the WAIM and W-PAIM, polypropylene (PP) is selected as the molding polymer for its good molding properties of WAIM. The parameters of Cross-WLF model of PP are obtained from Moldflow material database and shown in Table 1.

As the water and melt are free surface flows without mutual penetration between the two phases, the volume-of-fluid (VOF) method can be used to track the free interface of water/melt two-phase flow. The continuity equation of volume fraction is given by

$$\frac{\partial\alpha_i}{\partial t}+u_i\frac{\partial\alpha_i}{\partial x_i}=0, \tag{9}$$

where α_i is the volume fraction of the ith phase, which varies between 0 and 1. α_i takes the value greater than 0 and less than 1 which is referred to as the i phase front.

2.2. Test Case Model and Boundary Conditions. A pipe with straight and curved segments was modeled as a test case to investigate the penetration behavior of the projectile during the water injection stage of W-PAIM process. It has a sectional diameter of 16 mm, a deflection angle of 60°, and a bending radius of 20 mm, as shown in Figure 1. A hollow projectile with a cylinder and a rounded head was used, as shown in Figure 2.

Table 1: Cross-WLF viscosity model parameters of PP.

n	τ^*(Pa)	T_g(K)	D_1(Pa·s)	A_1	A_2	D_3
0.3083	16834.4	263.15	6.7266×10^{13}	30.441	51.6	0

In order to solve the mathematical model, the boundary and initial conditions must be specified. Boundary conditions include the inlet, outlet, and wall boundaries, as shown in Figure 1 and specified as follows.

The inlet is a circle with a diameter of 6 mm. Pressure inlet boundary condition is specified and the pressure at the inlet is water injection pressure. The pressure at the outlet is specified as atmospheric pressure. The temperature of inlet equals to water injection temperature:

$$\begin{aligned}p_{\text{inlet}}&=p_{\text{water}},\\ p_{\text{outlet}}&=0,\\ T_{\text{inlet}}&=T_{\text{water}}.\end{aligned} \tag{10}$$

The wall meets no-slip boundary condition, and the fixed temperature boundary condition is specified, that is

$$\begin{aligned}U_{\text{wall}}&=0,\\ T_{\text{wall}}&=T_{\text{mold}}.\end{aligned} \tag{11}$$

The boundary condition of the moving projectile is specified as wall without thermal properties.

The molding process of simulation is full shot method of W-PAIM, which means the mold cavity is completely filled with melt before the water injection. Therefore, the whole flow field can be initialized as follows: the volume fraction of melt is 1, the velocity of the melt is 0, and the temperature of the melt is the melt injection temperature.

The values of processing parameters are shown in Table 2.

The physical properties of PP and water shown in Table 3 are treated to be constant.

2.3. Numerical Procedure. Gambit software was applied for modeling and meshing of the test model. The numerical simulations were performed on FLUENT 16.0, a very famous fluid field simulation platform. A user-defined function was coded to calculate the melt viscosity.

In order to deal with the motion of rigid projectile, dynamic mesh in six degrees of freedom model, spring smoothing method, and local remeshing method were applied in the simulation.

The VOF model was adopted to track the free interface of water/melt two-phase flow. The pressure-implicit with splitting of operators (PISO) algorithm was used to solve the pressure-velocity coupling equation for its high accuracy and capability to deal with unsteady flow. The volume fraction discrete item is "QUICK," the pressure discrete item

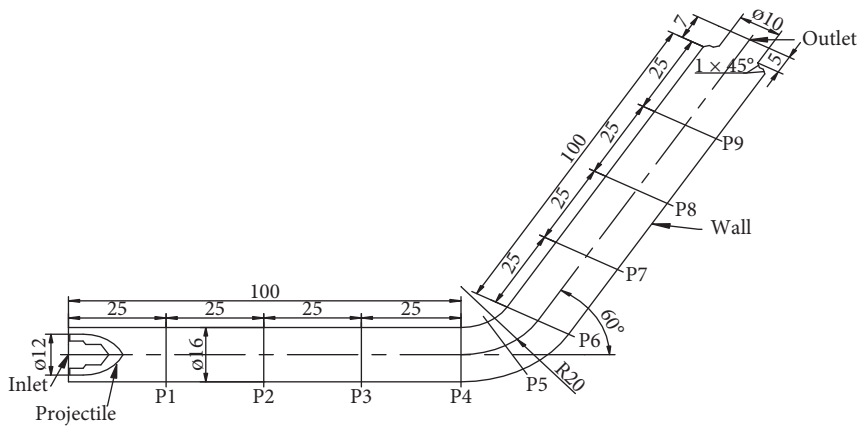

Figure 1: CFD model of a pipe with straight and curved segments for the simulations. All dimensions are in millimeters (no projectile for WAIM process).

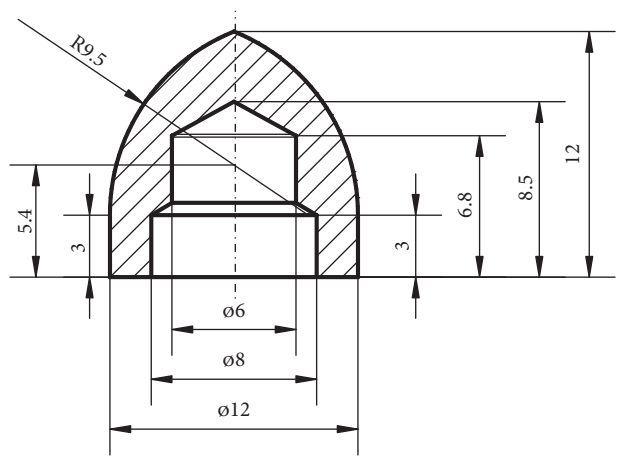

Figure 2: Projectile used in the simulation of W-PAIM process (All dimensions are in millimeters).

Table 2: Processing parameters in the simulation.

Melt temp (K)	Water pressure (MPa)	Melt injection pressure (MPa)	Holding time (s)	Water delay time (s)	Mold temp (K)
483	5	6	5	0	300

Table 3: Physical properties of melt and water in the simulation.

Material	Density ($kg \cdot m^{-3}$)	Cp ($J \cdot kg^{-1} \cdot K^{-1}$)	Thermal conductivity ($W \cdot m^{-1} \cdot K^{-1}$)	Viscosity ($kg \cdot m^{-1} \cdot s^{-1}$)	Standard state enthalpy ($J \cdot kg^{-1} \cdot mol^{-1}$)	Reference temperature (K)
PP	775	3450	0.1875		387940	483
Water	998.2	4182	0.6	1.003	-2.858×10^{8}	298

is "PRESTO!", and the other items are "First-Order Upwind". For convergence and smoothness of solutions, the underrelaxation factors are all set to 0.3 and the time step size is fixed as 1E-5 s.

3. Results and Discussion

3.1. RWT. Figures 3(a) and 3(b)show the penetration interface of WAIM and W-PAIM, respectively. As can be seen from that, both penetrations of water and projectile are successfully completed. Figure 3(c) shows the quantitative comparison of the RWTs at the specified positions between them. At the straight segments, the RWT of the WAIM pipe is about 2.1 mm, while that of the W-PAIM pipe is about 1.4 mm. At the curved segments, the RWTs of the WAIM pipe are 1.2 mm at the inner concave side and 2.8 mm at the outer convex side, while the RWTs of the W-PAIM pipe are 0.8 mm at the inner concave side and 2.0 mm at the outer convex side. The RWTs of the W-PAIM pipe are much thinner than those of the WAIM pipe. In

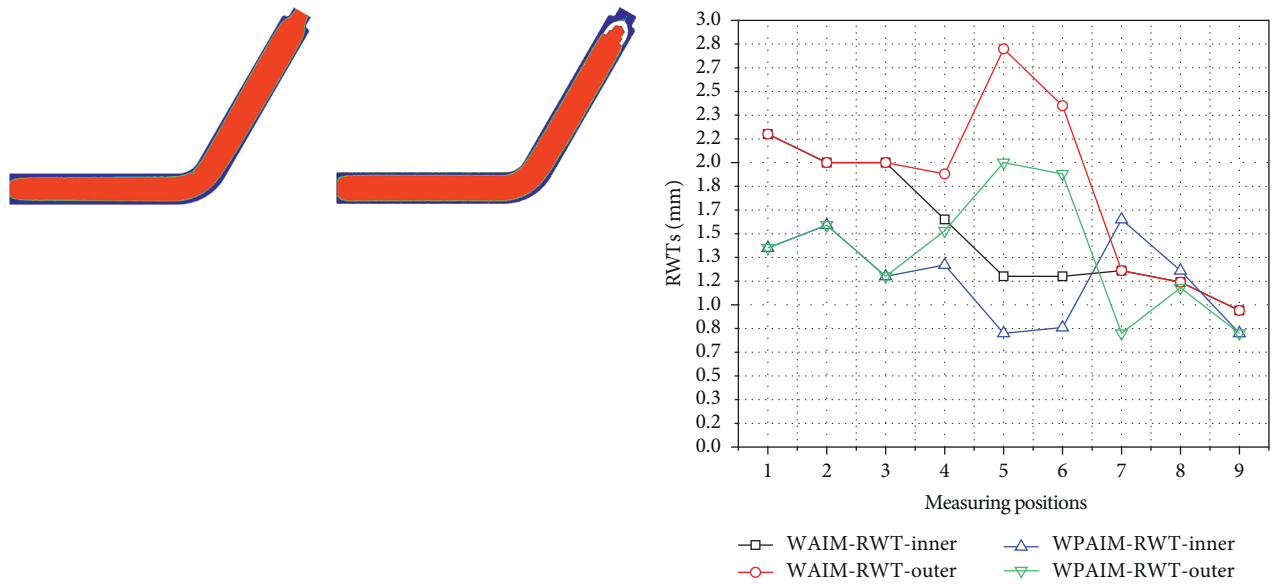

(a) (b) (c)

Figure 3: Comparison of penetration interfaces and RWTs between WAIM and W-PAIM pipe: (a) penetration interface of WAIM pipe, (b) penetration interface of W-PAIM pipe, and (c) RWTs.

addition, at the curved segments, the RWTs are thinner at the inner concave side and thicker at the outer convex side. This means that the penetrations of water in WAIM and the projectile in W-PAIM are relatively stable at the straight segment and always close to the inner concave side. The simulation results are in good agreement with the experimental results obtained by Hopmann and Behmenburg [17] and our preliminary work [19]. Obviously, the projectile has a crucial influence on the RWT. Moreover, it can be seen for both pipes that the RWTs at the second straight segments near the outlet show a decreasing trend along the flow direction. This is because in the simulation the outlet boundary is set to atmospheric pressure and the inlet pressure is water injection pressure. As the penetration proceeds, the pressure gradient in the melt in front of the penetration front increases gradually, and the penetration cross section increases correspondingly. The uniform penetration cross section can be obtained by designing a slender rather than a bulky overflow cavity.

In order to investigate the effects of different projectile diameters on RWT, different diameters projectile designs, such as 0 mm (0 mm represents the water-assisted injection molding experiment without a projectile), 6 mm, 8 mm, 10 mm, and 12 mm, were explored and compared with WAIM.

As shown in Figure 4, the RWT measurement scheme is that six pipe samples are taken for each group experiment and each pipe takes four-section positions (P1, P2, P3, and P4) along the flow direction. Each section takes four equal points (P5, P6, P7, and P8) to measure wall thickness. All wall thickness data were recorded and the arithmetic mean was used to acquire the average RWT. The expression illustrating the arithmetic mean method for solving the RWT is as follows:

$$t_{P1} = \frac{t_{P5} + t_{P6} + t_{P7} + t_{P8}}{4},$$
$$T_{P1} = \frac{t_{P1} + t_{P2} + t_{P3} + t_{P4}}{4}, \quad (12)$$
$$A_0 = \frac{T_{P1} + T_{P2} + T_{P3} + T_{P4} + T_{P5} + T_{P6}}{4},$$

where t_{Pi} is the average RWT at ith transverse section position at the same pipe, T_{Pi} is the average RWT at ith pipe, and A_i is the average RWT at ith type of pipe.

Figure 5 shows the comparison of the cross section of test samples molding by different projectile diameters, including transverse section (Figure 5(a)) and longitudinal section (Figure 5(b)). It might be seen that the RWT of the pipe shaped with a cross-sectional diameter of 6 mm is large. The wall thickness distribution of the pipe is nonuniform. When the diameter of the projectile is less than 10 mm, there is a certain deflection phenomenon during projectile passing the melt, which makes the wall thickness distribution of the pipe uneven. Therefore, the RWT of the pipe is mainly affected by the extrusion of the projectile and the water pushing the melt. At the same time, to obtain the average RWT, enough measuring data points of each test sample will be taken. More samples are measured. As shown in Figure 5(c), it can be found that when the diameter of the projectile is 6 mm, the RWT of the pipe is 2.78 mm. When the diameter of the projectile is 8 mm, the RWT of the pipe is 2.39 mm. According to the result of the error bar, the figure shows that when the diameter of the projectile is less than 10 mm, the RWT fluctuates greatly. However, when the diameter of the projectile is larger than 10 mm, the RWT of the pipes is mainly affected by the size of the projectile. The RWT is thinner than the WAIM process. According to the trend of

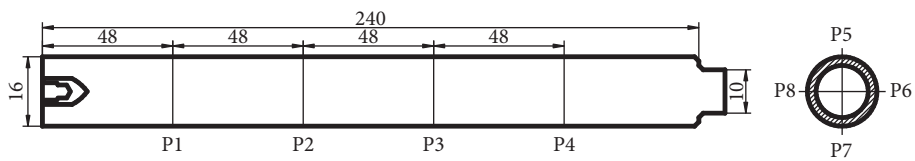

Figure 4: RWT measurement scheme.

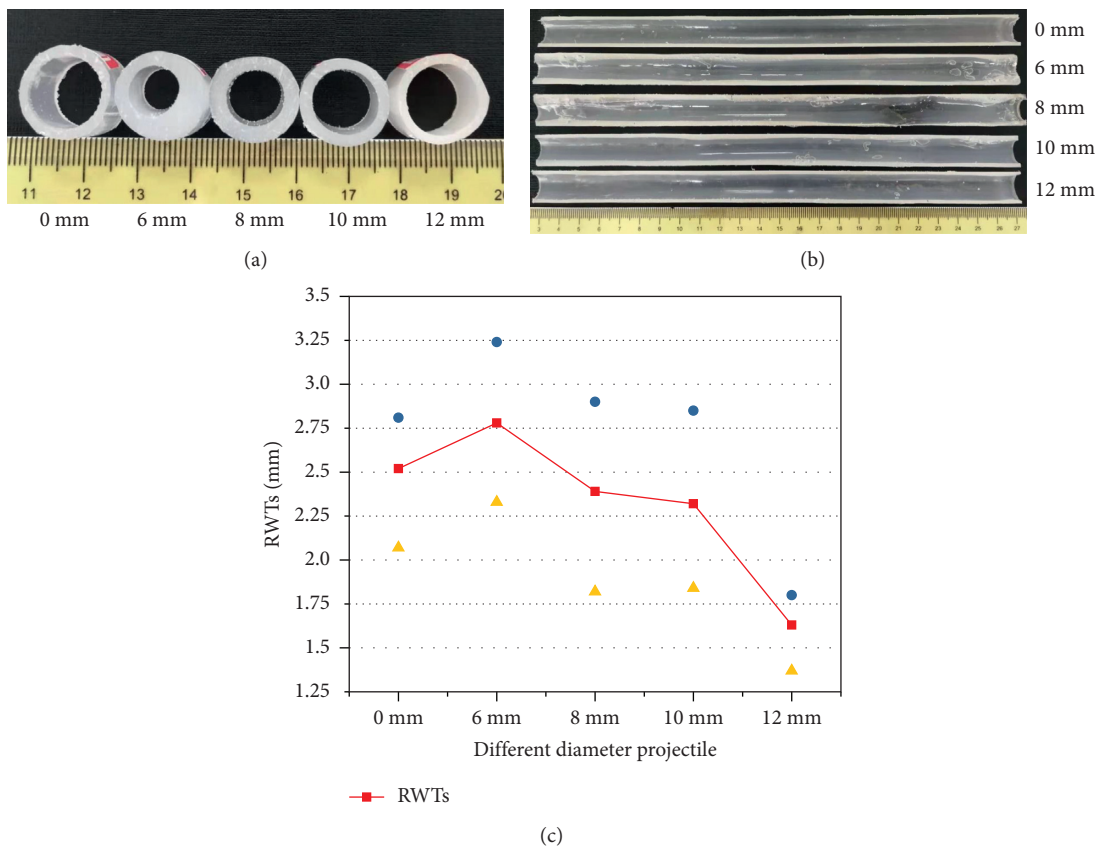

Figure 5: Comparison of RWTs between WAIM and different diameters projectile W-PAIM pipe: (a) transverse section of WIAM and W-PAIM pipes, (b) longitudinal section of WIAM and W-PAIM pipes, and (c) RWTs and error bar.

the graph, it can be concluded that the RWT of the pipes shaped by the W-PAIM process decreases with the increase in the diameter of the projectile.

3.2. Penetration Behavior of the Projectile at Straight Segment. In order to investigate the penetration behavior of the projectile at the straight segment, the velocity, pressure, and strain rates near the penetration front were explored and compared with those of WAIM.

Figure 6 shows the comparison of the velocity distribution near the penetration front at the middle location of the straight segment between WAIM and W-PAIM. For the convenience of observation, the penetration interfaces are overlay-displayed on the velocity magnitude contour, as shown in Figures 6(a) and 6(b). It can be seen for both processes the cross sections of the velocity field near the penetration front increase remarkably and the velocity fields in front of the penetration fronts are very uniform. The quantitative comparison of the velocity at three positions of 0.04, 0.05, and 0.06 mm from the entrance, marked by x-0.04, x-0.05, and x-0.06, is shown in Figures 6(c)–6(e), respectively. Both the velocity profiles of WAIM and W-PAIM at x-0.04, the position behind the penetration front, are approximately parabolic, which is a characteristic of pressure flow of Newtonian fluid. The velocities near the wall, or rather in the RWT zone, are almost zero. That means the RWTs would be almost unchanged after the penetration. Compared with the velocity profile of WAIM, the velocity profile of W-PAIM has a wider radial range and a smaller value at the center of cavity for its larger penetration section and the block of the rigid projectile. The velocity at the center in WAIM reaches 12 m/s and that in W-PAIM is about 10 m/s. Both velocities are much faster than 0.34 m/s, a critical velocity of laminar flow and turbulence of water. Therefore, water flows in turbulent state. It shows the rationality of using the turbulent model for water in the simulation. At the current position of the penetration front, that is, x-0.05, the velocity profile of W-PAIM showed

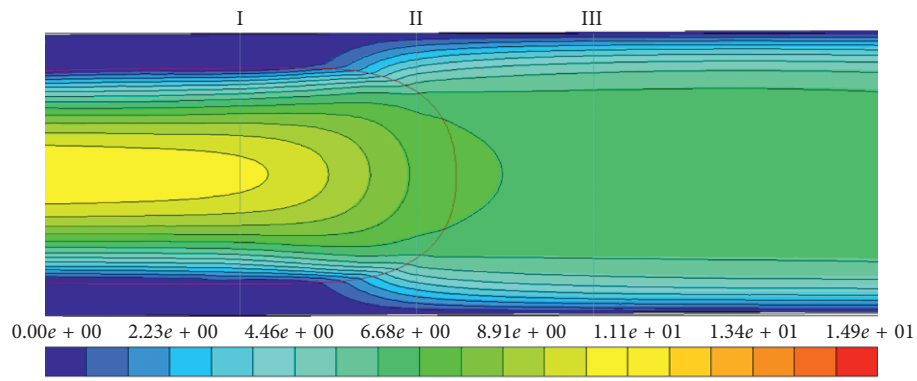

(a)

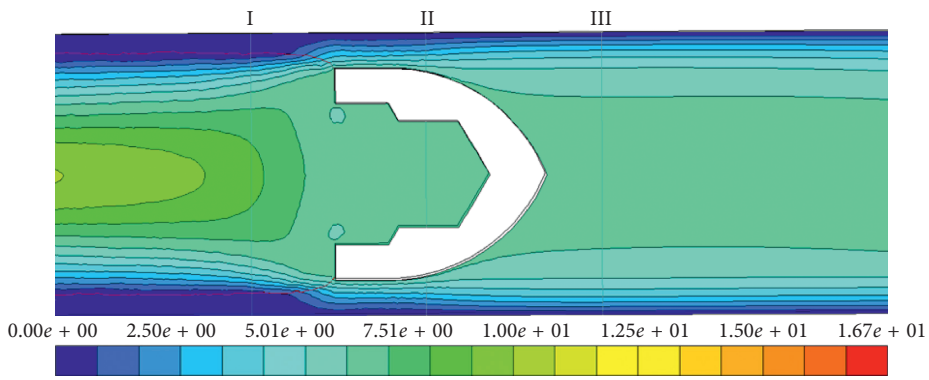

(b)

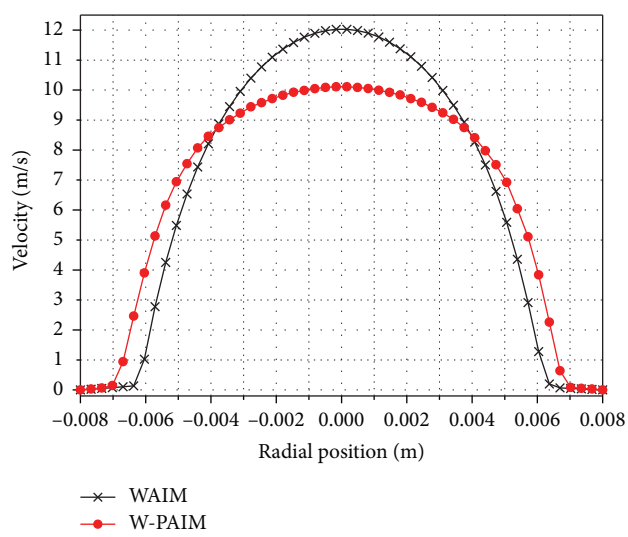

(c)

Figure 6: Continued.

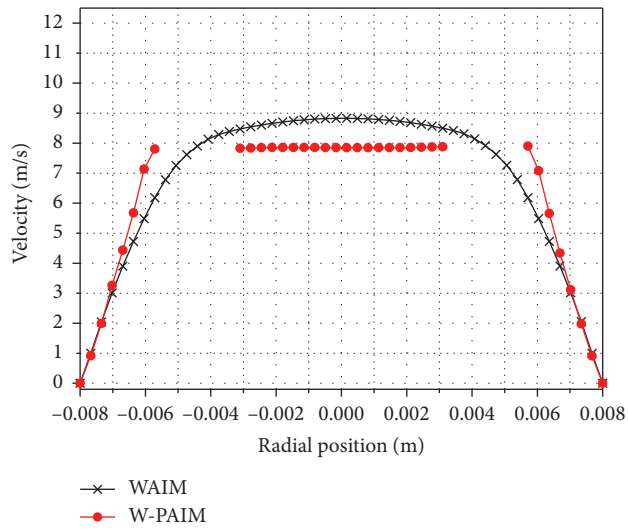

(d)

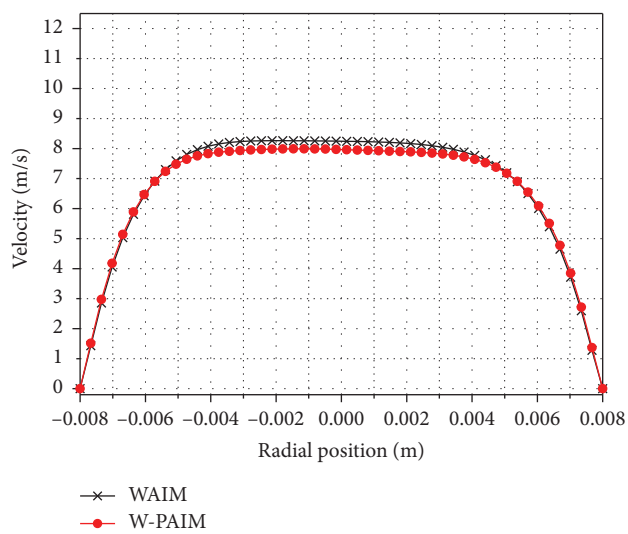

(e)

Figure 6: Comparison of the velocity distribution near the penetration front at the middle location of straight segments between WAIM and W-PAIM: (a) velocity magnitude contour of WAIM, (b) velocity magnitude contour of W-PAIM, (c) velocity profiles at position I, (d) velocity profiles at position II, (e) velocity profiles at position III (I denotes the location of 0.04 mm, II is 0.05 mm, and III is 0.06 mm).

the shape of an isosceles trapezoid without velocity segments of near zero. The horizontal segment at the middle represented the velocity of the water trapped by the projectile. The linear segments on both sides were the velocity of the melt at the outside of the projectile, which implied that the melt flow at the outside of the projectile is drag flow. Moreover, the velocity of the drag flow at the outside of the projectile is faster than that of the subsequent pressure flow near the wall. Consequently, the water followed the projectile is partially supplemented to the drag flow area. Therefore, the simulated RWT is thinner than the radius difference between the part cavity and the projectile. Compared with the velocity field at x-0.04, the cross sections of the velocity field at x-0.05 increase remarkably and the velocity profile has relatively flat middle segments, which indicates the flow there is a plunger flow. The velocity at the center in WAIM is decreased and close to 9 m/s and that in W-PAIM is about 8 m/s. The velocity profile of WAIM at x-0.06, the position in front of the penetration front, is similar to that of W-PAIM. Both of them have flat middle segments, which indicate the flow before the penetration front is a typical plunger flow of pseudoplastic flow of the melt with a non-Newtonian index of 0.3. The highest velocity in WAIM is further reduced to near 8.3 m/s and that in W-PAIM basically keeps constant of about 8 m/s.

The pressure fields of WAIM and W-PAIM processes when the penetration front reaches the middle of the straight section are also compared, as shown in Figure 7. For both processes, the pressure behind the penetration front is the injection pressure due to almost no pressure loss in water. The pressure contours after a short distance to the penetration front in W-PAIM are similar to those in WAIM. The difference is that the pressure contours in front of the W-PAIM

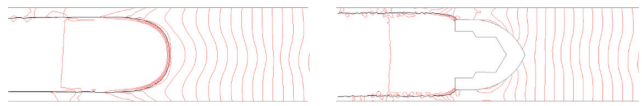

(a) (b)

Figure 7: Comparison of the pressure contours near the penetration front at the middle location of straight segments between WAIM and W-PAIM: (a) WAIM and (b) W-PAIM.

projectile are straight lines for the existence of the rigid projectile, while the pressure contours in front of the WAIM penetration front are curves with shape like the penetration front.

Figure 8 shows the comparison of the strain rate distribution near the penetration front at the middle location of the straight segment between WAIM and W-PAIM. In order to observe conveniently, the penetration interfaces are overlay-displayed on the strain rate magnitude contour, as shown in Figures 8(a) and 8(b). It can be seen for both processes that the strain rate peak behind the penetration front locates at the penetration interface, while that before the penetration front locates near the wall. The quantitative comparison of the velocity at three positions of 0.04, 0.05, and 0.06 mm from the entrance is shown in Figures 8(c)–8(e), respectively. At x-0.04, the strain rate peak of W-PAIM is 5500 1/s and locates in the radius range of 0.0065 mm, while that of WAIM is 5100 1/s and locates at a radial position of 0.006 mm. Moreover, in WAIM, the strain rate closer to the center of cavity is lower,while the strain rate of W-PAIM is relatively uniform near to the center of cavity for the block of projectile. At x-0.05, the current position of penetration front, the strain rate profiles are quite different between WAIM and W-PAIM. In WAIM, the strain rate peak locates near the wall, and the strain rate is relatively uniform in the radius range of 0.004. While the strain rate peak in W-PAIM locates at the surface of projectile, and closer to the wall, the strain rate is lower. At the location of x-0.06, the strain rate profile of W-PAIM is similar to that of WAIM. The strain rate peak locates close to the wall and is about 4500 s^{-1}. The strain rate is almost zero in the radius range of 0.004.

3.3. Penetration Behavior of the Projectile at Curved Segment. The penetration behavior of the projectile at the curved segment was explored by observing the velocity, pressure, and strain rates near the penetration front and compared with those of WAIM.

Figure 9 shows the comparison of the velocity distribution near the penetration front at the curved segment between WAIM and W-PAIM. For the convenience of investigation, the penetration interfaces are overlay-displayed on the velocity magnitude contour, as shown in Figures 9(a) and 9(b). It can be seen for both processes the cross sections of the velocity field near the penetration front increase remarkably and the velocity fields in front of the penetration fronts near the center of cavity are very uniform. The quantitative comparison of the velocity at position 4, position 5, and position 6, marked by IV, V, and VI, is shown in Figures 9(c)–9(e), respectively. The left side of the zero position is the outer convex side of the curved section and the right side is the inner concave side.

At the start position of the curved segment, as it can be seen from Figure 9(c) that both the velocity profiles of WAIM and W-PAIM are like parabolic and slightly skewed to the right, which is the inner concave side of the curved section. That indicates that the penetration tends to be close to the inner concave side at the start position of the curved segment. Compared with the velocity profile of WAIM, the velocity profile of W-PAIM has a wider range and a smaller value near the center of cavity. The velocity at the center in WAIM reaches 16 m/s and that in W-PAIM is about 12 m/s.

At the current position of the penetration front, as it can be seen from Figure 9(d) that the projectile velocity close to the outer convex side in W-PAIM is above 12.5 m/s and higher than that close to the inner concave side, which is about 8.5 m/s. Therefore, the projectile turns accordingly. However, the velocity profile of WAIM is still slightly skewed to the inner concave side with a maximum of about 13 m/s. The velocity profile of WAIM at VI, the position in front of the penetration front, is similar to that of W-PAIM. Both are skewed to the left, which is the outer convex side of the curved section. It can be seen from Figures 9(a) and 9(b) that the velocity contours with high value after the bending segment in both WAIM and W-PAIM processes deflect from the outer convex side to the center of cavity and tend to be symmetrical.

The pressure fields of WAIM and W-PAIM processes when the penetration reaches the middle of the curved section are also compared, as shown in Figure 10. The pressure contours near the penetration front in W-PAIM are similar to those in WAIM.

Figure 11 shows the comparison of the strain rate distribution near the penetration front at the curved segment between WAIM and W-PAIM. In order to observe conveniently, the penetration interfaces are overlay-displayed on the strain rate magnitude contour, as shown in Figures 11(a) and 11(b). It can be seen for both processes that the maximum strain rate behind the penetration front locates at the penetration interface, while that before the penetration front locates near the wall. The quantitative comparison of the velocity at three positions of IV, V, and VI is shown in Figures 11(c)–11(e), respectively. At position IV, the strain rate peak of W-PAIM near the outer convex side is about 5600 1/s and locates in the radius of 0.0055 mm, and it is about 9500 1/s near the inner concave side and locates in the radius of 0.0065 mm. That is to say, the strain rate on the outside is higher than that on the inside. However, the strain rate peak of WAIM near the outer convex side is about 10000

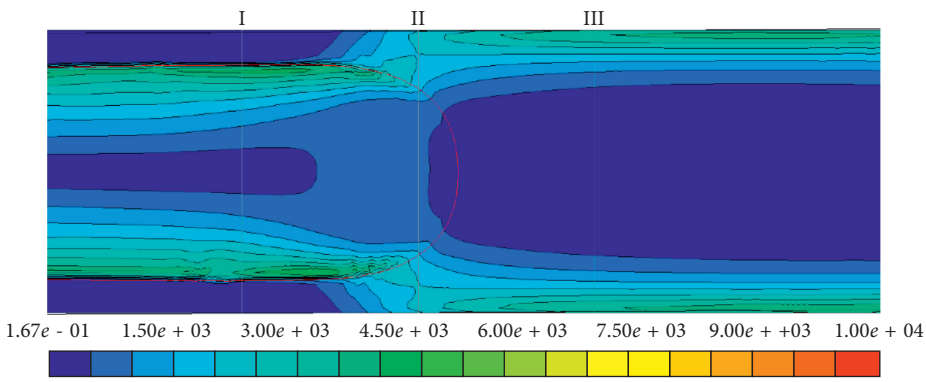

(a)

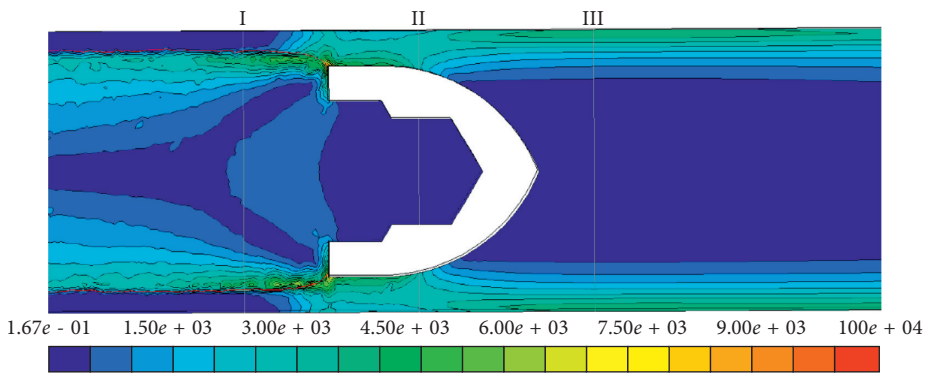

(b)

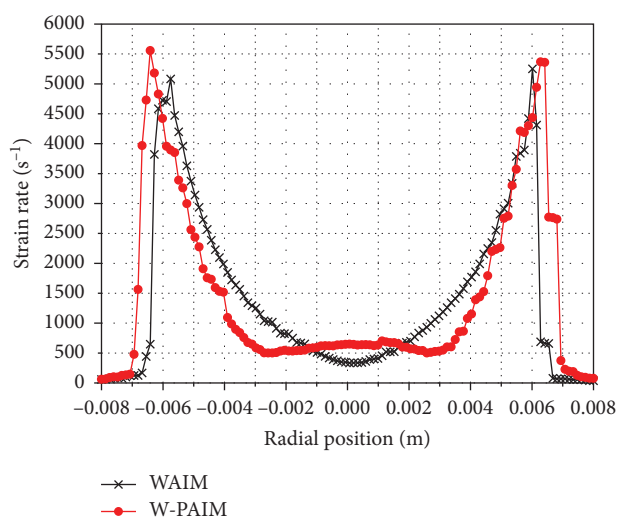

(c)

Figure 8: Continued.

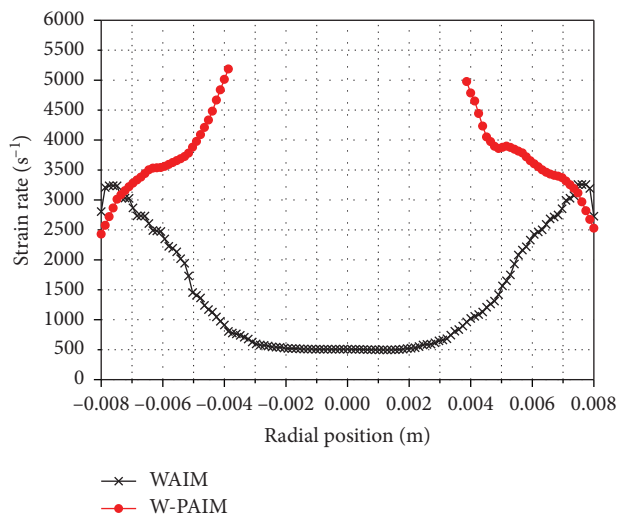

(d)

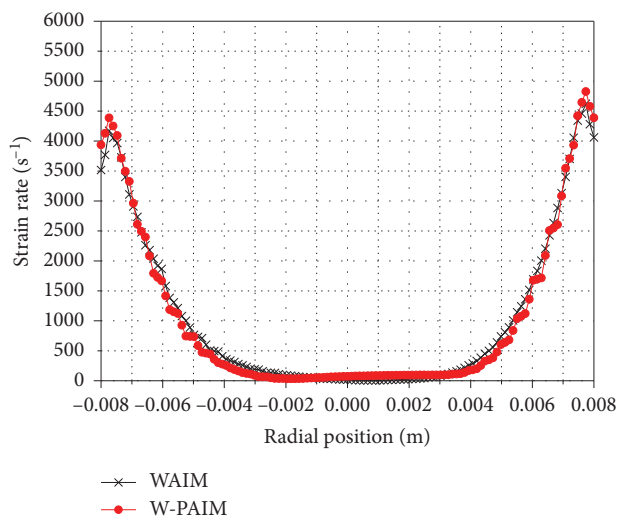

(e)

Figure 8: Comparison of the strain rate distribution near the penetration front at the middle location of straight segments between WAIM and W-PAIM: (a) strain rate magnitude contour of WAIM, (b) strain rate magnitude contour of W-PAIM, (c) strain rate profiles at position I, (d) strain rate profiles at position II, and (e) strain rate profiles at position III (I denotes the location of 0.04 mm, II is 0.05 mm, and III is 0.06 mm).

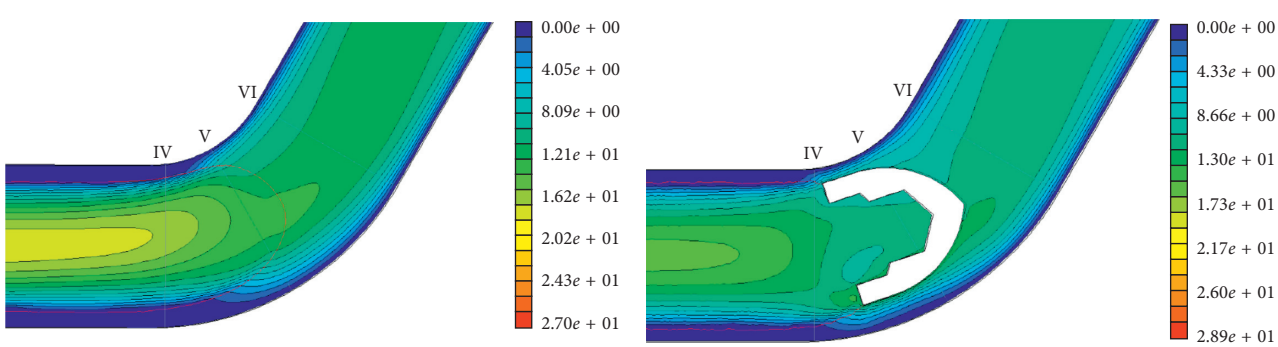

(a) (b)

Figure 9: Continued.

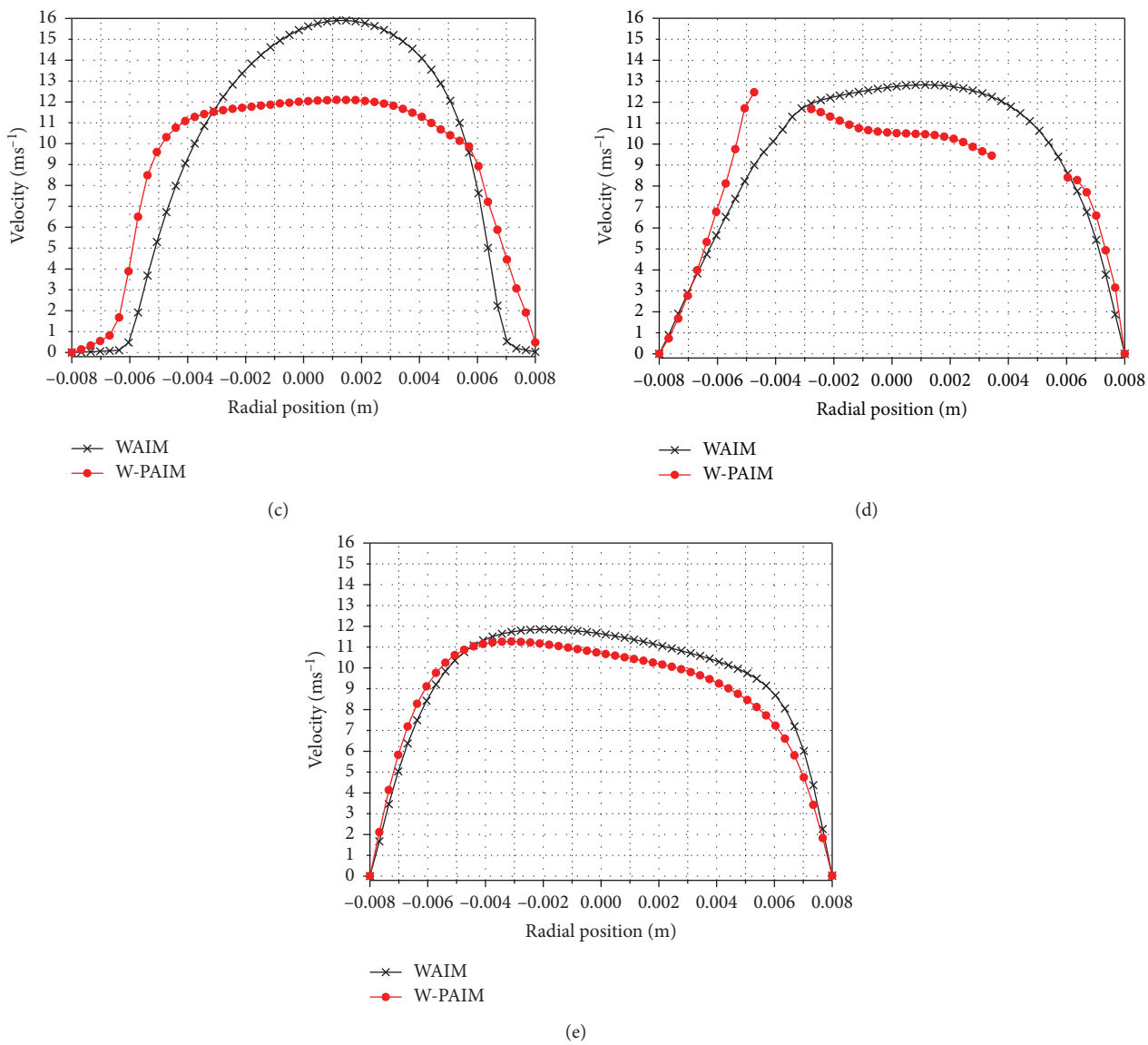

Figure 9: Comparison of the velocity distribution near the penetration front at the middle location of curved segments between WAIM and W-PAIM: (a) velocity magnitude contour of WAIM, (b) velocity magnitude contour of W-PAIM, (c) velocity profiles at position IV, (d) velocity profiles at position V, and (e) velocity profiles at position VI (IV, V, and VI denote the beginning, middle, and end of the curved segments, respectively. Negative radial positions are near the outer convex side of curved segments, while the positive radial positions are near the inner concave side).

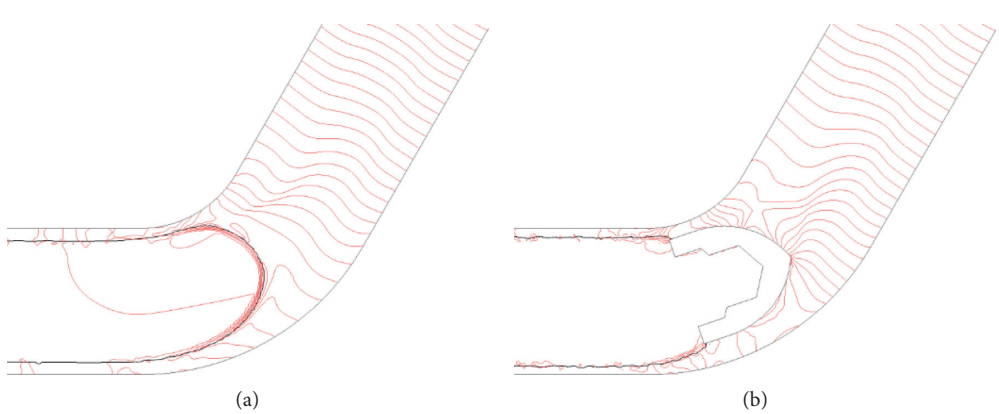

Figure 10: Comparison of the pressure contours near the penetration front at the middle location of curved segments between WAIM and W-PAIM: (a) WAIM and (b) W-PAIM.

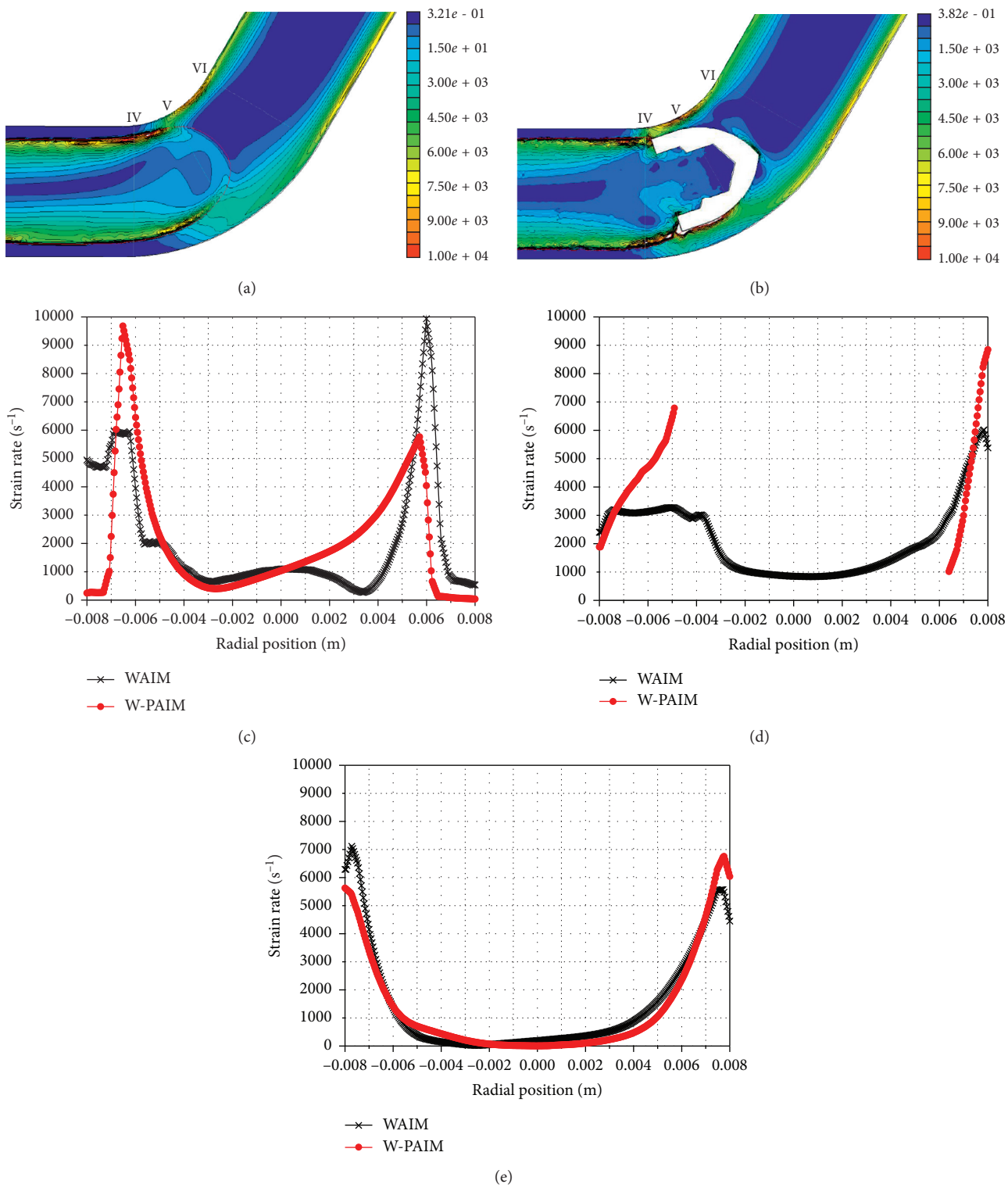

Figure 11: Comparison of the straight rate distribution near the penetration front at the middle location of curved segments between WAIM and W-PAIM: (a) straight rate magnitude contour of WAIM, (b) straight rate magnitude contour of W-PAIM, (c) velocity profiles at position IV, (d) straight rate profiles at position V, and (e) straight rate profiles at position VI (IV, V, and VI denote the beginning, middle, and end of the curved segments, respectively. Negative radial positions are near the outer convex side of curved segments, while the positive radial positions are near the inner concave side).

1/s and locates in the radius of 0.006 mm, and it is about 6000 1/s near the inner concave side and locates in the radius of 0.0065 mm. At the start position of the curved section, the strain rate peak on the outside is about 4000 1/s higher than that on the inside in W-PAIM, while it is opposite in WAIM. At position V, the current position of penetration front, both

the strain rate peaks in WAIM and W-PAIM near the inner concave side are close to the wall. The strain rate peak in W-PAIM near the outer convex side is close to the projectile, while that in WAIM is uniform. At position VI, the strain rate profile of W-PAIM is approach to that of WAIM with the peak close to the wall. The strain rate peak of W-PAIM near the outer convex side is about 5500 1/s, and it is about 6700 1/s near the inner concave side. The strain rate peak of WAIM near the outer convex side is about 7100 1/s, and it is about 5500 1/s near the inner concave side. In other words, at the end position of curved section, the strain rate peak on the outside is about 1000 1/s less than that on the inside in W-PAIM, while it is opposite in WAIM.

4. Conclusion

According to the simulation results of the water injection stage of a W-PAIM pipe with straight and curved segments and the comparison with those of WAIM pipe, the following conclusions can be drawn:

(1) When the diameter of the projectile is 12 mm, the RWTs of the W-PAIM pipe are much thinner than those of the WAIM pipe in the case studied. In addition, at the curved segments, the RWTs are thinner at the inner concave side and thicker at the outer convex side. The projectile has a crucial influence on the RWT. The penetrations of the projectile in W-PAIM are relatively stable at the straight segment and always close to the inner concave side. Moreover, the uniform RWT near the end of part cavity can be obtained by designing a slender rather than a bulky overflow cavity for a constant pressure gradient. When the diameter of the projectile is less than 10 mm, there is a certain deflection phenomenon during projectile passing the melt and the RWT fluctuates greatly. The RWT of the pipes shaped by the W-PAIM process decreases with the increase in the diameter of the projectile.

(2) At the straight segment, both the velocity profiles of WAIM and W-PAIM at the position behind the penetration front are approximately parabolic for the pressure flow of Newtonian fluid there. The velocities in the RWT zone are almost zero. Compared with the velocity profile of WAIM, the velocity profile of W-PAIM has a wider radial range for the larger penetration section and a smaller value at the center of cavity for the block of the rigid projectile. At the position of the penetration front, the velocity profile of W-PAIM showed the shape of an isosceles trapezoid, which implies the melt flow at the outside of the projectile is drag flow. The velocity profile of W-PAIM at the position in front of the penetration front is approach to that of WAIM. Both have characteristics of a typical plunger flow of pseudoplastic flow of the melt with a non-Newtonian index of 0.3.

(3) At the curved segment, both the velocity profiles of WAIM and W-PAIM at the position behind the penetration front are like parabolic and slightly skewed to the inner concave side. That indicates the penetration tends to be close to the inner concave side. At the position of the penetration front, the projectile velocity close to the outer convex side in W-PAIM is higher than that close to the inner concave side, and the projectile's turning is realized. While the velocity profile of WAIM is still slightly skewed to the inner concave side. The velocity profile of W-PAIM at the position in front of the penetration front is similar to that of WAIM and both are skewed to the outer convex side and higher at that side. The velocity contours at the straight segment after the curved segment in both WAIM and W-PAIM processes deflect from the outer convex side to the center of cavity and tend to be symmetrical again.

(4) The pressure fields of W-PAIM and WAIM are very similar in both straight and curved segments. The existence of the projectile only affects the pressure field in a very small region around its location.

(5) In both W-PAIM and WAIM, the strain rate peak behind the penetration front locates at the penetration interface, while that in front of the penetration front locates near the wall. At the penetration front in straight segment, the strain rate peak of WAIM locates near the wall, while that of W-PAIM locates near the projectile outer surface. At the penetration front in the curved segment, the strain rate peak near the inner concave side in both WAIM and W-PAIM locates near the wall, while that near the outer convex side in W-PAIM locates near the penetration interface.

Data Availability

The data used to support the findings of this study are available from the corresponding author upon request.

Conflicts of Interest

The authors declare that there are no conflicts of interest regarding the publication of this paper.

Acknowledgments

This study was supported financially by the National Natural Science Foundation of China (NSFC) (nos. 51563010 and 21664002) for which the authors are very grateful. And this work was also supported financially by the Natural Science Foundation of China of Jiangxi Province (no. 20181BAB206014) for which the authors are grateful.

References

[1] M. R. Kamal, A. I. Isayev, and S. J. Liu, Eds., *Injection Molding: Technology and Fundamentals*, Hanser Gardner Publications, Cincinnati, OH, USA, 2009.

[2] S. J. Liu, "Water assisted injection molding: a review," *International Polymer Processing*, vol. 24, no. 2, pp. 315–325, 2009.

[3] W. Michaeli, A. Brunswick, and T. Pohl, "A comparison of gas and water," *Kunststoffe-Plast Europe*, vol. 89, no. 9, pp. 56–60, 1999.

[4] S. Sannen, J. De Keyzer, and P. Van Puyvelde, "The influence of melt and process parameters on the quality and occurrence of part defects in water-assisted injection molded tubes," *International Polymer Processing*, vol. 26, no. 5, pp. 551–559, 2011.

[5] S. Sannen, M. De Munck, P. Van Puyvelde, and J. De Keyzer, "Water penetration behavior in water-assisted injection molding (WAIM): a study of product quality for different process and material parameters," *International Polymer Processing*, vol. 27, no. 5, pp. 602–616, 2012.

[6] IIDA and ISAO, "Manufacture of hollow body," IIDA, ISAO, Waterford, Ireland, JPH04208425, 1992.

[7] H. Eckardt, "Making parts lightweight strong with new technologies," *Plastics Technology*, vol. 52, no. 2, 2012.

[8] S.-J. Liu and Y.-C. Wu, "Dynamic visualization of cavity-filling process in fluid-assisted injection molding-gas versus water," *Polymer Testing*, vol. 26, no. 2, pp. 232–242, 2007.

[9] A. Polynkin, L. Bai, J. F. T. Pittman et al., "Water assisted injection moulding: development of insights and predictive capabilities through experiments on instrumented process in parallel with computer simulations," *Plastics, Rubber and Composites*, vol. 37, no. 2-4, pp. 131–141, 2008.

[10] T. Kuang, C. Yu, and Y. Deng, "Influence of cross section of cavity on water penetration during overflow water-assisted injection molding process," *Journal of Chemical Industry and Engineering*, vol. 65, no. 10, pp. 4176–4182, 2014.

[11] Y. Chen, H. Zhou, Z. Zhang, and H. Kong, "Comparison research on residual wall thickness of water-assisted and gas-assisted injection molded parts," *China Plastics*, vol. 26, no. 6, pp. 71–75, 2012.

[12] H.-X. Huang and Z.-W. Deng, "Effects and optimization of processing parameters in water-assisted injection molding," *Journal of Applied Polymer Science*, vol. 108, no. 1, pp. 228–235, 2008.

[13] J. Yang, X. Zhou, and G. Luo, "Study of water penetration length and processing parameters optimization in water-assisted injection molding," *The International Journal of Advanced Manufacturing Technology*, vol. 69, no. 9-12, pp. 2605–2612, 2013.

[14] J. Yang, X. Zhou, and Q. Niu, "Model and simulation of water penetration in water-assisted injection molding," *The International Journal of Advanced Manufacturing Technology*, vol. 67, no. 1-4, pp. 367–375, 2013.

[15] C. Hopmann, W. Michaeli, M. Gründler, O. Grönlund, and A. Neuss, "Process development of the projectile injection technique (PIT)," in *Proceedings of the Annual Technical Conference of the Society of Plastics Engineers 2011, (ANTEC 2011)*, pp. 1706–1710, Boston, MA, USA, May 2011.

[16] C. Hopmann and C. Behmenburg, "Hollow bodies using the projectile injection technique," in *Proceedings of the Annual Technical Conference of the Society of Plastics Engineers 2013, (ANTEC 2013)*, pp. 282–285, Cincinnati, OH, USA, April 2013.

[17] C. Hopmann and U. Recht, "Manufacturing of fibre-reinforced, elastomeric parts using the injection molding process," in *Proceedings of the Annual Technical Conference of the Society of Plastics Engineers 2015, (ANTEC 2015)*, pp. 1728–1732, Orlando, FL, USA, March 2015.

[18] T. Kuang, J. Pan, Q. Feng et al., "Residual wall thickness of water-powered projectile-assisted injection molding pipes," *Polymer Engineering & Science*, vol. 59, no. 2, pp. 295–303, 2019.

[19] W. Liu, T. Kuang, and D. Lai, "Preliminary experimental investigation on the fluid-projectile-assisted injection molding pipes," *China Plastics Industry*, vol. 44, no. 11, pp. 138–142, 2016.

Hindawi
Advances in Polymer Technology
Volume 2020, Article ID 7654249, 9 pages
https://doi.org/10.1155/2020/7654249

Research Article

Optimization of Injection-Molding Process Parameters for Weight Control: Converting Optimization Problem to Classification Problem

Peng Zhao,[1,2,3] **Zhengyang Dong**,[1,2] **Jianfeng Zhang**,[1,2] **Yi Zhang**,[1,2] **Mingyi Cao**,[1,2] **Zhou Zhu**,[4] **Hongwei Zhou**,[5] **and Jianzhong Fu**[1,2]

[1]*The State Key Laboratory of Fluid Power and Mechatronic Systems, College of Mechanical Engineering, Zhejiang University, Hangzhou 310027, China*
[2]*Key Laboratory of 3D Printing Process and Equipment of Zhejiang Province, College of Mechanical Engineering, Zhejiang University, Hangzhou 310027, China*
[3]*Jiangsu Jianghuai Magnetic Industry Co., Ltd., Xuyi 211700, China*
[4]*College of Mechanical Engineering, Zhejiang University of Technology, Hangzhou 310014, China*
[5]*Tederic Machinery Co., Ltd., Hangzhou 311224, China*

Correspondence should be addressed to Peng Zhao; pengzhao@zju.edu.cn

Received 4 July 2019; Revised 12 August 2019; Accepted 16 September 2019; Published 26 March 2020

Academic Editor: Leandro Gurgel

Copyright © 2020 Peng Zhao et al. This is an open access article distributed under the Creative Commons Attribution License, which permits unrestricted use, distribution, and reproduction in any medium, provided the original work is properly cited.

Product weight is one of the most important properties for an injection-molded part. The determination of process parameters for obtaining an accurate weight is therefore essential. This study proposed a new optimization strategy for the injection-molding process in which the parameter optimization problem is converted to a weight classification problem. Injection-molded parts are produced under varying parameters and labeled as positive or negative compared with the standard weight, and the weight error of each sample is calculated. A support vector classifier (SVC) method is applied to construct a classification hyperplane in which the weight error is supposed to be zero. A particle swarm optimization (PSO) algorithm contributes to the tuning of the hyperparameters of the SVC model in order to minimize the error between the SVC prediction results and the experimental results. The proposed method is verified to be highly accurate, and its average weight error is 0.0212%. This method only requires a small amount of experiment samples and thus can reduce cost and time. This method has the potential to be widely promoted in the optimization of injection-molding process parameters.

1. Introduction

Injection molding is regarded as the most important method for mass-producing plastic parts [1–4], and it is complicated because of steep thermal gradients and complex flow geometries; many studies have been conducted in this field [5–10]. The product weight of a plastic part is considered one of the most significant properties, especially for plastic parts with high precision requirements, such as plastic lenses. The product weight can reflect other quality properties such as impact strength. [11]. Weight control is also of great commercial interest for manufacturers, as it reduces the cost of materials in mass production [12]. Therefore, the weight control of products is a critical issue in injection molding.

For a specific material and product, process parameters are the most important factors affecting product weight, and many studies have been conducted to explore the relationship between process parameters and product weights. Hassan [13] determined that product weight has a positive correlation with packing pressure. López et al. [14] applied the design of experiments (DOE) method to explore the influence of parameters on products with different geometries. Yang and Gao [11] found that the settings for packing pressure, barrel temperature, and mold temperature have

the most significant effects on the product weight. Hence, it is of vital importance to select optimal process parameters before the part is molded. However, the procedure for selecting optimal process parameters remains challenging. Most parameters are coupled with each other, and it is therefore difficult to construct an accurate mathematical model. The traditional parameter optimization method is an inefficient trial-and-error process based on personal experience, and it is not suitable for complex plastic parts [15].

Because of these challenges, researchers have conducted many studies to explore the approaches to take in order to optimize injection-molding parameters. The design of experiments (DOE), such as the Taguchi method, is applied to improve the quality of manufactured goods by analyzing the signal-to-noise (S/N) ratio and the analysis of variance (ANOVA) [16–21]. The Taguchi method is unsuitable for the problem in this study because process parameters are continuous. Thus, the Taguchi method is unable to assist technologists in obtaining optimal process parameters [22]. The DOE approach also requires that technologists understand both statistics and the injection-molding process in experiment planning [23]. Because of the shortcomings of the DOE method, researchers have proposed new optimization methods by applying surrogate models, such as the artificial neural network (ANN) [24], and iterative methods, such as the genetic algorithm (GA) [25, 26]. Xu et al. [27] developed a backpropagation neural network model combined with particle swarm optimization (PSO) to map the complex nonlinear relationship between process parameters and the mechanical performance of the product. Chen et al. [28] applied a backpropagation neural network, genetic algorithms, and engineering optimization concepts to achieve competitive advantages in both quality and cost. However, defining the structure of a neural network is a time-consuming procedure due to the lack of uniform structure. Technologists need to determine the number of layers and nodes in the network, as well as the connection relations between nodes. In addition, to guarantee accuracy, ANN usually requires a large number of experiment samples, which is difficult to acquire in practice.

In this study, the optimization objective is to generate process parameters for the molding of optimal products of a standard weight. Because the weight of the molded product has an either positive or negative error, the optimization problem can be converted into a classification problem. The support vector machine (SVM) method is now widely applied in classification problems, such as separating defective and nondefective products. Yu [29] applied the SVM and DOE methods for predicting process windows to ensure robust, high-quality injection moldings. Gao [30] proposed a method using SVM to optimize process parameters that could provide more stable product quality than traditional methods. Shin et al. [31] pointed out that SVM generally has better accuracy than ANN as the data size decreases. Due to the advantages of SVM, this study proposes a classifier model using the support vector machine method, called the support vector classifier (SVC), to construct a hyperplane which separates products that are heavier or lighter than the standard weight. Optimal process parameters are presumed to be located on the hyperplane constructed by the SVC model. Having established an SVC model, a particle swarm optimization (PSO) algorithm is applied to improve the SVC model by tuning hyperparameters in order to minimize the error between the experimental result and the SVC prediction value. The outline of this paper is as follows: Section 2 introduces the implementation procedure of the proposed optimization method and its key algorithms. In Sections 3 and 4, a case of plastic lenses is carried out to verify the presented algorithm. The conclusions are provided in the last section.

2. Method Implementation

The implementation procedure for the proposed optimization method is described in Section 2.1. Section 2.2 illustrates the SVC algorithm in detail, and the method for tuning the hyperparameters of SVC using PSO is introduced in Section 2.3.

2.1. Implementation Procedure. The standard weight of a plastic product is determined by technologists prior to molding. The product weight can be regarded as a function of the process parameters throughout the injection-molding process. Each experiment sample under different process parameters could be heavier or lighter than the standard weight and can therefore be labeled as a positive sample (heavier) or a negative sample (lighter). The molding parameters for the desired product with a standard weight should be located between the molding parameters for the positive and negative samples. Hence, this study intends to search for the parameter classification boundary between the positive and negative classes, as shown in Figure 1. The larger the weight error of a sample is, the further away the point is from the boundary, and the points on the boundary correspond to a zero-weight error.

In this study, an SVC model is employed to classify products by their weights. Products under different process parameters are injection-molded and weighed. These products are labeled as either positive or negative samples, and they are employed as training data for the SVC. As illustrated in Figure 1, the SVC constructs a maximum-margin hyperplane, which is also known as the classification boundary, to separate the positive and negative samples. The distance between the samples and the hyperplane corresponds to weight errors. Optimal parameters should be located on the hyperplane of the trained SVC model. Because of the linearly nonseparable problem, further modifications of the SVC model are required, including the selection and calculation of the kernel function [32], as well as the determination of the slack variable [33]. Mathematical principles are illustrated in Section 2.2 in detail. The kernel parameter of the kernel function and the penalty parameter of the slack variable have a great influence on the performance of the SVC model. The determination of these hyperparameters for the SVC is therefore significant. In this study, a particle swarm optimization (PSO) method is adopted. The implementation procedure for the proposed method can be summarized as follows:

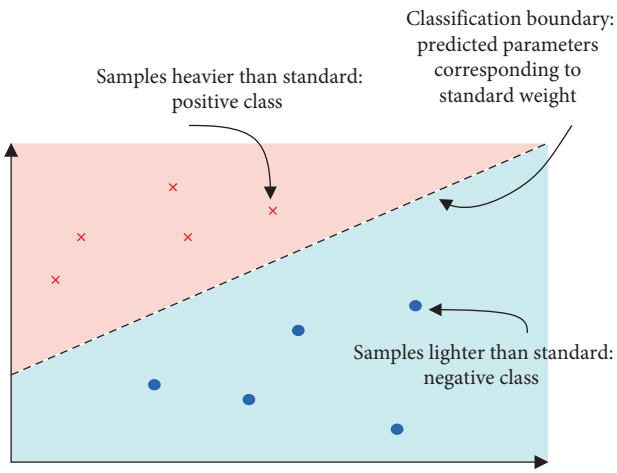

Figure 1: Schematic diagram of converting the parameter optimization problem to a classification problem.

Step 1: initialize parameter range. Choose molding parameters, and then set their initial range. The initial parameter range should cover all the feasible parameters.

Step 2: perform experiments. Carry out experiments under each process parameter. Then, evaluate experimental results by comparing the product weight with the standard weight.

Step 3: train the SVC model. Label these samples, and prepare the data sets for the SVC. Select proper kernel function, and train the SVC with sample data.

Step 4: tune SVC hyperparameters. Apply PSO to determine hyperparameters. A hyperplane that separates underweight and overweight samples can be obtained. The optimal process parameters are located on that hyperplane.

Step 5: perform verification experiments.

2.2. Support Vector Classifier Algorithm. The support vector classifier is a machine learning algorithm based on statistical learning theory. It minimizes the structural risk and improves the generalization ability of the learning machine. The target of a classification is to estimate a function f using the training data $(\mathbf{x}_1, y_1)\cdots(\mathbf{x}_n, y_n)$, where $\mathbf{x} = (\mathbf{x}_1, \ldots, \mathbf{x}_n) \in R^N$ is the matrix of the process parameters in this study and $y \in \{+1, -1\}$ is the label, indicating whether a product is heavier or lighter than the standard weight.

Considering a linear case as shown in Figure 1, the classification function can be written as

$$f(\mathbf{x}) = \mathbf{w}^T\mathbf{x} + b, \tag{1}$$

where w is a normal vector and b is the intercept. When $f(\mathbf{x}) = 0$, x is a point located on the hyperplane. For all points that satisfy $f(\mathbf{x}) < 0$, the corresponding label y_i is -1, and for all points that satisfy $f(\mathbf{x}) > 0$, the corresponding label y_i is 1. It can also be written as

$$y_i \times \left(\mathbf{w}^T\mathbf{x} + b\right) \geq 1. \tag{2}$$

The margin between two classes is

$$\text{margin} = \left(\overrightarrow{\mathbf{x}_+} - \overrightarrow{\mathbf{x}_-}\right) \cdot \frac{\vec{w}}{||\vec{w}||} = \frac{1 + b - (-1 + b)}{||\vec{w}||}. \tag{3}$$

Moreover, the target is to find the hyperplane that makes the margin the largest. For mathematic convenience, maximize $2/\|\vec{w}\|$ is equal to minimize $(1/2)\|w\|^2$. Thus, the optimization problem becomes

$$\begin{cases} \min \dfrac{1}{2}\|\mathbf{w}\|^2 \\ \text{s.t. } y_i \cdot \left(\mathbf{w}^T x + b\right) \geq 1. \end{cases} \tag{4}$$

Because of the linear inseparability of the data set, a kernel function must be adopted to map the data (input space) to a high-dimensional space (feature space) where a linear separating hyperplane can be constructed. One kernel commonly used in training nonlinear SVCs is the Gaussian kernel which maps data to an infinite-dimensional space. The Gaussian kernel on two samples $\mathbf{x}$ and $\mathbf{y}$ is defined as

$$K(\mathbf{x}, \mathbf{y}) = \exp\left(-\frac{||\mathbf{x} - \mathbf{y}||^2}{2\sigma^2}\right) = \exp\left(-\gamma||\mathbf{x} - \mathbf{y}||^2\right), \tag{5}$$

where $\gamma = 1/2\sigma^2$ represents the width and height of the Gaussian function.

Although the probability of linear separation is increased by introducing the kernel function, it is still difficult to deal with the noise in a data set. Noisy data, also known as "outliers," have a great influence on the SVC model, especially when outliers become support vectors. The slack variable ξ_i is therefore introduced. After considering outliers, the constraint condition in equation (4) is

$$y_i\left(\mathbf{w}^T\mathbf{x}_i + b\right) \geq 1 - \xi_i, \quad i = 1, 2, \ldots, n. \tag{6}$$

The slack variable means that the accurate classification of the outliers is abandoned, which is an additional loss to the classifier and should be added to the objective function. Thus, the optimization problem becomes

$$\begin{cases} \min \dfrac{1}{2}\|\mathbf{w}\|^2 + C\displaystyle\sum_{i=1}^{n} \xi_i \\ \text{s.t. } y_i\left(\mathbf{w}^T\mathbf{x}_i + b\right) \geq 1 - \xi_i \\ \xi_i \geq 0, \end{cases} \tag{7}$$

where C is the penalty parameter, which refers to the sensitivity of the SVC model to outliers. The weight error between each sample and the standard weight can be calculated, which means each sample should have a different penalty parameter. The further away the sample is from the standard, the more emphasis the SVC should put on the sample, which means the penalty parameter C for this sample should be larger. For this reason, we should modify C for each sample according to its own weight error. The

determinant of penalty parameter C is as follows: first, expand the value of C to an $n \times 1$ matrix and then calculate the updated penalty parameter matrix $\mathbf{C}_{\text{sample}}$ as

$$\mathbf{C}_{\text{sample}} = \mathbf{C} \odot \mathbf{W}_e, \tag{8}$$

where $\mathbf{W}_e$ is an $n \times 1$ matrix of the weight error of n samples and "$\odot$" is the denotation of componentwise multiplication. From equation (7), it can be clearly seen that it is a convex optimization problem with linear constraint. The final optimization goal is

$$\begin{cases} \min\limits_{\alpha} \sum\limits_{i=1}^{n} \alpha_i - \dfrac{1}{2} \sum\limits_{i=1}^{n} \sum\limits_{j=1}^{n} \alpha_i \alpha_j y_i y_j K\left(\mathbf{x}_i, \mathbf{x}_j\right) \\ \text{s.t. } 0 \le \alpha_i \le C \\ \sum\limits_{i=1}^{n} \alpha_i y_i = 0, \end{cases} \tag{9}$$

where α_i is a nonnegative Lagrange multiplier and $K(\mathbf{x}_i, \mathbf{x}_j)$ is the kernel function, as shown in equation (5).

It should be noted that the performance of an SVC model depends largely on the parameters γ and C. Parameter γ determines the sphere of influence of each support vector. A large value of γ is conducive to the situation in which the support vectors affect only the nearby area, which can lead to high variance of the model and overfitting. Parameter C controls the tradeoff between achieving a low training error and the ability to generalize the model to unseen data. Because of the absence of prior knowledge of the choice of parameters, some types of model selection (parametric search) must be conducted. Several approaches have been proposed, such as K-folder cross validation [34] and grid search [35]. K-folder cross validation is often combined with grid search as a method of parameter evaluation. Via this method, hyperparameters can be modified by improving the classification accuracy of the model. However, this criterion only applies to a model with a large number of samples. Because of the small data set in this study, a new criterion to modify SVC model must be proposed.

2.3. Determination of SVC Hyperparameters Using Particle Swarm Optimization. Particle swarm optimization is an algorithm that simulates the foraging behavior of a flock of birds. The basic idea is to find the optimal solution via collaboration and information sharing among individuals in the group. A group of particles (candidate solutions) is randomly initialized in the solution space. Each particle is evaluated by calculating its fitness value. The optimal solution is then found by iteration. In each iteration, the particle updates its own velocity and position by tracking "Pbest" (the best known position of the current individual) and "Gbest" (the best known position of the current group). The updated formula for particle $i\,(i = 1, 2, \ldots, n)$ can be written as

$$\begin{cases} v_i = \omega \times v_i + c_1 \times \text{rand} \times \left(P\text{best}_i - x_i\right) \\ \quad + c_2 \times \text{rand} \times \left(G\text{best}_i - \mathbf{x}_i\right), \\ \mathbf{x}_i = \mathbf{x}_i + v_i, \end{cases} \tag{10}$$

where v_i and x_i are the velocity and position of the particle, respectively, rand is a random value between $(-1, 1)$, c_1 and c_2 are learning factors, and under normal conditions, $c_1 = c_2 = 2$, and ω is known as the inertia weight factor. In order to achieve better convergence, ω is set to linearly decrease with the iteration:

$$\omega = \omega_{\min} + \left(\omega_{\max} - \omega_{\min}\right) \frac{i_{\max} - i}{i_{\max}}, \tag{11}$$

where ω is the inertia weight for each iteration, $\omega_{\min}$ and $\omega_{\max}$ are the minimum and maximum inertia weights, respectively, which are set to 0.2 and 0.6 in this study, and i refers to the current iteration step. By applying a linear decrease, particles can quickly converge to the approximate optimal solution with a large step size at the beginning and then converge to the exact solution with a small step size.

In this study, PSO is applied to improve the accuracy of the SVC model by determining its hyperparameters. The key to applying PSO in this optimization problem is to construct a proper fitness function. In order to acquire the most precise result, the prediction value of the SVC should be the same as the actual value from experiments. By tuning the hyperparameters of the SVC model, the position of the hyperplane can be modified. Thus, the distance between the hyperplane and the samples is as close as possible to the actual weight error. The calculation of fitness of particles is

$$\text{fitness} = \|\mathbf{p} - \mathbf{e}\|^2, \tag{12}$$

where $\mathbf{p}$ is the normalized vector of the distance between the sample and the hyperplane and $\mathbf{e}$ is the normalized vector of the product weight error. $\mathbf{p}$ and $\mathbf{e}$ are calculated by

$$\begin{aligned} \mathbf{p} &= \frac{\mathbf{p} - \min(\mathbf{p})}{\max(\mathbf{p}) - \min(\mathbf{p})}, \\ \mathbf{e} &= \frac{\mathbf{e} - \min(\mathbf{e})}{\max(\mathbf{e}) - \min(\mathbf{e})}. \end{aligned} \tag{13}$$

Through PSO, all particles converge to the position where the fitness value is reduced to the minimum. The optimal position corresponds to the modified combination of hyperparameters of the SVC. With this method, the parameters γ and C can be calculated.

3. Experimental Design

To demonstrate the accuracy of the proposed method, an experiment using a plastic lenses is presented in this section. A high-precision electrical injection-molding machine, Zhafir VE400 (Zhafir Plastics Machinery GmbH, China), is employed in this study and is depicted in Figure 2(a). The injection mold and molded plastic lenses are shown in Figure 2(b) and Figure 2(c), respectively. A single lens has a diameter of 30 mm and a maximum thickness of 2 mm. The resin used in this study is poly(methyl methacrylate) (PMMA, HT55X produced by Sumipex, Japan [36]). To weigh the product, an electronic balance FA2004 (Shanghai Sunny Hengping Scientific Instrument Co., Ltd, China) is employed, the measurement accuracy of which is 0.0001 g (see Figure 2).

(a) (b) (c)

Figure 2: Experimental setup: (a) injection-molding machine; (b) injection mold; (c) molded plastic lenses.

Many process parameters have large effect on product weight, including packing pressure, packing time, injection pressure, injection time, and injection temperature. The effect of these parameters depends on the type of the resin [13] and the structure of the product [14]. According to Yang, Hassan and López [11–14], the injection temperature and packing pressure are the two parameters which have the most significant influence on product weight. On purpose of demonstrating the optimization results more clearly, this study selects only these two parameters as optimization variables. The initial range of injection temperature is divided into 4 levels, namely, 235°C, 245°C, 255°C, and 265°C, according to the recommended temperatures provided by the material supplier. A relatively wide range of packing pressure, from 70 MPa to 120 MPa in increments of 10 MPa, is set as the initial range. Subsequently, a total number of 24 injection-molding analyses with different process parameters are carried out. After obtaining the experiment samples, all runners are removed, because the weight of the additional plastic in runners is not concerned in this study. Only the four lenses of one sample are weighted. The total standard weight of four lenses is 8.16 g. The experiment results are shown in the following section.

4. Results and Verification

4.1. Experimental Results. The product weight under the condition of each process parameter is presented in Table 1 and Figure 3. A positive weight error value indicates that the product weight is larger than the standard value, and vice versa.

From the experimental results, we can observe that the product weight has a positive correlation with both the packing pressure and injection temperature. This phenomenon agrees well with the research of Hamdy [13] and Yang and Gao [11]. Due to the high viscosity, PMMA has a poor fluidity and the melt viscosity is sensitive to injection temperature. The fluidity of the PMMA melt improves with an increase in the injection temperature, which leads to more plastic melt flowing into the mold. In addition, the melt solidifies quickly due to the small thickness of the product. When the injection temperature is higher, the time to reach solidification increases. Therefore, more melt can pass through the gate during a longer time. With an increase in the packing pressure, more materials can be packed into the cavity in the packing phase.

Table 1: Weight under each parameter set.

No.	Process parameters		Product weight (g)	Weight error (g)
	Packing pressure (MPa)	Injection temperature (°C)		
1	70	235	8.0968	−0.0632
2	80	235	8.1324	−0.0276
3	90	235	8.1040	−0.0560
4	100	235	8.0920	−0.0680
5	110	235	8.1456	−0.0144
6	120	235	8.1664	0.0064
7	70	245	8.0944	−0.0656
8	80	245	8.0896	−0.0704
9	90	245	8.1100	−0.0500
10	100	245	8.1248	−0.0352
11	110	245	8.1716	0.0116
12	120	245	8.2104	0.0504
13	70	255	8.1316	−0.0284
14	80	255	8.1624	0.0024
15	90	255	8.2028	0.0428
16	100	255	8.2404	0.0804
17	110	255	8.2836	0.1236
18	120	255	8.3288	0.1688
19	70	265	8.4116	0.2516
20	80	265	8.5212	0.3612
21	90	265	8.7520	0.5920
22	100	265	8.7608	0.6008
23	110	265	8.6756	0.5156
24	120	265	8.8624	0.7024

As the SVC is a supervised machine learning model, the data set must be labeled. In this study, we regard all the negative values with a -1 label and the positive values with a +1 label. The two key parameters (C and γ) of the SVC are optimized through PSO, and the convergence procedure is shown in Figure 4. From the result of PSO, the performance of the SVC model is determined to be the best with $C = 2451.3$ and $\gamma = 5.74$. The hyperplane that separates the overweight and underweight samples is exhibited in Figure 5; each dot indicates an experimental sample, and the size of the dot corresponds to the magnitude of the weight error. The product weight under process parameters that are located on the hyperplane should be equal to the standard weight of 8.16 g.

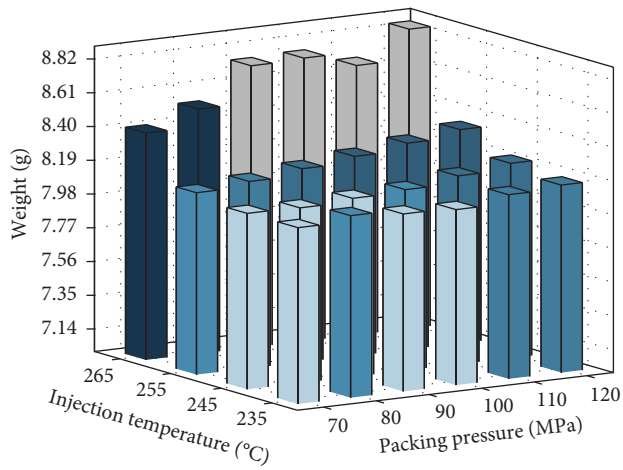

Figure 3: Product weight under varying process parameters.

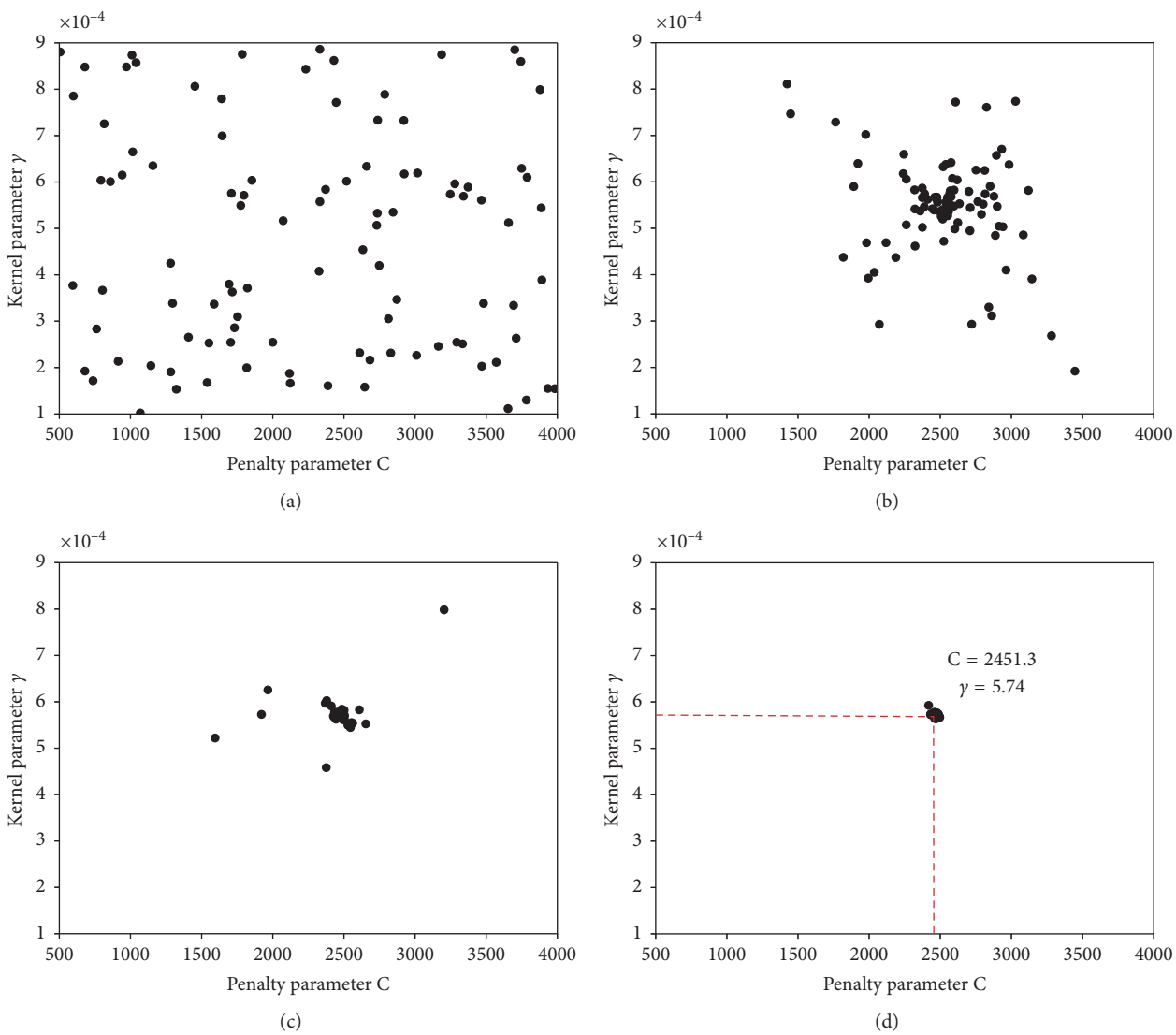

Figure 4: PSO convergence procedure: (a) random initialization; (b) 8th iteration step; (c) 54th iteration step; (d) 261st iteration step, converge at $C = 2451.3$ and $\gamma = 5.74$.

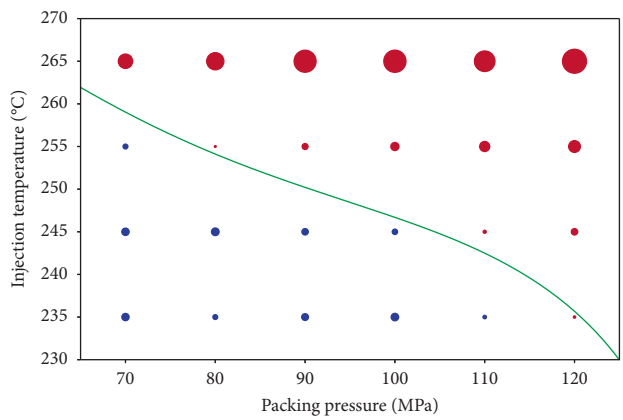

Figure 5: Classification hyperplane (green curve); red dots are overweight samples; blue dots are underweight samples.

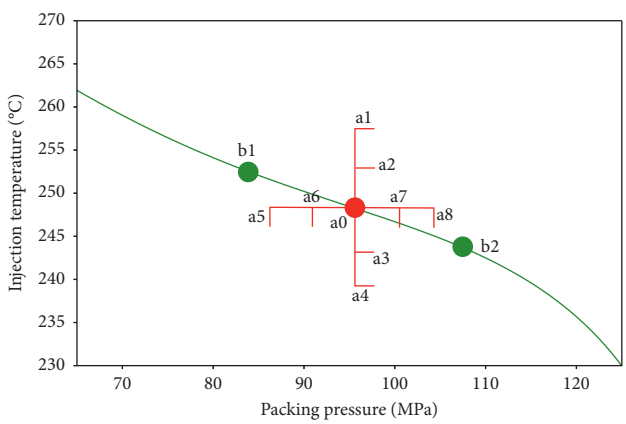

Figure 6: Verification experiments scheme: a0, b1, and b2 are process parameters on the hyperplane, while a1, a2, ..., a8 are process parameters not on the hyperplane.

4.2. Verification. In order to evaluate the hyperplane obtained from the proposed method, a set of verification experiments are carried out. The verification experiment scheme is illustrated in Figure 6. The points a0, a1, a2, . . ., a8, and b1 and b2 represent different injection-molding process parameters.

To verify that a single point located on the hyperplane is the best parameter combination among the other points around it, the center point (a0) with a packing pressure of 95 MPa and an injection temperature of 248°C is selected as the verification point. A series of experiments (a1, a2, a3, and a4) is first conducted with a fixed packing pressure of 95 MPa and varying injection temperatures from 242°C to 254°C in increments of 3°C. Then, several experiments (a5, a6, a7, and a8) were conducted with a fixed injection temperature of 248°C and varying packing pressures from 89 MPa to 101 MPa in increments of 3 MPa. In total, 9 sets of experiments are conducted. For each parameter combination, 30 products are molded and weighed. The results are provided in Figure 7, and the statistics are listed in Table 2 and 3. Although there are fluctuations during the injection-molding process, the product weight under the optimized parameters is the closest to the standard weight. The average

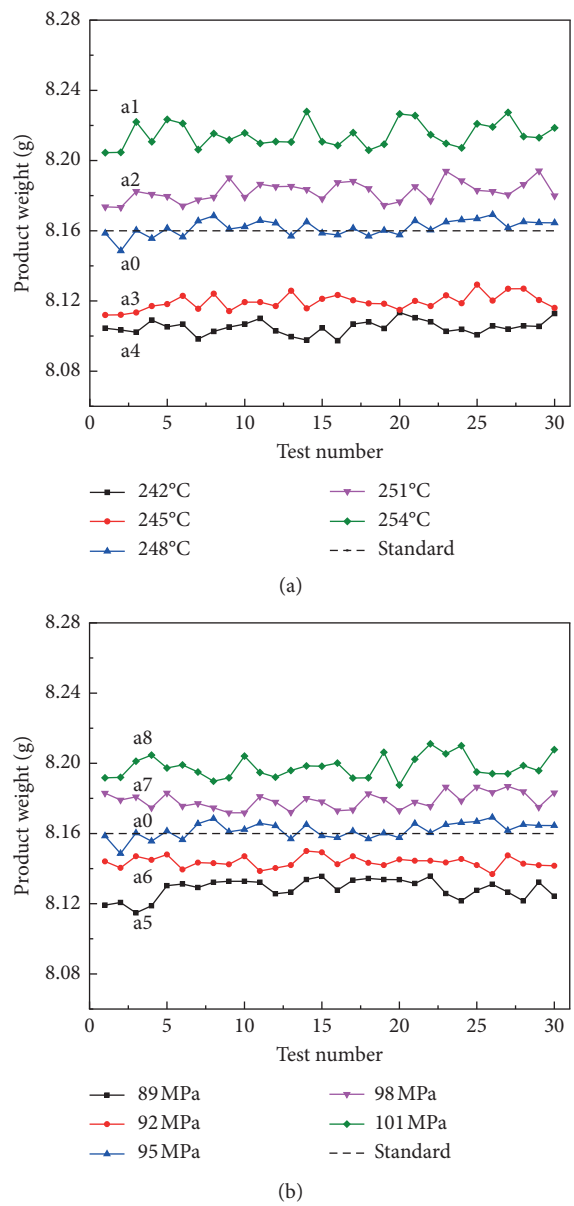

Figure 7: Verification results: product weight under (a) varying injection temperature; (b) varying packing pressure.

weight error can reach 0.0212%, which is smaller than any other parameter combinations around it.

In the case in which a single point on the hyperplane is known as an optimal parameter set, the second step is to verify that other points on the hyperplane are also feasible. Experiments under two other parameter combinations on the hyperplane (b1: 85 MPa/252.5°C and b2: 105 MPa/244.8°C) are carried out. Their weights are 8.1645 g and 8.1634 g, respectively, and the results are presented in Figure 8. We can presume that the product weight under other parameters on the hyperplane is also close to the standard weight. Other feasible process parameters offer more choices, so the technologists can pick up the parameter that fits the current product the best according to the product structure and the type of the resin.

Table 2: Product weight under varying injection temperature.

Injection temperature (°C)	Average weight (g)	Error (%)	Standard deviation (g)
242	8.1050	−0.6746	0.00401
245	8.1194	−0.4973	0.00445
248	8.1617	0.0212	0.00453
251	8.1823	0.2736	0.00564
254	8.2147	0.6705	0.00705

Table 3: Product weight under varying packing pressure.

Packing pressure (MPa)	Average weight (g)	Error (%)	Standard deviation (g)
242	8.1286	−0.3852	0.00562
245	8.1437	−0.1998	0.00310
248	8.1617	0.0212	0.00453
251	8.1787	0.2288	0.00464
254	8.1979	0.4647	0.00623

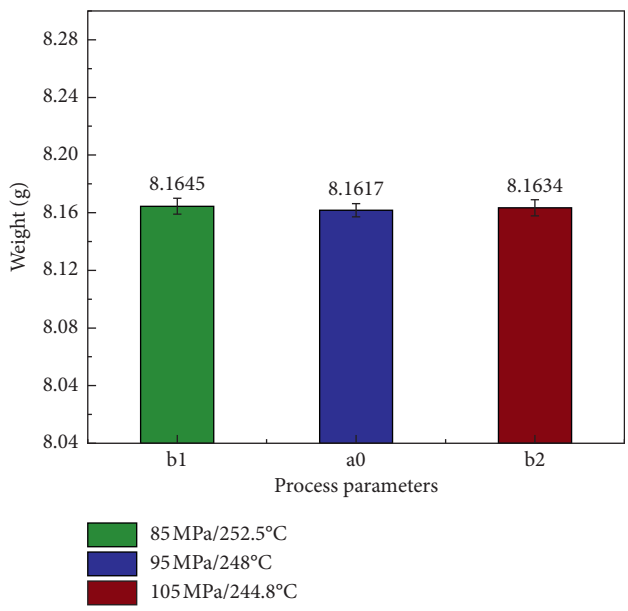

Figure 8: Product weight under three parameters on the hyperplane.

5. Conclusions

This study proposed a new method for optimizing process parameters to mold products with a standard weight. The parameter optimization problem is converted into a weight classification problem according to whether the sample is heavier or lighter than the standard weight. The support vector classifier and particle swarm optimization algorithm are adopted to construct the classification hyperplane, which separates samples. A new criterion for the classification model is introduced in order to improve accuracy. The product weight under parameter sets located on the classification hyperplane should be the same as the standard weight. Based on the results obtained in this study, the following conclusions can be drawn: (1) The product weight under optimized parameters is rather close to the standard weight. Experimental results indicate that the weight error can reach 0.0212%. The hyperplane obtained from the SVC has a high level of correspondence with the verification result. (2) The idea of converting an optimization problem to a classification problem is proven useful for process parameter optimization. (3) The accuracy of the classification model can be improved by applying the PSO method and the criterion proposed in this study. (4) In contrast to the shortcomings in the traditional Taguchi method, this approach for the optimization of process parameters can deal with the situation in which the process parameters are continuous and nonlinear. In general, the proposed method has the advantages of a small data set requirement, high accuracy, and the ability to deal with nonlinear problems.

The ongoing studies will serve to solve the following problems: (1) apply this method to multiple parameters optimization problems; (2) drive the mathematical model to a tool for design algorithms to determine the process window; (3) promote the proposed method to other parameter optimization problems for other polymer processing techniques, such as extrusion molding and blow molding.

Data Availability

The data used to support the findings of this study are available from the corresponding author upon request.

Conflicts of Interest

The authors declare that they have no conflicts of interest.

Acknowledgments

The authors would like to acknowledge the financial support of the Zhejiang Provincial Natural Science Foundation of China (No. LZ18E050002), the Key Research and Development Plan of Zhejiang Province (No. 2020C01113), and the National Natural Science Foundation Council of China (No. 51875519 and No. 51635006).

References

[1] H. Zhou, *Computer Modeling for Injection Molding*, John Wiley & Sons, Hoboken, NJ, USA, 2013.

[2] B. Ozcelik and T. Erzurumlu, "Comparison of the warpage optimization in the plastic injection molding using ANOVA, neural network model and genetic algorithm," *Journal of Materials Processing Technology*, vol. 171, no. 3, pp. 437–445, 2006.

[3] J. Yao, "A review of current developments in process and quality control for injection molding," *Advances in Polymer Technology*, vol. 24, no. 3, pp. 165–182, 2010.

[4] C. Fernandes, A. J. Pontes, J. C. Viana, and A. Gaspar-Cunha, "Modeling and optimization of the injection-molding process: a review," *Advances in Polymer Technology*, vol. 37, no. 2, pp. 429–449, 2018.

[5] Y. Zhao, P. Zhao, J. Zhang, J. Huang, N. Xia, and J. Fu, "On-line measurement of clamping force for injection molding

machine using ultrasonic technology," *Ultrasonics*, vol. 91, pp. 170–179, 2019.

[6] G. Shan, "Flow properties of polymer melt in longitudinal ultrasonic-assisted microinjection molding," *Polymer Engineering & Science*, vol. 57, no. 8, pp. 797–805, 2017.

[7] J. Zhang, P. Zhao, Y. Zhao, J. Huang, N. Xia, and J. Fu, "Online measurement of cavity pressure during injection molding via ultrasonic investigation of tie bar," *Sensors and Actuators A: Physical*, vol. 285, pp. 118–126, 2019.

[8] N. Xia, P. Zhao, J. Xie, C. Zhang, J. Fu, and L.-S. Turng, "Defect diagnosis for polymeric samples via magnetic levitation," *NDT & E International*, vol. 100, pp. 175–182, 2018.

[9] N. Xia, P. Zhao, T. Kuang, Y. Zhao, J. Zhang, and J. Fu, "Nondestructive measurement of layer thickness in water-assisted coinjection-molded product by ultrasonic technology," *Journal of Applied Polymer Science*, vol. 135, no. 33, p. 46540, 2018.

[10] C. Fernandes, A. J. Pontes, J. C. Viana, J. M. Nóbrega, and A. Gaspar-Cunha, "Modeling of plasticating injection molding - experimental assessment," *International Polymer Processing*, vol. 29, no. 5, pp. 558–569, 2014.

[11] Y. Yang and F. Gao, "Injection molding product weight: online prediction and control based on a nonlinear principal component regression model," *Polymer Engineering & Science*, vol. 46, no. 4, pp. 540–548, 2006.

[12] M. R. Kamal, A. E. Varela, and W. I. Patterson, "Control of part weight in injection molding of amorphous thermoplastics," *Polymer Engineering & Science*, vol. 39, no. 5, pp. 940–952, 1999.

[13] H. Hassan, "An experimental work on the effect of injection molding parameters on the cavity pressure and product weight," *The International Journal of Advanced Manufacturing Technology*, vol. 67, no. 1-4, pp. 675–686, 2013.

[14] A. López, J. Aisa, A. Martinez, and D. Mercado, "Injection moulding parameters influence on weight quality of complex parts by means of DOE application: case study," *Measurement*, vol. 90, pp. 349–356, 2016.

[15] H. GAO, Y. Zhang, X. Zhou, and D. Li, "Intelligent methods for the process parameter determination of plastic injection molding," *Frontiers of Mechanical Engineering*, vol. 13, no. 1, pp. 85–95, 2018.

[16] M. D. Azaman, S. M. Sapuan, S. Sulaiman, E. S. Zainudin, and A. Khalina, "Optimization and numerical simulation analysis for molded thin-walled parts fabricated using wood-filled polypropylene composites via plastic injection molding," *Polymer Engineering & Science*, vol. 55, no. 5, pp. 1082–1095, 2015.

[17] M. Cao, F. Gu, C. Rao, J. Fu, and P. Zhao, "Improving the electrospinning process of fabricating nanofibrous membranes to filter PM2.5," *Science of The Total Environment*, vol. 666, pp. 1011–1021, 2019.

[18] P. Zhao, M. Cao, H. Gu et al., "Research on the electrospun foaming process to fabricate three-dimensional tissue engineering scaffolds," *Journal of Applied Polymer Science*, vol. 135, no. 46, p. 46898, 2018.

[19] H. Oktem, T. Erzurumlu, and I. Uzman, "Application of Taguchi optimization technique in determining plastic injection molding process parameters for a thin-shell part," *Materials & Design*, vol. 28, no. 4, pp. 1271–1278, 2007.

[20] X. Sánchez-Sánchez, A. Elias-Zuñiga, and M. Hernández-Avila, "Processing of ultra-high molecular weight polyethylene/graphite composites by ultrasonic injection moulding: Taguchi optimization," *Ultrasonics Sonochemistry*, vol. 44, pp. 350–358, 2018.

[21] J. Zhao and G. Cheng, "An innovative surrogate-based searching method for reducing warpage and cycle time in injection molding," *Advances in Polymer Technology*, vol. 35, no. 3, pp. 288–297, 2016.

[22] C.-T. Su and H.-H. Chang, "Optimization of parameter design: an intelligent approach using neural network and simulated annealing," *International Journal of Systems Science*, vol. 31, no. 12, pp. 1543–1549, 2000.

[23] S. L. Mok, C. K. Kwong, and W. S. Lau, "Review of research in the determination of process parameters for plastic injection molding," *Advances in Polymer Technology*, vol. 18, no. 3, pp. 225–236, 1999.

[24] W.-C. Chen and D. Kurniawan, "Process parameters optimization for multiple quality characteristics in plastic injection molding using Taguchi method, BPNN, GA, and hybrid PSO-GA," *International Journal of Precision Engineering and Manufacturing*, vol. 15, no. 8, pp. 1583–1593, 2014.

[25] C. Fernandes, A. J. Pontes, J. C. Viana, and A. Gaspar-Cunha, "Using multiobjective evolutionary algorithms in the optimization of operating conditions of polymer injection molding," *Polymer Engineering & Science*, vol. 50, no. 8, pp. 1667–1678, 2010.

[26] C. Fernandes, A. J. Pontes, J. C. Viana, and A. Gaspar-Cunha, "Using multi-objective evolutionary algorithms for optimization of the cooling system in polymer injection molding," *International Polymer Processing*, vol. 27, no. 2, pp. 213–223, 2012.

[27] Y. Xu, Q. Zhang, W. Zhang, and P. Zhang, "Optimization of injection molding process parameters to improve the mechanical performance of polymer product against impact," *The International Journal of Advanced Manufacturing Technology*, vol. 76, no. 9–12, pp. 2199–2208, 2015.

[28] W.-C. Chen, G.-L. Fu, P.-H. Tai, and W.-J. Deng, "Process parameter optimization for MIMO plastic injection molding via soft computing," *Expert Systems with Applications*, vol. 36, no. 2, Part 1, pp. 1114–1122, 2009.

[29] S. Yu, "Offline prediction of process windows for robust injection molding," *Journal of Applied Polymer Science*, vol. 131, no. 18, 2014.

[30] H. Gao, "Process parameters optimization using a novel classification model for plastic injection molding," *The International Journal of Advanced Manufacturing Technology*, vol. 94, no. 1–4, pp. 357–370, 2018.

[31] K.-S. Shin, T. S. Lee, and H.-j. Kim, "An application of support vector machines in bankruptcy prediction model," *Expert Systems with Applications*, vol. 28, no. 1, pp. 127–135, 2005.

[32] B. E. Boser, I. M. Guyon, and V. N. Vapnik, "A training algorithm for optimal margin classifiers," in *Proceedings of the Fifth Annual Workshop on Computational Learning Theory*, July 1992.

[33] C. Cortes and V. Vapnik, "Support-vector networks," *Machine Learning*, vol. 20, no. 3, pp. 273–297, 1995.

[34] K. Duan, S. S. Keerthi, and A. N. Poo, "Evaluation of simple performance measures for tuning SVM hyperparameters," *Neurocomputing*, vol. 51, pp. 41–59, 2003.

[35] F. Friedrichs and C. Igel, "Evolutionary tuning of multiple SVM parameters," *Neurocomputing*, vol. 64, pp. 107–117, 2005.

[36] Ltd., S.C.A.P. PMMA/MMA, https://www.sumitomo-chem.com.sg/petrochemicals-plastics/pmma-mma/.

Hindawi
Advances in Polymer Technology
Volume 2020, Article ID 3161068, 15 pages
https://doi.org/10.1155/2020/3161068

Research Article

Microstructure, Tensile Property, and Surface Quality of Glass Fiber-Reinforced Polypropylene Parts Molded by Rapid Heat Cycle Molding

Feng Liu,[1,2] **Taidong Li**,[1] **Fuyu Xu**,[1] **Jiquan Li**,[1] **and Shaofei Jiang**[1]

[1]*College of Mechanical Engineering, Zhejiang University of Technology, Hangzhou 310014, China*
[2]*School of Mechanical and Automotive Engineering, Zhejiang University of Water Resources and Electric Power, Hangzhou 310018, China*

Correspondence should be addressed to Shaofei Jiang; jsf75@zjut.edu.cn

Received 26 July 2019; Revised 7 September 2019; Accepted 17 September 2019; Published 26 March 2020

Academic Editor: Huamin Zhou

Copyright © 2020 Feng Liu et al. This is an open access article distributed under the Creative Commons Attribution License, which permits unrestricted use, distribution, and reproduction in any medium, provided the original work is properly cited.

The microstructure of a molded product considerably influences its macroscopic properties. In this study, the influence of molding process on microstructure, tensile property, and surface quality was explored on the glass fiber-reinforced polypropylene (GFRPP) parts molded by rapid heat cycle molding (RHCM) and conversion injection molding (CIM). Tensile strength and surface gloss were chosen to measure macroscopic properties of the molded parts. The microstructure including multilayer, fiber orientation, crystallinity, and fiber-matrix bonding strength were analyzed by simulations, scanning electron microscopy, wide-angle X-ray diffraction, and dynamic mechanical analysis. The relationship between the macroscopic properties and microstructure of the RHCM samples was also discussed. The results indicate that as the mold cavity surface temperature increases, the tensile strength increases firstly and decreases thereafter. The tensile strength of RHCM parts reached the maximum at the mold heating temperature of 60°C. It is also observed that the surface gloss of the sample increases as the mold cavity surface temperature rises, and the increase of surface gloss decreases distinctly with the mold heating temperature higher than 90°C.

1. Introduction

Short glass fiber-reinforced polypropylene (GFRPP) composites are recyclable materials with good mechanical properties, high chemical resistance, excellent thermal stability, and attractive performance-cost ratio. In view of these advantages, the GFRPP is widely used in structural applications in the fields of aerospace, automotive, civil, and marine engineering [1–5]. It is well known that the macroscopic performance of the product is substantially dependent on its microstructure [6–8]. In the past, considerable efforts have been devoted to adapt the microstructures of GFRPP products and improve their macroscopic performance [9–15]. It is presumed that the mechanical properties of GFRPP products significantly depend on the combined effects of glass fiber orientation and distribution, fiber-matrix interface bonding strength conditions, and state of matrix crystallization, while some surface defects, such as flow marks, floating fibers, weld lines, and jetting marks cannot be avoided through the CIM process [16, 17]. The rapid heat cycle molding (RHCM) process is a relatively new technique that can not only significantly reduce or even eliminate surface defects but also significantly shorten the production cycle and reduce energy consumption and environmental pollution [18]. The most evident difference between the RHCM and CIM processes is that the former employs dynamic mold temperature control technology whereby the mold temperature is rapidly increased to a preset temperature before the mold is filled with the melt. During the filling and packing stage, high temperature is maintained; thereafter, the melt is quickly cooled to demold it before proceeding to the next stage of the production cycle [19–21]. Thus, the RHCM process has a more complex thermomechanical history than the CIM process [22].

To date the research works on the relationship between microstructure and macroscopic properties of products molded by the RHCM process have received increasing attention. Wang et al. [23] investigated the effect of mold cavity surface temperature in the filling process on the crystallization state of virgin PP in injected plastic part layers with different thicknesses. They also explored the relationship between the surface quality of plastic parts, crystallinity, and residual stress in the RHCM. Recently, Speranza et al. [24] reported that the mold surface temperature markedly influenced the molecular orientation and morphology developed in injection-molded samples, and the combination of flow fields and cooling rate experienced by the virgin polymer determined the multilayer structure of samples. Under strong flow field and high temperature conditions, a tightly packed structure (called shish-kebab) aligned along the flow direction was observed, whereas the formation of β-phase in cylindrite form was observed in weak flow fields. Li et al. [22] proposed a novel method to acquire the crystallization evolution information of virgin polymers during the RHCM process. The influence of temperature and shear rate on crystallization was considered in this method, thereby the method was beneficial to the optimization of the RHCM molding process for the manufacture of high-quality products. Liparoti et al. [25] analyzed the effect of the operative conditions of injection molding process on the morphology distribution inside molded products and found that the shear layer thickness was reduced in samples produced at high mold temperatures. It was particularly noted that the shear layer disappeared when the packing pressure and heating time were 360 bar and 20 s, respectively.

Based on the foregoing investigations, literature studies are mainly focused on the virgin polymer. So far, limited research works are about short glass fiber-reinforced polymer under the RHCM process. Li et al. [9] established a novel model describing the confluent process for the fiber-reinforced melt in the RHCM and described the relationship between the mold temperature and appearance of the confluent region. Furthermore, they presented the effect of fiber orientation in the confluent region on the impact strength of resultant parts. Wang et al. [26] used two reinforced plastics including ABS/PMMA/nano-$CaCO_3$ and 20% fiber-reinforced polypropylene to investigate the influence of cavity surface temperature immediately before filling on the surface appearance and texture of the molded reinforced plastic parts using the RHCM. The roughness, gloss, and morphology of the surface are characterized with white light interferometer, gloss meter, and optical microscope, respectively. They found that the mold surface temperature immediately before filling has a significant influence on the surface appearance of the molded part. In another work, the same research group [27] found that for fiber-reinforced plastics of PP + 20% glass fiber produced through the RHCM, the cavity surface temperature set to 118°C at the filling stage reduced the tensile strength of the part without a weld mark but slightly increased that of the part with a weld mark.

The aforementioned studies indicate that the microstructure (e.g., multilayer structure, fiber orientation, state of crystallization, interfacial bonding strength, and surface morphology) and macroperformance (e.g., tensile strength and surface gloss) of GFRPP product molded by RHCM have not been established. This makes the processing and parameter adjustment of the RHCM have great blindness. Hence, it is crucial to obtain the microstructure evolution law of reinforced thermoplastics produced by the RHCM process to reveal the mapping relationship between the macroscopic properties and microstructure of RHCM products. In this study, an electric heating RHCM is employed to understand the different cavity surface temperature action mechanisms that regulate the tensile strength and the surface appearance quality of a reinforced polymer product without a weld line. The macroscopic properties and microstructure are tested and analyzed by scanning electronic microscope (SEM), wide-angle X-ray diffraction (WAXRD), dynamic thermomechanical analysis (DMA), Autodesk Moldflow™, surface roughness meter, and surface gloss meter. The corelationships between the macroscopic properties, microstructure, and processing of RHCM products are explored.

2. Materials and Methods

2.1. Materials. The testing material adopted in this study is PP with 30% short glass fibers (supplied by Suzhou Yulian Engineering Plastics Co. Ltd., China) with a density of 1.18 g/cm^3 (ASTM D792), melt flow rate of 1.8 g/10 min (ASTM: D1238), and heat deflection temperature of 140°C (ASTM: D648).

2.2. Experimental Setup and Procedure. The employed electric heating RHCM apparatus (Figure 1 [28]) is mainly composed of electric heating rods, K-type thermocouple sensor, and mold temperature controller MTS-32II system (Beijing CHN-TOP Machinery Group Co. Ltd., China) to measure, regulate, and display the mold surface heating temperature, and a two-plate RHCM mold (the cavity surface is polished to achieve a glossy mirror surface with a roughness Ra of about 57 nm). Electrical heating rods are only deployed at the fixed side of the mold to heat this side rapidly before filling. The regular water-cooling tunnels are used to cool both movable and fixed sides of the mold with turbulent room temperature cooling water after the packing stage. An injection molding machine (HTFX5 series, Haitian Plastic Machinery Group Co. Ltd., China) is used. All process parameters are listed in Table 1.

And only the samples produced after stabilizing the process parameters are used. For each set of molding conditions, no less than five samples are employed for the subsequent measurements and analysis.

2.3. Specimen Preparation. The sample position is selected as shown in Figure 2. To facilitate description, the samples molded with cavity surface temperatures of 60, 90, and 120°C are designated as RHCM60, RHCM90, and RHCM120, respectively. All of the RHCM test samples are selected and processed on the side of the fixed half mold. The injection-

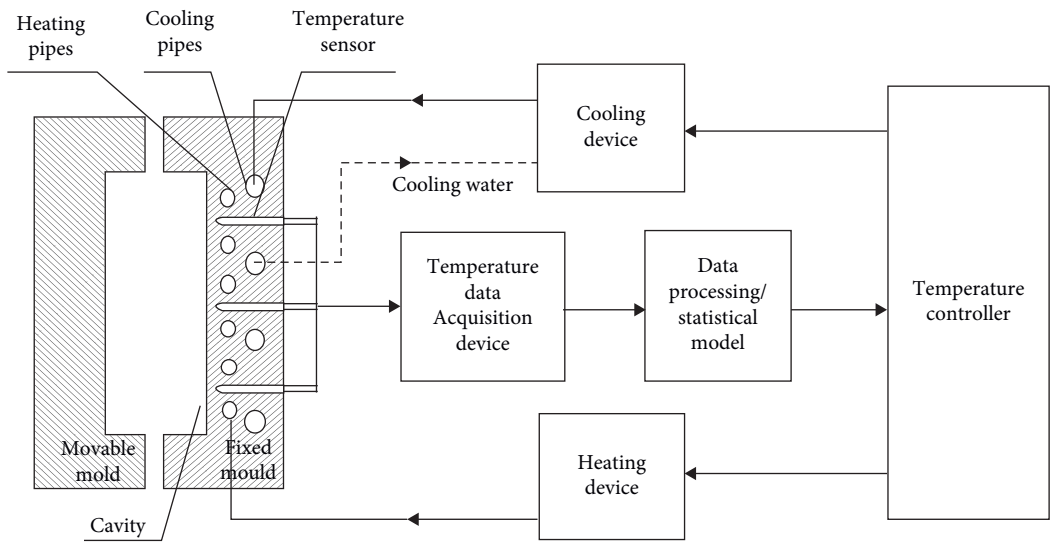

Figure 1: Schematic diagram of RHCM apparatus [32].

Table 1: Processing parameters used in RHCM tests.

Melt temperature (°C)	Injection pressure (MPa)	Injection velocity (%)	Packing time (s)	Packing pressure (MPa)	Mold heating temperature (°C)	Cooling time (s)
240	60	45	9	50	60/90/120	30

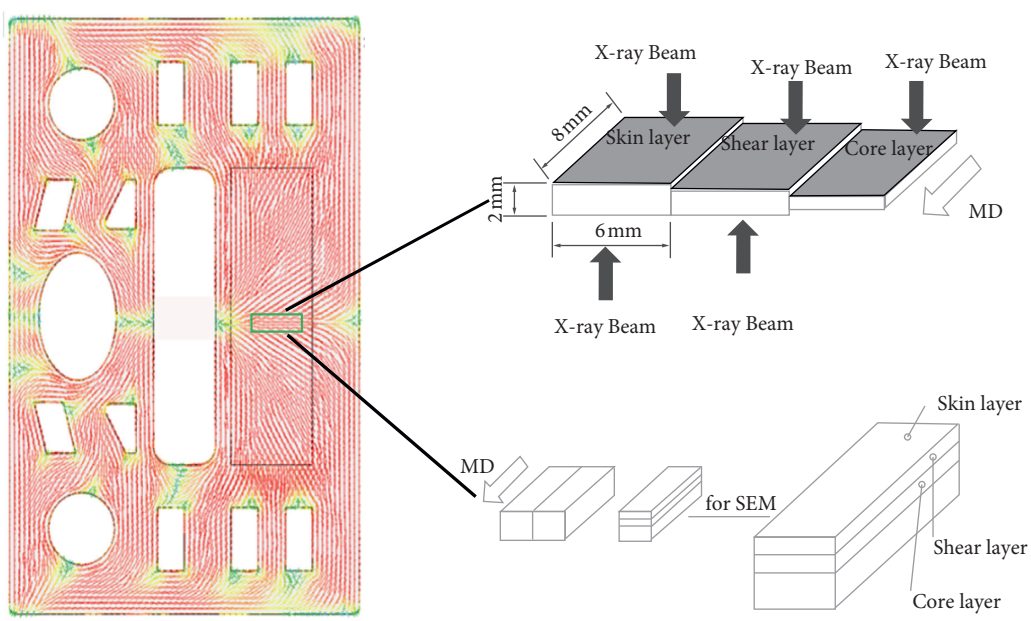

Figure 2: Schematic of parts and locations of tested samples.

molded samples are placed in liquid nitrogen and thereafter fractured as illustrated in Figure 2.

2.4. Performance Testing. According to ASTM D638, tensile tests are conducted on a universal testing instrument (INSTRON-8872, USA). The sample surface roughness is measured by a roughness meter (Mitutoyo SJ-410, Japan). The sample surface gloss is measured according to ASTM D523 using a gloss meter (WGG-60, Tongfu Electromechanical Equipment Co., Ltd., China).

2.5. Microstructure Analysis. All fractured surfaces for examination are polished in sequence using metallographic sandpaper with particle sizes of 300#, 600#, and 1500# on a grinding and polishing machine. The polished cross section is sputtered with gold in a vacuum; thereafter, the

microstructure of the sample is observed with a scanning electron microscope (Hitachi S-4700, Japan). The scanning voltage is 15.0 kV, and a total magnification of 150X is applied. The WAXRD technique is employed to estimate the crystallinity in each specified layer across the sample thickness. The sample position is specifically selected along the thickness, as illustrated in Figure 2. The WAXD is performed with an X'Pert PRO X-ray diffraction instrument (PANalytical B.V., Almelo, Netherlands) with a Cu Kα source and an average wavelength of 0.154056 nm. The equipment is operated at 40 kV and 40 mA in ambient temperature with a diffraction angle (2θ) range of 10°–40° and a 2°/min scan rate. The interfacial bonding strength of GFRPP composites can be characterized by the DMA test using DMAQ800 (TA instruments, America). Rectangular test samples (each 3 mm × 1 mm × 2 mm) are heated from −20 to 40°C at a rate of 2°C/min. The single cantilever mode is employed to test the samples at an oscillation amplitude and frequency of 10 μm and 1 Hz, respectively.

Autodesk Moldflow™ is utilized to evaluate the glass fiber orientation distribution in the sample thickness direction. In the simulation, the material properties and corresponding boundary conditions are set according to the parameters used in the actual CIM and RHCM experiments.

3. Results and Discussion

3.1. Effect of RHCM Process on Multilayer Microstructure of GFRPP. The SEM micrographs of multilayer structures are shown in Figure 3, which appear in the cross sections of CIM and RHCM60 samples. In the cross section of samples, the CIM sample exhibits a distinct symmetric skin-shear-core structure, whereas RHCM samples present an asymmetric multilayer structure. The layers thicknesses on the fixed mold side are considerably different from those on the movable mold side. This asymmetric structure is mainly attributed to the heating of the cavity surface in the fixed half mold with dynamic mold temperature control technology, and it well demonstrates the effect of different heating temperatures on the microstructures of RHCM samples. Figure 4 exhibits the skin layer thickness variation trends in RHCM and CIM samples produced at different cavity surface temperatures before filling. Based on the SEM images of specimen cross sections, the thickness of multilayers is determined by taking the average of multiple measurements with the aid of JMICROVISION software.

Figure 5(a) shows that the skin layer thickness of the sample decreases as the cavity temperature before filling increases, and such a decreasing tendency can be interpreted as temperature gradient distribution. Compared with the RHCM process, the CIM process has the largest temperature gradient between the melt and the cavity surface; hence, the entering melt rapidly cools upon contact with the cold cavity surface and immediately condenses and forms the skin layer, and accordingly, the CIM sample has the thickest skin layer. With the increase of temperature, the temperature gradient decreases. According to the foregoing, it is not difficult to sort the skin layer thickness in descending order as the cavity temperature before filling increases.

In Figure 5(b), the shear layer thickness in all RHCM samples is thicker than the shear layer thickness in the CIM sample. According to the previous analysis, the CIM process produces the thickest skin layer. Evidently, this skin layer provides the best heat insulation effect for the melt and weakens the heat exchange between the melt and mold wall and thereafter decreases the temperature gradient below the CIM skin layer; as a result, the shear layer thickness in the CIM sample is the thinnest. Compared with CIM sample, as the cavity surface temperature further increases, the skin layer thermal insulation performance further weakens and the shear layer thickness of the RHCM samples presents a descending order.

In Figure 5(c), it can be observed that the core layer thickness in the RHCM samples increases with the increase in the cavity surface temperature, and the core layer thickness in the CIM sample is thicker than that in the RHCM samples processed at cavity surface temperatures of 60 and 90°C. This phenomenon can be attributed to the fact that the thicker skin layer in the CIM sample has a good heat insulation effect, the temperature gradient in the melt under the skin layer is smaller, and consequently, the core layer thickness in the CIM sample is relatively thicker. In the RHCM process, the temperature difference between the cavity surface and melt gradually decreases with the increase in the cavity surface temperature; this explains the gradual increase in the core layer thickness. When the cavity surface temperature rises to 120°C, the core layer reaches its maximum thickness.

3.2. Effect of RHCM Process on Fiber Orientation in the GFRPP Microstructure. The model is constructed using tetrahedral elements with 11 layers meshed in the thickness direction. Figure 6 shows the meshed model established with the software. The fiber orientation distribution in different layers on the side of the fixed half mold is obtained by Moldflow™ simulation, as shown in Figure 7.

In the CIM process, the shear layer has the highest fiber-reinforced orientation parallel to the flow direction, followed by the skin layer. In the core layer, the fibers are observed to be oriented randomly. These results confirm those reported in literature [6, 29, 30]. Figure 7(a) shows the skin layer fiber orientation tensors obtained at different cavity surface temperatures. As the cavity surface temperature increases, the cooling and freezing rates of the skin layer are slowed down. These afford ample time for the fibers to be oriented in the flow direction as well as more time for the molecular orientation to relax. Under this condition, both shearing and stretching coupled with the molecular orientation effect are strengthened. These factors have opposite effects on the skin layer fiber orientation, and the final fiber orientation results are determined by these two competing effects. For RHCM60, the shearing and stretching effects are more predominant in the skin layer fiber orientation; accordingly, this sample has a relatively higher skin layer fiber orientation than the CIM sample. On the other hand, because the melt cooling rate in RHCM90 is lower than that in RHCM60, the skin layer is in a high elastic state over a longer period. The

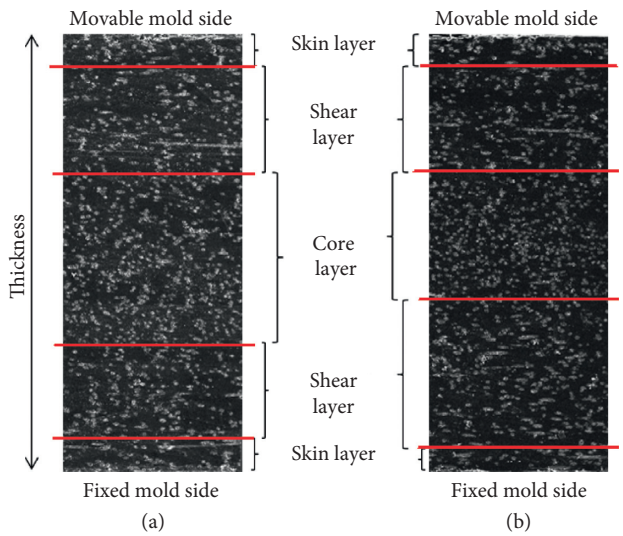

Figure 3: SEM micrographs of inner multilayer thickness distribution. Trend of tested samples: (a) CIM sample; (b) RHCM sample.

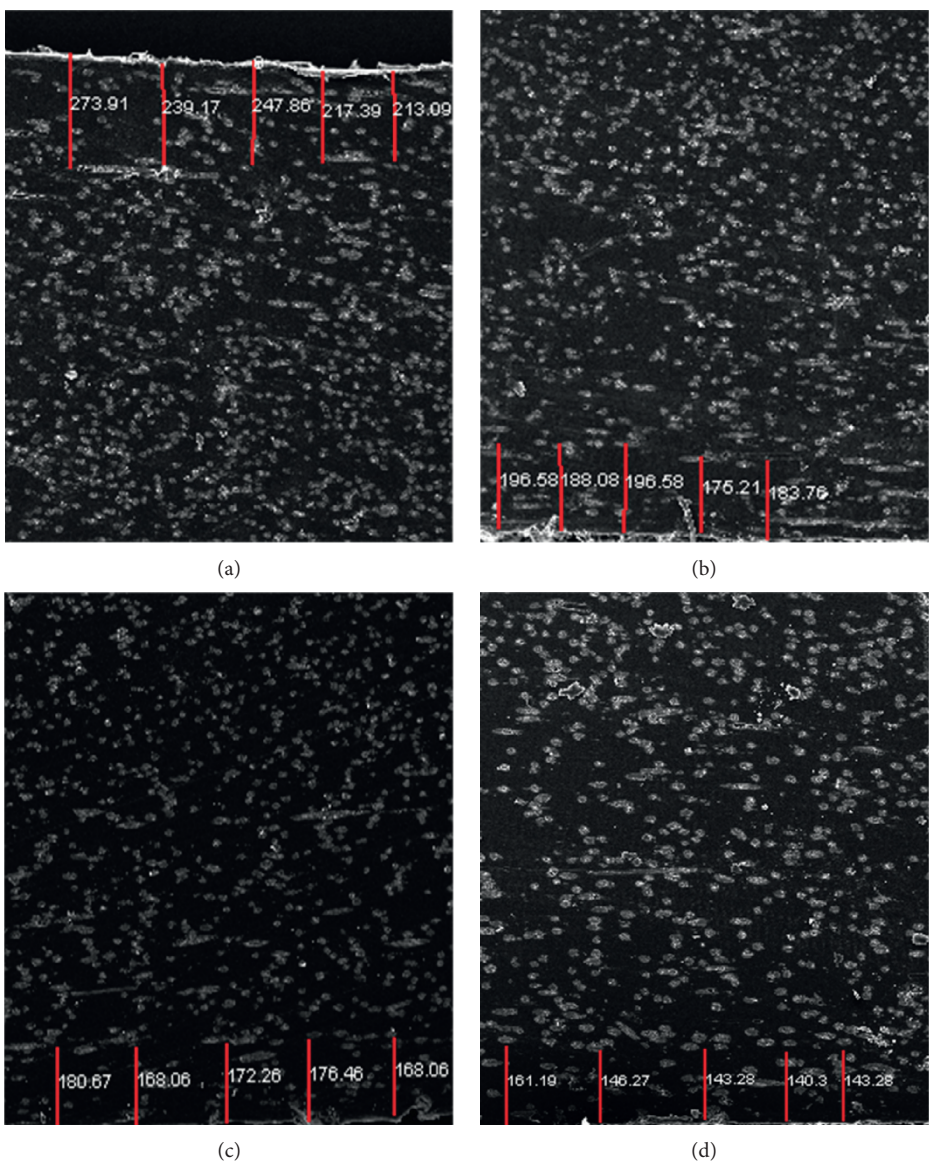

Figure 4: SEM micrographs of skin layer thickness in RHCM and CIM samples produced at different cavity surface temperatures before filling: (a) CIM; (b) RHCM60; (c) RHCM90; (d) RHCM120 (unit: μm).

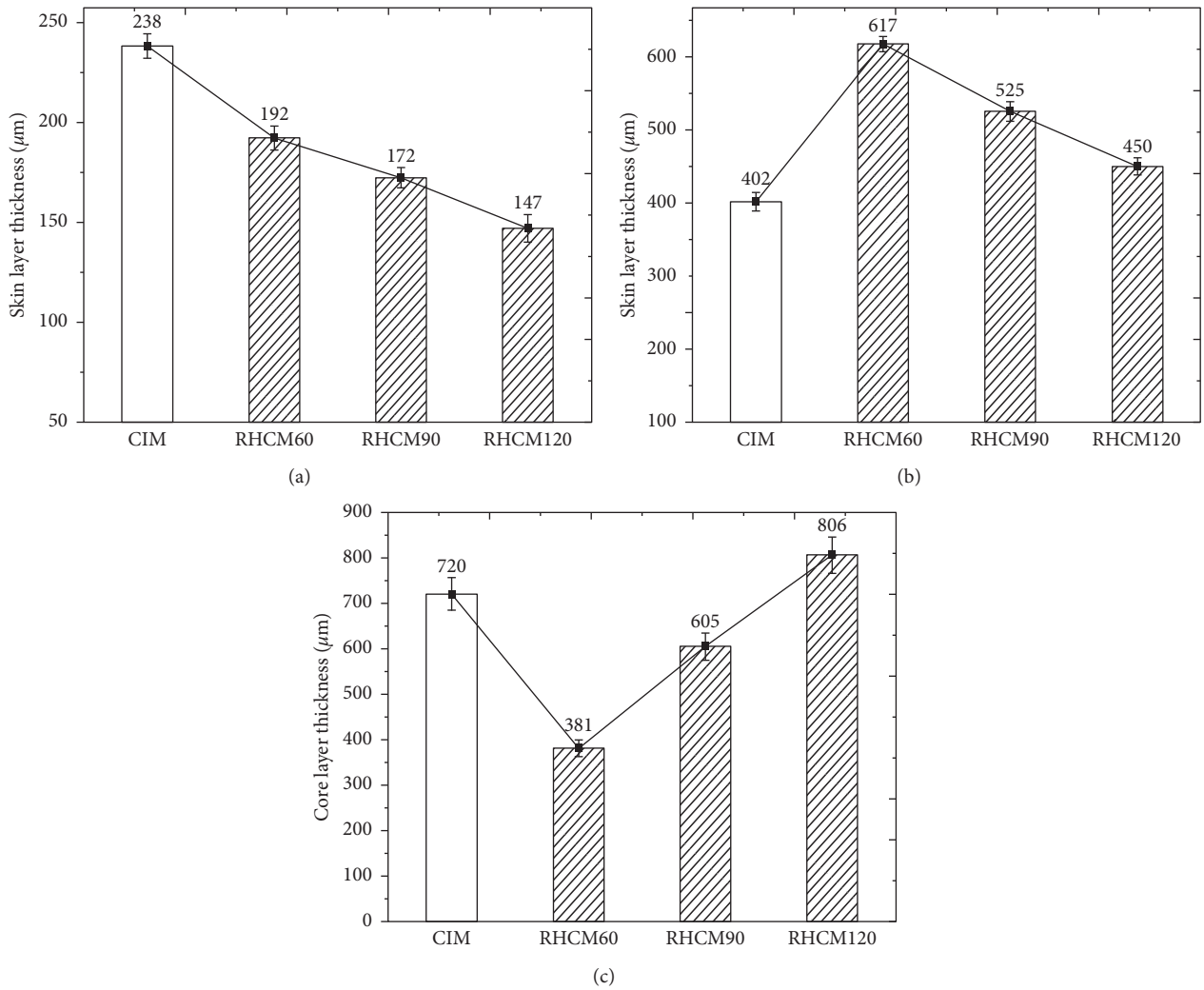

Figure 5: Schematic of each layer thickness change trend in RHCM and CIM samples: (a) skin layer thickness; (b) shear layer thickness; (c) core layer thickness.

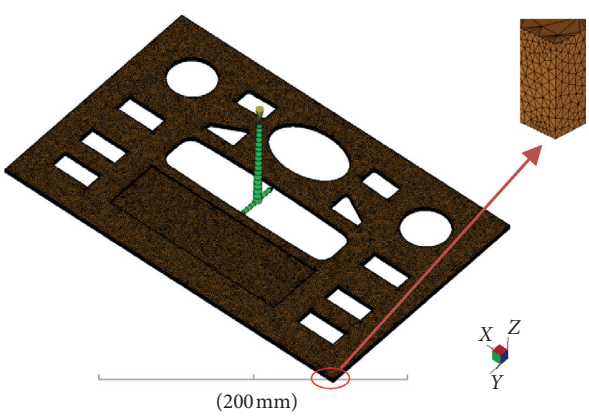

Figure 6: Schematic of the simulation model.

shearing and stretching effects are weaker because the velocity gradient is further reduced under this condition, and the internal fibers undergo a certain random movement based on the high temperature relaxation effect of the oriented polymer macromolecular chains. All of the these allow RHCM90 sample to have a relatively lower skin layer fiber orientation than the CIM sample. In the RHCM120 process, the cooling rate is the slowest, the oriented molecular chain relaxation is the most sufficient, and the skin layer fiber orientation is basically unoriented.

Figure 7(b) shows the fiber orientation tensor of the shear layer in the RHCM samples. It can be observed that RHCM60 sample has the highest shear layer fiber orientation. In the RHCM process, the melt in the shear layer is subjected to a lower shearing force compared with that experienced in the skin layer. However, the shear action time is longer, and the inner fibers have sufficient time to be oriented. Hence, the degree of fiber orientation in the shear layer is relatively higher than that in the skin layer. Moreover, notice that the fiber orientation tensor in the shear layer decreases drastically with the increase in mold temperature. Recall that as the heating temperature of the mold increases, the temperature gradient in the melt decreases; this causes the flow velocity difference among the layers to

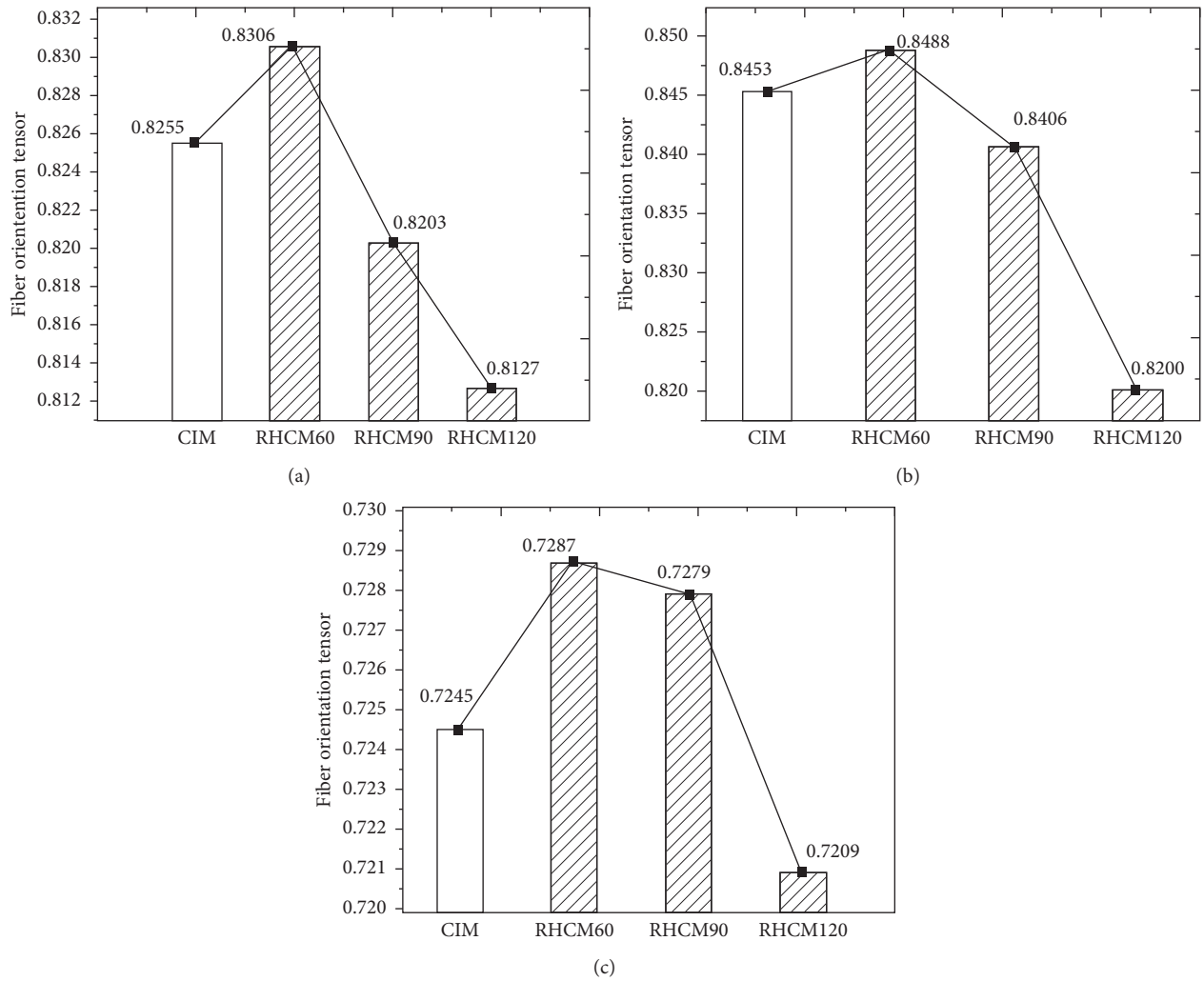

Figure 7: Schematic of layer fiber orientation tensor change trend in RHCM and CIM samples: (a) within skin layer; (b) within shear layer; (c) within core layer.

decrease. Thereafter, the shearing effect among the layers is weakened, particularly in RHCM120 sample. Figure 7(c) shows the core layer fiber orientation tensor of samples. In general, the core layer fiber orientation in all RHCM and CIM samples is relatively low. Compared with the skin and shear layers, the core layer has a uniform temperature distribution and a melt temperature that can be maintained higher than the glass transition temperature in both RHCM and CIM processes. Moreover, it has practically no shearing effect that can impact its fibers, and its polymer molecules have sufficient time to relax. Accordingly, with its fibers freely oriented, the core layer has a low fiber orientation.

3.3. Effect of RHCM Process on Crystallinity in the Microstructure of GFRPP. The statistical results of crystallinity in each layer in all samples are shown in Figure 8. The inner crystallization variation trend in the CIM sample is the same as the study result obtained by Salah et al. [31]. And the

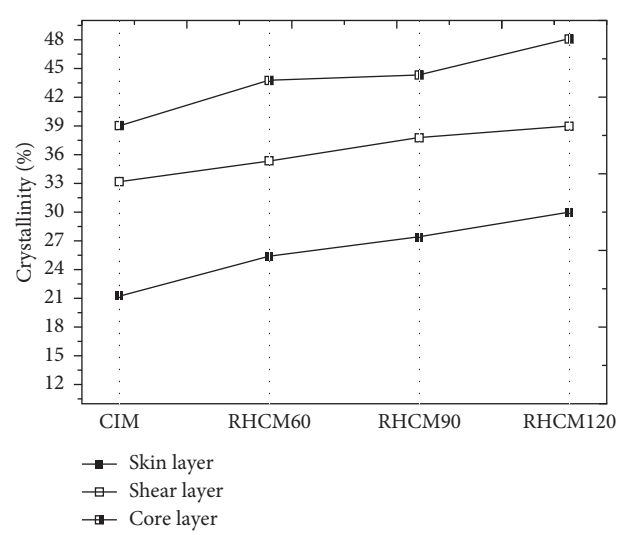

Figure 8: Statistical results of crystallinity in each layer in CIM and RHCM samples.

crystallinity in each layer in the RHCM samples is higher than that in the CIM sample; furthermore, the crystallinity in all layers increases continuously as the cavity surface temperature increases. In the RHCM process, when the melt comes into contact with the cavity surface having a higher temperature, the melt experiences a temperature range that is suitable for crystallization. And it is widely known that good fluidity results in less pressure loss in the melt flow direction and enhances the subsequent packing effects and, hence, decreases the free volume in the melt and increases the melt density; thereafter, the orientation of the molecular chains formed in the filling stage is further strengthened during the subsequent packing stage, and all these factors facilitate crystallization.

Additionally, it is found that the crystallinity in all layers increases continuously as the cavity surface temperature increases, the core layer has a higher crystallinity than the shear layer, and the skin layer has the lowest crystallinity. The heat exchange between the melt and the mold cavity surface is weakened because of the skin layer's heat insulation effect, at the same time the temperature in the shear layer is higher than that in the skin layer, and the crystallization time is relatively longer. And the intensive shear stress field in the shear layer triggers shear-induced crystallization. Thus, it can be concluded that as the heating temperature of the mold increases, both crystallization rate and crystallization time increase, and the crystallinity in shear layer is higher than that in skin layer. Additionally, both skin and shear layers act as insulating layers to further reduce the heat exchange between the mold surface and core layer; the core layer has a relatively longer and better crystallization time and zone. Thus, the core layer in each sample has the highest crystallinity, followed by the shear layer and skin layer in sequence.

3.4. Effect of RHCM Process on Fiber-Matrix Bonding Strength of GFRPP Composites. The interfacial bonding strength determines the stress transfer between the reinforcing fiber and matrix and is recognized as the key factor in the global mechanical performance of composites [10, 12, 32, 33]. To estimate the interfacial bonding strength of GFRPP composites under different mold cavity surface temperatures, the DMA test is employed [34]. The damping factor (tan δ) curves indicate the interfacial bonding strength of GFRPP composites, as shown in Figure 9.

As the mold cavity surface temperature increases, the peak of the mechanical loss in the sample gradually decreases, which indicates that the bonding strength between the reinforcing fiber and PP matrix increases as the temperature increases. It can be explained as follows: the global crystallinity in the sample increases under this condition, which causes the crystal area to expend, and the free movement volume of the molecular chain to reduce; these factors limit the movement of polymer molecular chains. Hence, the friction between molecular chains and fibers is decreased, and the sample's mechanical loss (tan δ) peak gradually decreases. Accordingly, the fiber-matrix bonding strength increases gradually with the increase of cavity surface temperature.

3.5. Relationship between Microstructure and Tensile Property. Figure 10 shows the tensile strength of samples produced by different CIM and RHCM processes. RHCM60 sample has the highest tensile strength, which reaches 57.61 MPa; this indicates that the RHCM process effectively improves the tensile property of the GFRPP composites. However, it is also found that as the mold cavity temperature before filling increases, the tensile strength of the RHCM sample gradually decreases, and even the tensile strength of RHCM120 sample is lower than that of the CIM sample. The tensile strength difference can be illustrated by the microstructure of the molded samples.

Figure 11 shows the microstructure comparison of RHCM60 and CIM samples. It is observed that the shear layer thicknesses with highly oriented fibers of RHCM60 increase by 53.5% compared with the CIM sample. However, the thicknesses of the skin and core layers, with the relatively lower fiber orientation tensors, are reduced by approximately 19.3% and 47.1%, respectively. Meanwhile, both crystallinity and fiber orientation in each layer in RHCM60 are higher than those in the CIM sample. The crystallinity in the skin, shear, and core layers increased by 19.4%, 6.5%, and 12.1%, respectively. Thus, the overall crystallinity and fiber orientation of RHCM60 in the cross section are higher than those in the CIM sample. When the external force exerts a tensile load on the sample, the increase in fiber orientation causes more fibers to bear the load transmitted by the substrate. The increase in matrix crystallinity indicates that the contact area between the crystal and amorphous regions increases; this also aids in the loads transfer from the matrix to the fiber. Hence, the tensile strength of RHCM60 is higher than that of the CIM sample.

It is evident in Figure 12 that as the cavity temperature is increased, the thicknesses of the skin and shear layers with higher fiber orientations are considerably reduced with decrements of 10.4%, 14.5%, and 14.9%, 14.3%, respectively. The thickness of the core layer with low fiber orientation is increased significantly with increments of 58.8% and 33.2%. Hence, as the cavity surface temperature is increased, the overall fiber orientation in the thickness direction of the sample is drastically lowered. Moreover, the crystallinity in each layer has different degrees of increment, ranging from 1.3% to 9.4%; the overall crystallinity in the RHCM samples increases continuously as the temperature increases. Although the high crystallinity matrix under this condition is advantageous for sustaining more applied loads, it is presumed that the effect of drastic reduction in the thickness of the shear layer with high fiber orientation on the tensile strength is more distinct.

3.6. Relationship between Microstructure and Surface Gloss. As shown in Figure 13, the RHCM process can effectively and continuously improve the surface gloss of the sample from 37.5 to 78.8 Gs as the surface temperature rises. The sample surface gloss is determined by the surface morphology of the product.

Table 2 summarizes the surface roughness measurement result of each sample. It indicates that the surface roughness

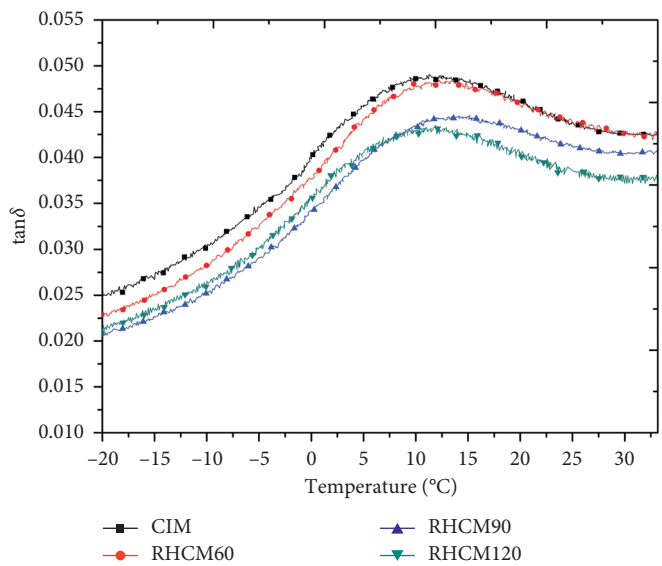

Figure 9: Mechanical loss (tan δ) curve of RHCM and CIM samples.

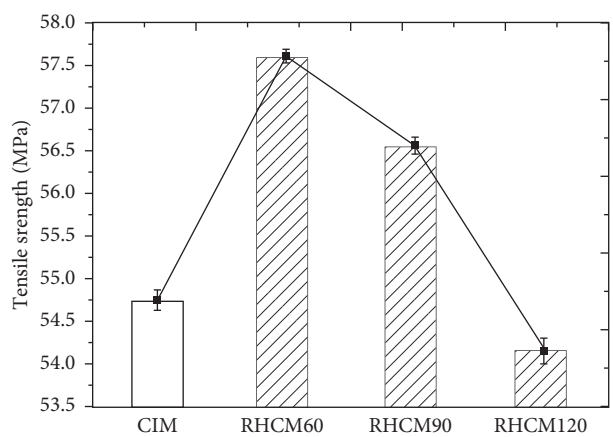

Figure 10: Tensile strength of RHCM and CIM samples.

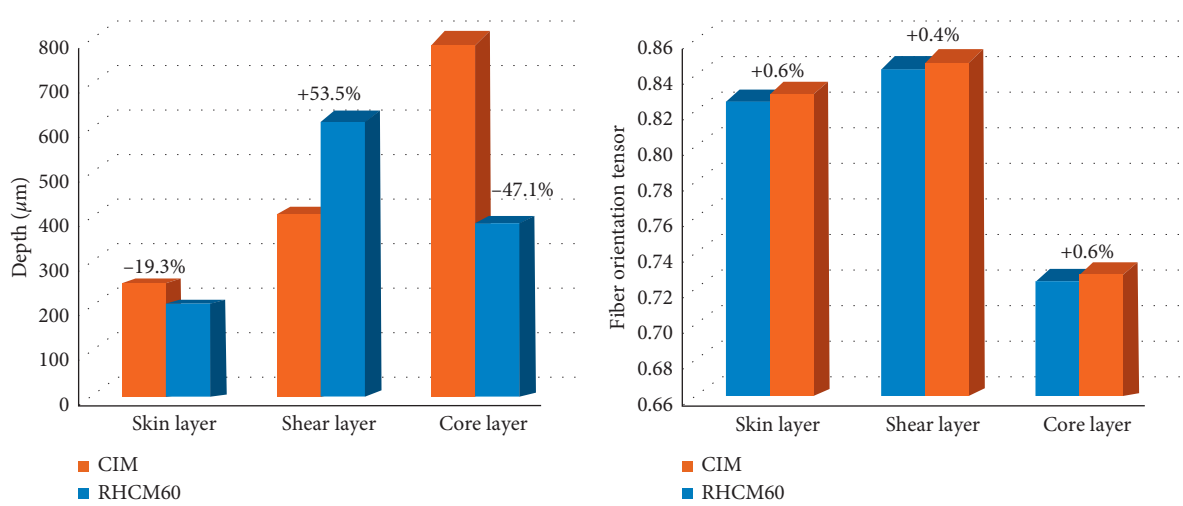

Figure 11: Continued.

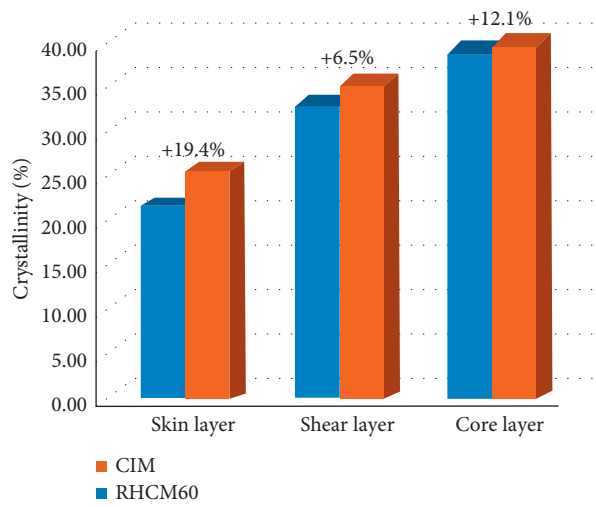

(c)

Figure 11: Comparison of microstructure layers in RHCM60 and CIM samples: (a) depth; (b) fiber orientation tensor; (c) crystallinity.

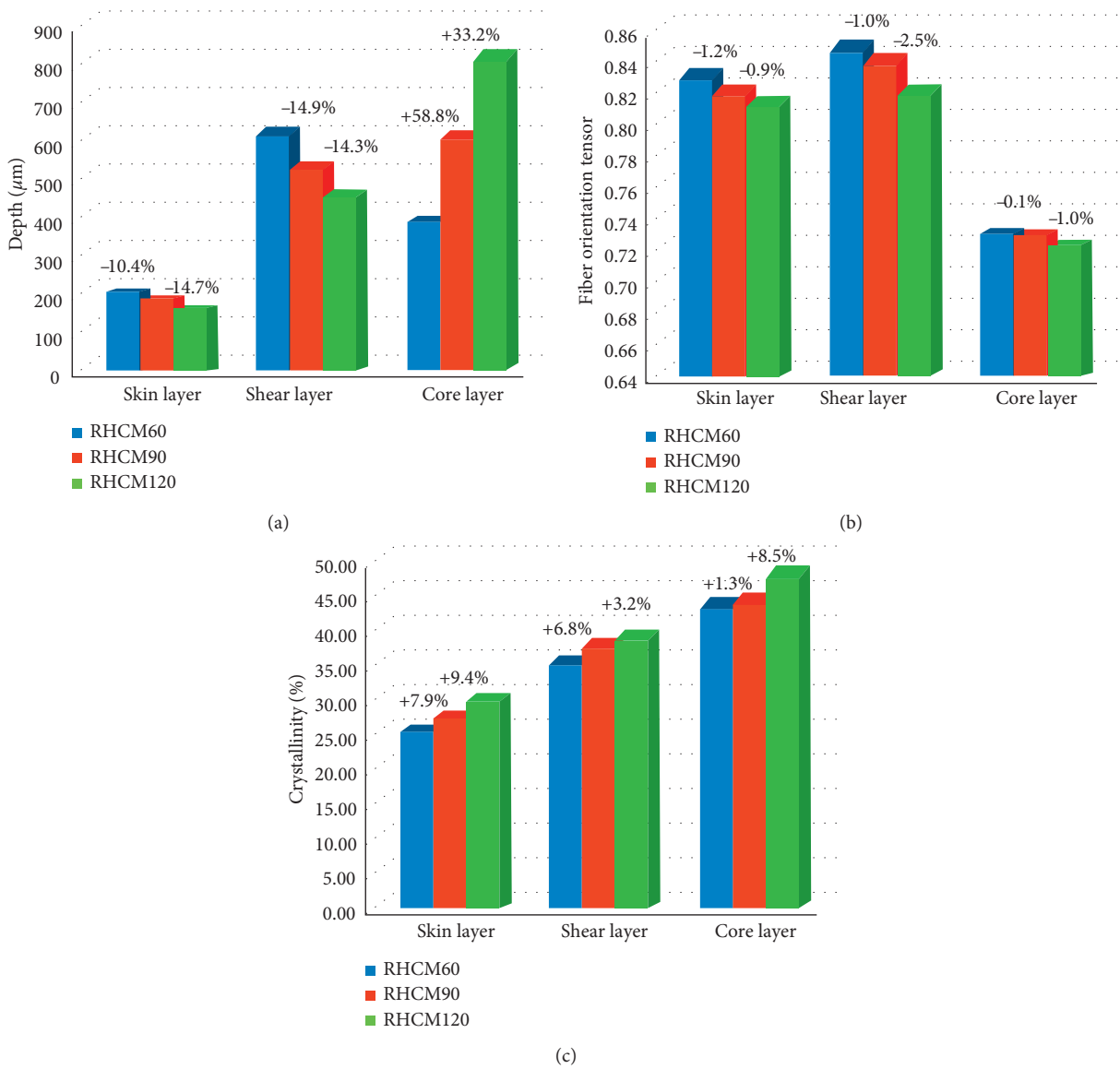

Figure 12: Comparison of microstructure layers in RHCM samples. (a) depth; (b) fiber orientation tensor; (c) crystallinity.

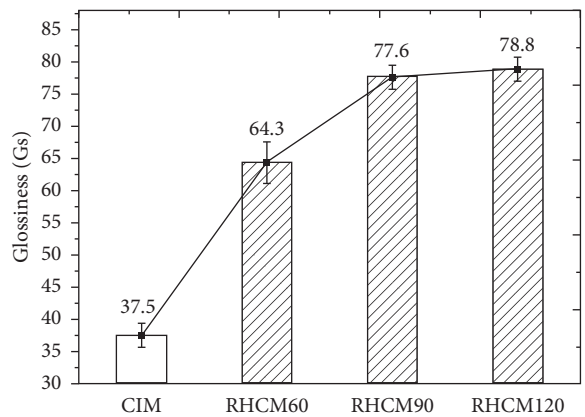

Figure 13: Glossiness variance trends of samples molded at different cavity surface temperatures.

Table 2: Surface roughness of test samples.

Roughness	Ra (μm)					Average
Sample	1	2	3	4	5	
CIM	0.944	1.042	0.668	0.636	0.895	0.837
RHCM60	0.352	0.431	0.336	0.337	0.358	0.363
RHCM90	0.181	0.234	0.212	0.189	0.216	0.206
RHCM120	0.196	0.235	0.190	0.213	0.155	0.198

of the sample can be effectively improved by increasing the mold surface temperature. In the RHCM process, as the mold cavity surface temperature increases, the number of exposed surface fibers decreases because the fluidity of the polymer in the skin layer is enhanced. It is easier for the polymer melt to fill in the gap formed between the fiber and cavity surface, and the fiber of the skin layer can be well-wrapped by the polymer matrix without being exposed outside the skin layer.

Figure 14 shows the microsurface images of GFRPP samples molded at different cavity surface temperatures immediately before filling. With the temperature rising, a smooth mold surface can be accurately reproduced; hence, the surface roughness of the product is gradually decreased. The greater the surface roughness, the larger the undulation of the microscopic surface of the product and the stronger the scattering of light; this means that the gloss of the product becomes lower with the increase in surface roughness. Figure 14 further shows that the surface gloss increase is not distinct after the surface temperature reaches 90°C; this phenomenon is consistent with results found by Wang et al. [33]. They attributed this high gloss surface to the amorphous phase, which completely wrapped all crystalline phases on the surface; finally, the surface presented a pure and uniform amorphous phase. However, this conclusion differs from the observations of other researchers [17, 21, 31] who indicated that the surface of the PP sample is composed of both crystalline and amorphous phases. Another researcher (Wang et al. [35]) pointed out that, for the virgin PP, the surface gloss exhibited a different trend: instead of increasing, it tended to decrease as the cavity surface temperature continued to rise after reaching 110°C.

To better comprehend the mechanism involved in attaining the best gloss quality exhibited by RHCM120, WAXRD technology is employed to estimate the surface crystallization. The WAXRD patterns of RHCM90 and RHCM120 are shown in Figure 15. Note that the orientation parameters of these two samples are practically the same; however, the surface crystallinity of RHCM120 is relatively higher than that of RHCM90. This is because the higher mold surface temperature not only substantially increases the surface crystallization rate of the product, but also increases the crystallization time; thus, the crystallinity on the surface of RHCM120 is relatively high. The high surface crystallinity indicates that the surface crystal area is large, and the molecular chains on the surface are regularly arranged; this can effectively suppress light scattering and thereby improve surface gloss.

The foregoing analysis indicates that when the mold heating temperature is below 90°C, the increase in the surface gloss of the sample is mainly because of the reduction in the surface-exposed floating fibers and the improvement in the melt surface replication ability. When the cavity surface temperature is more than 90°C, the surface gloss increase is primarily attributed to the increase in surface crystallinity combined with the higher surface replication ability of the melt.

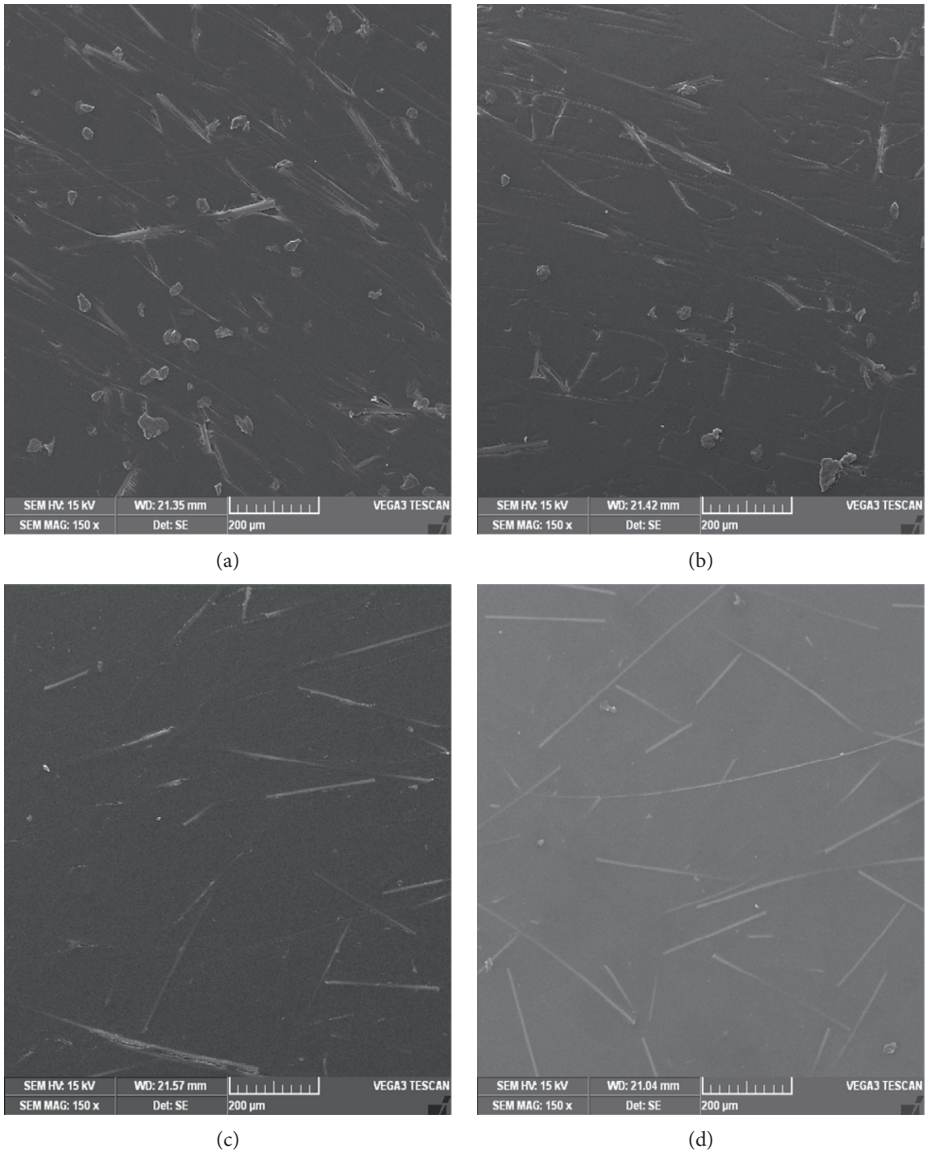

Figure 14: Microsurface images of GFRPP samples molded at different cavity surface temperatures immediately before filling: (a) CIM; (b) RHCM60; (c) RHCM90; (d) RHCM120.

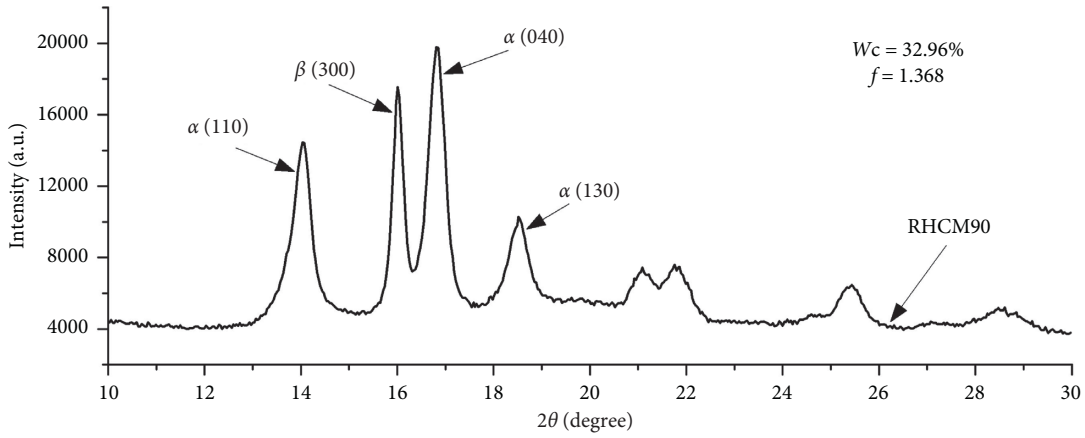

(a)

Figure 15: Continued.

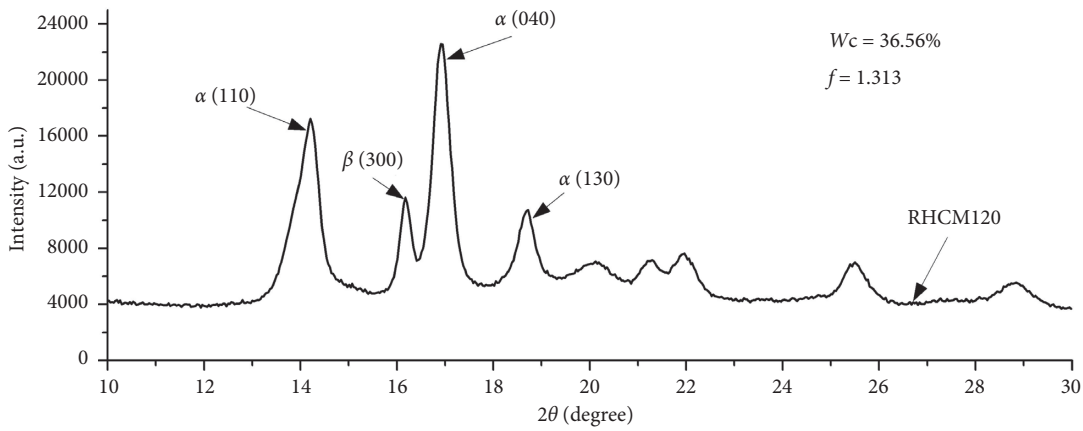

(b)

Figure 15: X-ray diffraction curves of (a) RHCM90 and (b) RHCM120.

4. Conclusions

In this study, the effect of mold cavity surface temperature on the tensile and surface gloss properties is investigated in 30% short glass fiber-reinforced PP composites without weld lines. The influence mechanisms of temperature are discussed and revealed by coupling simulation, SEM, WAXRD, DMA, roughness meter, and surface gloss meter. The corelationship between the macroscopic properties (tensile strength and surface gloss), microstructure, and processing of RHCM samples are discussed. The main conclusions drawn are as follows.

(1) The tensile strength first increases and then decreases as the cavity surface temperature increases before filling. RHCM60 sample has the highest tensile strength followed by RHCM90 and CIM samples; RHCM120 sample has the lowest tensile strength. These differences are mainly because the microstructure of GFRPP composites considerably depends on the preassigned cavity surface temperature.

(2) With increasing cavity surface temperature before filling, the thickness of skin layer with a medium fiber orientation along the flow direction decreases continuously. The thickness of the shear layer with a strong fiber orientation first increases and then decreases, and all the shear layers of RHCM samples are thicker than that of the CIM sample; RHCM60 sample has the widest shear layer thickness. The thickness of the core layer with a weak fiber orientation first decreases and thereafter increases; RHCM120 and RHCM60 samples have the thickest and thinnest core layers, respectively.

(3) Each layer fiber orientation in all samples exhibits an increasing and thereafter decreasing trend with increasing cavity surface temperature. Each layer fiber orientation in RHCM60 sample is higher than that in the CIM sample. The crystallinity in each layer in all samples increases with increasing cavity surface temperature, and the same variance trend can be observed between the fiber-matrix interfacial bonding strength in all samples and cavity surface temperature.

(4) The sample surface gloss increases with the increase in the surface temperature of the mold cavity; however, when the temperature exceeds 90°C, the growth trend sharply slows down. Moreover, among all samples, the surface crystallinity in RHCM120 sample is the highest. When the mold heating temperature is lower than 90°C, the increase in surface gloss is mainly attributed to the reduction in the exposed floating fiber and the enhancement of the melt surface replication ability. When the mold heating temperature is more than 90°C, the surface gloss increases mainly because of the increase in the surface crystallinity coupled with the high level of the mirror surface replication ability of the melt.

Data Availability

All data used to support the findings of this study are included with the article.

Conflicts of Interest

The authors declare that there are no conflicts of interest regarding the publication of this paper.

Acknowledgments

The authors acknowledge the financial support of the Zhejiang Provincial Natural Science Foundation of China (Grant nos. LY19E050004 and LY19E050009), the National Natural Science Foundation of China (Grant nos. 51575491 and U1610112), and the Zhejiang Provincial Department of Education Foundation of China (Grant no. Y201737711).

References

[1] A. R. Albooyeh, "The effect of addition of Multiwall Carbon Nanotubes on the vibration properties of Short Glass Fiber

reinforced polypropylene and polypropylene foam composites," *Polymer Testing*, vol. 74, pp. 86–98, 2019.

[2] K. Friedrich and A. A. Almajid, "Manufacturing aspects of advanced polymer composites for automotive applications," *Applied Composite Materials*, vol. 20, no. 2, pp. 107–128, 2013.

[3] G. Colucci, H. Simon, D. Roncato, B. Martorana, and C. Badini, "Effect of recycling on polypropylene composites reinforced with glass fibres," *Journal of Thermoplastic Composite Materials*, vol. 30, no. 5, pp. 707–723, 2017.

[4] H. Ikbal, Q. Wang, A. Azzam, and W. Li, "GF/CF hybrid laminates made through intra-tow hybridization for automobile applications," *Fibers and Polymers*, vol. 17, no. 9, pp. 1505–1521, 2016.

[5] E. I. Kurkin and V. O. Sadykova, "Application of short fiber reinforced composite materials multilevel model for design of ultra-light aerospace structures," *Procedia Engineering*, vol. 185, pp. 182–189, 2017.

[6] R. S. Bay, *Fiber Orientation in Injection-Molded Composites: A Comparison of Theory and Experiment*, St Edmundsbury Press, Suffolk, UK, 1991.

[7] S. Liparoti, A. Sorrentino, V. Speranza, and G. Titomanlio, "Multiscale mechanical characterization of iPP injection molded samples," *European Polymer Journal*, vol. 90, pp. 79–91, 2017.

[8] Z. Wang, G. Zheng, B. Wang et al., "Suppressing the skin-core structure in injection-molded HDPE parts via the combination of pre-shear and UHMWPE," *RSC Advances*, vol. 5, no. 103, pp. 84483–84491, 2015.

[9] X. P. Li, N. N. Gong, Z. Gao et al., "Fiber orientation in melt confluent process for reinforced injection molded part," *International Journal of Advanced Manufacturing Technology*, vol. 90, no. 5–8, pp. 1457–1463, 2017.

[10] C. Kahl, M. Feldmann, P. Sälzer, and H.-P. Heim, "Advanced short fiber composites with hybrid reinforcement and selective fiber-matrix-adhesion based on polypropylene—characterization of mechanical properties and fiber orientation using high-resolution X-ray tomography," *Composites Part A: Applied Science and Manufacturing*, vol. 111, pp. 54–61, 2018.

[11] J. L. Thomason and G. E. Schoolenberg, "An investigation of glass fibre/polypropylene interface strength and its effect on composite properties," *Composites*, vol. 25, no. 3, pp. 197–203, 1994.

[12] J. Hou, G. Zhao, G. Wang, G. Dong, and J. Xu, "A novel gas-assisted microcellular injection molding method for preparing lightweight foams with superior surface appearance and enhanced mechanical performance," *Materials & Design*, vol. 127, pp. 115–125, 2017.

[13] E. Haberstroh and H. Wehr, "Rubber processing with gas-assisted injection moulding (R-GAIM)," *Macromolecular Materials and Engineering*, vol. 284-285, no. 1, pp. 76–80, 2000.

[14] X. H. Liu, Y. M. Pan, G. Q. Zheng et al., "Overview of the experimental trends in water-assisted injection molding," *Macromolecular Materials & Engineering*, vol. 303, no. 8, pp. 1–13, 2018.

[15] D. Mi, R. La, T. Wang, X. Zhang, and J. Zhang, "Hierarchic structure and mechanical property of glass fiber reinforced isotactic polypropylene composites molded by multiflow vibration injection molding," *Polymer Composites*, vol. 38, no. 12, pp. 2707–2717, 2017.

[16] D. Yao, S.-C. Chen, and B. H. Kim, "Rapid thermal cycling of injection molds: an overview on technical approaches and applications," *Advances in Polymer Technology*, vol. 27, no. 4, pp. 233–255, 2008.

[17] G. L. Wang, G. Q. Zhao, and Y. J. Guan, "Thermal response of an electric heating rapid heat cycle molding mold and its effect on surface appearance and tensile strength of the molded part," *Journal of Applied Polymer Science*, vol. 128, no. 3, pp. 1339–1352, 2013.

[18] S.-C. Chen, Y.-W. Lin, R.-D. Chien, and H.-M. Li, "Variable mold temperature to improve surface quality of microcellular injection molded parts using induction heating technology," *Advances in Polymer Technology*, vol. 27, no. 4, pp. 224–232, 2008.

[19] S. Liparoti, A. Sorrentino, G. Guzman, M. Cakmak, and G. Titomanlio, "Fast mold surface temperature evolution: relevance of asymmetric surface heating for morphology of iPP molded samples," *RSC Advances*, vol. 5, no. 46, pp. 36434–36448, 2015.

[20] L. Crema, M. Sorgato, F. Zanini, S. Carmignato, and G. Lucchetta, "Experimental analysis of mechanical properties and microstructure of long glass fiber reinforced polypropylene processed by rapid heat cycle injection molding," *Composites Part A: Applied Science and Manufacturing*, vol. 107, pp. 366–373, 2018.

[21] Z. Shayfull, S. Sharif, A. M. Zain et al., "Potential of conformal cooling channels in rapid heat cycle molding: a review," *Advances in Polymer Technology*, vol. 33, no. 1, pp. 725–738, 2014.

[22] J. Li, T. Li, Y. Jia, S. Yang, S. Jiang, and L.-S. Turng, "Modeling and characterization of crystallization during rapid heat cycle molding," *Polymer Testing*, vol. 71, pp. 182–191, 2018.

[23] W. H. Wang, G. Q. Zhao, Y. J. Guan et al., "Effect of rapid heating cycle injection mold temperature on crystal structures, morphology of polypropylene and surface quality of plastic parts," *Journal of Polymer Research*, vol. 22, no. 5, pp. 1–11, 2015.

[24] V. Speranza, S. Liparoti, R. Pantani, and G. Titomanlio, "Hierarchical structure of iPP during injection molding process with fast mold temperature evolution," *Materials*, vol. 12, no. 3, p. 424, 2019.

[25] S. Liparoti, A. Sorrentino, and G. Titomanlio, "Rapid control of mold temperature during injection molding process: effect of packing pressure," *American Institute of Physics*, vol. 1965, pp. 0200521–0200524, 2015.

[26] G. Wang, G. Zhao, and X. Wang, "Effects of cavity surface temperature on reinforced plastic part surface appearance in rapid heat cycle moulding," *Materials & Design*, vol. 44, pp. 509–520, 2013.

[27] G. Wang, G. Zhao, and X. Wang, "Effects of cavity surface temperature on mechanical properties of specimens with and without a weld line in rapid heat cycle molding," *Materials & Design*, vol. 46, pp. 457–472, 2013.

[28] J. Li, W. Zheng, S. Jiang, and G. Chai, "An experimental study of skin layer in rapid heat cycle molding," *Polymer-Plastics Technology and Engineering*, vol. 53, no. 5, pp. 488–496, 2014.

[29] X. P. Li, G. Q. Zhao, and C. Yang, "Effect of mold temperature on motion behavior of short glass fibers in injection molding process," *International Journal of Advanced Manufacturing Technology*, vol. 73, no. 5–8, pp. 639–645, 2014.

[30] Y. G. Zhou, B. Su, and L. S. Turng, "Mechanical properties, fiber orientation, and length distribution of glass fiber-reinforced polypropylene parts: influence of water-foaming technology," *Polymer Composites*, vol. 39, no. 12, pp. 4368–4399, 2018.

[31] H. B. H. Salah, H. B. Daly, J. Denault, and F. Perrin, "Morphological aspects of injected polypropylene/clay nanocomposite materials," *Polymer Engineering & Science*, vol. 53, no. 5, pp. 905–913, 2013.

[32] M. A. Kashfipour, N. Mehra, and J. H. Zhu, "A review on the role of interface in mechanical, thermal, and electrical properties of polymer composites," *Advanced Composites & Hybrid Materials*, vol. 1, no. 3, pp. 415–439, 2018.

[33] G. L. Wang, G. Q. Zhao, and X. X. Wang, "Experimental research on the effects of cavity surface temperature on surface appearance properties of the moulded part in rapid heat cycle moulding process," *International Journal of Advanced Manufacturing Technology*, vol. 68, no. 5–8, pp. 1293–1310, 2013.

[34] L. A. Pothan, Z. Oommen, and S. Thomas, "Dynamic mechanical analysis of banana fiber reinforced polyester composites," *Composites Science and Technology*, vol. 63, no. 2, pp. 283–293, 2003.

[35] M. H. Wang, J. J. Dong, W. H. Wang et al., "Optimal design of medium channels for water-assisted rapid thermal cycle mold using multi-objective evolutionary algorithm and multi-attribute decision-making method," *International Journal of Advanced Manufacturing Technology*, vol. 68, no. 9–12, pp. 2407–2417, 2013.

Hindawi
Advances in Polymer Technology
Volume 2020, Article ID 7573693, 7 pages
https://doi.org/10.1155/2020/7573693

Research Article

Advances in Polymer Technology Application of Pareto-Based Genetic Algorithm in Determining Layout of Heating Rods for a Plastic Injection Mold

Yipeng Li, Ningning Gong, Yaohui Wang, Yuntao Chen, Bowen Wang, and Xiping Li

College of Engineering, Zhejiang Normal University, Jinhua 321004, China

Correspondence should be addressed to Ningning Gong; gnn@zjnu.cn

Received 23 June 2019; Revised 2 August 2019; Accepted 11 November 2019; Published 21 March 2020

Academic Editor: Huamin Zhou

Copyright © 2020 Yipeng Li et al. This is an open access article distributed under the Creative Commons Attribution License, which permits unrestricted use, distribution, and reproduction in any medium, provided the original work is properly cited.

The Pareto-based genetic algorithm is an effective way to solve complex optimization design problems in engineering. In this study, first, the principles of Pareto optimal solutions and multiobjective genetic algorithm were presented. Second, to investigate the influence of the mold temperature on the products' performances, a multicavity experiment injection mold was designed whose temperature could be controlled by the heating rods. To obtain a homogeneous temperature distribution across the multicavity surfaces after the heating stage, multiobjective optimization models for the heating rods layout were established based on the heat transfer process of the mold. Finally, the Pareto-based genetic algorithm and finite element method were combined to solve the optimized models to obtain the optimal solution. After a finite element analysis and experimental injection, it is proved that the optimized distribution of the heating rods in the mold is necessary for the experiment and production.

1. Introduction

Injection products quality mainly depends on the history of plastic melt experienced in the mold cavity. Mold temperature, cavity pressure, and other injection molding process parameters all play an important role in the quality of products. Especially, the mold temperature could greatly affect the melt flow process, solidification process, and the final shape and dimensional precision of the products. At suitable mold temperature, the plastic melt fills the mold cavity easily, the shrinkage and warpage of the molded part are very small, and the surface quality and mechanical properties are also relatively high. Therefore, studying and analysing the influences of the mold temperature on the product quality attaches great importance to the researchers. Lin et al. [1] investigated the effect of mold temperature field on the injection molding process of polypropylene (PP) parts. The warpage of the relevant parts due to the asymmetry of the mold temperature was examined. It was found that the part warpage decreased with the increasing mold temperature. Zhao et al. [2, 3] analysed the effect of rapid changing mold temperature on improving microscopic feature replication and molded part appearance. The results showed that the rapid heating of the cavity helped the polymer melt to replicate the surface topography of the mold. Li et al. [4] discussed the impact of cavity surface temperature on the surface topography and texture of molded reinforced plastic parts, and it was shown that the increase of cavity surface temperature can improve the surface appearance of the injected parts. Recently, literatures [5–8] focusing on the influences of mold temperature and other parameters on the weldline properties are also attracting more attention. However, concerning the relationship between the mold temperature and the part performances, there are still many problems that are not clear. For example, the effects of the same mold temperature on different plastic materials' performances, the effects of different mold temperature on the same material performances, and especially, the formation and disappearing processes of the weldline on the injection part are still

ambiguous. Thus, it is still very necessary to do further studies on the relationship between the mold temperature and the part performances.

For this purpose, according to the American Society for Testing and Materials (ASTM) standard, an experimental injection mold with multiple cavities including tensile specimen cavity, impact specimen cavity, and bend specimen cavity was designed. Several heating rods were installed in the mold to control the mold temperature by controlling the heating time of the rods. To study different properties of the specimens in a same mold temperature, the temperature of each cavity surface must be the same and distributes uniformly before the melt injected. It is required that the installed location of the heating rods in the mold must be properly optimized. According to the characteristics of the design mold and the heat transfer process, a multiobjective model indicating the uniformity of temperature distribution and efficiency of heating mold was established by combining the finite element analysis (FEA) with Pareto's genetic algorithm (GA). Finally, the effectiveness of the proposed optimization method is proved by practical experiment.

2. Multiobjective Optimization Algorithms

2.1. Pareto Optimal Solutions. In engineering applications, conflicts often occur when it comes to optimization problems with multiobjective functions. It is foreseeable that no optimal design point can achieve optimal results for all objective functions at the same time. If an objective function is optimized with only one variable, the other parameters may be opposite to the target function value. Therefore, the traditional method of converting multiple targets into a single target by mathematical operations is greatly limited. Unlike the traditional optimization method, the weight is difficult to be clear, and the Pareto-based multiobjective optimization algorithm pays more attention to obtaining several better solutions. Designers can choose the best solution from the Pareto optimal solutions obtained according to different situations. Therefore, the Pareto optimal solution is only a compromise solution for the feasible solution domain and has been used in many engineering applications in recent years. [9–13].

2.2. Multiobjective Genetic Algorithm. The Genetic Algorithm (GA) develops on the basis of population. Every time you perform a GA operation, more than one solution can be obtained. It eliminates replacement inferior solutions by comparing them to each other in all solutions. Then, in each iteration operation, the optimal solution of the previous operation is used instead of the new variable to approximate the optimal solution. Therefore, a solution that meets certain accuracy can be considered the best solution. Therefore, GA is the same with solving multiobjective problems in engineering applications, especially the Pareto optimal solution. Poirier et al. [14] applied GA for the multiobjective optimization of steel sandwich panels under prescribed quasi-static loads. The results demonstrated that the proposed methodology could be applied to the design of light-weight laser-welded steel sandwich panels with outstanding structural performance.

Chattaraj and Ganguli [15] used GA for multiobjective optimization. Analysis shows that for thick flexible extensions, the extended length provides a Pareto optimal solution for multiobjective optimization. Guo et al. [16] considered the differences between plants, production departments, and processes for multiobjective order scheduling in production planning in complex environments. The Pareto optimization model and the NSGA II optimization process are used to address this issue. Experiments based on industry data verify the effectiveness of the optimization model. Bandyopadhyay et al. [17] used a multiobjective genetic algorithm to simultaneously minimize the yield stress and R value to obtain the anisotropic yield function coefficients. Results showed that the yield function coefficients optimized were commendably calculating the deformation behaviour of various anisotropic metal plates. According to the literature, the GA and Pareto-based optimization are very efficient to deal with multiobjective problems. Following is an optimization process based on Pareto's multiobjective genetic algorithm. Firstly, bring design variables into the operation in the form of autosomal, which contain the information concern solutions. Secondly, the initial population composed of individuals is given default values. Next, the objective function value is used to evaluate the results of individual adaptability. By replication, crossover, and mutation, all individuals with high fitness can be passed on to the next generation to ensure genetic diversity, so as to obtain new individuals with better optimization results and finally to form a new population. Finally, the algorithm terminates when the maximum algebra is generated or the level of suitability is satisfactory. Otherwise, the process will continue to loop through the second subsequent steps until the termination condition is met. The problem presented in the current article and the details of the optimization process are described in the following text.

3. Establishment of the Optimization Model

3.1. Structure of the Experimental Injection Mold. To investigate the mold temperature influences on surface appearance, mechanical properties, and weldline formation, and disappearing process of the part, a multicavity mold including tensile, impact, and bend strength specimen is designed by the authors. Specimens with both single and double injection gates are designed for the convenience of comparing the performance of the injected part with weldline and nonweldline. Several heating rods are installed in the mold to control the mold temperature. Figure 1 shows the internal structure of the cavity.

3.2. Establishment of Multiobjective Optimization Models. For studying properties of different injection specimen with the same injection parameters, the temperature of the inner surface of the cavity should be basically the same and distributes uniformly after heating stage. For considering the

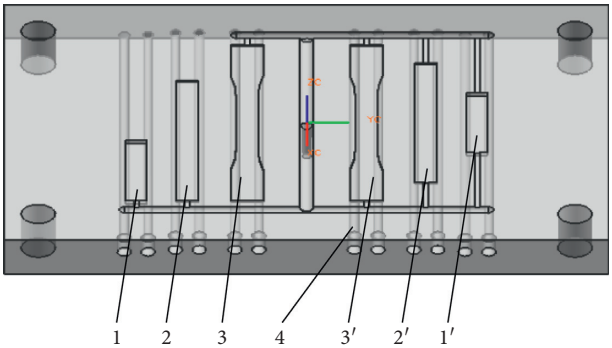

Figure 1: Structure of the designed mold and the standard specimen. (1, 1′): Standard tensile specimens with single gate and double gates, (2, 2′): standard bending specimens with single gate and double gates, (3, 3′): standard impact specimens with by single gate and double gates, and (4): heating rods.

experiment cost and the mold structure, two heating rods are installed under each cavity surface to heat the mold. If the interval between the two rods on the cavity does not reach an optimum distance, the temperature on the surface of the mold cavity will be inhomogeneous and the temperature difference will be large in general. Therefore, the optimization of the arrangement or position of the heaters in the cavity plate is of great significance, which can ensure the temperature distribution as well as the heating efficiency. Since the heating rods are symmetrical about the center line of the cavity plate, only half of the cavity plate cross section is set as the simplified model for studying the heat transfer process and temperature distribution analysis. The temperature distribution analysis model is shown in Figure 2.

3.2.1. Design Variables. Assuming that the interval from the heater to the surface of the cavity is the same and set to 7.5 mm, the interval from the left side to the center of each heater is set as variables to optimize the heat transfer process. Then, the lower left corner of the geometric model is set as the reference coordinate system origin. Therefore, the horizontal ordinate of the horizontal heating rod is determined as a design variable and is represented by x_i, where $i = 1$–6.

Design variables should have certain limitation before performing the optimization process. As presented in Figure 2, the boundary conditions of variables must be limited as

$$\begin{aligned} &a_1 \le x_1 \le b_1, a_2 \le x_2 \le b_2, a_3 \le x_3 \le b_3, \\ &a_4 \le x_4 \le b_4, a_5 \le x_5 \le b_5, a_6 \le x_6 \le b_6, \end{aligned} \tag{1}$$

where a_i, b_i ($i = 1$–5) are the lower and upper limits of the design variables, and they are defined based on the following regulations.

(1) Based on the previous optimization results, the position of the heating rods was redefined, and the FEA model of the cavity was supplemented by the analysis of meshing and recalculation. So, the design variables should satisfy the expressions:

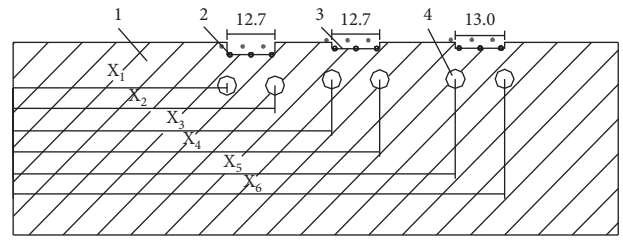

Figure 2: Optimization model for the designed mold (Unit: mm). 1: Cavity plate. 2: Temperature tracking points. 3: Cavity surface. 4: Heating rods.

$$b_1 + D \le a_2, b_2 + D \le a_3, b_3 + D \le a_4, b_4 + D \le a_5, b_5 + D \le a_6, \tag{2}$$

where D represents the diameter of the heating rods. In this case, the adjacent rods will not intersect with each other in the optimization process

(2) The two heating rods under each corresponding cavity should not be very far away from the cavity in the interest of heating efficiency

Based on the abovementioned rules and mold design experience, the boundary conditions for the design variables are defined in Table 1.

3.2.2. Objective Functions

(1) Objective Function of Heating Efficiency. To conveniently measure the temperature on the cavity surface, three suitable equidistant points are used for tracking the temperature of the cavity surface. The average value of the tracking points in determined heating time is used to define the heating efficiency. Meanwhile, the average temperature is proportional to heating time. According to the next objective function of temperature uniformity distribution, the reciprocal of average temperature can be considered as the minimum objective function. Therefore, the following function can be used to represent the objective function of heating efficiency.

$$\min F_1(X) = \min \frac{1}{\overline{T}} = \min\left(\mathrm{OBJ}_w\left(x_1, x_2, x_3, x_4, x_5, x_6\right)\right), \tag{3}$$

where $(\overline{T})$ indicates the average value of the temperature tracking points. $X = x_1, x_2, x_3, x_4, x_5, x_6$ is a coordinate vector, and $x_1, x_2, x_3, x_4, x_5, x_6$ are design variables of vector X.

(2) Objective Function of Temperature Distribution Uniformity. In this study, the difference between the tracking point temperature and the average temperature is applied for characterizing whether the temperature distribution is uniform. The smaller the variance, the more uniform the temperature distribution. Therefore, the objective function of uniformity of temperature distribution can be expressed by the following functions:

Table 1: Boundary conditions of the design variables (mm).

Variables	x_1	x_2	x_3	x_4	x_5	x_6
Lower limits	60	77	92	112	132	146
Upper limits	70	85	105	125	139	155

$$\begin{aligned} \min F_2(X) &= \min\left(\sum_i^n \left(T_i - \overline{T}\right)^2\right) \\ &= \min\left(\mathrm{OBJ}_f\left(x_1, x_2, x_3, x_4, x_5, x_6\right)\right), \end{aligned} \tag{4}$$

where, T_i is the tracking point temperature at the end of the heating stage, $i = 1, 2, \ldots$ and n is used to identify the location of each temperature tracking point. $F_1(X)$ or OBJ_w $(x_1, x_2, x_3, x_4, x_5, x_6)$ and $F_2(X)$ or OBJ_f $(x_1, x_2, x_3, x_4, x_5, x_6)$ are used to represent the subobjective functions, respectively. According to the correlation characteristics of the abovementioned objective functions, it is known that, when the objective functions take a smaller value, the heating efficiency is relatively higher and the temperature distribution is much more uniform. Therefore, the parameters of the design variables should be such that the two objective functions are simultaneously minimized in order to achieve the desired value.

4. Optimization Procedure and Discussion of Results

In the present work, the optimization procedure is separated into three parts, i.e., establishing and analysing the model, simplifying the operation with clear information, and FEA simulation and Pareto-based GA optimization. Firstly, an analytical model is built by using computer-aided design software under the constraints, including initial and boundary values for design variable. Secondly, the temperature distribution on the surface of the cavity is simulated by the finite element method. For the sake of facilitating the calculation of the objective function, the corresponding subroutines are compiled and the results of temperature distribution are rearranged. Finally, the Pareto and GA-based optimization algorithms can be used to optimize the results, and the optimal values are obtained.

Considering the experiment cost and quality, P20 steel is used to manufacture the injection mold. The material properties are shown in Table 2. It is considered that these properties are invariable in the process of FEM simulation. The heating rods, which are fabricated by MISUMI cooperation, are installed in the mold, and their power is 15 w/cm^2.

By far, we have known all the constraints and initial variables needed before optimization beginning. Each optimization iteration is accompanied by multiple simulation operations to get better results. When optimization starts, few Pareto solutions are available to solve the problem. But, as the number of iteration increases, more and more Pareto solutions are produced. Meanwhile, much better solutions are gradually used to eliminate or replace the inferior solutions until the optimal solution of the problem is obtained.

It is easy to observe from Figure 3 that the optimal solutions of heating efficiency and uniformity of temperature distribution are obtained when the iteration operation is carried out to the 50th generation. Each point in the graph represents a Pareto optimal solution. From the figure, we can also know that the smaller the value of OBJ_w, the higher the heating efficiency, and OBJ_f is inversely related to OBJ_w. There isn't a same variable value to make both of the objective functions to be optimal at the same time. Therefore, the designer is required to select a compromise scheme to satisfy the user's requirements based on the two objective function values. Finally, FEA and experimental application verify that the optimal solution obtained in this paper meets the application requirements. The discussion is carried out in Section 5.

5. Finite Element Analysis and Experimental Application

5.1. Finite Element Analysis. From the function diagram, it is impossible to achieve optimal values for both objective functions at the same time. However, to meet the design requirement, only a compromise solution can be adopted. It was finally found that the optimized average temperature varied between 81.3°C and 90.1°C, while the OBJ_f which represents the temperature distribution uniformity varied from 67.2 to 648.2. Considering the experimental purpose, the quality of the obtained samples plays a very important role for the subsequent performance tests, and the quality of the samples mainly depends on the temperature uniformity of the mold. Besides, it is easy to improve the average temperature of the cavity surface by increasing the heating time. Therefore, it can be confirmed that the OBJ_f function plays a much more important role than the heating efficiency function. Accordingly, in the actual mold design, the variable values resulting in an optimal temperature distribution uniformity are empolyed. Based on the optimal design variables determined in Table 3, the optimized cavity average temperature is reduced from 84.4 $(1/1.185 \times 10^{-2})$°C to 81.1 $(1/1.233 \times 10^{-2})$°C. The optimized value representing temperature distribution uniformity also decreases from 561.4 to 62.8, proving that the presented optimized process is very effective. Although the uniformity of temperature distribution after optimization has been greatly improved, it inevitably leads to a slight reduction in heating efficiency, which does not affect the experimental efficiency.

Finally, FEA simulation software was used for calculating the heat transfer process of the cavity surface under different conditions. Figure 4 is a schematic diagram of simulated results by using the initial and optimized variable values, respectively. It is found that the optimized mold temperature distribution is much more uniform than the initial temperature distribution.

The temperature of the twelve tracking points before and after optimization is illustrated in Figure 5. According to the figure, the temperature of the cavity surface varies from 71.5°C to 94.7°C with the initial design variable values, and the maximum temperature difference is 23.2°C. However, after optimization, the temperature is between 78.5°C and

Table 2: Material properties.

Density (g·cm^{-3})	Specific heat, J (kg·C)$^{-1}$	Thermal conductivity, W (m·C)$^{-1}$	Modulus of elasticity (MPa)	Coefficient of thermal expansion (°C^{-1})
7.78	4.60×10^2	30	2.05×10^5	1.16×10^{-5}

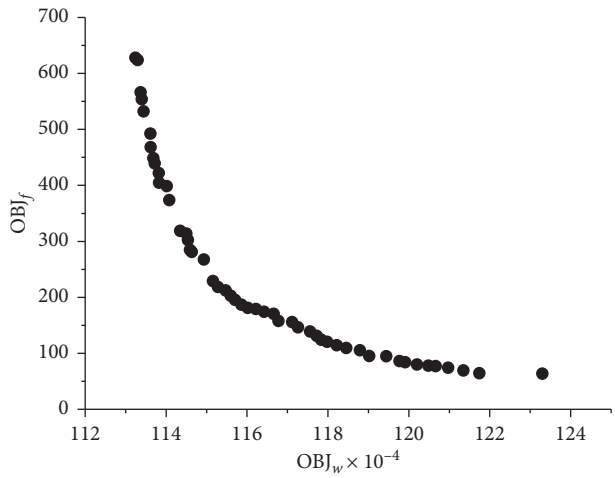

Figure 3: Pareto optimal solutions.

Table 3: Values of the initial and optimal design variables.

Design variables/objective	Initial values	Optimal values
x_1 (mm)	70.4	67.2
x_2 (mm)	84.5	78.4
x_3 (mm)	100.5	99.3
x_4 (mm)	114.5	116.2
x_5 (mm)	135.5	138.9
x_6 (mm)	149.5	153.4
OBJ$_f$ (°C^2)	561.4	62.8
(OBJ$_w$)$^{-1}$ (°C^{-1})	1.185×10^{-2}	1.233×10^{-2}

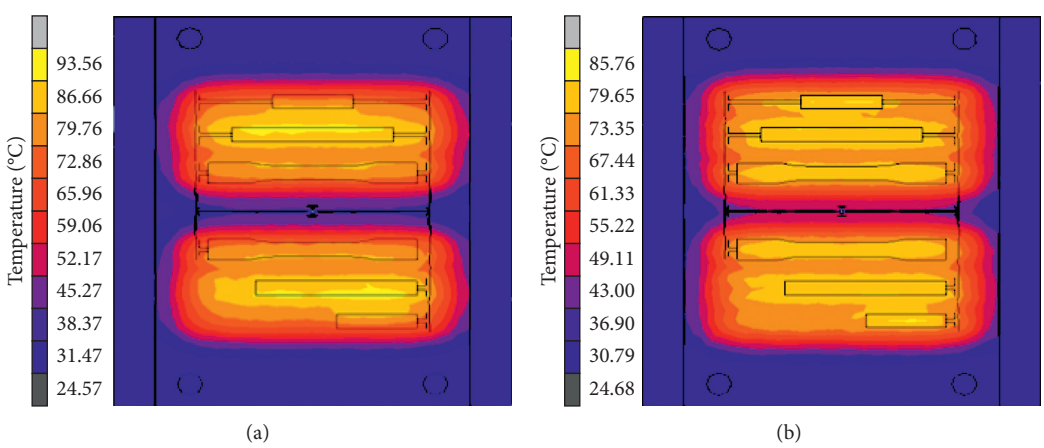

Figure 4: Temperature distribution of the designed mold. (a) Initial temperature distribution. (b) Optimal temperature distribution.

84.8°C, and the maximum difference in temperature is only 6.3°C. The optimized structure reduced the maximum temperature difference by 16.9°C. It can be known that the temperature value of the tracking point after optimization is much more stable and distributed much more uniform than that of the initial mold design. Therefore, we can conclude that the optimized design is very necessary and effective.

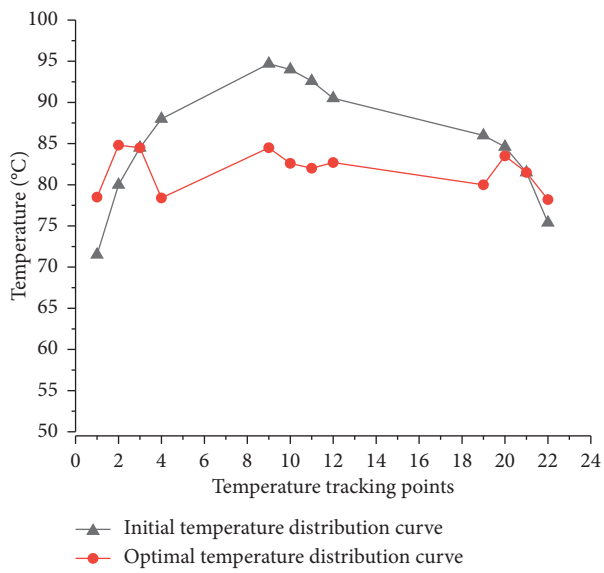

Figure 5: Temperature distribution curves. 1: Initial temperature distribution curve. 2: Optimal temperature distribution curve.

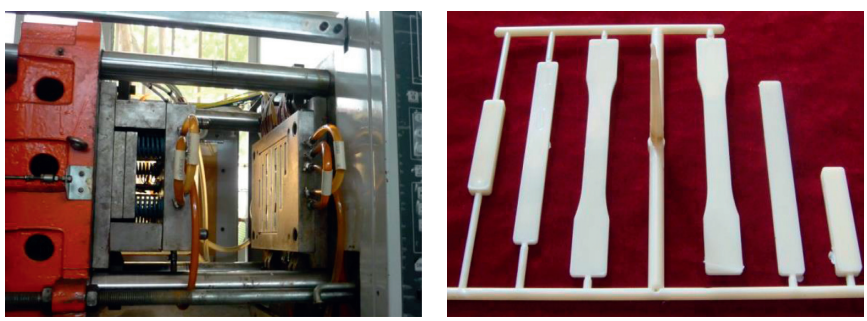

(a) (b)

Figure 6: Injection experiment in the laboratory. (a) Experiment mold installed in an injection machine. (b) Produced samples.

5.2. Experiment Applications. According to the optimized results, this paper designs an experiment mold to study the influence of the mold temperature on the part performances. The layout of heating rods in the mold is designed and manufactured according to the optimized parameters. The mold temperature could be controlled by the rods, and sound samples could be successfully produced at different mold temperatures. Figure 6(a) gives the photograph of the fabricated mold in opening state installed in the injection machine in our laboratory, and Figure 6(b) shows the samples injected with a mold temperature of 85°C.

6. Conclusions

A Pareto-based multioptimization method can be used to obtain a couple of optimal feasible domain compromise solutions. According to different requirements, users can choose the most efficient solution from Pareto optimal solutions. The sidedness of traditional optimization methods is avoided. By determining proper coordinates for the established model in this paper, a multiobjective model including uniform temperature distribution and the heating efficiency of cavity surface was established. In the simulation process, an FEA method and Pareto-based GA are used to obtain optimal values of design variables. As a result, the objective function of the uniform temperature distribution reduced from 648.2 to 67.2, and the maximum temperature difference of the cavity surface is reduced from 23.2°C to 6.3°C. There is obvious improvement for the uniformity of temperature distribution. Accordingly, an experimental injection mold is designed and manufactured. Very good injection products are produced with the optimal values. The presented optimization method can also be used to solve other multiobjective problems.

Data Availability

The data used to support the findings of this study are available from the corresponding author upon request.

Conflicts of Interest

The authors declare that there are no conflicts of interest regarding the publication of this paper.

Acknowledgments

The research work was supported by the Natural Science Foundation of Zhejiang Province (LY18E050011 and LY20E050008) and National Natural Science Foundation of China (51675489).

References

[1] Y.-H. Lin, H.-L. Chen, S.-C. Chen, and Y.-C. Lin, "Effect of asymmetric cooling system on in-mold roller injection molded part warpage," *International Communications in Heat and Mass Transfer*, vol. 61, pp. 111–117, 2015.

[2] G. Dong, G. Zhao, L. Zhang, J. Hou, B. Li, and G. Wang, "Morphology evolution and elimination mechanism of bubble marks on surface of microcellular injection-molded parts with dynamic mold temperature control," *Industrial & Engineering Chemistry Research*, vol. 57, no. 3, pp. 1089–1101, 2017.

[3] G. Wang, Y. Hui, L. Zhang, and G. Zhao, "Research on temperature and pressure responses in the rapid mold heating and cooling method based on annular cooling channels and electric heating," *International Journal of Heat and Mass Transfer*, vol. 116, pp. 1192–1203, 2018.

[4] X. Li, N. Gong, Z. Gao, and C. Yang, "Fiber orientation in melt confluent process for reinforced injection molded part," *The International Journal of Advanced Manufacturing Technology*, vol. 90, no. 5-8, pp. 1457–1463, 2016.

[5] J. Gómez-Monterde, M. Sanchez-Soto, and M. Maspoch, "Influence of injection molding parameters on the morphology mechanical and surface properties of ABS foams," *Advances in Polymer Technology*, vol. 37, no. 8, pp. 2707–2720, 2018.

[6] K.-H. Kim, J. Cheon Park, Y. Suh, and B.-H. Koo, "Interactive robust optimal design of plastic injection products with minimum weldlines," *The International Journal of Advanced Manufacturing Technology*, vol. 88, no. 5-8, pp. 1333–1344, 2016.

[7] C. Leisen, M. Wolf, and D. Drummer, "Influence of the mold temperature on the material properties and the vibration welding process of crosslinked polyamide 66," *Polymer Engineering & Science*, vol. 58, no. S1, pp. E207–E214, 2017.

[8] S. Kitayama, K. Tamada, M. Takano, and S. Aiba, "Numerical optimization of process parameters in plastic injection molding for minimizing weldlines and clamping force using conformal cooling channel," *Journal of Manufacturing Processes*, vol. 32, pp. 782–790, 2018.

[9] D. Alanis, P. Botsinis, Z. Babar et al., "A quantum-search-aided dynamic programming framework for pareto optimal routing in wireless multihop networks," *IEEE Transactions on Communications*, vol. 66, no. 8, pp. 3485–3500, 2018.

[10] Z. Bao, X. Ren, Y. Yang, J. Zhu, C. Wang, and R. Yin, "Multi-objective integration of flexible collaborative planning and fuzzy flexible lot-splitting scheduling based on the pareto optimal," *International Journal of Hybrid Information Technology*, vol. 8, no. 7, pp. 305–318, 2015.

[11] Y. Li, B. Feng, G. Li, J. Qi, D. Zhao, and Y. Mu, "Optimal distributed generation planning in active distribution networks considering integration of energy storage," *Applied Energy*, vol. 210, pp. 1073–1081, 2018.

[12] J. Razmi, E. Jafarian, and S. H. Amin, "An intuitionistic fuzzy goal programming approach for finding pareto-optimal solutions to multi-objective programming problems," *Expert Systems with Applications*, vol. 65, pp. 181–193, 2016.

[13] N. Wang, W.-J. Zhao, N. Wu, and D. Wu, "Multi-objective optimization: a method for selecting the optimal solution from Pareto non-inferior solutions," *Expert Systems with Applications*, vol. 74, pp. 96–104, 2017.

[14] J. D. Poirier, S. S. Vel, and V. Caccese, "Multi-objective optimization of laser-welded steel sandwich panels for static loads using a genetic algorithm," *Engineering Structures*, vol. 49, pp. 508–524, 2013.

[15] N. Chattaraj and R. Ganguli, "Multi-objective optimization of a triple layer piezoelectric bender with a flexible extension using genetic algorithm," *Mechanics of Advanced Materials and Structures*, vol. 25, no. 9, pp. 785–793, 2017.

[16] Z. X. Guo, W. K. Wong, Z. Li, and P. Ren, "Modeling and Pareto optimization of multi-objective order scheduling problems in production planning," *Computers & Industrial Engineering*, vol. 64, no. 4, pp. 972–986, 2013.

[17] K. Bandyopadhyay, K. Hariharan, M.-G. Lee, and Q. Zhang, "Robust multi objective optimization of anisotropic yield function coefficients," *Materials & Design*, vol. 156, pp. 184–197, 2018.

Hindawi
Advances in Polymer Technology
Volume 2020, Article ID 8405745, 13 pages
https://doi.org/10.1155/2020/8405745

Research Article

Numerical Investigation of the Effect of Viscoelasticity on Drop Retraction and the Evaluation of Interfacial Tension between Polymer Melts

Lin Deng,[1,2] **Yun Zhang**,[3] **Shaofei Jiang**,[2] **Jiquan Li**,[2] **and Huamin Zhou**[3]

[1]*School of Mechanical and Electrical Engineering, Wuhan Institute of Technology, Wuhan, China*
[2]*Key Laboratory of E & M, Zhejiang University of Technology, Hangzhou, China*
[3]*State Key Laboratory of Material Processing and Die & Mold Technology, Huazhong University of Science and Technology, Wuhan, China*

Correspondence should be addressed to Yun Zhang; marblezy@hust.edu.cn

Received 22 July 2019; Accepted 21 September 2019; Published 12 March 2020

Academic Editor: Gyorgy Szekely

Copyright © 2020 Lin Deng et al. This is an open access article distributed under the Creative Commons Attribution License, which permits unrestricted use, distribution, and reproduction in any medium, provided the original work is properly cited.

The purpose of this paper is twofold. The first is to numerically investigate and reveal the effect of polymer viscoelasticity on the retraction of a deformed drop using the lattice Boltzmann (LB) method and polymer kinetic theory. More importantly, the second is to propose a novel method to evaluate the interfacial tension between polymer melts based on the numerical study. Compared with the conventional deformed drop retraction method (DDRM), the present method is designed to greatly reduce the impact of polymer viscoelasticity on measuring interfacial tension. To verify, the interfacial tension between molten PP and POE is evaluated using the proposed method and obviously closer result to the true value is shown.

1. Introduction

By blending two or more polymers, it is an inexpensive and convenient way of obtaining new excellent materials that are complementary in performance. In recent years, polymer blends have been increasingly ubiquitous in the plastics industry, i.e., semiconductors [1], nanofiltration [2], fibers [3], and printing [4], and thus have become a very active area of research in materials science. The final properties of the polymer blends depend on not only that of each polymer component but also its internal microstructure, which is the result of the processing conditions as well as the interfacial tension [5, 6]. Therefore, it is of nontrivial science and engineering significance to measure the interfacial tension between polymers accurately for predicting and controlling the structure and properties of polymer blends.

Although the measurement technology for polymer has developed at increasingly faster pace in recent years [7–12], it still has been a challenging problem to obtain the interfacial tension experimentally due to the intrinsic viscoelasticity of polymers [13–15]. These measuring technologies can be divided into two categories: the equilibrium methods and the dynamic methods [14]. The equilibrium methods, including the pendant drop method [16–18], the sessile drop method [5, 6, 19], and the spinning drop method [20–22], establish the equation of the drop shape in a mechanically balanced state and the extrapolate the interfacial tension between the polymers. Although they are applicable for both purely viscous and viscoelastic fluids with very good accuracy, it requires the matrix transparency, comparatively low viscosity of the polymer, and long time to reach equilibrium, with increased risk of thermal degeneration of the polymers. On the contrary, the dynamic methods, including the breaking thread method [23–25], imbedded fiber method [26–29], and deformed drop retraction method [30–34], obtain the interfacial through the morphology evolution equation. For example, the deformed drop retraction method establishes an equation that describes the shape variation of a deformed drop during retraction. The dynamic methods are comparatively more straightforward

and fit for very viscous polymers. Nonetheless, the underlying theory of the existing dynamic methods is only valid for purely viscous fluids. If applied to polymers, the dynamic method will inevitably produce an error that is difficult to estimate. Some research studies on characterization technology are reported to be an inspiration for this problem, but the effect is not clear yet [35].

Therefore, prior to proposing an improved dynamic method for polymers, the effect of viscoelasticity on the drop dynamics, i.e., deformed drop retraction, should be understood first, and then, attempt is made to reduce the effect.

To the author's knowledge, many simulation research studies have focused on the dynamics of viscoelastic drop. Yu and Zhou integrated the Boussinesq–Scriven viscoelastic interfacial constitutive equation in the perturbation analysis on the flow field inside and outside the drop [36]. Mukherjee et al. simulated the shape relaxation of a sheared drop in the case that either or both phases are Oldroyd-B fluids by the finite difference method and front tracking algorithm [37]. Yue et al. used the 2D diffuse-interface method to simulate retraction of a Oldroyd-B drop in quiescent matrix [38]. Yue et al. incorporated the Oldroyd-B viscoelasticity constitutive equation into the phase-field framework of Cahn–Hilliard equation with the adaptive meshing scheme and studied the interfacial dynamics of the drop dynamics [39]. Yu et al. extended Batchelor's approach to viscoelastic fluids and calculated the creeping flow around the drop [40]. The common idea of these studies is the combination of the Navier–Stokes equations, interface tracking algorithm, and the viscoelasticity constitutive model of polymer, i.e., the Maxwell model [41], the Voigt–Kelvin model [42, 43], the transient network model [44, 45], the Oldroyd-B model [46], the upper convected Maxwell model [46], and the FENE-P model [46, 47]. The above review highlights the complex dynamics of viscoelastic drops and the difficulties in modeling. However, most studies are restricted to low viscosity cases and fail to simulate high Debora number (viscoelasticity), due to the limitation of their numerical model and the constitutive model.

In this paper, the effect of viscoelasticity on drop retraction is studied by the LB method and polymer kinetic theory, and then, a novel method for measuring the interfacial tension between polymer melts is proposed. The LB method is a special version of the Boltzmann equation that describes evolution of particles interacting on fixed lattices [48]. It has a kinetic, microscopic origin with a characteristic scale between nanometer and millimeter. On the contrary, the LB method can be Chapman–Enskog expanded to recover the full time-dependent incompressible and compressible Navier–Stokes equations. The LB method models the fluid by an ensemble of particles, so the macroscopic properties such as density and velocity can be easily constructed once an LB solution is obtained. The advantages of the LB method include the ease in dealing with arbitrary geometries and intricate multiphase flows, while its intrinsic parallel algorithm can be solved efficiently and affordably in massively parallel computers. During the past few decades, the LB method has been proved to be a promising tool for the simulation of complex fluid flow [49], i.e., microfluidics [50–52], flow through porous media [53–55], capillary flow [56–58], non-Newtonian flow [59–61], and more importantly, the multiphase flow [62–64]. The automatic-phase separation mechanism and straightforward interface tracking technology are both attractive characteristics of the LB method for simulating drop morphology evolution and has been successfully applied in research [65–68]. Different from the constitutive model of polymer viscoelasticity, the polymer kinetic theory explains the origin of viscoelasticity in a microscopic way, as the net effect of the dynamics of a large collection of constituent molecules with internal degrees of freedom. Interestingly, the macroscopic constitutive models, such as the upper-convected Maxwell (UCM) model and Oldroyd-B, can be derived based on the kinetic theory [46]. For the microscopic nature of both, Onishi et al. for the first time integrated the LB method and kinetic theory and succeeded in modeling the polymeric fluids [69, 70]. Osmanlic and Körner applied the LB-kinetic theory framework to the simulation of Oldroyd-B fluids [71]. This paper combines the LB method and polymer kinetic theory to simulate the retraction of the deformed drop and analyze the effect of viscoelasticity.

The rest of the paper is organized as follows. In Section 2, the retraction process of a deformed drop is simulated using a coupled model of the pseudo-potential multiphase LB scheme and a dumb-bell model of polymer molecule. The effect of viscoelasticity on drop dynamics is analyzed and a novel evaluation method of the interfacial tension is devised. Then, in Section 3, the interfacial tension between molten polypropylene (PP) and polyolefin elastomer (POE) is measured by the proposed method and the original deformed drop retraction method, respectively. Through comparison the better accuracy of the proposed method is verified. Finally, a conclusion is drawn in Section 4.

2. Numerical Investigation

In essence, the LB method is a pseudoparticle method, which streams and collides on the lattice sites over discretized time and space. By tracking the evolution of the distribution function of the pseudoparticles, the fluid flow and drop morphology evolution is captured. On the contrary, the kinetic theory of polymer chains is rewritten in the lattice scheme. So the LB method-based computational framework consists of three ingredients: the pseudopotential multiphase model [72] for drop morphology evolution, the FENE dumbbell model for the polymer viscoelasticity [70, 71], and an appropriate coupling strategy. The outline of the three-dimensional numerical method is briefed in this section, while the details are presented in Appendix. Using the established model, several simulation cases of the deformed drop retraction is implemented and the effect of the viscoelasticity on the retraction process is analyzed. Finally, a novel evaluation method of interfacial tension is proposed.

2.1. Modeling. Among all the multiphase models of the LB method, the pseudopotential approach first proposed by Shan and Chen [72] and improved by Shan and Doolen [73]

is the most widely used by virtue of its simplicity and versatility and thus employed in this paper. The distribution functions of the two components, $f_{d,i}(\mathbf{x},t)$ and $f_{m,i}(\mathbf{x},t)$, which interact through pseudopotential force, describe the multiphase flow and result in the drop morphology evolution. The governing equation of the distribution functions is elaborated in Appendix, as equation (A.2). The term F_i' denotes the interaction between different components and gives rise to spontaneous phase separation (shown in Figure 1).

This automatic mechanism of phase separation is an attractive feature of the pseudopotential model because the two-phase interface is no longer a mathematic boundary, but a postprocessing variable that can be characterized by monitoring the density change of the fluid components so that any specific interface tracking or interface capturing technology is not required as in conventional CFD methods.

From the microscopic point of view, the multiphase phenomenon and polymer viscoelasticity are a result of the intermolecular forces and the stretch and relaxation of polymer chain [74], and thus, it is feasible to model the macroscopic dynamics of viscoelastic polymer blends through the mesoscale polymer kinetics. The viscoelasticity of polymer is modeled based on the polymer kinetics theory; herein, the finitely extensible nonlinear elastic (FENE) dumbbell model is chosen, where two beads are connected by a string, as illustrated in Figure 2.

The conformation of the dumbbell can be defined by the tensor $\mathbf{q}$ that contains the length and orientation of polymer chain. Similar to the idea of the LB method, the function $\psi(\mathbf{q},\mathbf{x},t)$ is defined to indicate the probability distribution of given polymer dumbbell conformation $\mathbf{q}$ at position $\mathbf{x}$ and time t. By solving the governing equation of the evolution of $\psi(\mathbf{q},\mathbf{x},t)$, equation (A.15), namely, the Fokker–Planck equation [75], the conformations of the polymer dumbbells are updated all over the space with time. Then, the viscoelastic stress is calculated according to the conformation according to equation (A.20).

The evolution of the drop morphology and the polymer chain conformation is simulated simultaneously and separately and are coupled through rewriting the equilibrium function f^{eq} ((A.24)). That is, the elastic stress originating from the dumbbell conformation act as a forcing term in Guo's scheme [76].

2.2. Simulation. Before implementing the simulation, it is noteworthy that the simulation of the drop retraction process is based on two fundamental assumptions about the initial condition and the drop shape. Firstly, in terms of initial conditions, there is no residual stress in the drop/matrix sample before the drop is set to retract. This is because in common practice of experiments, the drop is always heated after preparation in order to eliminate the residual stress. Secondly, the drop maintains an axisymmetric ellipsoid during the retraction process with two minor axes B and W of equal length, as illustrated in Figure 3. This seemingly ideal situation can be achieved as long as the sample is well fabricated and the density difference between the drop and matrix is negligible.

The primary aim of the simulation is to study the effect of polymer viscoelasticity on retraction of the deformed drop. For this purpose, all the physical parameters but viscoelasticity strength of the polymers are equal in each simulation case so as to exclude the influence of other factors. The viscosities of both the drop and matrix components, μ_d and μ_m, are set to be 1000 Pa s, the density, ρ_d and ρ_m, 1000 kg/m^3, and the interfacial tension between the drop and the matrix, σ, 0.116 mN/m.

The pseudopotential parameter $g_{\sigma\bar{\sigma}}$ of LB is related to σ according to the Laplace law and decided through trials and error. The spring constant H is set to be 1.

These parameters are kept constant during the drop retraction process. Since the drop retracts very slowly during the process, and the ambient temperature is maintained unchanged somehow, the influence of temperature could be neglected in the simulation.

The strength of the polymer viscoelasticity is characterized by the Deborah number, as expressed below:

$$\mathrm{De} := \frac{\lambda_H}{t_c}, \tag{1}$$

which defines the ratio of relaxation time λ_H and the characteristic time t_c. It is obvious that the larger the De, the stronger the viscoelasticity, and a zero De indicates purely viscous polymer.

The shape of the ellipsoid drop is defined by two parameters, equivalent radius R and the deformability D:

$$\begin{aligned} R &:= \frac{1}{2}\sqrt[3]{LB^2}, \\ D &:= \frac{L^2 - B^2}{L^2 + B^2}. \end{aligned} \tag{2}$$

Of all the simulation cases, the initial values of R and D are set to be 0.12 mm and 0.14, respectively. In addition, for the sake of characterization of the extent to which the ellipsoid drop retracts to sphere, a new parameter, the deformation recovery degree $\varphi(t)$, is defined:

$$\varphi(t) := \ln \frac{L^2(t) - B^2(t)}{(L^2 - B^2)_{t=0}}. \tag{3}$$

In terms of the boundary conditions, periodic boundaries are applied on all the outer boundaries of the simulation domain.

Three numerical cases that only differ in viscoelasticity strength, De = 0, De = 1, and De = 5, are carried out. As expected, in all cases, the drop shape gradually changes from ellipsoid to sphere under the force of interfacial tension. Take the purely viscous case (De = 0) as an instance, and the shape evolution of the drop is shown in Figure 4.

The major and minor axis length of the ellipsoid drop is calculated according to the component distribution of the drop by the eigenvalue method [77]. In all cases, the drop gradually retracts from an ellipsoid to a sphere, while φ continuously decreases from 0 to $-\infty$ overtime, as plotted in Figure 5.

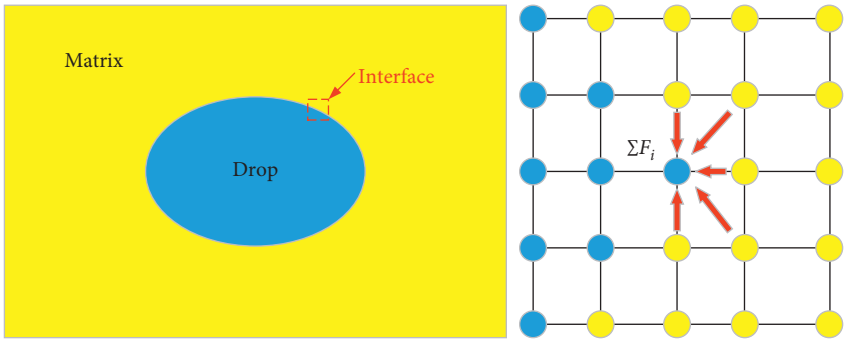

Figure 1: The principle of the pseudopotential model: (a) the schematic of the drop-interface-matrix structure; (b) the pseudopotential force between particles at interface.

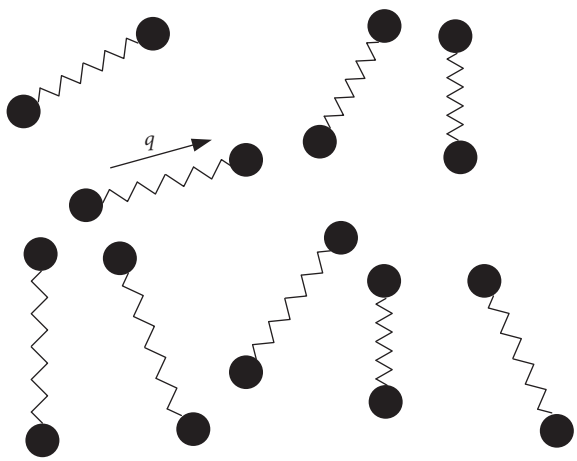

Figure 2: Polymer molecules modeled as an ensemble of bead-spring-spring chains.

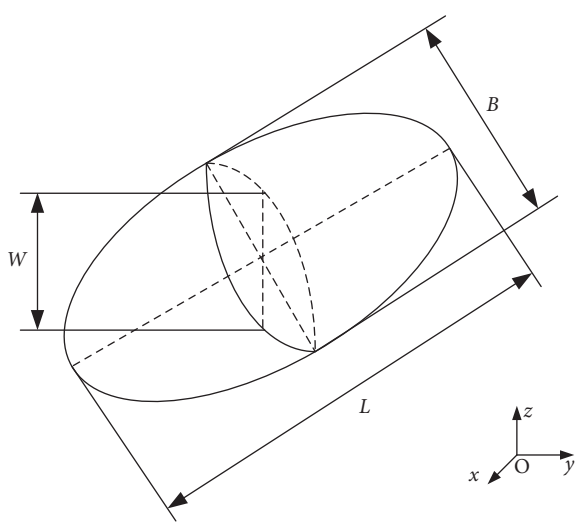

Figure 3: Ellipsoid drop with the major axis of length L and two minor axes of lengths B and W.

From the above simulation results, it can be seen that when the polymer is purely viscous (De = 0), the deformation recovery degree φ is in good linearity with the time, consistent with the small deformation theory (equation (4)). It means that, in this condition, the original DDRM is valid:

$$\varphi(t) = -\frac{40(\lambda+1)}{(2\lambda+3)(19\lambda+6)}\frac{\sigma}{\eta_m R_0}t = -\frac{t}{t_c}. \quad (4)$$

When the drop is viscoelastic (De = 1 and De = 5), the larger the De, the more curved the φ-t results. With the purely viscous case as a reference, the retraction process of the viscoelastic case can be divided into two distinct stages. In the first stage, $t < 3000$ s, the drop retracts at a comparatively faster rate, and φ decreases rapidly, but when the time elapses after about 3000 s~3500 s (1.856~2.165 t_c), the retraction rate of the drop gradually slows down. This is because the viscoelasticity of the polymer has a certain inhibitory effect on the retraction process. At the initial moment, the polymer chains do not elastically deform, so this resistance is relatively small. As the drop continues to retract, the elastic stress keeps growing due to the extension and compression of the dumbbells. In the second stage, the stress has grown to a considerable level so that its inhibitory effect obviously reduces the retraction rate of the drop. Using the data of different stages to implement parameter fitting with equation (4), the values of the obtained interfacial tension are as shown in Figure 6.

In Figure 6, label "$t < 3500$" indicates that the interface tension is obtained by fitting with data from before 3500 s "$t > 3500$," after 3500 s, and "whole stage" all the data. It should be noted that when De = 0, the DDRM is correct and the obtained value of the interfacial tension represents the true two-phase interfacial tension set in the simulation. When De $\neq$ 0, the viscoelasticity of the matrix affects the shape of the curve and the interfacial tension obtained using different stages of the simulation data has apparent discrepancy with the true value. Specifically, using the data of $t < 3500$ produces the fitted interfacial tension much closer to the true one, and the gap is nearly insignificant.

From the above simulations and analysis, it is obvious that, in case of viscoelastic polymers, the original DDRM faces inherent error caused by polymer viscoelasticity which will be augmented with the strengthening of viscoelasticity, whereas at the initial retraction stage, its effect is very weak in comparison to that of the second stage. If only picking the data of the first stage of the drop retraction for fitting with equation (4), then the deviation between the measurement and the true value can be greatly reduced so that a credible result can be obtained.

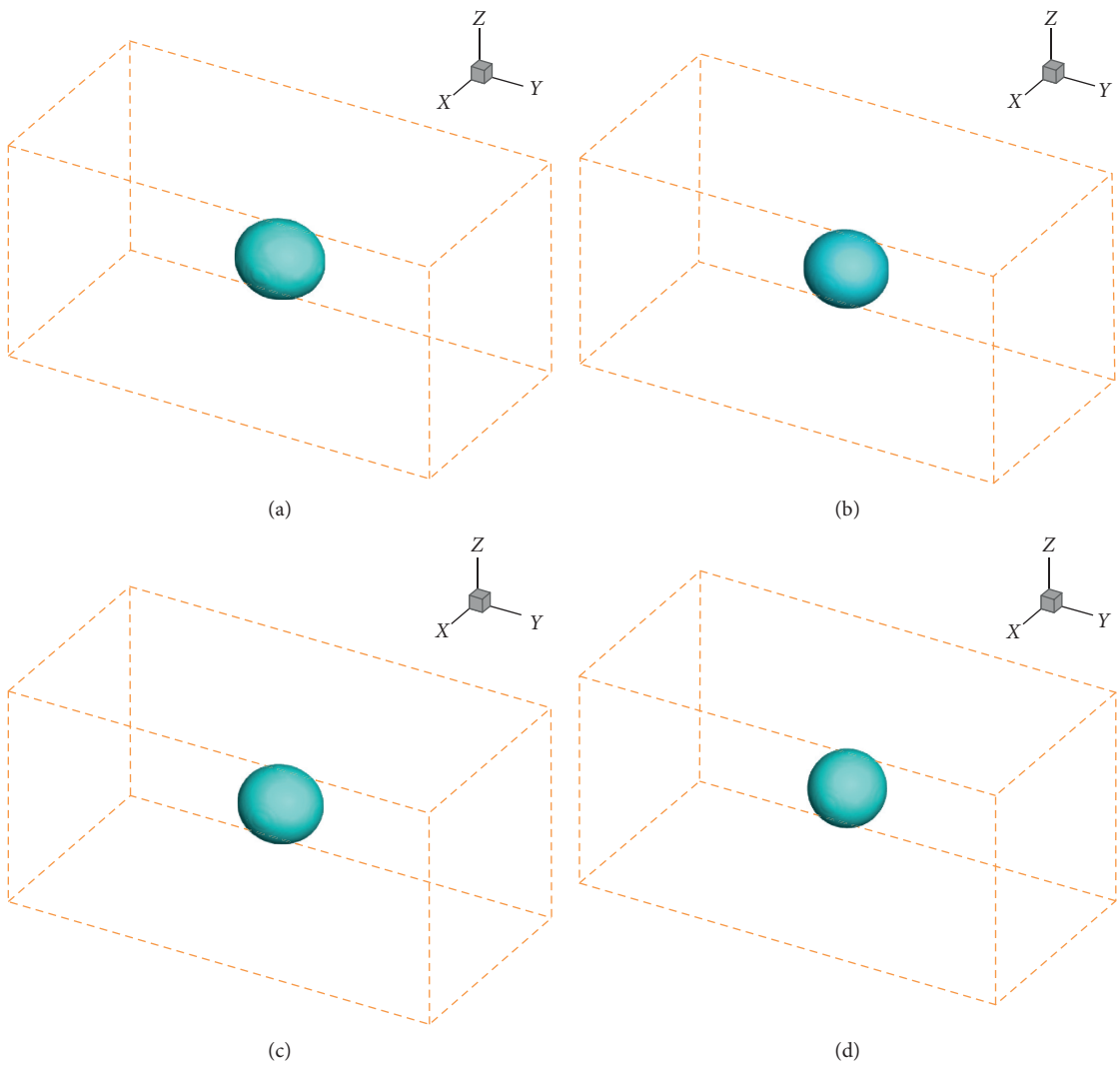

Figure 4: Drop shapes during the retraction process in case of De = 0 with various deformability: (a) 0.15; (b) 0.12; (c) 0.06; (d) 0.

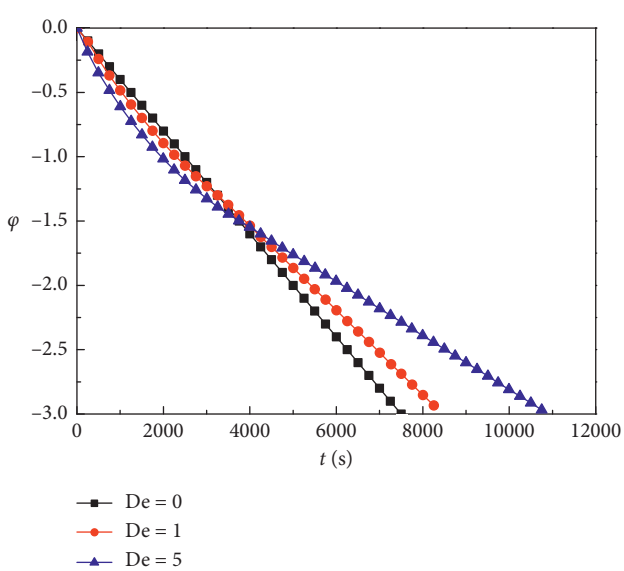

Figure 5: The simulated retraction degree variation with time of different viscoelasticity of the drop with different viscoelasticity (De).

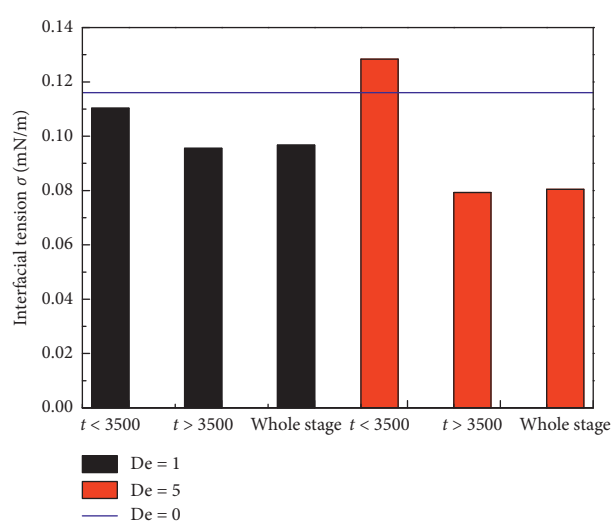

Figure 6: The interfacial tension obtained using the data of t<3500 s, t>3500 s, and the whole stage.

Herein, a novel method to evaluate the interfacial tension is proposed according to the deformed drop retraction. Other than fitting the data of the whole process with equation (4) during which the drop retracts from an ellipsoid to a sphere, only the data from the onset of retraction t_0 to the time $\varphi(t_u) = \varphi_u$ are utilized. The duration between t_0 and t_u is the first stage of the drop retraction, and empirically, the value φ_u is more appropriate to set -1.5.

It should be noted that this treatment also agrees with the dumbbell model. The dumbbell model of polymer molecules suggests that only the terminal polymer relaxation dynamics is relevant. It is just the elasticity that makes the original DDRM invalid. Therefore, the neglect of polymer dynamics at intermediate time scales and thereafter (which actually gives rise to the elastic component of viscoelasticity) will alleviate the effect of elasticity on drop retraction.

3. Experimental Study

3.1. Materials and Set-Up. Polypropylene (PP) is a widely produced, versatile, commodity polymer with a series of desirable properties, and it is often blended with polyolefin elastomer (POE) (see Figure 7) to improve its toughness and impact strength, alleviating notch sensitivity and low-temperature brittleness. In this section, the interfacial tension between PP and POE melt is measured using the proposed method in an optical microscope equipped with a heating stage. PP, with the trademark *T*36 F, supplied by Chevron (Zhangjiagang) Chemical Co., Ltd, composes the drop. POE, with the trademark 8150, supplied by Dow DuPont (USA) Co., Ltd, composes the matrix. POE is a typical kind of viscoelastic polymer, while the viscoelasticity of PP is negligible compared to POE, so PP is considered purely viscous.

Before the experiment, necessary major properties of the two polymers are measured and shown in Table 1.

The experiment consists of three steps, that is, the preparation of experimental samples, getting PP and POE in full contact, and observing the drop retraction process sequentially.

3.1.1. Preparation of Experimental Samples. First, the PP fiber is drawn in molten state on a melt indexer instrument. Since the melting temperature of the PP is about 170°C, the heating temperature of the apparatus is set to 230°C. By adding different weights to the melt indexer to apply different drawing forces, PP fibers of different diameters, 0.2 mm, 0.3 mm, and 0.4 mm, are obtained and then cut them into short fibers with the aspect ratio of roughly 3~4.

Then, the POE sheet is molded out on a compression molding press. The temperature of the upper and lower boards of the machine is set to be 180°C to make two POE sheets with the thickness of about 0.5~0.6 mm.

Finally, one piece of PP short fiber is embedded between two POE sheets to make a sample by stepwise heating and packing, and the parameters are shown in Table 2.

Through the above treatment, the air bubbles trapped between the POE sheets are pressed out, and the sample is compact enough, the structure of which is similar to the hot dog bread, as illustrated in Figure 8.

On the contrary, in order to relieve the stress generated in the preparation of the sample, the sample is subsequently placed in a vacuum drier, annealed at 100°C for 3 hours, and then cooled in air.

3.1.2. Getting PP Short Fiber and POE Sheet in Full Contact. After the above preparations, there may be still small amount of air remaining in the vicinity of the contact surface of the fiber and sheets. If not eliminated, bubbles will generate and aggregate when the sample melts, causing interference to the observation. In order to remove the air totally, the sample is put into the vacuum dryer again and heated at 200°C under vacuum condition for 10 min. In this process, the air largely escapes out of the sample when the POE sheets soften and warps the PP short fiber.

3.1.3. Experimental Observation and Data Processing. The test sample is placed on a slide of the hot table, and the temperature is raised to 120°C at the rate of 40°C/min by program setting and kept for 10 min to further eliminate the residual stress in the sample. Next, the heating temperature of the sample is increased to 220°C, at which the PP and POE are melted, and the shape evolution of PP short fibers with diameters of 0.2 mm, 0.3 mm, and 0.4 mm, is observed, respectively, while a camera takes consecutive shots of the process.

When all the cases have finished, the software Scion image is used to measure the length of the major and minor axes of the ellipsoid drop, L and B, at each shot time and the radius R when the spherical drops are restored.

4. Results and Discussion

The retraction process of the 0.2 mm diameter PP fiber in POE sheets is shown in Figure 9. From the figure, it is clear that the retraction process of the drop can be divided into two phases: at the first phase, shape of the fiber changes from a rod to an ellipsoid and at the second phase, from the ellipsoid to a sphere.

Likewise, the PP short fiber with the diameter of 0.3 mm and 0.4 mm has the similar morphology evolution process.

From the recorded images, the length of the major and minor axes of the ellipsoid drop, L and B, at different times is measured by the software Scion image and then the variation in the deformation recovery degree $\varphi(t)$ over time is calculated, as shown in Figure 10. A common first-fast-then-slow retraction process is observed, and from the simulation results, it could be inferred that even if the experiments were performed much longer, a second stage with slower retraction will probably not occur.

There are twofold reasons for using a set of three PP short fiber of different diameters. Easy to see, measuring several times and averaging the results are good for improving accuracy. More important, it is reported that the influence of polymer viscoelasticity on drop dynamics decreases with the increase in the drop size [78, 79], so trying experiments with different drop sizes from small to large will gradually approach the true value of the interfacial tension.

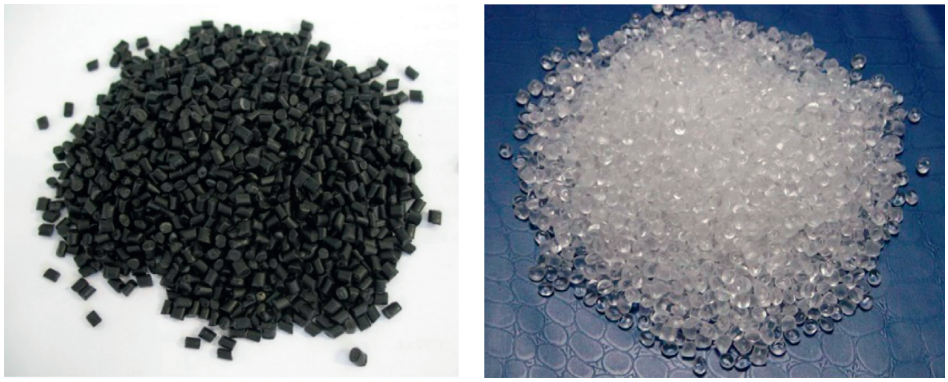

(a) (b)

Figure 7: Blend components: (a) polypropylene (PP); (b) polyolefin elastomer (POE).

Table 1: Mechanical, thermal, and rheological properties of PP and POE.

Property parameter	PP	POE
Melt density (g/cm^3)	0.738	0.776
Thermal conductivity J/(kg·°C)	2755	2380
Specific heat capacity W/(m·°C)	0.173	0.236
Zero shear viscosity at 220°C (Pa·s)	7766.894	4972.087

Table 2: Stepwise heating and mold pressing of the sample.

Molding pressure (MPa)	Heating time (min)	Heating temperature (°C)
5	5	180
10	5	180
15	5	180

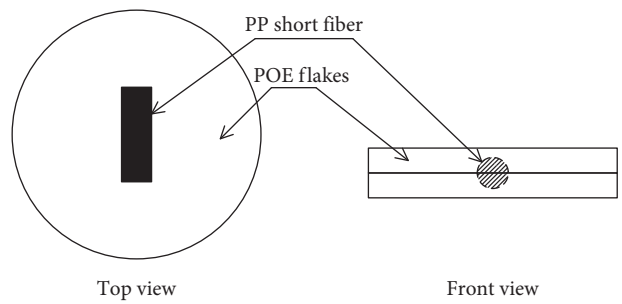

Figure 8: Illustration of the experimental sample prepared for interfacial tension measurement.

In the following, it is demonstrated that, using the proposed evaluation method of interfacial tension, even with the comparative small-sized drop, a desirable accuracy is attained.

The principal difference between the proposed method and the original DDRM lies in the way of deriving the interfacial tension from the shape evolution of drop retraction. Their measurement results are shown in Table 3. The label "DDRM" indicates that the interfacial tension is obtained by fitting with all the experimental data, while the label "I-DDRM" indicates that only the data spanning from the beginning of the drop retraction to the time when φ reduces to φ_u is used to fit equation (4).

At the bottom of Table 3, the results fluctuation $\mathrm{fluc}(A)$ characterizes the impact of drop size on the measurement results:

$$\mathrm{fluc}(A) := \frac{\max(A) - \min(A)}{\mathrm{ave}(A)} \times 100\%, \tag{5}$$

where A is the set of all the measured data, $\max(A)$ is the minimum value in A, and $\mathrm{ave}(A)$ is the average of A. From Table 3, it is noteworthy that using the conventional DDRM, the measurement result is apparently dependent on the drop size and the fluctuation is as high as 28.66%. The reason behind this phenomenon is the effect of polymer viscoelasticity. By contrast, when using the proposed evaluation method, the measurement results are very stable with whatever size drop and the fluctuation of the measurement results is strikingly reduced to 3.98%. On the contrary, the interfacial tension obtained by the conventional DDRM with the smallest drop (0.4 mm diameter) is thought to be the closest to the true value. This measurement value is approximately the one obtained by the proposed method in all the three cases of different drop sizes. The experimental comparison and analysis agree well with the revelation in Section 2 and validate the interfacial tension evaluation method proposed by this paper.

To supplement, the proposed method has another implication. There is no need to try a beforehand unknown number of experiments with different drop sizes to dampen the effect of polymer viscoelasticity and approximate the true value step by step, as is done now in the conventional DDRM. By employing the novel evaluation method proposed in this paper, the value of the interfacial tension between viscoelastic polymers can be evaluated close to the true value reliably and once for all.

Finally, the effects of temperature and polymer molecular weights on the drop retraction process and interfacial tension should be mentioned. Kamal et al. [80] and Biresaw et al. [81] showed that higher molecular weight systems showed a weaker dependence of interfacial tension on temperature than lower molecular weight systems. So, the interfacial tension

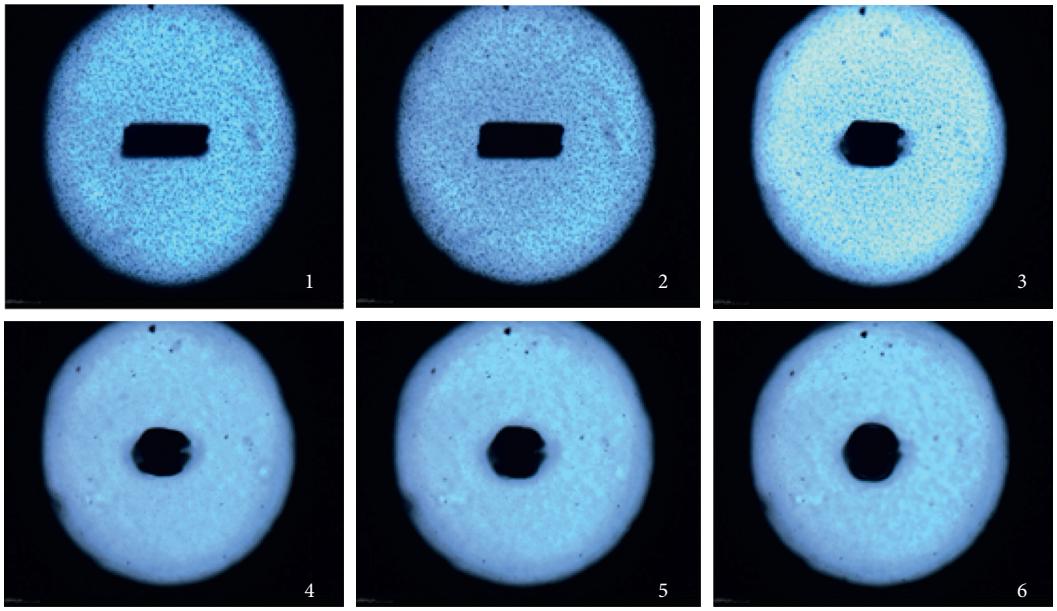

Figure 9: SEM image of the retraction process of PP short fiber in POE matrix.

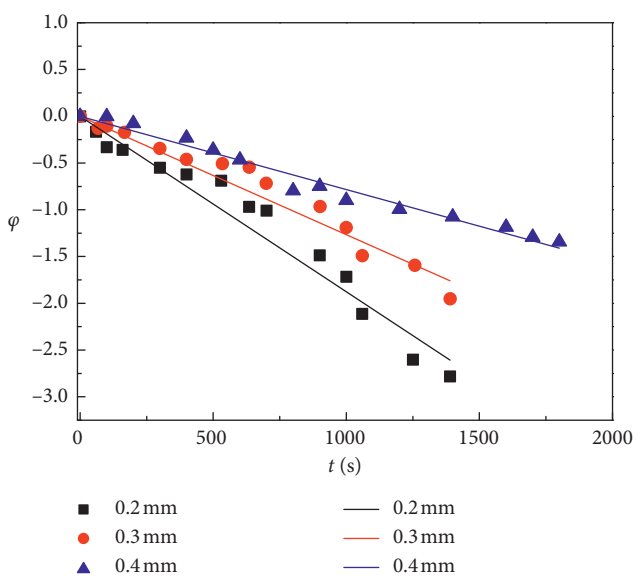

Figure 10: The retraction of PP fibers with a diameter of 0.2 mm, 0.3 mm, and 0.4 mm in the POE sheets. The symbols denote the experimental data, and the lines are obtained by data fitting.

Table 3: The interfacial tension between PP and POE obtained by DDRM and I-DDRM.

PP fiber diameter (mm)	Interfacial tension between PP and POE (mN/m)	
	DDRM	I-DDRM
0.2	12.255	9.093
0.3	11.638	9.060
0.4	9.102	9.132
Result fluctuation	28.66%	3.98%

between the same polymers of different molecular weights is not the same and needs measuring separately.

5. Conclusion

In this paper, the deformed drop retraction process is simulated taking account of the fluid viscoelasticity and its effect on the shape evolution of the drop is revealed. Compared with the case of purely viscous blend, the drop retraction process follows the "first fast then slow" law. Then, a novel evaluation method of the interfacial tension is put forward that only takes advantage of the first stage of the experimental data. The evaluation method is successfully validated by measuring the interfacial tension between PP and POE. Compared to the original DDRM, the obtained interfacial tension is close to the true value, but the experimental times are reduced to only once. Due to the complexity of polymer viscoelasticity, the dumbbell chain model is a simplified model and has its own limitations. It cannot describe more complicated spatial configurations of the polymer molecule, let alone the entanglement phenomenon of polymer chain in the melt. Therefore, to advance the measuring for interfacial tension between polymers, making more thorough insights into polymer dynamics is desired.

Appendix

A. Pseudopotential Lattice Boltzmann Model

In this paper, three-dimensional LB method is implemented on the D3Q19 lattice, which is one of the most commonly used lattice types nowadays (Figure 11).

As illustrated in Figure 11, in D3Q19, the velocity space is discretized into a set of 19 discrete velocities:

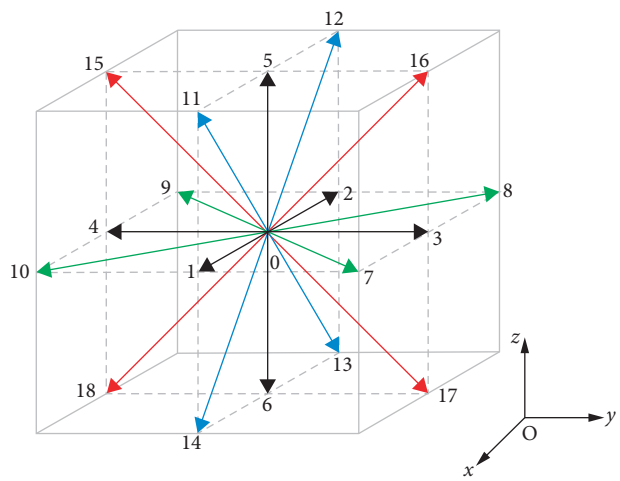

Figure 11: The structure of the D3Q19 lattice with lattice vectors.

$$c = \begin{bmatrix} 0 & 1 & -1 & 0 & 0 & 0 & 0 & 1 & -1 & 1 & 1 & -1 & 1 & -1 & 0 & 0 & 0 & 0 & 0 \\ 0 & 0 & 0 & 1 & -1 & 0 & 0 & 1 & 1 & -1 & 0 & 0 & 0 & 0 & 1 & 1 & -1 & 1 & -1 \\ 0 & 0 & 0 & 0 & 0 & 1 & -1 & 0 & 0 & 0 & 1 & 1 & -1 & -1 & 1 & 1 & 1 & -1 & -1 \end{bmatrix} c, \tag{A.1}$$

where $c = \boldsymbol{\delta} x / \boldsymbol{\delta} t$ is the lattice speed, $\boldsymbol{\delta} x$ is the lattice spacing, and $\boldsymbol{\delta} t$ is the time step.

Using the multirelaxation time collision operator MRT, the governing equation of f_i can be written as

$$f_i(\mathbf{x} + \mathbf{c}_i \boldsymbol{\delta} t, t + \boldsymbol{\delta} t) - f_i(\mathbf{x}, t) = \boldsymbol{\Omega}_i + \boldsymbol{\delta} t \mathbf{F}_i', \tag{A.2}$$

where Ω_i is the collision operator and defined by

$$\boldsymbol{\Omega}_i = -\left(\mathbf{M}^{-1}\mathbf{S}\mathbf{M}\right)_{ij}\left[f_i(\mathbf{x}, t) - f_j^{\mathrm{eq}}(\mathbf{x}, t)\right]. \tag{A.3}$$

f_t is the density distribution function associated with velocity $\mathbf{c}_i$ at position $\mathbf{x}$ and time t, and their moments satisfy

$$\begin{aligned} \rho &= \sum_i f_i, \\ \rho \mathbf{u} &= \sum_i \mathbf{e}_i f_i + \frac{1}{2} \boldsymbol{\delta} t \mathbf{F}, \end{aligned} \tag{A.4}$$

where $\mathbf{F}$ represents the interaction force between components. F_i' is the discrete forcing term accounting for the interaction force $\mathbf{F}$:

$$\mathbf{F}' = \mathbf{M}^{-1}\left(\mathbf{I} - \frac{\mathbf{S}}{2}\right)\mathbf{M}\widetilde{F}, \tag{A.5}$$

where $\mathbf{I}$ is the unit matrix, while $\widetilde{\mathbf{F}}$ is defined by

$$\widetilde{F}_i = w_i\left[\frac{\mathbf{c}_i \cdot \mathbf{F}}{c_s^2} + \frac{(\mathbf{u}\mathbf{F} + \mathbf{F}\mathbf{u}) : (\mathbf{c}_i\mathbf{c}_i - I)}{2c_s^4}\right]. \tag{A.6}$$

In the collision operator, $\mathbf{M}$ is the constant transformation matrix and $\mathbf{S}$ is a diagonal nonnegative relaxation time matrix that is decided by fluid properties.

For multicomponent flow, $f_{\sigma,i}^{\mathrm{eq}}$ is the corresponding equilibrium distribution of component $\boldsymbol{\sigma}$ and is determined by

$$f_{\sigma,i}^{eq} = w_i \boldsymbol{\rho}_\sigma(\mathbf{x}, t)\left[1 + \frac{\mathbf{e}_i \cdot \mathbf{u}^{eq}}{c_s^2} + \frac{(\mathbf{e}_i \cdot \mathbf{u}^{eq})^2}{2c_s^4} - \frac{(\mathbf{u}^{eq})^2}{2c_s^2}\right], \tag{A.7}$$

where w_i is the weight associated with the velocity $\mathbf{e}_i$:

$$w_i = \begin{cases} \dfrac{1}{3}, & |\mathbf{e}_i|^2 = 0 \\ \dfrac{1}{18}, & |\mathbf{e}_i|^2 = 1 \\ \dfrac{1}{36}, & |\mathbf{e}_i|^2 = 2. \end{cases} \tag{A.8}$$

$\mathbf{u}_\sigma^{eq}$ is the equilibrium macroscopic velocity in consideration of the component interaction:

$$\mathbf{u}_\sigma^{\mathrm{eq}} = \mathbf{u}' + \boldsymbol{\tau}_\sigma \boldsymbol{\delta} t \frac{\mathbf{F}}{\boldsymbol{\rho}_\sigma}, \tag{A.9}$$

where u' satisfies the momentum equation without the external force:

$$\mathbf{u}' = \frac{\sum_\sigma \boldsymbol{\rho}_\sigma \mathbf{u}_\sigma / \boldsymbol{\tau}_\sigma}{\sum_\sigma \boldsymbol{\rho}_\sigma / \boldsymbol{\tau}_\sigma}, \tag{A.10}$$

in which $\boldsymbol{\rho}_\sigma$ and $\boldsymbol{\mu}_\sigma$ are the macroscopic density and velocity of component.

$\mathbf{F}$ is the interaction between the particles of different components, when only considering the nearest neighbor, it can be written as

$$\mathbf{F}_{\sigma\bar{\sigma}}(\mathbf{x}) = -g_{\sigma\bar{\sigma}} \boldsymbol{\rho}_\sigma(\mathbf{x}) \mathbf{c}_s^2 \sum_i^N w\left(|\mathbf{e}_i|^2\right) \boldsymbol{\rho}(\mathbf{x} + \mathbf{e}_i) \mathbf{e}_i, \tag{A.11}$$

where $g_{\sigma\bar{\sigma}}$ denotes the interaction strength between components σ and $\bar{\sigma}$. When $g_{\sigma\bar{\sigma}}$ is positive, the repulsive force is generated between the particles, and when the $g_{\sigma\bar{\sigma}}$ is negative, the attraction between the particles is generated.

With the modified equilibrium distribution and pseudopotential forcing term, the Navier–Stokes equations can be recovered from the lattice Boltzmann equation in the limit of small Mach number by the Chapman–Enskog analysis and Taylor expansion:

$$\frac{\partial \rho_\sigma}{\partial t} + \nabla \cdot (\rho_\sigma \mathbf{u}) = -\nabla \cdot \mathbf{j}_\sigma, \qquad \frac{\partial \rho}{\partial t} + \nabla \cdot (\rho \mathbf{u}) = 0, \tag{A.12}$$

as well as the momentum equation of the blend flow:

$$\frac{\partial}{\partial t}(\rho \mathbf{u}) + \nabla \cdot (\rho \mathbf{u}\mathbf{u}) = -\nabla p + v \nabla \cdot (\nabla p \mathbf{u}), \tag{A.13}$$

where v is the kinematic viscosity of the blend:

$$v = \frac{1}{D+2}\left(\sum_\sigma \frac{\rho_\sigma}{\rho}\boldsymbol{\tau}_\sigma - \frac{1}{2}\right). \tag{A.14}$$

B. FENE Dumbbell Model

Likewise, the conformation distribution function $\psi_j(\mathbf{x}, t)$ follows the discrete Fokker–Planck equation on D3Q19 lattice:

$$\psi_j(\mathbf{x}, t+1) - \psi_j(\mathbf{x}, t) = -\frac{1}{\tau_\psi + 1/2}\left[\psi_j(\mathbf{x}, t) - \psi_j^{\mathrm{eq}}(\mathbf{x}, t)\right] + \frac{\tau_\psi}{\tau_\psi + 1/2} M_j(\mathbf{x}, t) + \Delta\psi_j(\mathbf{x}, t). \tag{A.15}$$

As the polymer melt is thought isotropic at equilibrium, the equilibrium conformation distribution function ψ_j^{eq} is equal to w_j:

$$\psi_j^{\mathrm{eq}} = \begin{cases} \frac{1}{3}, & \left|\mathbf{q}_j\right|^2 = 0 \\ \frac{1}{18}, & \left|\mathbf{q}_j\right|^2 = 1 \\ \frac{1}{36}, & \left|\mathbf{q}_j\right|^2 = 2. \end{cases} \tag{A.16}$$

τ_ψ is the single relaxation time of $\psi_j(\mathbf{x}, t)$ towards ψ_j^{eq}. M_j accounts for the elongation and rotation of the dumbbell:

$$M_j = \omega_j \frac{H}{k_B T_m}\left[\mathbf{q}_j\mathbf{q}_j - \frac{k_B T_m}{H}\mathbf{I}\right] : (\nabla \mathbf{u})^T \cdot \frac{H}{k_B T_m}\langle \mathbf{q}_j \mathbf{q}_j \rangle. \tag{A.17}$$

$\Delta\psi_j(\mathbf{x}, t)$ is the convection of dumbbells between lattice sites due to the flow and can be written as

$$\delta m_i = f_{\bar{i}}(\mathbf{x} + c\mathbf{e}_\alpha \Delta t, t) - f(\mathbf{x}, t), \tag{A.18}$$

$$\Delta\psi_j(x, t) = \sum_k \begin{cases} \dfrac{\delta m_k}{\rho(\mathbf{x} + c\mathbf{e}_\alpha \Delta t, t)}\psi_j(x + c\mathbf{e}_\alpha \Delta t, t), & \delta m_i > 0, \\ \dfrac{\delta m_k}{\rho(\mathbf{x}, t)}\psi_j(\mathbf{x}, t), & \delta m_i < 0. \end{cases} \tag{A.19}$$

Solving the equation (A.2) and equation (A.15) simultaneously, the conformations of the dumbbells can be updated during the flow simulation. Then, the macroscopic elastic stress is linked with the dumbbell conformation through the Kramers formula:

$$\tau_p = \boldsymbol{\rho} \sum_j \mathbf{q}_j \mathbf{F}_j^C \psi_j + \boldsymbol{\rho} \sum_j \mathbf{q}_j \mathbf{F}_j^C \psi_j^{eq}, \tag{A.20}$$

where $\mathbf{F}_j^c$ is the spring force acted on the dumbbell beads:

$$\mathbf{F}_j^C = \frac{H}{1 - \left(q_j^2/q_b^2\right)}\mathbf{q}_j. \tag{A.21}$$

When applied the Chapman–Enskog expansion, the equation (A.15) results in the macroscopic Oldroyd-B constitutive model:

$$\lambda_H \overset{\nabla}{\tau}_p + \tau_p = -\mu_p\left(\nabla \mathbf{u} + (\nabla \mathbf{u})^T\right). \tag{A.22}$$

The model parameters λ_H and u_p are linked to that of the lattice Fokker–Planck equation by the following relations:

$$\lambda_H = \tau_\psi, \qquad \mu_p = \frac{1}{3} n_p H \tau_\psi. \tag{A.23}$$

As mentioned above, the flow field changes the conformation of the dumbbells; in turn, the conformation of the dumbbells contributes to the local stress and thus alters the flow field. In the modeling, they are coupled through the rewriting of f^{eq}:

$$f_{\sigma,i}^{eq} = \boldsymbol{\omega}_i \rho_\sigma(\mathbf{x}, t)\left[1 + \frac{\mathbf{e}_i \cdot \mathrm{u}^{eq}}{c_s^2} + \frac{\left(\mathbf{e}_i \cdot \mathbf{u}^{eq}\right)^2}{2c_s^4} - \frac{(\mathbf{u}^{eq})^2}{2c_s^2}\right] + \frac{9}{2}\boldsymbol{\omega}_i\left(\frac{\mathbf{e}_i e_i}{c^2} - \frac{1}{3}\mathbf{I}\right) : \frac{\boldsymbol{\tau}_p}{k_B T_m}. \tag{A.24}$$

It is noticeable that the modified expression reflects the effect of polymer viscoelasticity through the introduction of $9/2\omega_i(\mathbf{e}_i\mathbf{e}_i/c^2 - (1/3)\mathbf{I}) : \boldsymbol{\tau}_p/k_B T_m$ into f^{eq}. After the modification, the second-order moment of the distribution function contains both viscous and elastic stress:

$$\tau = \sum f_i(\mathbf{x}, t)\mathbf{e}_i\mathbf{e}_i = \boldsymbol{\tau}_N + \boldsymbol{\tau}_p, \tag{A.25}$$

where $\boldsymbol{\tau}_N$ is the viscous stress, $\tau_N = \mu(\nabla \mathbf{u} + (\nabla \mathbf{u})^T)$, so that viscoelastic Navier–Stokes equation can be recovered from equation (A.2).

The numerical procedure for each time step at each lattice site reads as follows:

(1) Stream the component distribution functions $f_{\sigma,i}$ between the adjacent lattice sites (left-hand side of equation (A.2)) and calculate the velocity u and density ρ (equation (A.3))

(2) Calculate the convection of the dumbbell conformation $\Delta\psi_j(\mathbf{x}, t)$ (equation (A.20)) and the elongation and rotation of the dumbbells M_j due to the polymer flow (equation (A.18))

(3) Update the new conformation functions $\psi_j(\mathbf{x}, t)$ (equation (A.15)

(4) Sum the viscous and elastic stress to calculate the total local stress $\boldsymbol{\tau}$ (equation (A.25))

(5) Collide and update the new component distribution functions $f_{\sigma,\alpha}$ (right-hand side of equation (A.2))

(6) Repeat the procedures (1)~(5) until the simulation ends

Data Availability

The experimental data used to support the findings of this study are included within the article. The software code data used to support the findings of this study are available on request to the Lin Deng via hust.smart@gmail.com.

Conflicts of Interest

The authors declare that they have no conflicts of interest.

Acknowledgments

This work was financially supported by the National Natural Science Foundation of China (no. 51805379).

References

[1] A. Gumyusenge, X. Luo, H. Zhang, G. M. Pitch, A. L. Ayzner, and J. Mei, "Isoindigo-based binary polymer blends for solution-processing of semiconducting nanofiber networks," *ACS Applied Polymer Materials*, vol. 1, no. 7, pp. 1778–1786, 2019.

[2] G. Ignacz, F. Fei, and G. Szekely, "Ion-stabilized membranes for demanding environments fabricated from polybenzimidazole and its blends with polymers of intrinsic microporosity," *ACS Applied Nano Materials*, vol. 1, no. 11, pp. 6349–6356, 2018.

[3] R. Zhang, Q Du, and L. Wang, "Unlocking the response of lignin structure for improved carbon fiber production and mechanical strength," *Green Chemistry*, vol. 21, no. 18, pp. 4981–4987, 2019.

[4] Z. C. Kennedy, J. F. Christ, B. W. Arey, L. Zhong, and C. A. Barrett, "Tunable porosity in fused filament 3D-printed blends of intrinsically porous polymer and thermoplastic aliphatic polyesters polycaprolactone and polylactic acid," *ACS Applied Polymer Materials*, vol. 1, no. 3, pp. 482–492, 2019.

[5] J. Hamuyuni, P. Taskinen, G. Akdogan, and S. M. Bradshaw, "Measurement of surface tension of molten matte phases by an improved sessile drop method," *Mineral Processing and Extractive Metallurgy*, vol. 121, no. 3, pp. 173–177, 2012.

[6] L. B. Direktor, V. M. Zaichenko, and I. L. Maikov, "An improved method of sessile drop for determining the surface tension of liquids," *High Temperature*, vol. 48, no. 2, pp. 176–180, 2010.

[7] J. Pavlíček, G. Bogdanić, and I. Wichterle, "Simple apparatus for the measurement of total pressure of polymer-solvent mixtures," *Chemical Engineering & Technology*, vol. 42, no. 8, p. 1726, 2019.

[8] H. Naseem and H. Murthy, "A simple thermal diffusivity measurement technique for polymers and particulate composites," *International Journal of Heat and Mass Transfer*, vol. 137, pp. 968–978, 2019.

[9] H. R. Z. Moghadam, S. A. Faghidian, M. Jamal-Omidi, and S. Rahmati, "Micro-residual stress measurement in nanocomposite reinforced polymers," *International Polymer Processing*, vol. 34, no. 3, pp. 356–366, 2019.

[10] B. H. Jang, S. Kwon, and J. H. Kang, "Measurement of the magnetic susceptibility of subtle paramagnetic solutions using the diamagnetic repulsion of polymer microparticles," *Lab on a Chip*, vol. 19, no. 14, pp. 2356–2361, 2019.

[11] I. Dolezal, L. Hes, and K. Bal, "A non-destructive single plate method for measurement of thermal resistance of polymer sheets and fabrics," *International Journal of Occupational Safety and Ergonomics*, vol. 25, no. 4, pp. 562–567, 2019.

[12] P. Zhao, Y. Zhao, H. Kharbas et al., "In-situ ultrasonic characterization of microcellular injection molding," *Journal of Materials Processing Technology*, vol. 270, pp. 254–264, 2019.

[13] Y. Son, "Comparative measurement of interfacial tension by transient dynamic methods," *Journal of Applied Polymer Science*, vol. 99, no. 4, pp. 1910–1918, 2006.

[14] N. R. Demarquette, "Evaluation of experimental techniques for determining interfacial tension between molten polymers," *International Materials Reviews*, vol. 48, no. 4, pp. 247–269, 2003.

[15] P. Xing, M. Bousmina, D. Rodrigue, and M. R. Kamal, "Critical experimental comparison between five techniques for the determination of interfacial tension in polymer blends: model system of polystyrene/polyamide-6," *Macromolecules*, vol. 33, no. 21, pp. 8020–8034, 2000.

[16] D. Morais, T. S. Valera, and N. R. Demarquette, "Evaluation of the surface tension of poly (vinyl butyral) using the pendant drop method," *Macromolecular Symposia*, vol. 245-246, no. 1, pp. 208–214, 2006.

[17] A. Morita, D. Carastan, and N. Demarquette, "Influence of drop volume on surface tension evaluated using the pendant drop method," *Colloid & Polymer Science*, vol. 280, no. 9, pp. 857–864, 2002.

[18] S. Wan, Z. Wei, X. Chen, and J. Gao, "Pendant drop method for interfacial tension measurement based on edge detection," in *Proceedings of the 2009 2nd International Congress on Image and Signal Processing*, Tianjin, China, October 2009.

[19] F. K. Hansen and J. Hveem, "The interfacial tension between acrylic monomers and polymers and non-ionic surfactants investigated by the automatic sessile drop method," *Journal of Colloid and Interface Science*, vol. 210, no. 1, pp. 144–151, 1999.

[20] N. R. Demarquette and M. R. Kamal, "Comparação entre o método da gota pendente e o método da gota girante para medida da tensão interfacial entre polímeros," *Polímeros*, vol. 7, no. 3, pp. 63–70, 1997.

[21] J. J. Elmendorp and G. De Vos, "Measurement of interfacial tensions of molten polymer systems by means of the spinning

drop method," *Polymer Engineering and Science*, vol. 26, no. 6, pp. 415–417, 1986.

[22] J. Viades-Trejo and J. Gracia-Fadrique, "Spinning drop method," *Colloids and Surfaces A: Physicochemical and Engineering Aspects*, vol. 302, no. 1-3, pp. 549–552, 2007.

[23] P. H. M. Elemans, J. M. H. Janssen, and H. E. H. Meijer, "The measurement of interfacial tension in polymer/polymer systems: the breaking thread method," *Journal of Rheology*, vol. 34, no. 8, pp. 1311–1325, 1990.

[24] L. Minkova, H. Yordanov, S. Filippi, and N. Grizzuti, "Interfacial tension of compatibilized blends of LDPE and PA6: the breaking thread method," *Polymer*, vol. 44, no. 26, pp. 7925–7932, 2003.

[25] G. Palmer and N. R. Demarquette, "New procedure to increase the accuracy of interfacial tension measurements obtained by breaking thread method," *Polymer*, vol. 44, no. 10, pp. 3045–3052, 2003.

[26] C. J. Carriere and A. Cohen, "Evaluation of the interfacial tension between high molecular weight polycarbonate and PMMA resins with the imbedded fiber retraction technique," *Journal of Rheology*, vol. 35, no. 2, pp. 205–212, 1991.

[27] C. J. Carriere, A. Cohen, and C. B. Arends, "Estimation of interfacial tension using shape evolution of short fibers," *Journal of Rheology*, vol. 33, no. 5, pp. 681–689, 1989.

[28] A. Cohen and C. J. Carriere, "Analysis of a retraction mechanism for imbedded polymeric fibers," *Rheologica Acta*, vol. 28, no. 3, pp. 223–232, 1989.

[29] G. Palmer and N. R. Demarquette, "Evaluation of imbedded fiber retraction phenomenological models for determining interfacial tension between molten polymers," *Polymer*, vol. 46, no. 19, pp. 8169–8177, 2005.

[30] H. Y. Mo, C. X. Zhou, and W. Yu, "A new method to determine interfacial tension from the retraction of ellipsoidal drops," *Journal of Non-newtonian Fluid Mechanics*, vol. 91, no. 2-3, pp. 221–232, 2000.

[31] D. Pan, H. He, H. Ren et al., "Study on the interfacial tension of immiscible polystyrene/polypropylene blend with deformed drop retraction method," *Journal of Thermoplastic Composite Materials*, vol. 32, no. 2, pp. 205–215, 2019.

[32] Y. Son and K. B. Migler, "Interfacial tension measurement between immiscible polymers: improved deformed drop retraction method," *Polymer*, vol. 43, no. 10, pp. 3001–3006, 2002.

[33] Y. Son and J. T. Yoon, "Measurement of interfacial tension by a deformed drop retraction method," *Polymer*, vol. 42, no. 16, pp. 7209–7213, 2001.

[34] W. Yu, M. Bousmina, and C. X. Zhou, "Determination of interfacial tension by the retraction method of highly deformed drop," *Rheologica Acta*, vol. 43, no. 4, pp. 342–349, 2004.

[35] J. Li, T. Li, Y. Jia, S. Yang, S. Jiang, and L.-S. Turng, "Modeling and characterization of crystallization during rapid heat cycle molding," *Polymer Testing*, vol. 71, pp. 182–191, 2018.

[36] W. Yu and C. Zhou, "Dynamics of droplet with viscoelastic interface," *Soft Matter*, vol. 7, no. 13, pp. 6337–6346, 2011.

[37] S. Mukherjee and K. Sarkar, "Effects of viscoelasticity on the retraction of a sheared drop," *Journal of Non-newtonian Fluid Mechanics*, vol. 165, no. 7-8, pp. 340–349, 2010.

[38] P. Yue, J. J. Feng, C. Liu, and J. Shen, "Diffuse-interface simulations of drop coalescence and retraction in viscoelastic fluids," *Journal of Non-newtonian Fluid Mechanics*, vol. 129, no. 3, pp. 163–176, 2005.

[39] P. Yue, C. Zhou, J. J. Feng, C. F. Ollivier-Gooch, and H. H. Hu, "Phase-field simulations of interfacial dynamics in viscoelastic fluids using finite elements with adaptive meshing," *Journal of Computational Physics*, vol. 219, no. 1, pp. 47–67, 2006.

[40] W. Yu, M. Bousmina, C. Zhou, and C. L. Tucker, "Theory for drop deformation in viscoelastic systems," *Journal of Rheology*, vol. 48, no. 2, pp. 417–438, 2004.

[41] J. C. Maxwell, "The Bakerian lecture: on the viscosity or internal friction of air and other gases," *Philosophical Transactions of the Royal Society of London*, vol. 156, pp. 249–268, 1866.

[42] N. W. Tschoegl, *The Phenomenological Theory of Linear Viscoelastic Behavior: An Introduction*, Springer Science & Business Media, Berlin, Germany, 2012.

[43] D. John and L. Ronald, *Structure and Rheology of Molten Polymers from Structure to Flow Behavior and Back Again*, Hanser Publishers/Hanser Gardner Publications, Cincinnati, OH, USA, 2006.

[44] M. Yamamoto, "The visco-elastic properties of network structure I. General formalism," *Journal of the Physical Society of Japan*, vol. 11, no. 4, pp. 413–421, 1956.

[45] M. Yamamoto, "The visco-elastic properties of network structure III. normal stress effect (Weissenberg effect)," *Journal of the Physical Society of Japan*, vol. 13, no. 10, pp. 1200–1211, 1958.

[46] R. B. Bird, R. C. Armstrong, and O. Hassager, *Dynamics of Polymeric Liquids: Fluid Mechanics*, A Wiley-Interscience Publication, John Wiley & Sons, Hoboken, NJ, USA, 1987.

[47] A. Peterlin, "Streaming birefringence of soft linear macromolecules with finite chain length," *Polymer*, vol. 2, pp. 257–264, 1961.

[48] E. Monaco, K. H. Luo, and R. S. Qin, *Lattice Boltzmann Simulations for Microfluidics and Mesoscale Phenomena*, Springer Berlin Heidelberg, Berlin, Heidelberg, 2009.

[49] C. K. Aidun and J. R. Clausen, "Lattice-Boltzmann method for complex flows," *Annual Review of Fluid Mechanics*, vol. 42, no. 1, pp. 439–472, 2010.

[50] J. Zhang, "Lattice Boltzmann method for microfluidics: models and applications," *Microfluidics and Nanofluidics*, vol. 10, no. 1, pp. 1–28, 2011.

[51] Z. Guo, T. S. Zhao, and Y. Shi, "A lattice Boltzmann algorithm for electro-osmotic flows in microfluidic devices," *The Journal of Chemical Physics*, vol. 122, no. 14, p. 144907, 2005.

[52] Z. Yu, O. Hemminger, and L.-S. Fan, "Experiment and lattice Boltzmann simulation of two-phase gas-liquid flows in microchannels," *Chemical Engineering Science*, vol. 62, no. 24, pp. 7172–7183, 2007.

[53] Z. Guo and T. Zhao, "Lattice Boltzmann model for incompressible flows through porous media," *Physical Review E*, vol. 66, no. 3, Article ID 036304, 2002.

[54] C. Pan, L.-S. Luo, and C. T. Miller, "An evaluation of lattice Boltzmann schemes for porous medium flow simulation," *Computers & Fluids*, vol. 35, no. 8-9, pp. 898–909, 2006.

[55] C. Manwart, "Lattice-Boltzmann and finite-difference simulations for the permeability for three-dimensional porous media," *Physical Review E*, vol. 66, no. 1, Article ID 016702, 2002.

[56] H.-J. Vogel, J. Tölke, V. P. Schulz, M. Krafczyk, and K. Roth, "Comparison of a lattice-Boltzmann model, a full-morphology model, and a pore network model for determining capillary pressure-saturation relationships," *Vadose Zone Journal*, vol. 4, no. 2, pp. 380–388, 2005.

[57] M. L. Porter, M. G. Schaap, and D. Wildenschild, "Lattice-Boltzmann simulations of the capillary pressure-saturation-interfacial area relationship for porous media," *Advances in Water Resources*, vol. 32, no. 11, pp. 1632–1640, 2009.

[58] B. Ahrenholz, J. Tölke, P. Lehmann et al., "Prediction of capillary hysteresis in a porous material using lattice-Boltzmann methods and comparison to experimental data and a morphological pore network model," *Advances in Water Resources*, vol. 31, no. 9, pp. 1151–1173, 2008.

[59] S. Papenkort and T. Voigtmann, "Lattice Boltzmann simulations of a viscoelastic shear-thinning fluid," *Journal of Chemical Physics*, vol. 143, no. 4, 2015.

[60] A. Vikhansky, "Construction of lattice-Boltzmann schemes for non-Newtonian and two-phase flows," *The Canadian Journal of Chemical Engineering*, vol. 90, no. 5, pp. 1081–1091, 2012.

[61] T. N. Phillips and G. W. Roberts, "Lattice Boltzmann models for non-Newtonian flows," *Ima Journal of Applied Mathematics*, vol. 76, no. 5, pp. 790–816, 2011.

[62] M. L. Shan, "Pseudopotential multi-relaxation-time lattice Boltzmann model for cavitation bubble collapse with high density ratio," *Chinese Physics B*, vol. 25, no. 10, 2016.

[63] Y. Q. Zu and S. He, "Phase-field-based lattice Boltzmann model for incompressible binary fluid systems with density and viscosity contrasts," *Physical Review E*, vol. 87, no. 4, Article ID 043301, 2013.

[64] H. Liu, A. J. Valocchi, and Q. Kang, "Three-dimensional lattice Boltzmann model for immiscible two-phase flow simulations," *Physical Review E*, vol. 85, no. 4, Article ID 046309, 2012.

[65] P. Berghout and H. E. A. Van Den Akker, "Simulating drop formation at an aperture by means of a multi-component pseudo-potential lattice Boltzmann model," *International Journal of Heat and Fluid Flow*, vol. 75, pp. 153–164, 2019.

[66] F. Milan, M. Sbragaglia, L. Biferale, and F. Toschi, "Lattice Boltzmann simulations of droplet dynamics in time-dependent flows," *The European Physical Journal E*, vol. 41, no. 1, p. 6, 2018.

[67] D. Lycett-Brown, I. Karlin, and K. H. Luo, "Droplet collision simulation by a multi-speed lattice Boltzmann method," *Communications in Computational Physics*, vol. 9, no. 5, pp. 1219–1234, 2011.

[68] R.-Q. Duan, S. Koshizuka, and Y. Oka, "Two-dimensional simulation of drop deformation and breakup at around the critical Weber number," *Nuclear Engineering and Design*, vol. 225, no. 1, pp. 37–48, 2003.

[69] J. Onishi, Y. Chen, and H. Ohashi, "Dynamic simulation of multi-component viscoelastic fluids using the lattice Boltzmann method," *Physica A: Statistical Mechanics and Its Applications*, vol. 362, no. 1, pp. 84–92, 2006.

[70] J. Onishi, Y. Chen, and H. Ohashi, "A lattice Boltzmann model for polymeric liquids," *Progress in Computational Fluid Dynamics, An International Journal*, vol. 5, no. 1/2, p. 75, 2005.

[71] F. Osmanlic and C. Körner, "Lattice Boltzmann method for Oldroyd-B fluids," *Computers & Fluids*, vol. 124, pp. 190–196, 2016.

[72] X. Shan and H. Chen, "Lattice Boltzmann model for simulating flows with multiple phases and components," *Physical Review E*, vol. 47, no. 3, pp. 1815–1819, 1993.

[73] X. Shan and G. Doolen, "Multicomponent lattice-Boltzmann model with interparticle interaction," *Journal of Statistical Physics*, vol. 81, no. 1-2, pp. 379–393, 1995.

[74] G. R. Strobl and G. R. Strobl, *The Physics of Polymers*, Springer, Berlin, Germany, 1997.

[75] M. Lemou, M. Picasso, and P. Degond, "Viscoelastic fluid models derived from kinetic equations for polymers," *SIAM Journal on Applied Mathematics*, vol. 62, no. 5, pp. 1501–1519, 2002.

[76] Z. H. Chai and T. S. Zhao, "Effect of the forcing term in the multiple-relaxation-time lattice Boltzmann equation on the shear stress or the strain rate tensor," *Physical Review E*, vol. 86, no. 1, 2012.

[77] H. Xi and C. Duncan, "Lattice Boltzmann simulations of three-dimensional single droplet deformation and breakup under simple shear flow," *Physical Review E*, vol. 59, no. 3, pp. 3022–3026, 1999.

[78] W. Yu, C. Zhou, and M. Bousmina, "Theory of morphology evolution in mixtures of viscoelastic immiscible components," *Journal of Rheology*, vol. 49, no. 1, pp. 215–236, 2005.

[79] D. C. Tretheway and L. G. Leal, "Deformation and relaxation of Newtonian drops in planar extensional flows of a Boger fluid," *Journal of Non-newtonian Fluid Mechanics*, vol. 99, no. 2-3, pp. 81–108, 2001.

[80] M. R. Kamal, R. Lai-Fook, and N. R. Demarquette, "Interfacial tension in polymer melts. Part II: effects of temperature and molecular weight on interfacial tension," *Polymer Engineering and Science*, vol. 34, no. 24, pp. 1834–1839, 1994.

[81] G. Biresaw, C. J. Carriere, and R. L. Sammler, "Effect of temperature and molecular weight on the interfacial tension of PS/PDMS blends," *Rheologica Acta*, vol. 42, no. 1-2, pp. 142–147, 2003.

Hindawi
Advances in Polymer Technology
Volume 2020, Article ID 2075434, 11 pages
https://doi.org/10.1155/2020/2075434

Research Article

Five-Axis Tool Path Generation of Injection Mold Represented by T-Spline Surface

Ce Shang,[1,2] Hongyao Shen,[1,2] Jianzhong Fu,[1,2] Yangfan Sun,[1,2] Shuhua Yue,[1,2] and Jianfeng Zhang[1,2]

[1]*State Key Laboratory of Fluid Power and Mechatronic Systems, College of Mechanical Engineering, Zhejiang University, Hangzhou 310027, China*
[2]*Key Laboratory of 3D Printing Process and Equipment of Zhejiang Province, College of Mechanical Engineering, Zhejiang University, Hangzhou 310027, China*

Correspondence should be addressed to Hongyao Shen; shenhongyao@zju.edu.cn

Received 4 June 2019; Revised 7 August 2019; Accepted 16 August 2019; Published 9 March 2020

Guest Editor: Yun Zhang

Copyright © 2020 Ce Shang et al. This is an open access article distributed under the Creative Commons Attribution License, which permits unrestricted use, distribution, and reproduction in any medium, provided the original work is properly cited.

Injection molding is widely used in industries to produce polymeric products. At present, compound NURBS surfaces are commonly used to represent freeform surfaces in mold models. This work uses T-spline surface with extraordinary control points instead of NURBS to represent freeform surfaces in mold models. Compared with NURBS, T-splines' higher-order continuity facilitates the mold quality control especially at the patch boundary. And, its patch layout information can be utilized for tool path planning. We propose an algorithm to determine the patch processing order and generate nonretraction tool path for T-spline surface models. The tool paths are generated patch by patch using isoparametric strategy. Actual machining and injection molding experiments have been conducted. The result shows the feasibility of the proposed method, and the final product is in good quality.

1. Introduction

In today's industry, polymer is one of the most widely used materials. To produce polymeric products, injection molding (IM) is extensively used and is characterized by low cost, high precision, high productivity, and production of complex products. In the past few decades, injection molding has achieved rapid development due to the growth of new applications in automotive, transportation, electronics, etc. Currently, about one-third of all polymeric products are produced by injection molding. Many researchers are dedicated to make progress in the field of injection molding. Hot research topics include mathematical modeling [1], online measurement, parameter optimization [2–4], mold design, and manufacturing methods [5–7].

One of the main goals in IM is the improvement of molded product quality. To produce high-quality molded product, a high precision mold has to be provided. As a typical situation of mechanical manufacturing, mold manufacturing also has its particularity. For example, as the geometric shape of a mold is usually complex, mold manufacturing is usually finished by milling operations. And, because the mold sometimes contains deep cavities, the five-axis milling is usually applied to avoid unintended gouges and collision. A lot of research has been reported about mold manufacturing including automatic polishing [8], machining parameter optimization [9, 10], and optimum parting direction determination [11].

Another major characteristic of mold manufacturing is that the mold is usually represented by freeform surfaces. Nonuniform rational B-splines (NURBS) are widely used in the last few decades to represent freeform surfaces for design and manufacturing. To represent a simple shape, a single-patched NURBS surface model might be enough. To represent a complex shape, several NURBS patches are utilized, and each patch might be trimmed as needed. This kind of model is called compound NURBS surface model. Although the compound NURBS surface model is widely applied in CAD and CAM, it still has some disadvantages in use. The redundant control points in NURBS surface increase the

required storage space. Cracks or ripples usually appear between adjacent patches. And, the patch layout in compound NURBS surface model is usually not clearly defined. These disadvantages of NURBS trouble the CAD area for decades. And, in CAM area, these disadvantages also make tool path generation difficult. Generally, there are three major strategies to generate a tool path for a freeform surface model [12], isoparamtric [13, 14], isoplanar [15] and isoscallop [16]. The isoparametric strategy uses a series of isoparametric lines as the cutter contact paths. For compound NURBS surface model, isoparametric strategy has to be applied patch by patch as the boundary between adjacent NURBS patches is usually discontinuous. The discontinuity may cause problems such as uncut material at patch boundaries. And, a retraction is usually needed to connect the tool path of two different patches. The machining time might become longer in this situation. The isoplanar strategy uses the intersection lines between the surface model and a series of planes as the cutter contact paths. Although this strategy is less sensitive to the model continuity, it assumes that the direction of the normal vectors of the surface does not change too much over the entire model. Thus, it is not a suitable method when the model has a complex geometry. The isoscallop strategy controls the scallop between two adjacent tool paths to be a constant. It is usually applied patch by patch like the isoparametric strategy. And, it also has the aforementioned shortcoming as the isoparametric strategy.

To overcome the defects of the compound NURBS surface model, T-splines were introduced by Sederberg et al. in 2003 [17]. As a generalization of NURBS, T-splines inherit most of the advantages of NURBS. Besides, T-splines have three attractive features over NURBS. Firstly, T-junctions are allowed in the control mesh of T-splines to avoid redundant control points. The computational cost can be significantly reduced for complex models. Secondly, the preimage of a T-spline surface does not have to be a rectangular region. Holes and irregular boundaries are allowed for a single T-spline patch. Thirdly, T-splines introduce extraordinary control points. Thus, a multipatched model can be merged into a watertight T-spline surface model with high-order continuity [18]. And, the patch layout information is clear in T-splines. With all these advantages, T-spline technique has been regarded as a promising technique. And, it has been regarded as a possible candidate for the future industry standard. In recent years, several works have been reported about T-spline CAM. Gan et al. proposed an improved SFC method to generate a nonretraction tool path for T-spline surfaces with irregular boundary [19]. Zhao et al. developed a STEP-compliant CNC system which uses T-spline surfaces to represent the freeform surface model in the system [20, 21]. And, Feng et al. proposed a T-spline surfaces direct slicing algorithm for FDM 3D printing [22]. Currently, all these existing T-spline CAM research focuses on the situation that the model does not contain extraordinary control points. However, the representation ability of a T-spline surface without extraordinary control point is quite limited. The T-spline surface without an extraordinary control point is no more complex than a single-trimmed NURBS patch. Therefore, T-spline CAM for mold manufacturing has to consider T-spline surface models with extraordinary control points to fully take advantage of T-splines. Thus, the aforementioned works are not suitable in the mold manufacturing application.

In this work, we propose to use T-splines instead of traditional compound NURBS surfaces to represent injection molds. We propose a five-axis tool path generation algorithm facing the T-spline surface model with extraordinary control points. The isoparametric strategy is applied as it is a simple and robust way to control the machining scallop. And, the T-spline patch layout is utilized to generate a nonretraction tool path. The rest of the article is constructed as follows. Section 2 briefly introduces the basic theories of T-splines. Section 3 introduces the proposed algorithm to generate the five-axis tool path. The experimental examples include machining and injection molding are given in Section 4. And, Section 5 summarizes the whole paper and gives the conclusion.

2. Basic Theories of T-Splines

2.1. T-Spline Surface. The basic theory of T-splines can be found in detail in [17]. The algebraic formula of T-spline surface $\mathbf{S}(u, v)$ is the same as it of NURBS, which is defined as follows:

$$\mathbf{S}(u, v) = \frac{\sum_{i=1}^{n} w_i B_i(u, v)\mathbf{P}_i}{\sum_{i=1}^{n} w_i B_i(u, v)}, \tag{1}$$

where $\mathbf{P}_i$ is the i-th control point, w_i is the weight of the control points, n is the number of 96 the control points, $B_i(u, v)$ is the blending function which can be calculated according to the famous de Boor Cox recursion formula while the knot vector is defined using the ray-intersection method in [17]. Figure 1 gives a T-spline surface example, and the enlarged drawing on the right shows the control mesh topology and marked the T-junctions in the control mesh. The existence of T-junctions avoids the redundant control points and also reduces the computational consumption.

2.2. T-Spline Surface with Extraordinary Control Points. A surface with a complex topology cannot be represented using T-splines with a single global u-v parametric representation [23]. Besides, making isoparametric lines align with principal curvature direction will also benefit the shape representation [24]. Extraordinary control points are introduced to improve T-splines from these two perspectives. For T-spline surface with extraordinary control points, the entire surface model is constructed with several T-spline patches. Each patch has its own u-v parametric representation just like a NURBS patch in compound NURBS surface models. And, the parametric representation between the adjacent patches can be transformed with a translation and rotation transform. The basis functions of control points near the patch boundary have C^2 continuity at the patch boundary. Thus, the patch boundary of T-splines has high-

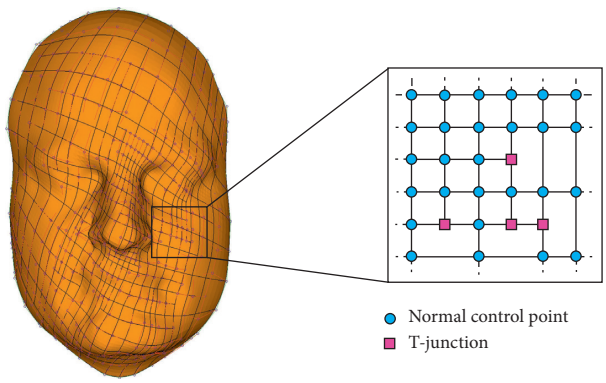

Figure 1: A face model with only one T-spline surface patch. The enlarged drawing shows the T-junctions in the control mesh topology.

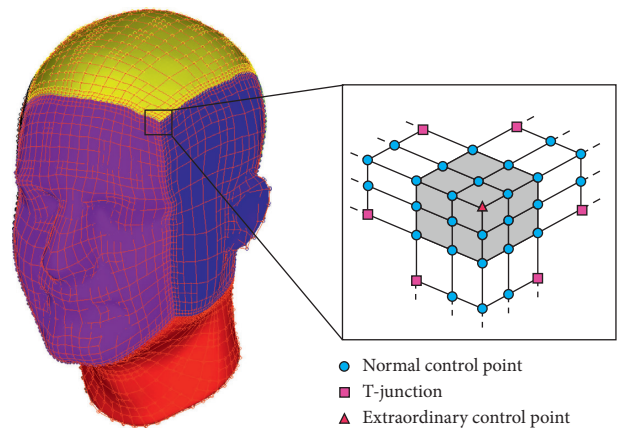

Figure 2: A head model which contains 6 patches and 8 extraordinary control points. Different patches are drawn in different colors. The enlarged drawing shows the extraordinary control point at the patch corner, and the extraordinary region is marked in gray.

order continuity just like the interior of a patch. For the control point at the patch corner, if the number of patches that sharing this corner is not four, this control point is called an extraordinary control point. The region near the extraordinary control point (usually its two-ring neighbor) is called extraordinary region. Figure 2 gives an example of a T-spline surface model with 6 patches and 8 extraordinary control points. An extraordinary control point and its corresponding extraordinary region are show in the figure. To evaluate the surface in extraordinary region, special treatment has to be applied [25]. In the very first definition of T-splines, a subdivision rule is applied to evaluate the surface in extraordinary region. This kind of model is called T-NURCCs (Nonuniform rational Catmull–Clark surfaces with T-junctions). And latter, as T-splines with extraordinary control points become commonly used, this kind of model is also called T-splines. As the subdivision rule used in T-NURCCs is not quite compatible with NURBS, several research have been reported about handling extraordinary control points by using template [26] or knot interval duplication [27] to avoid subdivision.

For the treatment of extraordinary control points, refer [27] for a good survey. And in this work, we handle the extraordinary control points with the original T-NURCCs subdivision rule. And thus the entire surface model is at least C^2 continues except the extraordinary position. The extraordinary position is the position on the surface associated with the extraordinary control point on the control mesh. At the extraordinary position, the surface is G^1 continues. For other extraordinary control points handling methods, the obtained continuity in extraordinary regions might be worse than the subdivision based method. But as long as the continuity is not worse than G^1, the machining error at the patch boundaries can be ensured by ensuring the error of each patch. Thus, the proposed method is still capable of generating a suitable tool path.

The proposed algorithm regards the input model as a few rectangular patches. A pair of adjacent patch shares an entire edge of the patch. This perspective is consistent with many modeling approaches [23, 24]. Notice that if there are too many extraordinary control points or holes in the mesh, the size of a patch might be too small. In this situation, the tool path generated by the proposed method will be less efficient as we utilize a patch-by-patch machining process. But, as the T-spline design usually tries to minimize the number of extraordinary control points, the proposed algorithm is suitable in general.

2.3. Evaluation of the Geometric Properties. Local geometric properties of the surface are useful in path generation. In order to evaluate local geometric properties of the surface, partial differential of the surface should be established. The derivation of the geometric properties of T-splines can be found in [19]. For equation (1), we use the notation $\mathbf{B} = \sum_{i=1}^{n} w_i B_i(u,v)\mathbf{P}_i$, $W = \sum_{i=1}^{n} w_i B_i(u,v)$ and $\mathbf{S} = \mathbf{B}/W$. The first and second derivatives of the T-spline surface are as follows:

$$\begin{cases} \mathbf{S}_u = \dfrac{\mathbf{B}_u - W_u\mathbf{S}}{W}, \\ \mathbf{S}_v = \dfrac{\mathbf{B}_v - W_v\mathbf{S}}{W}, \\ \mathbf{S}_{uu} = \dfrac{\mathbf{B}_{uu} - 2W_u\mathbf{S}_u - W_{uu}\mathbf{S}}{W}, \\ \mathbf{S}_{uv} = \dfrac{W(\mathbf{B}_{uv} - W_{uv}\mathbf{S} - W_u\mathbf{S}_v) + W_uW_v\mathbf{S} - \mathbf{B}_uW}{W^2}, \\ \mathbf{S}_{vv} = \dfrac{\mathbf{B}_{vv} - 2W_v\mathbf{S}_v - W_{vv}\mathbf{S}}{W}. \end{cases} \tag{2}$$

The surface normal can be calculated as

$$\mathbf{n} = \frac{\mathbf{S}_u \times \mathbf{S}_v}{|\mathbf{S}_u \times \mathbf{S}_v|}. \tag{3}$$

And, the first and second fundamental forms of the surface are

$$\begin{cases} E = \mathbf{S}_u^2, \\ F = \mathbf{S}_u \mathbf{S}_v, \\ G = \mathbf{S}_v^2, \\ L = \dfrac{1}{\sqrt{EG - F^2}} \langle \mathbf{S}_{uu}, \mathbf{S}_u, \mathbf{S}_v \rangle, \\ M = \dfrac{1}{\sqrt{EG - F^2}} \langle \mathbf{S}_{uv}, \mathbf{S}_u, \mathbf{S}_v \rangle, \\ N = \dfrac{1}{\sqrt{EG - F^2}} \langle \mathbf{S}_{vv}, \mathbf{S}_u, \mathbf{S}_v \rangle. \end{cases} \tag{4}$$

In the equations above, $\langle \cdot \rangle$ denotes mixed product and $|\cdot|$ denotes Euclidean norm. And, the symbols with subscripts denote its partial derivatives. As the partial derivative and first and second fundamental forms are calculated, the geometric properties such as local curvature can be easily obtained using the principle of differential geometry.

For the extraordinary region, the geometric properties are obtained using the same equations. But some conversion of control points and basic functions are needed according to extraordinary region handling strategy. For subdivision-based method, the control mesh has to be refined several times using the local refinement rule of T-NURCCs [17]. After local refinement, a part of the original extraordinary region will be evaluable and the local geometric properties can be evaluated using the aforementioned equations according to the refined control mesh. For the remaining part of the original extraordinary region, the local refinement rule can be applied iteratively, until it becomes evaluable.

3. Tool Path Generation

3.1. Algorithm Overview. The workflow of the proposed tool path generation algorithm is shown in Figure 3. The input of the algorithm is a T-spline surface model probably with several extraordinary control points. And, the output is a nonretraction tool path. The proposed algorithm includes the following steps. The connectivity of patches is analysed first. The topology layout of patches is obtained and represented as an undirected weighted graph. Then, the patch order is determined by solving a TSP problem using LKH solver. The transit corners of the tool path are selected using a back-tracking algorithm. For simple models, these steps can also be manually finished in consideration of the machining time or product texture. After patch order and transit corners are determined, the tool path is generated patch by patch using isoparametric strategy. In this step, we proposed a scallop tuning algorithm to make the tool path finish at the selected transit corner. In this work, we consider using ball-end mill as the tool. And, the posture of the tool is set to avoid gouge.

3.2. Patch Neighboring Relation Analysis. In the T-spline surface model, there are two kinds of patch neighboring relation, corner connection, and boundary connection. Two patches have a boundary connection means they share a boundary edge. And, two patches have a corner connection means they share a corner node but do not have a common boundary edge. The connection of the patches can be represented as an undirected weighted graph. An example of a patch layout and the corresponding undirected weighted graph is shown in Figure 4. And, patches are colored according to its neighboring relation with patch 0. The blue patches are boundary connected with patch 0. The green patches are corner connected with patch 0. And, gray patches are not connected with patch 0. In the undirected weighted graph, two kinds of connections can be distinguished using different weights. And, they are represented using different kinds of lines in the figure.

Except for the neighboring relation, we also care about which corner or boundary edge of a patch is shared with the other. To denote corners and edges of a patch, consider a parametric surface patch whose parameter domain is a unit square in R^2 ($[0, 1] \times [0, 1]$); the corner with coordinate $u = 0, v = 0$ is called the lower left corner of this patch. Similarly, the boundary edge with the algebraic expression $u = 1$ is called the right boundary edge of this patch. For a patch neighboring relation, it has to be clear which corner or boundary is shared by the two patches. This information usually can be obtained from the T-splines' data structure. And, in the following discussion, we consider it as obtainable for algorithms.

3.3. Patch Order Determination. To generate a nonretraction tool path, the patch processing order has to be determined. The output of patch order determination and transit corner selection is a processing list containing several processing data element. And, each processing data element in the list contains the information including processing patch (patch ID), starting corner, finishing corner, and preferred crossfeed direction. The patch order and preferred crossfeed direction are first determined, and the transit corners are selected later. One limiting condition here is that the starting corner of a processing data element must be the same point as the finishing corner of the former processing data element. The preferred crossfeed direction in the record is used to define which crossfeed direction will be utilized when both crossfeed directions are acceptable. Consider that this process might be manually designed or modified especially when the patch layout is simple. For implementation, the processing list is saved as a file and input to the subsequent isoparametric tool path generation procedure.

The patch order has to ensure that two patches that are processed successively are adjacent in position. This problem can be regarded as a traveling salesman problem (TSP) to some degree. The TSP problem can be described as given a list of cities and the distance between each pair of cities and find the shortest possible route that visits each city exactly once and returns to the origin city. Here, we regard each patch as a city and regard each neighboring relation as a road

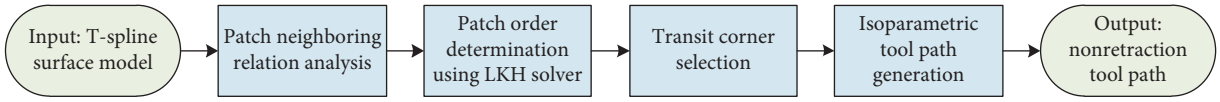

Figure 3: The workflow of the proposed tool path generation algorithm.

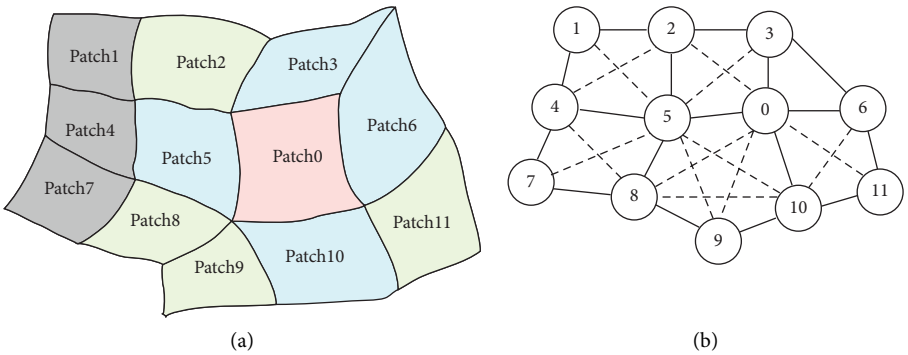

Figure 4: The neighboring relation of a model with 12 patches; (a) the patch layout, for each patch, its neighboring relation with patch 0 is represented in the figure using a different color; (b) the undirected weighted graph generated from the neighboring relation in (a); boundary connections are represented using solid lines and corner connections are represented using dashed lines.

between cities. And, convert the patch order determination problem into a TSP problem. The neighboring relation between patches can be obtained from the undirected weighted graph. The distance weight of the same kind of connection is set to be the same value. To facilitate transit corner selection, boundary connection is preferred than corner connection. Thus, a large distance weight is assigned to a corner connection edge. And, because the tool path does not need to go back to the original position like the TSP problem, we add a zero-weighted link between the starting patch and the suggested finishing patch. The starting patch and suggested finishing patch can be set manually or randomly decided. The weight of this link is set to be zero because we prefer it to appear at the end of the TSP solution to virtually link the finishing patch and the starting patch. If this link appears at the beginning of the TSP solution, the patch order in the solution (except the first one) has to be reversed to put the finishing patch at the end.

To solve the TSP problem here, we use the LKH solver. The LKH is an efficient TSP solver which is published online. With LKH, for a typical 100-city problem, the optimal solution can be found in less than a second. It is also used to generate a kind of TSP tool path for freeform surfaces in other research [28, 29]. One possible zero-weighted link and a corresponding TSP solution for the graph in Figure 4 is shown in Figures 5(a) and 5(b). Figures 5(c) and 5(d) give an patch layout that a corner connection must be included in a TSP solution.

The preferred crossfeed direction is used to facilitate users to choose the crossfeed direction to optimize the machining time or control the machining texture. As default, the preferred crossfeed direction can be set to be u-direction or the direction results in a shorter isoparametric tool path to process this patch.

3.4. Transit Corner Selection. After the patch order is determined, the starting corner and the finishing corner have to be defined for each patch. These starting and finishing corners are the transit corners of the entire tool path to connect the adjacent patches. The proposed transit corner selection algorithm roughly consists of two parts, main loop of the algorithm and the back tracking part. In the main loop, the starting corner of the first patch (the starting corner point of the entire tool path) is randomly defined. Then, if the current patch and the next patch share a boundary edge, there are two possible situations and there will be at least one possible finishing corner for the current patch. If the current patch and the next patch only share a corner, there are three different situations. All these five situations are shown in Figure 6. The finishing corner will be selected from all the possible finishing corners. If there are two possible finishing corners, the one which is compatible with the preferred crossfeed direction will be selected. If both of them are compatible with the preferred crossfeed direction, the finishing corner will be randomly selected. After the finishing corner of the current patch is determined, the starting corner of the next patch is determined and the finishing corner of the next patch can be selected in the same way. This process continues until the starting corner of the last patch is determined. And, the finishing corner of the last patch can be randomly selected. For a patch connected with the next patch with a corner connection, if the shared corner is the same as its starting corner, there is no possible finishing corner. In this situation, the algorithm turns into the back tracking loop and tries to back track to the former patch, set the currently used finishing corner as unusable, and keep searching for the possible solution. If the algorithm goes back to the first patch and still could not find a possible solution, the current patch order cannot generate a

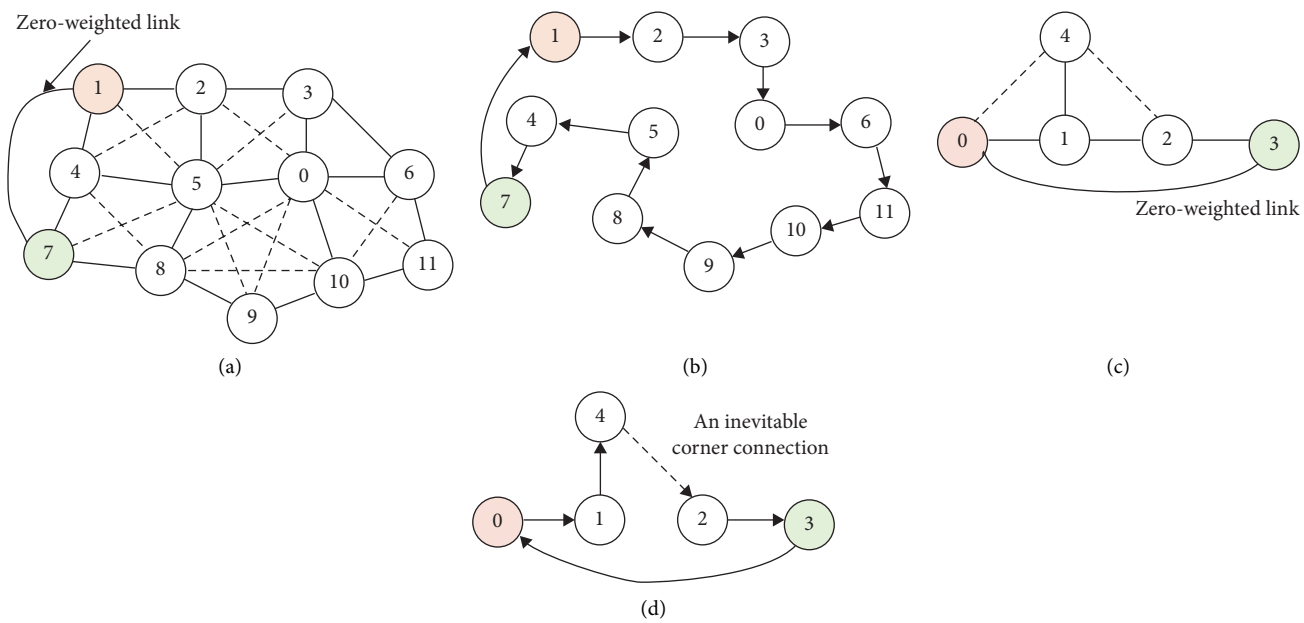

Figure 5: The patch order obtained by solving TSP problem, the starting patch is marked in red, the suggested finishing patch is marked in green, and a zero-weighted link is added; (a) the patch layout in Figure 4; (b) one possible TSP solution for the graph in (a); (c) a patch layout that corner connection link must be included in the TSP solution; (d) one possible TSP solution for the graph in (c).

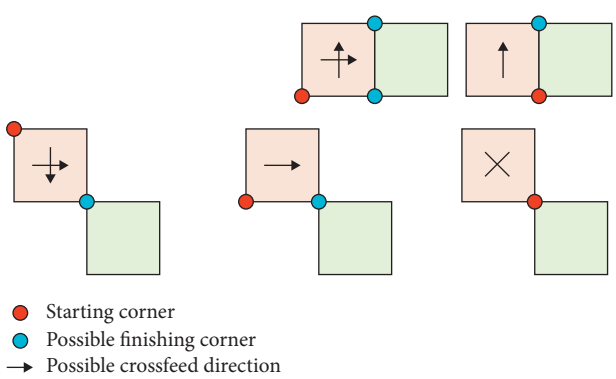

Figure 6: Five possible situations for determining the finishing corner. The current patch are drawn in red and the next patch is drawn in green.

nonretraction tool path. In this situation, it is suggested to adopt a retraction at the patch where the path generation is failed or tries to select another starting patch and generate a new patch order. Fortunately, this is not likely to happen, as we always take the boundary connection as the first choice in TSP solution. The flowchart of the transit corner selection algorithm is shown in Figure 7. And, one possible result of the patch layout in Figure 4 with the patch order in Figure 5 is shown in Figure 8.

3.5. Isoparametric Tool Path Generation. After the processing order is determined, the remaining task is to generate a tool path with the defined starting corner, finishing corner, and preferred crossfeed direction for each patch. This can be achieved easily using the isoparametric strategy. If the starting and finishing corners are at the same side of the patch, there is only one possible crossfeed direction. And, if the starting and finishing corners are located in the diagonal of the patch, the preferred crossfeed direction in the processing data record will be selected as the crossfeed direction.

Given the starting corner, the crossfeed direction, the tool radius, and the acceptable scallop height, there are various methods to generate an isoparametric tool path for a parametric surface with rectangular topology [19, 28]. Consider the situation that the lower left corner is the starting corner and the crossfeed direction is the u-direction. The first tool path has the algebraic expression $u = 0$. Then, a side step Δu in parameter space is calculated according to the tool radius, the scallop height, and the geometric property of the surface. To calculate the side step Δu, we first sample a number of points on the current tool path. Then, for each point, calculate the side step in physical space using the following equation:

$$g = \sqrt{\frac{8hrR}{R + \text{sign} \cdot r}}. \tag{5}$$

As shown in Figure 9, g is the side step in physical space, r is tool end radius, R is the surface curvature, h is the scallop height, and sign is an operator whose value is 0 for flat surface, 1 for convex surface and −1 for concave surface. And, Δu can be calculated for each sampling point by mapping the side step g in physical space back into the parameter space. The calculation formula of Δu is given in equation (6). And, for patches with v-direction as the crossfeed direction, the calculation formula of Δu is also given in equation (6). The minimum Δu among them is utilized as the side step in parameter space, and the second tool path can be generated by offset the first tool path with a

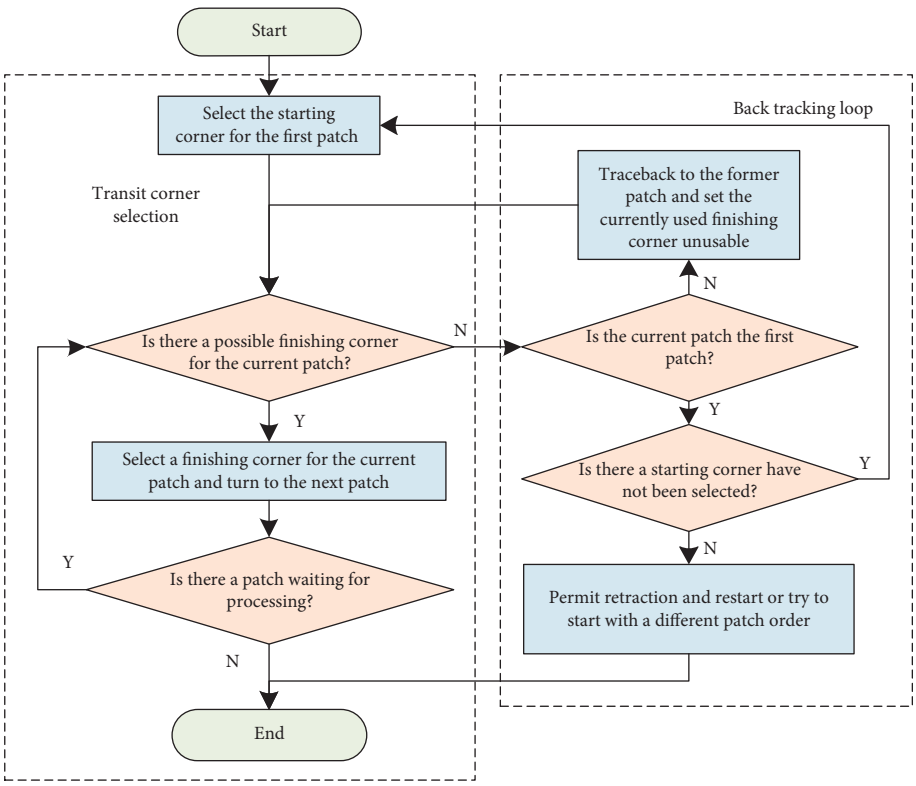

Figure 7: The flow chart of the transit corner selection algorithm.

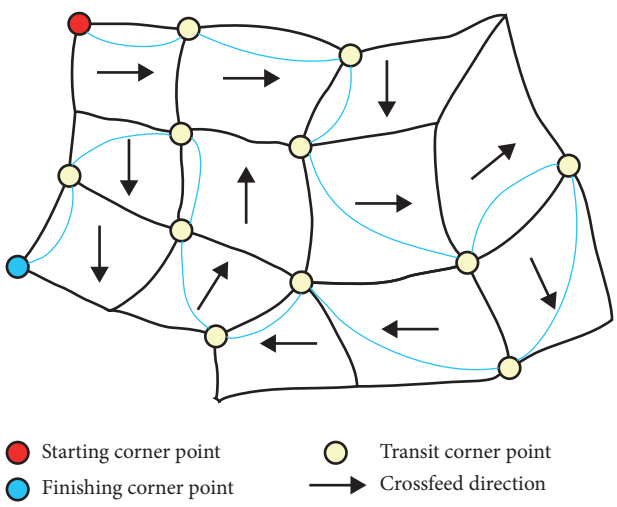

Figure 8: One possible processing order generated using the proposed algorithm for the patch layout in Figure 4 and the patch order in Figure 5. The blue curves in the figure connect the starting and finishing corners for each patch.

parametric distance Δu. And a series of iso-parametric lines can be generated by repeatedly performing this process. These isoparametric lines are the tool paths of this surface patch:

$$\begin{cases} \Delta u = \dfrac{gF}{\sqrt{E^2G - EF^2}}, \\ \Delta v = \dfrac{-gF}{\sqrt{EG^2 - F^2G}}. \end{cases} \tag{6}$$

To avoid retraction, the isoparametric lines are usually connected in a zig-zag way. As shown in Figure 10, for an isoparametric tool path starting from its lower left corner with u-direction as the crossfeed direction, there are two possible finishing corners. Before path generation, we cannot predict which corner will the zig-zag path finish at. In order to ensure the tool path finished at the expected corner, we propose utilizing a scallop tuning for patches that the isoparametric tool path does not finish at the expected finishing corner. Obviously, the finishing corner is decided by the odevity of

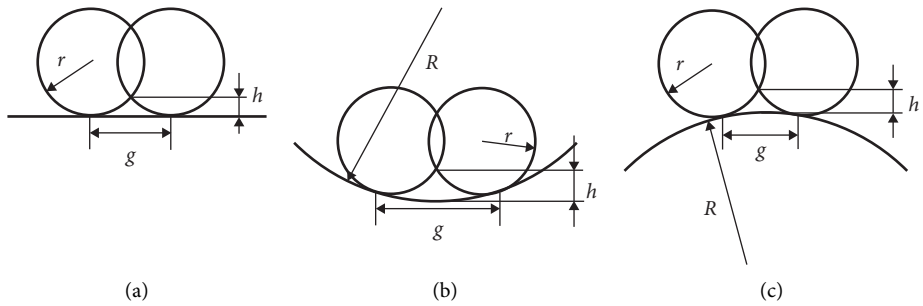

Figure 9: Side step calculation under scallop limit.

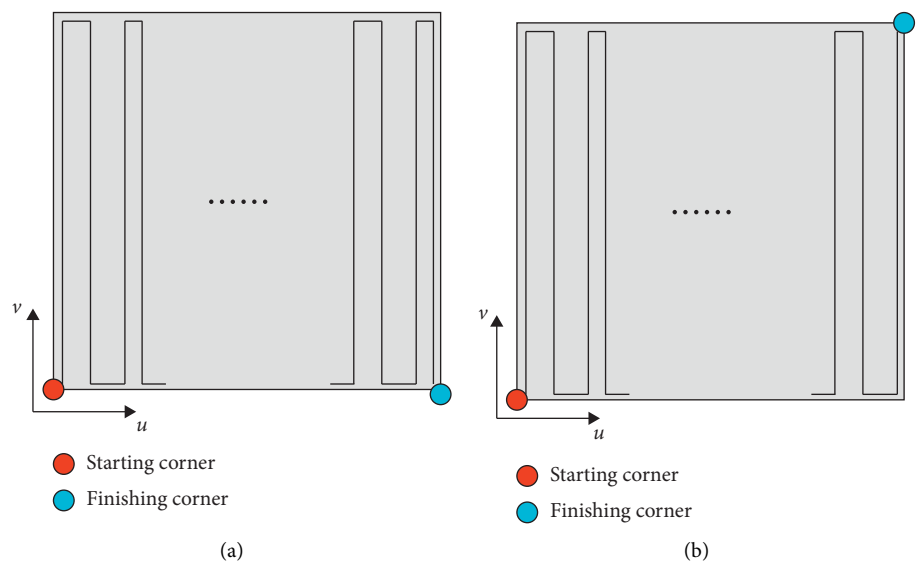

Figure 10: Two different finishing corners of the isoparametric tool path starting from the lower left corner with u-direction as the crossfeed direction.

the number of the isoparametric lines. If the path number of the generated isoparametric lines is n and the finishing corner is not the expected one, generate a tool path with $n+1$ isoparametric lines correcting the finishing corner. Thus, we slightly decrease the scallop height used in the tool path generation of this patch. For instance, if the original scallop is h, it is first decreased by a constant step length such as $0.1h$. Then, an isoparametric tool path is generated with $0.9h$ scallop. If the number of isoparametric lines is still n, the scallop will be decreased again with the step length 321. If the number of isoparametric lines is $n+1$, the generated tool path of 322 can be used as the final result. Otherwise, if the number of isoparametric lines is greater than $n+1$, the bisection method can be utilized to find a proper scallop between the current scallop and the original scallop and produce a tool path with $n+1$ isoparametric lines.

For five-axis machining, the tool posture has to be determined for a tool path. As we consider ball-end mill as the machining tool in this work, the posture is set to avoid gouge. Without loss of generality, the direction of the tool axis direction which is gouge free and most close to the Z-axis is set to be the tool axis direction for five-axis machining. For other kinds of tools, posture can also be determined by other standard such as surface curvature matching.

4. Experimental Results

To verify the effectiveness of the proposed algorithm, experimental results are given in this section. The test model is a keycap model with five T-spline patches and four extraordinary control points. As the work focuses on the machining of freeform surfaces, the model ignores the connecting structure of the keycap and only uses the shell part. The procedure of experiment is shown in Figure 11. Different patches in the model are shown in different color. The model is first input to the test program. The program generates the five-axis tool path using the proposed algorithm, and the corresponding Gcode file is also generated. The Gcode file is first simulated in Varicut software. And, the molds are machined using a five-axis machining center. After the molds are manufactured, the injection experiment is conducted on an injection molding machine to get the final product.

The machining center used here is a Mikron UCP 600 five-axis machining center. The injection molding machine

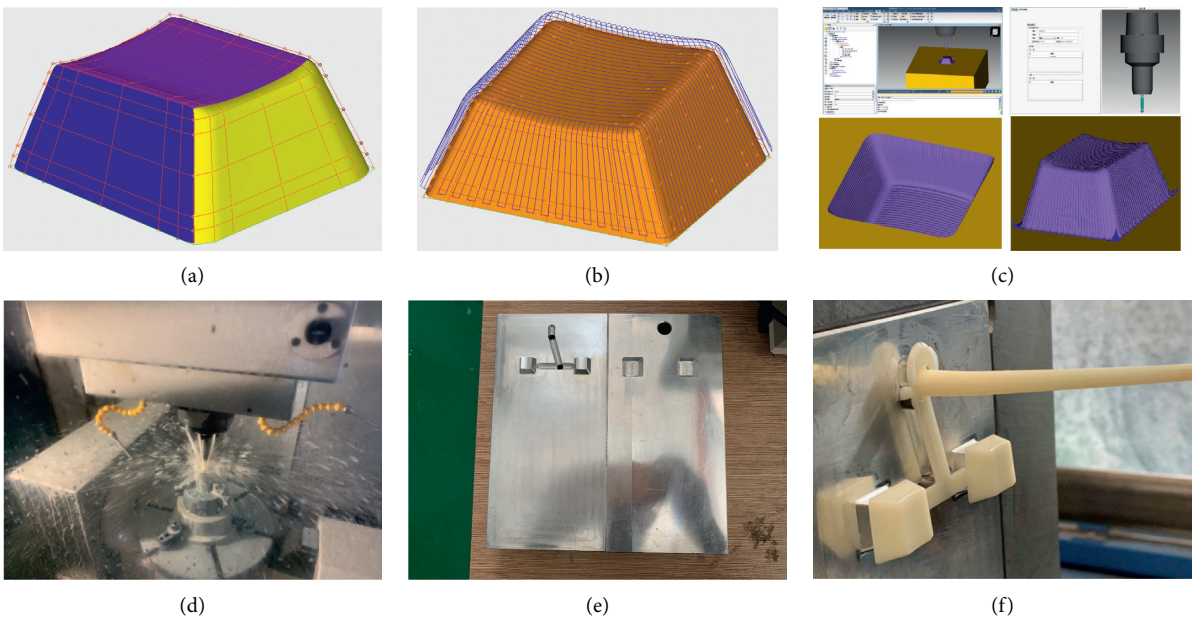

Figure 11: The procedure of experiment. (a) Input T-spline model, (b) tool path generation, (c) tool path simulation, (d) five-axis machining, (e) injection molds, and (f) polymetric product.

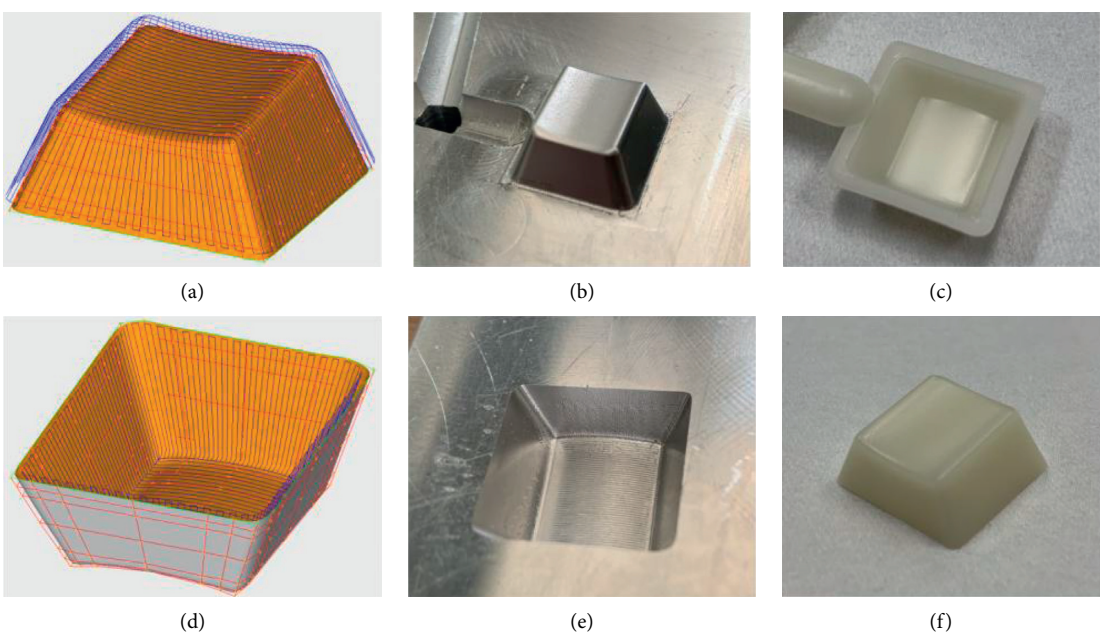

Figure 12: Tool path, injection molds, and final ABS product for the keycap model.

is ONGO Z70/JD. Mold material is 6061 aluminium alloy. The injection molding material is ABS. The convex model is in size of 14.4 mm × 14.4 mm × 6.8 mm, and the concave model is in size of 18 mm × 18 mm × 8.6 mm. To avoid local gouge or overcut, the finish machining cutting tool is a ball-end mill with 0.5 mm end radius. And, the scallop height limit is set to be 0.005 mm.

The experimental results are shown in Figure 12. The proposed method successfully generates a nonretraction tool path for the T-spline surface model with extraordinary control points. In each surface patch, the tool path is a zig-zag isoparametric tool path. These tool paths are end to end. And, the machining of the molds is finished at once without retraction. As shown in Figure 11, the boundaries of the T-spline patches are located near the edges of the keycap model. It can be seen in Figure 12 that the quality of the molds and the polymeric products is quite good in all places. And, there is no visible defect at these patch boundaries.

5. Conclusions

In this paper, we proposed a new five-axis tool path generation algorithm facing the T-spline surface model with extraordinary control points. Mold manufacturing is a typical application of this algorithm. One major advantage of using T-splines instead of NURBS is that the mold quality can be well controlled especially at patch boundaries as the T-spline surface model has high level continuity all over the model. Besides, the proposed algorithm utilizes the patch layout information of T-spline models to generate a nonretraction tool path. And, we also performed the mold machining and injection test to manifest the proposed method.

So far, there are still lots of potential improvements to the current work. Firstly, the proposed method still generates the tool path in a patch-by-patch manner. One possible improvement is to merge the tool path in adjacent patch to further reduce the processing time. Machining texture is also a worthwhile topic to improve the surface quality of the model. In the experiment, we can see some machining texture which will somehow influence the surface smoothness of the final product. Another interesting research direction is the T-spline-based mold design. However, there are already many T-spline modeling algorithms and T-spline-based CAD software such as Rhino and Fusion 360. They are not facing the injection mold design situation. Functions such as parting surface design are needed for mold design.

Data Availability

No data were used to support this study.

Conflicts of Interest

The authors declare that they have no conflicts of interest.

Acknowledgments

This work was financially supported by the National Nature Science Foundation of China (no. 51575483), Science Fund for Creative Research Groups of National Natural Science Foundation of China (no. 51821093), Key Research and Development Plan of Zhejiang Province (no 2018C01073), and the Fundamental Research Funds for the Central Universities (no. 2019QNA4004).

References

[1] C. Fernandes, A. J. Pontes, J. C. Viana, and A. Gaspar-Cunha, "Modeling and optimization of the injection-molding process: a review," *Advances in Polymer Technology*, vol. 37, no. 2, pp. 429–449, 2018.

[2] J. Gómez-Monterde, M. Sánchez-Soto, and M. L. Maspoch, "Influence of injection molding parameters on the morphology, mechanical and surface properties of ABS foams," *Advances in Polymer Technology*, vol. 37, no. 8, pp. 2707–2720, 2018.

[3] F. Liu, Y. Zhang, Y. Zhang et al., "Experimental investigation of the effects of process conditions on the morphology in injection molding of polymer blends," *Advances in Polymer Technology*, vol. 36, no. 3, pp. 341–351, 2017.

[4] M. C. Song, Z. Liu, M. J. Wang, T. M. Yu, and D. Y. Zhao, "Research on effects of injection process parameters on the molding process for ultra-thin wall plastic parts," *Journal of Materials Processing Technology*, vol. 187-188, pp. 668–671, 2007.

[5] L. Guangming, F. Hui, Z. Lixuan, and Y. Bin, "Research on optimal design of the injection mold parting direction based on preference relation," *The International Journal of Advanced Manufacturing Technology*, vol. 79, no. 5–8, pp. 1027–1034, 2015.

[6] I. Matin, M. Hadzistevic, J. Hodolic, D. Vukelic, and D. Lukic, "A CAD/CAE-integrated injection mold design system for plastic products," *The International Journal of Advanced Manufacturing Technology*, vol. 63, no. 5–8, pp. 595–607, 2012.

[7] Z. Li, X. Zhou, W. Liu, Q. Niu, and C. Kong, "A similarity-based reuse system for injection mold design in automotive interior industry," *The International Journal of Advanced Manufacturing Technology*, vol. 87, no. 5-8, pp. 1783–1795, 2016.

[8] X. Pessoles and C. Tournier, "Automatic polishing process of plastic injection molds on a 5-axis milling center," *Journal of Materials Processing Technology*, vol. 209, no. 7, pp. 3665–3673, 2009.

[9] Y. Jiang, L. Zhenliang, and M. Li, "Application of fuzzy and rough sets theory in the optimization of machining parameters for mold milling operations," *The International Journal of Advanced Manufacturing Technology*, vol. 28, pp. 1071–1077, 2006.

[10] H. U. Cho, J. W. Park, and Y. C. Chung, "Computation of optimal tool length for 5-axis ball-ended milling of molding die," *Journal of Mechanical Science and Technology*, vol. 26, no. 10, pp. 3097–3101, 2012.

[11] L. A. Sarmiento-Merida, A. Guevara-Morales, and U. Figueroa-López, "Determining the optimum parting direction in plastic injection molds based on minimizing rough machining time during mold manufacturing," *Advances in Polymer Technology*, vol. 37, no. 1, pp. 194–201, 2018.

[12] A. Lasemi, D. Xue, and P. Gu, "Recent development in CNC machining of freeform surfaces: a state-of-the-art review," *Computer-Aided Design*, vol. 42, no. 7, pp. 641–654, 2010.

[13] W. He, M. Lei, and H. Bin, "Iso-parametric CNC tool path optimization based on adaptive grid generation," *The International Journal of Advanced Manufacturing Technology*, vol. 41, no. 5-6, pp. 538–548, 2009.

[14] S. Sarkar and P. P. Dey, "A new iso-parametric machining algorithm for free-form surface," *Proceedings of the Institution of Mechanical Engineers, Part E: Journal of Process Mechanical Engineering*, vol. 228, no. 3, pp. 197–209, 2014.

[15] S. Ding, M. A. Mannan, A. N. Poo, D. C. H. Yang, and Z. Han, "Adaptive iso-planar tool path generation for machining of free-form surfaces," *Computer-Aided Design*, vol. 35, no. 2, pp. 141–153, 2003.

[16] Z. Lin, J. Fu, H. Shen, and W. Gan, "A generic uniform scallop tool path generation method for five-axis machining of freeform surface," *Computer-Aided Design*, vol. 56, pp. 120–132, 2014.

[17] T. W. Sederberg, J. Zheng, A. Bakenov, and A. Nasri, "T-splines and T-NURCCs," *ACM Transactions on Graphics*, vol. 22, no. 3, pp. 477–484, 2003.

[18] T. W. Sederberg, G. T. Finnigan, X. Li, H. Lin, and H. Ipson, "Watertight trimmed NURBS," *ACM Transactions on Graphics*, vol. 27, no. 3, pp. 1–8, 2008.

[19] W.-F. Gan, J.-Z. Fu, H.-Y. Shen, Z.-Y. Chen, and Z.-W. Lin, "Five-axis tool path generation in CNC machining of -spline surfaces," *Computer-Aided Design*, vol. 52, pp. 51–63, 2014.

[20] G. Zhao, Y. Liu, W. Xiao, O. Zavalnyi, and L. Zheng, "STEP-compliant CNC with T-spline enabled toolpath generation capability," *The International Journal of Advanced Manufacturing Technology*, vol. 94, no. 5–8, pp. 1799–1810, 2018.

[21] G. Zhao, O. Zavalnyi, Y. Liu, and W. Xiao, "Prospects for using T-splines for the development of the STEP-NC-based manufacturing of freeform surfaces," *The International Journal of Advanced Manufacturing Technology*, vol. 102, no. 1–4, pp. 1–16, 2019.

[22] J. Feng, J. Fu, Z. Lin, C. Shang, and B. Li, "Direct slicing of T-spline surfaces for additive manufacturing," *Rapid Prototyping Journal*, vol. 24, pp. 709–721, 2018.

[23] H. Wang, Y. He, X. Li, X. Gu, and H. Qin, "Polycube splines," *Computer-Aided Design*, vol. 40, no. 6, pp. 721–733, 2008.

[24] M. Campen and L. Kobbelt, "Quad layout embedding via aligned parameterization," *Computer Graphics Forum*, vol. 33, no. 8, pp. 69–81, 2014.

[25] X. Li, F. Chen, H. Kang, and J. Deng, "A survey on the local refinable splines," *Science China Mathematics*, vol. 59, no. 4, pp. 617–644, 2016.

[26] W. Wang, Y. Zhang, G. Xu, and T. J. R. Hughes, "Converting an unstructured quadrilateral/hexahedral mesh to a rational T-spline," *Computational Mechanics*, vol. 50, no. 1, pp. 65–84, 2012.

[27] L. Liu, Y. J. Zhang, and X. Wei, "Handling extraordinary nodes with weighted T-spline basis functions," *Procedia Engineering*, vol. 124, pp. 161–173, 2015.

[28] Z. Lin, J. Fu, H. Shen, W. Gan, and S. Yue, "Tool path generation for multi-axis freeform surface finishing with the LKH TSP solver," *Computer-Aided Design*, vol. 69, pp. 51–61, 2015.

[29] Z. Lin, J. Fu, Y. Sun, Q. Gao, G. Xu, and Z. Wang, "Non-retraction toolpath generation for irregular compound free-form surfaces with the LKH TSP solver," *The International Journal of Advanced Manufacturing Technology*, vol. 92, no. 5–8, pp. 2325–2339, 2017.

Hindawi
Advances in Polymer Technology
Volume 2020, Article ID 3793505, 8 pages
https://doi.org/10.1155/2020/3793505

Research Article

Reducing the Sink Marks of a Crystalline Polymer using External Gas-Assisted Injection Molding

Shaofei Jiang, Taidong Li, Xinxin Xia, Xiang Peng, and Jiquan Li

Key Laboratory of E&M, Ministry of Education, Zhejiang University of Technology, Hangzhou 310014, China

Correspondence should be addressed to Jiquan Li; lijq@zjut.edu.cn

Received 26 June 2019; Accepted 30 July 2019; Published 29 February 2020

Copyright © 2020 Shaofei Jiang et al. This is an open access article distributed under the Creative Commons Attribution License, which permits unrestricted use, distribution, and reproduction in any medium, provided the original work is properly cited.

External gas-assisted injection molding (EGAIM) has been used to reduce the sink marks of amorphous polymer products, but that of crystalline polymer products has not yet been reported. EGAIM of a crystalline polymer product was investigated in this study, and the influences of process parameters on the sink marks were discussed based on experiments. An isotactic polypropylene (iPP) product was fabricated by EGAIM under different process conditions. A uniform design was applied as an experimental design to investigate the influences of the process parameters on the sink marks. A regression equation was established to describe the quantitative relationship between the important parameters and sink marks in which a data-processing method was applied to determine the optimal value of F_α at significant level α to reduce the possibility of omission of some important parameters. The results show that EGAIM was effective in reducing the sink marks in these iPP products, and the most important parameters were the cooling time, gas pressure, and gas time. This study also provides the quantitative relationship between the important parameters and sink marks as reference for the research of EGAIM on crystalline polymer.

1. Introduction

External gas-assisted injection molding (EGAIM) is an unconventional molding process that efficiently fabricates products with high precision and high surface quality, especially in significantly reducing sink marks [1–3]. A sink mark is usually defined as "an unwanted depression or dimple on the surface of a molding due to localized shrinkage." [4, 5]. The distinct localized shrinkage commonly results from a local thick-wall structure, such as ribs, bosses, and other similar structures [3, 6], which is also greatly affected by the process parameters in injection molding [7–9], including the melt temperature [10–12], packing pressure [13, 14], packing time [15], cooling time [16], injection pressure [17], and injection speed [18].

EGAIM is more complicated than the conventional injection molding (CIM) because of the introduction of gas. Gas with certain pressure is injected between the cavity surface of the mold and the solidified polymer formed during filling, after the cavity was filled by polymer. The gas pressure is maintained until the cooling process is terminated. The pressure on the solidified polymer pushes it to move and deform, which compensate the polymer shrinkage caused by temperature decrease during packing and cooling and reduce the sink marks.

The advantages and complexity of EGAIM have attracted the attention of researchers. Chen et al. [19] investigated the packing effects of EGAIM on the shrinkage and sink marks of plastic parts (ABS) under various rib designs and compared them with those of CIM. The results showed that EGAIM could further reduce the part shrinkage when the gas pressure and gas-packing time were both increased. Su et al. [20] also reduced the ghost marks in plastic parts of PA using EGAIM. Moreover, the quality of the parts was improved by increasing the mold temperature, melt temperature, injection speed, and pressure, although some limitations were experienced. Jiang et al. [21] discussed the relationship between the process parameters and part quality of ABS using the single-factor test method and developed a physical model that described the influence of gas-melting interaction on the sink marks [22].

The aforementioned studies focused on amorphous polymer products and did not explore the application of EGAIM to crystalline polymer products. Crystalline polymers are an important component in industrial production [23], aerospace [24], and pharmaceutical production [25]. In addition, the shrinkage of crystalline polymers is usually more obvious than that of amorphous polymers [26], and the sink marks of crystalline polymer products are usually larger than those of amorphous polymer products. Therefore, investigating

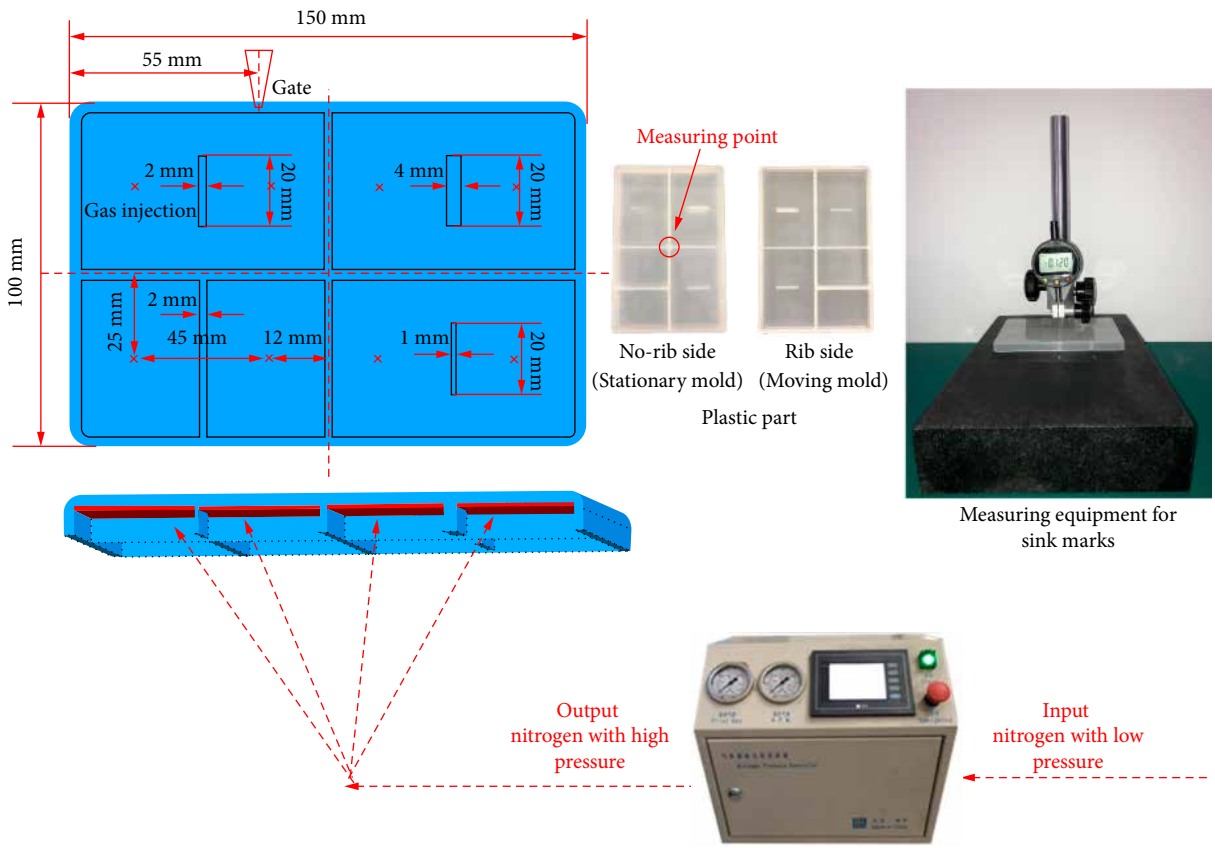

Figure 1: The equipment of EGAIM and measuring instruments.

the application of EGAIM to crystalline polymer products is important. In the present study, an iPP product was manufactured using EGAIM, and the influences of the process parameters on the sink marks of the iPP products were discussed. A regression equation was established to investigate the quantitative influence based on the experimental results in which a data-processing method was applied to determine the optimal value of F_α at significant level α to reduce the possibility of omission of some important parameters. To verify the reduction of the sink marks of these iPP products by EGAIM, experiments with or without gas were carried out under an optimal condition, as calculated by the regression equation.

2. Experiments

A semi-crystalline iPP (T30S, Zhenhai Branch of Sinopec Corp., China) product was used in this study, and its parameters were as follows: melt flow index of 2.5 g/10 min, melting point of 167°C, density of 0.91 g/cm^3, and isotactic index of more than 94%. An injection molding machine (MA3800/2250, Haitian International Holdings Ltd., China) was used to manufacture the products with dimensions of 150 mm × 100 mm × 3 mm. After filling at a later time (delay time), an inert gas (N_2) with certain pressure was injected between the solidified polymer and cavity surface of the moving mold using a nitrogen pressure controller (C8-01, Beijing Chn-Top Machinery Group Co., Ltd., China). The sink marks of the crystalline polymer products were measured by a dial indicator (A0-12.7, Shanghai Siwei Instrument Manufacturing Co., Ltd., China), which has a measurement range of 12.7 mm and accuracy of 0.001 mm. The locations of gate, gas injections and measuring point are shown in Figure 1.

To study the efficiency of EGAIM on the reduction of sink marks in the crystalline polymer products, almost all of the process parameters were considered, including the material temperature, injection pressure, injection speed, packing pressure, packing time, cooling time, gas pressure, gas time, and delay time. The uniform design focuses on the uniform distribution of test points within the test range to obtain the largest available information with the least number of tests. Thus, the design is especially suitable for a multi-factor test, and the system model is completely unknown [29]. A uniform design is chosen to design the experiments using uniform table remarking $U_{30}(3^1 \times 5^1 \times 6^2 \times 10^5)$. The levels and parameters are listed in Table 1, where X_1–X_9 represent the material temperature, injection pressure, injection speed, packing pressure, packing time, cooling time, gas pressure, gas time, and delay time, respectively. The nine parameters were selected referring some studies of the sink marks [10–18].

3. Data-Processing Method

Regression analysis is a set of statistical processes that estimates the relationship between the parameters and results. More specifically, regression analysis helps us understand how the

Table 1: Uniform table remarking $U_{30}(3^1 \times 5^1 \times 6^2 \times 10^5)$ in EGAIM.

Number	Parameter X								
	X_1 (°C)	X_2 (MPa)	X_3 (mm/s)	X_4 (MPa)	X_5 (s)	X_6 (s)	X_7 (MPa)	X_8 (s)	X_9 (s)
1	180	65	25	10	1	10	0	5	0
2	200	70	30	20	2	15	1	10	0.5
3	220	75	35	30	3	20	2	15	1
4	—	80	40	40	4	25	3	20	1.5
5	—	85	45	50	5	30	4	25	2
6	—	90	50	60	—	35	5	30	2.5
7	—	95	55	70	—	40	6	—	—
8	—	100	60	80	—	45	7	—	—
9	—	105	65	90	—	50	8	—	—
10	—	110	70	100	—	55	9	—	—

Table 2: Uniform table.

Number N_j	Parameter X_l				Result Y
	X_1	X_2	$\cdots$	X_P	$Y = X_{P+1}$
N_1	X_{11}	X_{12}	$\cdots$	X_{1P}	$Y = X_{1(P+1)}$
N_2	X_{21}	X_{22}	$\cdots$	X_{2P}	$Y = X_{2(P+1)}$
$\cdots$	$\cdots$	$\cdots$	$\cdots$	$\cdots$	$\cdots$
N_n	X_{n1}	X_{n2}	$\cdots$	X_{nP}	$Y = X_{n(P+1)}$

typical values of parameters change when any one of the results is varied [28]. One of the most important steps in regression analysis is the determination of optimal value F_α at significant level α, which directly determines whether parameters are introduced into the regression equation. In general, significant level $\alpha = 0.05$ is commonly used in statistics [29]. However, some important parameters are sometimes omitted in injection molding. Thus, a data-processing method was applied in this study to establish the optimal value of F_α at significant level α, which would reduce the possibility of omission of some important parameters. The data in the uniform table need to be dealt with by this processing method.

A uniform table was designed using a uniform design to reduce the number of experiments. The uniform table consists of N_j ($j = 1, 2, \ldots, n$) experiments, X_l ($l = 1, 2, \ldots, P$) parameters, and Y(recorded as X_j, where $j = P + 1$) results. The value of parameter X_l in the jth experiment is X_{jl}, and result Y is recorded as $X_{j(P+1)}$, as listed in Table 2.

Correlation coefficient r_{ij} accurately describes the reliability between the parameters and results. The value of r_{ij} is positively correlated with the reliability between the parameters and results, as expressed in Equation. (1) [30]

$$r_{ij} = \frac{l_{ij}}{\sqrt{l_{ii} l_{jj}}} = \frac{\sum_{k=1}^{n}\left[\left(X_{ki} - \frac{1}{n}\sum_{k=1}^{n} X_{ki}\right)\cdot\left(X_{kj} - \frac{1}{n}\sum_{k=1}^{n} X_{kj}\right)\right]}{\sqrt{\sum_{k=1}^{n}\left(X_{ki} - \overline{X}_i\right)^2 \cdot \sum_{k=1}^{n}\left(X_{kj} - \overline{X}_j\right)^2}};$$
$$i = 1, 2, \ldots, P+1,\ j = 1, 2, \ldots, n, \tag{1}$$

where l_{ij} and l_{ii} are the sum of the products of the mean deviation and sum of squares of the deviation from the mean, respectively. $\overline{X}_i$ is the average value of X_{jl} ($l = 1, 2, \ldots, P+1$, $j = 1, 2, \ldots, n$). The important parameters were selected by comparing the values of correlation coefficient r_{ij}.

The r_{ij} forms the matrix of the correlation coefficients, as expressed in Equation. (2) [31].

$$\left[r_{ij}\right] = \begin{bmatrix} r_{11} & r_{12} & \cdots & r_{1P} & r_{1(P+1)} \\ r_{21} & r_{22} & \cdots & r_{2P} & r_{2(P+1)} \\ r_{31} & r_{32} & \cdots & r_{3P} & r_{3(P+1)} \\ \cdots & \cdots & \cdots & \cdots & \cdots \\ r_{n1} & r_{n2} & \cdots & r_{nP} & r_{n(P+1)} \end{bmatrix} \tag{2}$$

Generally, F should be calculated for every parameter in the regression analysis and is compared with pre-determined F_α at significant level α to determine whether the parameter is retained or not. In this study, the important parameters were obtained by comparing the correlation coefficients that should be included in the regression analysis. If the commonly used significant level, i.e., $\alpha = 0.05$, in the statistics is applied to the regression analysis in EGAIM, some important parameters might be omitted. Thus, this study introduced a method for modifying significant level α and corresponding F_α.

In this work, the data processing can be summarized by the following steps.

Step 1. A set of significant level α in a certain range and corresponding F_α are obtained using the critical value table of the F distribution.

Step 2. The F_{X_l} values of the important parameters are calculated using Equation (3) [32],where subscript X_l represents the selected important parameters using the comparison of the correlation coefficients.

$$F_{X_l} = \frac{\left[\frac{\left(r_{i(P+1)}\right)^2}{r_{ii}}\right] \times (n-3)}{r_{ii} - \left[\frac{\left(r_{i(P+1)}\right)^2}{r_{ii}}\right]}; i = 1, 2, \ldots, P+1 \tag{3}$$

Step 3. Minimum F_{X_l} is compared with F_α using Equation (4). If minimum F_{X_l} is less than F_α, F_α cannot ensure that the important parameters are included in the regression equation. If minimum F_{X_l} is larger than or equal to F_α, F_α is suitable for the regression analysis.

Table 3: Values of the sink marks of the crystalline polymer products.

Number	Parameter X_l									Sink mark Y
	X_1 (°C)	X_2 (MPa)	X_3 (mm/s)	X_4 (MPa)	X_5 (s)	X_6 (s)	X_7 (MPa)	X_8 (s)	X_9 (s)	$Y = X_{10}$ (mm)
1	180	105	40	10	5	35	3	5	1.5	0.264
2	220	110	35	80	2	25	8	10	2	0.155
3	220	70	60	90	3	10	1	30	1.5	0.0723
4	180	75	25	50	2	25	2	20	2	0.121
5	200	100	50	100	1	40	6	30	0.5	0.098
6	200	110	60	50	5	50	7	25	2	0.067
7	180	85	65	90	2	45	9	5	1	0.202
8	200	95	30	40	2	40	0	15	2.5	0.168
9	220	85	35	70	4	45	3	30	2.5	0.143
10	180	90	35	60	5	20	8	30	1	0.127
11	200	110	25	40	3	10	40	25	0	0.040
12	180	90	70	40	1	15	4	10	0.5	0.176
13	220	85	40	30	1	30	90	25	0	0.073
14	220	95	25	100	4	50	5	15	1	0.157
15	220	65	55	50	5	35	70	10	0	0.154
16	180	70	30	20	4	40	6	15	0.5	0.107
17	180	65	45	80	1	35	5	25	2	0.080
18	180	95	70	30	4	30	0	25	1.5	0.213
19	200	80	60	20	2	45	40	30	0	0.066
20	200	80	45	80	5	15	0	15	0.5	0.120
21	220	75	70	60	3	55	6	20	1.5	0.132
22	200	70	40	30	3	55	8	5	1.5	0.208
23	180	100	55	70	3	10	7	15	2.5	0.112
24	220	105	65	10	2	20	5	20	1	0.079
25	180	105	45	90	3	55	10	20	0	0.117
26	200	75	50	10	4	15	9	20	2.5	0.044
27	220	90	50	20	1	50	1	10	2	0.240
28	220	100	55	60	4	25	2	5	0.5	0.167
29	200	65	30	70	1	20	2	5	1	0.172
30	200	80	65	100	5	30	4	10	2.5	0.145

$$\begin{cases} \min F_{X_l} < F_\alpha; \text{unsuitable} \\ \min F_{X_l} \geq F_\alpha; \text{suitable} \end{cases} \quad (4)$$

Step 4. Correspondingly, this condition results in many suitable F_α values based on Step (2), but not all F_α values are optimal F_α. To improve the accuracy, maximum F_α is considered as the optimal value from a large number of suitable F_α values.

The aforementioned data-processing method provides the basis for selecting F_α at significant level α by comparing it with F_{X_l} of the important parameters, which reduces the possibility of omission of some important parameters in the regression equation and improves the accuracy of this equation.

4. Results and Discussion

4.1. Correlation Coefficients of the Parameters. The sink marks of the crystalline polymer products measured by the dial indicator are listed in Table 3.

The matrix of the correlation coefficients is shown in the form of a heat map by combining Equations (1) and (2) to intuitively express the relationship between the parameters and sink marks, as shown in Figure 2. In the heat map, red and blue represent the positive and negative effects, respectively, and the number and shade of the colors indicate the correlation between the abscissa and ordinate. The value of the correlation coefficient between the gas time and sink marks is the largest value, which reaches −0.71. Thus, gas time is the most important parameter in EGAIM, and the negative sign indicates that the relationship between the gas time and sink marks is positive. The longer the gas time is, the smaller is the sink-mark value. The correlation coefficients of the cooling time and gas pressure are also large, which reach 0.32 and −0.23, respectively. Therefore, the gas time, cooling time, and gas pressure are important in the sink marks of the crystalline polymer products. The value of the correlation coefficient between the delay time and gas pressure is also large, which reaches 0.27. Thus, the influence of the delay time and gas pressure should not be neglected. The determination of the important parameters establishes a basis for exploring the

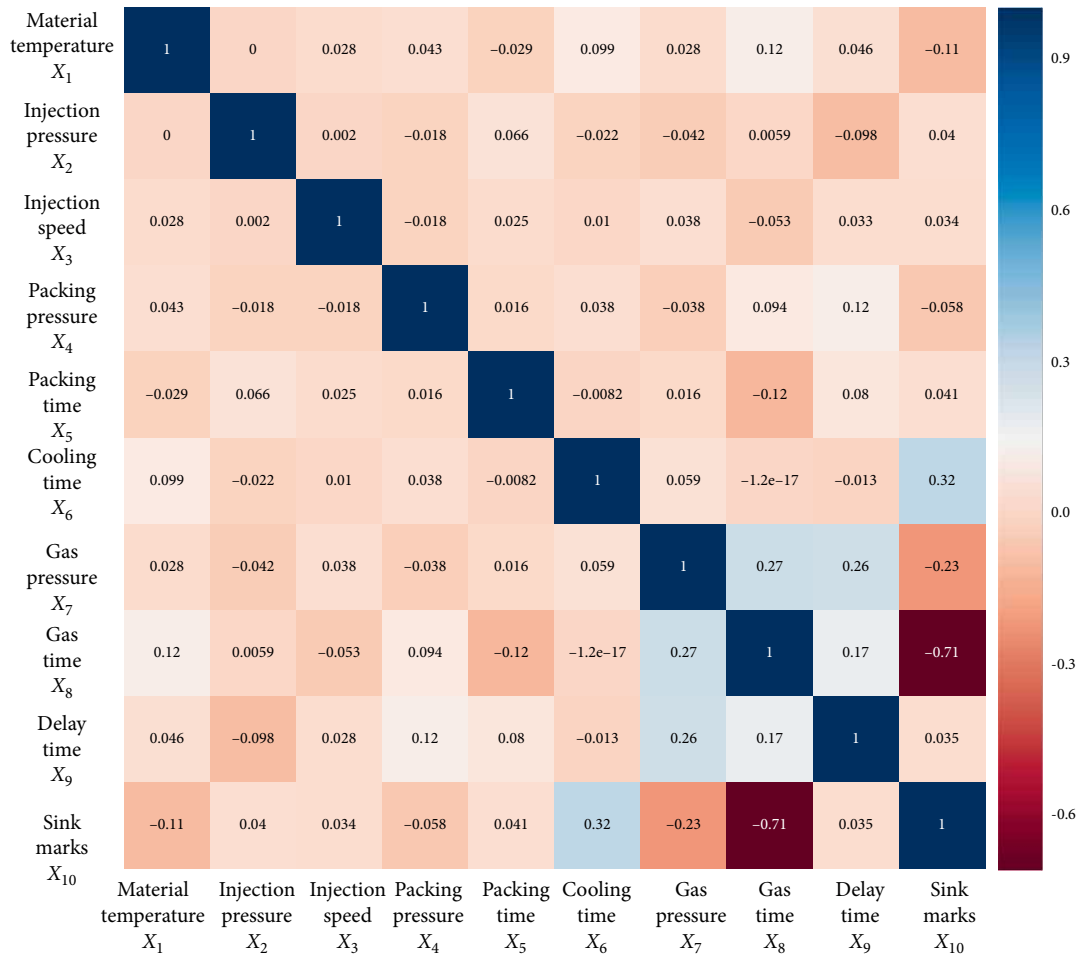

Figure 2: Heat map of the matrix of the correlation coefficients.

quantitative relationship between the parameters and sink marks of the crystalline products in EGAIM.

4.2. Establishment of the Regression Equation. According to the calculation by Equation (3), the F_{X_i} values of the cooling time, gas pressure, and gas time, were 3.19, 1.56, and 28.46, respectively. F_{X_i} of the interaction of the gas pressure and delay time was 2.03. One of the most important steps in considering the regression equation is to determine F_α at significant level α to select the parameters. In general, F_α at significant level α should be defined before exploring the regression equation. However, F_α depends on the preferences of different people. α is generally defined in statistics as 0.05, and $F_\alpha = 2.9$ at significant level $\alpha = 0.05$. If $F_\alpha = 2.9$ is used to investigate the EGAIM parameters, the cooling and gas times are considered in the regression equation because $F_{X_i} > F_\alpha = 2.9$. However, the gas pressure is omitted from the equation, which is unacceptable according to the aforementioned discussion. Significant level α was thus adjusted to $\alpha = 0.3$ to ensure that all important parameters were included into the regression equation. $F_\alpha = 1.4$ at $\alpha = 0.3$. All the F_{X_i} values of the important parameters were larger than F_α, which avoided omitting the important parameters.

To obtain the quantitative relationship between the parameters and sink marks, the square term of the parameters and the interaction among the parameters were considered in the regression equation. The regression equation was investigated using the comparison between F_{X_i} and $F_\alpha = 1.4$, as expressed in Equation (5),

$$\begin{aligned} Y = {} & 0.0879 + 0.003025 \times X_6 + 0.02563 \times X_7 - 0.01050 \times \\ & X_5 + 0.1185 \times X_9 + 0.000223 \times X_5^2 - 0.03374 \times X_9^2 \\ & - 0.000514 \times X_7 \times X_8 - 0.00621 \times X_7 \times X_9 \end{aligned} \quad (5)$$

The ratio of variation to the total variation for Equation (5) was described by the important coefficient R^2, which is a measure of the degree of fit. When R^2 more approaches unity, the response model fits the actual data better. The value of R^2 in Equation (5) is 85.37%, which is acceptable.

The regression equation of the sink marks in EGAIM was obtained according to the analysis of the correlation coefficients, which revealed the quantitative relationship between the important parameters and sink marks of the crystalline polymer products in EGAIM.

4.3. Discussion on the Regression Equation. The regression equation explores the influence of important parameters

Table 4: Uniform table remarking $U_{15}(3^1 \times 5^4)$, including the unimportant parameters designed using the uniform design.

Number	Parameter X_l					Result Y
	Material temperature (°C) X_1	Injection pressure (MPa) X_2	Injection speed (mm/s) X_3	Packing pressure (MPa) X_4	Packing time (s) X_5	Sink marks (mm) $Y = X_{10}$
1	180	110	40	80	5	0.116
2	220	110	50	20	4	0.111
3	200	110	60	60	1	0.096
4	180	80	60	20	4	0.096
5	200	100	40	20	2	0.092
6	180	100	70	40	3	0.103
7	220	100	30	100	3	0.102
8	200	80	70	100	4	0.096
9	200	70	50	80	3	0.089
10	200	90	30	40	5	0.096
11	180	90	50	100	1	0.085
12	220	90	70	80	2	0.087
13	220	80	40	40	1	0.091
14	220	70	60	60	5	0.085
15	180	70	30	60	2	0.103

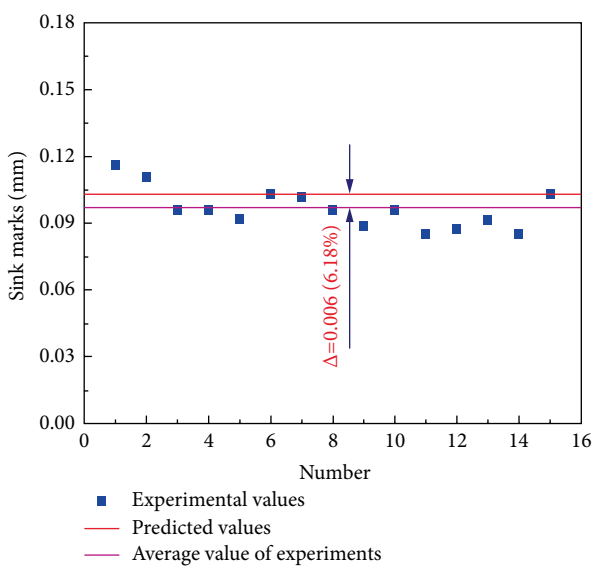

Figure 3: Comparison between the experiments and predictions in the regression equation.

on the sink marks of the crystalline polymer products. The minimum value of the sink marks was obtained by calculating the regression equation, which was equal to 0.103 mm when the cooling time, gas pressure, gas time, and delay time were 55 s, 9 Mpa, 30 s, and 1 s, respectively.

According to the previous research, when the important parameters were defined, the influence of the unimportant parameters on the sink marks of crystalline polymers could be ignored, including the material temperature, injection pressure, injection speed, packing pressure and packing time. When the important parameters were the same as those of the aforementioned values, i.e., the cooling time, gas pressure, gas time, and delay time were 55 s, 9 Mpa, 30 s and 1 s, respectively, and the other unimportant parameters were combined according to the uniform design in a certain range, the sink marks of the crystalline polymer under different unimportant parameters are as those listed in Table 4.

The experimental results are shown in Figure 3, and the values of the sink marks under different unimportant parameters fluctuate from the average value and reach 0.097 mm. The difference between the average and predicted values of the regression equation is 0.006 mm and reaches 6.18%, which indicates that the accuracy of the regression equation and the influence of these parameters on the sink marks of crystalline polymer products are almost negligible. The regression equation establishes the quantitative relationship between the important parameters and sink marks of the crystalline polymer products in EGAIM.

4.4. Reduction of Sink Marks Using EGAIM. The aforementioned research obtained the optimal important parameters for the sink marks, including a cooling time of 55 s, gas pressure of 9 Mpa, gas time of 30 s, and delay time of 1 s. the other unimportant parameters were randomly determined from no. 14 in Table 4, and the material temperature, injection pressure, injection speed, packing pressure, and packing time are 220°C, 70 Mpa, 60 mm/s, 60 Mpa, and 5 s, respectively. The sink marks of the crystalline polymer products with or without gas are compared and shown in Figure 4. Figure 4(a) shows that the sink mark of the crystalline polymer products without the gas is 0.365 mm, whereas that with the gas is only 0.085 mm, as shown in Figure 4(b). The difference in the sink marks of the crystalline polymer products with or without gas is 0.280 mm. Thus, EGAIM significantly reduces the sink marks of the crystalline polymer products. Therefore, EGAIM obviously reduces the sink marks of these iPP products. The results provide sufficient evidence for the application of crystalline polymers in EGAIM.

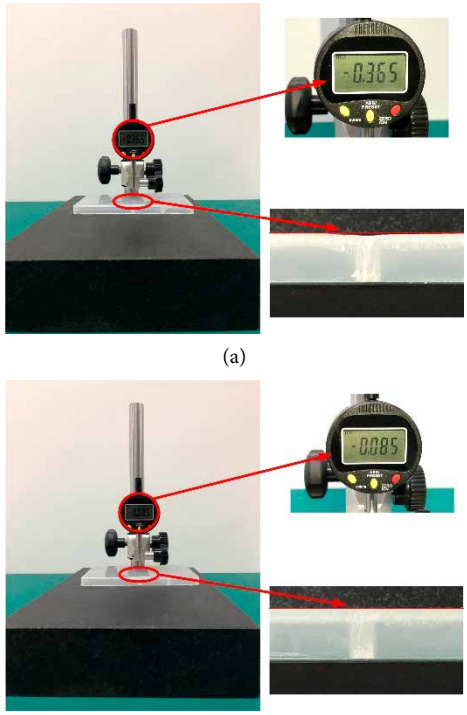

(a)

(b)

Figure 4: The values of sink marks of crystalline polymer products without gas (a) and with gas (b).

5. Conclusion

In this study, the application of EGAIM to an iPP product was investigated by experiment. According to the results of this study, the following conclusions can be drawn. (1) EGAIM can significantly reduce the sink marks of these iPP products. (2) The cooling time, gas pressure, and gas time are important parameters that affect the sink marks of the crystalline polymer products according to the correlation coefficients. (3) The regression equation can correctly predict the sink marks of the crystalline polymer products when the important parameters in EGAIM are constant. In general, this study verifies the effectiveness of EGAIM on reducing the sink marks of crystalline polymer products and provides the quantitative relationship between the important parameters and sink marks of crystalline polymer products in EGAIM.

Data Availability

The data used to support the findings of this study are available from the corresponding author upon request.

Conflicts of Interest

The authors declare that they have no conflicts of interest.

Acknowledgments

This work was supported by the National Natural Science Foundation under Grant Nos. 51575491, 51875525, and U1610112 and by the Natural Science Foundation of Zhejiang Province under Grant Nos. LY19E050004 and LY18E050020.

References

[1] S.-C. Nian, M.-H. Li, and M.-S. Huang, "Warpage control of headlight lampshades fabricated using external gas-assisted injection molding," *International Journal of Heat and Mass Transfer*, vol. 86, pp. 358–368, 2015.

[2] H.-Y. Su, S.-C. Nian, and M.-S. Huang, "Reducing ghost marks in injection-molded plastic parts by using external gas-assisted holding pressure," *International Communications in Heat and Mass Transfer*, vol. 66, pp. 1–10, 2015.

[3] S.-J. Liu, C.-H. Lin, and Y.-C. Wu, "Minimizing the sinkmarks in injection-molded thermoplastics," *Advances in Polymer Technology*, vol. 20, no. 3, pp. 202–215, 2001.

[4] D. Mathivanan and N. S. Parthasarathy, "Prediction of sink depths using nonlinear modeling of injection molding variables," *International Journal of Advanced Manufacturing Technology*, vol. 43, no. 7-8, pp. 654–663, 2009.

[5] J. Yu, H. Yong, L. Zhao, K. Agnieszka, Y. Wantai, and N. Jun, "Effect of monomer structure on real-time UV-curing shrinkage studied by a laser scanning approach," *Advances in Polymer Technology*, vol. 32, no. 1, pp. 4186–4193, 2013.

[6] C. Shen, L. Wang, W. Cao, and Q. Li, "Investigation of the effect of molding variables on sink marks of plastic injection molded parts using Taguchi DOE technique," *Polymer-Plastics Technology and Engineering*, vol. 46, no. 3, pp. 219–225, 2007.

[7] Y. Wang, L. Y. Chen, and X. M. Yang, "Numerical optimization of shrinkage and warpage on the injection molding process parameters of electrical connector," *Applied Mechanics and Materials*, vol. 868, pp. 183–191, 2017.

[8] M. C. R. Garcia, A. C. S. Netto, and A. J. Pontes, "Experimental stu dy of shrinkage and ejection forces of reinforced polypropylene based on nanoclays and short glass fibers," *Polymer Engineering and Science*, vol. 58, no. 1, pp. 55–62, 2017.

[9] X. Wang, J. Gu, and C. Shen, "Warpage optimization with dynamic injection molding technology and sequential optimization method," *The International Journal of Advanced Manufacturing Technology*, vol. 78, no. 1, pp. 177–187, 2015.

[10] B. Y. Tay, L. Liu, N. H. Loh, S. B. Tor, Y. Murakoshi, and R. Maeda, "Injection molding of 3D microstructures by μPIM," *Microsystem Technologies*, vol. 11, no. 2–3, pp. 210–213, 2005.

[11] R.-D. Chien, "Micromolding of biochip devices designed with microchannels," *Sensors and Actuators A: Physical*, vol. 128, no. 2, pp. 238–247, 2006.

[12] N.-S. Ong, H. L. Lee, and M. A. Parvez, "Influence of processing conditions and part design on the gas-assisted injection molding process," *Advances in Polymer Technology*, vol. 20, no. 4, pp. 270–280, 2001.

[13] C. D. Greene and D. F. Heaney, "The PVT effect on the final sintered dimensions of powder injection molded components," *Materials & Design*, vol. 28, no. 1, pp. 95–100, 2007.

[14] V. Speranza, U. Vietri, and R. Pantani, "Adopting the experimental pressure evolution to monitor online the shrinkage in injection molding," *Industrial & Engineering Chemistry Research*, vol. 51, no. 49, pp. 16034–16041, 2012.

[15] F. D. Santis, R. Pantani, V. Speranza, and G. Titomanlio, "Analysis of shrinkage development of a semicrystalline polymer during

injection molding," *Industrial&Engineering Chemistry Research*, vol. 49, no. 5, pp. 2469–2476, 2010.

[16] R. Elleithy, I. Ali, M. Al-haj Ali, and S. M. Al-Zahrani, "Different factors affecting the mechanical and thermo-mechanical properties of HDPE reinforced with micro-$CaCO_3$," *Journal of Reinforced Plastics&Composites*, vol. 30, no. 9, pp. 769–780, 2011.

[17] Y.-J. Xu, W. Yang, B.-H. Xie, Z.-Y. Liu, and M.-B. Yang, "Effect of injection parameters and addition of nanoscale materials on the shrinkage of polypropylene copolymer," *Journal of Macromolecular Science Part B*, vol. 48, no. 3, pp. 573–586, 2009.

[18] J. Pomerleau and B. Sanschagrin, "Injection molding shrinkage of PP: experimental progress," *Polymer Engineering & Science*, vol. 46, no. 9, pp. 1275–1283, 2010.

[19] S.-C. Chen, Y.-C. Lin, and S.-W. Huang, "Study on the packing effects of external gas-assisted injection molding on part shrinkage in comparison with conventional injection molding," *Polymer Engineering & Science*, vol. 50, no. 11, pp. 2085–2092, 2010.

[20] H.-Y. Su, S.-C. Nian, and M.-S. Huang, "Reducing ghost marks in injection-molded plastic parts by using external gas-assisted holding pressure," *International Communications in Heat & Mass Transfer*, vol. 66, pp. 1–10, 2015.

[21] S. Jiang, W. Zheng, J. Zhang, and J. Li, "Experimental study on the Influence of parameters on the plastic parts quality of external gas-assisted injection molding," *Applied Mathematics & Information Sciences*, vol. 6, no. 3, pp. 665–671, 2012.

[22] S. Jiang, J. Tao, and J. Li, "Study on the mechanism of the packing process and sink mark in external gas-assisted injection molding," *Advances in Mechanical Engineering*, vol. 6, 853142 pages, 2014.

[23] M. Altan, "Reducing shrinkage in injection moldings via the Taguchi, ANOVA and neural network methods," *Materials & Design*, vol. 31, no. 1, pp. 599–604, 2010.

[24] D. Garcia-Gonzalez, S. Garzon-Hernandez, and A. Ariasb, "A new constitutive model for polymeric matrices: application to biomedical materials," *Composites Part B: Engineering*, vol. 139, pp. 117–129, 2018.

[25] R. P. Brannigan and A. P. Dove, "Synthesis, properties and biomedical applications of hydrolytically degradable materials based on aliphatic polyesters and polycarbonates," *Biomaterials Science*, vol. 5, no. 1, pp. 9–21, 2017.

[26] D. L. Poerschke, A. Braithwaite, D. Park, and F. Lauten, "Crystallization behavior of polymer-derived Si-O-C for ceramic matrix composite processing," *Acta Materialia*, vol. 147, pp. 329–341, 2018.

[27] A. R. Higgs, M. J. Maughon, R. T. Ruland, and M. C. Reade, "Effect of uniform design on the speed of combat tourniquet application: a simulation study," *Military Medicine*, vol. 181, no. 8, pp. 753–755, 2016.

[28] K-. H. Kim, J. C. Park, Y. S. Suh, and B-. H. Koo, "Interactive robust optimal design of plastic injection products with minimum weldlines," *The International Journal of Advanced Manufacturing Technology*, vol. 88, no. 5–8, pp. 1333–1344, 2017.

[29] J. F. Mudge, T. J. Barrett, K. R. Munkittrick, and J. E. Houlahan, "Negative consequences of using $\alpha = 0.05$ for environmental monitoring decisions: a case study from a decade of canada's environmental effects monitoring program," *Environmental Science & Technology*, vol. 46, no. 17, pp. 9249–9255, 2012.

[30] W-.Y. Zhang, Z. W. Wei, B-.H. Wang, and X-.P. Han, "Measuring mixing patterns in complex networks by spearman rank correlation coefficient," *Physica A: Statistical Mechanics and its Applications*, vol. 451, no. 1, pp. 440–450, 2016.

[31] M. Z. Belmecheri, M. Ahfir, and I. Kale, "Automatic heart sounds segmentation based on the correlation coefficients matrix for similar cardiac cycles identification," *Biomedical Signal Processing & Control*, vol. 43, pp. 300–310, 2018.

[32] L. P. Ma, *Regression Analysis: Regression Analysis [M]*, Machinery Industry Press, p. 150, 2014.

Hindawi
Advances in Polymer Technology
Volume 2020, Article ID 6910535, 9 pages
https://doi.org/10.1155/2020/6910535

Research Article

Design and Research of Skin Injection Molded TPE Materials Based on Genetic Algorithm

Kui Yan,[1,2] Yizhe Chen,[1,2] Hui Wang,[1,2] Cheng Gao,[1,3] and Qiuyang Bai[1,3]

[1]*Hubei Key Laboratory of Advanced Technology for Automotive Components, Wuhan University of Technology, Wuhan 430070, China*
[2]*Hubei Collaborative Innovation Center for Automotive Components Technology, Wuhan 430070, China*
[3]*Hubei Engineering Research Center for Green & Precision Material Forming, Wuhan 430070, China*

Correspondence should be addressed to Yizhe Chen; yzchen@whut.edu.cn and Hui Wang; huiwang@whut.edu.cn

Received 31 May 2019; Revised 7 August 2019; Accepted 6 February 2020; Published 29 February 2020

Guest Editor: Peng Zhao

Copyright © 2020 Kui Yan et al. This is an open access article distributed under the Creative Commons Attribution License, which permits unrestricted use, distribution, and reproduction in any medium, provided the original work is properly cited.

Thermoplastic elastomer (TPE) is a kind of new automotive interior material with high elasticity and strength. Traditional TPE materials were difficult to meet the new requirements of large-scale automotive interior parts with complex shape. In this study, the TPE material was prepared using different mass ratios with homopolymer polypropylene (PP), styrene-ethylene/butene-styrene copolymer (SEBS), naphthene oil (NO), magnesium stearate (MGST), and polytetrafluoroethylene (PTFE). A quality-prediction and multiobjective optimization method based on a genetic algorithm was applied. The parameters that had an important effect on the forming quality were selected using an orthogonal testing method. Results showed that using the proposed method, a new TPE material is obtained with excellent scratch resistance ability and high MFI. The mechanisms of the addition of PTFE and MGST were analysed according to SEM images. The peel strength of the optimized part was measured to prove the coating quality of TPE material.

1. Introduction

Soft tactile interior has great advantages in visual and tactile aspects, which became the mainstream of interior materials in the automotive field. The processing technologies of soft tactile interior mainly include slush, cathode mould, and positive film. But these processes have disadvantages of low utilization rate of materials, high equipment costs and requirements [1]. Skin injection molding indicates the process of two-step injection. The core material is injected into the mold firstly. After the curing of the core material, the skin material is injected into the mold, covering the core material [2]. This technology can be used to make soft touch materials covering the interior parts by injecting soft tactile materials on the surface. In the skin injection molding process, reasonable process parameter design [3] and accurate process parameter measurement [4] can improve the quality of the molded component. Compared with traditional forming methods, this process has positive effects of low cost, high production efficiency and material utilization rate. It can improve the design freedom of the products [5, 6]. Thermoplastic elastomer (TPE) is a new material with low density, soft surface, and high elasticity and strength, which can be formed using injection. It is widely used as small interior decoration cladding parts such as automobiles and aeronautics. However, due to its poor fluidity and insufficient composite ability with polypropylene (PP), it cannot be used in large-size automotive door trim panels, dashboards, and other skin injection molding components. Srinivasan and Gupta [7] and Li H et al. [8] studied the mechanical properties and morphology of PP/SEBS/PC blends. It was found that adding SEBS into PP can improve the large deformation ability. But the small deformation performance was reduced. The addition of SEBS to PP/PC reduced the stress concentration of the blends and increased the overall yield strength of the matrix. Tiggemann et al. and Tomacheski et al. studied the influence of clay on the properties of SEBS/PP/oil thermoplastic elastomer [9, 10]. It was found that the addition of clay enhanced the tensile strength of the material. When a certain amount of clay was added, the

material showed the best mechanical properties. Ayaz et al. [11], Daneshpayeh et al. [12], and Ghasemi et al. [13] studied the impact strength and flexural strength of PP/LLDPE/TiO_2/SEBS nanocomposites by the Taguchi test. Kim et al. [14] and Vuluga et al. [15] studied the effect of repeated recycling on the structure and morphology of SEBS/PP composites. It was found that repeated recycling would degrade the triblock copolymer in SEBS, resulting in a slight decrease in hardness and a significant increase in viscosity. Sengupta et al. [16, 17] studied the effects of compositions and processing conditions on the morphology and properties of SEBS/PP/oil thermoplastic elastomer blends. It was found that SEBS/PP/oil blends had a continuous morphology, their SEBS phases were oriented together, and PP phases were decomposed in the polystyrene domain under high strain, which increased the elongation of the blends.

Current research mainly focused on the modification of TPE materials, changing the proportion of materials and additives, so as to improve the mechanical properties and meet the needs of production and life. However, the problems of low material fluidity, poor composite ability, and scratch resistance ability were not solved well.

In this study, TPE materials with different mass ratios of SEBS, PP, NO, MGST, and PTFE were prepared, and the materials with high MFI and excellent scratch resistance were designed by using genetic algorithm. The materials had better mold adaptability in injection moulding and could meet the requirements of large-size automobile interior parts with complex shape. The mechanisms of the addition of PTFE and MGST were analysed according to SEM images. The peel strength of the optimized part was carried out to prove the coating quality of TPE material.

2. Materials and Methods

2.1. Experimental Materials, Instruments, and Optimization Method. The materials used in this study were homopolymer polypropylene (PP), styrene-ethylene/butene-styrene copolymer (SEBS), naphthene oil (NO), magnesium stearate (MGST), and polytetrafluoroethylene (PTFE). Compared with other lubricants, MGST can reduce the adsorption of the surface powder and improve the fluidity. The same quality of MGST is better than talc and magnesia. The reason for choosing PTFE is that it has the lowest friction coefficient, and a lubricious film can be formed on the surface of the part. It has good lubricity and wear resistance under shearing force and better performance under high load conditions. The detailed information of these materials can be found below.

The melt mass flow rate of PP is 37 g/10 min. The properties of PP including density, hardness, notched impact strength, and tensile strength of PP are 0.98 g/cm^3, 70R, 22 J/m^2, and 32 MPa, respectively. This material was produced by Sinopec Co., Ltd.

The YH-503 powdery SEBS has low viscosity. The mass ratio of S and B is 30/70. The tensile strength, elongation, and hardness of the material are 26.5 MPa, 480%, and 75A, respectively. The SEBS was obtained from Yueyang Petrochemical Company.

The KN4010 naphthene oil also has low viscosity. The viscosity at the temperature of 100°C is 10.06 mm^2/s. The density and flash point of NO are 899.3 kg/m^3 and 215°C. This material was obtained from Xinjiang Karamay Company.

The density and melting point of pure MGST are 1.028 g/cm^3 and 132°C. For the PTFE powder used in this study, the particle size, density, and crystallinity are 0.2 μm, 2.3 g/cm^3, and 90–95%, respectively. The authors bought MGST and PTFE from DuPont Company of USA.

The high-speed mixer used in this study is SHR-25A from Zhangjiagang Light Industry Machinery Factory Co., Ltd.

The screw extruder applied in the current research is SHJ-20 from Nanjing Janet Electrical and Mechanical Co., Ltd. In the forming process, the temperature of the feeding section was 170°C. The temperature of the compression section and the metering section was 240°C. The temperature of the head section was 220°C and the screw speed was first stabilized at a lower speed, and the molten material was discharged. After the head was extruded, the screw speed was stabled at 20 rpm.

The skin injection molding machine is HDX50, produced by Guangdong Haida Injection Molding Machine Co., Ltd. The injection conditions are shown in Table 1. For the injection molding process, mold temperature was important for the crystallinity of material. From Zhao's work, it can be found that low mold temperature was beneficial for the improvement of crystallinity degree but negative for the uniformity of crystallinity. Therefore, the mold temperature was chosen as 40°C in the current study [18].

The melt flow rate instrument was MFI-1211 bought from Chengde Jinjian Testing Instrument Co., Ltd. The mechanical test machine was CMT6104 from Metis Industrial Systems (China) Co., Ltd. The electric cross gravimeter was 430P-I from Erichsen Company, Germany. The type of chromometer was X-Rite Color-Eye 7000A from American Aceroy Company. The SEM analysis was conducted using JSM-IT300 in Wuhan University of Technology.

The multiobjective optimization method developed by our team in the paper [19] was used to confirm the raw material ratio of the TPE material. In this method, the parameters that have an important effect on the responses are selected using an orthogonal testing method, and then a central composite design experiment is performed using these parameters. A mathematical model considering a response and impact factors is developed using the response surface method. The optimal combination of the impact parameters is finally determined using the NSGA-II (Nondominated Sorting Genetic Algorithm II). Detailed algorithm of this method can be found in our previous paper, but the difference is in TPE material here. Optimization can be performed based on the mass ratios of SEBS, PP, NO, MGST, and PTFE. The solving process of the method is illustrated in Figure 1.

2.2. Sample Preparation. SEBS and PP were placed in a vacuum drying chamber and dried at 100°C for more than 12 hours to ensure that their moisture content was below

Table 1: Injection conditions.

Parameters	Value	
	Skeleton	Coatings
Melt temperature (°C)	200	240
Mold temperature (°C)	40	40
Injection temperature (°C)	104	
Injection time (s)	3.0	0.8
V/P switching (filling volume percentage)	98	98
Holding pressure (percentage of filling pressure)	80	80
Holding time (s)	20	10
Cooling time (s)	—	20

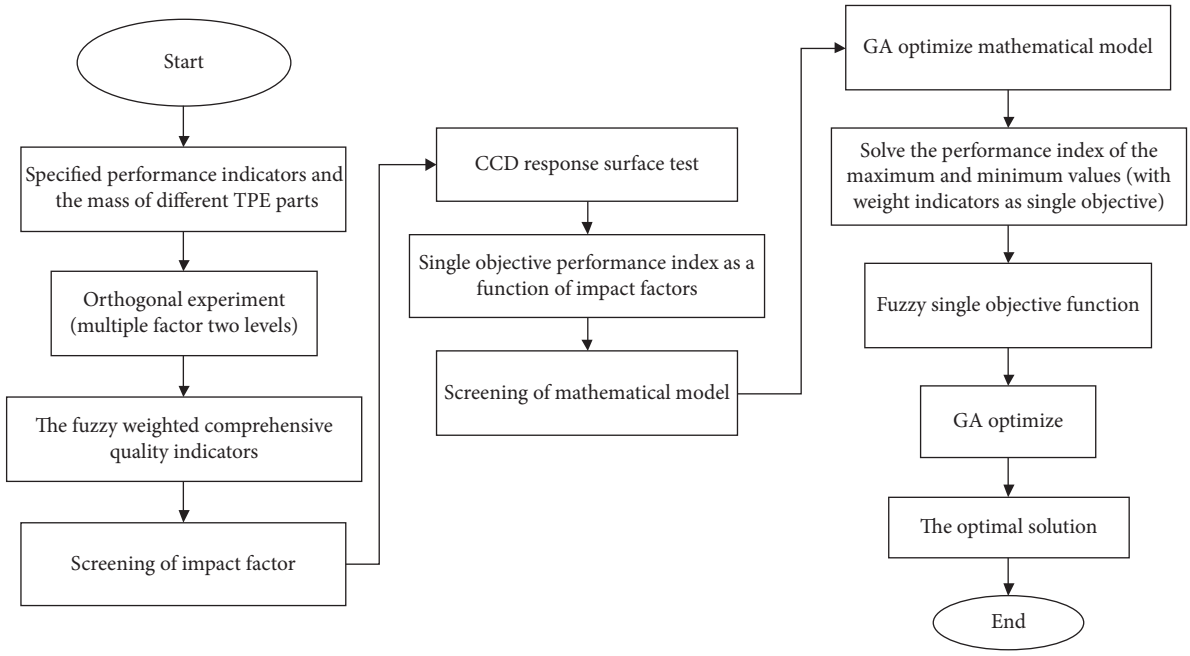

Figure 1: Solving process of the optimization method [19].

0.02%. The ratio of SEBS, NO, PP, MGST, and PTFE was defined as $A:B:C:D:E$. Firstly, the SEBS was put into the SHB-25A high-speed mixer, and then the temperature was decreased to room temperature. The NO was evenly sprinkled and mixed at a low speed of 500 r/min for 5 min. The PP material, MGST, and PTFE were added to the mixer with a high speed of 1000 r/min for 5 min, and then extruded in a TSE-40B twin-screw extruder. The pellets were then cut into test specimens by injection molding machine, as shown in Figure 2. Figure 2 shows a surface performance test piece based on the ISO7724 standard with a side length of 50 mm and a thickness of 4 mm. Since the mass ratio of each component has a great influence on the performance of the TPE material, the mass ratio of SEBS, NO, PP, MGST, and PTFE was determined by orthogonal experimental design. The general notation for orthogonal tables is Ln(ap), where p is the number of columns in the table (the number of factors), n is the number of rows in the table, and a is the number of levels. In this paper, 5 factors and 3 levels are selected; thus, the orthogonal table L27 (53) is used. The factors and levels are shown in Table 2.

According to the L27 (53) orthogonal table, at the same time, according to the factor level table shown in Table 2, 27 sets of test variable combinations were obtained, as shown in Table 3.

The formulations of TPE were designed with different mass ratio. Then the material was granulated by an extruder. The melt index was tested. The TPE material was then injected into a square test piece for injection performance testing. For a goal of consistent results, each experiment was repeated three times.

3. Results and Discussion

3.1. Performance Testing and Characterization. The melt index was tested according to ASTM D1238-95. The test temperature is 230°C, and the load is 2.16 kg. The melt index of each group mixture is shown in Table 4.

Scratch resistance ability was tested according to the following steps: the surface performance test samples of each component in Table 3 are taken, and each component was tested three times. The test load was 1 kg, and the scratch rate

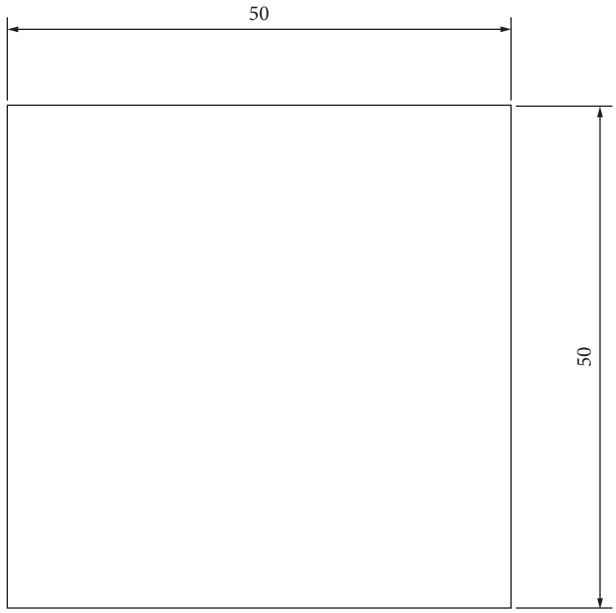

Figure 2: Test sample of surface performance.

Table 2: Factors and levels.

Level	Factors				
	A (SEBS)	*B* (NO)	*C* (PP)	*D* (MGST)	*E* (PTFE)
1	100	120	50	0	0
2	110	130	60	20	20
3	120	140	70	40	40

Table 3: Test variables.

No.	*A*	*B*	*C*	*D*	*E*
1	100	120	50	0	0
2	100	120	50	0	20
3	100	120	50	0	40
4	100	130	60	20	0
5	100	130	60	20	20
6	100	130	60	20	40
7	100	140	70	40	0
8	100	140	70	40	20
9	100	140	70	40	40
10	110	120	60	40	0
11	110	120	60	40	20
12	110	120	60	40	40
13	110	130	70	0	0
14	110	130	70	0	20
15	110	130	70	0	40
16	110	140	50	20	0
17	110	140	50	20	20
18	110	140	50	20	40
19	120	120	70	20	0
20	120	120	70	20	20
21	120	120	70	20	40
22	120	130	50	40	0
23	120	130	50	40	20
24	120	130	50	40	40
25	120	140	60	0	0
26	120	140	60	0	20
27	120	140	60	0	40

Table 4: Test average of TPE material properties.

No.	MFI (g/10 min)	Scratch resistance ΔL^*
1	106.25	1.49
2	95.43	0.96
3	79.21	0.47
4	139.55	1.82
5	121.32	1.27
6	96.28	0.55
7	162.33	2.42
8	147.32	1.58
9	126	0.69
10	152.45	2.15
11	131.12	1.42
12	110.35	0.58
13	109.42	1.36
14	97.24	0.89
15	81.24	0.43
16	140.25	1.75
17	122.41	1.09
18	97.26	0.49
19	159.34	1.97
20	143.21	1.24
21	106.32	0.64
22	155.23	2.04
23	133.87	1.57
24	111.75	0.66
25	110.84	1.21
26	99.43	0.78
27	86.88	0.39

was 1000 mm/min. At least 20 parallel scratch lines were produced with a spacing of 2 mm. Each sample was subjected to 5 separate tests, one in the middle and four in the corner (as shown in Figure 3), and the result was the average of the five values. The scratch resistance of each group of surface test samples is shown in Table 4. ΔL^* is the amount

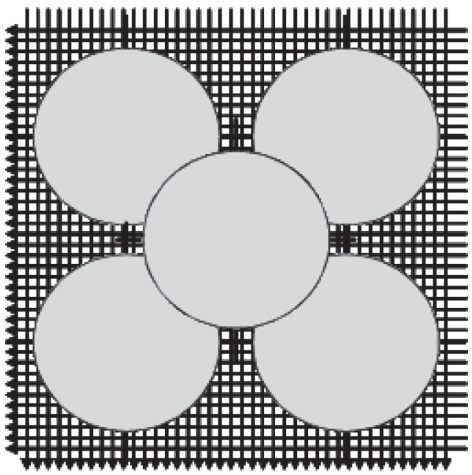

Figure 3: Test point location.

of the variation of value before and after the test. The smaller the value of ΔL^*, the better the scratch resistance of the surface of the model.

In order to find the best mathematical model of the two goals of MFI and scratch resistance, considering the interaction of each variable, the fitting method of linear interaction curve was adopted in the software Minitab to obtain the relationship between the melt index and the variable. The fitting relationship is shown in the following formula:
\openup3

$$\begin{aligned}
\text{MFI} &= -1178 + 12.34A + 16.50B - 16.92C \\
&\quad + 1.140 \quad D + 34.1E - 0.1535\,A * B \\
&\quad + 0.1332\,A * C - 0.213\,A * E \\
&\quad + 0.0157\,B * C - 0.299\,B * E \\
&\quad - 0.153\,C * E - 0.00540\,D * E \\
&\quad + 0.00187\,A * B * E - 0.00047\,A \\
&\quad * C * E + 0.00164\,B * C * E, \\
\text{Scratch resistance} &= -12.2 + 0.217A + 0.1729B - 0.315\,C \\
&\quad + 0.01971\,D - 0.111\,E - 0.002267\,A \\
&\quad * B + 0.001267\,A * C - 0.00013\,A \\
&\quad * E + 0.001317\,B * C - 0.00147\,B \\
&\quad * E + 0.00653\,C * E - 0.000448\,D \\
&\quad * E + 0.000021\,A * B * E - 0.000041\,A \\
&\quad * C * E - 0.000016\,B * C * E.
\end{aligned} \tag{1}$$

The multiobjective optimization of the surface qualities during the injection molding was developed according to the regression fitting, and the mathematical model is described as

$$\begin{aligned}
&\text{minimize} \quad y1,\ y2, \\
&\qquad y1 = -1178 + 12.34A + 16.50B \\
&\qquad\quad - 16.92C + 1.140 \\
&\qquad\quad D + 34.1E - 0.1535A \\
&\qquad\quad * B + 0.1332A * C \\
&\qquad\quad - 0.213A * E + 0.0157B \\
&\qquad\quad * C - 0.299B * E - 0.153C \\
&\qquad\quad * E - 0.00540 \\
&\qquad\quad D * E + 0.00187A \\
&\qquad\quad * B * E - 0.00047A * C \\
&\qquad\quad * E + 0.00164B * C * E, \\
&\qquad y2 = -12.2 + 0.217A + 0.1729B \\
&\qquad\quad - 0.315C + 0.01971 \\
&\qquad\quad D - 0.111E - 0.002267A \\
&\qquad\quad * B + 0.001267A * C \\
&\qquad\quad - 0.00013A * E \\
&\qquad\quad + 0.001317B * C \\
&\qquad\quad - 0.00147B * E + 0.00653C \\
&\qquad\quad * E - 0.000448 \\
&\qquad\quad D * E + 0.000021A * B \\
&\qquad\quad * E - 0.000041A * C * E \\
&\qquad\quad - 0.000016B * C * E, \\
&\text{S.T.} \qquad\quad - 1 < A, B, C, D, E < 1,
\end{aligned} \tag{2}$$

where $y1$ and $y2$ denote the MFI and scratch resistance, respectively, and A, B, C, D, and E are the impact parameters in Tables 2 and 3.

The multiobjective genetic algorithm was used to perform the optimization. The multiobjective optimization was implemented by the following steps:

Step 1: the min/max values for MFI ($\text{Min}_{\text{MF}}/\text{Max}_{\text{MF}}$) and scratch resistance ($\text{Min}_{\text{SR}}/\text{Max}_{\text{SR}}$) were determined within the specified domain of the impact factors by using min and max functions.

Step 2: the objective functions (MFI and scratch resistance) were fuzzy, where the parameters a and b for the MFI and scratch resistance were set as minimum and maximum, respectively, and $k = 1$ was used. The mapped objective functions were set as the multiobjective fitness functions and were described as

$$\begin{aligned}
f_1 &= \frac{1}{(\text{Max}_{\text{MF}} - \text{Min}_{\text{MF}})}\,(y_1 - \text{Min}_{\text{MF}}), \\
f_2 &= \frac{1}{(\text{Max}_{\text{SR}} - \text{Min}_{\text{SR}})}\,(y_2 - \text{Min}_{\text{SR}}).
\end{aligned} \tag{3}$$

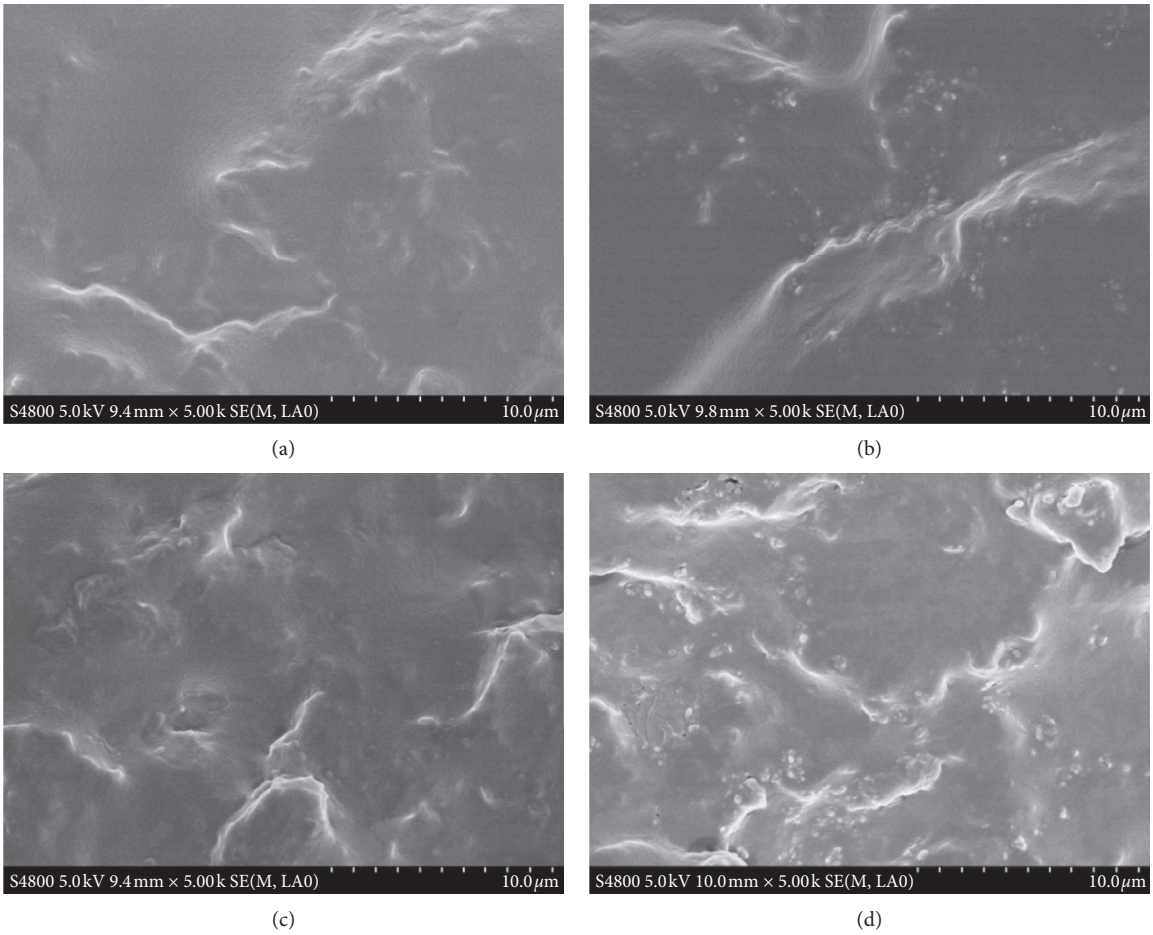

Figure 4: SEM images of samples of (a) original TPE, (b) TPE with MGST, (c) TPE with PTFE, and (d) TPE with MGST and PTFE.

Step 3: the optimal front set, population, and fitness function deviation were set to be 50,200 and 1e-100. The multiobjective genetic algorithm was used to calculate its Pareto optimal solution set. According to the requirements of the quality of the components, MFI and scratch resistance are both very important. Therefore, the nearest solution to the origin of the distance coordinates was selected as the final solution of this study. The optimal parameters were obtained: SEBS is 109.972, naphthenic oil is 139.978, PP is 40.01, MGST is 38.7, and PTFE is 7.23. The combination of these parameters yielded a maximum MFI of 170.25 mm and minimum scratch resistance of 0.29.

3.2. Mechanism Analysis. It is well known that the MGST and PTFE have obvious influence on the scratch resistance ability. Therefore, the surface topographies of the samples with or without these two compositions were obtained using SEM observation, as shown in Figure 4. Figure 4(a) is the image of the original TPE (the material contains only SEBS, NO and PP, and without MGST and PTFE). Figure 4(b) is an SEM image of TPE with additional PTFE sample, and Figure 4(c) is a TPE sample with MGST. Figure 4(d) is the SEM image of the sample with the addition of MGST and PTFE.

Comparing Figures 4(a) and 4(b), it can be seen that after the addition of PTFE to the TPE matrix, granules appear in the dispersed phase of the matrix. Since PTFE is a layered crystal structure formed with van der Waals force, the molecules are easily released. Therefore, when PTFE and TPE matrix are mixed, melted, granulated, and injected, the molecules of PTFE fall off and combine with TPE. The dual-preferred transfer film is preferentially formed on the dual surface. The adhesive wear changes to abrasive wear, which significantly improves the scratch resistance of the material. Comparing Figures 4(a) and 4(c), it can be seen that after the addition of MGST to the TPE matrix, the originally larger dispersed phase is changed to a large number of small dispersed phases. The interfacial tension of the material, while some of the potholes are filled by the small dispersed phase, can significantly increase the melt index of the material. Comparing Figures 4(c) and 4(d), it can be seen that with the addition of MGST and PTFE to the TPE matrix, the PTFE abrasive particles can be combined with the small dispersion. The MFI is reduced due to the lower cohesion and adhesion of the abrasive particles. At the same time, since MGST is more likely to be adhesive wear, the material

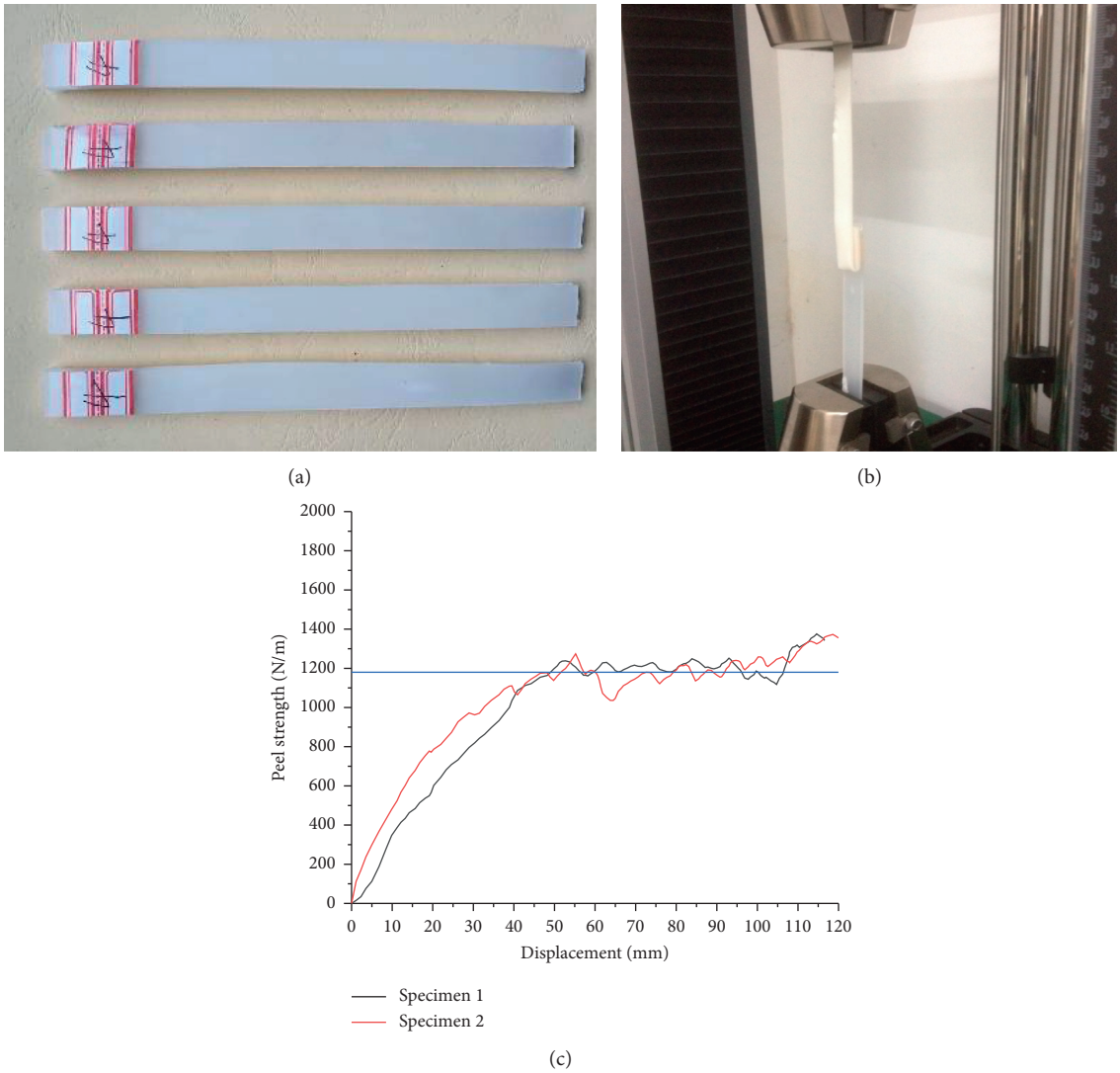

Figure 5: (a) Testing sample, (b) testing process, and (c) strength-displacement curve.

is mainly characterized by abrasive wear accompanied with slight adhesive wear.

3.3. Peel Strength Verification. In order to get the mechanical properties of optimized material, the peel strength test was carried out. As shown in Figure 5(a), the formed sample was processed into a rectangular spline (170 × 10 mm) to perform a peeling test. The test was referred to GB/T2790-1995, the peeling rate was 50 mm/min, and the test was carried out at room temperature. In most interior parts of automobiles, the adhesion of the surface cladding to the skeleton needs to be greater than 525 N/m (refer to GMW 14892-2012). In the peeling test, a part of the TPE material was previously separated from the PP material. The TPE and PP materials were, respectively, placed on the upper and lower ends of the testing machine (as shown in Figure 5(b)). As the displacement of the tester beam increased, the deformation was carried out. The tensile force of the TPE material was also improved continuously. Finally, as the peeling progressed, the peeling force of the two materials gradually stabilized. As shown in Figure 5(c), the average peel strength at which the spline peel strength tends to be stable is indicated by a horizontal straight line. It can be seen from the figure that the curve shows an upward trend when the displacement is <50 mm, and the peel strength tends to be stable after the displacement ≥50 mm. The average peeling value is close to 1200 N/m (greater than 525 N/m), indicating that the optimized sample has good coating properties.

4. Conclusion

The automotive interior material requires soft touch, excellent injection performance, and good surface scratch resistance. In order to achieve these goals, the TPE material was modified to obtain the optimal ratio of components by using genetic algorithm. The ideal material with low surface hardness, high MFI, and excellent scratch resistance was obtained. The specific results are as follows:

(1) The parameters were selected using an orthogonal testing method. The optimized ratio of SEBS, PP, NO, MGST, and PTFE of TPE material can be obtained using genetic algorithm. The optimal parameters were obtained as follows: SEBS is 109.972, NO is 139.978, PP is 40.01, MGST is 38.7, and PTFE is 7.23. Using the optimized results, the TPE material has higher MFI of 170.25 and scratch resistance of 0.29.

(2) When PTFE and TPE matrix were mixed, melted, granulated, and injected, the molecules of PTFE fall off and combine with TPE. The dual-preferred transfer film was preferentially formed on the dual surface. The adhesive wear changed to abrasive wear, which significantly improved the scratch resistance of the material.

(3) After the addition of MGST to the TPE matrix, the originally larger dispersed phase was changed to a large number of small dispersed phases. The interfacial tension of the material, while some of the potholes were filled by the small dispersed phase, can significantly increase the MFI of the material.

(4) When both MGST and PTFE were added to the original TPE material, the PTFE abrasive particles can be combined with the small dispersion. The MFI was reduced due to the lower cohesion and adhesion of the abrasive particles. The material was mainly characterized by abrasive wear accompanied with slight adhesive wear. The results of peel strength test proved that the average peeling value is close to 1200 N/m (greater than 525 N/m), indicating that the optimized sample had excellent coating properties.

Data Availability

The data used to support the findings of this study are included within the article.

Conflicts of Interest

The authors declare that they have no conflicts of interest.

Acknowledgments

The authors would like to acknowledge the financial support from the National Natural Science Foundation Council of China (Grant nos. 51775398 and 51805392), the 111 Project (Grant no. B17034), the Program for Innovative Research Team in University of Education Ministry (Grant no. IRT_17R83), the Nature Science Foundation of Hubei Province (Grant no. 2018CFB595), and the Fundamental Research Funds for the Central Universities (Grant nos. WUT:2018III074GX and 2018III067GX).

References

[1] W. Zhang, H. Chang, Y. Dou et al., "Polyurethane slush powders for instrument panel of automobiles: composition, processing and rheological properties," *Materials Review*, vol. 32, no. 12, pp. 4392–4397, 2018.

[2] M. Viana, D. Martino, A. J. Pontes, and J. C. au, "Co-injection molding of immiscible polymers: skin-core structure and adhesion studies," *Polymer Engineering & Science*, vol. 51, no. 12, pp. 2398–2407, 2011.

[3] H. Daniel, "Multivariate process analysis for the prediction of injection molded part quality," 2019.

[4] J. Zhang, P. Zhao, Y. Zhao, J. Huang, N. Xia, and J. Fu, "On-line measurement of cavity pressure during injection molding via ultrasonic investigation of tie bar," *Sensors and Actuators A: Physical*, vol. 285, pp. 118–126, 2019.

[5] L. Y. Hsieh and K.-H. Chang, "Yield improvement on in-mold decoration manufacturing through parameter optimization," *International Journal of Precision Engineering and Manufacturing*, vol. 14, no. 10, pp. 1823–1828, 2013.

[6] V Goodship, "Design and manufacture of plastic components for multifunctionality," in *Injection Molding of Thermoplastics*, pp. 103–170, Springer, Berlin, Germany, 2016.

[7] K. R. Srinivasan and A. K. Gupta, "Mechanical properties and morphology of PP/SEBS/PC blends," *Journal of Applied Polymer Science*, vol. 53, no. 1, pp. 1–17, 1994.

[8] H. Li, X. Sui, and X. M. Xie, "Correlation of morphology evolution with superior mechanical properties in PA6/PS/PP/SEBS blends compatibilized by multi-phase compatibilizers," *Chinese Journal of Polymer Science*, vol. 36, no. 7, pp. 848–858, 2018.

[9] H. M. Tiggemann, V. F. Ribeiro, F. Celso, and S. M. B. Nachtigall, "Effect of commercial clays on the properties of SEBS/PP/oil thermoplastic elastomers. Part 1: physical, mechanical and thermal properties," *Applied Clay Science*, vol. 109-110, pp. 151–156, 2015.

[10] D. Tomacheski, M. Pittol, C. E. Ermel, D. N. Simões, V. F. Ribeiro, and R. M. C. Santana, "Influence of processing conditions on the mechanical properties of SEBS/PP/oil blends," *Polymer Bulletin*, vol. 74, no. 11, pp. 1–15, 2017.

[11] M. Ayaz, S. Daneshpayeh, and A. Noroozi, "Enhancing the impact and flexural strength of PP/LLDPE/TiO2/SEBS nanocomposites by using Taguchi methodology," *Composites Science and Technology*, vol. 129, pp. 61–69, 2016.

[12] S. Daneshpayeh, F. Ashenai Ghasemi, I. Ghasemi, and M. Ayaz, "Predicting of mechanical properties of PP/LLDPE/TiO_2 nano-composites by response surface methodology," *Composites Part B: Engineering*, vol. 84, pp. 109–120, 2016.

[13] F. A. Ghasemi, S. Daneshpayeh, I. Ghasemi, and M. Ayaz, "An investigation on the Young's modulus and impact strength of nanocomposites based on polypropylene/linear low-density polyethylene/titan dioxide (PP/LLDPE/TiO_2) using response surface methodology," *Polymer Bulletin*, vol. 73, no. 6, pp. 1741–1760, 2016.

[14] J.-K. Kim, C.-H. Kim, and M.-H. Park, "Effects of multiple recycling on the structure and morphology of SEBS/PP composites," *Bulletin of the Korean Chemical Society*, vol. 37, no. 6, pp. 820–825, 2016.

[15] Z. Vuluga, D. M. Panaitescu, C. Radovici, C. Nicolae, and M. D. Iorga, "Effect of SEBS on morphology, thermal, and mechanical properties of PP/organoclay nanocomposites," *Polymer Bulletin*, vol. 69, no. 9, pp. 1073–1091, 2012.

[16] P. Sengupta and J. W. M. Noordermeer, "Effects of composition and processing conditions on morphology and properties of thermoplastic elastomer blends of SEBS-PP-oil and dynamically vulcanized EPDM-PP-oil," *Journal of Elastomers & Plastics*, vol. 36, no. 4, pp. 307–331, 2004.

[17] W. G. F. Sengers, P. Sengupta, J. W. M. Noordermeer, S. J. Picken, and A. D. Gotsis, "Linear viscoelastic properties of olefinic thermoplastic elastomer blends: melt state properties," *Polymer*, vol. 45, no. 26, pp. 8881–8891, 2004.

[18] P. Zhao, W. Yang, X. Wang, J. Li, B. Yan, and J. Fu, "A novel method for predicting degrees of crystallinity in injection molding during packing stage," *Proceedings of the Institution of Mechanical Engineers, Part B: Journal of Engineering Manufacture*, vol. 233, no. 1, pp. 204–214, 2019.

[19] Z. Yuan, H. Wang, X. Wei et al., "Multiobjective optimization method for polymer injection molding based on a genetic algorithm," *Advances in Polymer Technology*, vol. 2019, Article ID 9012085, 17 pages, 2019.

Hindawi
Advances in Polymer Technology
Volume 2020, Article ID 6154694, 10 pages
https://doi.org/10.1155/2020/6154694

Research Article

Optimization of Residual Wall Thickness Uniformity in Short-Fiber-Reinforced Composites Water-Assisted Injection Molding Using Response Surface Methodology and Artificial Neural Network-Genetic Algorithm

Haiying Zhou,[1,2] **Hesheng Liu**,[1,2] **Tangqing Kuang**,[3] **Qingsong Jiang**,[2] **Zhixin Chen**,[2] **and Weiping Li**[2]

[1]*School of Mechanical and Electrical Engineering, Nanchang University, Nanchang 330031, China*
[2]*Jiangxi Province Key Laboratory of Polymer Micro/Nano Manufacturing and Devices, East China University of Technology, Nanchang 330013, China*
[3]*School of Mechanical and Electrical Engineering, East China Jiaotong University, Nanchang 330013, China*

Correspondence should be addressed to Hesheng Liu; hsliu@vip.163.com

Received 17 June 2019; Accepted 29 July 2019; Published 26 February 2020

Guest Editor: Yun Zhang

Copyright © 2020 Haiying Zhou et al. This is an open access article distributed under the Creative Commons Attribution License, which permits unrestricted use, distribution, and reproduction in any medium, provided the original work is properly cited.

This study aimed at improving the residual wall thickness uniformity (RWTU), which was closely related to the mechanical properties of plastic parts with a hollow cross-section, in short-fiber reinforced composites (SFRC) overflow water-assisted injection molding (OWAIM). The influences of five independent process parameters (melt temperature, mold temperature, delay time, water pressure, and water temperature) on RWTU were investigated through the methods such as central composite design, regression equation, and analyses of variance. Response surface methodology (RSM) and artificial neural network (ANN) optimized by genetic algorithm (GA) were employed to map the relationship between the process parameters and the standard deviation (SD) depicting the RWTU. Comparison assessments of three models (RSM, ANN, and ANN-GA) were carried out through some statistical indexes. It was concluded that the effect of melt temperature, delay time, and water temperature were significant to RWTU; the hybrid ANN-GA model had the best performance for predicting SD compared with RSM and ANN; the least SD obtained in optimization using ANN-GA as a fitness function was 0.0972.

1. Introduction

Overflow water-assisted injection molding (OWAIM) is a promising method for producing functional plastic parts with hollow sections and thin residual wall thickness (RWT) [1–3]. The process of OWAIM includes two steps. First, the functional part cavity is filled with the melted polymer. Second, after a short delay time, the high-pressure water is injected into the core to push the melt into the overflow cavity to form a functional part with a hollow cross-section. This technology has many advantages such as polymer saving, short cycle time, lower injection pressure, less warpage, better surface quality, enhanced flexibility in mold design, etc., [4].

Great attention has been paid to the RWT which is an important indicator for assessing the quality of overflow water-assisted injection molded parts [5–9]. The experiments and simulations indicated that the distribution of the RWT was uneven in OWAIM. The plastic parts with thin, uneven RWT are difficult to meet the mechanical performance requirement in special application. Using short-fiber reinforced composites (SFRC) as raw materials can significantly improve the mechanical properties of a plastic part [10, 11]. But it makes the process of OWAIM more complicated which results in a more uneven RWT. The residual wall thickness uniformity (RWTU) of a plastic part is related to the overall mechanical properties. Thus, for the wide application in different fields, it is urgent to improve the RWTU of plastic parts in OWAIM.

In the traditional plastic manufacturing industry, product quality improvement mainly depends on the workers' experience and trial and error, which is costly, time-consuming, and greatly

decrease the product competitiveness [12]. Fortunately, the development of information processing technology, using statistical methods, and artificial intelligence algorithm for modeling and optimizing quality objectives, significantly shorten the cycle time of product designing and reduce the product cost [13–15]. RWTU is influenced by the many factors such as material properties, mold structure, process parameter, etc. Generally, adjusting the process parameter setting for optimization is an approach adopted by industry plants. Thus, it is crucial to construct the relationships between the process parameters and RWTU.

Response surface methodology (RSM), based on statistical theory, is a classic and effective approach and has been widely applied for modeling and optimization. RSM is very useful for developing, improving, and optimizing the responses that are affected by multiple independent variables [16, 17]. RSM can be applied to evaluate the correlation between the responses and the independent variables and define the influences of the independent variables individually or in combination. However, the nonlinearity of OWAIM processes may be difficult for RSM to achieve better model accuracy and generalization. Artificial neural network (ANN), as an effective method for mapping linear and nonlinear relationships between factors and targets, is widely used for modeling, prediction, classification, and pattern recognition [18, 19]. However, the performance of ANN trained by the gradient decent algorithm is greatly affected using the inappropriate initial weights and bias, which causes local minima [20]. Genetic algorithm (GA), inspired by the biological evolution theory, is a global optimization tool and can be used to search the optimal initial weights and bias for ANN. The combination of ANN and GA (ANN-GA) has been successfully used in optimization studies [21, 22].

Up to our knowledge, limited worthwhile research has been implemented for the improvement of RWTU in SFRC OWAIM. In this study, the numerical experiments, arranged using a central composite design (CCD), have been carried out. RSM and ANN-GA were employed to map the relationship between the RWTU and the process parameters (melt temperature, mold temperature, delay time, water pressure, and water temperature). The significance of five process parameters was studied through the analyses of variance (ANOVA). The prediction performance of RSM, ANN, and ANN-GA models were compared using the linear regression equation and statistical indicators. Finally, the model with the best prediction performance was used as the fitness function of the GA to optimize the RWTU of the plastic part in SFRC OWAIM.

2. Methods

2.1. Related Mathematical Model. During the simulation of OWAIM, the melt flow is regarded as nonisothermal, transient, and nonNewtonian. It is assumed that the melt is incompressible, laminar, and the inertia term is ignored. The basic governing equations for melt flow are as follows.

$$\frac{\partial P}{\partial t} + \nabla \cdot \rho \boldsymbol{u} = 0, \tag{1}$$

$$\frac{\partial}{\partial t}(\rho \boldsymbol{u}) + \nabla \cdot (\rho \boldsymbol{u}\boldsymbol{u} - \boldsymbol{\tau}) = \rho g, \tag{2}$$

$$\rho C_p \left(\frac{\partial T}{\partial t} + \boldsymbol{u} \cdot \nabla T \right) = \nabla \cdot (k \nabla T) + \eta \gamma^2, \tag{3}$$

$$\boldsymbol{\tau} = -p\boldsymbol{I} + \eta\left(\nabla \boldsymbol{u} + \nabla \boldsymbol{u}^T\right), \tag{4}$$

where P is the pressure; T the temperature; t the time; $\boldsymbol{u}$ the speed; $\boldsymbol{\tau}$ the stress tensor; ρ the density; η the viscosity; k the thermal conductivity; C_p the specific heat; and γ the shear strain.

A constitutive equation with seven parameters is used to describe the relationship between melt viscosity and temperature and shear rate.

$$\eta(\dot{\gamma}, T, P) = \frac{\eta_0(T, P)}{1 + \left(\eta_0 \dot{\gamma}/\tau^*\right)^{1-n}}, \tag{5}$$

$$\eta_0(T, P) = D_1 \exp\left(\frac{-A_1(T - T_c)}{A_2 + (T - T_c)} \right), \tag{6}$$

$$T_c = D_2 + D_3 P, \tag{7}$$

$$A_2 = \widetilde{A}_2 + D_3 P, \tag{8}$$

where η is the viscosity; η_0 the zero shear viscosity; $\dot{\gamma}$ the shear rate; τ^* the material constant; n the power rate index; T the melt temperature; T_c the glass transition temperature; D_1, D_2, D_3, A_1, and $\widetilde{A}_2$ are the relative constants associated with the selected material.

In the high-pressure water filling stage, the volume of fluid (VOF) model is used to track the interface of the melt and water. F_i is the volume fraction of the i-th phase, and $0 \le F_i \le 1$. When a unit is completely occupied by the i-th phase, F_i takes a value of 1. When a unit does not have the i-th phase, F_i takes a value of zero.

$$\frac{\partial F_i}{\partial t} + \nabla \cdot (\boldsymbol{u} F_i) = 0. \tag{9}$$

2.2. Geometric Model in Simulation. As shown in Figure 1, the geometric model used in the simulation was composed of a runner, an overflow cavity and a functional plastic part with a diameter 16 mm and two elbows. The model built by Pro/E was meshed using the commercial software of Moldex3D. The numbers of mesh nodes and mesh elements were 60175 and 195118, respectively. The short glass fiber reinforced PP (Fiberfil J-68/20/E with a short fiber mass fraction of 20% and an aspect ratio of 20) was selected as the raw material in the simulation and its properties were available in the data bank of Moldex3D.

2.3. Definition of Residual Wall Thickness Uniformity. The values of RWT were measured at ten different locations along the central axis of the functional part as shown in Figure 2. Standard deviation (SD), which reflects the degree of dispersion among individuals in a group, was defined as an indicator for evaluating the RWTU. The formula of SD can be expressed as the following:

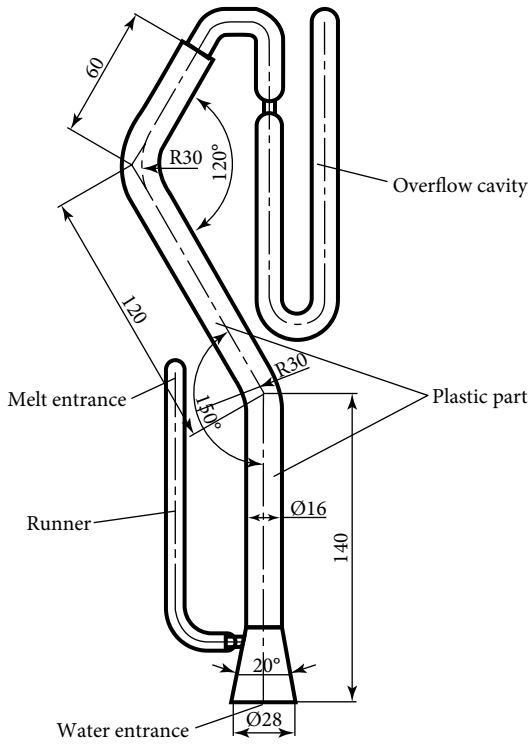

Figure 1: Geometric model for simulation.

$$\mathrm{SD} = \sqrt{\frac{1}{N}\sum_{i=1}^{N}\left(R_i - R_{\mathrm{avg}}\right)^2}, \quad (10)$$

where R_i is the value of RWT measured at the i-th point; R_{avg} is the average value of RWT; N is the total number of points.

2.4. Experimental Design. The process parameters such as melt temperature, mold temperature, delay time, water pressure, and water temperature were considered in this study. In general, those process parameters were easily controlled in the experiments and production for adjusting the important indicators of plastic parts. The process windows recommended for OWAIM were melt temperature [210°C, 230°C], mold temperature [42°C, 62°C], delay time [1 s, 5 s], water pressure [8 MPa, 12 MPa], and water temperature [20°C, 30°C]. In order to reduce the experiment times and comprehensively examine the influences of the process parameters on RWTU, the CCD based on RSM was applied to arrange the simulation experiments. The coded and actual values of five independent process parameters are shown in Table 1. Fifty experiments composed of 42 factorial and axial points and 8 center points are demanded for the CCD with three levels and five factors. The center points with the same process parameters result in the same RWT in the simulations. Therefore, the total number of experiments is 43. The details of the arrangements are revealed in Table 2.

2.5. Response Surface Methodology. The method of RSM based on the statistical technology was employed for the multiple regression analysis of experimental data obtained from the CCD. The relationship between the independent process parameters and the response SD is depicted using a second-order polynomial equation.

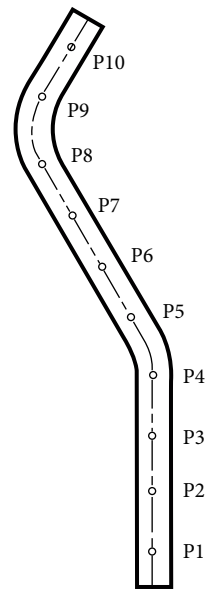

Figure 2: Locations for measuring residual wall thickness.

Table 1: Factors and level of process parameters.

Process parameter	Level		
	Low	Mean	High
Melt temperature (X_1)/[°C]	−1 (210)	0 (220)	1 (230)
Mold temperature (X_2)/[°C]	−1 (42)	0 (52)	1 (62)
Delay time (X_3)/[s]	−1 (1)	0 (3)	1 (5)
Water pressure (X_4)/[MPa]	−1 (8)	0 (10)	1 (12)
Water temperature (X_5)/[°C]	−1 (20)	0 (25)	1 (30)

$$\mathrm{SD} = \beta_0 + \sum_{i=1}^{5}\beta_i X_i + \sum_{i=1}^{4}\sum_{j=i+1}^{5}\beta_{ij}X_iX_j + \sum_{i=1}^{5}\beta_{ii}X_i^2, \quad (11)$$

where X_i and X_j are the independent process parameters; β_0 is the intercept constant; β_i is the linear coefficient; β_{ij} is the interaction coefficient and β_{ii} is the quadratic coefficient. The regression studies and ANOVA were implemented using the software of Design-Expert 8.0.

2.6. Artificial Neural Network. ANN inspired by biologic neural system is a computing model used to map linear or nonlinear factors and responses relationships. An ANN model comprises three parts: one input layer, one or more hidden layers, and one output layer. Each layer consists of a number of neurons. The numbers of neurons in the input layer and the output layer are determined by the numbers of factors and responses, respectively. In this study, an ANN model with one hidden layer was employed for modeling. The gradient descent algorithm was used for training model. The transfer functions of "*Tansig*" and "*Purelin*" were applied in the hidden layer and the output layer, respectively. By changing the number of neurons in the hidden layer from 5 to 15, the ANN topology of 5–11–1 was determined according to the minimum mean square error between the targets and the outputs. The ANN model is demonstrated in Figure 3.

Table 2: Experimental matrix and corresponding results.

No.	X_1	X_2	X_3	X_4	X_5	SD	No.	X_1	X_2	X_3	X_4	X_5	SD
1	0	0	−1	0	0	0.177	23	−1	1	−1	−1	1	0.180
2	−1	−1	−1	1	1	0.185	24	0	0	0	0	0	0.150
3	1	−1	1	1	1	0.183	25	1	−1	1	−1	−1	0.125
4	0	0	0	−1	0	0.164	26	0	0	0	1	0	0.163
5	−1	−1	1	−1	1	0.163	27	1	1	−1	1	1	0.189
6	−1	−1	−1	1	−1	0.224	28	1	−1	1	−1	1	0.215
7	1	1	1	−1	1	0.239	29	−1	−1	1	1	1	0.16
8	1	−1	−1	1	1	0.230	30	−1	1	−1	1	1	0.207
9	1	−1	−1	−1	1	0.200	31	−1	1	−1	1	−1	0.187
10	0	0	0	0	−1	0.162	32	1	0	0	0	0	0.190
11	1	−1	−1	−1	−1	0.201	33	0	0	1	0	0	0.158
12	1	1	1	1	−1	0.154	34	−1	1	1	1	1	0.157
13	1	−1	−1	1	−1	0.214	35	1	1	−1	−1	1	0.231
14	−1	−1	1	−1	−1	0.163	36	1	1	1	1	1	0.187
15	−1	1	1	1	−1	0.112	37	−1	1	1	−1	1	0.138
16	0	0	0	0	1	0.157	38	1	−1	1	1	−1	0.154
17	−1	1	−1	−1	−1	0.150	39	−1	−1	−1	−1	1	0.173
18	0	−1	0	0	0	0.165	40	0	1	0	0	0	0.177
19	−1	−1	1	1	−1	0.148	41	−1	0	0	0	0	0.130
20	1	1	−1	−1	−1	0.169	42	1	1	1	−1	−1	0.135
21	−1	−1	−1	−1	−1	0.151	43	1	1	−1	1	−1	0.190
22	−1	1	1	−1	−1	0.167							

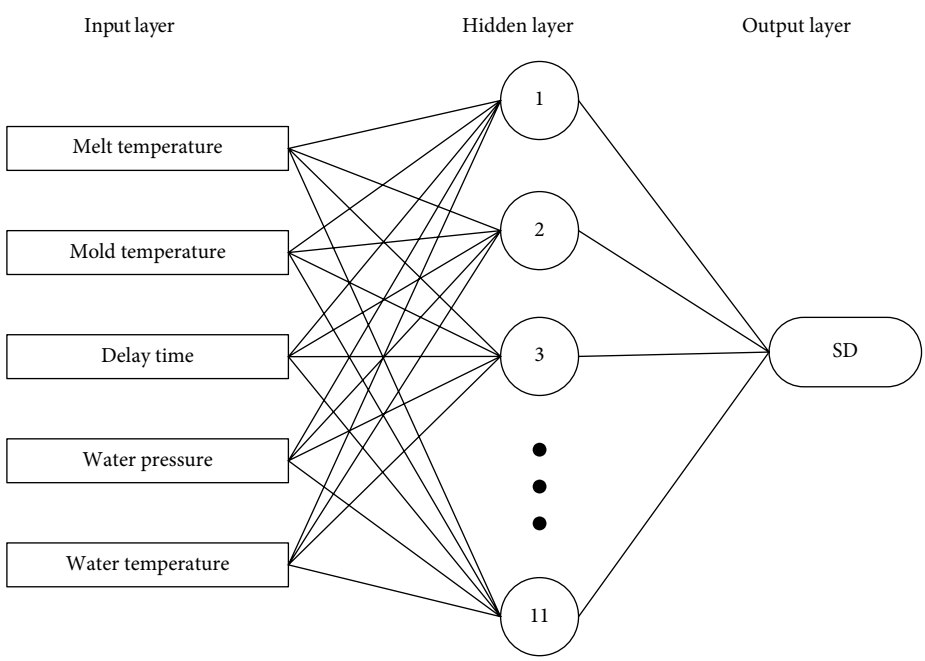

Figure 3: Topology of artificial neural network.

2.7. Genetic Algorithm. The genetic algorithm based on natural selection and survival of fitness is a global searching algorithm, and it is widely used in the fields of optimization, pattern recognition, robots, and prediction. Compared with other optimization methods, GA has many advantages including being not easy to be trapped into the local minima, requiring little prior information about the searched objectives, and easy identification of the optima in a complex search space.

The major operations of GA are summarized as follows: (1) Selection: individuals are selected based on their fitness so that better individuals are given a higher chance of being chosen, (2) Crossover: exchange the information of the two parents to generate a new individual according to the crossover probability, (3) Mutation: randomly alter the information of each chromosome according to the mutation probability.

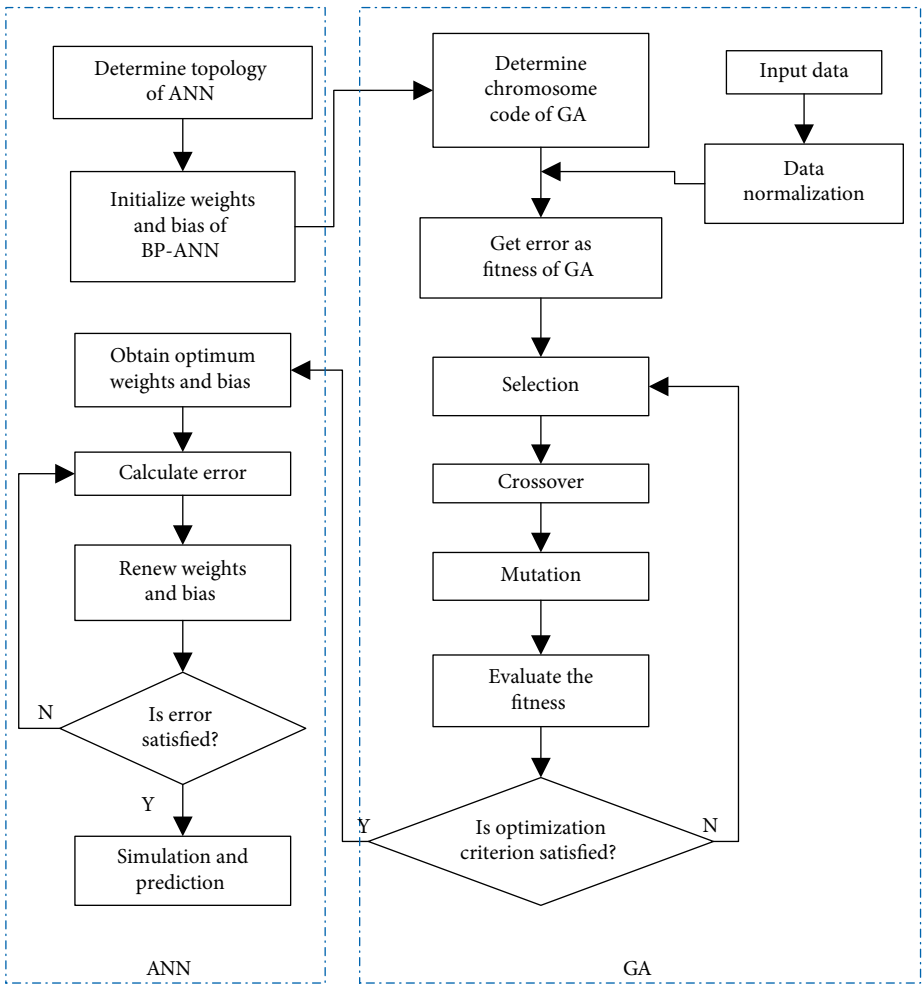

Figure 4: Flow chart of the hybrid model of ANN-GA.

2.8. Hybrid Model of Artificial Neural Network and Genetic Algorithm. GA was utilized to optimize the initial weights and bias for improving the prediction performance of ANN. The flow chart of ANN-GA is illustrated in Figure 4. The chromosome codes of GA consisted of the weights and bias of ANN. The mean square error between the experimental value and the prediction of ANN was used as the fitness function of GA. Then, genetic operations, such as selection, crossover, and mutation, were conducted to reproduce the new generation. As the new individuals replaced the parent individuals, the populations of GA were renewed. The abovementioned process repeated until the predefined generation number or the optimization criterion was satisfied.

Before training model, all the process parameter vectors and the observations in the simulations were normalized into the range [−1, 1] using the "mapmaxmin" function. All the calculations and optimizations were conducted under the environment of Matlab R2015b.

2.9. Statistical Analysis. To evaluate the performance of the different model for predicting SD, two statistic indicators including root mean square error (RMSE) and correlative coefficient (R) were calculated. These statistical parameters are defined as the following:

$$\mathrm{RMSE} = \sqrt{\frac{\sum_{i=1}^{N}(y_i - x_i)^2}{N}}, \tag{12}$$

$$\mathrm{R} = \frac{\sum_{i=1}^{N}(x_i - x_{\mathrm{avg}})(y_i - y_{\mathrm{avg}})}{\sqrt{\sum_{i=1}^{N}(x_i -)^2 \sum_{i=1}^{N}(y_i - y_{\mathrm{avg}})^2}}, \tag{13}$$

where x_i is the experimental value; y_i is the corresponding prediction; x_{avg} is the average of the experimental values; y_{avg} is the average of the predictions; N is the total number of simulations.

3. Results and Discussion

3.1. Simulation Results. The process of OWAIM includes a melt filling stage and a high-pressure filling stage. As shown in Figure 5(a), the mold cavity of the functional plastic part is filled with the high-temperature melt. During the short delay time, the outer layer of the melt is affected by the mold cavity, resulting in a decrease of temperature. Therefore, a thin melt layer with high viscosity is formed due to the heat conduction. Figure 5(b) demonstrates the result of high-pressure water

Table 3: ANOVA for Response Surface Quadratic Model.

Source	Sum of squares	df	Mean square	F value	p-value prob > F	
Model	0.03	20	1.51E–03	4.61	0.0001	Significant
X_1	4.97E–03	1	4.97E–03	15.2	0.0005	Significant
X_2	2.13E–04	1	2.13E–04	0.65	0.4266	
X_3	7.35E–03	1	7.35E–03	22.5	<0.0001	Significant
X_4	1.88E–04	1	1.88E–04	0.58	0.454	
X_5	4.43E–03	1	4.43E–03	13.55	0.0009	Significant
X_1X_2	5.25E–05	1	5.25E–05	0.16	0.6914	
X_1X_3	9.03E–06	1	9.03E–06	0.028	0.8691	
X_1X_4	3.71E–04	1	3.71E–04	1.14	0.2952	
X_1X_5	2.30E–03	1	2.30E–03	7.02	0.0129	Significant
X_2X_3	8.78E–05	1	8.78E–05	0.27	0.6082	
X_2X_4	5.53E–04	1	5.53E–04	1.69	0.2036	
X_2X_5	5.70E–04	1	5.70E–04	1.74	0.1971	
X_3X_4	2.13E–03	1	2.13E–03	6.51	0.0162	Significant
X_3X_5	9.57E–04	1	9.57E–04	2.93	0.0977	
X_4X_5	8.30E–04	1	8.30E–04	2.54	0.1218	
X_1^2	2.18E–07	1	2.18E–07	6.66E–04	0.9796	
X_2^2	3.16E–04	1	3.16E–04	0.97	0.3338	
X_3^2	1.50E–04	1	1.50E–04	0.46	0.503	
X_4^2	3.57E–05	1	3.57E–05	0.11	0.7435	
X_5^2	1.02E–07	1	1.02E–07	3.13E–04	0.986	
Residual	9.48E–03	29	3.27E–04			
Lack of fit	9.48E–03	22	4.31E–04			
Pure error	0	7	0			
Cor total	0.04	49				

Table 4: Optimal weights and bias for ANN-GA model.

Hidden layer						Output layer	
Weights					Bias	Weights	Bias
−0.045	0.411	−0.219	0.327	−0.389	−0.209	0.307	−0.243
0.426	0.463	0.239	−0.256	−0.302	−0.058	−0.240	
0.358	0.336	−0.062	0.349	−0.042	−0.381	0.065	
0.419	−0.104	0.147	0.428	−0.221	−0.220	−0.480	
−0.007	0.348	−0.322	−0.248	0.489	0.188	−0.187	
0.229	0.316	0.388	0.454	0.258	0.113	−0.141	
0.439	−0.174	−0.413	−0.289	0.171	−0.002	−0.411	
0.414	0.471	−0.374	0.078	0.055	0.286	0.075	
−0.166	0.453	0.077	0.004	0.491	−0.454	0.002	
0.471	0.452	0.362	−0.397	−0.316	−0.403	0.285	
−0.074	−0.175	−0.020	0.394	0.271	0.035	−0.088	

penetration. After the delay time, water is injected into the mold cavity and penetrates along the core with the least flow resistance. The melt is pushed forward to form a plastic part with a hollow cross-section.

3.2. Multiple Regression and Analysis of Variance. Based on the CCD, the results of the experiments are listed in Table 2. A second-order polynomial equation depicting the relationship between five independent process parameters and SD was determined.

$$\begin{aligned}\mathrm{SD} = {} & 0.15 + 0.012X_1 - 0.0025X_2 - 0.015X_3 + 0.0024X_4 \\ & + 0.011X_5 + 0.0013X_1X_2 + 0.0005X_1X_3 - 0.0034X_1X_4 \\ & - 0.0084X_1X_5 + 0.0017X_2X_3 - 0.0042X_2X_4 + 0.0042X_2X_5 \\ & - 0.0082X_3X_4 + 0.0055X_3X_5 - 0.0051X_4X_5 + 0.0003X_1^2 \\ & + 0.011X_2^2 + 0.0078X_3^2 + 0.0038X_4^2 - 0.0002X_5^2. \end{aligned} \tag{14}$$

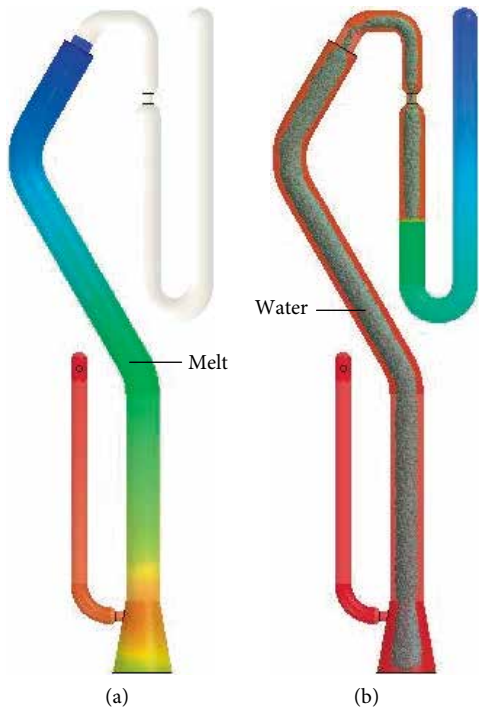

Figure 5: Simulation result and (a) melt filling stage, (b) water filling stage.

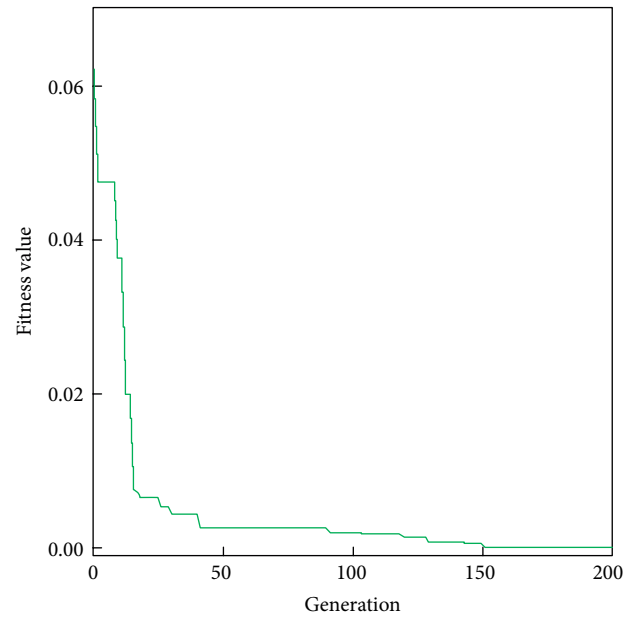

Figure 6: Evolution of fitness value for optimizing ANN-GA model.

The adequacy and fitness of the quadratic model were further studied by ANOVA (Table 3). p-value <0.05 is a criterion for judgment about the significance of each term, and shows significant variables at 95% confidence level. The regression model ($F = 4.61$ and $p = 0.0001$) was statistically significant, which indicates that there was a good fit between the experimental data and predicted data obtained by RSM. As listed in Table 3, the linear coefficients of melt temperature, delay time, and water temperature were noted to be significant with the F- and p-value of ($F = 15.2$, $p = 0.0005$), ($F = 22.5$, $p < 0.0001$) and ($F = 13.55$, $p = 0.0009$), respectively; the interaction between melt temperature and water temperature seemed to be predominant with F- and p-value of ($F = 7.02$, $p = 0.0129$), which was followed by the interaction between delay time and water pressure ($F = 6.51$, $p = 0.0162$); all quadratic coefficients were insignificant.

3.3. Initial Weights and Bias of ANN-GA. The optimization of the initial weights and bias of ANN was implemented using GA. 37 of the 43 data sets were used to train the ANN-GA, and the rest were used to test this model. The mean square error between the predicted values and experimental values was used as a fitness function. As shown in Figure 6, during the training process, the fitness value firstly decreased sharply and then ran steadily after the 150th generation. The minimum fitness value was 4.3E–4 after the preset generations, which meant that the predictions were in good agreement with the targets. The initial weights and bias (Table 4) were fixed and assigned to ANN-GA model.

3.4. Comparison of the Prediction Ability of RSM, ANN and ANN-GA. Figures 7 (a)–7(c) showed the comparative plots of the experimental values to predicted values obtained by three models (RSM, ANN, and ANN-GA). The linear coefficient of the fitting line for RSM, ANN, and ANN-GA models were 0.8147, 0.9839, and 1.001, respectively. The data points of RSM were scattered on both sides of the fitting line, while the data points of ANN and ANN-GA were very close to the fitting line. Moreover, the effectiveness of RSM, ANN, and ANN-GA models was statistically evaluated in terms of RMSE and R values between the experimental values and predicted values. Table 5 gives the statistical parameters of RMSE and R for RSM, ANN, and ANN-GA models, respectively. In general, the closeness of the RMSE value to zero and the R value to unity represents more accuracy of response predicted by three models. Through the analysis abovementioned, it was concluded that the three models (RAM, ANN, and ANN-GA) could well map the relationship between the independent process parameters and SD, and therefore can provide predictions with acceptable accuracy for unseen data sets; the best performance of prediction was ANN-GA followed by ANN and RSM, which indicates that the ANN-GA model has the strongest ability to be generalized. Hence, the ANN-GA model was selected as the final prediction model in the optimization process.

3.5. Optimization Result of ANN-GA and Validation. The optimization of RWTU was carried out with the principle "the smaller, the better". The expression based of ANN-GA for calculating SD was used as the fitness function of GA. The evolution of this optimization process was recorded in Figure 8. The lines representing fitness value run steadily after the 40th generation. The optimized process parameters of melt temperature = 219°C, mold temperature = 59.8°C, water injection delay time = 5 s, water pressure = 10.2 MPa and water temperature = 20°C were considered. With the optimized

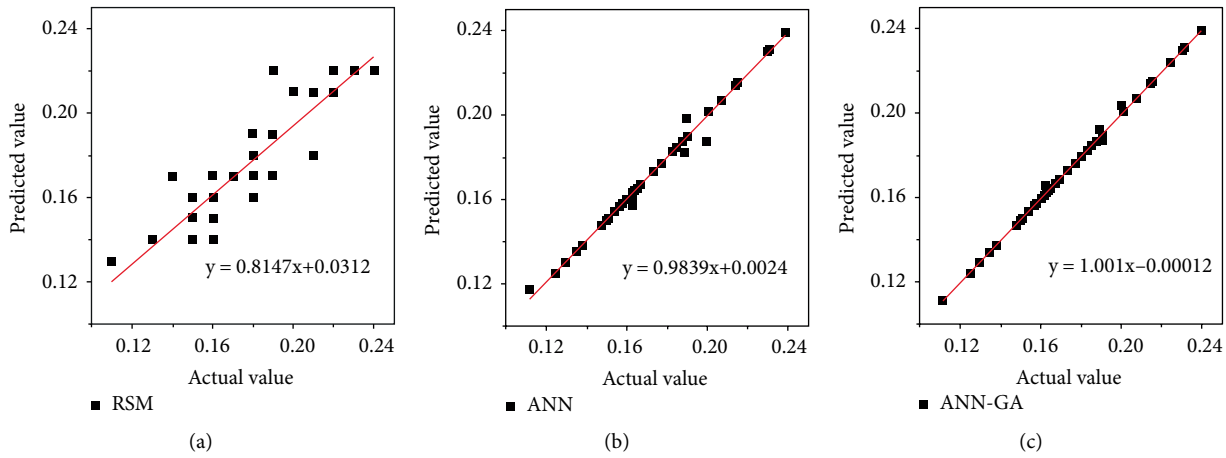

Figure 7: Predicted values versus the actual values, (a) RSM, (b) ANN, (c) ANN-GA.

Table 5: Statistical parameters of RSM, ANN and ANN-GA model.

Model	RMSE	R
RSM	0.0142	0.8731
ANN	0.0114	0.9397
ANN-GA	0.0010	0.9994

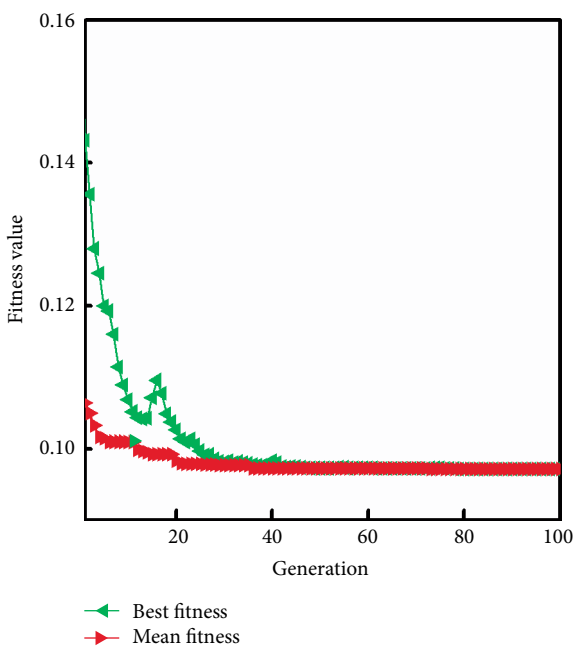

Figure 8: Evolution of fitness value in 100 generations.

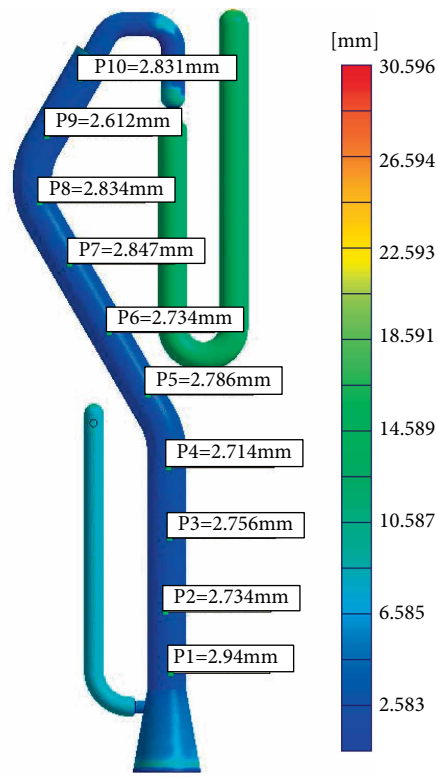

Figure 9: Simulation results with optimal process parameters.

process parameters, the SD predicted by ANN-GA model was 0.0972, which was smaller than any observation in simulation.

Using the optimal process parameters, a simulation experiment and real experiments were carried out to verify the optimization results. As shown in Figure 9, the value of SD obtained by the simulation experiment was 0.09, which was slightly smaller than the predicted value of ANN-GA and smaller than any observation in the simulation experiments (Table 2). The results of the real experiments showed that the RWTU obtained by the optimal process parameters was improved.

4. Conclusions

The simulations of SFRC OWAIM were carried out, and the SD was used to characterize the RWTU of plastic parts with hollow cross-sections. RSM-CCD with five independent variables (melt temperature, mold temperature, delay time, water pressure, and water temperature) at three levels and ANN-GA with one hidden layer were employed to construct models for predicting SD. The influences of five process parameters on RWTU were studied using ANOVA, indicating melt temperature, delay time, and

water temperature were predominant. The prediction abilities of three models (RSM, ANN, and ANN-GA) were compared through some statistical criteria and the results demonstrated that the ANN-GA model had the best performance followed by ANN and RSM. The optimization of RWTU was implemented using ANN-GA as a fitness function and got the minimum SD 0.097 which was smaller than any other experimental result. It is noteworthy that our interesting findings will be provided new solutions for the subsequent optimization of warpage and shrinkage of plastic parts in SFRC OWAIM.

Data Availability

The data used to support the findings of this study are available from the corresponding author upon request.

Conflicts of Interest

The authors declare that they have no conflicts of interest.

Acknowledgments

The work in this paper is funded by the National Natural Science Foundation of China (Grant nos. 21664002 and 51563010) and the Science and Technology Project of Education Department of Jiangxi, China (Grant no. GJJ150609). The authors would like to express their sincere gratitude to those who made comments on the changes proposed in this article.

References

[1] J. G. Yang, X. H. Zhou, and Q. Niu, "Model and simulation of water penetration in water-assisted injection molding," *The International Journal of Advanced Manufacturing Technology*, vol. 67, no. 1–4, pp. 367–375, 2013.

[2] L. Li, Y. Peng, and W. Wei, "Recent advances on fluid assisted injection molding technique," *Recent Patents on Mechanical Engineering*, vol. 7, no. 1, pp. 82–91, 2014.

[3] T.-Q. Kuang, K. Zhou, L.-X. Wu, G.-F. Zhou, and L.-S. Turng, "Experimental study on the penetration interfaces of pipes with different cross-sections in overflow water-assisted coinjection molding," *Journal of Applied Polymer Science*, vol. 133, no. 1, 2016.

[4] T. Kuang, C. Yu, B. Xu, and L. S. Turng, "Experimental study of penetration interfaces in the overflow fluid-assisted co-injection molding process," *Journal of Polymer Engineering*, vol. 36, no. 2, pp. 139–148, 2016.

[5] P. Olley, L. Mulvaney-Johnson, and P. D. Coates, "Non-isothermal experimental and simulation study of residual wall thickness in gas assisted injection moulding," *Plastics, Rubber and Composites*, vol. 35, no. 2, pp. 47–58, 2006.

[6] K.-Y. Lin, F.-A. Chang, and S.-J. Liu, "Using differential mold temperatures to improve the residual wall thickness uniformity around curved sections of fluid assisted injection molded tubes," *International Communications in Heat and Mass Transfer*, vol. 36, no. 5, pp. 491–497, 2009.

[7] H. Park and B. Rhee, "Effects of the viscosity and thermal property of fluids on the residual wall thickness and concentricity of the hollow products in fluid-assisted injection molding," *The International Journal of Advanced Manufacturing Technology*, vol. 86, no. 9–12, pp. 3255–3265, 2016.

[8] H.-P. Park, B.-S. Cha, S.-B. Park et al., "A study on the void formation in residual wall thickness of fluid-assisted injection molding parts," *Advances in Materials Science and Engineering*, vol. 2014, Article ID 238251, 6 pages, 2014.

[9] T. Pudpong, P. Buahom, S. Areerat, W. Rungseesantivanon, I. Satoh, and T. Saito, "The effects of processing parameters on the residual wall thickness distribution at the sharp angle corner of water assisted injection molded parts," *International Polymer Processing*, vol. 28, no. 5, pp. 528–540, 2013.

[10] H.-X. Huang, R.-H. Zhou, and C. Yang, "Fiber orientation propelled by high-pressure water penetration in water-assisted injection molded fiber-reinforced thermoplastics part," *Journal of Composite Materials*, vol. 47, no. 2, pp. 183–190, 2013.

[11] S.-J. Liu, M.-J. Lin, and Y.-C. Wu, "An experimental study of the water-assisted injection molding of glass fiber filled polybutylene-terephthalate (PBT) composites," *Composites Science and Technology*, vol. 67, no. 7–8, pp. 1415–1424, 2007.

[12] C. Shen, L. Wang, and Q. Li, "Optimization of injection molding process parameters using combination of artificial neural network and genetic algorithm method," *Journal of Materials Processing Technology*, vol. 183, no. 2–3, pp. 412–418, 2007.

[13] P. Pan, W. Jin, X. Li et al., "Optimization of multiplex quantitative polymerase chain reaction based on response surface methodology and an artificial neural network-genetic algorithm approach," *PLoS ONE*, vol. 13, no. 7, Article ID e0200962, 2018.

[14] S. Jacob and R. Banerjee, "Modeling and optimization of anaerobic codigestion of potato waste and aquatic weed by response surface methodology and artificial neural network coupled genetic algorithm," *Bioresource Technology*, vol. 214, pp. 386–395, 2016.

[15] N. Salim, A. Santhiagu, and K. Joji, "Process modeling and optimization of high yielding L-methioninase from a newly isolated *Trichoderma harzianum* using response surface methodology and artificial neural network coupled genetic algorithm," *Biocatalysis and Agricultural Biotechnology*, vol. 17, pp. 299–308, 2019.

[16] J.-X. Yang and G.-B. Hong, "Optimized extraction for active compounds in *Glossogyne tenuifolia* using response surface methodology," *Journal of Food Measurement and Characterization*, vol. 13, no. 1, pp. 663–676, 2019.

[17] A. A. B. M. Zin and M. Moradi, "An experimental investigation of price elasticity in electricity markets using a response surface methodology," *Energy Efficiency*, vol. 12, no. 3, pp. 667–680, 2019.

[18] Y. Horie, T. Yoshio, K. Aoyama et al., "Diagnostic outcomes of esophageal cancer by artificial intelligence using convolutional neural networks," *Gastrointestinal Endoscopy*, vol. 89, no. 1, pp. 25–32, 2019.

[19] A. Dehghanbanadaki, M. A. Sotoudeh, I. Golpazir, A. Keshtkarbanaeemoghadam, and M. Ilbeigi, "Prediction of geotechnical properties of treated fibrous peat by artificial neural networks," *Bulletin of Engineering Geology and the Environment*, vol. 78, no. 3, pp. 1345–1358, 2018.

[20] D. Wang, M. Zhang, Z. Li et al., "System impairment compensation in coherent optical communications by using

a bio-inspired detector based on artificial neural network and genetic algorithm," *Optics Communications*, vol. 399, pp. 1–12, 2017.

[21] S. Ghanavati Nasab, A. Semnani, A. Teimouri, H. Kahkesh, T. Momeni Isfahani, and S. Habibollahi, "Removal of congo red from aqueous solution by hydroxyapatite nanoparticles loaded on zein as an efficient and green adsorbent: response surface methodology and artificial neural network-genetic algorithm," *Journal of Polymers and the Environment*, vol. 26, no. 9, pp. 3677–3697, 2018.

[22] S. Bahrami, F. Doulati Ardejani, and E. Baafi, "Application of artificial neural network coupled with genetic algorithm and simulated annealing to solve groundwater inflow problem to an advancing open pit mine," *Journal of Hydrology*, vol. 536, pp. 471–484, 2016.

Hindawi
Advances in Polymer Technology
Volume 2019, Article ID 6135270, 10 pages
https://doi.org/10.1155/2019/6135270

Research Article

Simulation and Optimization of Short Fiber Circumferential Orientation in Short-Fiber-Reinforced Composites Overflow Water-Assisted Injection Molded Tube

Haiying Zhou,[1,2] **Hesheng Liu**,[1,2] **Tangqing Kuang**,[3] **Qingsong Jiang**,[2] **Zhixin Chen**,[2] **and Weiping Li**[2]

[1] *School of Mechanical and Electrical Engineering, Nanchang University, Nanchang 330031, China*
[2] *Jiangxi Province Key Laboratory of Polymer Micro/Nanomanufacturing and Devices, East China University of Technology, Nanchang 330013, China*
[3] *School of Mechanical and Electrical Engineering, East China Jiaotong University, Nanchang 330013, China*

Correspondence should be addressed to Hesheng Liu; hsliu@vip.163.com

Received 9 May 2019; Revised 8 July 2019; Accepted 18 July 2019; Published 19 August 2019

Guest Editor: Yun Zhang

Copyright © 2019 Haiying Zhou et al. This is an open access article distributed under the Creative Commons Attribution License, which permits unrestricted use, distribution, and reproduction in any medium, provided the original work is properly cited.

The mechanical properties of the water-assisted injection molded tube can be enhanced by the increase in the short fiber circumferential orientation (SFCO). Thus, the numerical method verified by experiments is used to simulate the SFCO distribution in the overflow water-assisted injection molding (OWAIM), with the mechanism of short fiber orientation analyzed as well. The effect of parameters (filling time, melt temperature, mold temperature, delay time, water pressure, and water temperature) on the SFCO is explored by range analysis and variance analysis of the orthogonal experimental scheme. Moreover, both of artificial neural network (ANN) and genetic algorithm (GA) are used to model and optimize process parameters. Results show that the melt temperature, delay time, and water pressure are predominant parameters. The evolution of SFCO increases with the increase of melt temperature and water pressure, whereas the changes in delay time reverse. The value of the maximum SFCO tensor obtained by GA optimization is found to be 0.234.

1. Introduction

Injection molding is the main process used to produce plastic products [1, 2]. Water-assisted injection molding (WAIM), similar to the gas-assisted injection molding (GAIM), fills the high-temperature melt followed by the injection of high-pressure water after a short delay time and forms a plastic part with hollow channel finally. Due to the incompressibility, high thermal conductivity, and high heat capacity of the medium water, WAIM has the characteristics of thin residual wall thickness (RWT) and high production efficiency and has obvious technological advantages in the preparation of hollow shaped plastic parts. At present, the research mainly focuses on the influence of factors (such as process parameters and material properties) on primary penetration, secondary penetration, and RWT distribution of plastic parts [3–6].

Short-fiber-reinforced composites (SFRC) can effectively improve the mechanical properties of water-assisted injection molded parts [7]. Liu et al. [8] have used the short-fiber reinforced polypropylene as raw material in short water-assisted injection molding (SWAIM). Results showed that the short fibers in RWT oriented mostly along the melt flow direction. Meanwhile, the orientation of the poly-butylene-terephthalate composites containing 15% glass fiber has been studied by Liu et al. [9]. They have found that the short fibers near the mold surface are arranged mainly along the melt flow direction, and the orientation gradually decreased with the increase of thickness. In order to further explore the orientation distribution characteristics of short fibers in

SWAIM, Huang et al. [10] have proposed that the short fiber orientation along the melt flow direction in the cross section near the high-pressure water inlet decreases gradually with the increasing thickness.

The mechanical properties of SFRC are closely related to the orientation of short fibers, and the reinforcing effect is mainly controlled by the direction of short fibers arrangement [11–13]. Experimental studies show that the short fibers of RWT in WAIM are mainly oriented along the axial direction and weakly oriented in the circumferential and radial directions. This implies that the mechanical properties of the parts in the circumferential direction are far below the axial direction. In order to improve the pressure resistance, friction resistance, and aging resistance of the water-assisted injection molded pipe, it is desirable to have more short fibers oriented in the circumferential direction. In general, the orientation distribution of the short fibers can be adjusted by altering the melt flow pressure and velocity field distribution in WAIM through appropriate process parameters [14–16].

Up to our knowledge, due to the difficulty in assessment of the performing quantitative experimental characterization, various researches focus on the qualitative observation of the short fiber orientation using scanning electron microscopy (SEM). To quantitatively characterize the short fiber orientation of RWT, it is crucial to carry out effective numerical simulation for WAIM. Thus, based on the improved Anisotropic Rotary Diffusion model and Retarding Principal Rate Model (iARD-RPR) proposed by Tseng [17–19], the numerical simulation of short fiber orientation distribution in overflow water-assisted injection molding (OWAIM) is implemented. The validity of the model and mechanism of short fiber orientation are analyzed. For this purpose, the orthogonal experimental scheme is designed to obtain the sample data. Meanwhile, an artificial neural network (ANN) is used to map the nonlinear relationship between process parameters and short fiber circumferential orientation (SFCO). In addition, the genetic algorithm (GA) uses the ANN model as the fitness function to optimize the process parameters for the maximum circumferential orientation.

2. Methods

2.1. Related Mathematical Models. The numerical simulation of short fiber orientation in OWAIM is based on the fiber orientation tensor evolution equation and the fluid mechanics governing equation. According to the fiber orientation theory, a single fiber is usually regarded as a rigid cylindrical rod. As shown in Figure 1, the orientation of a single fiber can be described by the unit vector [20].

$$P = \begin{pmatrix} \sin\theta\cos\varphi \\ \sin\theta\sin\varphi \\ \cos\theta \end{pmatrix} \tag{1}$$

where P is the direction of the fiber; θ and φ are the angles between P and the coordinate axis.

The orientation tensor A is defined to succinctly depict the orientations of a large amount of short fibers [17].

$$A = \oint \psi(P)\, PPdP = \begin{bmatrix} A_{11} & A_{12} & A_{13} \\ A_{12} & A_{22} & A_{23} \\ A_{13} & A_{23} & A_{33} \end{bmatrix} \tag{2}$$

$$A_{11} + A_{22} + A_{33} = 1 \tag{3}$$

where $\psi(P)$ is the probability density distribution function of the whole orientation space; A is a symmetric matrix, and when A=I/3, it represents the orientation state isotropic, where I is an identity matrix. The diagonal Components A_{11}, A_{22}, and A_{33} represent orientation tensors in the axial, circumferential, and radial directions, respectively.

Tseng has proposed the iARD-RPR fiber orientation prediction model composed of three parts, such as hydrodynamic model $\dot{A}^{HD}$, improved anisotropic rotational diffusion model $\dot{A}^{iARD}$ [20], and delayed principal rate model $\dot{A}^{RPR}$ [21].

$$\dot{A} = \dot{A}^{HD} + \dot{A}^{iARD}(C_I, C_M) + \dot{A}^{RPR}(\alpha) \tag{4}$$

$$\dot{A}^{HD} = (W \bullet A) - (A \bullet W) + \xi\left(D \bullet A + A \bullet D - 2A_4 : D\right) \tag{5}$$

$$\dot{A}^{iARD} = \dot{\gamma}\left[2D_r - 2\mathrm{tr}\left(D_r\right)A - 5D_r \bullet A - 5A \bullet D_r + 10A_4 : D_r\right] \tag{6}$$

$$D_r = C_I\left(I - C_M\frac{D^2}{\|D^2\|}\right) \tag{7}$$

$$\dot{A}^{RPR} = -R \bullet \dot{\Lambda}^{IOK} \bullet R^T \tag{8}$$

$$\dot{\Lambda}^{IOK}_{ii} = \alpha\dot{\lambda}_i, \quad i, j, k = 1, 2, 3 \tag{9}$$

where $\dot{A}^{iARD}$ contains two effective parameters: interfiber interaction factor C_I ($0 < C_I < 0.1$) and fiber-matrix interaction factor C_M ($0 < C_M < 1$); $\dot{A}^{RPR}$ contains a parameter α ($0 < \alpha < 1$), used to slow down the response speed of fiber orientation. W is the vortex tensor; D is the deformation rate tensor; ξ is a dimensionless number. The fourth-order orientation tensor A_4 is determined by the higher order polynomial approximation of second-order tensor A; $\dot{\Lambda}^{IOK}$ is the diagonal tensor material derivative and its superscript is the intrinsic orientation kinetic assumption; $\dot{\Lambda}^{IOK}_{ii}$ is the i-th diagonal component of $\dot{\Lambda}^{IOK}$; R is a rotation matrix; λ_i is the eigenvalue of the matrix A ($\lambda_1 > \lambda_2 > \lambda_3$).

In the injection molding process, the initial condition of the fiber orientation tensor at the entrance was set as the isotropic state. The movement of short fibers in the polymer melt is a transient, non-Newtonian, and nonisothermal process. In the numerical simulation, the melt is regarded as incompressible, laminar, and the inertia term is ignored. The

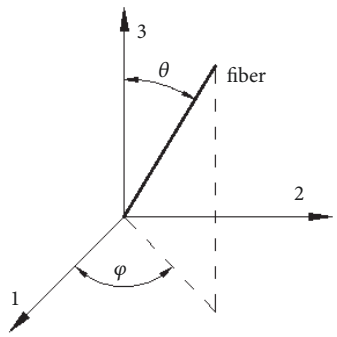

Figure 1: Schematic diagram of short fiber orientation.

Table 1: Related process parameters in simulation.

Process parameter	Values
Filling time /s	1.5-3.5
Melt temperature / °C	220-260
Mold temperature / °C	40-80
Delay time /s	2-6
Water pressure / MPa	6-8
Water temperature /°C	20-40
C_I	0.005
C_M	0.1
α	0.7

basic governing equations for transient and nonisothermal melt motion in OWAIM include the following [17]:

$$\frac{\partial \rho}{\partial t} + \nabla \bullet \rho \boldsymbol{u} = 0 \tag{10}$$

$$\frac{\partial}{\partial t}(\rho \boldsymbol{u}) + \nabla \bullet (\rho \boldsymbol{u}\boldsymbol{u} - \boldsymbol{\sigma}) = \rho \boldsymbol{g} \tag{11}$$

$$\boldsymbol{\sigma} = -\mathrm{p}\mathbf{I} + \eta\left(\nabla \boldsymbol{u} + \nabla \boldsymbol{u}^T\right) \tag{12}$$

$$\rho C_p\left(\frac{\partial T}{\partial t} + \boldsymbol{u} \bullet \nabla T\right) = \nabla \bullet (k \nabla T) + \eta \dot{\gamma}^2 \tag{13}$$

where ρ is the melt density; $\mathbf{u}$ is the velocity vector; t is the time; $\boldsymbol{\sigma}$ is the total stress tensor; $\boldsymbol{g}$ is the gravity acceleration vector; η is the viscosity; P is the pressure; C_p is the specific heat capacity; T is the temperature; k is the thermal conductivity; $\dot{\gamma}$ is the shear rate.

The seven-parameter Cross-WLF viscosity model is used as the constitutive equation, which can well describe the nonlinear relationship between polymer melt viscosity, temperature, and shear [18].

$$\eta(\dot{\gamma}, T, P) = \frac{\eta_0(T, P)}{1 + \left(\eta_0 \dot{\gamma}/\tau^*\right)^{1-n}} \tag{14}$$

$$\eta_0(T, P) = D_1 \exp\left(\frac{-A_1(T - T_c)}{A_2 + (T - T_c)}\right) \tag{15}$$

$$T_c = D_2 + D_3 P \tag{16}$$

$$A_2 = \widetilde{A}_2 + D_3 P \tag{17}$$

where η is the viscosity; η_0 is the zero shear viscosity; $\dot{\gamma}$ is the shear rate; τ^* is the material constant; n is the power law index in high shear rate; T is the melt temperature; T_c is the glass transition temperature; D_1, D_2, D_3, A_1, and $\widetilde{A}_2$ are the Constants associated with the selected material.

2.2. Geometric Model and Process Parameters. The geometric model (Figure 2) consists of two parts: an overflow cavity and a plastic part with length 280 mm and diameter 20 mm. The 3D solid combination model is built using Pro/E and meshed in Moldex Designer. The total number of mesh nodes and mesh elements is 205,056 and 2,208,359, respectively. The 3D solid meshed model is imported into the commercial software Moldex3D for material selection and process parameter settings. The PP (Fiberfil J-68/30/E) containing 30% short glass fiber with the fiber aspect ratio 20 is used as material in simulation of OWAIM. First, the melt was injected into the mold cavity of the plastic part. Second, after a short delay time, the high-pressure water was injected into the melt and penetrates along the position with the least flow resistance and pushed the melt into the overflow cavity to form a plastic part with a hollow cross-section. The process parameters considered in this study are shown in Table 1.

2.3. Experimental Verification. The experiment of OWAIM was carried out in the laboratory using the same process parameters as the simulation to verify the prediction result of short fiber orientation distribution. The platform includes an injection molding machine, a high pressure water injection system, a mold temperature control system, and a water temperature control system. The injection molding machine is the TTI-250FT automatic injection molding machine produced by Donghua Machinery Co., Ltd. The high-pressure water injection system is composed of a control system, a high pressure pump, and a water injection nozzle. The maximum water injection pressure is 20 MPa. The raw material is short-fiber-reinforced polypropylene (PP/GH43 with a short glass fiber mass fraction of 30%) produced by South Korea's Samsung Total Co., Ltd.

As shown in Figure 3, a section was taken in the middle of the plastic part along the axial direction. The orientation distribution of the short fibers was observed by SEM (Nova NanoSEM 450) with an acceleration voltage of 5kV. The sample was first immersed in liquid nitrogen and cryofractured after two hours. The prepared specimen was gold-sputtered before the observation.

2.4. Orthogonal Experimental Design. During the injection molding process, the melt is sheared and stretched by the surrounding melt due to the difference in viscosity gradient, pressure, and velocity field distribution. The shearing action leads the short fibers to be aligned along the melt flow direction, and the stretching effect induces the short fibers to orient in the stretching direction. The process parameters of OWAIM considered in this research include filling time, melt

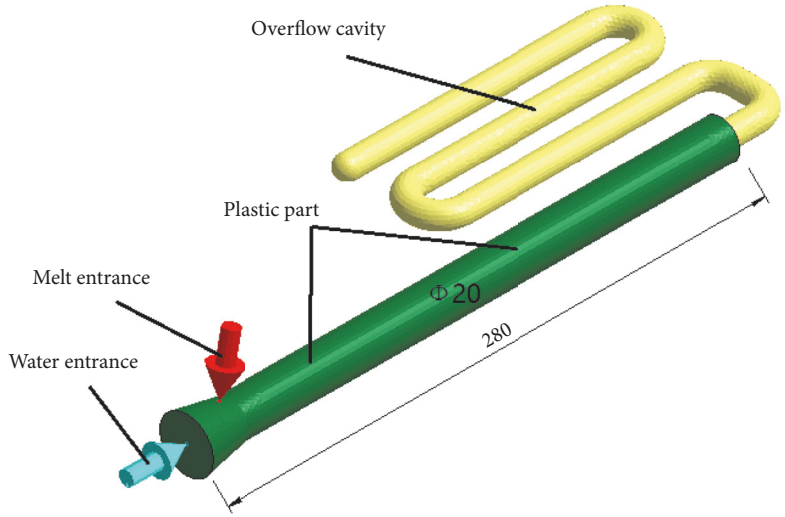

Figure 2: Geometry of the overflow water-assisted injection molding.

Table 2: Factors and levels of orthogonal experiment design.

Process parameter	Level				
	1	2	3	4	5
Filling time (A) /[s]	1.5	2	2.5	3	3.5
Melt temperature (B) /[°C]	220	230	240	250	260
Mold temperature (C) /[°C]	40	50	60	70	80
Delay time (D) /[s]	2	3	4	5	6
Water pressure (E) /[MPa]	6	6.5	7	7.5	8
Water temperature (F) /[°C]	20	25	30	35	40

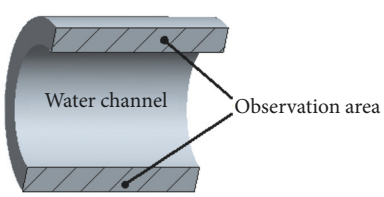

Figure 3: Schematic representation of specimen preparation for SEM observation.

temperature, mold temperature, delay time, water pressure, and water temperature. Set the range of values of each process parameter based on the software's recommendation for the selected material. In order to reduce the number of experiments and comprehensive investigation of the effect of process parameters on the SFCO, orthogonal experimental design (L_{25} (5^6)) with six factors and five levels is arranged, as shown in Tables 2-3. The objective A_{22} represents the fiber orientation in the circumferential directions of the pipe. The values of circumferential component of orientation tensor were taken at eighteen different points along the thickness direction of RWT, and A_{22} is the average value of these points.

2.5. Artificial Neural Network (ANN). ANN inspired by biologic neural system is a computing model used to map linear or nonlinear relationships between factors and responses. ANN can work as a human brain to establish a sample model from the perspective of information processing, without prior information or heuristic assumptions. An ANN model comprises three parts: one input layer, one or more hidden layers, and one output layer. The numbers of neurons in the input and output layer are determined by the numbers of

Table 3: Orthogonal experimental arrangement and results of simulation.

No.	A	B	C	D	E	F	A_{22}
1	1	1	1	1	1	1	0.195
2	1	2	2	2	2	2	0.196
3	1	3	3	3	3	3	0.197
4	1	4	4	4	4	4	0.194
5	1	5	5	5	5	5	0.201
6	2	1	2	3	4	5	0.203
7	2	2	3	4	5	1	0.182
8	2	3	4	5	1	2	0.187
9	2	4	5	1	2	3	0.193
10	2	5	1	2	3	4	0.201
11	3	1	3	5	2	4	0.19
12	3	2	4	1	3	5	0.202
13	3	3	5	2	4	1	0.217
14	3	4	1	3	5	2	0.192
15	3	5	2	4	1	3	0.191
16	4	1	4	2	5	3	0.205
17	4	2	5	3	1	4	0.187
18	4	3	1	4	2	5	0.193
19	4	4	2	5	3	1	0.188
20	4	5	3	1	4	2	0.221
21	5	1	5	4	3	2	0.193
22	5	2	1	5	4	3	0.207
23	5	3	2	1	5	4	0.213
24	5	4	3	2	1	5	0.185
25	5	5	4	3	2	1	0.189

factors and responses, respectively. In general, the number of neurons in hidden layer is determined by trial and error. The relationship between factors and responses can be depicted as follows:

$$O_k = f_o \left[\sum_j w_{kj} \bullet f_h \left(\sum_i w_{ji} I_i + b_j \right) + b_k \right] \quad (18)$$

where I_i denotes the i-th factor in input layer, w_{ji} denotes the weight between the i-th neuron in input layer and the j-th neuron in hidden layer, w_{kj} denotes the weight between the j-th hidden layer and the k-th output layer, b_j and b_k denote the bias assigned to j-th neuron in hidden layer and k-th neuron in output layer, respectively, f_h denotes the transfer function employed in the hidden layer, f_o denotes the transfer function employed in the output layer, and O_k denotes the k-th response in output layer.

According to Kolmogorov's theorem [22], an ANN model with a single hidden layer has the ability to map any complex nonlinear relationship between the factors and responses. In this study, an ANN model with one hidden layer was used for modeling circumferential component of orientation tensor. The transfer functions used in the hidden and output layer are "*Tansig*" and "*Purelin,*" respectively. The Levenberg-Marquardt algorithm was used to train the ANN model, and ANN can converge with much fewer iterations. By changing the number of neurons in the hidden layer from 5 to 15, the ANN topology of 6-13-1 was determined according to the minimum mean square error between the targets and the outputs, indicating that there were six neurons in the input layer, thirteen neurons in the hidden layer, and one neuron in the output layer (Figure 4).

2.6. Genetic Algorithm (GA). Genetic algorithm based on natural selection and survival of fitness is a global searching algorithm and is widely used in the fields of optimization, pattern recognition, robots, and prediction [23]. Compared with other optimization methods, it has many advantages including being not easy to be trapped into the local minima, requiring little prior information about the searched objectives, and easy identifying of the optima in a complex search space.

The flow chart of genetic algorithm is shown in Figure 5. The major operations of GA are summarized as follows. (1) Selection: individuals are selected based on their fitness so that better individuals are given a higher chance of being chosen. (2) Crossover: exchange the information of the two parents to generate a new individual according to the crossover probability. (3) Mutation: randomly alter the information of each chromosome according to the mutation probability. After the predefined evolution generations or the resulting solution is satisfied, the genetic algorithm is stopped.

3. Results and Discussion

3.1. Short Fiber Circumferential Orientation Distribution in RWT. After the simulation is completed, a cross-section extracted from the middle of the model is used to observe

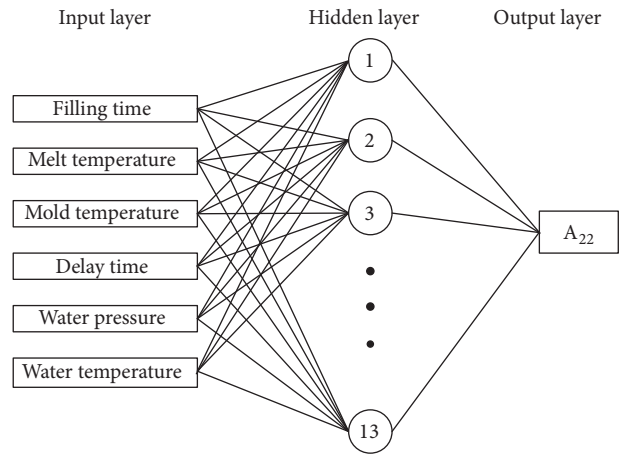

Figure 4: Topology of artificial neural network.

the short fiber orientation distribution. As shown in Figure 6, the SFCO distribution in the RWT of the tube has a distinct layered structure. The outer layer has a small SFCO distribution with a component of orientation tensor about 0.15. The SFCO distribution in the inner layer near the water channel increases significantly. The component of orientation tensor in the region near the water channel is about 0.33, indicating that the short fibers tend to be freely oriented.

Figure 7 is a typical short fiber orientation distribution state of RWT in OWAIM. The RWT can be divided into two regions according to the characteristics of the short fiber orientation distribution. The short fibers in the region near the mold wall are arranged mainly along the axial direction, while these near the water channel are irregularly arranged. Figure 7(a) is a magnified view of the area selected from the inner layer, in which there are dense holes caused by the cryofractured process, indicating many short fibers oriented in the circumferential direction. Figure 7(b) is a magnified view of the area selected from the outer layer of the RWT, in which the existing short fibers have a regular arrangement in the axial direction. The number of holes in outer layer is significantly reduced, and many elongated vacancies parallel to the axial direction are left in the photograph, revealing the short fibers in outer layer mainly arranged in the axial direction and very few short fibers oriented in the circumferential direction. A conclusion can be inferred from Figure 7 that the value of A_{22} in the inner layer is larger than that in the outer layer. Compared with the result obtained in Figure 6, it can be found that the iARD-RPR model is well suited for the short fiber orientation prediction in OWAIM.

3.2. Orientation Mechanism Analysis of the Short Fibers. The process of OWAIM includes a melt filling stage and a high-pressure water filling stage. Figure 8 shows the components of orientation tensor in the position where the RWT is located during two filling stages. The melt filling stage of OWAIM is similar to that of conventional injection molding, in which the large shear stress and velocity gradient changes exist between the thin layers near the mold cavity. This makes the short fibers highly orient along the axial direction due to the shear action. There are very few short fibers aligned in the

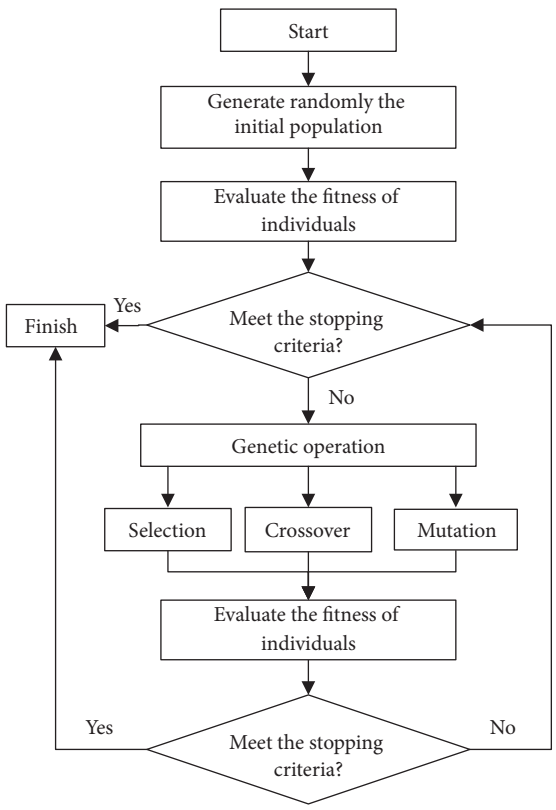

Figure 5: Chart of genetic algorithm.

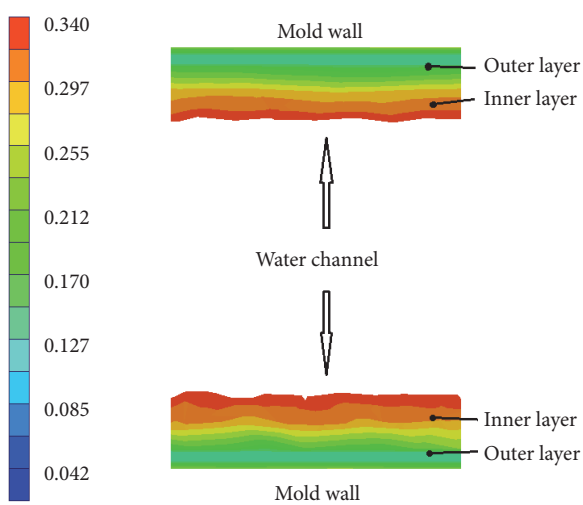

Figure 6: Contour of the circumferential component of orientation tensor.

circumferential direction and A_{22} is small in the whole RWT after melt filling stage. After the delay time, influenced by the low temperature of the mold cavity, the temperature of the surface melt is lowered to form a high-viscosity layer, wherein the short fiber orientation is solidified. During the penetration process of high-pressure water, the water column is in a turbulent state because of the short injection time. The residual melt is squeezed and rubbed by the water column at the interface between the melt and the water column. In addition, the flowing melt driven by the water column stretches the residual melt. The short fibers in the layer near the water channel, which are originally oriented along the axial direction, readjust the orientation posture, so that A_{11} decreases and A_{22} increases.

3.3. Sensitivity Analysis of Process Parameters. Table 3 shows the values of A_{22} in the orthogonal experimental scheme. The results of range analysis are listed in Table 4, in which K_i is the sum value of A_{22} of all level in each factor. According to the magnitude of the range R, the order of sensitivity of A_{22} to the six process parameters is determined as follows: water pressure, delay time, melt temperature, filling time, water temperature, and mold temperature. The optimal process parameters combination recommended by range analysis is A4B3C5D1E4F3, that is, melt filling time 3s, melt temperature 240°C, mold temperature 80°C, delay time 2s, water pressure 7.5MPa, and water temperature 30°C. From the analysis of variance (Table 5), it is concluded that melt temperature, delay time, and water pressure are the predominant factors with the F values of 7.782, 12.875, and 21.231, respectively, while filling time, mold temperature, and water temperature have no significant effects on the A_{22} with F values of 1.918, 0.938, and 1.061, respectively.

3.4. Modeling the Process Parameters Using ANN. Experimental data (Table 3), obtained from orthogonal experimental design, were divided randomly into three data sets. 19 of overall 25 points were used to train the ANN model, and the other points (3+3) were used to validate and test this model, respectively. The trained neural network was used to predict the values of A_{22} in the orthogonal experimental scheme. The predicted values shown in Figure 9, which are very consistent with the expected value, indicate that the neural network has established a nonlinear relationship between the process parameters and the A_{22}.

3.5. Effect of Significant Factors on the SFCO. Figure 10 shows the effect of a single significant parameter on the A_{22} predicted by the ANN model. It indicates that the values of A_{22} increase as the melt temperature and water pressure increase, while A_{22} has a reverse relation with the delay time. As mentioned above, the interferences of high-pressure water column with the inner layer of RWT result in an increase in A_{22}. The greater the melt temperature and water pressure are, the higher the disturbance to the inner layer is, causing an increase in A_{22}. The longer delay time is, the larger thickness of solidified layer is, and the thinner thickness of melt is disturbed by the high-pressure water, leading to the decrease of the A_{22}.

Figures 11–13 are the response surface contours indicating the interaction effects of two significant process parameters on A_{22}. Figure 11 shows the interaction effect of melt temperature and delay time. The value of A_{22} varies within the range of [0.195, 0.210], and maximum of A_{22} is obtained with delay time 2s and melt temperature 260°C. Figure 12 shows the interaction effect of delay time and water pressure. The value of A_{22} varies within the range of [0.185, 0.215], and maximum

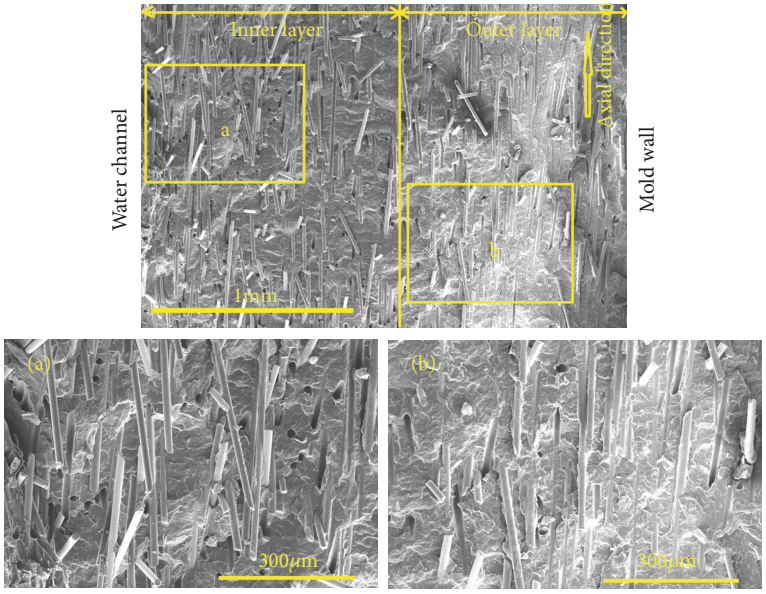

Figure 7: Representative SEM micrographs of RWT and Magnified views of (a) inner layer and (b) outer layer.

Table 4: Results of range analysis.

Factors	A	B	C	D	E	F
K_1	0.983	0.986	0.988	1.024	0.945	0.971
K_2	0.966	0.974	0.991	1.004	0.961	0.989
K_3	0.992	1.007	0.975	0.968	0.981	0.993
K_4	0.994	0.952	0.977	0.953	1.042	0.985
K_5	0.987	1.003	0.991	0.973	0.993	0.984
Optimal level	4	3	5	1	4	3
R	0.028	0.055	0.016	0.071	0.097	0.022
Order of importance			E>D>B>A>F>C			

Table 5: Results of variance analysis.

Factors	sum of squares	Degree of freedom	Mean square	F value	F_a	Significance
A	9.944E-5	4	2.486E-5	1.918		
B	0.403E-3	4	0.101E-3	7.782		* * *
C	4.864E-5	4	1.21E-5	0.938		
D	0.667E-3	4	0.167E-3	12.875	$F_{0.05}(4,8)=3.838$	* * *
E	1.101E-3	4	0.275E-3	21.231	$F_{0.01}(4,8)=7.006$	* * *
F	5.504E-5	4	1.376E-5	1.061		
Err.	0.104E-3	8	1.296E-5			
Sum	2.375E-3	24				

**indicates being significant.
* * * indicates being highly significant.

A_{22} appears with delay time 2s and water pressure 8MPa. As shown in Figure 13, the value of A_{22} varies within the range of [0.182, 0.204] for the interaction effect of melt temperature and water pressure, and the maximum A_{22} is got with melt temperature 260°C and water pressure 8MPa.

3.6. Optimization and Verification of the Circumferential Orientation. Taking the trained ANN model as the fitness function, the optimization of A_{22} was carried out using the solver of "ga, genetic algorithm" in the MATLAB R2015b optimization toolbox, with the principle "the larger, the better." The parameters of GA were set as the follows: population size 50, initial range [0; 1], crossover Fraction 0.8, mutation function 0.01, and generation 100. The evolution of optimization process is recorded in Figure 14. After 100 generations, the optimized A_{22} is found to be 0.234. The corresponding process parameters are filling time 3.5s, melt temperature 260°C, mold temperature 80°C, delay

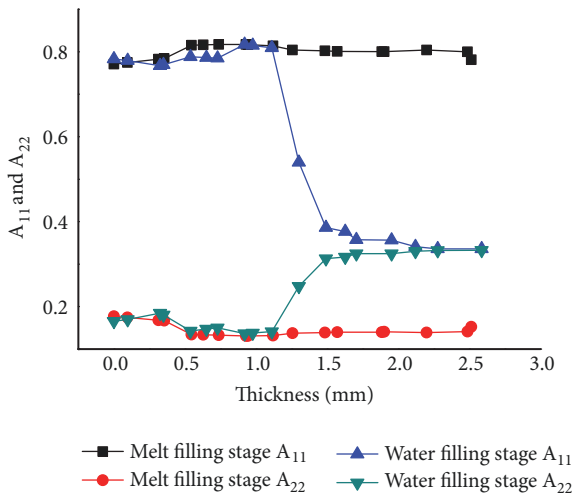

FIGURE 8: Short fiber orientation of RWT in the melt and water filling stages.

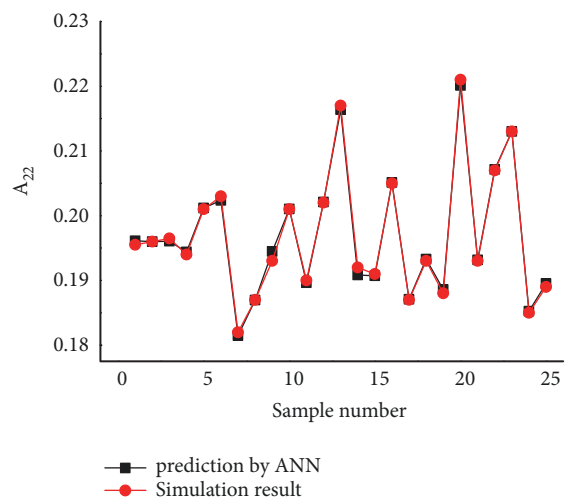

FIGURE 9: Comparison between experimental values and ANN predictions.

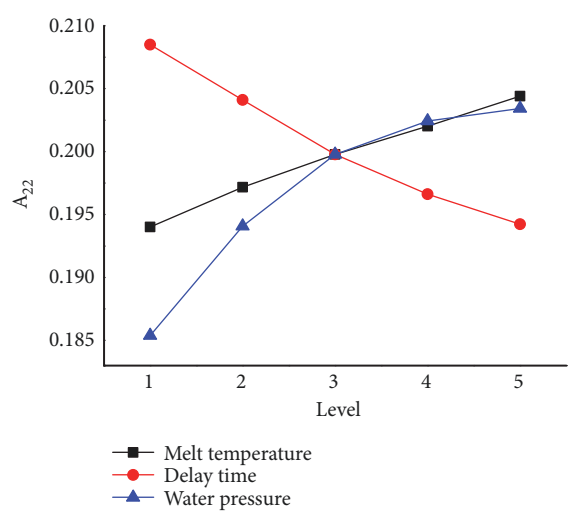

FIGURE 10: Effect of significant influence parameters on A_{22}.

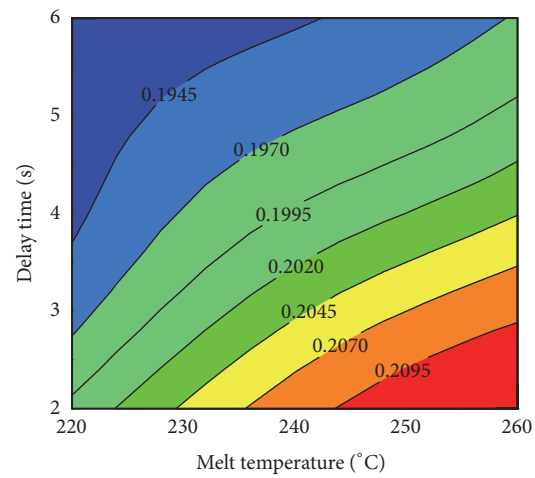

FIGURE 11: Interaction effect of melt temperature and delay time on A_{22}.

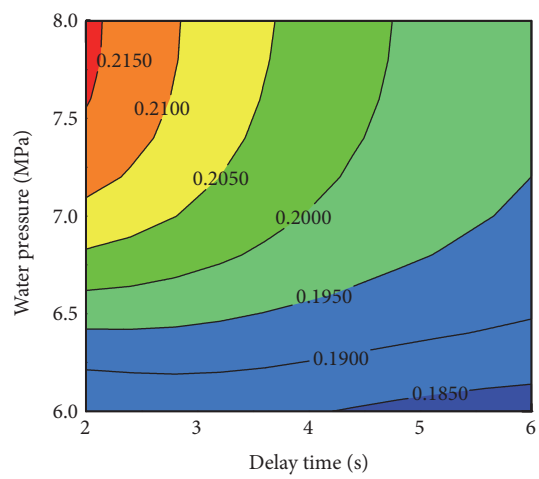

FIGURE 12: Interaction effect of delay time and water pressure on A_{22}.

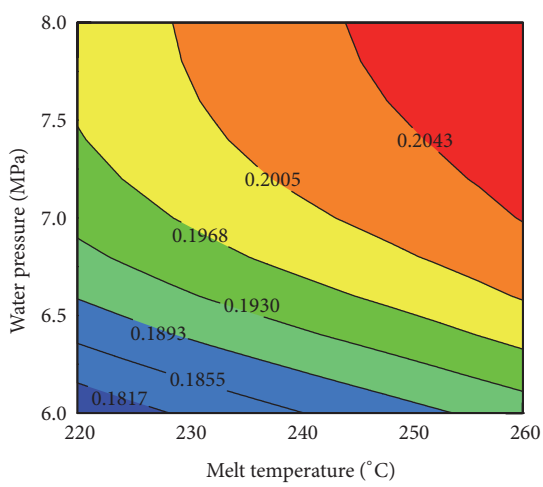

FIGURE 13: Interaction effect of delay time and water pressure on A_{22}.

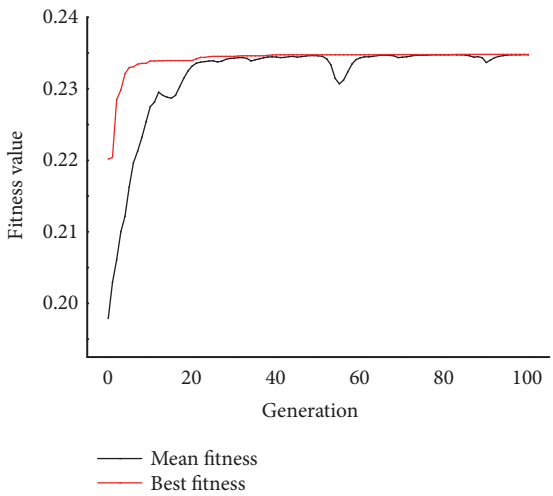

Figure 14: Evolution of the optimization.

time 2s, water pressure 8MPa, and water temperature 36°C, respectively. This value of A_{22} is greater than any set of experimental results in the orthogonal experimental scheme. The simulation experiments using the optimal parameters combination recommended by GA and range analysis are conducted by Moldex3D, and the obtained A_{22} are 0.233 and 0.228, respectively. Results show that the SFCO distribution is improved by two methods, and the combination of ANN and GA is better than that of range analysis in orthogonal experimental scheme.

4. Conclusions

In this research, the short fibers orientation distribution of RWT in OWAIM was simulated using the iARD-RPR model. Compared with the SEM micrographs, the simulation results indicated that this model was suitable for OWAIM. The simulation results showed that the value of A_{22} in the outer layer is small and that in the inner layer increases significantly. In addition, the simulations indicated that the penetration of water column readjusted the orientation state of short fibers, increasing the circumferential orientation of short fibers in the inner layer of RWT. Through the range analysis and variances analysis, it was found that melt temperature, delay time, and water pressure were significant factors. The values of A_{22} increase as the melt temperature and water pressure increase, while decreasing with the delay time rise. The maximum A_{22} was 0.234 in the optimization with the combination of ANN and GA. Compared with range analysis, the combination of ANN and GA resulted in a better optimization result. This study will help to further understand the orientation mechanism of short fibers in OWAIM.

Data Availability

The data used to support the findings of this study are available from the corresponding author upon request.

Conflicts of Interest

The authors declare that there are no conflicts of interest regarding the publication of this paper.

Acknowledgments

The work in this paper is funded by the National Natural Science Foundation of China (Grant No. 21664002, Grant No. 51563010) and Jiangxi Provincial Key Technology R&D Program (Grant No. 20161BBE50073). The authors would like to express their sincere gratitude to those who made comments on the changes proposed in this article.

References

[1] J. Zhang, P. Zhao, Y. Zhao, J. Huang, N. Xia, and J. Fu, "On-line measurement of cavity pressure during injection molding via ultrasonic investigation of tie bar," *Sensors and Actuators A: Physical*, vol. 285, pp. 118–126, 2019.

[2] P. Zhao, W. M. Yang, X. M. Wang, J. G. Li, B. Yan, and J. Z. Fu, "A novel method for predicting degrees of crystallinity in injection molding during packing stage," *Proceedings of the Institution of Mechanical Engineers, Part B: Journal of Engineering Manufacture*, vol. 233, no. 1, pp. 204–214, 2019.

[3] T. Q. Kuang, B. P. Xu, G. F. Zhou, and L. S. Turng, "Numerical simulation on residual thickness of pipes with curved sections in water-assisted co-injection molding," *Journal of Applied Polymer Science*, vol. 132, no. 34, pp. 1–10, 2015.

[4] N. Xia, P. Zhao, T. Kuang, Y. Zhao, J. Zhang, and J. Fu, "Nondestructive measurement of layer thickness in water-assisted coinjection-molded product by ultrasonic technology," *Journal of Applied Polymer Science*, vol. 135, no. 33, pp. 2–9, 2018.

[5] T.-Q. Kuang, K. Zhou, L.-X. Wu, G.-F. Zhou, and L.-S. Turng, "Experimental study on the penetration interfaces of pipes with different cross-sections in overflow water-assisted coinjection molding," *Journal of Applied Polymer Science*, vol. 133, no. 1, pp. 1–8, 2016.

[6] S.-J. Liu and S.-P. Lin, "Factors affecting the formation of fingering in water-assisted injection-molded thermoplastics," *Advances in Polymer Technology*, vol. 25, no. 2, pp. 98–108, 2006.

[7] Q. Jiang, H. Liu, Q. Xiao, S. Chou, A. Xiong, and H. Nie, "Three-dimensional numerical simulation of total warpage deformation for short-glass-fiber-reinforced polypropylene composite injection-molded parts using coupled FEM," *Journal of Polymer Engineering*, vol. 38, no. 5, pp. 493–502, 2017.

[8] S. Liu and Y. Chen, "The manufacturing of thermoplastic composite parts by water-assisted injection-molding technology," *Composites Part A: Applied Science and Manufacturing*, vol. 35, no. 2, pp. 171–180, 2004.

[9] S. J. Liu, M. J. Lin, and Y. C. Wu, "An experimental study of the water-assisted injection molding of glass fiber filled polybutylene-terephthalate (PBT) composites," *Composites Science and Technology*, vol. 67, no. 7-8, pp. 1415–1424, 2007.

[10] H. Huang, R. Zhou, and C. Yang, "Fiber orientation propelled by high-pressure water penetration in water-assisted injection molded fiber-reinforced thermoplastics part," *Journal of Composite Materials*, vol. 47, no. 2, pp. 183–190, 2012.

[11] I. Fiebig and V. Schoeppner, "Factors influencing the fiber orientation in welding of fiber-reinforced thermoplastics," *Welding in the World*, vol. 62, no. 5, pp. 997–1012, 2018.

[12] R. Taktak, N. Guermazi, and T. K. Kallel, "Effect of E-Glass fibre and ply orientation on the mechanical behaviour of FRP composites used for pressure pipe," *The International Journal of Advanced Manufacturing Technology*, vol. 92, no. 5-8, pp. 1741–1749, 2017.

[13] S. Mortazavian and A. Fatemi, "Effects of fiber orientation and anisotropy on tensile strength and elastic modulus of short fiber reinforced polymer composites," *Composites Part B: Engineering*, vol. 72, pp. 116–129, 2015.

[14] U. Delpy and G. Fischer, "Effect of mold-filling conditions on fiber distribution in injection-molded disks and on the mechanical properties of such disks," *Advances in Polymer Technology*, vol. 5, no. 1, pp. 19–26, 1985.

[15] S. Lee, D. Yang, J. Ko, and J. Youn, "Effect of compressibility on flow field and fiber orientation during the filling stage of injection molding," *Journal of Materials Processing Technology*, vol. 70, no. 1-3, pp. 83–92, 1997.

[16] K. Li, S. Yan, W. Pan, and G. Zhao, "Optimization of fiber-orientation distribution in fiber-reinforced composite injection molding by Taguchi, back propagation neural network, and genetic algorithm–particle swarm optimization," *Advances in Mechanical Engineering*, vol. 9, no. 9, pp. 1–11, 2017.

[17] H. Tseng, R. Chang, and C. Hsu, "Numerical prediction of fiber orientation and mechanical performance for short/long glass and carbon fiber-reinforced composites," *Composites Science and Technology*, vol. 144, pp. 51–56, 2017.

[18] H. Tseng, R. Chang, and C. Hsu, "Effect of the packing stage on fiber orientation for injection molding simulation of fiber-reinforced composites," *Journal of Thermoplastic Composite Materials*, vol. 31, no. 9, pp. 1204–1218, 2017.

[19] H. Tseng, R. Chang, and C. Hsu, "An objective tensor to predict anisotropic fiber orientation in concentrated suspensions," *Journal of Rheology*, vol. 60, no. 2, pp. 215–224, 2016.

[20] S. G. Advani and C. L. Tucker, "The use of tensors to describe and predict fiber orientation in short fiber composites," *Journal of Rheology*, vol. 31, no. 8, pp. 751–784, 1987.

[21] B. O. Agboola, D. A. Jack, and S. Montgomery-Smith, "Effectiveness of recent fiber-interaction diffusion models for orientation and the part stiffness predictions in injection molded short-fiber reinforced composites," *Composites Part A: Applied Science and Manufacturing*, vol. 43, no. 11, pp. 1959–1970, 2012.

[22] V. Kůrková, "Kolmogorov's theorem and multilayer neural networks," *Neural Networks*, vol. 5, no. 3, pp. 501–506, 1992.

[23] K. Li, S. Yan, W. Pan, and G. Zhao, "Warpage optimization of fiber-reinforced composite injection molding by combining back propagation neural network and genetic algorithm," *The International Journal of Advanced Manufacturing Technology*, vol. 90, no. 1-4, pp. 963–970, 2017.

Hindawi
Advances in Polymer Technology
Volume 2019, Article ID 3720127, 20 pages
https://doi.org/10.1155/2019/3720127

Research Article

Quality Indexes Design for Online Monitoring Polymer Injection Molding

Jian-Yu Chen,[1] Chien-Chou Tseng,[2] and Ming-Shyan Huang[2]

[1]*Bachelor's Program of Precision System Design, Feng Chia University, 100, Wenhua Rd., Seatwen Dist., Taichung City 407, Taiwan*
[2]*Department of Mechatronics Engineering, National Kaohsiung University of Science and Technology, 1, University Rd., Yanchao Dist., Kaohsiung City 824, Taiwan*

Correspondence should be addressed to Ming-Shyan Huang; mshuang@nkust.edu.tw

Received 1 April 2019; Revised 5 July 2019; Accepted 15 July 2019; Published 1 August 2019

Guest Editor: Yun Zhang

Copyright © 2019 Jian-Yu Chen et al. This is an open access article distributed under the Creative Commons Attribution License, which permits unrestricted use, distribution, and reproduction in any medium, provided the original work is properly cited.

Quality control is a crucial issue in the injection molding process with target of obtaining a high yield rate and reducing production cost. Consequently, effective methods for monitoring the injection conditions (e.g., pressure, velocity, and temperature) in real-time and adjusting these conditions adaptively as required to ensure a consistent part quality are essential. This study proposes a quality index based on the clamping force increment during the injection cycle, as determined by four strain gauges attached to the tie bars of the injection molding machine. Also, various quality indexes for online quality monitoring and prediction purposes based on the pressure, viscosity, and energy features extracted from the pressure profiles obtained at the load cell, nozzle, and molding cavity, respectively, are compared. The feasibility of the proposed quality indexes is investigated experimentally for various settings of the barrel temperature, back pressure, and rotational speed of the plasticizing screw. It is shown that all of the quality indexes are correlated with the injection-molded quality and hence provide a feasible basis for the realization of an on-line quality monitoring and control system. Particularly, the tie-bar elongation quality index requires no modification or invasion of the injection molding system or cavity and hence provides a particularly attractive solution for monitoring and controlling the part quality.

1. Introduction

Injection molding is a well-established technique for the mass production of plastic components. With its advantages of low cost, high efficiency, good versatility, and the ability to produce precise and complex components, injection molding is used in many fields nowadays, including electronics, sports goods, automobile components, and optical lenses. However, ensuring a consistent quality of injection-molded parts is highly challenging since the melt quality is readily affected by variations in the raw material properties, plasticizing and injection molding conditions, and machine motion characteristics. Importantly, even though current all-electric driven injection molding machines provide an extremely precise motion control, even very small variations in the raw material properties and/or plasticizing and injection molding conditions may result in significant variations in the molding quality. Furthermore, current inspection techniques focus mainly on the quality (e.g., geometrical dimensions and surface defects) of the final molded components. In other words, while they can confirm that the molded components satisfy the design criteria, in the event that they do not, they provide no clues as to why this is the case. Hence, such methods not only are time-consuming and expensive, but are also of only limited use in adjusting the injection molding conditions adaptively in such a way as to improve the consistency of the molding quality. Consequently, more effective methods for performing the on-line monitoring and control of the part quality are urgently required.

2. Literature Review

The injection molding process has traditionally been regarded as something of a "black box" since the flow behavior of the molten polymer within the cavity is unseen. Consequently, the process parameters are generally controlled through either statistical methods or simply the

personal experience of the operator. The plasticizing process in the injection molding procedure is usually performed using a reciprocating single screw that conveys, melts, and meters the molten polymer at a constant rotational speed. However, significant variations in the plasticizing quality are often observed, even when the screw motion is precisely controlled. Amano and Utsugi investigated the effects of the various injection molding parameters on the plasticizing quality and found that the quality was dominated by the shear heat in the metering zone and the absorption of the heat energy in the compression and feeding zones, which is determined primarily by the residual time of the molten polymer within the barrel [2–4]. In general, a long screw length is essential to ensure sufficient time for the raw materials to be properly heated as they pass through the feeding and compression zones, while a high rotational speed of the feed screw is necessary to expand the temperature variation of the molten polymer. Latif and Saidpour investigated the effect of the plasticizing parameters on the melt quality of PP, HDPE, and LLDPE polymer materials blended with master one percent batch colored pigment separately and found that a high back pressure and high screw rotational speed enhanced the shear rate of the molten polymer and improved the plasticization quality as a result [5]. Similar findings were also reported in the later studies of Tanoue et al. and Zhou et al., respectively [6, 7]. Khoshooee and Coates used the Taguchi robust design method to examine the effects of the back pressure, screw rotational speed, barrel temperature, screw retreat position, and speed on the plasticization quality of acrylonitrile butadiene styrene (ABS) materials [8]. The results showed that the melt quality was dominated by the barrel temperature and back pressure at slow rotational speeds of the screw. Jin et al. investigated the solid bed breakup behavior of a standard reciprocating injection screw and found that the breakage was determined mainly by the temperature and pressure of the molten polymer [9]. Hence, a careful control of the process parameters during the plasticizing process is essential to ensure the quality of the final molded components.

Modern all-electric driven injection molding machines provide highly precise and stable motion control. Moreover, the use of grey prediction methods to optimize the filling-to-packing switchover point can further enhance the quality consistency of the molded products [10]. However, minor changes in the melt quality inevitably occur during the injection molding process, and these variations cannot be entirely compensated by even the most precise motion control of the machine [11]. Even very small variations in the molten polymer quality may cause significant changes in the mechanical properties and dimensions of the molded part [12, 13]. As a result, it is essential that the melt quality be monitored in some way during the molding process such that the processing parameters can be modified if required. Accordingly, various p-V-T (pressure-volume-temperature) measuring methods have been proposed for predicting the melt quality [14–17]. Many studies have confirmed that an effective control of the p-V-T path of the molten polymer during the injection molding process improves the quality and consistency of the final product [18–21]. Wang and Mao showed that the injection molding quality is determined mainly by the pressure and temperature conditions [22]. However, in practical online quality inspection and motion control systems, the pressure signal is generally preferred since the response time is relatively quicker than that of the temperature signal [23–28].

The quality and reproducibility of injection molded components are highly correlated with the flow resistance (i.e., viscosity) of the molten polymer. However, the viscosity is traditionally measured off-line using a rheometer, and hence the measurement results are of little value in tuning the injection molding parameters adaptively in response to subtle changes in the melt quality. Hence, Gornik proposed an in-machine melt quality measurement system, in which the volumetric flow rate of the molten polymer passing through the nozzle in 10 minutes was detected using a special sensor installed within the nozzle [29]. The author additionally proposed a torque rheometer for online viscosity estimation based on the ratio of the energy consumption to the metering volume during the plasticizing stage. Aho and Syrjälä used a slit die equipped with pressure sensors to estimate the melt viscosity by measuring the ratio of the pressure gradient within the die to the volumetric flow rate of the molten polymer passing through it [30]. Kruppa et al. presented a feedback control method for calculating the viscosity of the molten polymer based on the detected nozzle pressure and temperature [31]. Asadizanjani and Gordon developed a multivariate sensor for controlling the melt quality based on pressure, temperature, and velocity measurements of the molten polymer [32, 33]. Montgomery and Gallo found that the change of the cavity pressure during the cavity filling stage ($\Delta P/\Delta t$) is proportional to the melt viscosity and hence provides a feasible means of predicting the part quality [34]. Lin et al. designed a pressure sensor bushing mounted around the nozzle for the online estimation of the molten polymer viscosity [35]. Chen et al. proposed an online melt quality monitoring system based on four quality indexes (i.e., the peak pressure, pressure gradient, viscosity index, and energy index) extracted from the signals collected from three pressure sensors mounted in the nozzle, runner, and cavity, respectively [36]. These quality indexes provide a convenient and effective means of monitoring shot-by-shot variations in the melt quality during continuous injection molding processes. As to the present study, we further proposed an online part quality inspection method based on quality indexes, in particular, a new quality index based on the clamping force increment during the injection cycle, as determined by four strain gauges attached to the tie bars of the injection molding machine. The tie-bar elongation quality index requires no modification or invasion of the injection molding system or cavity and hence provides a particularly attractive solution for monitoring and controlling the part weight quality.

During the filling phase of the injection molding process, molten polymer flows into the cavity under high temperature and pressure conditions. As the cavity fills, the pressure gradually increases. At the moment the voids in the cavity become completely full, the polymer material undergoes an instantaneous compression effect, which causes a sudden

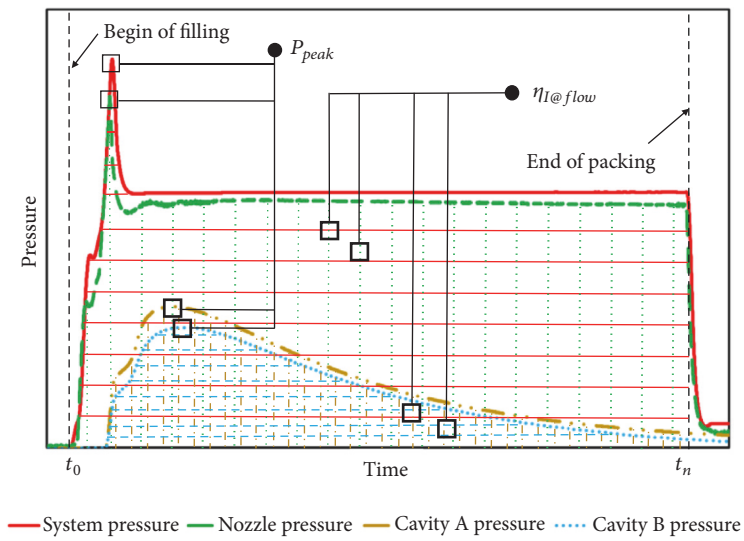

Figure 1: Peak pressure and viscosity indexes.

rise of the cavity pressure and a corresponding separation of the mold. Based on this observation, Chen et al. proposed a method for controlling the filling-to-packing switchover point by measuring changes in the tie-bar elongation profile using strain gauges attached to the tie bar structures [24, 37]. Yin et al. similarly presented a method for minimizing warpage in the injection molding process by optimizing the clamping force using a backpropagation neural network and a genetic algorithm [38]. Huang et al. confirmed that a proper setting of the clamping force is essential to enhance the quality and consistency of injection molded parts [39]. Zhao et al. developed a methodology based on ultrasonic technology to *in situ* detect clamping force [40, 41], and the advantages are simple, practical, and nondestructive.

In summary, current injection molding quality estimation methods generally exploit the signals obtained from pressure sensors located in or near the molding cavity. Such methods provide an effective approach for estimating the melt quality and tuning the processing conditions accordingly. However, they incur an additional cost in procuring the sensors and increase the time and expense of the mold setup process. Furthermore, an extremely precise positioning of the sensors is essential to prevent damage to the component during the molding process. Accordingly, the present study not only proposes three quality indexes based on the peak pressure, viscosity, and energy features extracted from the load cell, nozzle, and cavity pressure profiles, respectively, but also proposes an additional quality index based on the change in the clamping force during the injection cycle, as determined by four strain gauges mounted on the tie-bar surfaces. The feasibility of the various quality indexes for estimating the part quality is evaluated experimentally for various settings of the barrel temperature, back pressure, and rotational speed of the plasticizing screw, respectively.

3. Derivation of Quality Indexes

Figure 1 shows the pressure profiles detected by four sensors located at the load cell, nozzle, and two cavities of the injection mold, respectively, in the injection molding process. For each pressure profile, the peak pressure index, P_{peak}, indicates the maximum absolute pressure detected by the corresponding sensor during the filling, packing, and holding stages. In general, molten polymers with a higher viscosity have a relatively larger flow resistance and hence require a greater force to accomplish mold filling. According to Hele–Shaw theory, the flow behavior of the molten polymer in the molding cavity is analogous to that of viscous fluid flow within a slit [39]. Thus, the flow velocity in the x-direction varies as a function of the viscosity μ, the pressure drop ΔP over a flow distance L, and the width w and height h of the cavity [35], i.e.,

$$v_x(z) = \frac{1}{\mu}\frac{h^2}{8}\frac{\Delta P}{L}\left[1-\left(\frac{2z}{h}\right)^2\right]. \quad (1)$$

As shown in Eq. (1), the flow velocity profile is parabolic over the cavity height (i.e., the molded component thickness), and hence the maximum velocity, $v_{x,Max} = (h^2/8\mu)(\Delta P/L)$, appears in the mid-height position of the cavity. Averaging the flow velocity along the height direction, the Hele-Shaw flow formulation can be further derived as

$$v_{x,avg} = \frac{1}{h}\int_{-h/2}^{h/2} v_x(z)\,dz = \frac{h^2}{12\mu}\frac{\triangle P}{L}, \quad (2)$$

$$Q = v_{x,avg} \bullet hw = \frac{h^3 w}{12\mu}\frac{\triangle P}{L}, \quad (3)$$

where Q is the volumetric flow rate.

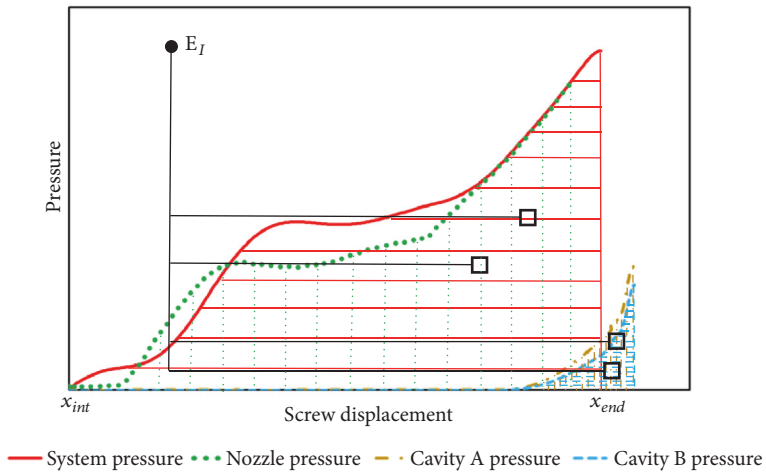

Figure 2: Energy index.

Furthermore, the instantaneous viscosity can be expressed as

$$\mu = \frac{h^2}{12L^2} \bullet \Delta P \bullet \Delta t. \tag{4}$$

In other words, the instantaneous viscosity of the molten polymer is directly proportional to the cavity height and pressure drop, ΔP, multiplied by a short time duration, Δt, and is inversely proportional to the flow distance L along the flow path during time Δt. For a given set of processing parameters (e.g., injection speed, holding pressure, and holding time), the injected volume of molten polymer in each shot is theoretically constant, and hence the flow distance L can also be taken as a constant for a uniform thickness h of the molded specimen.

The instantaneous viscosity given in Eq. (4) provides an indication of the flow resistance experienced by the molten polymer over a particular filling and holding distance. Hence, the present study proposes a new quality index designated as the melt viscosity index, $\eta_{I@flow}$, defined as

$$\eta_{I@flow} = C \int_{t_o}^{t_n} P(t)\, dt, \tag{5}$$

where C is a constant with a value which depends on the geometry of the mold cavity; $P(t)$ is the pressure signal detected over time by the corresponding sensor; and t_o and t_n represent the beginning and end times of the filling and holding process, respectively.

The mechanical energy consumed by the reciprocating screw in each shot is proportional to the viscosity of the molten polymer [29]. Accordingly, the present study proposes a further quality index, referred to as the energy index, E_I, which quantifies the energy consumed per shot by integrating the pressure profile with respect to the screw position (see Figure 2), i.e.,

$$E_I = A_{screw} \int_{x_{int}}^{x_{end}} P(x) \bullet dx, \tag{6}$$

where x_{int} is the initial position of the screw and x_{end} is the position of the screw at the end of the filling and holding process.

In injection molding systems, press-on strain sensors enclosed in a stainless steel protective foil and wrapped tightly around the cylindrical surface of the tie bars can be used to measure the surface strain directly at the mounting location in a manner similar to that of bonded tie-bar strain sensors used to measure the clamping force. In particular, the signals obtained from the press-on strain sensors yield the following measurements [38]:

$$\varepsilon_i = \frac{F_i}{EA}, \tag{7}$$

$$F_i = \frac{EA\varepsilon_i}{10^6}, \tag{8}$$

$$F_\Sigma = \sum_{i=1}^{n} F_i, \tag{9}$$

where ε_i is the strain of the ith tie bar in micrometers; E is Young's modulus of the tie bar material (i.e., 210,000 N/mm^2 for the injection molding machine used in the present study); A is the cross-sectional area of the tie bars in squared millimeters; F_i and F_Σ are the clamping force of the ith tie bar and the total clamping force (in kN), respectively, and n is the total number of tie bars. In Eq. (8), the item 10^6 in the denominator is used for the unit of clamping force to be kN.

Mold separation typically takes place during the period from the end of the filling stage to the end of the packing/holding stage and has a magnitude dependent on the cavity size and raw materials employed. While mold separation can often be tolerated within a limited range (e.g., 75 μm), larger separations result in flash and other undesirable quality defects. Hence, the clamping force must be carefully controlled. In practice, the mold separation effect induces an additional extension of the tie bars and hence increases the clamping force beyond the nominal value specified in

Table 1: Abbreviations of quality indexes.

Abbreviation	Definition
$P_{peak,S}$	Peak pressure index extracted from system pressure
$P_{peak,N}$	Peak pressure index extracted from nozzle pressure
$P_{peak,CavityA/B}$	Peak pressure index extracted from cavity pressure at cavity A/B
$\eta_{I@flow,S}$	Melt viscosity index extracted from system pressure
$\eta_{I@flow,N}$	Melt viscosity index extracted from nozzle pressure
$\eta_{I@flow,CavityA/B}$	Melt viscosity index extracted from cavity pressure at cavity A/B
$E_{I,S}$	Energy index extracted from system pressure
$E_{I,N}$	Energy index extracted from nozzle pressure
$E_{I,CavityA/B}$	Energy index extracted from cavity pressure at cavity A/B
$F_{\Sigma,increment}$	Total clamping force increment extracted from clamping force
$F_{\Sigma,increment@SGa}$	Clamping force increment of tie-bar A extracted from the strain gauge mounted on tie-bar A
t_{feeding}	Feeding time at the plasticization stage

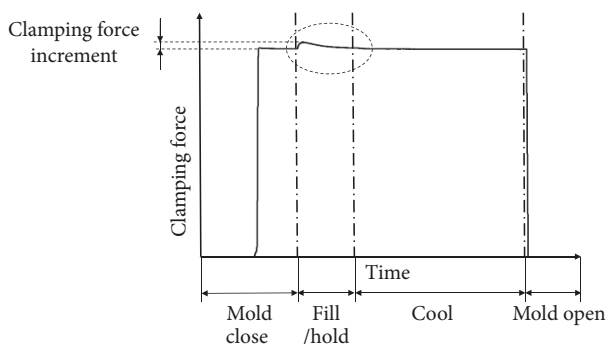

Figure 3: Clamping force increment index.

Figure 4: Photograph of experimental setup.

the design process. As shown in Figure 3, the clamping force increases rapidly toward the nominal design value as the filling, packing, and holding process proceeds and then suddenly spikes at the moment the cavity becomes completely full and the polymer resin undergoes compression. The increment in the clamping force, $F_{\Sigma,increment}$, is hence defined as an additional quality index in the present study, where it represents a measure of the degree of the mold filled with molten polymer from the injection unit. The description of quality indexes is shown in Table 1.

The quality of continuous injection molding processes is generally evaluated by comparing the part qualities of successive components. Accordingly, in the present study, the validity of the various pressure-based and force-based quality indexes described above was evaluated by examining the correlation between the quality indexes obtained at each of the monitoring positions (i.e., the load cell, nozzle, cavities, and tie bars) and the associated part quality, as determined by the thickness and weight of the molded component. In other words, for each quality index, the correlation index, r, was computed as

$$r = \frac{\sum (x - \overline{x})(y - \overline{y})}{\sqrt{\sum (x - \overline{x})^2}\sqrt{\sum (y - \overline{y})^2}}, \tag{10}$$

Table 2: Correlation index categories [1].

Strength	Correlation index
Strong	$\lvert r\rvert \geqq 0.7$
Middle	$0.7 > \lvert r\rvert \geqq 0.3$
Weak	$0.3 > \lvert r\rvert$

where x and y are quality indicators, respectively. Depending on the value obtained for the correlation index, the degree of correlation between the quality index and the melt viscosity was classified as "strong," "medium," or "weak," as shown in Table 2.

4. Experimental Setup

Figure 4 shows the general layout of the proposed online quality inspection system based on the four quality indexes described above. The experimental trials considered a dumbbell-shaped specimen with a length of 125 mm, a central width of 13 mm, an end width of 19 mm, and a thickness of 1.2 mm (Figure 5). The experiments were performed using two different ABS materials (both produced by Chi-Mei Corporation, Taiwan), namely, PA756 and PA756H. As shown in Table 3, the two materials have the same

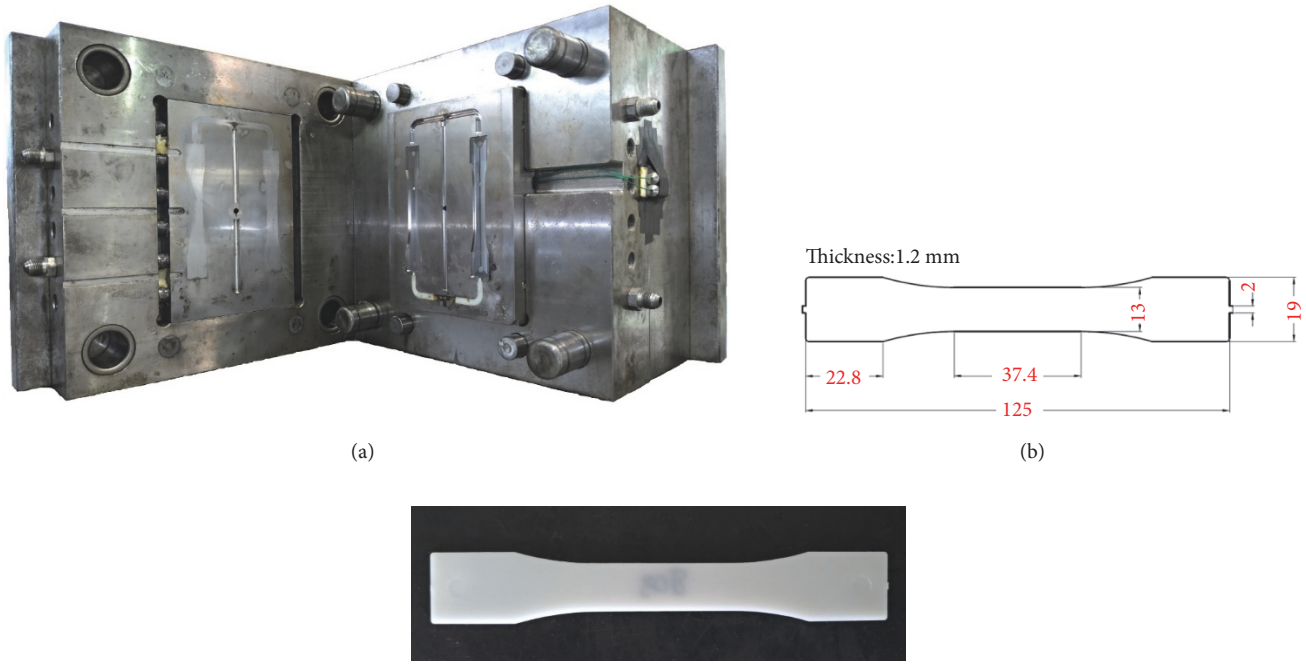

Figure 5: (a) Photograph of dual-cavity injection mold, (b) geometrical dimensions of dumbbell specimen, and (c) photograph of injection-molded part.

Table 3: Material properties and recommended processing conditions.

Property	ASTM test method	Materials	
		PA-756	PA-756H
Melt flow index (g/10min)	D1238	4.4	8
Tensile strength (MPa)	D638	48	40
Density (g/cm^3)	D792	1.05	
Hardness (R scale)	D785	115	
Processing conditions			
Mold Temp. (°C)	40-80	Solid. Temp. (°C)	120
Melt Temp. (°C)	180-230	Eject. Temp. (°C)	100

Table 4: Machine specification.

FANUC Roboshot S-2000i100B	Specification	Unit
Injection unit	Screw diameter (mm)	28
	Injection stroke (mm)	95
	Injection pressure (MPa)	240
	Injection speed (mm/s)	330
Clamping unit	Clamping force (kN)	1000

recommended processing conditions. However, the melt flow index (MFI) of PA756 is lower than that of PA756H. In other words, PA756 has a higher viscosity than PA756H under the same injection conditions. The injection molding trials were performed using an all-electric injection molding machine (ROBOSHOT S-2000i100B, FANUC, Japan) with the specification shown in Table 4.

As shown in Figures 6 and 7, the measuring system consisted of four pressure sensors located at the load cell, nozzle, and two cavities of the dumbbell molding chamber (CP_a and CP), respectively, and four strain gauge sensors (SG_a, SG_b, SG_c, and SG_d) attached to the four tie bars of the injection molding machine, respectively. The specifications of the various sensors are listed in Table 5. For each experimental

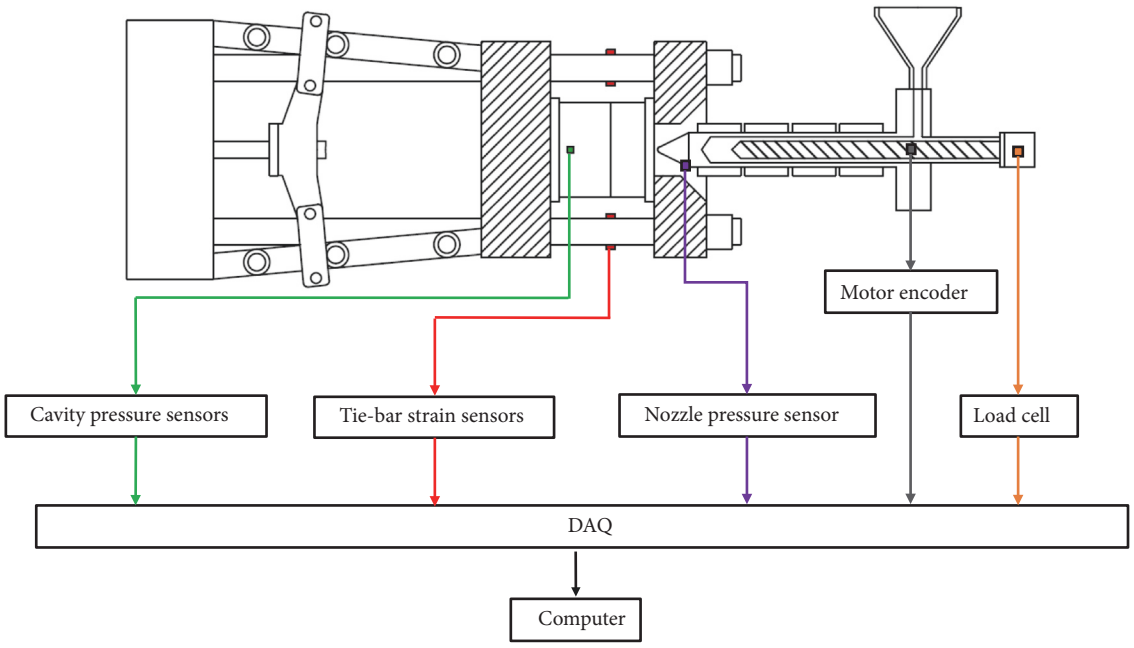

Figure 6: Schematic illustration of injection molding quality monitoring system.

Table 5: Sensor specifications.

Sensor	Supplier	Type
Nozzle pressure sensor	Kistler	9247A
Cavity pressure Sensor	Kistler	6159A
Tie-bar strain sensor	GEFRAN	GE1029
DAQ card	National Instruments	USB-6343

Table 6: Process parameter settings for varied plasticizing parameters experiments.

Fixed parameters			
Feeding stroke (mm)	40	Packing time (s)	5
Injection speed (mm/s)	90	Cooling time (s)	15
V/P switch (mm)	15	Mold temperature (°C)	60
Packing pressure (MPa)	105	Clamping force (kN)	600
Varied parameters			
Barrel temperature (°C)		205, *210*, 215, 220	
Back pressure (MPa)		5, *10*, 15, 20	
Screw rotational speed (rpm)		50, *100*, 150, 200	

Note: the italic letters act as fixed parameters as the one of them performs.

trial, the molding quality was evaluated by measuring the component weight and geometrical dimensions at points A_1, A_2, B_1, and B_2 (see Figure 7).

5. Results and Discussion

5.1. Effects of Melt Quality Fluctuations on Molded Part Quality. Injection molding experiments were performed to examine the effects of the three main processing parameters, namely, the barrel temperature, back pressure, and screw rotational speed, on the part quality (as determined by the part weight and thickness). Figure 8 shows the average part weight and average part thickness as measured over 30 continuous shots performed using PA756 as the raw material and various values of the three processing parameters. The parameter settings are listed in Table 6. For all values of the barrel temperature, back pressure, and screw rotational speed, a high correlation (r = 0.99) exists between the part thickness and the part weight. Therefore, the part weight can be regarded as a feasible indicator of the molded part quality.

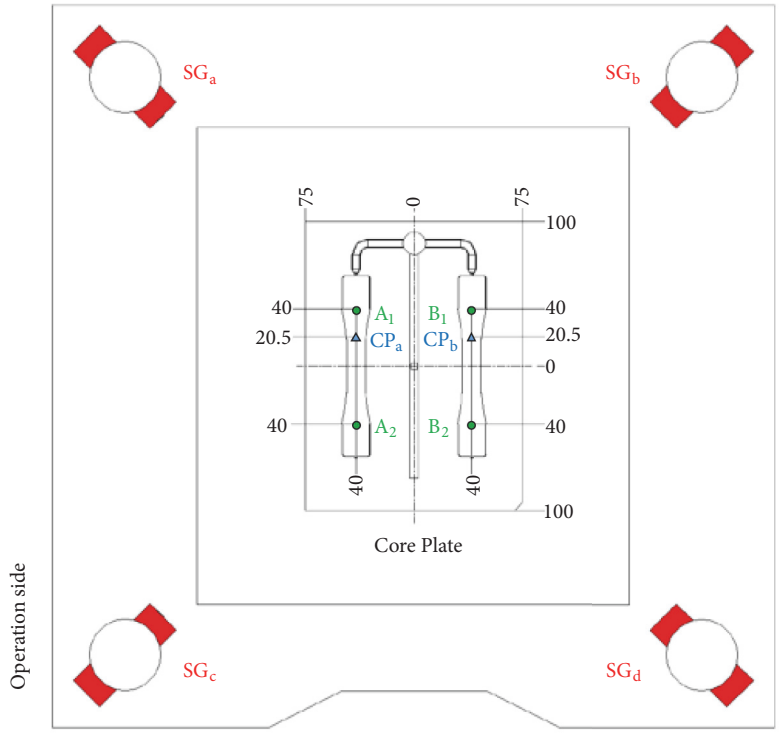

Figure 7: Detailed arrangement of cavity sensors ($CP_a - CP_b$) and strain gauge sensors ($SG_a - SG_d$).

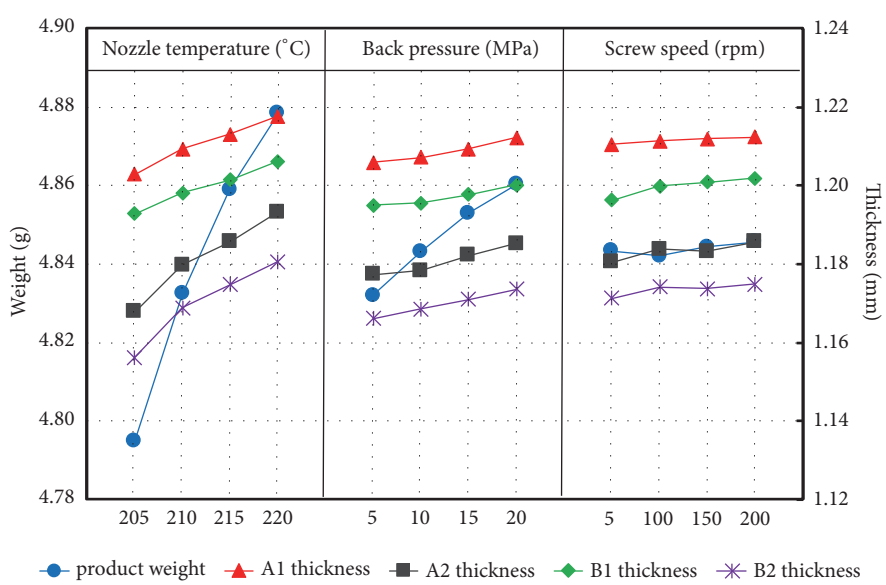

Figure 8: Variation of part weight and thickness for various plasticizing parameters.

5.1.1. Barrel Temperature. Table 7 shows the processing parameters used to investigate the effect of the barrel temperature (205, 210, 215, and 220°C) on the flow ability of the molten polymer during the injection molding process. Figure 9 shows the corresponding results obtained for the four quality indexes and the molded part weight. It is seen in Figures 9(a), 9(c), and 9(e) that the peak pressure, viscosity, and energy indexes derived from the load cell and nozzle pressure profiles reduce with an increasing barrel temperature. A higher barrel temperature reduces the viscosity of the molten polymer and therefore reduces the pressure required to drive the resin into the mold. As a result, the energy consumption also reduces. As the molten polymer leaves the nozzle and flows through the runner into the cavity, its

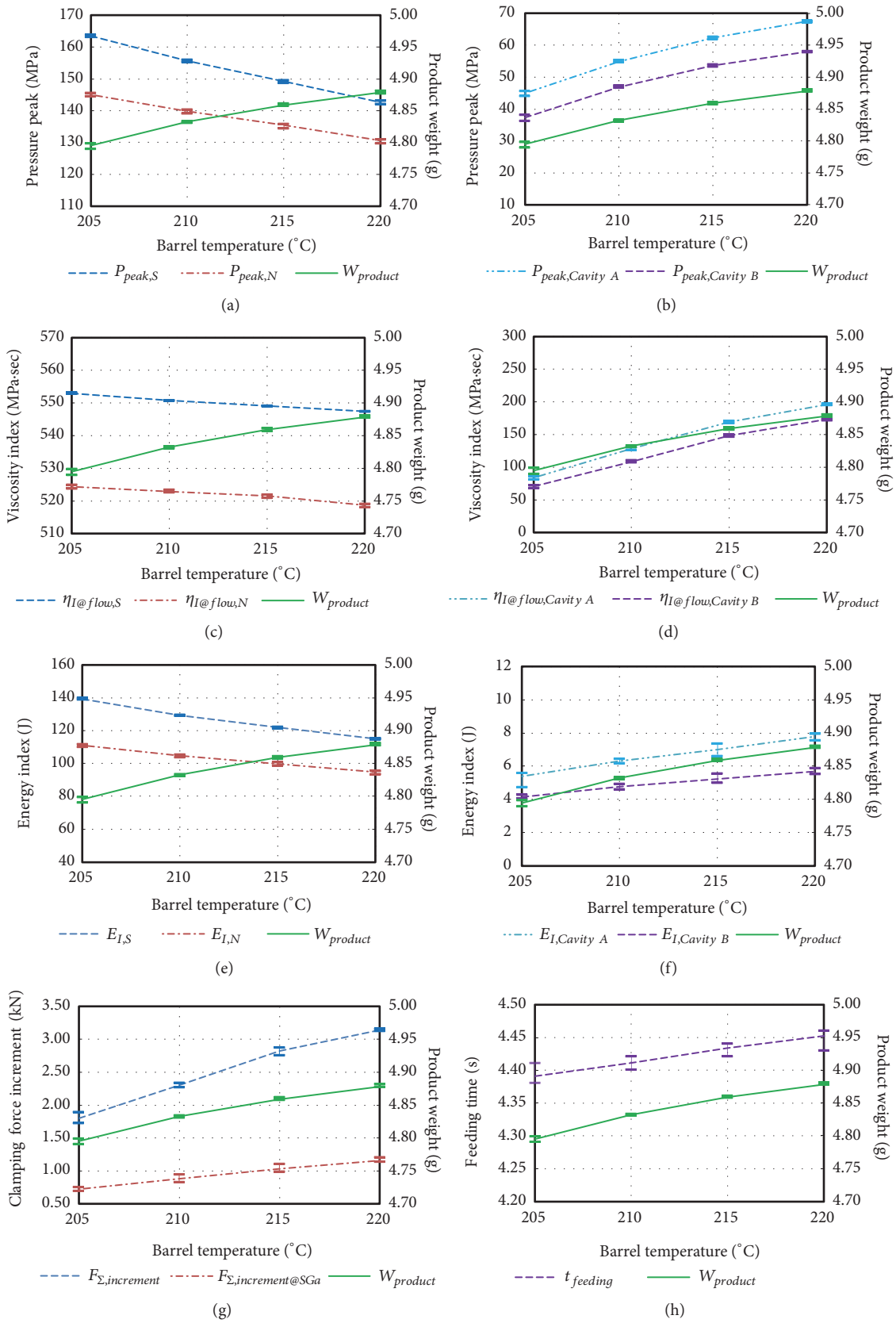

Figure 9: Variation of quality indexes and product weight with barrel temperature.

Table 7: Process parameter settings for varied barrel temperature experiments.

Fixed parameters			
Feeding stroke (mm)	40	Packing pressure (MPa)	105
Back pressure (MPa)	10	Packing time (s)	5
Screw rotational speed (rpm)	100	Cooling time (s)	15
Injection speed (mm/s)	90	Mold temperature (°C)	60
V/P switch (mm)	15	Clamping force (kN)	600
Varied parameter			
Barrel temperature (°C)		205, 210, 215, 220	

Table 8: Process parameter settings for varied back pressure experiments.

Fixed parameters			
Feeding stroke (mm)	40	Packing pressure (MPa)	105
Barrel temperature (°C)	210	Packing time (s)	5
Screw rotational speed (rpm)	100	Cooling time (s)	15
Injection speed (mm/s)	90	Mold temperature (°C)	60
V/P switch (mm)	15	Clamping force (kN)	600
Varied parameter			
Back pressure (MPa)		5, 10, 15, 20	

Table 9: Process parameter settings for varied screw rotational speed experiments.

Fixed parameters			
Feeding stroke (mm)	40	Packing pressure (MPa)	105
Barrel temperature (°C)	210	Packing time (s)	5
Back pressure (MPa)	10	Cooling time (s)	15
Injection speed (mm/s)	90	Mold temperature (°C)	60
V/P switch (mm)	15	Clamping force (kN)	600
Varied parameter			
Screw rotational speed (rpm)		50, 100, 150, 200	

flow and compressive abilities increase. Moreover, the gate-frozen time is delayed with an increasing barrel temperature. Consequently, more molten polymer is forced into the cavity, and thus the peak cavity pressure and part weight increase, as shown in Figures 9(b) and 9(d), respectively. The energy consumption also increases, as shown in Figure 9(f). The higher cavity pressure at higher barrel temperatures increases the mold separation effect, and hence the clamping force increment detected by the tie-bar elongation sensors also increases, as shown in Figure 9(g). Finally, Figure 9(h) shows that the screw feeding time increases by around 0.06 s as the barrel temperature increases from 205 to 220°C.

5.1.2. Back Pressure. Table 8 shows the processing parameters used to investigate the effect of the back pressure (5, 10, 15, and 20 MPa) on the flow ability of the molten polymer during the injection molding process. Figure 10 shows the corresponding results obtained for the four quality indexes and molded part weight, respectively. It is seen in Figures 10(a)–10(f) that the peak pressure index, viscosity index, and energy index all increase with an increasing back pressure. A higher back pressure results in a greater density and viscosity of the molten polymer and therefore increases the pressure required to drive the resin into the mold. As a result, the energy consumption also increases. As the molten polymer leaves the nozzle and flows through the runner into the cavity, the varying back pressure does not change the gate-frozen time. However, the greater amount of molten polymer injected in the filling stage leads to an increased part weight, as shown in Figure 10(f). Furthermore, the greater cavity pressure induced under a higher back pressure enhances the mold separation effect and therefore increases the clamping force increment, as shown in Figure 10(g). A higher back pressure prolongs the screw retreating time in the plasticizing stage. Hence, the screw feeding time increases by almost 1.1 s as the back pressure is increased from 5 to 20 MPa, as shown in Figure 10(h).

5.1.3. Screw Rotational Speed. The effect of the shear rate on the quality of the molten polymer was investigated by performing injection tests with screw rotational speeds of 50, 100, 150, and 200 rpm, respectively. The remaining processing parameters were set as shown in Table 9. Figure 11 shows the corresponding results for the four quality indexes and molded part weight, respectively. In general, the results show that the peak pressure, viscosity, and energy indexes which are obtained from the system, nozzle, and cavity pressure profiles vary only very slightly with the screw rotational speed

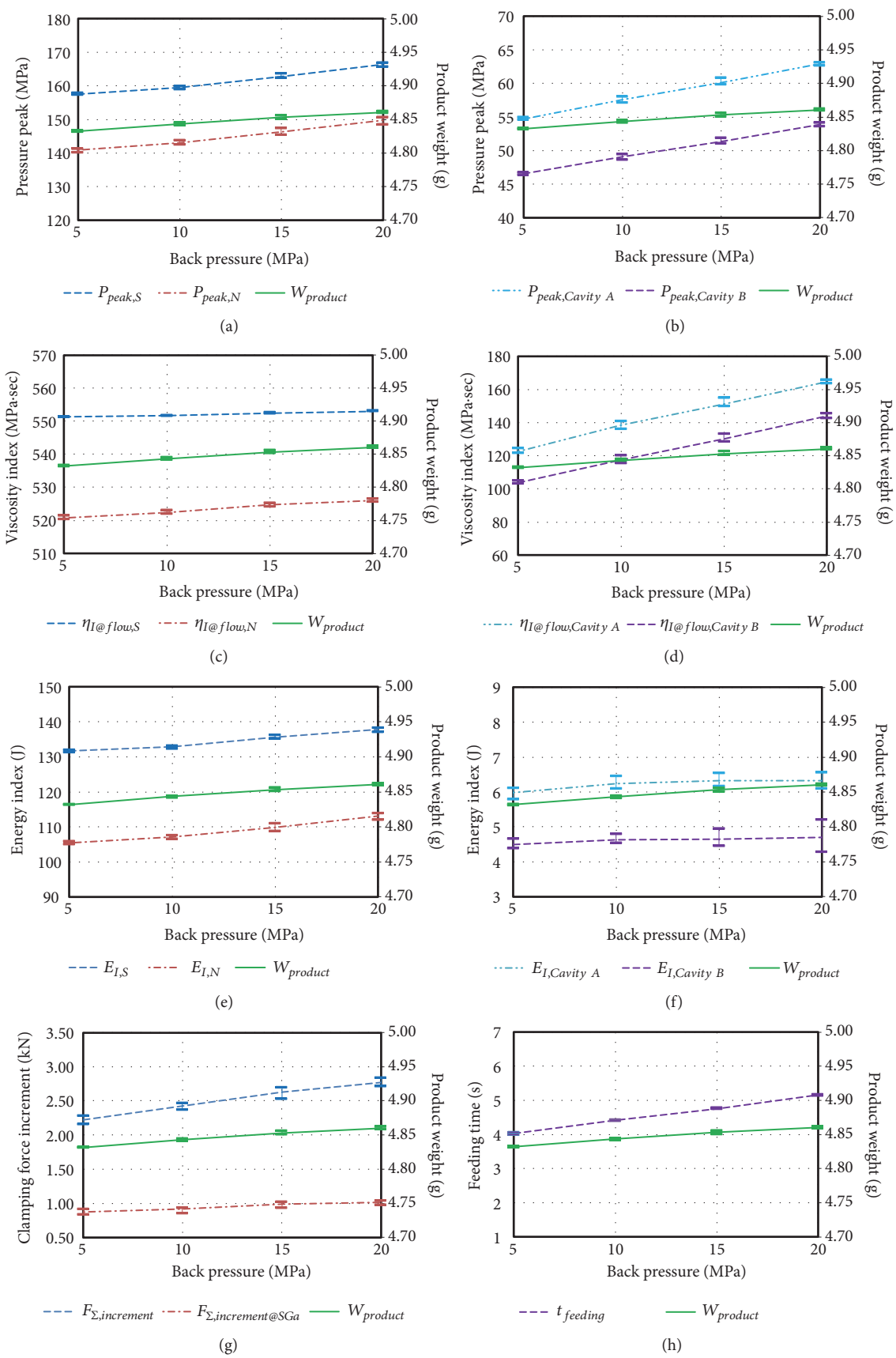

Figure 10: Variation of quality indexes and product weight with back pressure.

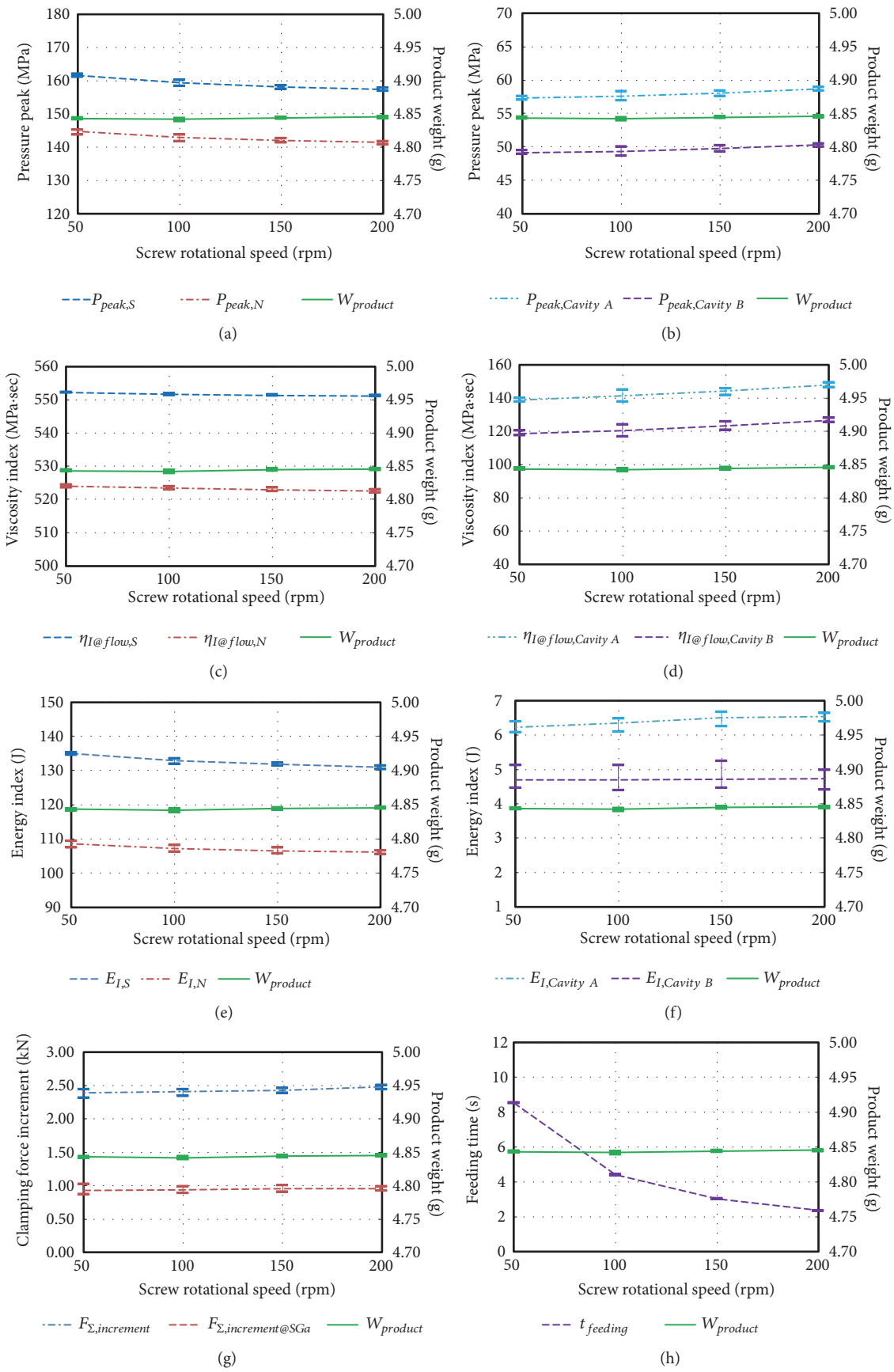

Figure 11: Variation of quality indexes and product weight with screw rotational speed.

Table 10: Process parameter settings for shot-by-shot melt viscosity fluctuation experiments.

Fixed parameters			
Feeding stroke (mm)	40	Packing pressure (MPa)	105
Barrel temperature (°C)	210	Packing time (s)	5
Back pressure (MPa)	10	Cooling time (s)	15
Injection speed (mm/s)	90	Mold temperature (°C)	60
screw rotational speed (rpm)	100	Clamping force (kN)	600
V/P switch (mm)	15		
Varying parameter (Blended materials)			
% of PA756/% of PA756H	100/0, 80/20, 60/40, 40/60, 20/80, 0/100		

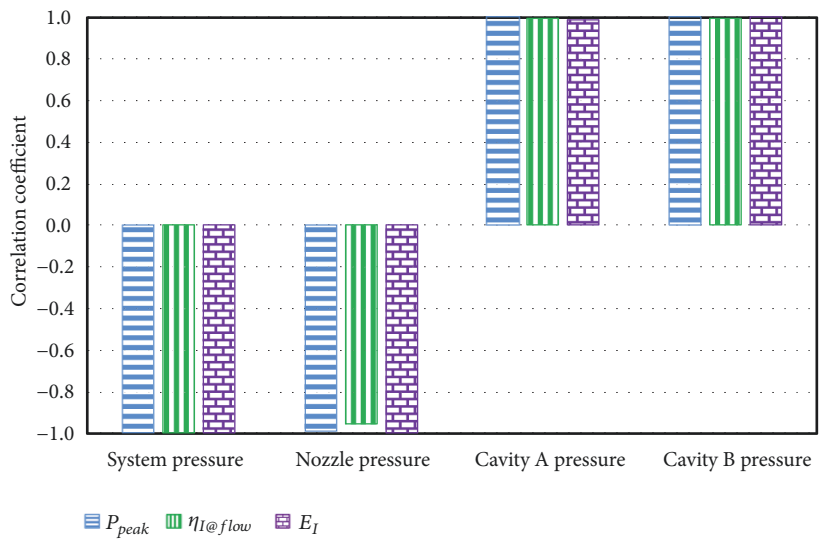

Figure 12: Correlation between pressure-based quality indexes and product weight for various barrel temperatures.

(see Figures 11(a)–11(f)). However, the part weight increases slightly as the screw rotational speed increases. Consequently, the clamping force increment also increases slightly, as shown in Figure 11(g). A higher screw rotational speed shortens the screw retreating time in the plasticizing stage. Consequently, the screw feeding time reduces by approximately 6.2 s as the screw rotational speed is increased from 50 to 200 rpm, as shown in Figure 11(h).

5.2. Correlation between Quality Indexes and Part Quality. As described in the previous section, the present study considered four different quality indexes, namely, the peak pressure, the viscosity, the energy, and the clamping force increment. Moreover, the first three indexes were monitored at four different positions, namely, the load cell of the injection molding system, the nozzle, and the two cavities of the mold die. The correlation between the index values and the quality (i.e., weight) of the injection-molded components was investigated for each of the processing conditions shown in Tables 7~9. For each experimental setting, 30 injection tests were performed using PA756 as the raw material. The correlation values obtained using Eq. (10) for each experimental setting were then averaged over the 30 samples to obtain a representative value for each index. Figures 12–14 show the corresponding results obtained for different barrel temperatures, back pressures, and screw rotational speeds, respectively. The results presented in Figure 12 confirm that the pressure-derived quality indexes are all highly correlated with the part quality for all values of the barrel temperature (i.e., r = -0.95~-1.00 for the load cell and nozzle indexes and r = 0.99~1.00 for the cavity indexes). For the experiments performed with different back pressures, the peak pressure, viscosity, and energy indexes present similarly high correlation values (r = 0.92~1.00), as shown in Figure 13. Finally, for the experiments performed with different screw rotational speeds, the peak pressure and viscosity indexes extracted from the load cell and nozzle pressure profiles exhibit a medium correlation with the part quality (r = -0.61~-0.77) and while those extracted from the cavity pressure profiles have a strong correlation with the part quality (r = 0.73~0.99) (see Figure 14).

Figure 15 shows the correlation coefficients between the clamping force index and the four molded part quality measures obtained in the experiments performed at different barrel temperatures, back pressures, and screw rotational speeds. The correlation coefficients for the experiments performed with different barrel temperatures and barrel speeds vary in the range of 0.96~0.99, while those for the experiments performed with different screw rotational speeds vary in the range of 0.76~0.89. In other words, the clamping force increment index has a good correlation with

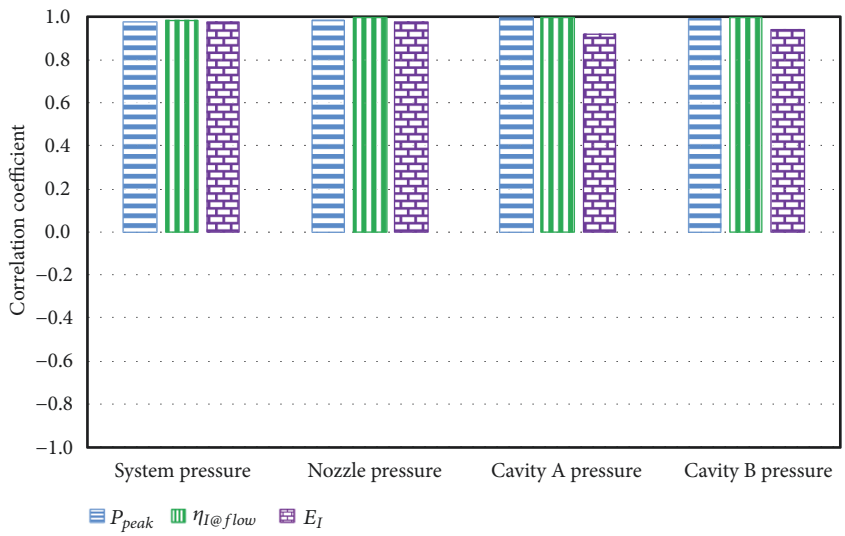

Figure 13: Correlation between pressure-based quality indexes and product weight for various back pressures.

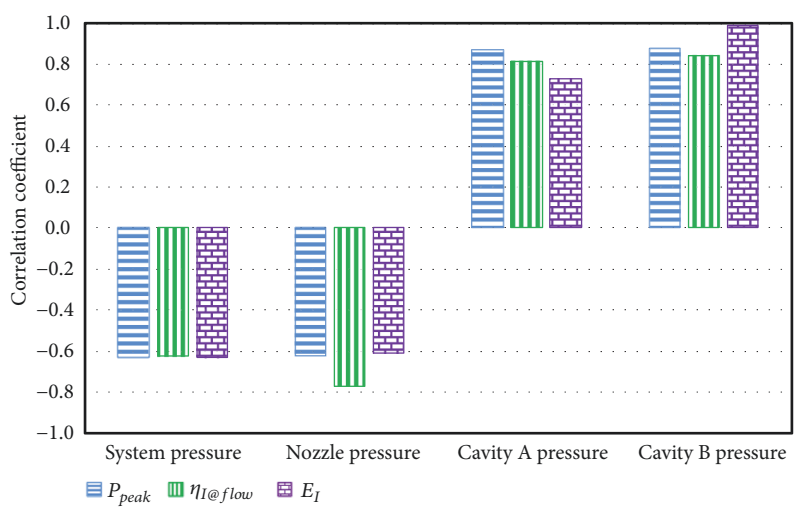

Figure 14: Correlation between pressure-based quality indexes and product weight for various screw rotational speeds.

the part quality under various injection conditions and thus provides a feasible means of estimating the molten polymer quality during the injection molding process.

Of the four pressure signals obtained from the proposed measurement system (i.e., the load cell pressure, the nozzle pressure, and the cavity void pressures (A and B)), only those obtained at the load cell and nozzle (i.e., upstream of the actual injection molding process) provide a full history of the rheological changes which take place during mold filling. Therefore, the quality indexes extracted at the load cell and nozzle provide a better indication of the mold filling quality than those extracted from the cavity. In particular, the quality indexes obtained from the load cell and nozzle pressure profiles provide a better indication of the viscosity variations which take place during the initial filling stage, while those extracted from the cavity pressure profiles provide a better indication of the viscosity variations which take place at the end of filling and hence give a better estimation of the final part quality.

In general the results presented in Figures 12–15 show that all four quality indexes provide an effective means of estimating the melt quality. However, the clamping force increment index is particularly attractive for monitoring and control purposes since it not only provides a good indication of the melt quality, but is also operationally straightforward since it can be implemented using simple stick-on strain gauges without the need for cavity invasion.

5.3. Detection of Melt Quality Fluctuations. To test the ability of the monitoring system to detect changes in the melt quality during continuous molding, injection molding experiments were performed using PA756 pellets for approximately 50 shots followed by the gradual addition of 20% PA756H pellets every 50 shots until 100% PA756H was achieved

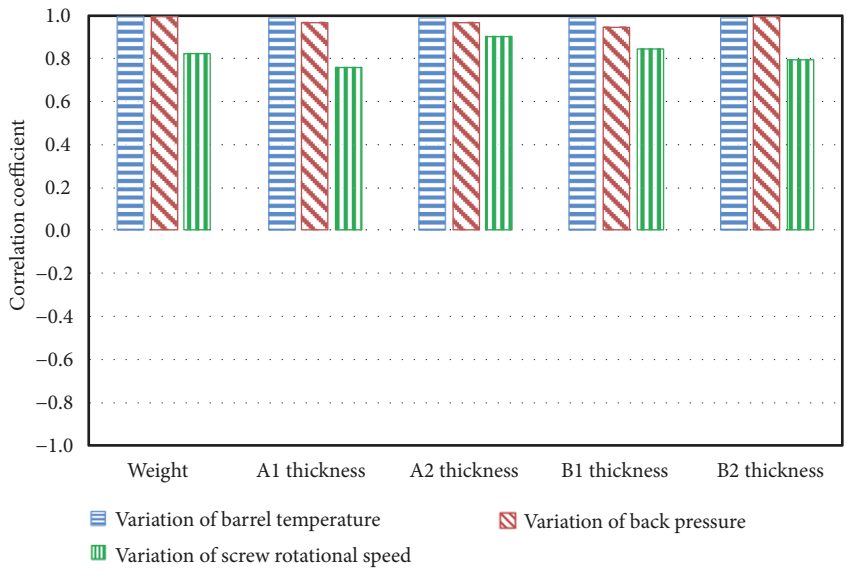

Figure 15: Correlation between clamping force increment index and molded part quality measures for various plasticizing parameters.

Table 11: Process parameter settings for varied V/P switchover position experiments.

Fixed parameters			
Feeding stroke (mm)	40	Packing pressure (MPa)	105
Barrel temperature (°C)	210	Packing time (s)	5
Back pressure (MPa)	10	Cooling time (s)	15
Injection speed (mm/s)	90	Mold temperature (°C)	60
screw rotational speed (rpm)	100	Clamping force (kN)	600
Varied parameter			
V/P switch (mm)	14, 16, 14.2, 15.8, 14.4, 15.6, 14.6, 15.4, 14.8, 15.2, 15		

(see Table 10). Notably, PA756 and PA756H have a similar rheological behavior. However, as mentioned earlier, the melt flow index (MFI) of PA756H is higher than that of PA756. In other words, PA756 has a greater viscosity than PA756H and is thus expected to induce significantly different quality index responses.

Figures 16 and 17 show the shot-by-shot variations in the clamping force increment index, peak pressure index, viscosity index, and energy index, respectively. The results confirm that when the PA756 pellets are gradually replaced with PA756H, the clamping force increment quality index and part weight increase (see Figures 16(a) and 16(b)). In other words, the ability of the proposed quality indexes to reveal crude changes in the viscosity of the molten polymer induced by a change in the raw material is confirmed. The peak pressure, viscosity, and energy quality indexes derived from the load cell and nozzle pressure profiles decrease with an increasing PA756H addition. By contrast, the quality indexes derived from the cavity pressure profiles increase. For both materials, all of the quality indexes fluctuate continuously over the course of the shot-by-shot injection process. In other words, all of the quality indexes provide the means to detect subtle changes in the viscosity (i.e., melt quality) from one shot to the next.

Figure 18 shows the correlation coefficients between the various quality indexes and the part weight, as evaluated using the measurement results obtained in the shot-by-shot injection tests. All of the quality indexes exhibit a strong correlation with the part weight. In particular, the quality indexes computed from the signals acquired at the load cell and nozzle, respectively, have a strong negative correlation with the part weight, while those derived from the cavity pressure signals and measured clamping force, respectively, exhibit a strong positive correlation with the part weight. Overall, the results confirm that all of the quality indexes can be used to predict the quality of the molded parts.

5.4. Detection of Changes in V/P Switchover Position. A final series of experiments was performed to confirm the ability of the clamping force increment quality index to detect variations in the part quality caused by changes in the V/P switchover position. Table 11 shows the corresponding processing parameters. As shown, the V/P point was initially set as 15 mm and was then adjusted to a new value every 5 shots. Figure 19 confirms that the clamping force quality index is strongly correlated with the part weight for all values of the V/P switchover position. For the nominal V/P position (15 mm), the total clamping force and clamping

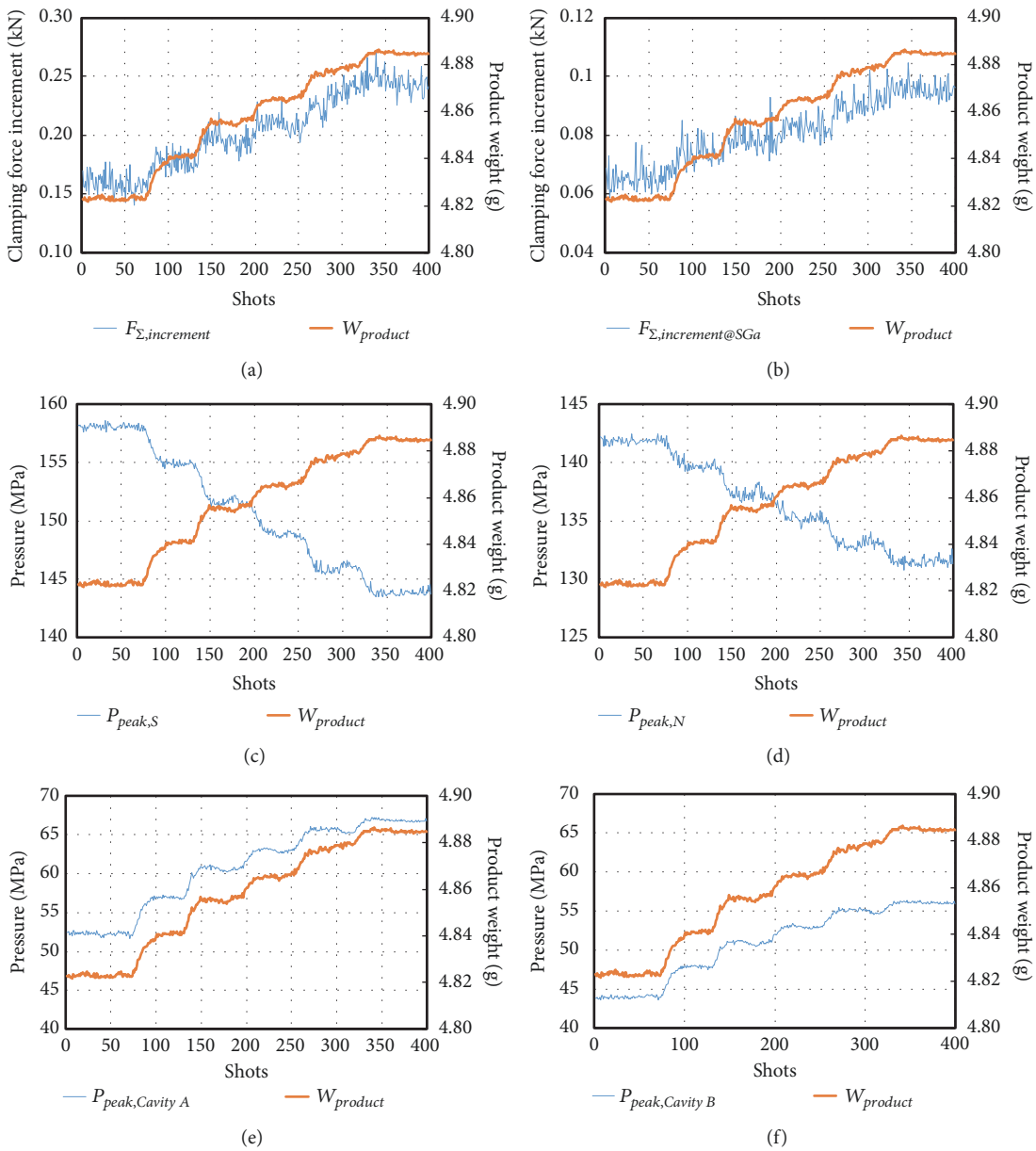

Figure 16: Melt quality fluctuation as revealed by force and pressure quality indexes.

force increment are 544 kN and 3.01 kN, respectively, while the average value and range of the part weight are 4.815 g and 0.010 g, respectively. In general, the results show that, for minor changes of the V/P switchover position from the nominal position, the part weight varies only very slightly. Nonetheless, this small change in the part weight can still be predicted by the single clamping force increment or total clamping force increment index. In other words, the feasibility of the proposed clamping force increment index for estimating the part quality is further confirmed.

6. Conclusions

The mechanical and physical properties of injection-molded components are critically dependent on the viscosity of the molten polymer. However, the polymer materials used in the injection molding process have a complex rheological behavior, and hence the viscosity tends to vary from cycle to cycle. Consequently, online methods for monitoring changes in the part quality are essential in predicting the quality of the final molded components and adjusting the processing parameters accordingly. This study has thus proposed three quality indexes derived from the pressure profiles obtained at the system load cell, nozzle, and molding cavities, respectively, and an additional quality index derived from the clamping force increment measured at the tie bars of the injection molding machine. These types of part quality indexes are revealed to monitor the quality variations of molten polymer. The experimental results support the following main conclusions.

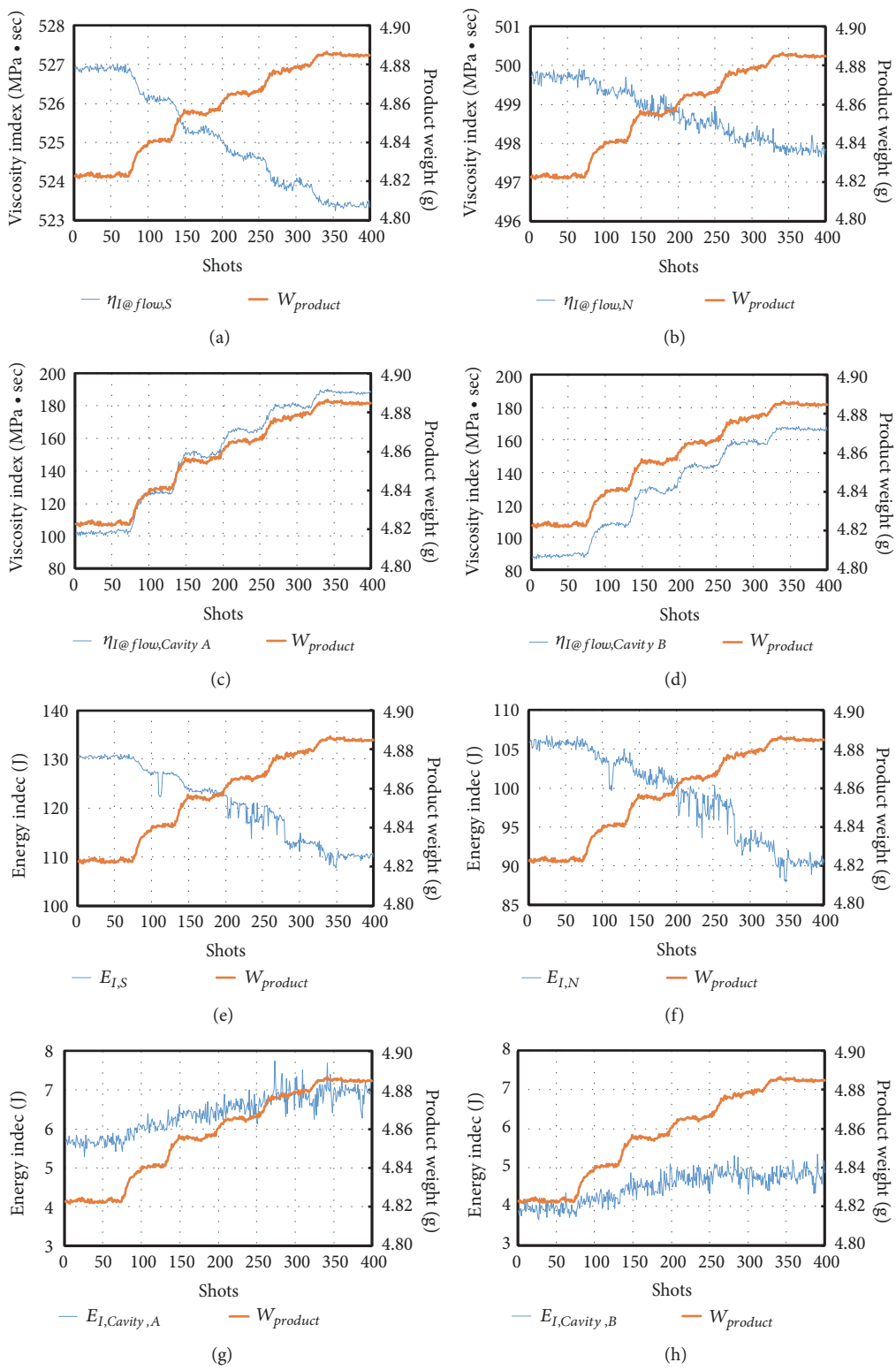

FIGURE 17: Melt quality fluctuation as revealed by viscosity and energy quality indexes.

(1) The plasticization parameter settings affect the initial quality of the molten polymer and therefore influence the final part weight. The barrel temperature and back pressure have a particularly strong effect on the part quality. By contrast, the screw rotational speed has a more minor effect since it acts for only a short duration. Overall, the results show that the three plasticization parameters can be ordered in terms of

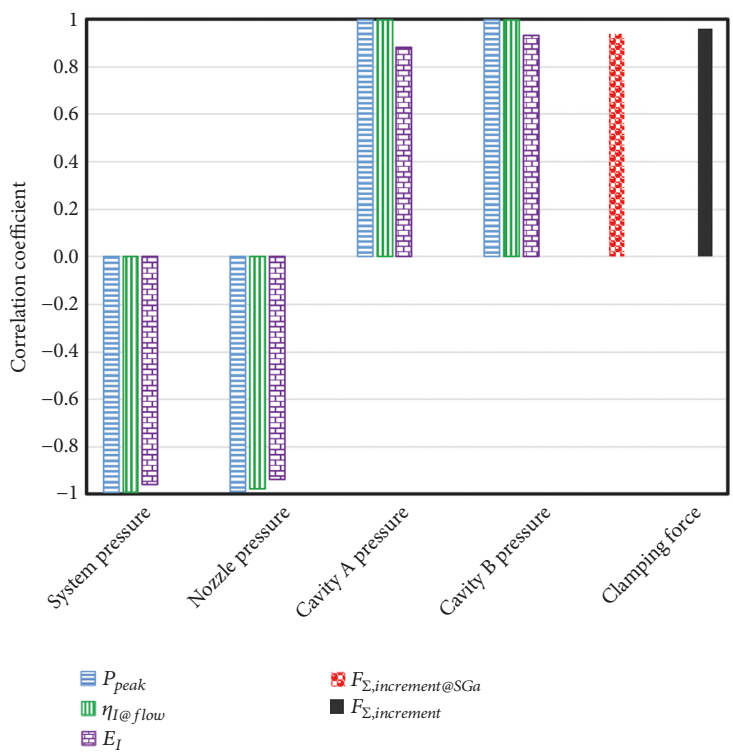

Figure 18: Correlation between quality indexes and product weight for various melt quality fluctuations.

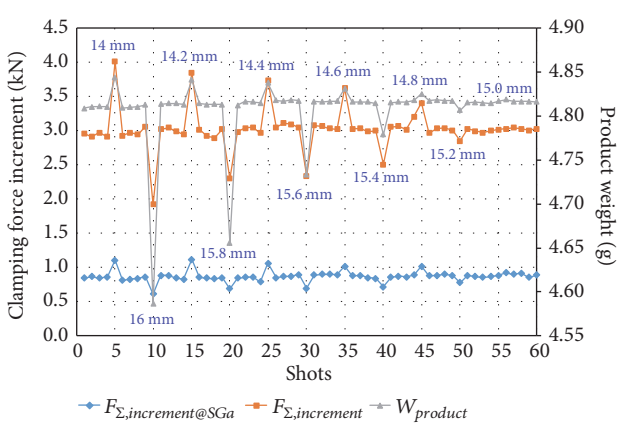

Figure 19: Shot-by-shot variation of clamping force quality index and product weight for various V/P switchover positions.

a decreasing effect on the part quality as follows: (i) barrel temperature, (ii) back pressure, and (iii) screw rotational speed.

(2) The quality indexes revealed in this work all provide a good indication of the injection molding quality under the considered processing conditions. Particularly, the quality of the molten polymer at the initial filling stage and the end of filling is quite different. The pressure signals obtained from upstream of the injection molding process provide a full history of the rheological change which takes place during mold filling. Therefore, the related quality indexes provide a good indication of the viscosity during the initial filling stage. By contrast, the quality indexes extracted from the downstream only reflect final molded part quality. Anyhow, these quality indexes, in particular with the clamping force increment index, have a strong correlation with the part qualities and they can all be used to predict the quality of the molded part.

(3) When PA756 pellets are gradually replaced with PA756H pellets with a lower viscosity, quality indexes derived from the cavity pressure signals and clamping force increase.

(4) The clamping force increment quality index is capable of detecting even very small (~0.2 mm) changes in the V/P switchover position.

(5) All of investigated quality indexes in this work provide a feasible means of detecting changes in molded part quality. In particular, clamping force increment quality index can be implemented using simple stick-on strain gauges and requires no modification or invasion of the injection molding system or cavity. Accordingly, it provides a particularly attractive solution for the online monitoring and control of the injection molding process.

Data Availability

Data is available upon request.

Conflicts of Interest

The authors declare that they have no conflicts of interest.

Acknowledgments

This work was supported financially by the Frontier Mould and Die Research and Development Center under The Featured Areas Research Center Program of the Higher Education Sprout Project of the Ministry of Education (MOE), Taiwan. Additional funding was also provided by the Ministry of Science and Technology, Taiwan, under Project No. 106-2218-E-327 -002 -MY2.

References

[1] J. Neter, W. Wasserman, and G. A. Whitemore, *Applied Statistics*, Pearson, New York, NY, USA, 4th edition, 1993.

[2] O. Amano and S. Utsug, "Temperature measurements of polymer melts in the heating barrel during injection molding. Part I. Temperature distribution along the screw axis in the reservoir," *Polymer Engineering & Science*, vol. 28, pp. 1565–1571, 1988.

[3] O. Amano and S. Utsugi, "Temperature measurements of polymer melts in the heating barrel during injection molding. Part 2: Three-dimensional temperature distribution in the reservoir," *Polymer Materials Science & Engineering*, vol. 29, p. 171, 1989.

[4] O. Amano and S. Utsugi, "Temperature measurements of polymer melts in the heating barrel during injection molding. Part 3: Effects of screw geometry," *Polymer Engineering & Science*, vol. 30, p. 385, 1990.

[5] L. Latif and H. Saidpour, "Assessment of plastic mixture quality in injection moulding process," *Polymer Testing*, vol. 16, no. 3, pp. 241–258, 1997.

[6] S. Tanoue, A. Hasook, T. Itoh, M. Yanou, Y. Iemoto, and T. Unryu, "Effect of screw rotation speed on the properties of polystyrene/organoclay nanocomposites prepared by a twin-screw extruder," *Journal of Applied Polymer Science*, vol. 101, no. 2, pp. 1165–1173, 2006.

[7] X. Zhou, Y. Zhang, T. Mao, and H. Zhou, "Monitoring and dynamic control of quality stability for injection molding process," *Journal of Materials Processing Technology*, vol. 249, pp. 358–366, 2017.

[8] N. Khoshooee and P. D. Coates, "Application of the Taguchi method for consistent polymer melt production in injection moulding," *Proceedings of the Institution of Mechanical Engineers, Part B: Journal of Engineering Manufacture*, vol. 212, pp. 611–620, 1998.

[9] Z. Jin, F. Gao, and F. Zhu, "An experimental study of solid-bed break-up in plasticization of a reciprocating-screw injection molding," *Polymer Engineering & Science*, vol. 44, pp. 1313–1318, 2004.

[10] M. S. Huang, "Cavity pressure based grey prediction of the filling-to-packing switchover point for injection molding," *Journal of Materials Processing Technology*, vol. 183, no. 419, 2007.

[11] Z. Chen and L. S. Turng, "A review of current developments in process and quality control for injection molding," *Polymers for Advanced Technologies*, vol. 24, pp. 165–182, 2005.

[12] S. C. Nian, C. Y. Wu, and M. S. Huang, "Warpage control of thin-walled injection molding using local mold temperatures," *International Communications in Heat and Mass Transfer*, vol. 61, pp. 102–110, 2015.

[13] S. C. Nian, M. H. Li, and M. S. Huang, "Warpage control of headlight lampshades fabricated using external gas-assisted injection molding," *International Journal of Heat and Mass Transfer*, vol. 86, p. 358, 2015.

[14] J. F. Luyé, G. Régnier, B. P. Le, D. Delaunay, and R. Fulchiron, "PVT measurement methodology for semicrystalline polymers to simulate injection-molding process," *Journal of Applied Polymer Science*, vol. 79, p. 302, 2001.

[15] S. Chakravorty, "PVT testing of polymers under industrial processing conditions," *Polymer Testing*, vol. 21, no. 3, pp. 313–317, 2002.

[16] C. B. Park, S. S. Park, D. Ladin, and H. E. Naguib, "On-line measurement of the PVT properties of polymer melts using a gear pump," *Polymers for Advanced Technologies*, vol. 23, p. 316, 2004.

[17] J. Wang, P. Xie, Y. Ding, and W. Yang, "On-line testing equipment of P–V–T properties of polymers based on an injection molding machine," *Polymer Testing*, vol. 28, pp. 228–234, 2009.

[18] H. Zuidema, G. W. M. Peters, and H. E. H. Meijer, "Influence of cooling rate on pVT-data of semicrystalline polymers," *Journal of Applied Polymer Science*, vol. 82, p. 1170, 2001.

[19] M. H. E. van der Beek, G. W. M. Peters, and H. E. H. Meijer, "A dilatometer to measure the influence of cooling rate and melt shearing on specific volume," *International Polymer Processing*, vol. 20, pp. 111–120, 2005.

[20] M. H. E. van der Beek, G. W. M. Peters, and H. E. H. Meijer, "The influence of cooling rate on the specific volume of isotactic poly(propylene) at elevated pressures," *Macromolecular Materials and Engineering*, pp. 443–455, 2005, vol. 290, no. 443, 2005.

[21] S. C. Chen, K. J. Wang, C. W. Chang, S. P. Sun, and K. H. Lee, "Verification of numerical approach and experiment in using PVT properties of polymer to control injection molded products," in *Proceedings of the SPE/ANTEC 2016*, vol. 1, pp. 1243–1248, Indianapolis, IN, USA, 2016.

[22] J. Wang and Q. Mao, "A novel process control methodology based on the PVT behavior of polymer for injection molding," *Advances in Polymer Technology*, vol. 32, pp. E474–E485, 2013.

[23] B. H. Min and J. Mater, "A study on quality monitoring of injection-molded parts," *Journal of Materials Processing Technology*, vol. 136, no. 1, 2003, 136, 1, 2003.

[24] Z. Chen and L. S. Turng, "Injection molding quality control by integrating weight feedback into a cascade closed-loop control system," *Polymer Engineering & Science*, vol. 47, p. 852, 2007.

[25] W. Michaeli and A. Schreiber, "Online control of the injection molding process based on process variables," *Polymers for Advanced Technologies*, vol. 28, p. 65, 2009.

[26] C. Hopmann and A. Reßmann, "Self-optimizing in injection molding and the problem at compensating viscosity fluctuations," in *Proceedings of the SPE/ANTEC 2014*, vol. 2, pp. 1706–1710, Las Vegas, NV, USA, 2014.

[27] F. A. Heinzler, M. Mistier, and J. Wortberg, "Quality improvement by enhanced pressure controlled injection molding," in *Proceedings of the SPE/ANTEC 2014*, vol. 2, pp. 1694–1699, Las Vegas, NV, USA, 2014.

[28] J. F. Zhang, P. Zhao, Y. Zhao, J. Y. Huang, N. Xia, and J. Z. Fu, "On-line measurement of cavity pressure during injection molding via ultrasonic investigation of tie bar," *Sensors and Actuators A: Physical*, vol. 285, p. 118, 2019.

[29] C. Gornik, "Viscosity measuring methods for feedstocks directly on injection molding machines," *Materials Science Forum*, vol. 591-593, pp. 174–178, 2008.

[30] J. Aho and S. Syrjälä, "Shear viscosity measurements of polymer melts using injection molding machine with adjustable slit die," *Polymer Testing*, vol. 30, no. 6, pp. 595–601, 2011.

[31] S. Kruppa, R. Schiffers, M. Würtele, and G. P. Holzinger, "Integrated process monitoring and process control of injection molding machines and molds," in *Proceedings of the SPE/ANTEC 2013*, vol. 1, pp. 1674–1679, Cincinnati, OH, USA, 2013.

[32] N. Asadizanjani, R. X. Gao, Z. Fan, and D. O. Kazmer, "Viscosity measurement in injection Molding using a multivariate sensor ASME/ISCIE 2012," in *Proceedings of the International Symposium on Flexible Automation*, vol. 1, pp. 231–237, St. Louis, MO, USA, 2012.

[33] G. Gordon, D. O. Kazmer, X. Tang, Z. Fan, and R. X. Gao, "Quality control using a multivariate injection molding sensor," *The International Journal of Advanced Manufacturing Technology*, vol. 78, p. 1381, 2015.

[34] S. Montgomery and V. Gallo, "Achieve process transparency with in-mold cavity sensors," *Plastics Technology*, vol. 39, 2012.

[35] C. C. Lin, W. T. Wang, C. C. Kuo, and C. L. Wu, "Experimental and theoretical study of melt viscosity in injection process," *International Journal of Chemical, Molecular, Nuclear, Materials and Metallurgical Engineering*, vol. 8, pp. 687–691, 2014.

[36] J. Y. Chen, K. J. Yang, and M. S. Huang, "Online quality monitoring of molten resin in injection molding," *International Journal of Heat and Mass Transfer*, vol. 122, no. 681, 2018.

[37] Z. Chen, L. S. Turng, and K. K. Wang, "Adaptive online quality control for injection-molding by monitoring and controlling mold separation," *Polymer Engineering & Science*, vol. 46, p. 569, 2006.

[38] F. Yin, H. Mao, and L. Hua, "A hybrid of back propagation neural network and genetic algorithm for optimization of injection molding process parameters," *Materials & Design*, vol. 32, p. 3457, 2011.

[39] M. S. Huang, S. C. Nian, J. Y. Chen, and C. Y. Lin, "Influence of clamping force on tie-bar elongation, mold separation, and part dimensions in injection molding," *Precision Engineering*, vol. 51, p. 647, 2018.

[40] Y. Zhao, P. Zhao, J. F. Zhang, J. Y. Huang, N. Xia, and J. Z. Fu, "On-line measurement of clamping force for injection molding machine using ultrasonic technology," *Ultrasonics*, vol. 91, p. 170, 2019.

[41] P. Zhao, Y. Zhao, J. F. Zhang, J. Y. Huang, N. Xia, and J. Z. Fu, "Ultrasonic measurement of clamping force for injection molding machine," *Journal of Polymer Engineering*, vol. 39, p. 388, 2019.

Hindawi
Advances in Polymer Technology
Volume 2019, Article ID 9012085, 17 pages
https://doi.org/10.1155/2019/9012085

Research Article

Multiobjective Optimization Method for Polymer Injection Molding Based on a Genetic Algorithm

Zhijun Yuan,[1,2] Hui Wang,[1] Xuebing Wei,[2] Kui Yan,[1] and Cheng Gao[1]

[1] *Hubei Key Laboratory of Advanced Technology for Automotive Components, Wuhan University of Technology, Wuhan 430070, China*
[2] *SAIC GM Wuling Automobile Company, Guangxi, Liuzhou 545007, China*

Correspondence should be addressed to Hui Wang; huiwang@whut.edu.cn

Received 20 March 2019; Revised 7 June 2019; Accepted 3 July 2019; Published 24 July 2019

Guest Editor: Srikanth Pilla

Copyright © 2019 Zhijun Yuan et al. This is an open access article distributed under the Creative Commons Attribution License, which permits unrestricted use, distribution, and reproduction in any medium, provided the original work is properly cited.

To solve the quality problem of polymer injection parts, a quality prediction and multiobjective optimization method is established. In this method, the parameters that have an important effect on the part quality are selected using an orthogonal testing method, and then a central composite design experiment is performed using these parameters. A mathematical model considering an objective and impact factors is developed using the response surface method. The optimal combination of the impact parameters is determined using a multiobjective genetic algorithm. The injection molding of a typical interior trim part of a car, i.e., the seat belt cover plate, is used as an example to demonstrate the method. The two most troublesome problems in this process—the sink marks and warpage—are multiobjectively analyzed using the established method, and the optimal combination of impact parameters that minimized the defects is determined. The errors of the sink marks and warpage between the experimental and theoretical values were 7.95% and 0.2%, respectively. The optimized parameters were tested in actual injection molding. The results show that the shrinkage and warpage of the parts are obviously improved by optimization using the proposed method, allowing the parts to satisfy the requirements of assembly and appearance.

1. Introduction

Because of low cost, complex molding ability, convenience, light weight, and corrosion resistance, polymer injection parts are widely used around the world [1]. Currently, over 30% of all the plastic parts are manufactured by injection molding [2, 3], and 80% of engineering plastic products are manufactured by injection molding [4].

However, polymer injection molding, which involves various processing parameters, is a complex process [5–7], and the final parts may have quality problems if the processing parameters are not carefully selected. Thus, many studies have been performed to solve the quality problems by optimizing the processing parameters. Warpage, i.e., deviation of the shape of an injection part from that of the cavity, is one of the most common defects in the injection molding process [8]. Because of its adverse effects on the appearance and performance of polymer injection parts, warpage has attracted increasing attentions. Regarding the polymer injection molding of thin-walled parts, warpage is likely to occur in the manufacturing process, degrading the surface quality. Numerous researchers have attempted to minimize the warpage in the polymer injection molding process. Lee et al. [9] optimized the processing parameters, including the wall thickness of the injection parts, the injection time, the pressure, the packing and cooling times, the melt temperature, and the coolant temperature by using the modified complex method to prevent warpage. Ozcelik et al. [10, 11] used the software Moldflow, combined with a back propagation neural network and a hybrid genetic algorithm (GA), to reduce the warpage by optimizing parameters such as the mold temperature, the melt temperature, the packing pressure, and the packing and cooling times. S-H. Tang et al. [12] reduced the warpage by optimizing the mold temperature, the injection time, the pressure, and the packing time via an orthogonal experimental design method. Gao et al. [13] minimized the warpage for a telephone part using the Kriging model, concluding that the injection time played the greatest role in the warpage. Farshi et al. [14] reduced the warpage by optimizing the mold temperature, the melt

temperature, the pressure, and the packing time. Wang et al. [15] optimized the warpage by improving the cooling system and processing parameters.

In the polymer injection molding of thin-wall parts, the warpage of parts is particularly obvious. By properly increasing the wall thickness of the part, its stiffness can be improved, and to a certain extent, the warpage can be reduced. However, shrinkage and dents are likely to occur during the injection molding of thicker wall parts. Rather than increasing the wall thickness, ribs are applied to increase the strength and stiffness of parts and effectively reduce the warpage. Thus, ribs are widely used in the design of injection parts. Nevertheless, ribs result in increased sink marks because of the thickness difference between a rib and its adjacent region. Deep sink marks seriously degrade the quality of injection parts.

Many studies have been performed on sink marks. Ni S. J. [16] reported that the geometric structure of parts, the mold structure, and the molding processing parameters were the main causes of sink marks. By combining experiments and a GA, Mathivanan D. [17] discovered that the melt temperature, the mold temperature, the packing pressure, and the ratio of the part thickness to the rib thickness were the most important factors for reducing sink marks. Guo et al. [1] experimentally studied the influence of parameters, such as the mold temperature, the melt temperature, the injection time, the V/P switch-over point, the packing pressure, the coolant temperature, the coolant Reynolds number, the direction of the rib, the thickness of the rib, and the distance between the rib and the injection gate on sink marks and optimized these parameters using a GA.

The optimization of the processing parameters was investigated in the aforementioned studies. However, most of the optimization methods considered only one objective. For different objectives, the optimized parameters may be different. The optimized parameters for one objective obtained by a single-objective optimization improve quality of the objective, but deteriorate quality of other objectives, such as the two objectives of warpage and sink marks. Guo et al. [1] showed that with the constant increase of the mold temperature between 20 and 80°C, the warpage gradually decreased, and the sink marks first increased and then decreased. When the melt temperature was increased in the range of 220–280°C, the warpage first increased and then decreased, while the sink marks constantly increased. When the packing pressure was increased in the range of 40%–120%, the warpage first decreased and then increased, while the sink marks constantly decreased. When the packing time was increased in the range of 2.5–20 s, the warpage first increased and then decreased, while the sink marks first decreased and then remained constant. When the coolant temperature was increased in the range of 0–50°C, the warpage first increased, and then decreased and became reduplicative, while the sink marks first increased and then decreased. Multiobjective optimization can not only be used to deal with these competing problems in injection molding [18, 19], but also is able to be used in other complex applications for novel design. In the innovative hybrid process that has been recently developed to manufacture metal-polymer composites, the multiobjective optimization can help to optimize the quality of polymeric part while still maintaining the requirement of sheet metal part [20, 21]. In the manufacture of a hybrid material structure via the injection of polypropylene (PP) with high ductility into a robust CF/Epoxy thermoset sheet, the multiobjective optimization can be used to optimize the formability and joinability [22]. On the other hand, in the existing optimization models, selection of the impact factors was more subjective, and most of them were determined via simple analysis as well as experience, owing to lack of reliable data [23].

To rationally select the impact factors with regard to the quality objective for polymer injection molding and comprehensively optimize the quality of injection parts, a systematic method for multiobjectively predicting and optimizing the quality of polymer injection parts is established. In this method, the parameters that have important effects on the part quality are identified via orthogonal testing, and a central composite design (CCD) experiment is performed on these parameters. Then, a mathematical model considering the optimization objective and the impact factors is developed using a response surface method (RSM). Finally, the optimal combination of the impact parameters is determined using a multiobjective genetic optimization algorithm. The injection molding of the seat belt cover plate in a car was used as an example, and the two most prominent problems in this process, i.e., the sink marks and warpage, were multiobjectively optimized according to the established method.

This paper is organized as follows. Section 2 describes the established optimization method. Section 3 is the verification. Finally, Section 4 summarizes our conclusions.

2. Multiobjective Optimization Method for Injection Molding

2.1. Optimization Strategy. The optimization process for polymer injection molding can be described by the following mathematical model:

$$\begin{aligned} &\text{Find} \quad \mathbf{x} = [x_1, x_2, \ldots, x_m]^T \\ &\text{Min} \quad \mathbf{y} = [y_1, y_2, \ldots, y_n] \\ &\text{S.T.} \quad x_{k\min} \le x_k \le x_{k\max}, \quad k = 1, 2, \ldots, m \end{aligned} \tag{1}$$

where $\mathbf{x}$ is the impact parameter vector, x_i denotes an impact parameter associated with the injection molding quality, m is the number of potential impact factors, $\mathbf{y}$ is the quality index vector of the polymer injection parts, y_j is a quality index, n is the number of concerned quality indices, and x_{kmin} and x_{kmax} denote the range of the impact parameters.

A method that can multiobjectively predict and optimize the quality of polymer injection molding is established. Its main flowchart is shown in Figure 1.

This method mainly includes a quality-factor selection module, a part-quality prediction module, and a multiobjective genetic optimization module. Firstly, for the quality-factor selection module, a multifactor two-level orthogonal experiment is employed. By using mean-value analysis, the order of various factors that affect the quality of the injection

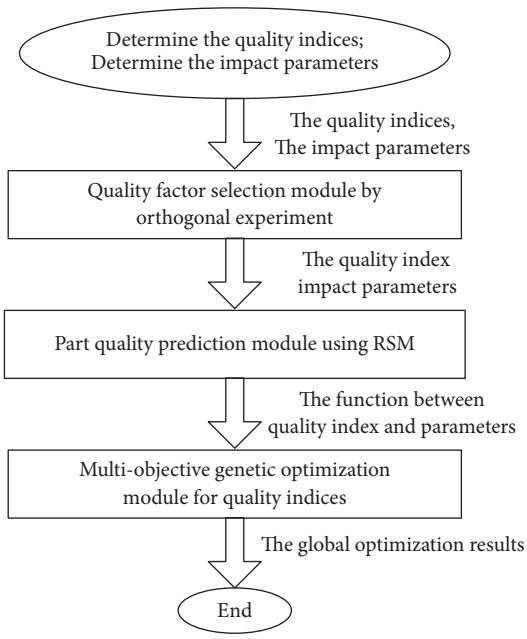

Figure 1: Flowchart of the method.

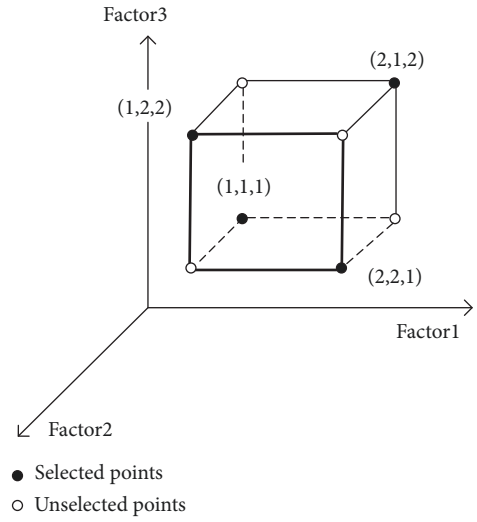

Figure 2: Space model of $L_4(2^3)$.

parts is identified, which provides scientific basis for choosing the quality impact factors. The part-quality prediction module based on the RSM is then applied to fit the single-objective function between the impact factors (such as processing parameters) and a target quality index according to CCD sample data. Finally, for the multiobjective genetic optimization module, the Pareto optimal solution set is obtained by using the Nondominated Sorting Genetic Algorithm II (NSGA-II) [24]. The design of the three aforementioned modules is described in detail in the following sections.

2.2. Quality-Factor Selection Module. In polymer injection molding, optimization can be performed from four aspects: the polymer resin, the part structure, the mold structure, and the processing parameters. For a specified part, the resin used is determined according to the performance and the cost, which are not easily changed. Therefore, the optimization is mainly realized by optimizing the part structure, the mold structure, and the processing parameters.

Orthogonal test design is a multifactor experimental design method wherein representative sample points are selected from the entire set of experimental sample points. The orthogonal test design is illustrated by the L_4 (2^3) space model shown in Figure 2, where each axis represents a factor, the eight cube vertices represent eight experimental points in the overall experiment, and the four sample points (black points) determined by the orthogonal table are evenly distributed. The projections of the sample points along a single axis do not overlap. The orthogonal experimental design is applied to characterize the overall experiment by using fewer tests. The procedure comprises four steps: (1) determine the number of experimental factors and levels, (2) select the proper orthogonal table, (3) list the experimental scheme and results, and (4) analyze the results of the orthogonal test design.

Before predicting and optimizing the quality of injection parts, the impact factors should be identified. The factors involved in the injection process are comprehensively considered. First, multifactor and two-level orthogonal design experiments are performed, and then several factors having the greatest effects on the injection parts are selected accordingly. For the multiobjective case, the influence of a factor on different objectives may be different.

The indices for the injection-part quality cannot be easily compared because of their different units and magnitudes, which is inconvenient for the comprehensive analysis of the indices. To eliminate this inconvenience, fuzzy mapping of the quality indices is applied. Here, each quality index is mapped to a fuzzy space $[0, 1]$ and is made dimensionless. Various fuzzy functions can be used in actual applications, e.g., the triangle function, the trapezoid function, the Gaussian function, the ridge function, the parabolic function, and the S shape function. In this study, the triangle fuzzy function is applied, which can be described as

$$\mu(x) = \begin{cases} 0 & x < a \\ \left(\dfrac{x-a}{b-a}\right)^k & a \le x \le b \\ 0 & x > b \end{cases} \tag{2}$$

where a, b, and k are the control parameters, which are determined by the index value.

Through fuzzy mapping, the quality index is translated to the space $[0, 1]$. Thus, the comprehensive impact of each factor on the quality of the injection parts is easily determined via the mean analysis of the orthogonal-experiment results, providing scientific basis for the selection of the quality factors.

2.3. Part-Quality Prediction Module. An RSM is used to establish an approximate model for evaluating the response

functions (quality indices) with respect to the design variables (impact factors), in order to perform prediction and optimization within the design space of the impact factors selected in Section 2.2.

When certain relationships exist between the impact factors and the response functions, a first- or second-order model describing the relationship between the responses and the impact factors can be obtained according to the experimental design. In the RSM, y is generally assumed to be a quality index of a part or a process. The relationship between y and the impact factors $x_1, x_2 \ldots x_k$ is given as follows:

$$y = f\left(x_1, x_2, \ldots, x_k\right) + \varepsilon \tag{3}$$

Here, the function f is unknown and may be very complicated and ε represents the error of the model. A first- or second-order Taylor expansion is generally used for the above function to approximate the real function over a small area. The first-order model is

$$y = \beta_0 + \sum_{i=1}^{k} \beta_i x_i + \varepsilon \tag{4}$$

The second-order model is

$$y = \beta_0 + \sum_{i=1}^{k} \beta_i x_i + \sum_{i=1}^{k} \beta_{ii} x_i^2 + \sum_{i<j} \sum_{j=2}^{k} \beta_{ij} x_i x_j + \varepsilon \tag{5}$$

In these two models, ε is random error, which follows a normal distribution. The random errors are independent of each other. The input variables are independent of each other.

The CCD is the most common and most recommended design in the RSM. It is an experimental design method based on two-level factors and partial experiments, wherein one zero point and two axial points are added for regression and evaluation of the relationship function between responses and factors.

2.4. Multiobjective Genetic Optimization Module. The idea of multiobjective optimization mainly studies on the simultaneous optimization of multiple objectives. Many scholars have proposed solutions for the multiobjective optimization problem, including the weighted-sum method, the goal programming method, the ε-constraint method, and other weight-based methods. With the development of artificial intelligence and its wide use in research and practice, many scholars have used artificial intelligence algorithms to solve multiobjective optimization problems. In this study, the quality of injection molding parts is optimized by the NSGA-II genetic algorithm [24], and its Pareto optimal solution [25] set is obtained. The NSGA-II is developed from the classic GA. In the NSGA-II, multiobjective related operations are involved, such as the nondominated solution [26], the Pareto front [25], and the crowding distance [24], which are explained in Appendix A.

The solution process of the module includes population initialization, selection, crossover, and mutation, recombination, crowding distance calculation, nondominated sorting, population update, and the final Pareto solution set output.

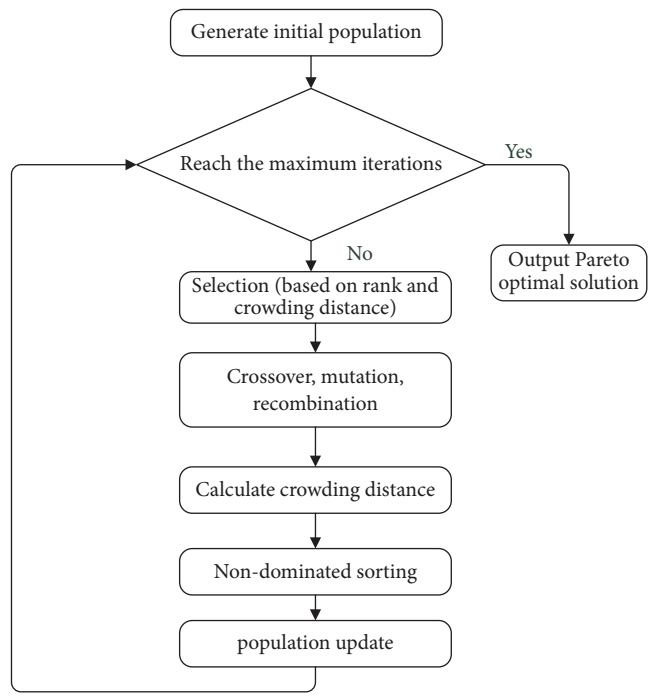

Figure 3: Flowchart of the NSGA-II.

The flowchart of the algorithm is shown in Figure 3. Algorithms of the key operators used in this module are provided in Appendix B.

2.5. Solving Process of the Method. Based on the method described above, its solving process is illustrated in Figure 4. First, quality indices concerned are identified for an injection part. Potential impact factors and their levels are preliminarily determined by experiences and trials. Then a multifactor two-level orthogonal experiment is performed, and the obtained quality indices are nondimensionalized by fuzzy mapping. The key impact factors are thus selected using mean-value analysis. Next, CCD experiment is performed for RSM, and each quality index is fitted as a single-objective function of the impact factors. Among the fitted models, the best one is determined according to goodness of fit. Afterwards, the minimum/maximum values for an index are calculated using its fitted function, which are then used to nondimensionalize the index function by fuzzy mapping. Finally, multiobjective optimization is performed using NSGA-II to obtain the Pareto optimal solution set, from which the optimal solution is determined according to product requirements.

3. Verification of the Method

MATLAB programming was used to establish the aforementioned multiobjective intelligent optimization method, and the experimental design modules of Minitab were used to design and analyze the required experiments. A seatbelt cover plate of a vehicle, for which significant quality issues such as warpage and surface sink marks were observed during

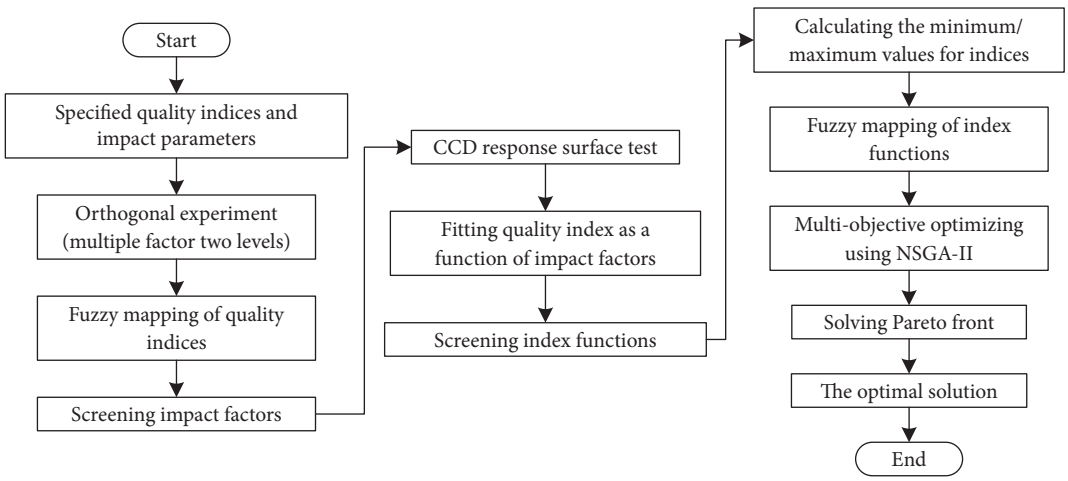

Figure 4: Solving process of the optimization method.

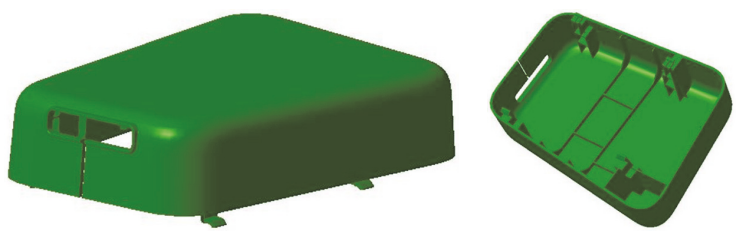

(a) (b)

Figure 5: Seatbelt cover plate model: (a) outer shape and (b) inner details.

the injection molding process, was considered, and the established multiobjective optimization method for polymer injection molding was adopted to ameliorate the quality problems. For conducting the plastic injection process, one commercial injection molding software, Autodesk® Moldflow V2014, was used. It is widely used to analyze injection molding, and has a good accuracy [11, 27]. The software is hybrid finite-element/finite-difference method for solving pressure, flow and temperature fields [10], which can provide fill time, sink marks, warpage, air traps, weld line, stress, and other results.

3.1. Case Setup

3.1.1. Geometric Model. The three-dimensional model of the seatbelt cover plate considered in this study is shown in Figure 5.

3.1.2. Material. In accordance with the molding process for the cover plate, the material for computer-aided engineering analysis was selected as TK-PP1, and its properties are listed in Table 1.

3.1.3. Mold. The mold system for practical manufacturing was employed to obtain a more accurate simulation output corresponding to the actual process. The cooling and feeding systems were set for the simulation analysis of the seatbelt cover, as shown in Figure 6.

Table 1: Material properties of TK-PP1.

Material properties	Value
Solid density(g/cm3)	1.0866
Melt density(g/cm3)	0.90867
Recommended mold temperature(°C)	30
Recommended melt temperature(°C)	230
Fibers/filler(talc-filled)	20% Talc
Material characteristics	PP
Elastic modulus(MPa)	2200
Shear modulus(MPa)	2270
Poisson's ratio	0.39

3.2. Factor Selection by Orthogonal Experiment

3.2.1. Experimental Factors

(a) Part Structure. The thickness, the height, and the root fillet of the rib have significant effects on the cooling time of the injection process, thereby affecting the surface qualities of the injection part. These factors should be considered in the rib design. The rib thickness varies with the thickness of the molding parts, and the rib height is related to the rib

Table 2: Experimental factors and their levels.

No.	Factors	Abbr.	Levels	
			Low	High
1	Rib radius (mm)	r	0	0.8
2	Rib relative thickness	t	0.4	0.8
3	Rib relative height	h	2	4
4	Sprue diameter (mm)	d	6	12
5	Gate location	s	A	B
6	Injection time (s)	$t_{inj.}$	1.97	2.17
7	Melt temperature (°C)	T_{melt}	210	250
8	Mold temperature (°C)	T_{mold}	20	40
9	Coolant temperature (°C)	T_{cool}	10	40
10	Coolant time (s)	t_{cool}	20	50
11	The Re number of coolant	RE	9000	11000
12	Cooling channel diameter (mm)	D	8	12
13	V/P switch-over point	V/P	90%	99%
14	Packing pressure (MPa)	P_{pack}	25	45
15	Packing time (s)	t_{pack}	6	14

Annotation: (1) wall thickness of the physical model presented in Section 3.1 was 2.33 mm.
(2) Diameter of the sprue was double that of the runner.

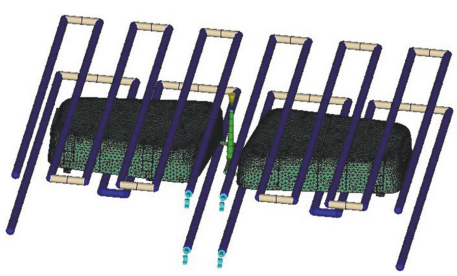

Figure 6: Simulation model.

thickness. Thus, the relative thickness (rib's/part's), relative height (height/thickness), and fillet angle radius of the rib were set as structural factors for the optimization of the surface quality of the cover plate.

(b) Mold Structure. Since the part structure and material were specified by the original designed manufacturer (ODM), the injection gate design of the mold becomes the key factor determining the ultimate quality of the molding part [28–31]. The position and diameter of the gate—the two main geometric parameters of the gate—were considered.

(c) Processing Parameters. In accordance with previous reports [9–16, 32], the melt and the mold temperature, the cooling time and the temperature, the packing pressure and the time, the injection time, the V/P switch-over point, and the Re number of the cooling liquid were used as processing parameters to optimize the surface qualities. The cooling-channel diameter has a remarkable effect on the cooling process, which significantly influenced the surface quality. Therefore, it was also considered in the quality-optimization analysis.

3.2.2. Design and Results of Orthogonal Experiment. According to the aforementioned experimental parameters for the polymer injection part with ribs, the factors considered in this study and their levels for the multiobjective optimization method of the cover plate are listed in Table 2. The injection gate position of Level A is shown in Figure 6, and that of Level B is symmetrical to Level A.

Orthogonal-experiment design was performed using Minitab with the factors listed in Table 2. The designed experimental sequence is presented in Table 3.

Moldflow simulations were conducted in accordance with the combination of the parameters listed in Table 3. Contours of sink marks and warpage of the cases No. 6 and No. 16 are shown in Figure 7 for example. From this figure, it can be seen that sink marks are found in the surface of the cover plate, and distinct warpage is observed at the groove position. The contours of the other cases are similar, and the results are illustrated in Figure 8. The sink marks and warpage vary inconsistently as the parameters change, indicating the significance of the multiobjective optimization for the molding part. However, the simulation results for the sink marks and warpage differ significantly, and the magnitude ratio of them is about 100.

3.2.3. Analysis of Orthogonal-Experiment Results. The fuzzy mapping of the indices is described in Section 2.2. The parameters a and b in the fuzzy functions for the sink marks and warpage, which are given by Eq. (2), were set as the minimum and maximum respectively, and k = 1 was assumed for simplification. The results are shown in Table 4.

The mapped values for the sink marks and warpage have the same order of magnitude after the fuzzy mapping. The results shown in Table 4 were orthogonally analyzed in Minitab, and the mean-value analysis is shown in Table 5.

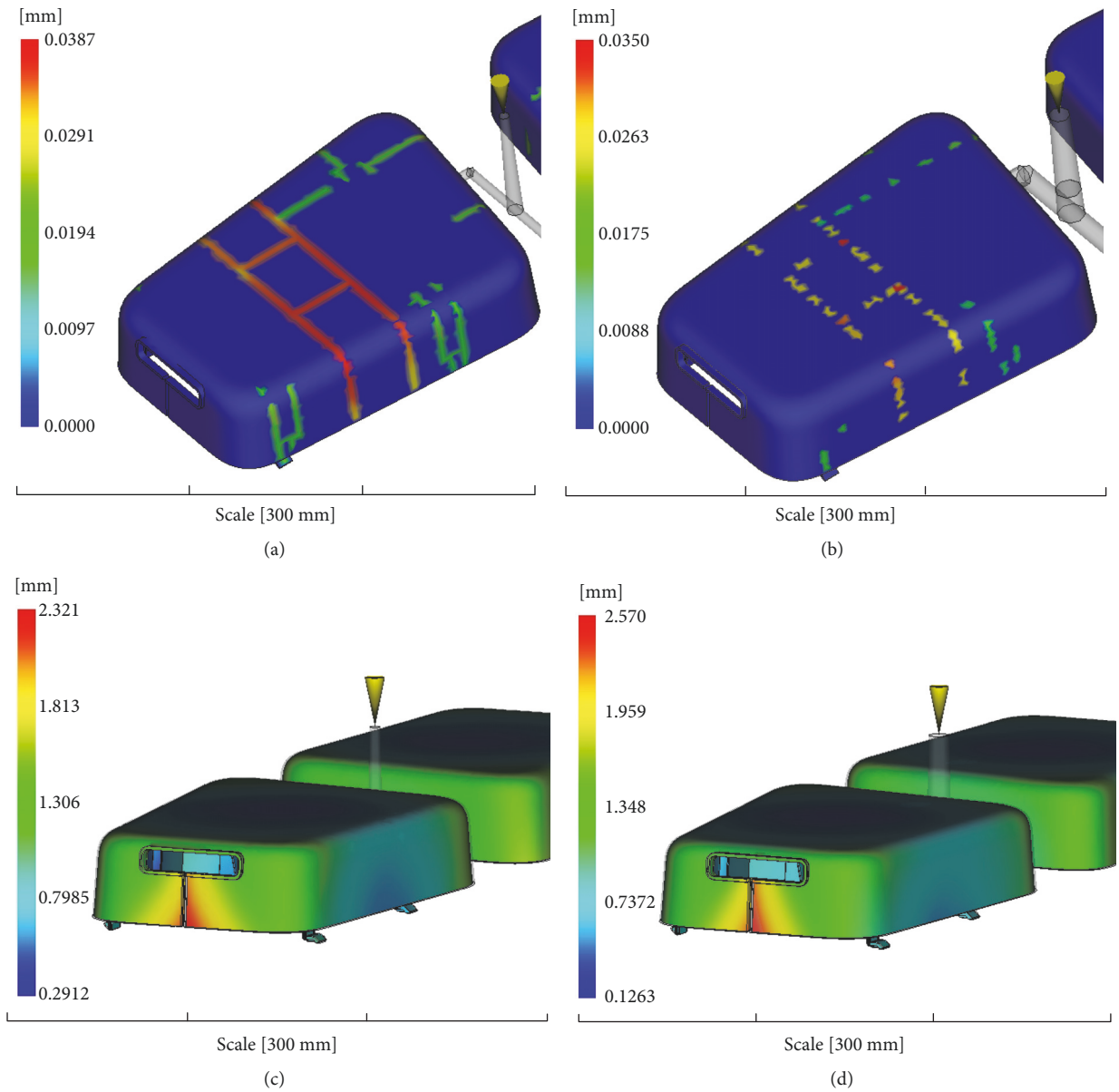

Figure 7: Contours of sink marks and warpage: (a) sink marks of Case No. 6, (b) sink marks of Case No. 16, (c) warpage of Case No. 6, and (d) warpage of Case No. 16.

From the mean-value analysis, the order of the influence of the factors is: the packing time, the mold temperature, the relative thickness of the rib, the melt temperature, the packing pressure, the V/P switch-over point, the radius of the rib fillets, the injection gate position, cooling-channel diameter, coolant temperature, cooling time, relative height of the rib, injection time, Re number of the coolant, and the sprue diameter.

The first five factors, which played dominant roles in the multiobjective optimization for the sink marks and warpage, were selected as the factors in the response surface experiment, to build the mathematical model for the sink marks and warpage versus the parameters, and thus the impact parameter vector **x** in Eq. (1) was identified.

3.3. Index Fitting by RSM

3.3.1. Design and Results of Response Surface Experiment. The levels for the five aforementioned factors are presented in Table 6, and the design for the response surface experiment using Minitab is shown in Table 7. The other ten parameters were set as the same with those in Case No.3 in the orthogonal test (Table 4), for the case exhibited the minimum value for the summation of the sink marks and warpage. Simulations were conducted in accordance with the response surface experiments detailed in Table 7, and the results are illustrated in Figure 9. From this figure, sink marks and warpage show different behaviors as the parameters change, and the relationship is discussed in the Sections 3.3.2 and 3.3.3.

Table 3: Orthogonal test.

No.	r	t	h	d	s	t_{inj}	T_{me}	T_{mo}	T_{co}	t_{co}	RE	D	V/P	P	t_{pa}
1	1	1	1	1	1	1	1	1	1	1	1	1	1	1	1
2	1	1	1	1	1	1	1	2	2	2	2	2	2	2	2
3	1	1	1	2	2	2	2	1	1	1	1	2	2	2	2
4	1	1	1	2	2	2	2	2	2	2	2	1	1	1	1
5	1	2	2	1	1	2	2	1	1	2	2	1	1	2	2
6	1	2	2	1	1	2	2	2	2	1	1	2	2	1	1
7	1	2	2	2	2	1	1	1	1	2	2	2	2	1	1
8	1	2	2	2	2	1	1	2	2	1	1	1	1	2	2
9	2	1	2	1	2	1	2	1	2	1	2	1	2	1	2
10	2	1	2	1	2	1	2	2	1	2	1	2	1	2	1
11	2	1	2	2	1	2	1	1	2	1	2	2	1	2	1
12	2	1	2	2	1	2	1	2	1	2	1	1	2	1	2
13	2	2	1	1	2	2	1	1	2	2	1	1	2	2	1
14	2	2	1	1	2	2	1	2	1	1	2	2	1	1	2
15	2	2	1	2	1	1	2	1	2	2	1	2	1	1	2
16	2	2	1	2	1	1	2	2	1	1	2	1	2	2	1

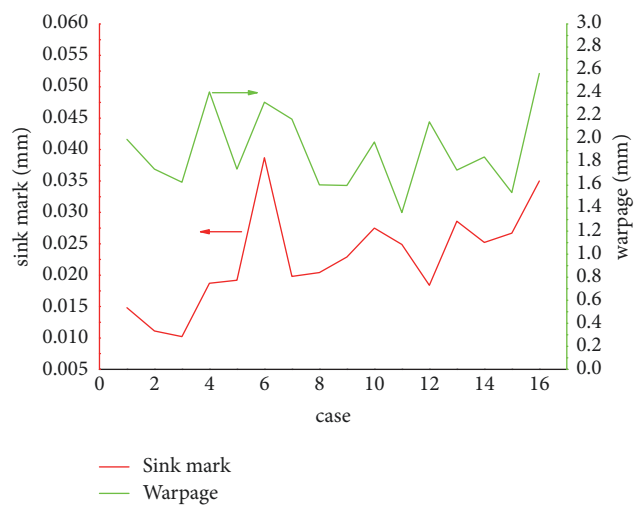

Figure 8: Results of sink marks and warpage.

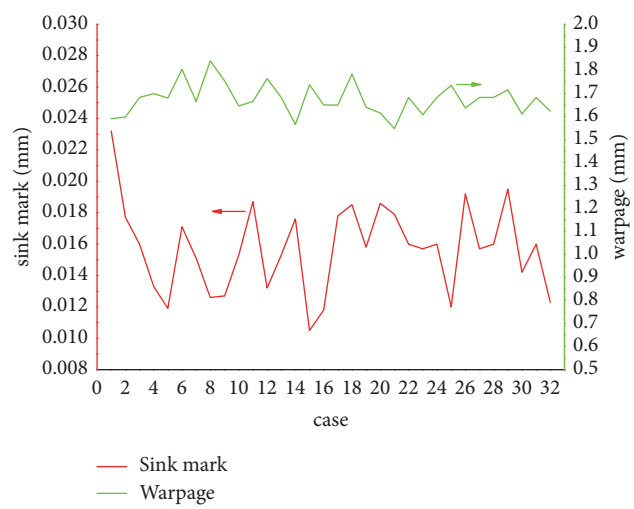

Figure 9: Results of sink marks and warpage.

3.3.2. Fitting of Sink Marks. Four fitting models were calculated, i.e., pure quadratic, linear + parabolic, linear + interactive, and linear. Fitting of the simulation results was performed using these four models respectively to obtain the mathematical function. The sink marks in Figure 9 were input as a response to conduct the response surface experiment. The results are shown in Table 8.

Comparison of R-sq, R-sq (adjustment) and R-sq (prediction) implies that the linear fitting model was the best one to fit the relationship between the sink marks and all the parameters, and the model was applied in this study. The values of the regression coefficients in the fitting model are shown in Table 9.

In the table, Coeff represents the coefficients in the linear fitting model. SE Coeff represents the errors for the coefficients. A lower SE Coeff value indicates higher precision. The SE Coeff values shown in Table 9 are small enough to ensure that the coefficients in the model are reasonable. T describes the ratio between the coefficient and its standard error, which is used to calculate the value P. P is set to assess the properties of the postulations. Factors with a low P value, especially less than 0.05, have significant effects on the sink marks.

The residual plot between the prediction and experiment is shown in Figure 10, where the residuals cluster near the standard line. The maximum residual was <0.003. According to the frequency distribution, most residuals are within a low level. The accuracy of the model is thus demonstrated.

3.3.3. Fitting of Warpage. The response surface experiment and analysis in Section 3.3.2 was reproduced here to obtain the relationship between the warpage and the factors; however, we adopted the linear + parabolic model, instead. The

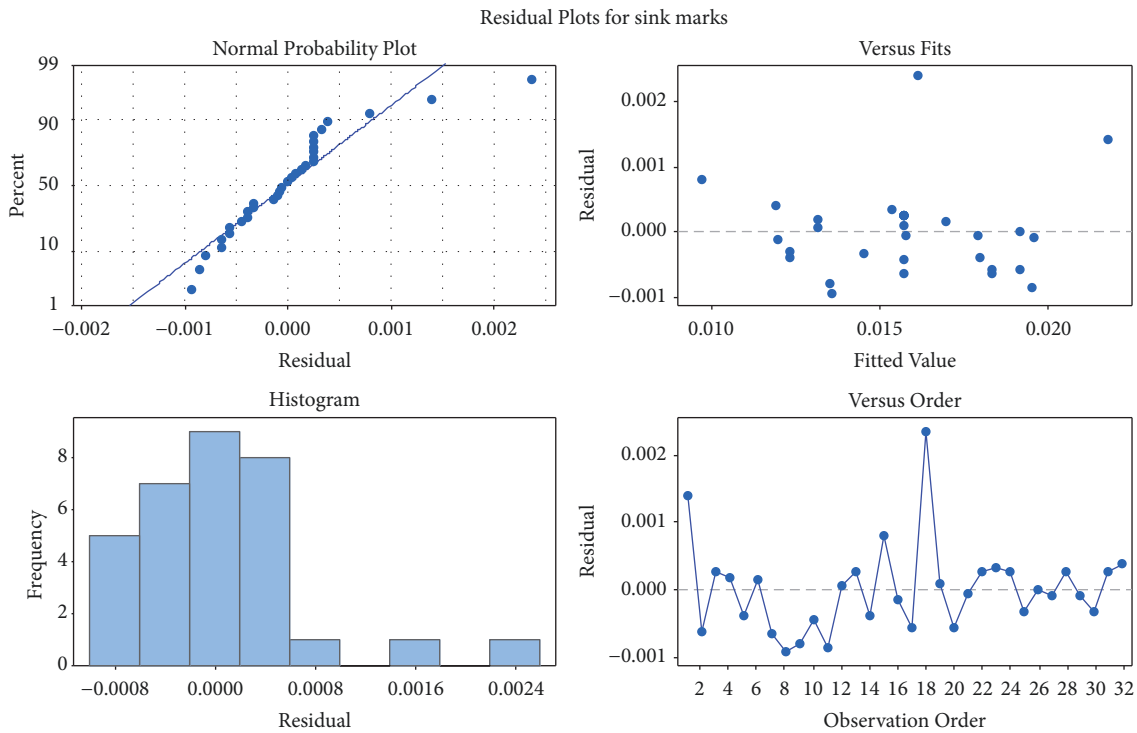

Figure 10: Residuals between the predicted and experimental values.

corresponding results are shown in Tables 10 and 11. Coeff, SE Coeff, T and P were similarly employed for the analysis of the warpage. Thus the quality index vector **y** in Eq. (1) was identified.

3.4. Multiobjective Optimization

3.4.1. Optimization Using GA. The multiobjective optimization of the surface qualities during the injection molding of the seatbelt cover plate were developed according to the regression fitting for the sink marks and warpage presented in the Sections 3.3.2 and 3.3.3, and the mathematical model of Eq. (1) is written as:

$$\begin{aligned}
&\text{Find} \quad [A, B, C, D, E] \\
&\text{Min} \quad [y_1, y_2] \\
&\quad y_1 \\
&\quad = 0.015875 - 0.000292 \times A + 0.000042 \times B \\
&\qquad + 0.003042 \times C - 0.000042 \times D - 0.000625 \\
&\qquad \times E \\
&\quad y_2 \\
&\quad = 1.68272 - 0.03713 \times A - 0.00171 \times B \\
&\qquad - 0.04379 \times C - 0.01929 \times D - 0.04304 \\
&\qquad \times E + 0.00266 \times A \times A - 0.00747 \times B \times B \\
&\qquad - 0.00522 \times C \times C - 0.00609 \times D \times D \\
&\qquad + 0.00553 \times E \times E \\
&\text{S.T.} \quad -2 < A, B, C, D, E < 2
\end{aligned} \tag{6}$$

Where, y_1 and y_2 denote the sink marks and warpage respectively, A, B, C, D, and E are the impact parameters in Table 6.

The multiobjective genetic algorithm was used to perform the optimization. The multiobjective optimization was implemented by the following steps:

Step 1. The minimum/maximum values for sink marks ($\text{Min}_{\text{SK}}/\text{Max}_{\text{SK}}$) and warpage ($\text{Min}_{\text{war}}/\text{Max}_{\text{war}}$) were determined within the specified domain of the impact factors by using the min and max functions.

Step 2. The objective functions (sink marks and warpage) were fuzzily mapped using Eq. (2), where the parameters a and b for the sink marks and warpage were set as the minimum and maximum respectively, and k = 1 was used. The mapped objective functions were set as the multiobjective fitness functions and were described as

$$\begin{aligned}
f_1 &= \frac{1}{(\text{Max}_{\text{SK}} - \text{Min}_{\text{SK}})}(y_1 - \text{Min}_{\text{SK}}) \\
f_2 &= \frac{1}{(\text{Max}_{\text{war}} - \text{Min}_{\text{war}})}(y_2 - \text{Min}_{\text{war}})
\end{aligned} \tag{7}$$

Table 4: Fuzzy mapping of the orthogonal results.

No.	Sink mark	Warpage	Sum
1	0.1614	0.5265	0.6879
2	0.0316	0.3129	0.3445
3	0.0000	0.2185	0.2185
4	0.2982	0.8675	1.1658
5	0.3158	0.3121	0.6279
6	1.0000	0.7939	1.7939
7	0.3368	0.6722	1.0090
8	0.3579	0.1987	0.5566
9	0.4456	0.1945	0.6402
10	0.6070	0.5066	1.1136
11	0.5158	0.0000	0.5158
12	0.2877	0.6531	0.9409
13	0.6456	0.3046	0.9502
14	0.5263	0.3998	0.9262
15	0.5789	0.1440	0.7230
16	0.8702	1.0000	1.8702

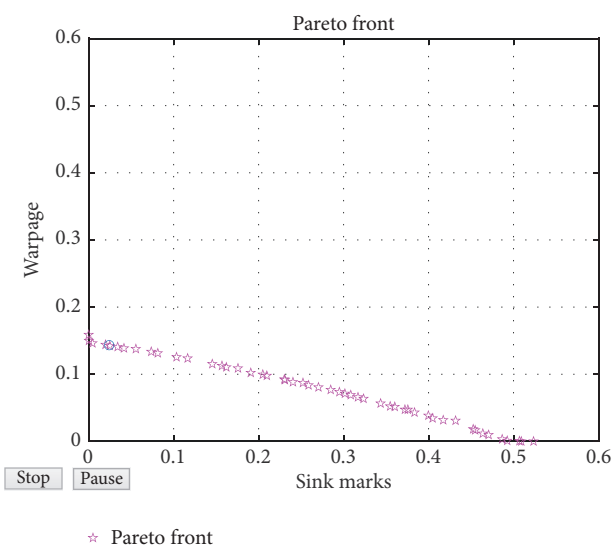

Figure 11: Solution of the GA.

Step 3. The optimal front set, population, and fitness function deviation were set to be 50, 200, and 1e-100. The multiobjective genetic algorithm was used to calculate its Pareto optimal solution set, and the result is shown in Figure 11. In this figure, the points are the nondominated solutions of the problem, and each solution represents a combination of the parameters in Table 6. For the solution of the left end point, the sink marks are the best, but the warpage is the worst. The closer a solution is to the left end, the better the sink marks become, and the worse the warpage becomes. On the contrary, for the solution of the right end point, the warpage is the best, but the sink marks are the worst. The closer a solution is to the right end, the better the warpage is, and the worse the sink marks are. According to the requirements of the quality of the seatbelt cover, sink marks and warpage are both very important, so the nearest solution to the origin (least square) was selected as the final solution of this study. The optimal parameters were obtained: a packing time of 13.748 s, mold temperature of 20.1325°C, relative rib thickness of 0.40123, melt temperature of 248.851°C, and packing pressure of 44.512 MPa. The combination of these parameters yielded a maximum sink mark of 0.0081 mm and warpage of 1.5433 mm.

3.4.2. Verification Experiment. The aforementioned parameters given by the GA were adopted in the simulation of Moldflow to verify the reliability of the optimization for the sink marks and warpage of the cover plate. The simulation results under the optimized parameters are shown in Figure 12, and those under the parameters of Level "-2", "0", and "2" in Table 6 are provided in Figure 13 for comparison. Parameters of Level "-2" and "2" are minimum and maximum values of the processing factors, and those of Level "0" are mean values. Compared with the other results, sink marks and warpage of the optimized results are both decreased obviously, which directly demonstrates effect of the optimization. It is noted that sink marks and warpage of the optimized results are not the minimal ones among all the results for this optimization. The warpage under the parameters of Level "2" in Figure 13(f) is smaller than that under the optimized parameters in Figure 12(b), but the sink marks are much worse. The results under the optimized parameters are not the best for a single objective but are the optimal for all of the objects. The simulation results under the optimized parameters are 0.0088 mm for the sink marks and 1.578 mm for the warpage. Compared with the optimization result by the GA, the errors are small: 0.0007 mm (7.95%) for the sink marks and 0.00347 mm (0.2%) for the warpage. Thus, the accuracy of the multiobjective optimization for the surface quality of the injection cover plate is high.

The optimized processing parameters were then adopted for the actual injection molding of the part. The manufactured cover plates are shown in Figure 14. Figures 14(a) and 14(c) show those without optimization, and the packing time of 10.0 s, mold temperature of 30.0°C, relative rib thickness of 0.6, melt temperature of 230.0°C, and packing pressure of 35 MPa were used, which took the parameters of Level "0" in Table 6. The other parameters were set as the same with those in Case No. 3 in Table 4. Obvious sink marks are observed in Figure 14(a) because of the rib design and molding process. Warpage occurred at the groove position of the cover plate owing to the molding process. Both of these seriously degraded the appearance of the cover plate. Figures 14(b) and 14(d) show parts manufactured with the optimized parameters, and the packing time of 13.7 s, mold temperature of 20.0°C, relative rib thickness of 0.4, melt temperature of 250°C, and packing pressure of 44.5 MPa were used, which approximated the optimized processing parameters as closely as possible. Comparison of Figures 14(a) and 14(b) reveals that the sink marks disappeared after the optimization. Likewise, Figures 14(c) and 14(d) indicate that the warpage was improved distinctly. Measurements showed that the warpage at the groove position of the cover plate was 64.8% without optimization and 35.4% with optimization.

Table 5: Results of mean-value analysis.

Label	r	t	h	d	s	t_{inj}	T_{melt}	T_{mold}	T_{cool}	t_{cool}	RE	D	V/P	P_{pack}	t_{pack}
1	0.8005	0.7034	0.8608	0.8855	0.938	0.8681	0.7414	0.6716	0.9243	0.9012	0.8731	0.93	0.7896	0.9859	1.1383
2	0.96	1.0571	0.8997	0.875	0.8225	0.8924	1.0191	1.089	0.8362	0.8594	0.8875	0.8306	0.9709	0.7747	0.6222
Delta	0.1595	0.3537	0.0389	0.0106	0.1155	0.0243	0.2778	0.4174	0.088	0.0418	0.0144	0.0994	0.1813	0.2112	0.5161
Rank	7	3	12	15	8	13	4	2	10	11	14	9	6	5	1

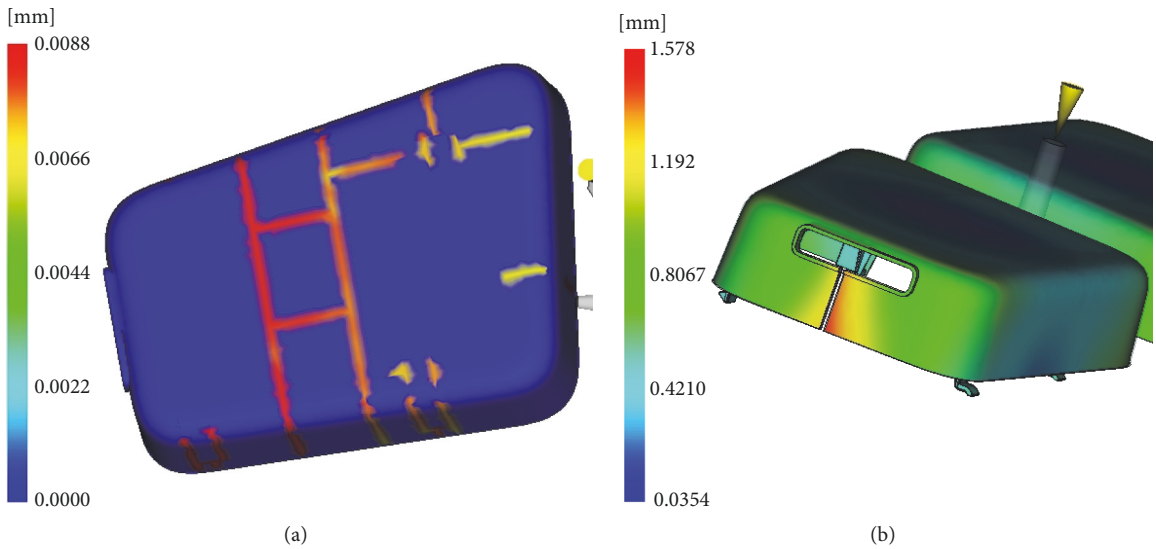

Figure 12: Simulation results under the optimized parameters: (a) sink marks and (b) warpage.

Table 6: Experimental factors and their levels.

Level	t_{pack} A	T_{mold} B	t C	T_{melt} D	P_{pack} E
-2	6	20	0.4	210	25
-1	8	25	0.5	220	30
0	10	30	0.6	230	35
1	12	35	0.7	240	40
2	14	40	0.8	250	45

The optimized result satisfied the appearance requirement of <40%.

4. Conclusions

We established a method of quality prediction and multiobjective optimization for injection molding. Firstly, the key impact factors for the objectives to be optimized are determined via orthogonal experiments. Secondly, RSM are performed to determine relationship function between an objective and impact factors. Finally, to determine the optimal combination of the impact factors, multiobjective GA is employed. The established optimization method was applied to the injection molding of a seatbelt cover plate as an example. The sink marks and warpage were selected as two objectives, which are two of the most prominent quality problems. We optimized the sink marks and warpage, and the prediction error was <8%. We used the optimized processing parameters to perform actual injection molding. The sink marks and warpage were significantly reduced, satisfying the requirements of actual assembly.

By analyzing the seatbelt cover by the proposed method, we confirmed the validity and accuracy of it. The proposed method provides not only scientific guidance for the injection molding process but also solutions and ideas for the multiobjective optimization of other similar problems. The authors intend to develop an integrated system by coding in MATLAB based on the established multiobjective optimization method, including user interfaces, experimental data input, factor selection, quality prediction, and optimization, and apply it in design of TPE (Thermoplastic Elastomer) overmolding.

Appendix

A. Specific Operations Used in Multiobjective Optimization

A.1. Nondominated Solution. Suppose p and q are two of all the feasible solutions. If at least one objective value for p is better than that of q and all the other objective values for p are not worse than those of q, it is defined as p dominates q or q is dominated by p. Dominant and nondominant solutions are illustrated in Figure 15. Points 1, 2, 3, and 4 represent four feasible solutions. In an optimization problem for the

Table 7: RSM experiments.

No.	A	B	C	D	E
1	0	0	2	0	0
2	-1	-1	1	1	1
3	0	0	0	0	0
4	1	1	-1	1	-1
5	-1	1	-1	1	1
6	0	0	0	0	-2
7	0	-2	0	0	0
8	-1	1	-1	-1	-1
9	-1	-1	-1	1	-1
10	0	2	0	0	0
11	-1	1	1	1	-1
12	1	-1	-1	-1	-1
13	0	0	0	0	0
14	1	-1	1	-1	1
15	0	0	-2	0	0
16	1	1	-1	-1	1
17	-1	1	1	-1	1
18	-2	0	0	0	0
19	0	0	0	2	0
20	1	-1	1	1	-1
21	1	1	1	1	1
22	0	0	0	0	0
23	2	0	0	0	0
24	0	0	0	0	0
25	-1	-1	-1	-1	1
26	1	1	1	-1	-1
27	0	0	0	-2	0
28	0	0	0	0	0
29	-1	-1	1	-1	-1
30	0	0	0	0	2
31	0	0	0	0	0
32	1	-1	-1	1	1

Table 8: Fitting results of the sink marks using the four regression models.

	R-sq	R-sq (adjustment)	R-sq (prediction)	regression model
Quadratic	97.51%	93.00%	37.95%	Sink mark1
Linear + parabolic	97.26%	95.96%	87.72%	Sink mark2
Linear + interaction	94.61%	89.56%	34.85%	Sink mark3
Linear	94.36%	93.28%	91.02%	Sink mark4

Annotation: R-sq was the goodness coefficient in regression fitting models.
Results for the four regression models:
Sink mark1 = 0.016148- 0.000292A + 0.000042B + 0.003042C- 0.00004 D - 0.000625E + 0.000227A×A-0.000273B×B + 0.000102C×C-0.000148 D×D-0.000273E×E + 0.000063A×B-0.000062A×C + 0.000062A×D + 0.000062A×E -0.000063B×C + 0.000063B×D + 0.000063B×E-0.000063C×D-0.000063C×E + 0.000063D×E.
Sink mark2 = 0.016148 - 0.000292A + 0.000042 B + 0.003042C- 0.000042D- 0.000625E + 0.000227A×A-0.000273B×B + 0.000102C×C- 0.000148 D×D - 0.000273E×E.
Sink mark3 = 0.015875-0.000292A + 0.000042B + 0.003042C- 0.000042D - 0.000625E + 0.000063A×B - 0.000062A×C+0.000062A×D + 0.000063A×E-0.000063B×C + 0.000063B×D + 0.000063B×E-0.000063C×D- 0.000063C×E + 0.000063D×E.
Sink mark4 = 0.015875-0.000292A + 0.000042B + 0.003042C - 0.000042D - 0.000625 E.

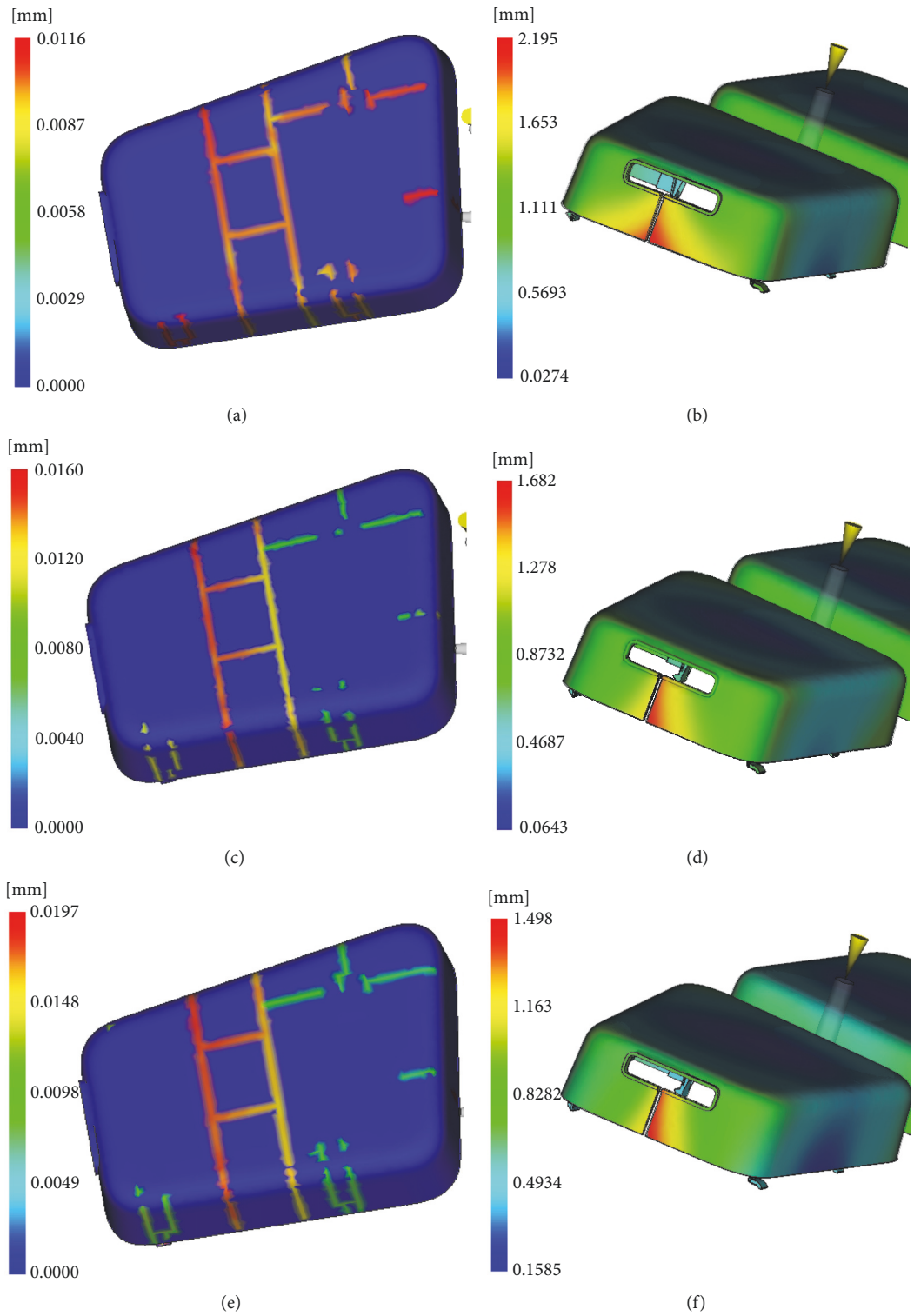

Figure 13: Simulation results under the parameters in Table 6: (a) sink marks and (b) warpage under Level "-2", (c) sink marks and (d) warpage under Level "0", and (e) sink marks and (f) warpage under Level "2".

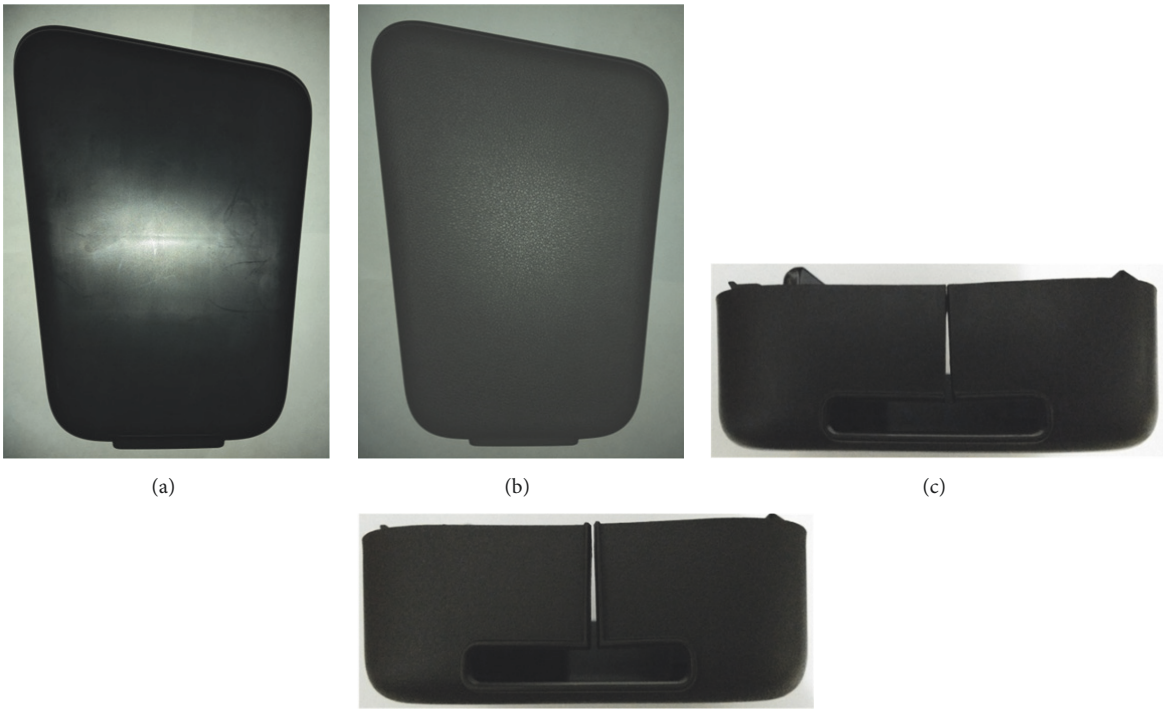

Figure 14: Comparison of the cover plate before and after optimization: (a) surface sink marks before optimization, (b) surface sink marks after optimization, (c) warpage before optimization, and (d) warpage after optimization.

Table 9: Regression-coefficient evaluation for the sink marks.

Term	Coeff	SE coeff	T	P
Constant	0.015875	0.00013	122.56	0
A	-0.000292	0.00015	-1.95	0.062
B	0.000042	0.00015	0.28	0.783
C	0.003042	0.00015	20.34	0
D	-0.000042	0.00015	-0.28	0.783
E	-0.000625	0.00015	-4.18	0

minimal solution, point 4 is the dominant solution, because both f1 and f2 of point 4 are smaller than the other solutions, where f1 and f2 are two objective functions of the problem. Points 2 and 3 are nondominated solutions for each other. f1 of point 2 is smaller than point 3, but f2 of point 2 is greater than point 3.

A.2. Pareto Optimal Set. If a solution p dominates q, the rank of p is smaller than q. If two solutions are nondominated to each other, the ranks of them are the same. The solutions with the rank of 1 (the smallest rank value) are added to a set, named the first front set. The solutions in the first front set are nondominated to each other. The Pareto optimal set is the first front set. As shown in the Figure 16, the curve A is the Pareto front, and the area B is the feasible solution domain.

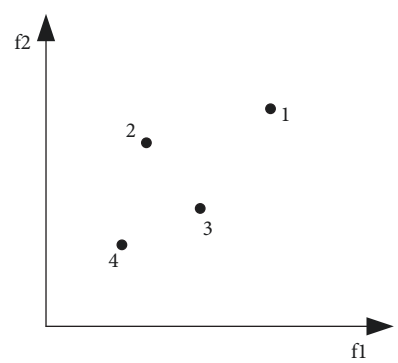

Figure 15: Dominant and nondominant solutions.

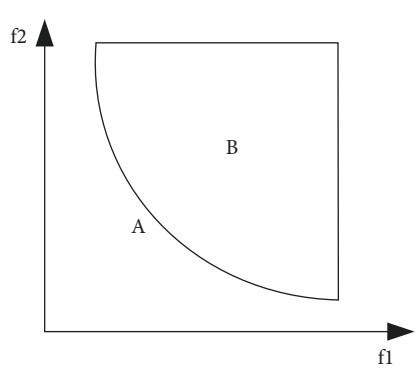

Figure 16: Pareto front.

Table 10: Fitting results of the warpage using the four regression models.

	R-sq	R-sq (adjustment)	R-sq (prediction)	regression model
Quadratic	98.18%	91.87%	51.38%	Warpage1
Linear + parabolic	96.40%	94.69%	88.19%	Warpage2
Linear + interaction	94.80%	89.92%	52.50%	Warpage3
Linear	93.02%	91.67%	88.81%	Warpage4

Annotation: the four regression models were followed:
Warpage1 = 1.68272 - 0.03713 A - 0.00171 B - 0.04379 C - 0.01929 D - 0.04304 E + 0.00266A×A - 0.00747B×B - 0.00522 C×C - 0.00609D×D + 0.00553 E×E - 0.00419A×B + 0.00069 A×C + 0.00706A×D - 0.00094 A×E+ 0.00069 B×C + 0.00031B×D + 0.00081B×E + 0.00569 C×D + 0.00594 C×E+ 0.00456 D×E.
Warpage2 = 1.68272 - 0.03713 A - 0.00171 B - 0.04379 C - 0.01929 D - 0.04304 E + 0.00266 A×A - 0.00747 B×B - 0.00522 C×C - 0.00609 D×D + 0.00553 E×E.
Warpage3 = 1.67478 - 0.03713 A - 0.00171 B - 0.04379 C - 0.01929 D - 0.04304 E - 0.00419A×B + 0.00069A×C + 0.00706 A×D - 0.00094 A×E + 0.00069 B×C + 0.00031B×D + 0.00081B×E + 0.00569C×D + 0.00594 C×E + 0.00456 D×E.
Warpage4 = 1.67478 - 0.03713 A - 0.00171 B - 0.04379 C - 0.01929 D - 0.04304 E.

Table 11: Regression-coefficient evaluation for the warpage.

Term	Coeff	SE coeff	T	P
Constant	1.68272	0.00623	269.97	0
A	-0.03713	0.00319	-11.64	0
B	-0.00171	0.00319	-0.54	0.598
C	-0.04379	0.00319	-13.73	0
D	-0.01929	0.00319	-6.05	0
E	-0.04304	0.00319	-13.49	0
A∗A	0.00266	0.00289	0.92	0.367
B∗B	-0.00747	0.00289	-2.59	0.017
C∗C	-0.00522	0.00289	-1.81	0.085
D∗D	-0.00609	0.00289	-2.11	0.047
E ∗E	0.00553	0.00289	1.92	0.069

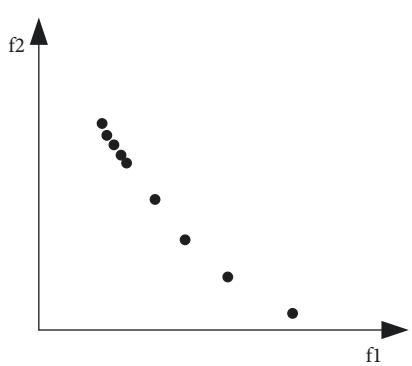

Figure 17: Crowding distance.

A.3. Crowding Distance. The crowding distance is used to describe the distance between two solutions in a front set. Obviously, the greater the distance is, the less crowded the solutions are, and the better the population diversity is. As shown in Figure 17, the crowding distance on the left side of the Pareto front is small, and many solutions are gathered in this area. This result is not ideal, so the crowding distance needs to be controlled. The calculation is described in Appendix B.

B. Algorithms of the Key Operators in the Multiobjective Genetic Optimization Module

B.1. Selection. The selection operator applied tournament selection algorithm based on rank and crowding distance. The algorithm is as in Algorithm 1.

B.2. Nondominated Sorting. Nondominated sorting was used to sort individuals in the combined population of parent and child populations so as to obtain the rank of each individual. The algorithm is as in Algorithm 2.

B.3. Crowding Distance Calculating. The process of the crowding distance calculation is as follows.

Step 1. Enter the population 'pop', the number of rows 'popSize', and the number of columns 'numDatta'. 'popSize' is the number of individuals, and 'numDatta' is the number of objective functions.

Step 2. Map the i-th objective function value of all individuals to interval (-1, 1).

Step 3. The mapped function values are sorted in ascending order.

Step 4. The crowding distance of the two ends is defined as infinite. The distance of other individuals is the function value difference of its two neighbor individuals, and thus the crowding distance of each individual under the i-th function value is obtained.

Step 5. Repeat Step 2, 3, and 4 until all objective functions have been calculated.

Step 6. The crowding distance for an individual is the sum of the calculated crowding distances for all objective functions.

Data Availability

The data used to support the findings of this study are included within the article

```
Input playerlist    // The list of athletes includes the 'nParents' groups, and each group
has 'tournamentSize' athletes.
for i=1 to nParents
   winner=plyer(1)
for j=2 to tournamentSize
   if rank(j)<rank(j-1)
winne(i)r=player(j)       // Athletes with small rank win, winners in group i are marked
as winner(i)
end if
if rank(j)=rank(j-1)
   if distance(j)>distance(j-1)
      winner(i)=player(j) //Individuals with greater crowding distance win,when they
have the same order value
   end if
end if
end for
Output winner
```

Algorithm 1: Selection tournament.

```
Input score    //Enter the objective function value, the number of rows 'popSize' is the
number of populations after the merger, the number of columns is the value of the
objective function
do
for p=1 topopSize
   if pis Sorted
      continue    // Perform the next cycle
end if
for q=1 to popSize
If there is a function value greater than p's in q and all of q's function values are not less
than p's
q dominate p;
   end if
end for
if p is not dominated
Assigns the current rank to p and p is sorted
end if
end for
rank++;
while all individuals are sorted
Output rank    //Output combined population order value
```

Algorithm 2: NonDominatedRank.

Conflicts of Interest

The authors declare that there are no conflicts of interest regarding the publication of this paper.

Acknowledgments

The authors would like to acknowledge the financial support from the National Natural Science Foundation Council of China (Grant no. 51775398), the 111 Project (Grant no. B17034), the Program for Innovative Research Team in University of Education Ministry (Grant no. IRT_17R83), Nature Science Foundation of Hubei Province (Grant no. 2018CFB595), and the Fundamental Research Funds for the Central Universities (Grants nos. WUT: 2018III074GX and 2018III067GX).

References

[1] W. Guo, L. Hua, and H. Mao, "Minimization of sink mark depth in injection-molded thermoplastic through design of experiments and genetic algorithm," *The International Journal of Advanced Manufacturing Technology*, vol. 72, no. 1-4, pp. 365–375, 2014.

[2] D. Mathivanan, M. Nouby, and R. Vidhya, "Minimization of sink mark defects in injection molding process – Taguchi approach," *International Journal of Engineering Science & Technology*, vol. 2, no. 2, 2010.

[3] Y. Zhao, P. Zhao, J. Zhang, J. Huang, N. Xia, and J. Fu, "On-line measurement of clamping force for injection molding machine using ultrasonic technology," *Ultrasonics*, vol. 91, pp. 170–179, 2019.

[4] Z. Jiao, P. Xie, W. Yang, and X. Wang, "Automatic control and energy-saving mechanism of internal circulation two-platen injection molding machine," in *Proceedings of the 2010 International Conference on Mechanic Automation and Control Engineering, MACE2010*, pp. 5491–5494, China, June 2010.

[5] P. Zhao, Y. Zhao, H. Kharbas et al., "In-situ ultrasonic characterization of microcellular injection molding," *Journal of Materials Processing Technology*, vol. 270, pp. 254–264, 2019.

[6] P. Zhao, W. M. Yang, X. M. Wang, J. G. Li, B. Yan, and J. Z. Fu, "A novel method for predicting degrees of crystallinity in injection molding during packing stage," *Proceedings of the Institution of Mechanical Engineers, Part B: Journal of Engineering Manufacture*, vol. 233, no. 1, pp. 204–214, 2019.

[7] J. F. Zhang, P. Zhao, Y. Zhao, J. Y. Huang, N. Xia, and J. Z. Fu, "On-line measurement of cavity pressure during injection molding via ultrasonic investigation of tie bar," *Sensors and Actuators A: Physical*, vol. 285, pp. 118–126, 2019.

[8] N. Li, H. B. Liu, and H. T. Wu, "The deformation analysis and optimization of the injection molded parts based on the moldflow and minitab software," *Advanced Materials Research*, vol. 753-755, no. 6, pp. 1180–1183, 2013.

[9] B. H. Lee and B. H. Kim, "Optimization of part wall thicknesses to reduce warpage of injection-molded parts based on the modified complex method," *Polymer-Plastics Technology and Engineering*, vol. 34, no. 5, pp. 793–811, 1995.

[10] B. Ozcelik and T. Erzurumlu, "Determination of effecting dimensional parameters on warpage of thin shell plastic parts using integrated response surface method and genetic algorithm," *International Communications in Heat and Mass Transfer*, vol. 32, no. 8, pp. 1085–1094, 2005.

[11] B. Ozcelik and T. Erzurumlu, "Comparison of the warpage optimization in the plastic injection molding using ANOVA, neural network model and genetic algorithm," *Journal of Materials Processing Technology*, vol. 171, no. 3, pp. 437–445, 2006.

[12] S. Tang, Y. Tan, S. Sapuan, S. Sulaiman, N. Ismail, and R. Samin, "The use of Taguchi method in the design of plastic injection mould for reducing warpage," *Journal of Materials Processing Technology*, vol. 182, no. 1-3, pp. 418–426, 2007.

[13] Y. Gao and X. Wang, "An effective warpage optimization method in injection molding based on the Kriging model," *The International Journal of Advanced Manufacturing Technology*, vol. 37, no. 9-10, pp. 953–960, 2008.

[14] B. Farshi, S. Gheshmi, and E. Miandoabchi, "Optimization of injection molding process parameters using sequential simplex algorithm," *Materials and Corrosion*, vol. 32, no. 1, pp. 414–423, 2011.

[15] C. Wang, J. Shen, and H. Zhu, "Warpage simulation and optimization for the shell of color liquid crystal display monitor based on Moldflow," in *Proceedings of the 2011 2nd International Conference on Mechanic Automation and Control Engineering, MACE 2011*, pp. 924–927, China, July 2011.

[16] S. Ni, "Preventing sink marks of injection molded parts using CAE analysis," in *Proceedings of the ANTEC*, pp. 453–455, 2000.

[17] D. Mathivanan and N. S. Parthasarathy, "Sink-mark minimization in injection molding through response surface regression modeling and genetic algorithm," *The International Journal of Advanced Manufacturing Technology*, vol. 45, no. 9-10, pp. 867–874, 2009.

[18] Q. Feng and X. Zhou, "Automated and robust multi-objective optimal design of thin-walled product injection process based on hybrid RBF-MOGA," *The International Journal of Advanced Manufacturing Technology*, vol. 101, no. 9-12, pp. 2217–2231, 2019.

[19] H. X. Li, K. Liu, D. Y. Zhao, M. J. Wang, Q. Li, and J. H. Hou, "Multi-objective optimizations for microinjection molding process parameters of biodegradable polymer stent," *Materials*, vol. 11, no. 11, p. 16, 2018.

[20] S. Farahani, A. Yelne, F. Akhavan Niaki, and S. Pilla, Numerical simulation for the hybrid process of sheet metal forming and injection molding using smoothed particle hydrodynamics method, 2019.

[21] S. Farahani, A. F. Arezoodar, B. M. Dariani, and S. Pilla, "An analytical model for nonhydrostatic sheet metal bulging process by means of polymer melt pressure," *Journal of Manufacturing Science and Engineering*, vol. 140, no. 9, 2018.

[22] H. Kazan, S. Farahani, and S. Pilla, Influences of process parameters on penetration in a hybrid single shot manufacturing of carbon fiber/epoxy- polypropylene structure, 2019.

[23] F. Yin, H. Mao, L. Hua, W. Guo, and M. Shu, "Back Propagation neural network modeling for warpage prediction and optimization of plastic products during injection molding," *Materials and Corrosion*, vol. 32, no. 4, pp. 1844–1850, 2011.

[24] K. Deb, A. Pratap, S. Agarwal, and T. Meyarivan, "A fast and elitist multiobjective genetic algorithm: NSGA-II," *IEEE Transactions on Evolutionary Computation*, vol. 6, no. 2, pp. 182–197, 2002.

[25] K. Miettinen, *Nonlinear Multiobjective Optimization*, Birkhaüser Verlag, 1999.

[26] E. Zitzler and L. Thiele, "Multiobjective optimization using evolutionary algorithms — a comparative case study," in *Proceedings of the International Conference on Parallel Problem Solving from Nature*, vol. 1498, pp. 292–301, 1998.

[27] H. Oktem, T. Erzurumlu, and I. Uzman, "Application of Taguchi optimization technique in determining plastic injection molding process parameters for a thin-shell part," *Materials and Corrosion*, vol. 28, no. 4, pp. 1271–1278, 2007.

[28] T. Tabi, A. Suplicz, F. Szabo et al., "The analysis of injection molding defects caused by gate vestiges," *Express Polymer Letters*, vol. 9, no. 4, pp. 394–400, 2015.

[29] V. Leo and C. Cuvelliez, "The effect of the packing parameters, gate geometry, and mold elasticity on the final dimensions of a molded part," *Polymer Engineering & Science*, vol. 36, no. 15, pp. 1961–1971, 1996.

[30] J. Dobránsky, P. Baron, M. KoČiško, L. BĚhálek, and E. Vojnová, "Solving depressions formed during production of plastic molding," *Metalurgija*, vol. 54, no. 3, pp. 496–498, 2015.

[31] M. Wegrzyn, O. Sahuquillo, A. Benedito, and E. Gimenez, "Morphology, mechanical performance, and nanoindentation behavior of injection molded PC/ABS-MWCNT nanocomposites," *Journal of Applied Polymer Science*, vol. 132, no. 22, 2015.

[32] T. Erzurumlu and B. Ozcelik, "Minimization of warpage and sink index in injection-molded thermoplastic parts using Taguchi optimization method," *Materials and Corrosion*, vol. 27, no. 10, pp. 853–861, 2006.

Hindawi
Advances in Polymer Technology
Volume 2019, Article ID 1591204, 13 pages
https://doi.org/10.1155/2019/1591204

Research Article

Improving the Consistency of Injection Molding Products by Intelligent Temperature Compensation Control

Yufei Ruan, Huang Gao, and Dequn Li

State Key Laboratory of Material Processing and Die & Mould Technology, Huazhong University of Science and Technology, Wuhan, 430074, China

Correspondence should be addressed to Huang Gao; gaohuang@hust.edu.cn

Received 10 April 2019; Revised 24 May 2019; Accepted 10 June 2019; Published 1 July 2019

Guest Editor: Srikanth Pilla

Copyright © 2019 Yufei Ruan et al. This is an open access article distributed under the Creative Commons Attribution License, which permits unrestricted use, distribution, and reproduction in any medium, provided the original work is properly cited.

Temperature stability is critical to the consistency of product quality in the injection molding process, and it is very necessary to improve the temperature control accuracy under dynamic conditions. However, due to the large time delay, strong coupling, and the dynamic characteristics existing in the system, it is not an easy task to achieve precise temperature control in the injection molding process. In this paper, a new intelligent temperature compensation control strategy for the injection molding process under dynamic conditions is proposed in order to solve two key problems in the compensation control strategy: the compensation time and compensation quantity. A data-based feedforward iterative learning control (ILC) algorithm is designed to learn the optimal compensation time. Once the optimal compensation time is learned, a deep Q-learning algorithm which combined Q-learning with an artificial neural network (ANN) is proposed to learn the optimal compensation quantity. An experimental platform is designed to validate the superiority of the proposed method. Experimental results show that the proposed method can effectively improve temperature control accuracy under dynamic conditions. Meanwhile, the product consistency has also been improved.

1. Introduction

Polymer injection molding is one of the most widely used processing methods for producing polymer products [1]. As a typical batch production process, product consistency is critical in the injection molding process [2]. Temperature is one of the two dominant factors that affect product consistency (the other one is pressure). And in the work reported by Gim et al. [3], temperature shows a stronger correlation. Therefore, improving the stability of temperature control is very important to improve product quality consistency. In general, in addition to the effects of machine design and materials, the stability of temperature is mainly determined by the following processing parameters: barrel temperature, screw rotation speed, back pressure, dwell time, and injection stroke. Limited by the processing technology and production efficiency, except for the barrel temperature, the other parameters are not controllable variables in the production process. Therefore, precise barrel temperature control is critical to improve the stability of melt temperature and product consistency.

However, it is challenging to achieve precise control of barrel temperature due to the two major particular characteristics, namely, large time delays and strong coupling [4]. Usually, the barrel is heated by using electrical resistance heating. The heaters are wrapped around the outside surface of the barrel. Therefore, heat is concentrated on the outside surface of the barrel and heating the material inside the barrel by means of heat conduction. Due to the thick barrel wall, it usually takes dozens of seconds or more until the heat is transferred to the internal part of the barrel. Thus, there is a huge time delay in the system. On the other hand, owing to the intermittent disturbances caused by (1) the ease of heat conduction, (2) the fresh raw materials entering, (3) changes in the environment, and (4) the shear heat generated during the operation, these make it a strong coupling system.

In most of the existing injection molding processes, the temperature is usually controlled by a proportional integral differential (PID) algorithm [5]. The PID algorithm has been widely applied in temperature control [6, 7]. It is easy to implement and can provide good robustness under static conditions. But the polymer injection molding process

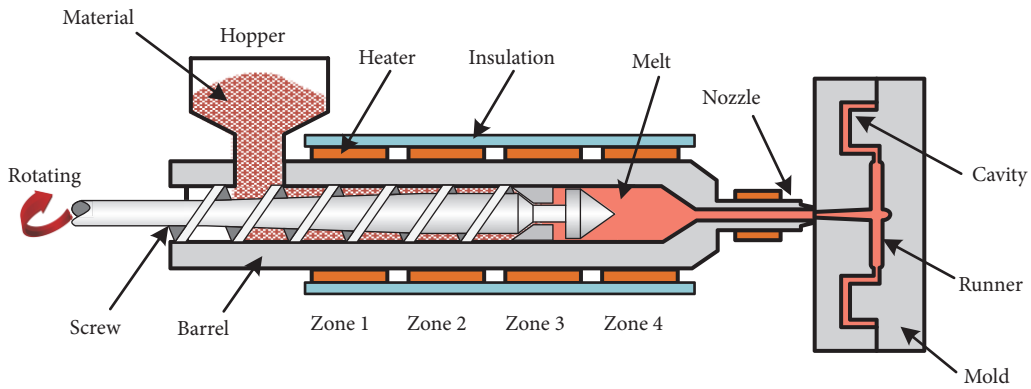

Figure 1: Structure diagram of an injection molding machine injection unit.

contains several iterative and repeated operations. Each operation is performed intermittently. Therefore, the barrel is in dynamic conditions during the injection molding process. Hence, the PID algorithm cannot provide a satisfactory barrel temperature control performance for the whole operation process. In the past decades, in order to solve the barrel temperature control problem, many advanced control methods have been proposed such as adaptive decoupling control [8], model predictive synchronous control [9], multivariable self-tuning predictive control [10], self-optimizing model predictive control [11], adaptive generalized predictive control [12], and response identification and internal model control [13]. These methods can effectively solve the problem of large time delay. However, most of these existing methods are based on feedback control strategies and cannot deal with the intermittent disturbances. On the other hand, these methods do not take into account the dynamic characteristics of the injection molding process.

Considering the repeated operation characteristics of the polymer injection molding process, it is feasible to use a feedforward compensation strategy to eliminate the effects of intermittent disturbances. For example, Yao et al. proposed a barrel temperature control method using the combination of a generalized predictive control with an iterative learning feedforward control [14]. The experimental results show that using a feedforward compensation strategy can effectively prevent large temperature variations caused by intermittent disturbances. There are two key points that must be confirmed when using a feedforward compensation strategy for the barrel temperature control: (1) the compensation time and (2) the compensation quantity. However, it is not an easy task to get the accurate compensation time and compensation quantity for the barrel temperature control. They are affected by many complex factors, such as raw materials, environment, injection molds, and process parameters. Therefore, it is difficult to obtain the accurate compensation time and compensation quantity through model-based methods.

According to the previous analysis, it is crucial to obtain the accurate compensation time and compensation quantity when using a feedforward compensation control strategy for the injection molding temperature control. Considering the repeated behavior of the system, iterative learning control (ILC) is recognized as an effective control method for the systems with repeated characteristics [15, 16]. ILC is a kind of data-based learning control method [17]. ILC generates feedforward control signals that apply to the next batch by using information from previous batches that have been stored. As a data-based control method, ILC does not require an accurate system model, so it can be easily adapted to a variety of complex conditions. Thus, it is feasible to use ILC to obtain the accurate compensation time. However, as a feedforward control strategy, ILC cannot achieve accurate compensation quantity control. As a typical batch production process, it is feasible to adopt a reinforcement learning (RL) algorithm to the control system [18].

In this paper, a new intelligent barrel temperature control method, which fully considers the dynamic characteristics of the injection molding process, is proposed. The proposed control method adopts a feedforward compensation strategy to improve the stability of temperature control under dynamic conditions. The proposed method first learns the optimal compensation time in each batch using a feedforward ILC algorithm. Subsequently, a deep Q-learning algorithm combining Q-learning with ANN is adopted to learn the optimal compensation quantity for each compensation period. With this innovation control strategy, the stability of temperature control can be effectively improved, and the product consistency can be significantly improved.

The rest of this paper is organized as follows. In Section 2, the system description is presented. Section 3 develops the feedforward compensation temperature control strategy. In Section 4, temperature control experiments with different conditions are performed. In Section 5, the product consistency experiments are given to verify the effectiveness of the developed control strategy in improving product consistency. Finally, conclusions are drawn in Section 6.

2. System Description

The typical structure diagram of an injection molding machine injection unit is shown in Figure 1. It mainly consists of a screw, a barrel, a nozzle, and a heating system. In general, the heating system has multiple heating zones. For each heating zone, there is a heater and a temperature sensor.

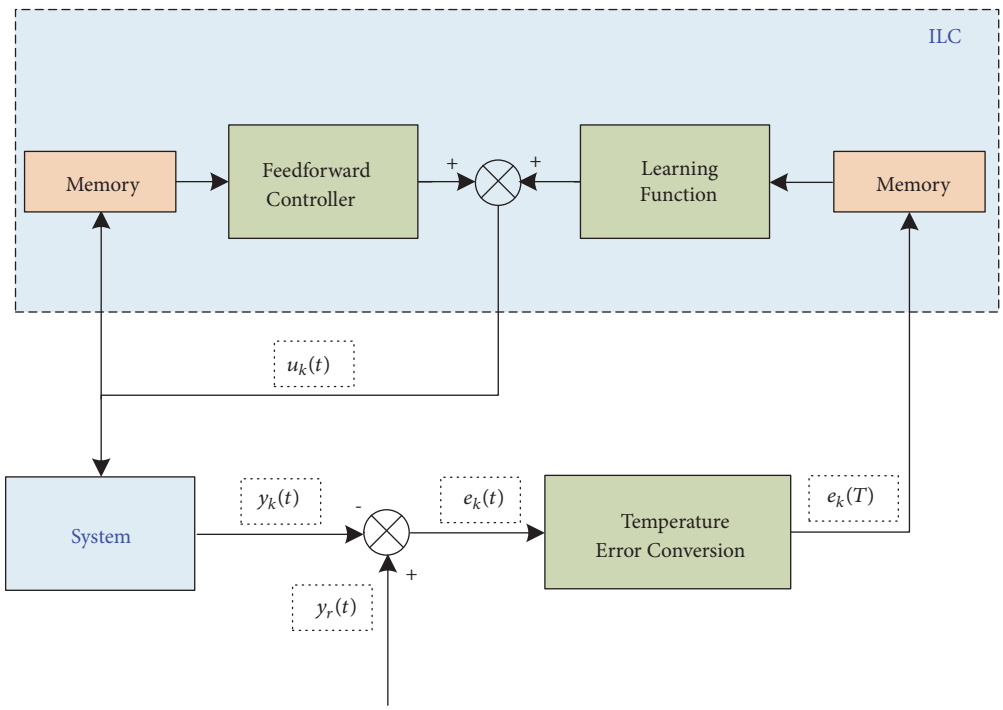

Figure 2: Schematic representation of the ILC-based compensation time control algorithm.

In most cases, the temperature set for each heating zone varies according to the requirements of the process. In order to save energy, the heating system is covered with a layer of thermal insulation materials. The system has no cooler system. Therefore, the cooling rate of the system is very slow.

During the injection molding process, the raw materials enter the barrel from the hopper. The raw materials are heated to molten state in the barrel. Then the screw rotates and retreats, thereby mixing the melt evenly and squeezing the melt to the front of the barrel. Finally, the screw moves forward to inject the melt into the mold. During this process, the temperature is affected by multiple factors:

(1) The heating coil around the outside of the barrel is the dominant factor under static conditions

(2) The shear heat, which is generated between the screw and the melt, is the other major factor affecting the temperature

(3) The thermal coupling is caused by the different temperature conditions of different heating zones and the excellent thermal conductivity of metal

(4) There are also the process parameters setting (screw rotation speed, back pressure, etc.), materials, molds, surrounding environment, and so on

Therefore, for such a complicated system, it is a great challenge to achieve precise temperature control. Previous studies have shown that it is impossible to solve this problem using a modeling approach [12].

3. Methodology

3.1. Feedforward ILC for Compensation Time Control. ILC is a data-based control method; compared to traditional model-based control methods, it does not require an accurate system model and only needs a small amount of historical data from previous batches. The objective of ILC is to generate a feedforward control signal by utilizing information from previous batches and reduce tracking error by iteration. In this paper, a feedforward ILC-based controller is designed to obtain the temperature compensation time.

The schematic representation of the ILC-based compensation time control algorithm is shown in Figure 2. $k = 1, 2, \ldots$ represents the number of iteration, $t = 0, 1, \ldots, T - 1$ represents the sample time, and T is the total number of samples in each batch. In batch k, $y_k(t)$ denotes the system output at step t, $u_k(t)$ denotes the input at step t, $y_r(t)$ denotes the control target at step t, $e_k(t)$ denotes the temperature error at step t, and $e_k(T)$ denotes the time error. The control algorithm included mainly consists of three parts: (1) a feedforward controller, (2) a learning function, and (3) temperature error conversion. The feedforward controller is used to handle the relationship between the previous batch input and the next batch input. The learning function is used to calculate input changes for the next batch. The temperature error is converted into compensation time error according to the temperature error conversion.

The purpose of the compensation time control algorithm is to obtain the optimal compensation time. In the practical control process, the temperature sensor returns the temperature of each sampling period. The data of each cycle in each

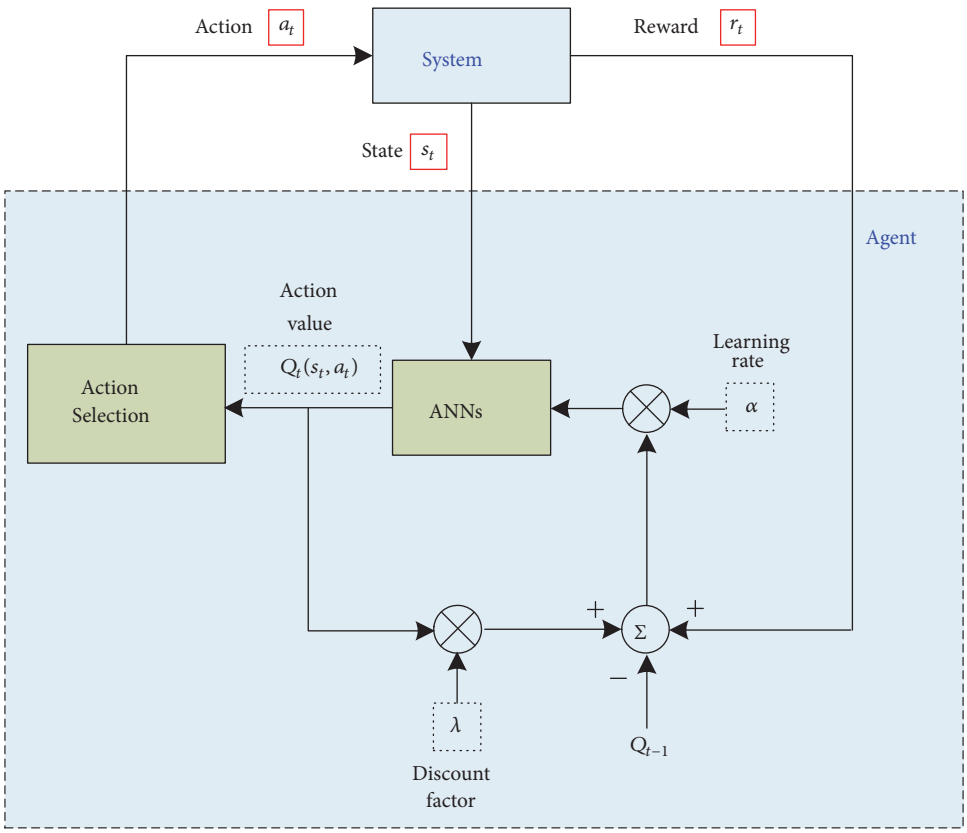

Figure 3: Schematic diagram of the RL-based compensation quantity control method.

batch are saved in the memory. At the end of a batch, the temperature error curve of the whole batch is obtained by comparing with the reference value. The time error $e_k(T)$ is obtained by analyzing the temperature error curve. The system input is given by

$$u_k(t) = Q(u_{k-1}(t)) + \Delta u_k(t), \tag{1}$$

where Q is a filter, $u_{k-1}(t)$ is the control input of the previous batch, and $\Delta u_k(t)$ is the change in control input of the next batch which is obtained by the learning function. It can be calculated as follows:

$$\min J_k = \sum_{t=0}^{T-1} [e_k(t)]^T A(t) [e_k(t)] + \sum_{t=0}^{T-1} [\Delta u_k(t)]^T B(t) [\Delta u_k(t)] \tag{2}$$

$$\frac{1}{2}\frac{\partial J_k}{\partial u_k} = -G^T A(t) e_k + B(t) \Delta u_k(t) = 0 \tag{3}$$

$$\Delta u_k(t) = B(t)^{-1} G^T A(t) e_k(t). \tag{4}$$

$A(t)$ and $B(t)$ represent the weighting matrices, and G is a Toeplitz matrix. In the learning process, a time constant, $e(T_0)$, is selected as the maximum permissible error. The learning process ends until the time error $e_k(T) \le e(T_0)$.

3.2. Reinforcement Learning for Compensation Quantity Control. In the problem of RL, an agent is able to improve its performance from its own experience by interacting with the environment [19]. A typical agent mainly consists of the following three parts: state s, action a, and reward r. The target of the agent is to learn the optimal action policy to maximize the total rewards it will receive in the future. In a time step t, the agent selects an action a_t based on the current state s_t; the system performs the selected action and returns a reward r_t and then goes to the next state s_{t+1}. Meanwhile, the state-action values $(s_t, a_t)_k$ are recorded. In this paper Q-learning is adopted to learn the optimal temperature compensation quantity. Q-learning is a form of model-free off-policy RL algorithm [20]. As a kind of widely used RL algorithm, Q-learning finds the optimal policy by learning the optimal action value function $Q_t(s_t, a_t)$ in each state.

The action value function $Q_t(s_t, a_t)$ is updated as follows:

$$Q_t(s_t, a_t) \longleftarrow Q_{t-1}(s_t, a_t) + \alpha\left[r_t + \lambda \max_{a \in A} Q_{t-1}(s_{t+1}, a) - Q_{t-1}(s_t, a_t)\right], \tag{5}$$

where $0 \le \lambda < 1$ is the discount factor, $0 < \alpha \le 1$ is the learning rate, and A is the action space.

The schematic representation of the RL-based temperature compensation quantity control method is shown in Figure 3. The sampling temperature y_t, temperature error e_t,

and control input u_t constitute the state space S_t; it can be expressed by

$$S_t = \{(y_t, e_t, u_t)\}. \tag{6}$$

The action space is expressed as

$$A_t = \{+\Delta u_t, 0, -\Delta u_t\}. \tag{7}$$

Δu_t is the minimum control voltage value, and $\Delta u_t = 0.1$ V. Three actions are available: increase input ($+\Delta u_t$), decrease input ($-\Delta u_t$), and 0 means no modification is made; the system performs the previous temperature control signal.

In order to prevent the algorithm from falling into the local optimal solution, the ε-greedy algorithm is adopted to choose the action. The algorithm chooses an action a_i in a state s_t with a probability $p(s_t, a_i)$. It can be described as

$$p(s_t, a_i) = \begin{cases} 1-\varepsilon, & a_i = \max\limits_{a'} Q(s_t, a') \\ \varepsilon, & \text{otherwise.} \end{cases} \tag{8}$$

ε is a small positive constant. During the control process, the algorithm will choose a greedy action with a probability $1-\varepsilon$ or randomly select an action with a probability ε.

The system will perform the selected action and return a reward r_t and then goes to the next state s_{t+1}. The agent will receive a positive reward (+1) if the temperature error $y_{e,t}$ is less than the maximum permissible error. If the temperature error is greater than the maximum permissible error, but less than the previous temperature error $y_{e,t-1}$, the agent will receive a small positive reward (+0.1). In other cases, the agent will receive a reward (-1). In summary, the reward function can be defined as follows:

$$r_{t+1} = \begin{cases} +1, & \text{if } |y_{e,t}| \le y_{e_0,t} \\ 0.1, & \text{if } |y_{e,t}| > y_{e_0,t} \text{ and } |y_{e,t}| \le |y_{e,t-1}| \\ -1, & \text{otherwise.} \end{cases} \tag{9}$$

Conventionally, the Q-learning method requires a lookup table to store the value of each state-action pair. However, it is impossible to build a lookup table for actual control problems. The state space of the temperature control process is very large. It may lead to a series of problems when using a lookup table. For example, it may cause high computational cost, or the algorithm cannot converge. In order to deal with the problem of a large number of state-action pairs in the temperature control, in this paper, neural networks are applied to approximate the optimal action value function. In each step t, the action value can be expressed as follows:

$$Q_t = \sum_{i=1}^{n} w_{t,i}^{(2)} d_{t,i}, \tag{10}$$

where

$$d_{t,i} = \frac{1}{1+e^{-h_{t,i}}} \tag{11}$$

$$h_{t,i} = \sum_{j=1}^{m} w_{t,ij}^{(1)} x_{t,j}. \tag{12}$$

n is the number of hidden nodes of the neural network, m is the number of neural network inputs, $h_{t,i}$ and $d_{t,i}$ represent the input and output of the ith hidden nodes, $w_{t,ij}^{(1)}$ and $w_{t,i}^{(2)}$ ($i = 1, 2, \ldots, n$; $j = 1, 2, \ldots, m$) are the connection weights, and $x_{t,j} \in S_t$ ($j = 1, 2, \ldots, m$) is the jth element of the state S_t.

According to (5), the weight matrix W_t of the ANN is updated as follows:

$$\Delta W_t = \alpha \left[r_{t+1} + \gamma \max_{a' \in A} Q_t(s_{t+1}, a') - Q_t(s_t, a_t) \right] \nabla_w Q_t. \tag{13}$$

W_t represents the connection weight matrix $W_t^{(1)}$ or $W_t^{(2)}$, and $\nabla_w Q_t = \partial Q_t / \partial W_t$ is a vector of the gradient, and it is calculated as follows:

$$\frac{\partial Q_t}{\partial w_{t,i}^{(2)}} = d_{t,i} \tag{14}$$

$$\frac{\partial Q_t}{\partial w_{t,ij}^{(1)}} = w_{t,i}^{(2)} d_{t,i} (1 - d_{t,i}) x_{t,j}. \tag{15}$$

Using neural networks to approximate the action value functions will solve some existing problems. However, some new problems will arise when RL is combined with neural networks. Firstly, there are the correlations between the state-action pairs [21]. In an actual control problem, the current state is usually very similar to the adjacent sampling period, so the correlation between the samples is very strong. Secondly, the target value is affected by network weight. The update of network weight in the current step will affect the target value of the other steps. Therefore, if network weights are updated in every step, this will lead to a very long time to converge or even to diverge.

In this paper, a mechanism called "experience replay" is adopted to solve the problems caused by using neural networks [22]. During the learning process, the state-action pair of every sampling period is first stored. Then you can randomly select data from the memory to update the network, thereby eliminating correlations between the state-action pairs. Furthermore, different from the traditional online neural network update strategy, the connection weights of the neural network are updated offline. The connection weights will be updated after the end of a batch. With this offline update strategy, the impact of weight update in the traditional online update strategy can be effectively eliminated. These innovations not only effectively reduce the computation time, but also make the proposed method more feasible.

4. Temperature Control Experiments

4.1. Experiment Setups. An experimental platform is designed to validate the proposed method, as shown in Figure 4. In order to meet the experimental needs, a modified injection molding machine is used for experiments. A new set of

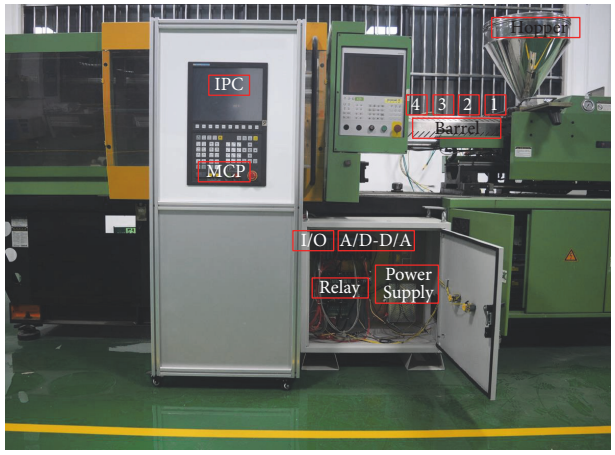

Figure 4: Experiment platform.

injection molding machine control system, as shown in Figure 4, is established on the original injection molding machine. The parameters of the injection molding machine related to the experiments are listed in Table 1. There are five heating zones including one-nozzle zone; the remaining four zones are numbered 1-4 from the hopper to nozzle. The materials used for the experiments are polypropylene (PP) and polystyrene (PS). The thermophysical properties of PP and PS are shown in Table 2. The parameters of the Q-learning algorithm are listed in Table 3.

4.2. Single Zone Temperature Control with Open Loop Control. To show the large time delays and strong coupling of the heating system, an open loop control strategy is applied to zone 3. The target temperature is set at 180°C, and all zones are heated from room temperature. In addition to zone 3, the other zones have no input. The temperature results of zone 3, zone 2, and zone 4 are shown in Figure 5(a). The control voltage is shown in Figure 5(b); 10 V means heating with the maximum power of the coil. The temperature of zone 3 reaches the target temperature after 1023 seconds; then stop heating. It can be seen that, after stopping heating, the temperature of zone 3 continues to rise until the maximum temperature (184.2°C) is reached at 1085 seconds. After that, the temperature of zone 3 gradually drops. During this process, the temperature of zone 2 and zone 4 will also rise owing to heat conduction. It can be observed that even if the temperature of zone 3 begins to decrease, the temperature of zone 2 and zone 4 will still rise as long as there are temperature differences. Therefore, the heating system is a large time delay and strong coupling system.

4.3. Temperature Control with Dynamic Conditions. As mentioned before, during the injection molding process, the heating system is in a dynamic condition. In order to validate the proposed temperature control strategy under dynamic conditions, several sets of comparative experiments are conducted. The proposed temperature control strategy is compared with the generalized predictive control (GPC) method and the PID method. The PID algorithm is the most widely used control algorithm in the field of temperature control; the discrete PID model can be expressed as follows:

$$\Delta u(t) = q_0 e(t) + q_1 e(t-1) + q_2 e(t-2), \tag{16}$$

where

$$\begin{aligned} q_0 &= K_p\left(1 + \frac{T}{T_i} + \frac{T_d}{T}\right) \\ q_1 &= -K_p\left(1 + 2\frac{T_d}{T}\right) \\ q_2 &= K_p\frac{T_d}{T}. \end{aligned} \tag{17}$$

$t = 2, 3, 4, \ldots$ represents the sample time, $\Delta u(t)$ represents the change in control input, $e(t)$, $e(t-1)$, and $e(t-2)$ are errors in different sampling periods, T is the control cycle, K_p is the proportional gain, T_i is the integral time, and T_d is the derivative time. The GPC algorithm has been widely used in the field of temperature control in recent years and has achieved excellent performance. It can be expressed as follows:

$$u(t) = u(t-1) + H_{N_c}\left(G^T G + \lambda I_{N_c}\right)^{-1} G^T (R - F), \tag{18}$$

where

$$H_{N_c} = [1, 0, 0, \ldots, 0]_{1\times N_c}$$

$$G = \begin{bmatrix} g_1 & 0 & \cdots & 0 \\ g_2 & g_1 & \cdots & 0 \\ \vdots & \vdots & \ddots & \vdots \\ g_{N_c} & g_{N_c-1} & \cdots & g_1 \\ \vdots & \vdots & \vdots & \vdots \\ g_{N_2} & g_{N_2-1} & \cdots & g_{N_2-N_c+1} \end{bmatrix}_{N_2\times N_c},$$

$$R = \begin{bmatrix} r(t+1) \\ r(t+1) \\ \vdots \\ r(t+N_2) \end{bmatrix}$$

$$F = \begin{bmatrix} \Delta u(t)\left[G_1\left(q^{-1}\right) - g_{1,0}\right] + F_1\left(q^{-1}\right) y(t) \\ \Delta u(t)\, q\left[G_2\left(q^{-1}\right) - \left(g_{2,1} - g_{2,0}\right) q^{-1}\right] + F_2\left(q^{-1}\right) y(t) \\ \vdots \\ \Delta u(t)\, q^{N_2-1}\left[G_{N_2}\left(q^{-1}\right) - \left(g_{N_2,N_2-1} - g_{N_2,N_2-2} - \cdots - g_{N_2,0}\right) q^{-(N_2-1)}\right] + F_{N_2}\left(q^{-1}\right) y(t) \end{bmatrix}. \tag{19}$$

$t = 0, 1, 2, \ldots$ represents the sample time, $u(t)$ represents the control input, $\lambda > 0$ is the weighting factor, and N_c is the step size of control time domain.

With material PS, a set of experiments are carried out. All experiments start from the static conditions. The temperature results of zone 3 are shown in Figure 6(a). The set temperature is 220°C. It can be observed that all the three control methods can obtain excellent control performance under static conditions. The temperature variations are very small at first. Then the system switches to dynamic conditions. Firstly, the screw moves forward to inject the melt. During this process, the raw material will flow into the barrel. Usually, the raw material is at the room temperature. Therefore, it will cause a temperature drop. As shown in Figure 6(a), there is a large temperature drop when using the GPC and PID control method. Particularly with the PID method, the temperature dropped by about 2.5°C. However, when using the proposed control method, the temperature has only dropped by about 0.4°C. At the same time, as shown in Figure 6(b), the control voltage will increase. But due to the time delay, the temperature will not rise immediately. After the injection is completed, the system enters the plastication process. The screw will rotate and retreat, and the screw speed is shown in Figure 6(c). During this process, the temperature will rise caused by the shear heat and the increased input. After the plastication process is finished, the system returns to static conditions again. Due to the influence of thermal inertia, the temperature will continue to rise for a while. Then, the temperature will slowly drop. Finally, the temperature will stabilize at the set value. Throughout this process, temperature overshoot will occur. It can be observed that the maximum temperature overshoot is only 0.5°C, when using the proposed method. However, when using the PID method, the maximum temperature overshoot is about 4.5°C. Large temperature overshoots will affect the quality of products or even lead to material decomposition. The GPC method can effectively reduce temperature overshoot. The maximum temperature overshoot is about 1.3°C under the GPC method.

4.4. Temperature Control with Different Materials. The thermophysical properties of different polymer materials vary greatly. The change of material will significantly affect the temperature control performance. In order to check the performance of the proposed method after changing the material, another experiment is conducted. In this experiment, the polymer material PS is replaced by PP. The screw periodically performs the action to simulate the actual production process. The other conditions remain the same.

The results are shown in Figure 7. It is observed that the temperature variations are very large at the beginning; the maximum temperature variation is larger than 2.5°C. This is mainly caused by the difference in heat capacity. As shown in Table 2, the heat capacity of PP is much larger than PS. After changing materials, the feedforward compensation strategy has not been updated. At this time, the learning process will be executed to learning the new compensation strategy. After about 1500 seconds, the maximum temperature variation is reduced to 0.5°C. This indicates that the system has already learned the new compensation strategy for PP. After that,

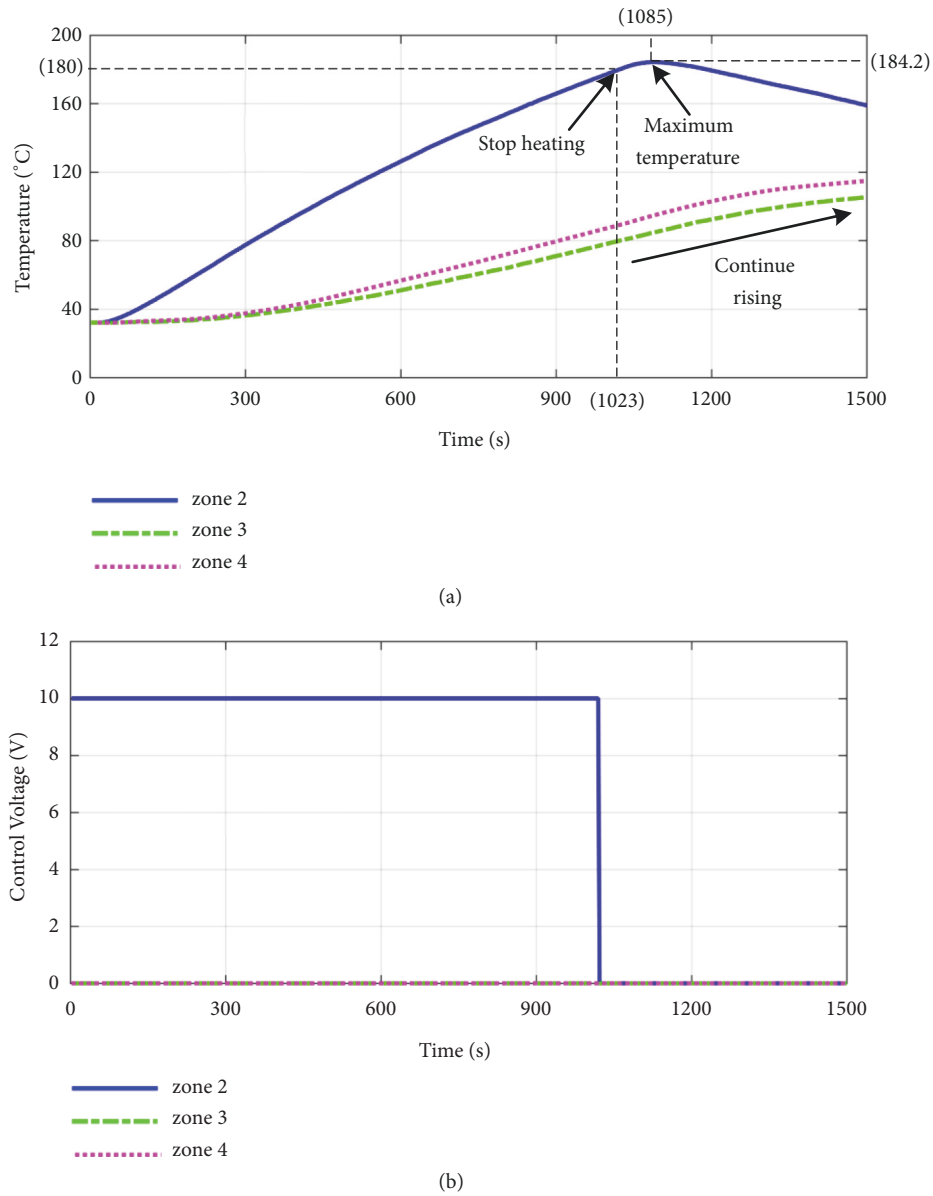

Figure 5: (a) Temperature, (b) control voltage with open loop control.

Table 1: The parameters of the injection molding machine.

Machine parameters	Values
Heating zones	5 (including one nozzle)
Maximum heating power (w)	1260 (nozzle 500)
Maximum screw speed (rpm)	196
Maximum injection pressure (MPa)	185
Maximum shot weight (g)	321

the learning process will temporarily stop, and the new compensation strategy will be stored. When the maximum temperature variation is larger than the set value, the learning process will be reactivated to obtain the new compensation strategy.

5. Products Consistency Experiments

As mentioned before, the barrel temperature control is critical to product consistency. And the purpose of this paper is to improve the consistency of injection molding products by improving the stability of the temperature. Thus, in this section, products consistency experiments are performed to further verify the validity of the proposed method by comparing with the GPC method and the PID method. In this paper, the product consistency is reflected by the product weight. There are multiple definitions of the quality of injection molding products such as weight, warpage, surface properties, mechanical properties, optical properties, and crystallization [23]. And warpage is an important factor reflecting product quality. Temperature unevenness is an important factor leading to warpage. But many other factors

Table 2: Thermophysical properties of PP and PS.

Material	Heat capacity (kj/(kg∗°C))	Density (kg/m^3)	Thermal conductivity (w/(m∗°C))
PP	1.926	900	0.138
PS	1.340	1050	0.126

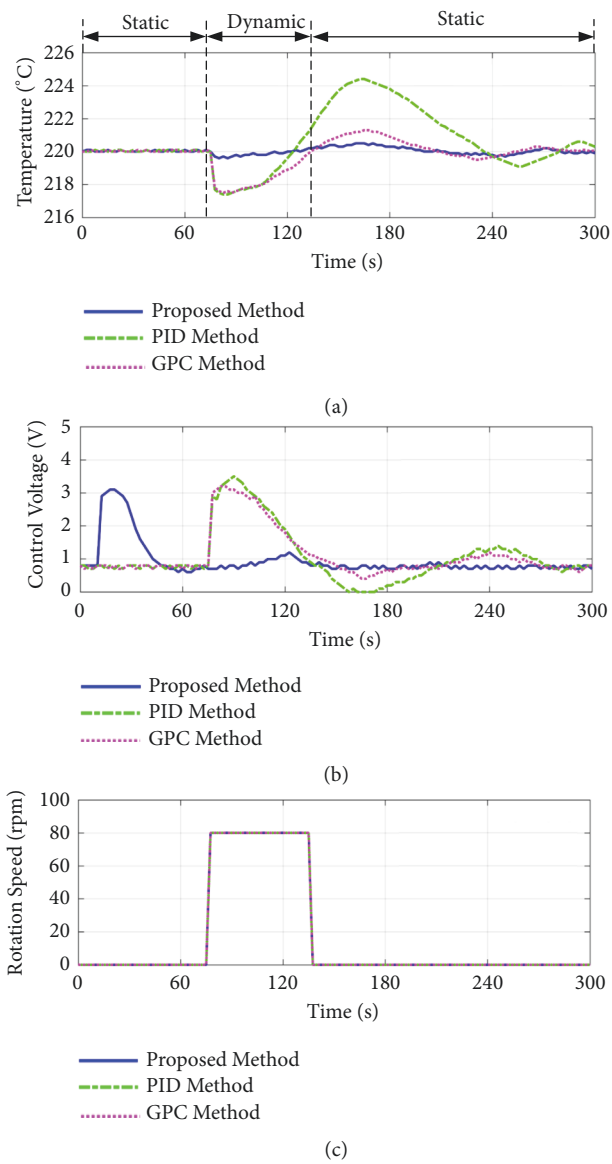

Figure 6: Comparison of the proposed method, PID, and GPC.

Table 3: The parameters of the Q-learning algorithm.

Parameters	Description	Values
α	Learning rate	0.6
λ	Discount factor	0.98
ε	Action selection policy	0.1

can also cause warpage, such as cooling time, ejection mechanism, and injection pressure. The purpose of this paper

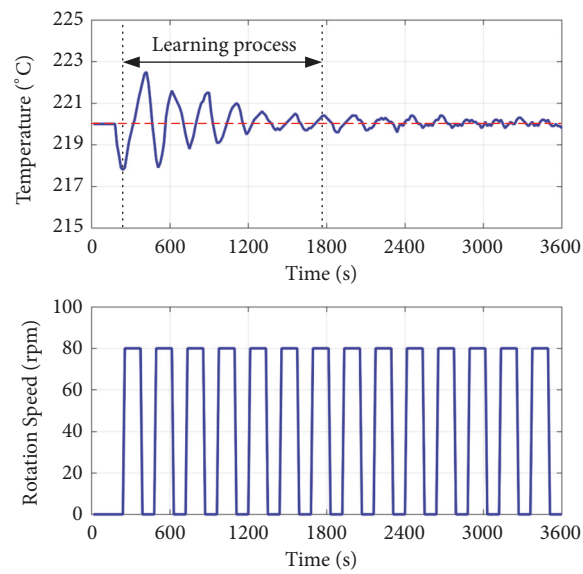

Figure 7: Temperature control performance with the proposed method after change of material.

is to improve the stability of the process through temperature compensation control to improve product consistency. Product weight can reflect process stability and product consistency very well. For example, in the work reported by Zhou et al. [24], they claimed that the product weight has a close relationship to other quality properties and the product weight can be a good indicator of process stability. On the other hand, the weight of the product can be very convenient to measure and quantify. Therefore, it is feasible to use the weight of the product to reflect the consistency of the product.

5.1. Experiment Setups. The experiments are conducted on the aforementioned experiment platform. A strip product is used for the experiments. The product is produced using a double cavity mold. The CAD model of the molded product is shown in Figure 8(a). The picture of the actual molded product is shown in Figure 8(b). The polymer material used in the experiments is PP. The settings of corresponding process parameters are listed in Table 4. In addition to these parameters that directly affect the melt temperature in the barrel, injection velocity is also an important factor that affects the temperature of the melt entering the cavity. And in order to eliminate the effects of different injection velocities, the injection velocities are set to the same for all experiments. The cooled products are weighted by a METTLER TOLEDO analytical balance LE204E with a minimum resolution 0.0001 g. Furthermore, in order to reduce the impact of machine fluctuations on product weight, a total of 80 cycles producing

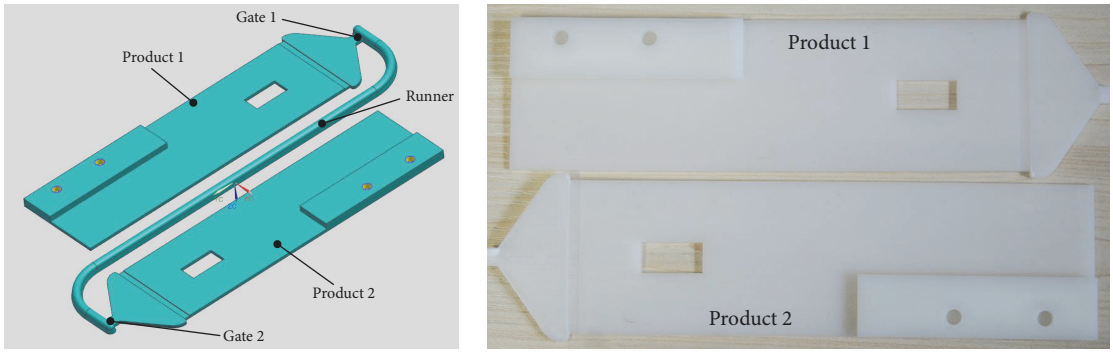

(a) (b)

Figure 8: Experimental injection product: (a) CAD model, (b) actual molded product.

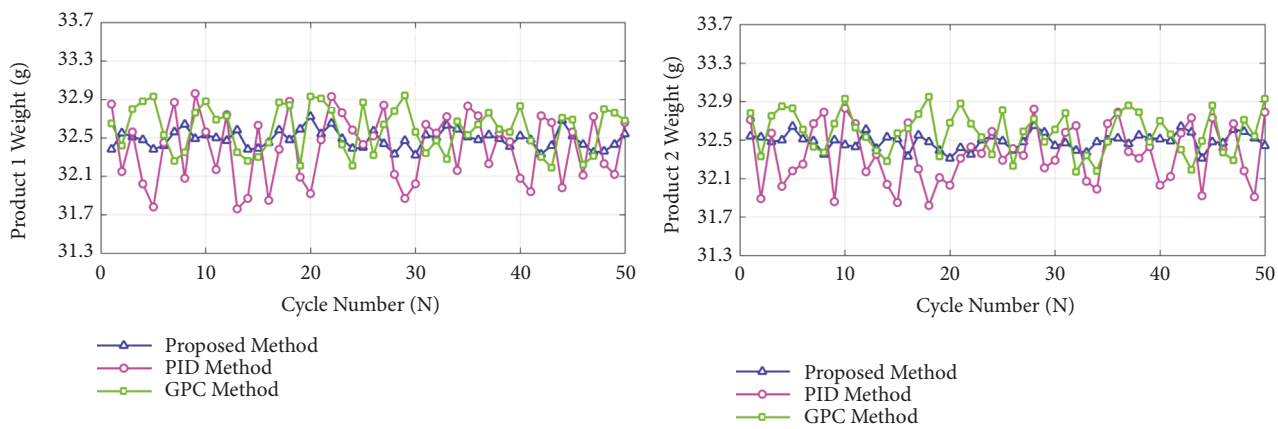

(a) (b)

Figure 9: Comparison of the product weight equipped with the proposed, GPC, and PID control methods: (a) product 1, (b) product 2.

Table 4: The settings of process parameters.

Process parameters		Value
Temperature (°C)	Zone 1	150
	Zone 2	215
	Zone 3	220
	Zone 4	225
	Nozzle	220
Screw rotation speed (rpm)		90
Back pressure (MPa)		2

will be conducted in each set of experiments. The first 30 cycles will be abandoned; only the remaining 50 cycles will be used for measurement.

5.2. Product Consistency under Different Temperature Control Methods. The results of the product weight are shown in Figure 9. It can be observed that, under the proposed temperature control method, both products have very small weight variations. The maximum weight variation is less than 0.4 g. This indicates that excellent product consistency can be achieved when using the proposed control method. However, when using the PID method, the product weight consistency deteriorated significantly. The maximum weight variation is about 1.2 g. Further, the difference in weight between product one and product two is sometimes very large even in the same batch. This indicates that there is a filling imbalance due to temperature variation. The weight consistency with the GPC method is better than the PID control method, but the product weight variations are still relatively large when compared with the proposed method.

Additionally, several statistical methods are used to analyze and compare the data. As shown in Table 5, the mean absolute deviation is used to describe the degree of data dispersion. The weight repeatability is calculated as follows:

$$\delta = \frac{\sqrt{(1/(n-1)) \sum_{i=1}^{n-1} (m_i - \overline{m})^2}}{\overline{m}} \times 100\%, \tag{20}$$

where $i = 1, 2, \ldots, n$ denotes the sample number, n is the total number of samples, $\overline{m}$ is the average weight, and m_i is the weight of sample. The smaller the value of δ, the better the weight repeatability. The statistical analysis of results shows that, under the proposed control method, the mean absolute deviation and the repeatability of product weight are much better than the PID and GPC method. On the other hand, the

Table 5: Statistical analysis of results under different control methods.

Method	Sample	Average weight (g)	Mean absolute deviation	Repeatability
Proposed	Product 1	32.4882	0.0739	0.2883%
	Product 2	32.4856	0.0636	0.2572%
	Sum	32.4869	0.0687	0.2718%
PID	Product 1	32.3956	0.3109	1.0855%
	Product 2	32.3532	0.2577	0.9396%
	Sum	32.3744	0.2864	1.0123%
GPC	Product 1	32.5868	0.2071	0.7253%
	Product 2	32.5814	0.1857	0.6744%
	Sum	32.5841	0.1965	0.6968%

difference between different cavities is also very small, which implies that excellent consistency can be achieved in different batches and different cavities.

5.3. Product Consistency with Different Process Parameters. In addition to the effect of barrel temperature, the melt temperature in the barrel is also affected by the following process parameters: screw rotation speed, back pressure, dwell time, and injection stroke. The effect of these process parameters on melt temperature consistency is shown in Table 6. It can be seen that, reducing the screw rotation speed, the heat generated by shearing will reduce, and the melt temperature difference due to the screw rotation speed will also reduce. Therefore, reducing the screw rotation speed can increase the consistency of the melt temperature to a certain extent. On the other hand, as the back pressure increases during the plastication process, the speed at which the screw retreats decreases. Thus, the melt stays longer in the barrel and the material in the barrel is denser. Therefore, increasing the back pressure can increase the consistency of the melt temperature and melt temperature. Increasing the dwell time allows the melt in the barrel to be warmed up for a longer period of time, and the heat conduction is more fully carried out, thereby improving the melt temperature consistency. However, it will increase the cycle time, which is unacceptable for a batch production process. In the actual production process, in order to increase production efficiency, the dwell time is usually set as small as possible. Therefore, in this paper, the dwell time is not selected. Decreasing the injection stroke can improve the melt temperature consistency. But the injection stroke is limited by the mold and cannot be adjusted at will during the production process. In summary, due to process conditions or production efficiency limitations, the screw rotation speed and back pressure are selected to justify the effectiveness of the proposed method.

In this set of experiments, the back pressure and screw rotation speed are selected as the variable. The other process parameters remain unchanged during the experiment. The experimental designs are listed in Table 7.

As shown in Figure 10(a), the back pressure changes from 2 MPa to 3 MPa after 20 cycles. Due to the change in back pressure, the shear heat generated during operation will change, and the temperature will also change. Therefore, the product consistency will be affected, resulting in a sudden change in product weight. Subsequently, as the temperature returns to stability, the product weight gradually returns to the original range. When using the proposed method, the product weight can return to the original range in about 5 cycles. However, when using the PID method and GPC method, it will take more than 10 cycles until the product weight returns to stability. Analogously, as shown in Figure 10(b), when the screw rotation speed changes from 90 rpm to 60 rpm, there is also a sudden change in the product weight. Different from back pressure changes, reducing the screw rotation speed will lower the temperature, leading to an increase in the product weight. With the proposed method, the product weight can quickly return to the original range due to the fast recovery of temperature. This indicates that the proposed method can effectively eliminate temperature changes due to process parameters change, thus improving product consistency.

The statistical analysis of results with process parameters change is listed in Table 8. It can be observed that as the process parameters change, the mean absolute deviation and repeatability will deteriorate. However, compared with the PID and GPC method, the proposed method can still achieve excellent results. On the other hand, it can be seen that, after reducing the screw rotation speed, the product consistency

Table 6: Effects of relevant process parameters on melt temperature consistency.

Process parameters	Change of parameters	Melt temperature consistency
Screw rotation speed	Decrease	Improved
Back pressure	Increase	Improved
Dwell time	Increase	Improved
Injection stroke	Decrease	Improved

Table 7: Experimental designs with different process parameters.

	Experiment 1		Experiment 2	
Process parameters	Back pressure		Screw rotation speed	
Variable value	2 MPa	3 MPa	90 rpm	60 rpm
Cycles	20	30	20	30

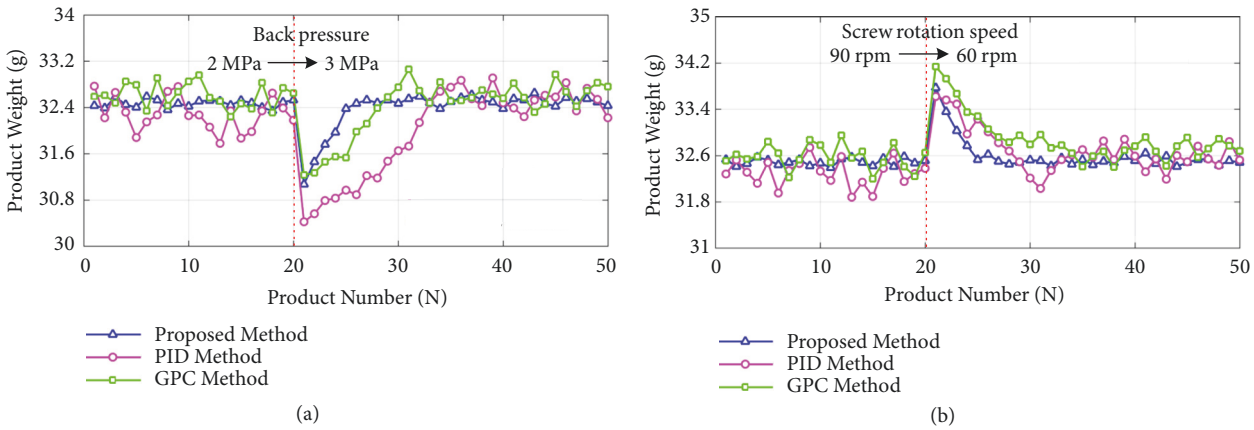

Figure 10: Product weight with variations in (a) back pressure, (b) screw rotation speed.

Table 8: Statistical analysis of results in the case of changes in process parameters.

Method	Variable	Average weight (g)	Mean absolute deviation	Repeatability
Proposed	Back pressure	32.4148	0.1475	0.8625%
	Rotation speed	32.5564	0.1185	0.7220%
PID	Back pressure	32.1168	0.5036	2.0190%
	Rotation speed	32.5394	0.2781	1.1851%
GPC	Back pressure	32.4822	0.2921	1.3028%
	Rotation speed	32.7690	0.2504	1.1501%

will improve. This implies that reducing the screw speed will make the temperature distribution more uniform and leads to an increase in product consistency.

6. Conclusions

In this paper, a new intelligent temperature compensation control strategy, which fully considers the dynamic characteristics of the injection molding process, is proposed. Based on the presented experimental results, the conclusions can be drawn as follows:

(1) The proposed barrel temperature control method significantly reduced the temperature variations under dynamic conditions. The experimental results indicated that the maximum temperature variation is about ±0.5°C under the proposed method, compared with GPC (±2.5°C) and PID (±4.5°C)

(2) The proposed method can effectively improve the consistency of injection molding products in different batches and different cavities. Statistical analysis of results showed that the repeatability is less than 0.3% when using the proposed method, which is much better than the PID method (about 1%) and GPC method (about 0.7%)

(3) The proposed strategy is a kind of data-based learning control method. It does not require an accurate system model, and the system can improve its performance by learning from its historical data. Therefore, it can be easily applied to different machines, materials, and process conditions

Data Availability

The data used to support the findings of this study are available from the corresponding author upon request.

Conflicts of Interest

The authors declare that there are no conflicts of interest regarding the publication of this paper.

Acknowledgments

This work is supported by the National Natural Science Foundation of China (Grant Numbers 51635006, 51675199) and the Fundamental Research Funds for the Central Universities (Grant Numbers 2016YXZD059, 2015ZDTD028).

References

[1] P. Zhao, H. Zhou, Y. Li, and D. Li, "Process parameters optimization of injection molding using a fast strip analysis as a surrogate model," *The International Journal of Advanced Manufacturing Technology*, vol. 49, no. 9-12, pp. 949–959, 2010.

[2] R. Zhang, R. Lu, A. Xue, and F. Gao, "Predictive functional control for linear systems under partial actuator faults and application on an injection molding batch process," *Industrial*

& Engineering Chemistry Research, vol. 53, no. 2, pp. 723–731, 2014.

[3] J. Gim, J. Tae, J. Jeon, J. Choi, and B. Rhee, "Detection method of filling imbalance in a multi-cavity mold for small lens," *International Journal of Precision Engineering and Manufacturing*, vol. 16, no. 3, pp. 531–535, 2015.

[4] K. Yao and F. Gao, "Optimal start-up control of injection molding barrel temperature," *Polymer Engineering & Science*, vol. 47, no. 3, pp. 254–261, 2007.

[5] C. Abeykoon, "Single screw extrusion control: a comprehensive review and directions for improvements," *Control Engineering Practice*, vol. 51, pp. 69–80, 2016.

[6] Y. Wang, Q. Jin, and R. Zhang, "Improved fuzzy PID controller design using predictive functional control structure," *ISA Transactions®*, vol. 71, pp. 354–363, 2017.

[7] N. Pachauri, A. Rani, and V. Singh, "Bioreactor temperature control using modified fractional order IMC-PID for ethanol production," *Chemical Engineering Research and Design*, vol. 122, pp. 97–112, 2017.

[8] C.-H. Lu and C.-C. Tsai, "Adaptive decoupling predictive temperature control for an extrusion barrel in a plastic injection molding process," *IEEE Transactions on Industrial Electronics*, vol. 48, no. 5, pp. 968–975, 2001.

[9] Y. Peng, W. Wei, and J. Wang, "Model predictive synchronous control of barrel temperature for injection molding machine based on diagonal recurrent neural networks," *Materials and Manufacturing Processes*, vol. 28, no. 1, pp. 24–30, 2012.

[10] C-C. Tsai and C.-H. Lu, "Multivariable self-tuning temperature control for plastic injection molding process," *IEEE Transactions on Industry Applications*, vol. 34, no. 2, pp. 310–318, 1998.

[11] R. Dubay, "Self-optimizing MPC of melt temperature in injection moulding," *ISA Transactions®*, vol. 41, no. 1, pp. 81–94, 2002.

[12] S. Huang, K. Tan, and T. Lee, "Adaptive GPC control of melt temperature in injection moulding," *ISA Transactions®*, vol. 38, no. 4, pp. 361–373, 1999.

[13] T. Liu, K. Yao, and F. Gao, "Identification and autotuning of temperature-control system with application to injection molding," *IEEE Transactions on Control Systems Technology*, vol. 17, no. 6, pp. 1282–1294, 2009.

[14] K. Yao, F. Gao, and F. Allgöwer, "Barrel temperature control during operation transition in injection molding," *Control Engineering Practice*, vol. 16, no. 11, pp. 1259–1264, 2008.

[15] L. Wang, F. Liu, J. Yu, P. Li, R. Zhang, and F. Gao, "Iterative learning fault-tolerant control for injection molding processes against actuator faults," *Journal of Process Control*, vol. 59, pp. 59–72, 2017.

[16] K. Liu, Y. Chen, T. Zhang, S. Tian, and X. Zhang, "A survey of run-to-run control for batch processes," *ISA transactions*, vol. 83, pp. 107–125, 2018.

[17] R. Chi, X. Liu, R. Zhang, Z. Hou, and B. Huang, "Constrained data-driven optimal iterative learning control," *Journal of Process Control*, vol. 55, pp. 10–29, 2017.

[18] K. Arulkumaran, M. P. Deisenroth, M. Brundage, and A. A. Bharath, "Deep reinforcement learning: a brief survey," *IEEE Signal Processing Magazine*, vol. 34, no. 6, pp. 26–38, 2017.

[19] R. S. Sutton and A. G. Barto, *Reinforcement Learning: An Introduction*, MIT Press, Cambridge, England, 1998.

[20] B. Luo, D. Liu, T. Huang, and D. Wang, "Model-free optimal tracking control via critic-only Q-learning," *IEEE Transactions on Neural Networks and Learning Systems*, vol. 27, no. 10, pp. 2134–2144, 2016.

[21] V. Mnih, K. Kavukcuoglu, D. Silver et al., "Human-level control through deep reinforcement learning," *Nature*, vol. 518, no. 7540, pp. 529–533, 2015.

[22] Y. Ruan, Y. Zhang, T. Mao, X. Zhou, D. Li, and H. Zhou, "Trajectory optimization and positioning control for batch process using learning control," *Control Engineering Practice*, vol. 85, pp. 1–10, 2019.

[23] P. Zhao, Y. Peng, W. Yang, J. Fu, and L.-S. Turng, "Crystallization measurements via ultrasonic velocity: study of poly (lactic acid) parts," *Journal of Polymer Science Part B: Polymer Physics*, vol. 53, no. 10, pp. 700–708, 2015.

[24] X. D. Zhou, Y. Zhang, T. Mao, and H. M. Zhou, "Monitoring and dynamic control of quality stability for injection molding process," *Journal of Materials Processing Technology*, vol. 249, pp. 358–366, 2017.

Hindawi
Advances in Polymer Technology
Volume 2019, Article ID 2604878, 8 pages
https://doi.org/10.1155/2019/2604878

Research Article

Effect of Process Parameters on Repeatability Precision of Weight for Microinjection Molding Products

Quan Wang,[1] Jinrong Wang,[1] Chongying Yang,[1] Kaihui Du,[1] Wenli Zhu,[2] and Xiaoli Zhang[3]

[1] *National Local Joint Engineering Laboratory of Intelligent Manufacturing Oriented Automobile Die & Mold, Tianjin University of Technology and Education, Tianjin 300222, China*
[2] *School of Mechanical & Automobile Engineering, Hubei University of Arts and Science, Hubei 441053, China*
[3] *College of Materials Science and Engineering, Zhengzhou University, Henan 450001, China*

Correspondence should be addressed to Quan Wang; wq2001126@163.com

Received 19 March 2019; Revised 3 May 2019; Accepted 16 May 2019; Published 4 June 2019

Guest Editor: Peng Zhao

Copyright © 2019 Quan Wang et al. This is an open access article distributed under the Creative Commons Attribution License, which permits unrestricted use, distribution, and reproduction in any medium, provided the original work is properly cited.

The repeatability precision of weight for injection molded products is important technical parameter to measure the quality and accuracy of injection molded products and evaluate the performance of injection molding machine. The influence of mold temperature, melt temperature, packing pressure, and packing time on the weight of microinjection molding products was studied by Taguchi orthogonal experiment. The influence of peak cavity pressure on the weight of products also was analysed. The experimental results show that the packing pressure is the most important process parameter affecting both the weight of the tensile and the impact specimens. With the increase of the packing pressure, the weight of the tensile and the impact specimens increases. When the peak cavity pressure reaches a certain value, the pressure value of the tensile specimen is 65 MPa, and the pressure value of the impact specimen is 68 MPa, the weight of the product increases quickly. The packing pressure increased from 85 MPa to 100 MPa, the weight of the tensile specimen increased from 0.544g to 0.559g, an increase of 2.7%, and the weight of the impact specimen increased from 0.418g to 0.425g, an increase of 1.7%.

1. Introduction

With the development of the synthesis and molding technology of polymer materials, more and more polymer precision products are applied to the advanced technology fields such as aerospace, medical instruments, biological engineering, precision optics, electronic communication, and so on [1–5]. More than 90% of the plastic molding products are the two main molding methods in the process of polymer molding, extrusion molding, and injection molding. This puts forward higher requirements for the quality precision of the polymer molding products, and the research on the factors affecting the quality precision and how to evaluate the quality of the molded products scientifically and effectively is the precondition of improving the precision of the molding quality.

Plastic injection molding is a widely used and complex process and is a highly efficient technique for producing a large quantity of plastic products, with high production requirement and tight tolerance. It is well-known as the manufacturing technique to produce products with various shapes and complex geometry at low cost [6–8]. The quality of parts produced by injection molding is a function of plastic material, part geometry, mold structure, and process conditions [9, 10].

The repeatability accuracy of injection molded products includes three aspects, such as size, appearance, and injection weight. It can measure the quality and accuracy of injection products [11–14]. However, the size and appearance of the products are different because of different products shape. It cannot be used to realize the quantitative comparison of the performance of different products and different machines. Therefore, the repetition precision of injection weight is usually used as a technical index to measure the quality accuracy of injection products and evaluate the performance of the injection molding machine [15]. The weight repetition

precision of the ordinary injection molding machine is about l%, which can reach 0.8%. The precision injection machine is lower than 0.5%, and the highest international level is less than 0.15% at present [16]. The improvement of the repetition precision of injection weight depends on the accuracy of mold processing and the rationality of the structure design, the performance of the raw materials, the rationality of the process parameters, and the control performance of the machine [17, 18]. Therefore, it is instructive for improving the repetition accuracy of injection weight to study the process parameters affecting the injection weight and the algorithm of repetition accuracy of injection weight which conforms to the characteristics of injection molding.

2. Calculation Method

The injection weight is the weight of the polymer melt from the nozzle of injection molding machine. The conventional injection weight based on the injection volume control method is related to the diameter of the injection screw and the injection stroke. The theoretical calculation formula is such as (1).

$$\begin{aligned} W &= \delta \frac{\pi}{4} D_s^2 S \rho = V_a \rho \\ V_a &= \delta \frac{\pi}{4} D_s^2 S \end{aligned} \tag{1}$$

where W is the injection weight, g; ρ is density of polymer resin in room temperature, g/cm^3; D_s is the diameter of the screw, cm; S is the stroke of screw, cm; V_a is actual injection capacity, cm^3; δ is injection coefficient, which varies with different raw materials.

In (1), the diameter D_s of the screw is given by the injection machine and δ is the empirical coefficient. The injection stroke S of the screw is accurately measured by the displacement sensor and controlled by the servo motor driving the ball screw; that is to say, V_a is kept constant. In the traditional injection volume control method, ρ is a constant value. The injection weight obtained from (1) is the weight of the injection product. However, in the actual injection process, ρ is not really constant. The change rate of melt density of polypropylene (Trademark T30S, MFR=3.2g/10min, supplied by Mao Ming Phoenix Ltd., China) is 6.44% when the pressure rises from 2 MPa to 30 MPa in temperature 190°C. When the temperature is 200°C, the change rate of polypropylene under the same pressure is 6.64% [19]. Therefore, the injection weight obtained by formula (1) is not the real weight of the injection molded product. Of course, the traditional volume control method cannot achieve the consistency of weight of injection products. According to the control technology of PVT in the injection process, the molding process, especially the temperature and pressure, has an important influence on the polymer melt ρ [20, 21]. Therefore, the effect of molding process on the injection weight accuracy of microinjection molding products is studied in this paper.

Repetitive precision refers to the degree of consistency between the results of continuous measurements of the same object under the same measurement conditions. It is the degree of repetition error in the measurement results. Therefore, the repetition accuracy of injection weight can be understood as the consistency between the weight of injection molded parts and the ideal weight of injection molded parts, which is a concept based on statistical process. There are two formulas for calculating the weight repeatability of products which are given as follows:

$$\delta_G = \frac{w_{max} - w_{min}}{\overline{w}} \times 100\% \tag{2}$$

$$\delta_G = \frac{\sqrt{(1/(n-1)) \sum_{i=1}^{n} (w_i - \overline{w})^2}}{\overline{w}} \times 100\% \tag{3}$$

$$\overline{w} = \sum_{i}^{n} \frac{w_i}{n} \tag{4}$$

where n is the number of sample products; w_i is the weight of the i product, g; w_{max} is the maximum weight of the product, g; w_{min} is the minimum weight of the product, g; $\overline{w}$ is the average weight of the sample, g; δ_G is the repetition precision of the product weight.

The denominators of (2) and (3) denote the arithmetic average weight of the sample product, and the numerator denotes the fluctuation of the sample data. Equation (2) is the sample range; and (3) is the sample standard deviation. Therefore, (2) is the polar difference algorithm, and (3) is the standard deviation algorithm. In order to objectively calculate the weight repetition accuracy of the products and eliminate the influence of abnormal values, (3) is chosen in the paper.

3. Experimental

3.1. Materials. The sample material used in this work was polypropylene in the form of pellets and with a trade mark 5090T (MFI=15g/10min), supplied by the Formosa petrochemical Corp, Taiwan.

3.2. Microinjection Molding Machine. The experimental work was carried out on an injection molding machine of type BOX XS concept having a maximum injection pressure 2298 bar, with screw diameter for plastication 14 mm and maximum weight of the product 6.1g as shown in Figure 1.

3.3. Mold. The multispline injection mold constructed from two parts (tensile specimen and impact specimen). The mold cavity thickness is 1 mm. The cavity pressure and temperature is measured in the mold cavity by the quartz sensor for mold cavity pressure type Kistler 6190CA, which has a front of 4.0 mm diameter. Data output from the amplifier is collected using a Kistler 5865 Como injection system. Computer is used to record the output reading of the acquisition system through an interface cart by the help of lab view program. The pressure sensors are installed in the middle of the specimens, respectively. The distance from the gate is 8 mm. The dimensions of specimen and gate are shown in Figure 2.

3.4. Mold Temperature Controller. The mold temperature controller (model TP6ZE) was adopted using PIOVAN Co. Ltd., Italia.

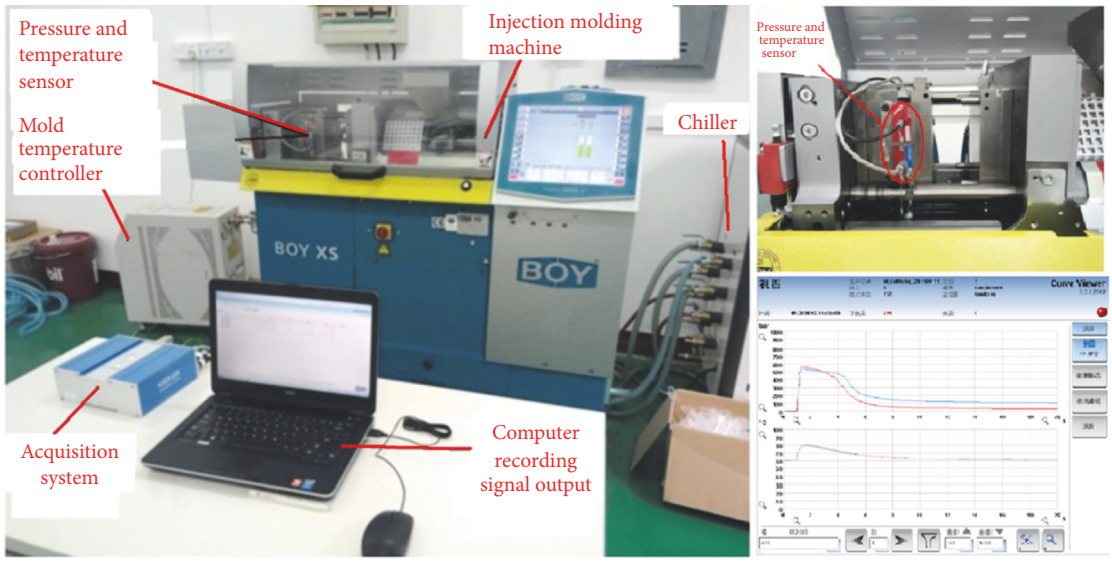

Figure 1: Experimental setup.

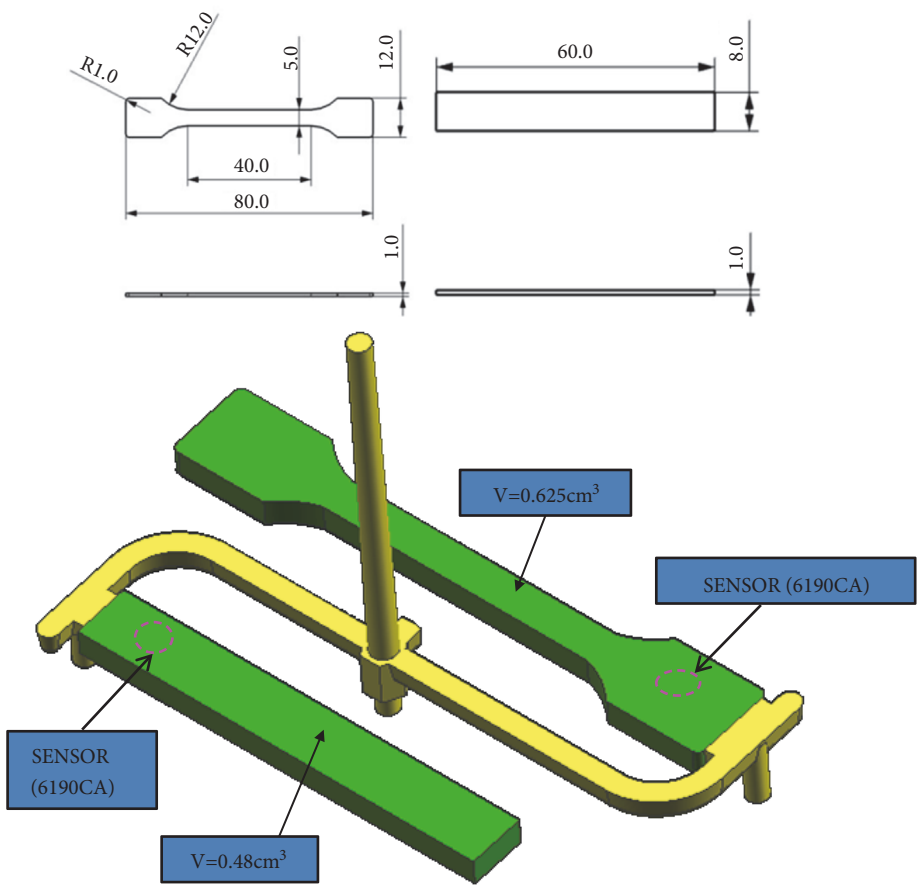

Figure 2: Dimension of specimen and gate.

Table 1: Parameters of injection molding process.

Level	melt temperature (°C)	mold temperature (°C)	Packing pressure (MPa)	Packing time (s)	Injection pressure (MPa)
1	220	40	85	5	85
2	230	50	90	10	90
3	240	60	95	15	95
4	250	70	100	20	100

3.5. Chiller. Chiller (model ML-CA03) was adopted Ming Lee Co. Ltd., Hong Kong, China.

3.6. Electronic Balance. Electronic balance (model CP214) was adopted OHAUS Co. Ltd., America. The accuracy is 0.1 mg.

Melt temperature, mold temperature, packing pressure, packing time, and injection pressure were chosen as the process parameters. Parameters of injection molding process are reported in Table 1.

Orthogonal design is a high-efficiency design method for tests to arrange multifactor tests and seek optimal level combinations. The design method of orthogonal tests is able to determine optimal parameters by simply calculating influences of each factor on test results, showing the influences in charts, and then comprehensively comparing differences. The calculation is carried out on orthogonal tables, so the whole process is simple and clear. In this way, enough information can be obtained through a few tests, thus saving costs. An $L_{16}(4^5)$ orthogonal array was selected for the experimental design for each of the five factors. The four levels for the five parameters were identified during the 16 experiments. The data of injection five molds were recorded under the same conditions and the peak cavity pressure also was recorded. Then, the process parameters were changed to continue the same procedures. The values of these parameters are presented in Table 2.

Table 2: Proposed L_{16} orthogonal array.

Level	A	B	C	D	E
1	1	1	1	1	1
2	1	2	2	2	2
3	1	3	3	3	3
4	1	4	4	4	4
5	2	1	2	3	4
6	2	2	1	4	3
7	2	3	4	1	2
8	2	4	3	2	1
9	3	1	3	4	2
10	3	2	4	3	1
11	3	3	1	2	4
12	3	4	2	1	3
13	4	1	4	2	3
14	4	2	3	1	4
15	4	3	2	4	1
16	4	4	1	3	2

4. Results and Discussion

The variance analysis of the relationship between the specimen weight and the process parameters was carried out, in which A stands for melt temperature (°C), B stands for mold temperature (°C), C stands for packing pressure (MPa), D stands for packing time (s), and E stands for injection pressure (MPa). Figure 3 shows that the packing pressure, mold temperature, and melt temperature have great influence on the weight of the product, while the packing time and injection pressure have little influence on the weight of the product.

The weight of the tensile and impact specimens increases with the increase of the melt temperature as illustrated in Figure 4. The weight of the tensile specimen increases faster than that of the impact specimen in the melt temperature range of 230°C to 240°C. When the melt temperature rises from 220°C to 250°C, the weight of the tensile specimen increases from 0.548g to 0.554g, by 1.1%. The weight increased from 0.419g to 0.423g, an increase of 0.9% for the impact specimen.

Figure 5 shows the effect of mold temperature on the weight of the product. The weight of the tensile specimen increases with the increase of mold temperature, but the impact specimen shows the opposite situation. This may be due to the filling unbalance of the two mold cavities because of different dimensions and weight of product. The cavity of impact specimen is filled before the tensile specimen, resulting in a large residual stress and shrinkage. In molding process, reasonable adjustment of process parameters should be made to achieve the best balance filling of two cavities. The weight of tensile specimen increased from 0.544g to 0.551g, an increase of 1.3%, and the weight of impact specimen decreased from 0.422g to 0.420g, a decrease of 0.47%. The increase of mold temperature can promote the filling of melt, the specimen is more compact, the melt fluidity will be guaranteed, and the mechanical properties of the specimen are improved.

Figure 6 is the effect of packing pressure on the weight. The weight of tensile and impact specimens increases with the increase of packing pressure, which is due to the increase of packing pressure, filling more melt in the cavity at the same time, the specimen is more compact, but excessive packing pressure will cause stress of products. The packing pressure increased from 85 MPa to 100 MPa, the weight of tensile specimen increased from 0.544g to 0.559g, an increase of 2.7%, and the weight of impact specimen increased from 0.418 g to 0.425 g, an increase of 1.7%.

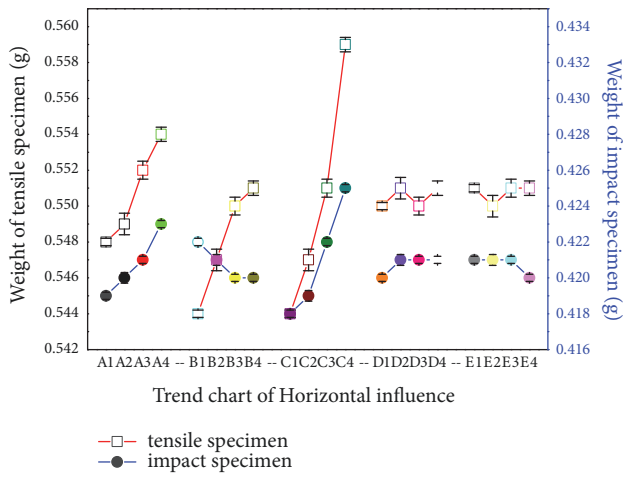

Figure 3: Horizontal trend chart of tensile and impact specimen.

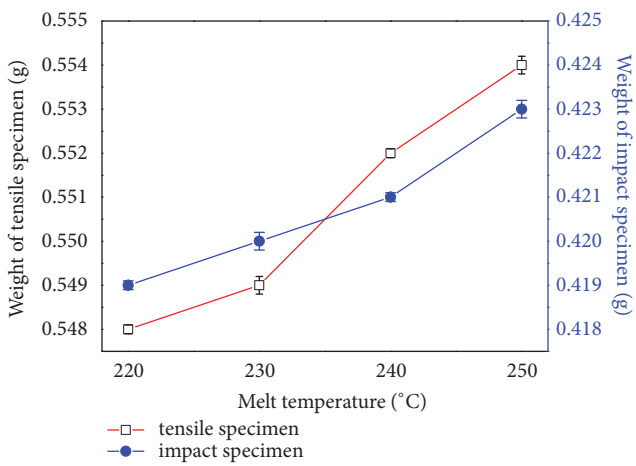

Figure 4: Influence of melt temperature on product weight.

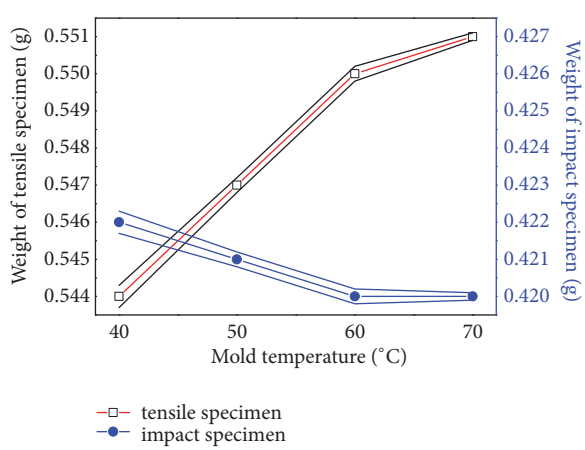

Figure 5: Influence of mold temperature on product weight.

Influence of packing time on product weight is illustrated in Figure 7. The packing time has little effect on the weight of the product, indicating that when the product is small, the gate has cooled, and increasing the packing time has little effect on the weight of the product.

Because the filling process of the cavity is not known in the molding process, the weights of the parts become important basis for verifying the defects of parts. In the process of injection molding, the pressure is not large enough to fill the cavity; short shots and other phenomena will

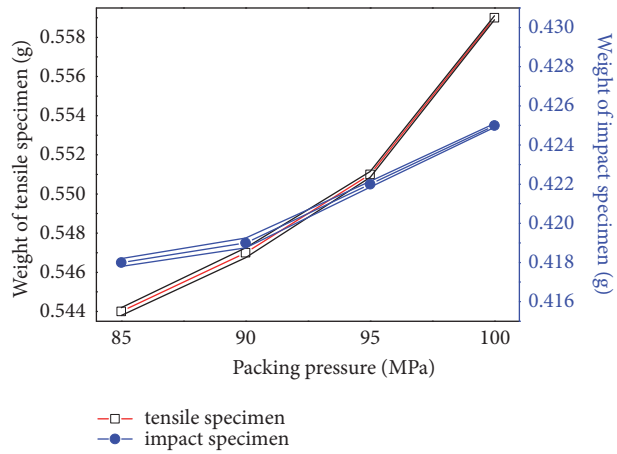

Figure 6: Influence of packing pressure on product weight.

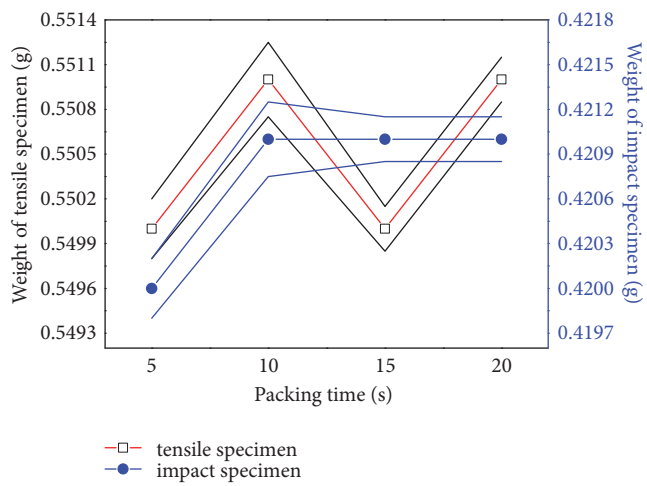

Figure 7: Influence of packing time on product weight.

occur. Injection molding pressure is one of the key processing parameters mentioned in several research works [22–25]. The peak cavity pressure and product weight have a certain relationship. Because the cavity pressure curve records the change of cavity pressure during the whole injection molding process, the relationship between them is studied to guide the production better.

The weight of the tensile and impact specimen increases with the increase of the peak cavity pressure as illustrated in Figure 8. This is because the larger the peak cavity pressure, the better the fluidity of melt, the more the melt injected into the cavity at the same time, and the greater the density of the specimen. At the same time, the weight of the specimen does not increase significantly before the cavity pressure reaches 65 MPa for tensile specimen. After the peak pressure reaches 65 MPa, the weight increases rapidly. The peak cavity pressure increases; the more melt is filled into the cavity in the same time. The density of specimen is enhanced, and the weight of the specimen increases. The pressure continues to pack in additional material which is low in viscosity. Therefore, the less viscous melt is able to fill up the cavity thoroughly and even created some flash without causing significant increase in pressure. Due to the fact that more material is in the cavity, the parts produced are heavier and denser although peak cavity pressure does not increase much. The maximum weight of impact specimen appears about 71 MPa. Because the peak cavity pressure has a high correlation with the weight of specimen, the pressure value and the actual parts can be recorded in actual molding process. It can be used as a reference in molding process. It can also be used to judge the actual injection process of specimen according to the peak cavity pressure.

5. Conclusions

An experimental work is carried out to study the effect of the microinjection molding parameters on the product weight in this paper. For the tensile and impact specimens, the packing pressure is the most important parameter affecting their weight. With the increase of packing pressure, the weight of both the tensile and impact specimens increases. The cavity pressure of impact specimen is larger than that of tensile specimen during injection molding because of unbalance filled. When the cavity pressure increases, the weight of the

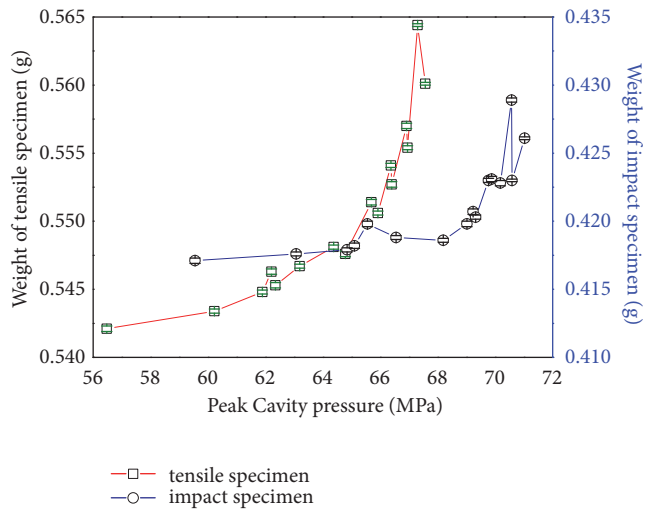

Figure 8: Effect of the peak cavity pressure on the tensile and impact specimen weight.

specimen will increase; when the peak cavity pressure reaches a certain value, the peak cavity pressure is about 65 MPa for tensile specimen and peak cavity pressure is about 68 MPa for impact specimen; when the peak cavity pressure increases, the weight of specimen increases significantly.

Data Availability

The data used to support the findings of this study are available from the corresponding author upon request.

Conflicts of Interest

The authors declared no potential conflicts of interest with respect to the research, authorship, and/or publication of this article.

Acknowledgments

The authors would like to acknowledge the financial support of the Excellent Young Talents Fund Program of Higher Education Institutions of Tianjin Province (RC180202), Research and Development Fund of Tianjin University of Technology and Education (KJ1808), and the National Natural Science Foundation of China (51403059) for financial support.

References

[1] M. Joglekar and B. G. Trewyn, "Polymer-based stimuli-responsive nanosystems for biomedical applications," *Biotechnology Journal*, vol. 8, p. 931, 2013.

[2] D. Ozdil and H. M. Aydin, "Polymers for medical and tissue engineering applications," *Journal of Chemical Technology & Biotechnology*, vol. 89, no. 12, pp. 1793–1810, 2014.

[3] D. J. Phillips and M. I. Gibson, "Towards being genuinely smart: 'isothermally-responsive' polymers as versatile, programmable scaffolds for biologically-adaptable materials," *Polymer Chemistry*, vol. 6, pp. 1033–1043, 2015.

[4] G. Tosello, H. N. Hansen, and S. Gaspaparin, "Applications of dimensional micro metrology to the product and process quality control in manufacturing of precision polymer micro components," *CIRP Annals - Manufacturing Technology*, vol. 58, pp. 467–472, 2009.

[5] L. S. Nair and C. T. Laurencin, "Biodegradable polymers as biomaterials," *Progress in Polymer Science*, vol. 32, no. 8-9, pp. 762–798, 2007.

[6] K. M. Tsai and J. K. Lan, "Correlation between runner pressure and cavity pressure within injection mold," *The International Journal of Advanced Manufacturing Technology*, vol. 79, no. 1-4, pp. 273–284, 2015.

[7] X. D. Zhou, Y. Zhang, T. Mao, and H. M. Zhou, "Monitoring and dynamic control of quality stability for injection molding process," *Journal of Materials Processing Technology*, vol. 249, pp. 358–366, 2017.

[8] M. R. Kamal, R. El Otmani, A. Derdouri, and J. S. Chu, "Flow and thermal history effects on morphology and tensile behavior of poly(oxymethylene) micro injection molded parts," *International Polymer Processing*, vol. 32, no. 5, pp. 590–605, 2017.

[9] B. R. Whiteside, M. T. Martyn, P. D. Coates, P. S. Allan, P. R. Hornsby, and G. Greenway, "Micromoulding: process characteristics and product properties," *Plastics, Rubber and Composites*, vol. 32, no. 6, pp. 231–239, 2003.

[10] G. Tosello, H. N. Hansen, and S. Gasparin, "Applications of dimensional micro metrology to the product and process quality control in manufacturing of precision polymer micro components," *Cirp Annals-Manufacturing Technology*, vol. 58, p. 467, 2009.

[11] J. Q. Li, T. D. Li, Y. D. Jia, S. G. Yang, S. F. Jiang, and L. S. Turng, "Modeling and characterization of crystallization during rapid heat cycle molding," *Polymer Testing*, vol. 71, pp. 182–191, 2018.

[12] Y. Zhao, P. Zhao, J. F. Zhang, J. Y. Huang, N. Xia, and J. Z. Fu, "On-line measurement of clamping force for injection molding machine using ultrasonic technology," *Ultrasonics*, vol. 91, p. 170, 2018.

[13] J. F. Zhang, P. Zhao, Y. Zhao, J. Y. Huang, N. Xia, and J. Z. Fu, "On-line measurement of cavity pressure during injection

molding via ultrasonic investigation of tie bar," *Sensors and Actuators A: Physical*, vol. 285, pp. 118–126, 2019.

[14] P. Zhao, W. M. Yang, X. M. Wang, J. G. Li, B. Yan, and J. Z. Fu, "A novel method for predicting degrees of crystallinity in injection molding during packing stage," *Proceedings of the Institution of Mechanical Engineers, Part B: Journal of Engineering Manufacture*, vol. 233, no. 1, p. 204, 2019.

[15] A. Lopez, J. Aisa, A. Martinez, and D. Mercado, "Injection moulding parameters influence on weight quality of complex parts by means of DOE application: Case study," *Measurement*, vol. 90, pp. 349–356, 2016.

[16] Q. Zhang, H. Xu, D. M. Wu, and Z. W. Yang, "Experimental analysis on main technological parameters which influences the weight repeatability precision of injection molding products," *Plastics*, vol. 45, no. 6, pp. 107–109, 2016.

[17] W. W. Kim, M. G. Gang, B. K. Min, and W. B. Kim, "Experimental and numerical investigations of cavity filling process in injection moulding for microcantilever structures," *The International Journal of Advanced Manufacturing Technology*, vol. 75, no. 1-4, pp. 293–304, 2014.

[18] G. Gordon, D. O. Kazmer, X. Y. Tang, Z. Y. Fan, and R. X. Gao, "Quality control using a multivariate injection molding sensor," *The International Journal of Advanced Manufacturing Technology*, vol. 78, no. 9-12, pp. 1381–1391, 2015.

[19] J. P. Qu, B. S. Shi, and H. Z. He, "Influence of vibration on density of polymer solid granules in single screw extruder," *Polymer-Plastics Technology and Engineering*, vol. 46, no. 3, pp. 233–237, 2007.

[20] C. Hopmann, A. Ressmann, and J. Heinisch, "Influence on product quality by pvT-optimised processing in injection compression molding," *International Polymer Processing*, vol. 31, no. 2, p. 156, 2016.

[21] X. J. Sun, X. M. Su, P. Tibbenham, J. H. Mao, and J. Tao, "The application of modified PVT data on the warpage prediction of injection molded part," *Journal of Polymer Research*, vol. 23, p. 86, 2016.

[22] T. Nguyen-Chung, C. Loser, G. Juttner, T. Pham, M. Obadal, and M. Gehde, "Simulation of the micro-injection moulding process: effect of the thermo-rheological status on the morphology," *Proceedings of the Institution of Mechanical Engineers, Part E: Journal of Process Mechanical Engineering*, vol. 225, p. 224, 2011.

[23] H. Hassan, "An experimental work on the effect of injection molding parameters on the cavity pressure and product weight," *The International Journal of Advanced Manufacturing Technology*, vol. 67, no. 1-4, pp. 675–686, 2013.

[24] M. Kurt, O. S. Kamber, Y. Kaynak, G. Atakok, and O. Girit, "Experimental investigation of plastic injection molding: Assessment of the effects of cavity pressure and mold temperature on the quality of the final products," *Materials and Corrosion*, vol. 30, no. 8, pp. 3217–3224, 2009.

[25] H. Zamani, S. Azmoudeh, and K. Shelesh-Nezhad, "Warpage characterization of thin and centrally-gated injection molded part by applying cavity pressure measurement," *Applied Mechanics and Materials*, vol. 446, pp. 1099–1103, 2014.